NASA CR-112119

# EVALUATION OF COATED COLUMBIUM ALLOY HEAT SHIELDS FOR SPACE SHUTTLE THERMAL PROTECTION SYSTEM APPLICATION

VOLUME I

PHASE I • ENVIRONMENTAL CRITERIA AND MATERIAL CHARACTERIZATION

June 1972

By
W. E. Black et al



GENERAL DYNAMICS
*Convair Aerospace Division*

NASA CR-112119

# EVALUATION OF COATED COLUMBIUM ALLOY HEAT SHIELDS FOR SPACE SHUTTLE THERMAL PROTECTION SYSTEM APPLICATION

VOLUME I

PHASE I + ENVIRONMENTAL CRITERIA AND MATERIAL CHARACTERIZATION

June 1972

By
W. E. Black et al

Prepared Under
Contract NAS1-9793

Prepared by
CONVAIR AEROSPACE DIVISION OF GENERAL DYNAMICS
San Diego, California

for
National Aeronautics and Space Administration
LANGLEY RESEARCH CENTER
Hampton, Virginia

## FOREWORD

This report was prepared by Convair Aerospace Division of General Dynamics — San Diego Operation under Contract NAS1-9793 for the National Aeronautics and Space Administration, Langley Research Center, Hampton, Virginia. It was administered under the direction of the Materials Division, Materials Application Branch, Metals Section with Mr. D. R. Rummler acting as the Technical Representative of the Contracting Officer. The Convair program manager was W. E. Black. Others who participated in this program and in the preparation of this report are: J. W. Baer, process development and deputy program manager; T. J. DeLacy, nondestructive evaluation; J. R. Kerr, environmental testing; R. T. Torgerson, static creep testing; R.S. Wilson and J. F. Fischer, Jr., structural analysis. The subcontract work performed by North American Rockwell Space Division was under the direction of L. J. Korb. Space Division personnel assisting were: C. B. Blumer, vehicle and flight environment; D. R. Dixon, mechanical properties testing; R. Heisman, manufacturing development (diffusion bonding); and M. J. Suppanz, plasma arc testing. W. K. McDonald and W. E. Elkington of the Wah Chang Albany Corporation provided assistance in performing metallography and analysis thereof.

This report covers the period from October 1970 to March 1972.

Page Intentionally Left Blank

CONTENTS

## FIGURES

Page

TABLES

# EVALUATION OF COATED COLUMBIUM ALLOY HEAT SHIELDS FOR SPACE SHUTTLE THERMAL PROTECTION SYSTEM APPLICATION

## VOLUME I

## Phase I

## Environmental Criteria and Material Characterization

By W. E. Black et al.
Convair Aerospace Division of General Dynamics

## 1 SUMMARY

In this three-phase program to evaluate columbium alloy thermal protection systems (TPS) for the Space Shuttle, Phase I was directed toward establishing design parameters and investigating material characteristics as applicable to heat shield environments.

Initially design goals and performance requirements for the TPS were established. These criteria were to be used throughout the program for the design, analysis, and test of elemental, subsize, small size, and full-scale components.

Three columbium alloys (Cb-752, C-129Y, and WC-3015) and two silicide coatings (R-512E and VH-109) were selected for evaluation. Material difficulties with the WC-3015 in the form of sheet delamination and coating process incompatibility rendered it unacceptable for complete testing. Hence, WC-3015 was not extensively evaluated. However, it exhibited the highest tensile properties and was the most weldable of the alloys examined. The Cb-752 was found fabricable with relative ease with only slight porosity problems associated with welding. No problems were encountered with C-129Y.

Two columbium alloys were fabricated into elemental specimens and tested through a simulated space shuttle flight profile. Cb-752 and C-129Y, protected from oxidation by R-512E silicide coating were successfully tested through 100 flight cycles that included temperature, external pressures, and applied mechanical loads. The four material systems evaluated survived a minimum of 42 cycles without structural failure. No coating failures were observed with the final selected system — Cb-752/R-512E. Structural joints for columbium alloy heat shields made by electron beam welding and by solid state diffusion bonding were found to retain their integrity through the full 100 thermal/mechanical flight cycles. No failures occured during this study in or near a joint while under test.

Plasma arc tests were run on specimens identical to those used in the flight simulation test series. A similar cyclic thermal profile with a static load representative of that expected at maximum temperature was used. The specimens were exposed for a maximum of 40 cycles. Those specimens not affected by the shock waves completed testing with results similar to the static air exposure.

Creep studies undertaken were of two types: static creep at various temperatures and cyclic creep during flight simulation testing. Although rational and consistent data evolved from each creep test method and for each material system, only limited correlation was found to exist between cyclic and static creep. Creep predictions for anticipated heat shield loadings were found to be 50 to 100 percent lower than observed creep with simulated boost - reentry environment and loads. Additional creep studies are needed to fully understand creep in heat shields.

The most severe type of coating deterioration resulted in substrate oxidation at isolated sites along the edges of structural elements. Spallation of oxidized coating from structural surfaces is continuous and is considered to be normal and not deleterious throughout thermal cycling. It is significant that even with edge damage and substrate oxidation, coated columbium alloys retained load carrying ability and survived numerous flight cycles after initial sighting of oxidation.

It is believed that a walk-around inspection of coated columbium heat shields will identify discrete coating damage sites requiring repair before reuse. Unaided visual inspection of coated surfaces is sufficient to detect signs of substrate oxidation. Conventional nondestructive test methods (thermoelectric, eddy current and stimulated emission radiography) are useful during manufacturing to assist process and quality control as well as to assess the general condition of as-coated hardware. However, these methods are not adequate for the evaluation of hardware which has been exposed to one or more thermal flight cycles.

The information and data presented in the sections on fabrication, material evaluation, and material characterization will be used in the ensuing phases for configuration evaluation and system scale-up.

The units used for physical quantities delineated in this report are given in both the U.S. Customary Units and in the International System of Units (SI). Conversion factors pertinent to the present investigation are presented in Appendix A.

# 2 INTRODUCTION

The economical development of manned systems for outer space depends on the development of low-cost, lightweight, reliable systems employed on reusable space booster and orbiter vehicles. The NASA approach to this development is to provide vehicles capable of earth landings and possessing the aerodynamic maneuvering characteristics of aircraft and yet able to withstand spacecraft reentry temperatures. This system has been designated the Space Shuttle.

The key element in the success of these vehicles is the thermal protection system (TPS). It must be capable of withstanding the structural static and dynamic loads as well as dissipating the frictional heat in aerodynamically slowing down the vehicle. Although several TPS concepts have been and are being studied, one of the most promising from a weight, cost, and reusability standpoint is that of metallic radiative heat shields. It is toward columbium alloys as applied to heat shields on a Space Shuttle orbiter that this study has been directed.

This is a 30-month, three-phase program that began in October 1970. The principal objective is to evaluate coated columbium alloy thermal protection systems by a logical sequence of analytical and experimental investigations involving simulated mission and environmental conditions. These efforts are directed toward the selection, characterization, and design of one material system (i.e., one columbium alloy with one coating), one heat shield configuration, and one support system with insulation. Reported herein are the results of Phase I of this study.

Phase I was initiated by selecting a model vehicle with an associated total environment from prelaunch to landing. This vehicle and environment would be the basis for the design conditions, design criteria, and test conditions used throughout the program. This selection was followed by an experimental and analytical evaluation of the properties of the material systems as applied to heat shields. Phase I culminates with the selection of two coating/substrate combinations for further application and test in Phase II.

Phase II, which is partially concurrent with Phase I, consists of two parts involving two types of panels. Part 1 involved the analytical investigation of several heat shield configurations. The two most promising concepts were selected for subsize panel testing followed by the design, fabrication, and testing of the concepts integrated into small-size TPS specimens. In Part 2 these small size specimens, which are

composed of heat shields, supports, insulation, and simulated primary structure, will undergo vibration and acoustic testing and either thermal-flow testing at one atmosphere or radiant heat-lamp testing with applied loads at reduced pressures. Part 2 will also investigate the forming, machining, and joining methods to be used for the manufacturing of complete thermal protection systems. Based on the performance of the two TPS configurations during the test program, the better concept will be selected for further evaluation in Phase III.

Two types of TPS will be designed, fabricated, and tested during Phase III. One will be designed for testing in the 50 megawatt electrogas dynamic facility of the Air Force Flight Dynamics Laboratory at Wright-Patterson Air Force Base, Ohio. This specimen is intended for the study of the hot gas flow effects on parallel and transverse heat shield joints. The second specimen will be a full-scale, nine-panel configuration representative of an orbiter vehicle lower surface. This specimen will be exposed to simulated mission duty cycles consisting of combined thermal, load, and vibration testing to verify structural adequacy. A test of combined thermal/acoustic environments is intended to further provide full scale verification of the design. Phase III will demonstrate the structural and thermal adequacy and the manufacturability of full-sized, coated columbium alloy thermal protection systems and provide data necessary to project the performance and cost of these systems for Space Shuttle vehicles.

# 3 VEHICLE ENVIRONMENT AND DESIGN CRITERIA

## 3.1 Vehicle Selection

The model vehicle selected to serve as the basis for heat shield design and test throughout this program was the North American Rockwell Space Division high cross-range orbiter designated NR SSV 134C (Reference 1). The launching of this vehicle was to be provided by the B-8D Convair booster. Figure 3-1 shows the relationship between the orbiter and booster in the mated position with the orbiter nose off-set nine inches (23 cm) behind that of the booster. A composite isotherm map of the maximum heat shield radiation equilibrium temperatures (using an assumed emittance of 0.80) during boost or reentry is shown in Figure 3-2. The region selected for study is located between stations X/L = 0.025 [53 inches (1.25 meters)] and 0.050 [106 inches (2.49 meters)] where L = 2120 inches (53.85 meters). A view of this area is shown in Figure 3-3. The vehicle cross-section at X/L = 0.025 is 64 inches (1.63 meters) and

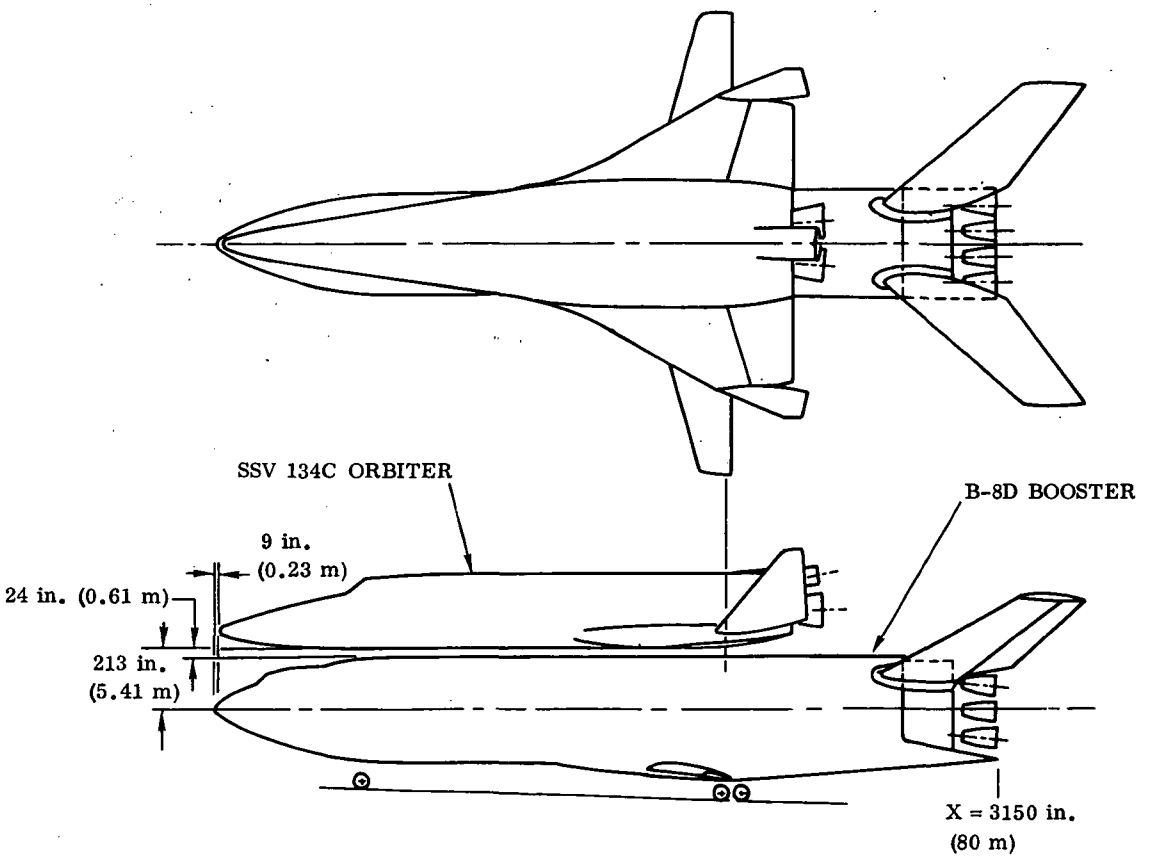


Figure 3-1. Baseline Orbiter/Booster Position

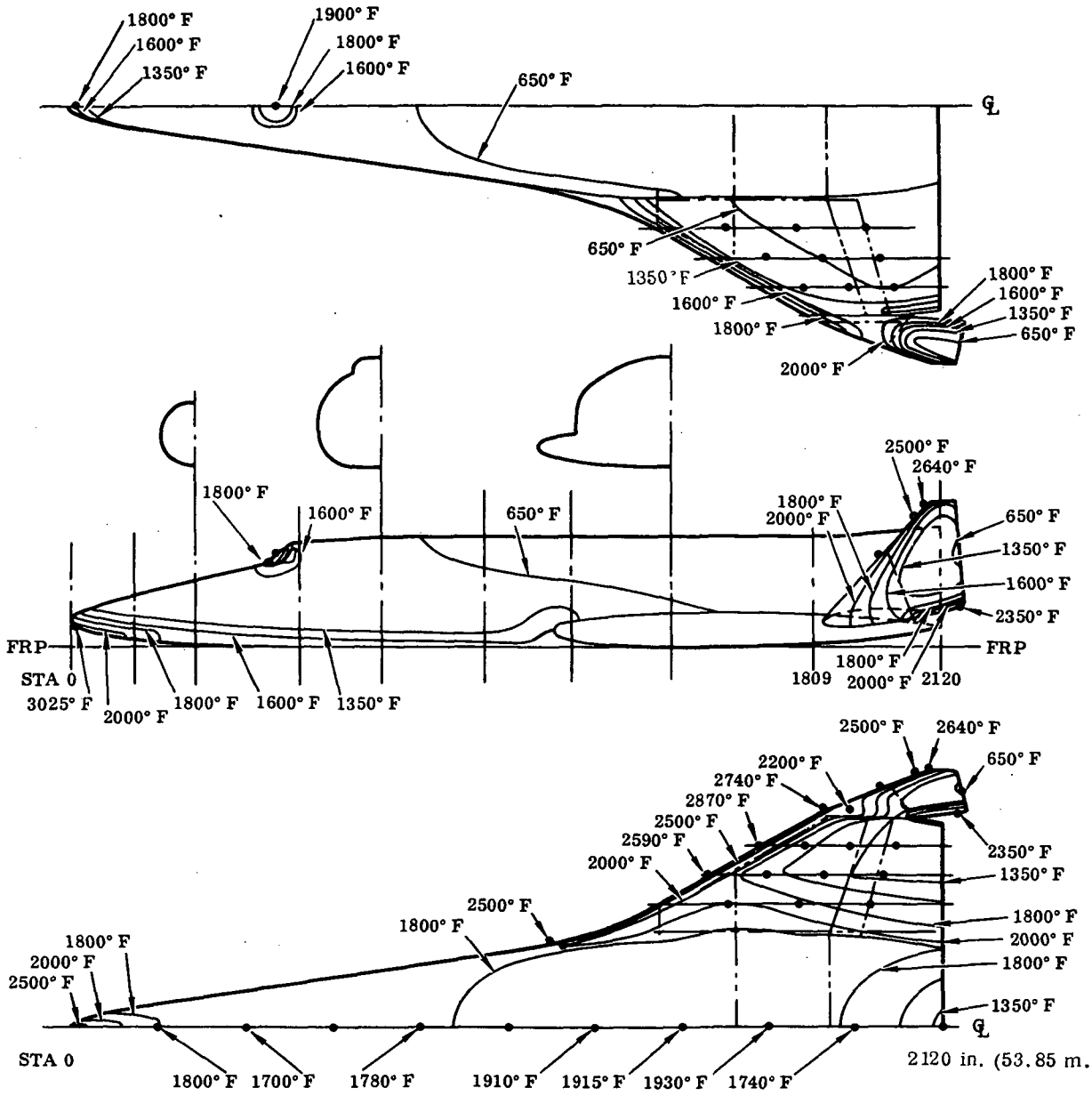


TEMPERATURE CONVERSION

| | |
|---|---|
| 650°F (616°K) | 2000°F (1366°K) |
| 1350°F (1005°K) | 2200°F (1477°K) |
| 1600°F (1144°K) | 2350°F (1561°K) |
| 1700°F (1200°K) | 2500°F (1644°K) |
| 1740°F (1222°K) | 2590°F (1694°K) |
| 1780°F (1244°K) | 2640°F (1722°K) |
| 1800°F (1255°K) | 2870°F (1850°K) |
| 1910°F (1316°K) | 3025°F (1936°K) |
| 1915°F (1320°K) | 2870°F (1850°K) |
| 1930°F (1328°K) | 3025°F (1936°K) |

RADIATION EQUILIBRIUM TEMPERATURES CALCULATED WITH AN ASSUMED EMITTANCE OF 0.80

ZERO LIFT BOOST TRAJECTORY
FOR ORBITER/BOOSTER COMBINATION
SSP 235 RE-ENTRY TRAJECTORY
($\alpha$ = 53-1/2° - 30° - 14°)

**Figure 3-2. Orbiter Maximum Surface Isotherm Map**

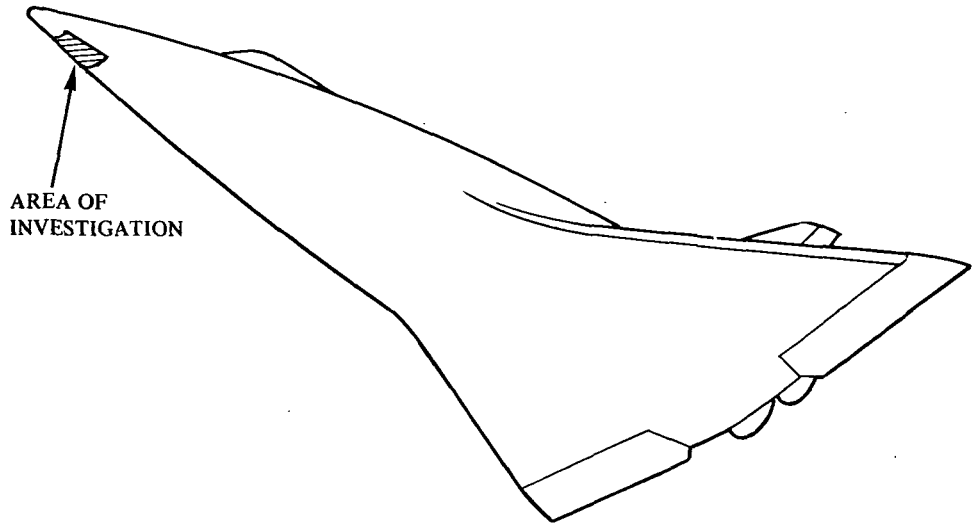


Figure 3-3. Orbiter Lower Surface Area of Investigation

at X/L = 0.050 is 90 inches (2.29 meters) in diameter. The maximum radiation equilibrium temperatures in the investigative region range from 2400°F (1589°K) to 2000°F (1366°K).

## 3.2 Design Environments

3.2.1 Boost. — The boost parameters, dynamic pressure, heating rate, and temperatures are presented in Figure 3-4 for a vehicle location of X/L = 0.025. It assumes a zero-lift ascent to separation at 183.5 seconds followed by a coast of 2.5 seconds between stages. Optimum pitch-plane steering of the powered orbiter continues until 434 seconds when the orbiter reaches the insertion orbit of 50 by 100 n. mi. (9.26 by 18.52 km) at a 55° inclination. After the orbit is circularized at 100 n. mi. (18.52 km), an additional burn is made to place the orbiter into a 100 by 270 n. mi. (18.52 by 50 km) path that is subsequently circularized into a nominal 270 n. mi. (50 km) by 55° inclination orbit. The maximum acceleration of the 3,500,000-pound (1,589,000 kg) fixed-gross-weight configuration was limited to 3 g.

The vibration response environment on the heat shield panels is the result of booster engine noise at ignition, aerodynamic noise during the transonic/maximum dynamic pressure period of boosted flight, and mechanical vibration of the orbiter boost engines. Booster engine liftoff noise levels were calculated on the basis of procedures contained in WADC TR 57-354 (Reference 2), and WADC TR 58-343, Volume II (Reference 3), modified by data from S&E ASTN/MSFC and published in Convair Report No. 76-549-4-151/AD-71-28 (Reference 4).

During the transonic period, aerodynamic shock waves will form at various locations and generally move aft. Turbulence in the boundary layer beneath these shocks

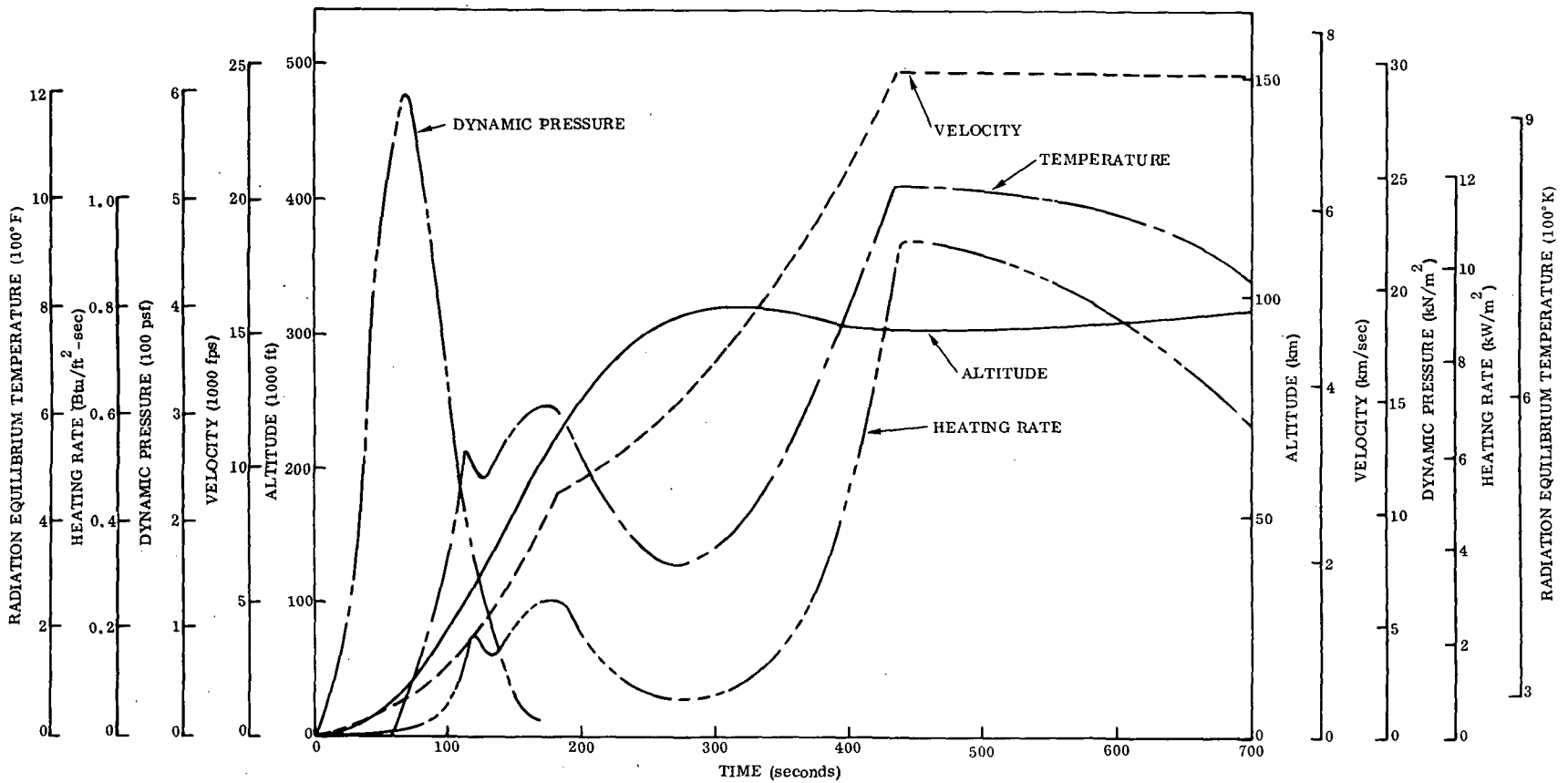


Figure 3-4. Selected Boost History — Lower Surface X/L = 0.025

will be amplified by their presence, providing significant vibratory excitation. In addition, shock waves from the booster will amplify the turbulence in the orbiter boundary layer, causing like effects. Also, separated flow will undoubtedly occur in the interference region between the booster and orbiter. The prediction procedures developed by Coe and Rechtien (Reference 5), Ailman (Reference 6), and Robertson (Reference 7), have been used based on information furnished on the steady aerodynamic flow conditions. The environment transmitted to the heat shield support structure during orbiter boost phase will depend on the engine support structure, the orbiter primary structure, and the heat shield support structure configuration. Methods developed during the Apollo CSM and Saturn S-II programs have been employed to calculate the vibration environment at the heat shield attach points. Figure 3-5 presents a time history of the external acoustic environment that may be expected during liftoff and atmospheric boost flight. The liftoff acoustic noise environment shown in Figure 3-6 was developed by modifying Saturn V liftoff noise data with corrections for engine size, chamber pressure, and distance from the source. The maximum dynamic pressure aerodynamic noise environment shown in Figure 3-6 combines shock-boundary layer interaction effects (below 160 Hz) at M = 1.4 with estimates of unperturbed flow (References 8, 9, and 10).

The orbiter boost engine mechanically transmitted vibration environment is shown in Figure 3-7. It presents a vibration spectrum at the heat shield attach points and was derived from Saturn S-II/J-2 engine-induced vibration data.

Orbiter surface pressure histories for the booster trajectory in the mated configuration were derived from wind tunnel data and were available for discrete Mach numbers (References 11 and 12). Figure 3-8 shows the results of one such wind tunnel test at Mach number $M_\infty = 1.16$, which is close to the Mach number coinciding with maximum dynamic pressure. The data is plotted using the worst-case conditions of boost where the angle of attack may vary from a maximum of -6.7° for a headwind condition [$q_{max}$ = 689 psf (40 kN/m$^2$)] to +3.0° for a tailwind [$q_{max}$ = 486 psf (23.3 kN/m$^2$)]. A tolerance of ± 0.5 psi (3.5 kN/m$^2$) was added for the ability of the passive vent system to maintain static pressure. These data were the basis for the positive 3 psi (20.7 kN/m$^2$) heat shield differential pressure criteria presented in Section 3.3.

3.2.2 Entry environment. — The atmospheric heating environment definition for the Space Shuttle system covers the entire range of convective heating analysis. Because of the complicated vehicle configurations and flow fields, experimental data is relied on heavily, and is correlated and extrapolated using analytical techniques to predict the heating environment. Analysis of Apollo flight test data has demonstrated the validity of this approach. Typical entry environments are presented as examples of the environments that were used to establish test requirements.

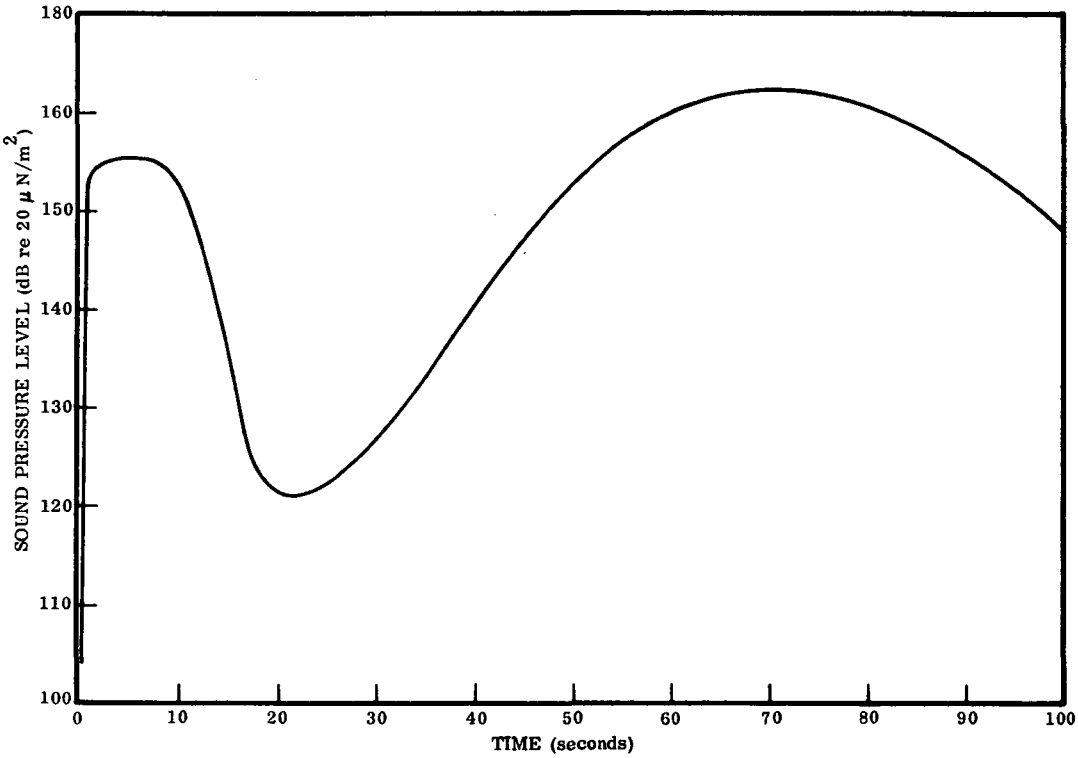


**Figure 3-5. Boost External Noise Time History**

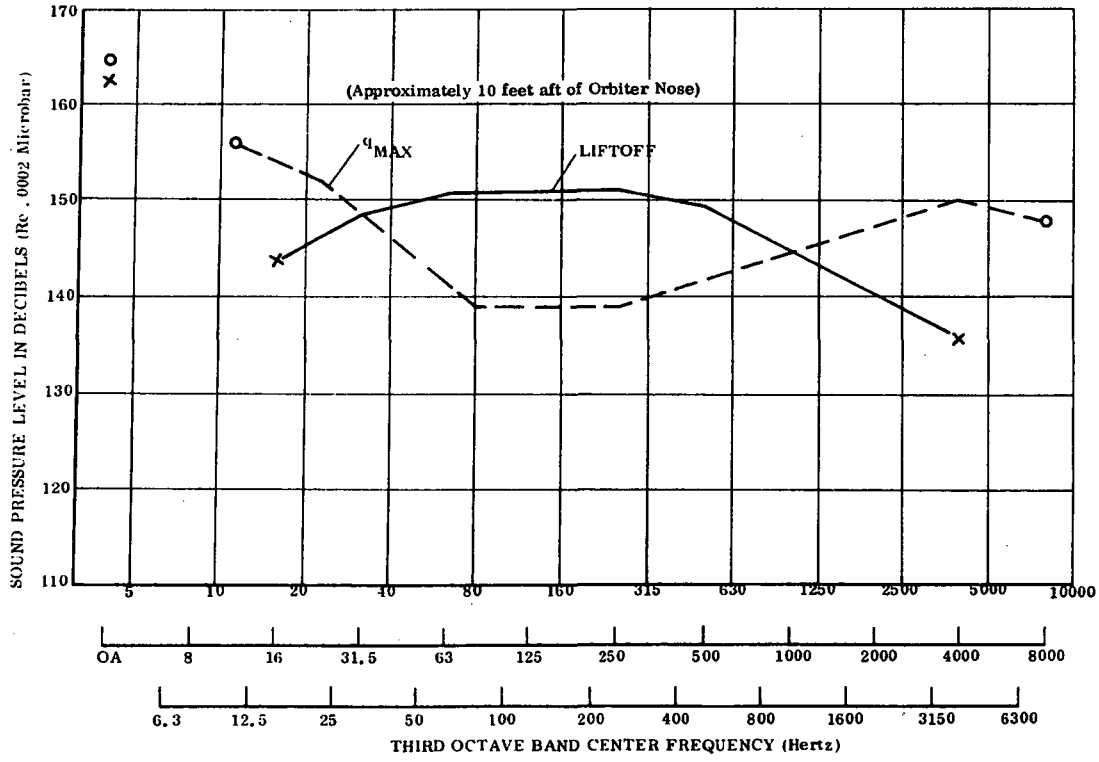


**Figure 3-6. Heat Shield Panel Acoustic Environment**

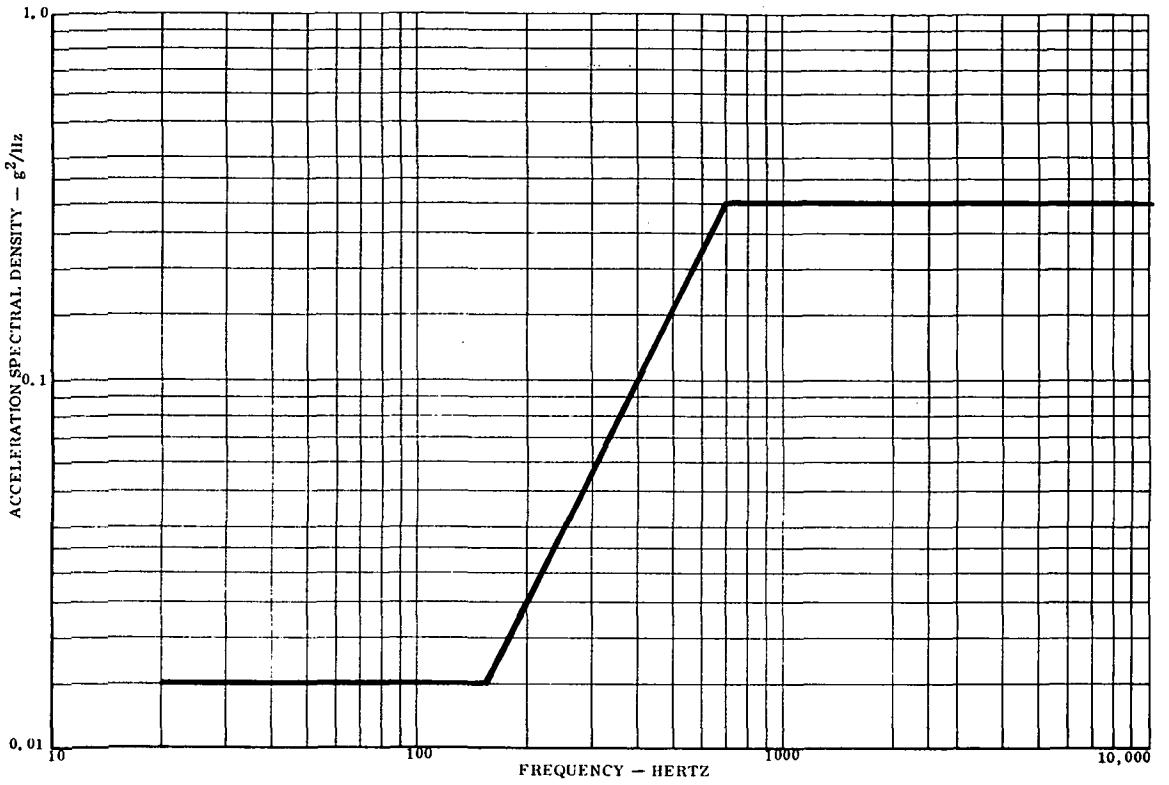


Figure 3-7. Boost Engine Vibration Spectrum at Heat Shield Attach Points

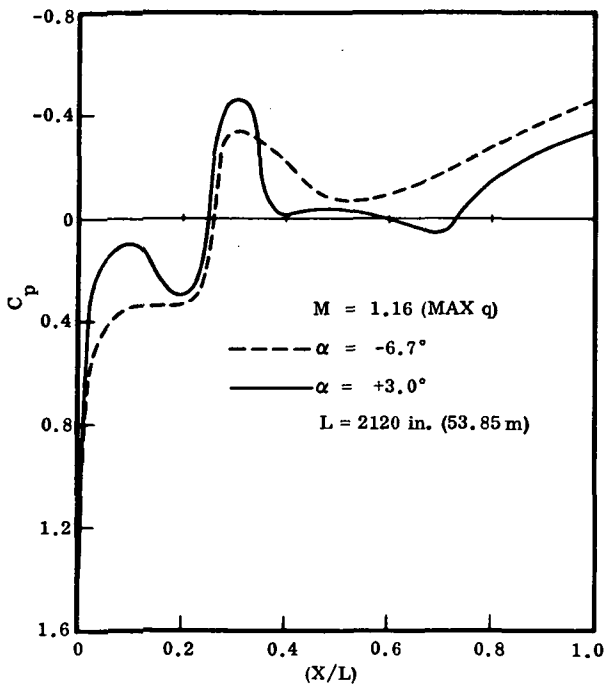


Figure 3-8. Orbiter Lower Fuselage Pressure Distribution for Mated (Orbiter/ Booster) Configuration (SSV 134C)

The vehicle is represented as a point mass, i. e. , translational equations of motion only are considered. Entry is assumed to begin at 400,000 feet (12,200 km) following a 435-fps (132. 6 m/sec) retro from a 270 n. mi. (50 km), 55° inclination orbit. The entry interface with a spherical rotating earth was at the ascending node. Roll maneuvers are performed about the velocity vector; therefore, the aerodynamics (i.e., heating distribution) remain symmetrical about the vehicle centerline. Figure 3-9 presents the entry histories. The apparent discontinuities in the heating and temperature curves may be correlated with the vehicle angle of attack changes. The spikes that initiate at approximately t= 2000 seconds result from a laminar-to-turbulent boundary layer transition.

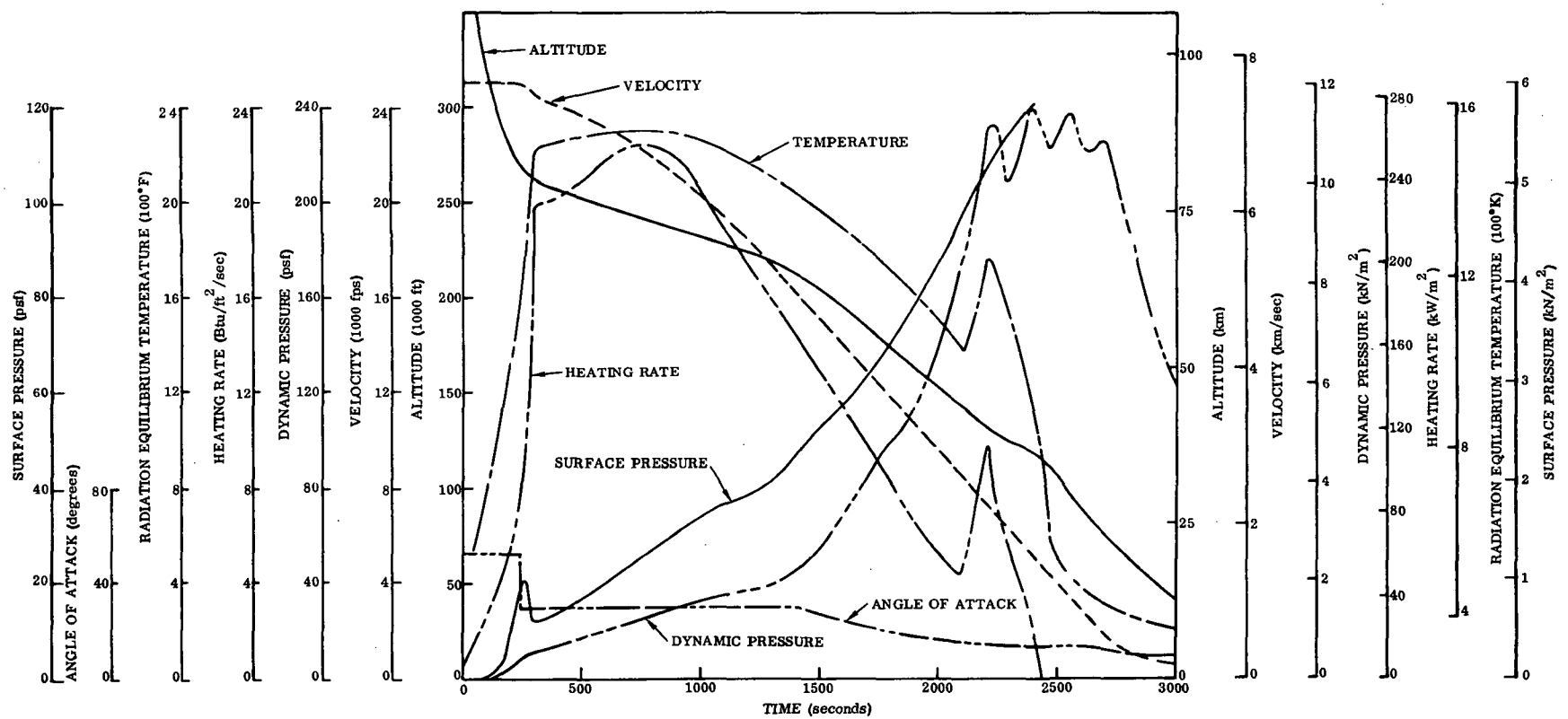


Figure 3-9. Selected Entry History — Lower Surface X/L = 0.025

The surface pressure history presented in Figure 3-9 is based on the hypersonic Newtonian pressure coefficient and is considered to be accurate to approximately 2400 seconds in the entry trajectory. The pressure spike results from a pitchover maneuver. During entry, pressures are low. The maximum surface pressure (assuming no venting) would vary between approximately 0.2 psi (1.4 $kN/m^2$) when the heat shield was at 2400° F (1589° K) to approximately 0.6 psi (4.1 $kN/m^2$) when temperatures dropped below 1500° F (1089° K). Venting of the panel underside would reduce this differential. The maximum pressure differential across the panel in the entry phase would occur during a 2.5 g maneuver, which could be made at any time after 2500 seconds of entry. At this time a 1 psi (6.9 $kN/m^2$) maximum pressure is experienced. For design purposes, an additional 1 psi (6.9 $kN/m^2$) was added for venting tolerances. The maximum panel temperature after 2500 seconds of entry would be below 400° F (478° K).

## 3.3 TPS Design Criteria

The main structural considerations are to design panels that: (1) have minimum weight and volume, (2) are reusable, (3) permit external removal from the vehicle, (4) permit inspection, and (5) accommodate thermal stress, deflections, and rotations. The critical design environments are established from the flight profile. Generally, the boost and entry environments design the outer heat shield panels, the boost environment sizes the heat shield and its supports, and the entry environment controls the materials. The entry environment generally causes the more severe thermal stresses. The outer heat shield panels are sized so that they sustain normal air loads, and are of sufficient stiffness to resist panel flutter. The standoffs are sized so that they transmit the panel air load to the structure, provide slip joints to accommodate thermal expansion, and minimize the number of thermal shorts. Initially, the panels and their components are sized to withstand the boost pressure loads that occur near maximum dynamic pressure and at low material temperatures. The panel size and gages are then checked for combined mechanical and thermal stresses at the maximum aerodynamic load condition and the maximum surface temperature condition, and the thermal distribution through the thermal protection and structural system is determined. In all cases, the panel size and the heat shield components are limited to a combined stress resulting from air load, inertia loads, and thermal loads that are below the selected material allowables for crippling, compressive yield, and tensile yield. Once the panel size has been established on a strength-stability-creep basis, the heat shield is examined to determine that no combinations of load (including dynamic load) and temperature produce deflections or rotations that would be structurally excessive (cause permanent set) or create hot spots.

The heat shield design criteria listed here consist of performance requirements (sometimes called failure modes or success criteria) and design goals.

3.3.1 Design goals. – The goals are:

(1) Have minimum weight

(2) Be reusable for 100 missions

(3) Permit external removal of heat shields

(4) Permit coating inspection between flights

3.3.2 Performance requirements. — Stress predictions will consider the actual effective structural material thickness and discount coating thickness. In materials where substrate thickness is a function of time, stress, temperature, and contact environment, it is necessary to consider the change of substrate thickness that is caused by these variables. The performance requirements are:

(1) Material rupture shall not be experienced during the service life of the vehicle. Material rupture shall be defined as a crack or hole that allows leakage of hot gases into the substructure and insulation. Rupture shall not occur even in an extreme flight maneuver or other circumstance where pressure and inertia loads are 1.5 times greater than the maximum predicted. In this case, however, it may be necessary to replace the panel before the next flight.

(2) Material yield shall not be experienced during periods of flight when temperatures are below the range of significant creep.

(3) Out-of-plane deflections occur during the boost and entry phases due to differential pressure and thermal gradient loadings respectively. In addition, there are deflections that result from permanent creep deformations. The heat shields shall be designed to minimize aerodynamic drag and temperature increases by limiting inflight panel waviness. In the region of the vehicle to be examined, the maximum permissible waviness shall vary as a straight line whose function is defined by: $\delta = 0.1 + 0.04\,L\,[(B.S.-12)/110]$, where L = the panel length (in inches) between supports and B.S. denotes the vehicle body station (Reference 13).

This deflection includes deflection of the supports, joints, and panels. It includes thermal and mechanical distortion as well as creep considerations. Creep effects shall be considered as accumulative over one service life (100 flights).

In the prediction of creep strain, consideration will be given restraining effects of adjacent material subjected to a different temperature/stress experience (e.g., plane sections remaining plane in beam cross-section). The residual stresses caused

by these restraints will be evaluated and considered in progressive load cycles. For example, it would be expected that no significant residual stresses existed on the first flight and that considerable residual stresses were present on the next-to-last. This condition will materially affect the creep experienced in the second flight being different than that experienced in the last.

(4) Stability of structural components shall be assured. Compressive loads shall not cause instabilities even when the pressure and inertia source of these loads become 1.5 times the maximum predicted. Bowing of members due to accumulative creep effects shall be considered. Creep buckling and panel deflections shall be considered accounting for material property changes as a function of temperature.

(5) In no case shall flaws increase in size to a point that any of the performance requirements are not achieved, e.g., cracks shall not grow through the material so that a gas leak is allowed, cracks shall not grow so that structural instabilities result.

(6) Panel flutter shall be prevented in all modes, including first-vibration mode flutter, and in traveling-wave and standing-wave phenomena as defined by NASA SP-8004.

External surfaces shall be free of panel flutter at all dynamic pressures up to (1) 1.5 times the local dynamic pressure expected to be encountered at any Mach number in flight, and (2) the maximum dynamic pressure expected for dispersed abort trajectories.

(7) The panels shall have the capability to dissipate a lightning strike defined by MIL-B-5087 without loss of vehicle or mission capability.

# 4 ELEMENTAL TESTING

## 4.1 Material Selection and Fabrication

4.1.1 Material selection. — Three sheet columbium alloys were selected for this program: Cb-752 (Cb-10W-2.5 Zr), C-129Y (Cb-10Hf-10W-0.1Y), and WC-3015 (Cb-30Hf-14W-5Ti-1 Zr). The Cb-752 and C-129Y alloys were selected on the basis of possessing the best combination of specific strength ($F/\rho$), formability, weldability, and availability. Both alloys were believed to have adequate creep strength for heat shield application since the potential configurations were not anticipated to be creep sensitive.

Of the three alloys, Cb-752 has received the most attention and application. Up to the time of initiation of this program (October 1970), the most extensive contractual evaluation of material properties and subsize panel testing for thermal protection system applications of Cb-752 was conducted by McDonnell-Douglas Astronautics Company-East (Reference 14). In addition, large scale TPS components of Cb-752 have been fabricated and tested by Lockheed-California Company (Reference 15). Also, Convair Aerospace has fabricated heat shields and hot structures of Cb-752, using a variety of forming and joining processes (References 16 and 17). All have been successfully tested in static thermal or hot gas flow conditions.

The selection of C-129Y was based primarily on the experience of Convair Aerospace in TPS components joining. While the forming characteristics of Cb-752 and C-129Y are similar, it was found that C-129Y produced cleaner weldments and minimized post-weld cracking. Several heat shields had been made of both Cb-752 and C-129Y and tested, with C-129Y being the more successful of the two alloys.

The third alloy selected for evaluation under this program was WC-3015. It was chosen because work at Convair Aerospace indicated greatly improved oxidation resistance when compared with other columbium alloys. While the alloy still required a protective coating, it offered some fail-safe capability in the event of a localized coating breakdown. In addition to its inherent oxidation resistance due to the high hafnium content, WC-3015 exhibited high strength throughout the applicable temperature regime.

All three sheet alloys were supplied by Wah Chang Albany Corporation of Albany, Oregon to comply with Convair Aerospace Engineering Specification 0-00947 (Reference 18). All material was to be supplied in the fully recrystallized condition. The sheet

material was nominally 0.015 inch (0.038 cm) thick and 24 inches (60.96 cm) wide by 24 inches (60.96 cm) long, except WC-3015, which was supplied in the size 12 inches (30.48 cm) wide by 12 inches (30.48 cm) long due to pilot plant rolling constraints. Only one heat of each alloy was supplied for all elemental testing conducted during Phase I of this program. The ingot chemistries for the three alloys supplied are presented in Table 4-1. Typical material properties from certifications are presented in Table 4-2.

Two oxidation resistant coatings were selected for application to the three columbium alloys. Both coatings are modified silicides applied to the base metal by a fused slurry technique. This type of coating for protecting Cb-752 and C-129Y at elevated temperatures has been the subject of numerous aerospace programs involving both materials studies as well as heat shields and hot structures. Little information was available on coatings for WC-3015. It was known, though not reported, that both candidate coatings had been applied to WC-3015 and tested to a limited degree.

Two candidate coatings were: R-512E, a silicon-20% chromium-20% iron coating, developed by Sylvania High Temperature Composites Laboratory, Chemical and Metallurgical Division at Hicksville, New York; and VH-109, a duplex coating containing silicon-hafnium-tantalum-chromium and iron, developed by Vac-Hyd Processing Corporation of Torrance, California.

Both coatings are applied to clean metal surfaces by dipping or spraying followed by air drying and baking at a low temperature to remove volatiles and carriers. A high-temperature [over 2500° F (1644° K)] fusing cycle, followed by a diffusion and homogenization treatment, complete the coating cycle. Both Sylvania and Vac-Hyd have applied these coatings to complex test hardware, and both companies have the skill and the capability to coat the large, full-scale heat shield panels required in Phase III of this program.

Coatings were specified to be applied to each of the three columbium alloys to a nominal thickness of 3 mils (0.008 cm) on all surfaces of the test specimens, with particular attention to be given to the specimen edges and test section.

4.1.2 Specimen fabrication. — Two configurations of specimens were fabricated for exposure testing in the flight simulation apparatus and for creep testing. They were: (1) a simple, tensile-type specimen 1-1/4 inches (3.18 cm) wide by 11 inches (27.94 cm) long with a 2-1/2 inch (6.35 cm) long by 1/2 inch (1.27 cm) test section; and (2) a static creep specimen 1-1/4 inches (3.18 cm) wide by 20 inches (50.80 cm) long and having a special test section with four sighting tabs. Figure 4-1 shows the dimensions of a typical tensile type specimen, and Figure 4-2 shows the creep specimen. The creep specimen was made long in order that the grip ends would be well out of the heated test zone, thus minimizing grip problems. The tabs in the

Table 4-1. Ingot Chemistries of Phase I Columbium Alloys

| Element | C-129Y Heat 572038 | | Cb-752 Heat 770022 | | WC-3015 Heat 590216 | |
|---|---|---|---|---|---|---|
| | Sample 1 | Sample 2 | Sample 1 | Sample 2 | Sample 1 | Sample 2 |
| | Composition in Percent by Mass | | | | | |
| Hf | 10.9 | 9.2 | | | 30.5 | 29.8 |
| Ta | | | | | 0.55 | 0.61 |
| Ti | | | | | 5.10 | 5.11 |
| W | 9.2 | 9.6 | 9.7 | 10.5 | 14.1 | 14.3 |
| Y | 0.06 | 0.18 | | | | |
| Zr | | | 2.8 | 2.6 | 1.3 | 1.3 |
| Cb | Bal. | Bal. | Bal. | Bal. | Bal. | Bal. |
| | Impurities in Parts per Million (ppm) | | | | | |
| Al | <20 | <20 | <20 | <20 | <20 | <20 |
| B | < 1 | < 1 | < 1 | < 1 | < 1 | < 1 |
| C | 40 | 60 | 70 | <40 | 620 | 570 |
| Cd | | | < 5 | < 5 | | |
| Co | <10 | <10 | <10 | <10 | | |
| Cr | | | <20 | <20 | | |
| Cu | <40 | <40 | | | <40 | <40 |
| Fe | <50 | <50 | <50 | <50 | <50 | <50 |
| H | 2.9 | 2.6 | 5 | 9 | 4.3 | 2.6 |
| Hf | | | 480 | 390 | | |
| Mg | <20 | <25 | <20 | <20 | | |
| Mn | <20 | <20 | <20 | <20 | | |
| Mo | 150 | 100 | 100 | 150 | 200 | 200 |
| N | 45 | 29 | 50 | 50 | 80 | 70 |
| Ni | <20 | <20 | <20 | <20 | | |
| O | 60 | 120 | 110 | 160 | 290 | 170 |
| Pb | <20 | <20 | <20 | <20 | | |
| Si | <50 | <50 | <50 | <50 | <50 | <50 |
| Sn | 10 | 25 | 15 | 10 | | |
| Ta | 3700 | 3700 | 3800 | 4300 | | |
| Ti | <40 | <40 | <40 | <40 | | |
| V | <20 | <20 | <20 | <20 | | |
| Y | | | | | 410 | 420 |
| Zr | 4000 | 3700 | | | | |

Table 4-2. Room Temperature Properties of As-Received Sheet Alloys

| Property | C-129Y Heat 572038 | Cb-752 Heat 770022 | WC-3015 Heat 590216 |
|---|---|---|---|
| $F_{TY}$ @ 2% offset, ksi ($MN/m^2$) | 71.2 (490.9) | 62.4 (430.2) | 139 (958.4) |
| $F_{TU}$, ksi ($MN/m^2$) | 87.9 (606.1) | 81.8 (564.0) | 143 (986.0) |
| Elongation, % | 25.5 | 26.0 | 13.5 |
| Hardness in BHN (avg.) | 202 | 188 | 280 |
| ASTM grain size | 9.0 | 9.5 | 11.0 |
| Nominal density, $lb/in^3$ ($gm/cm^3$) | 0.343 (9.49) | 0.326 (9.02) | 0.360 (9.96) |

test section were added to offer sighting targets for optical strain measurements at elevated temperatures.

Figure 4-3 identifies the various test specimens used in Phase I and shows the fabrication sequence for each type specimen. Tensile type specimens were prepared for parent metal testing and for testing electron beam welded and diffusion bonded joints for all six material systems (three alloys and two coatings). The creep specimens were made of parent metal without joints for Cb-752 and C-129Y only. Two materials systems were to be creep tested. In all cases, except for WC-3015, the long axis of the test specimens was aligned parallel with the rolling direction of the material. Only random lengths of WC-3015 were available on schedule, necessitating all WC-3015 specimens to be made with the long axis transverse to the rolling direction.

Two types of joints, typical of the kind and quality of joints anticipated for TPS application, were made and tested. These were an electron beam welded (simple butt joint) and a diffusion bonded (lap joint). The latter involved hot press diffusion bonding with a half-inch (1.27 cm) overlapped joint, interleafed with an 0.001 inch (0.003 cm) thick pure titanium foil. Bonding was accomplished at 1950° F (1339° K) under 1000 psi (6895 $kN/m^2$) pressure during a five to six hour cycle in a vacuum of less than five microns of Hg (0.67 $N/m^2$). Bonded joints were evaluated by the use of C-scan ultrasonic testing for 100% area bond. Welded joints were required to meet Convair Aerospace Engineering Specification 0-77008, with a 10% maximum mismatch allowed.

In the case of both types of joints, the joint halves were taken from the same sheet and, in most cases, both halves were generated by dividing a single panel. Tack welding of the ends of the panel joints prior to joining was permitted to facilitate positioning the halves during the joining process.

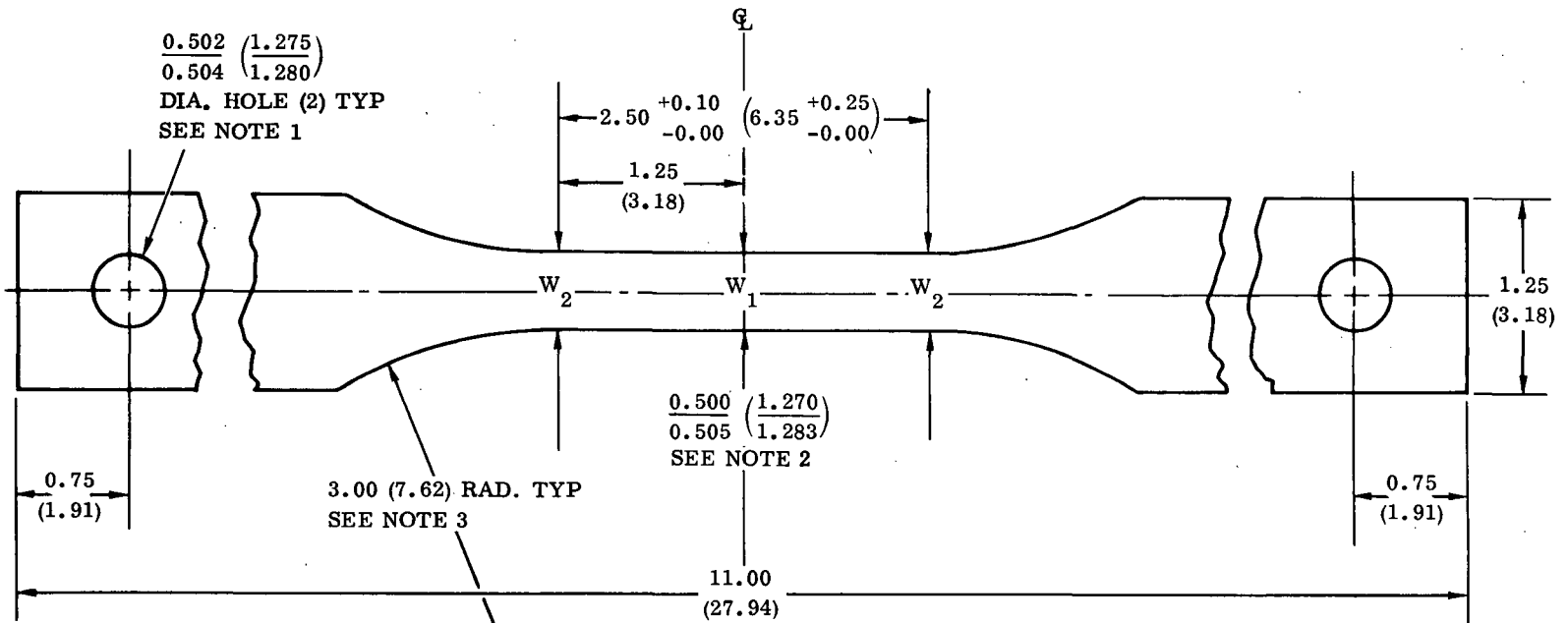


NOTES:

1. HOLES ON CENTERLINE OF TEST SECTION WITHIN ±0.005 (±0.013).
2. GRADUAL TAPER FROM $W_2$ TO $W_1$ of $0.005\ ^{+0.000}_{-0.002}$ $\left(0.013\ ^{+0.000}_{-0.005}\right)$.
3. NO UNDERCUT AT INTERSECTION OF RADII AND TEST SECTION.

PARENTHESIZED DIMENSIONS IN CENTIMETERS; ALL OTHER DIMENSIONS IN INCHES

Figure 4-1. Typical Flight Simulation and Tensile Specimen

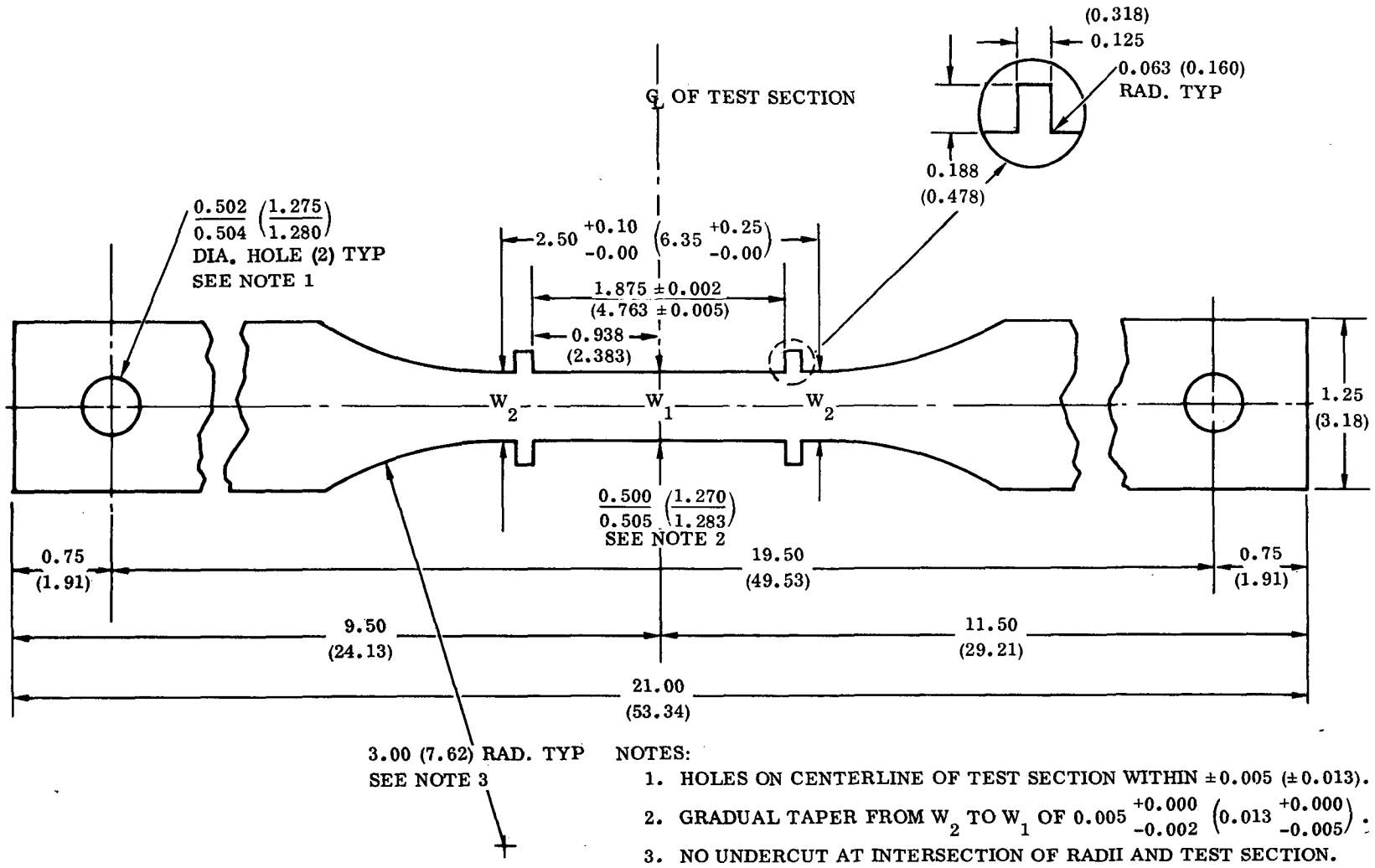


NOTES:

1. HOLES ON CENTERLINE OF TEST SECTION WITHIN ±0.005 (±0.013).
2. GRADUAL TAPER FROM $W_2$ TO $W_1$ OF $0.005\ ^{+0.000}_{-0.002}$ $\left(0.013\ ^{+0.000}_{-0.005}\right)$.
3. NO UNDERCUT AT INTERSECTION OF RADII AND TEST SECTION.

PARENTHESIZED DIMENSIONS IN CENTIMETERS; ALL OTHER DIMENSIONS IN INCHES

Figure 4-2. Typical Creep Specimen

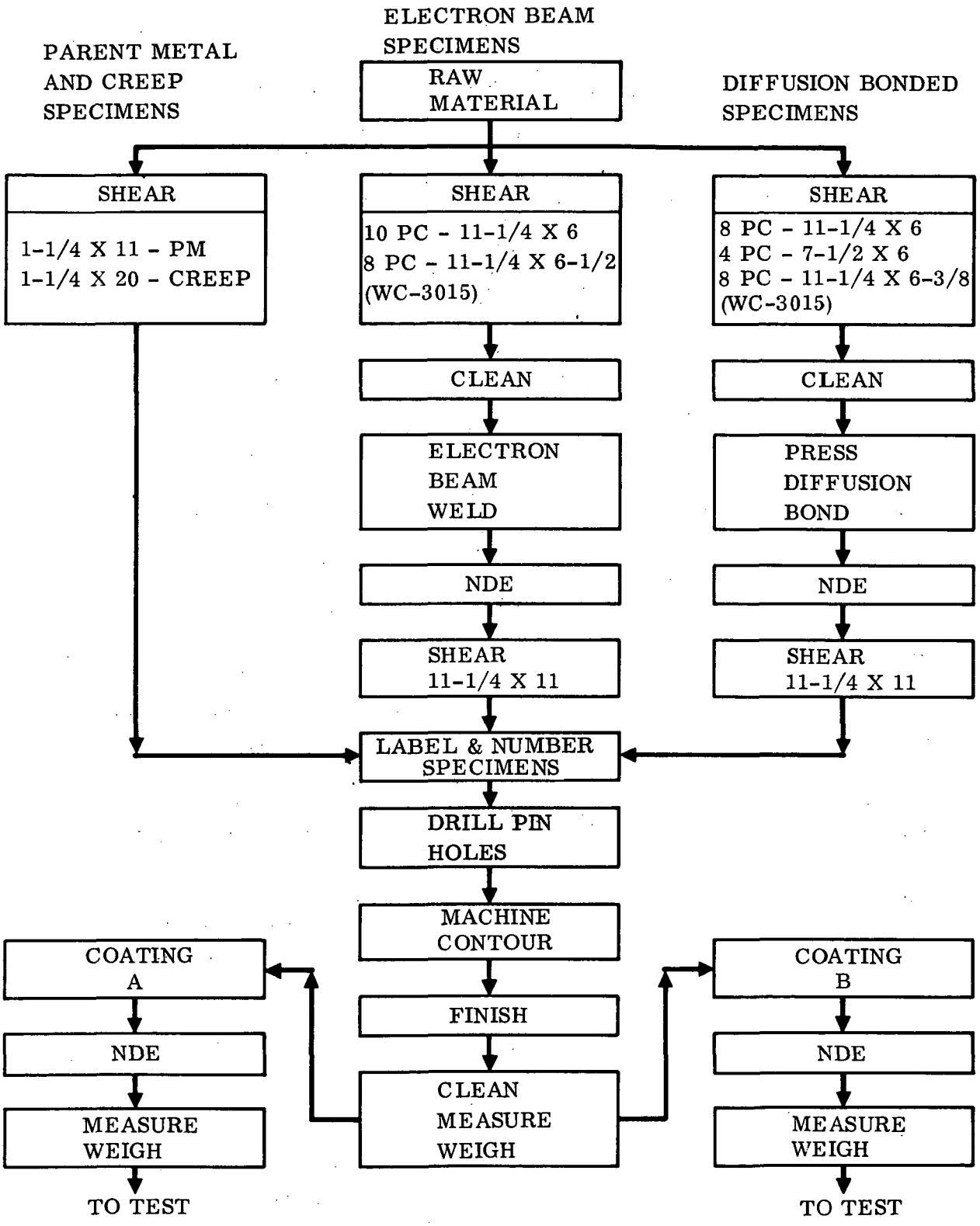


**Figure 4-3. Phase I Test Specimens**

Cleaning of the material for joining or prior to coating was done to Convair Aerospace Engineering Specification 0-73510 and involved both an alkaline degreasing treatment and nitric-hydrofluoric acid pickling.

After preparation and acceptance of the joints, the C-scan or X-ray records of individual joints were examined for selection of the best areas for the test specimens. Each joint panel was marked to differentiate the specimen regions and the scrap regions and were cut accordingly.

After machining of the specimens, a finishing operation was required to prepare the specimen edges for coating. This preparation consists of radiusing or rounding of all edges and corners of the specimen. This was accomplished by machine vibratory finishing after a light, hand deburring operation. The long creep specimens required additional hand radiusing in the tab areas after machine finishing because of process limitations and the flexibility of the long parts. The cross-section of a specimen edge in Figure 4-4 shows the typical radius produced on thin gage specimens by vibratory finishing. Radii were uniform from specimen to specimen with this process.

4.1.3 Material and fabrication problems and observations. —

(1) Several Cb-752 and C-129Y sheets were shipped from the mill without designation of grain direction. Before fabrication could proceed, it was necessary to determine if there was a directionality effect on the sheet properties due to rolling. Mechanical testing and metallurgical sampling produced no firm evidence of directionality on the C-129Y sheets and an insignificant difference between longitudinal and transverse properties for the Cb-752 sheets. Therefore, the C-129Y sheets were considered to have equal properties in either direction, and the Cb-752 sheets were assigned an apparent rolling direction with all specimens oriented accordingly.

(2) Electron beam welds in Cb-752 repeatedly showed evidence of porosity; welds in C-129Y and WC-3015 did not. The following observations were made relative to the weldability of the three alloys for this program when electron beam welded under identical conditions:

(a) The three alloys were readily weldable by the electron beam process.

(b) Weld cracking was not present in any welds.

(c) Parent material cracking adjacent to the weld (transverse) was a problem with Cb-752 but no problem with either of the other alloys.

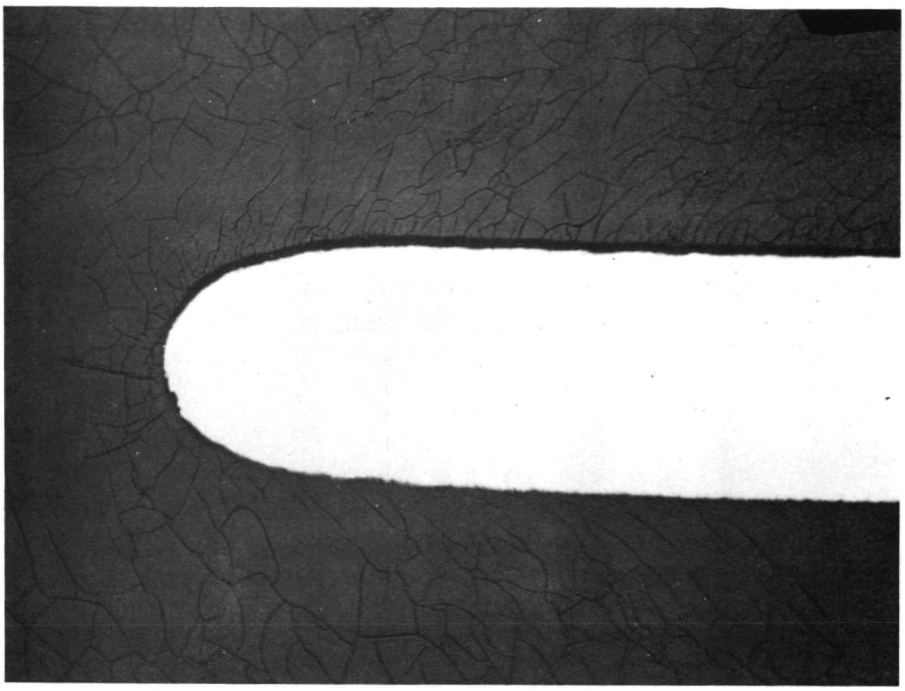

Figure 4-4. Radiused Edge of Tensile Specimen
100X (Photo C8647)

(d) Porosity was a significant problem with Cb-752 welds and a minor problem with the other alloys.

(e) Sheet mismatch resulting from welding was prevalent with Cb-752 and C-129Y.

(f) The three alloys ranked for weldability are WC-3015, C-129Y, and Cb-752.

(3) Alloy WC-3015 material encountered several problems during Phase I.

(a) Severe delamination was detected in several sheets when examined by C-scan ultrasonics. These delaminations were predominantly located at the corners and edges of the sheets.

(b) The material as received was not fully recyrstallized, having received only a 2000°F (1366°K) stress relief treatment. This put the material in the best condition for welding and for room temperature forming. Subsequent annealing or coating applications caused an increase in the ductile-to-brittle transition temperature (DBTT) and resulted in poor room temperature ductility (0 to 3%).

(c) Gross warpage was experienced by the WC-3015 specimens when coated with VH-109. Significant warpage occurred when WC-3015 specimens were coated with R-512E. Minor or insignificant warpage was experienced by C-129Y and Cb-752 when coated with either R-512E or VH-109.

(d) Diffusion bonded material became oxygen contaminated during a vendor's vacuum degassing operation prior to diffusion bonding. The bonded material had an oxygen level by gas analysis of 3 to 3-1/2 times that of the as-received material from the same sheets and heat. This contamination embrittled the material, and cracks or edge spalling developed during shearing, metal stamping, and machining of specimens.

During the early stages of this program it became readily apparent that WC-3015 must still be considered a developmental sheet alloy. It had demonstrated low yield from ingot to sheet, which limits the producible sheet widths and lengths, increases costs, and contributes to poor product quality. In the material supplied to Convair Aerospace, some process heat treatments and welding of the material had been found to embrittle the material by raising the DBTT above room temperature. Work at MSFC (Reference 19) has shown that significant improvement in the DBTT can be attained by adding a small amount of yttrium and reducing the tungsten concentration.

As a relatively new columbium alloy, WC-3015 has had limited application in TPS programs. Thus, there is little data on coatings, coated material properties, the effect of joining processes, or on general fabricability. It was anticipated that most of these would have been resolved before and during the early stages of this program.

In summary, specific problems with WC-3015 have been encountered during this program that directly impacted its continued consideration: (1) gross warpage was experienced on all specimens when coated, therefore producing questionable tensile and flight simulation test data; (2) the material as supplied by Wah Chang was to have been in its most fabricable condition; however, subsequent coating application raised the DBTT so that very low ductility was achieved at room temperature, negating its usefulness for heat shield applications; and (3) some of the as-received material was found to have areas of delamination.

In addition to the difficulties with this alloy as experienced by Convair Aerospace, McDonnell Douglas (Reference 20) had found a relatively high base metal consumption by the coating, severe distortion of coated specimens, and embrittlement of specimens after cyclic exposure with a significant loss (up to 38%) of strength.

It appears that many of the problems encountered with WC-3015 resulted from its premature consideration as a producible and fabricable sheet material. The work by Tavassoli (Reference 19) indicates that the alloy has potential with modifications in chemistry and heat treatment; however, for the reasons cited above, further work with the alloy on this program was discontinued.

## 4.2 Flight Simulation Testing

4.2.1 Test plan. — Flight simulation testing was the primary part of an experimental investigation of material characteristics for heat shield applications. Three columbium alloy substrates, each with two different silicide coatings were to be evaluated, and from the results two coating/substrate combinations were to be selected for further study in Phase II of the overall program. Parent metal, electron beam weld, and diffusion bonded specimens of each material system were tested. The test plan called for six specimens each of the three types of specimens to be subjected to 100 flight simulation cycles or to failure, whichever occurred first. During the simulation testing (at approximately 10 cycle intervals) cyclic creep measurements, NDE, visual examinations, and photographs were made. Following exposure cycling, specimens that survived 100 cycles were tensile tested, three at room temperature and three at 2400°F (1589°K). NDE and tensile testing procedures and results are presented in Sections 4.6 and 4.4 respectively. Extensive metallographic examinations were made of representative specimens, both those that failed during flight simulation testing and those that completed 100 flight cycles and were later tensile tested.

4.2.2 Test profile. — The elemental test profile (Figure 4-5) used for the flight simulation testing closely follows the predicted boost and entry trajectory histories shown in Figures 3-4 and 3-9. The total test time per cycle was 3600 seconds. All essential parameters could be performed within this time period, and it was consistent with equipment operating time. A ramp function temperature profile was selected to more easily analyze and correlate test results. The peak temperature during the simulated boost phase was 960°F (789°K), which was maintained for 220 seconds before returning to room temperature. The simulated entry temperature profile exhibited a peak temperature of 2400°F (1589°K) in 300 seconds and was held for 600 seconds. The temperature was decreased in 1000 seconds to 1600°F (1144°K) and was held for 400 seconds before returning to room temperature. The maximum simulated entry temperature of 2400°F (1589°K) was selected rather than the predicted temperature of 2300°F (1533°K). The test temperature is believed to be a realistic maximum nominal temperature for coated columbium alloys.

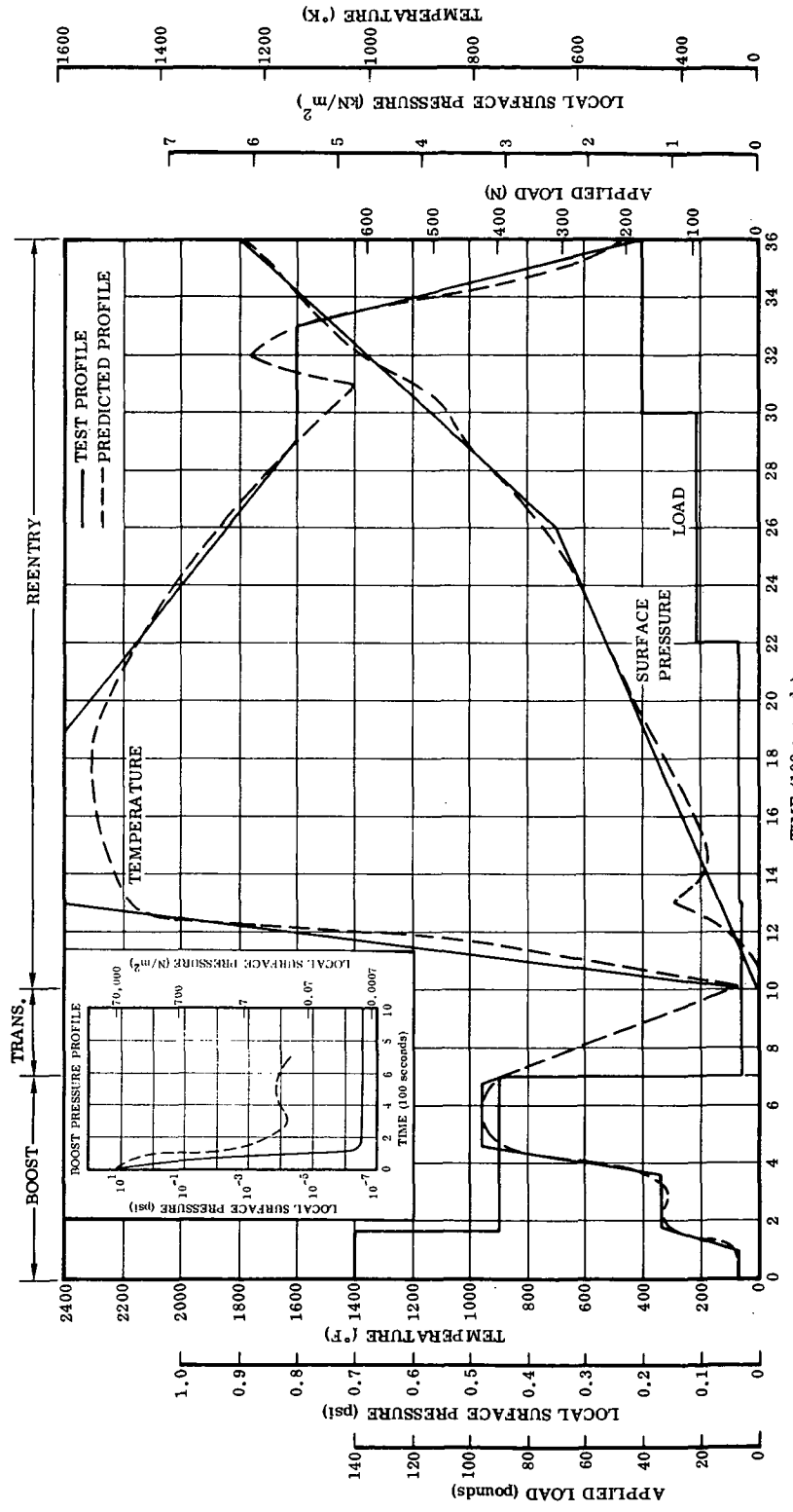


Figure 4-5. Elemental Test Profile

The variation of the chamber pressure (which simulates the local surface pressure) during the simulated boost results from the rapid but non-controllable operation of the roughing and diffusion pumps. The chamber pressure is decreased from one atmosphere to the $10^{-6}$ to $10^{-7}$ psi (7 to 70 mN/m$^2$) range in approximately 160 seconds. Since the temperature during this period did not exceed 300° F (422°K), the difference in the effect of the oxygen present was considered to be inconsequential. The chamber pressure during the entry portion closely followed the predicted heat shield external surface pressure. The pressure at the end of each test was 0.9 psi (6 kN/m$^2$).

The test load profile shown in Figure 4-5 represents the loads due to pressure differentials associated with the flight. That is, up to 3 psi (21 kN/m$^2$) might be experienced during the booster launch phase (t = 0 to 170 seconds) when the booster/orbiter interference effects might be present. This load represents a nominal stress level of 29 ksi (200 MN/m$^2$). Up to 2 psi (14 kN/m$^2$) might be experienced during the orbiter launch phase. This load represents a nominal stress level of 19 ksi (131 MN/m$^2$). The pressure differentials vary with entry and were raised slightly during the last step to account for maneuvers expected during the cruise phase. The nominal stress levels ranged from 1.5 ksi (10.3 MN/m$^2$) at maximum temperature [2400° F (1589°K)] to 4 ksi (27.6 MN/m$^2$) and to 8 ksi (55.2 MN/m$^2$) during the latter stages of the profile.

Using the load, temperature, and time cycle of Figure 4-5, stresses were determined in the following manner. Complete details can be found in Appendix B.

(1) Using a representative heat shield configuration it was determined that temperature gradients produced stresses considerably lower than the differential pressure loading. Therefore, it was assumed that stress would be primarily a function of pressure loading. Hence,

$$f = K(\Delta p)$$

(2) The pressure curve was factored by a constant (K) so that at no time during the cycle would the stress exceed:

$$f = K(\Delta p) \leq F_{ty} @ \theta$$

or

$$f = K(\Delta p)\ (UFS) \leq F_{tu} @ \theta$$

where

$\theta$ = temperature

UFS = ultimate factor of safety

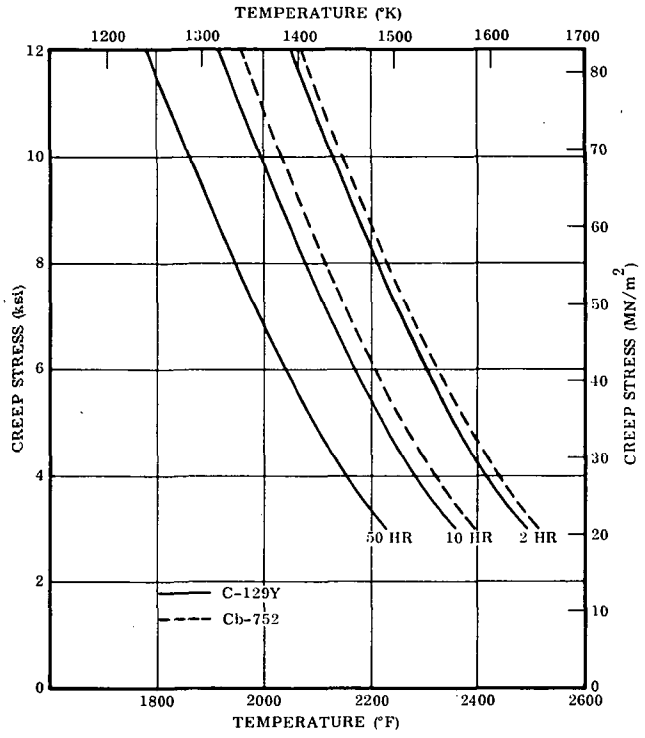


Figure 4-6. Allowable Stress for 1% Creep Strain (Based on Net As-Coated Section)

This procedure determined a stress level that was adequate to prevent short time yield or failure.

(3) Since the other failure criteria was creep, it was necessary to reduce the stress factor, K, such that the accumulated creep strain was below 1 percent for the 100 cycle life.

The creep data shown in Figure 4-6 were used to evaluate the allowable stress levels. A computer program (Reference 21) following the logic shown in Figure 4-7 was used to establish this creep constraint on the test stress level.

The applied load was based on a net base metal cross section at the end of 100 cycles. The uncoated specimen thicknesses varied from 0.0115 inch (0.0292 cm) to 0.0155 inch (0.0394 cm). For load compilation a mean of 0.015 inch (0.038 cm) was used. A nominal coating thickness of 0.003 inch (0.008 cm) per side was to be applied to each specimen. The assumption was made that the base metal thickness was initially reduced by 0.001 inch (0.003 cm) per side due to the coating diffusion. Although this diffusion zone is, in effect, capable of carrying load, it was considered to be non-structural for the determination of test loads. An assumption was also made that the effective base metal thickness would be reduced at a rate of 0.00001 inch (0.00003 cm) per side per cycle. That is, at the end of 100 thermal cycles the total specimen thickness would be reduced by 0.002 inch (0.005 cm) from the net as-coated thickness.

4.2.3 Test equipment. —

4.2.3.1 Environmental simulation: Simulation testing was performed in Convair Aerospace's Flight Simulation Facility. The unit consists of (1) a supporting stand, (2) four separate quartz lamp heated test chambers, (3) a common vacuum manifold, (4) a vacuum pumping station, (5) specimen mounting fixtures through which tensile loads can be applied, and (6) the associated control, regulation, and programming devices. Figure 4-8 shows the overall system; Figures 4-9 to 4-13 are closeups of some of the components.

1. Consider time element in cycle.

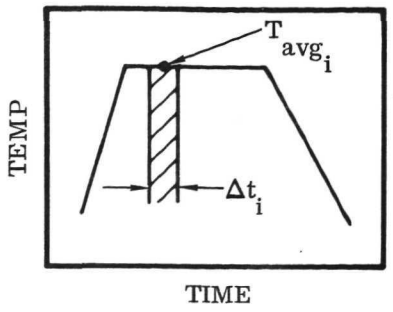


2. Find stresses required to reach 1% creep for the 3 times in Figure 4-6 at $T_{avg}$.

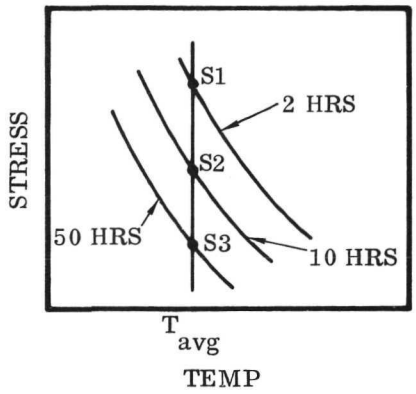


3. Knowing 3 points (s, t), establish "Time to Reach 1% Creep" curve as function of stress and find time for this particular time element.

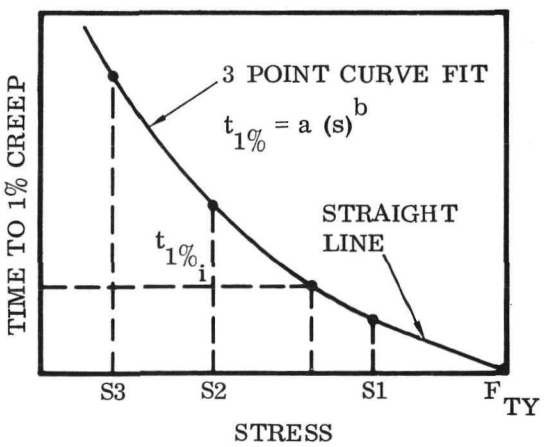


4. Compute strain contribution of this time element, $\epsilon_i = 0.01 \Delta t_i / t_{1\%_i}$.

5. Accumulate these elemental creep strains for one cycle, $\epsilon_c = \Sigma \epsilon_i$.

6. Multiply creep strain for one cycle by total number of cycles, $\epsilon_{c_{life}} = N_{life} \epsilon_c$.

7. If $\epsilon_{c_{life}} > 0.01$, reduce the stress levels by 5% and return to Step 3.

Figure 4-7. Creep Constraint Evaluation Sequence

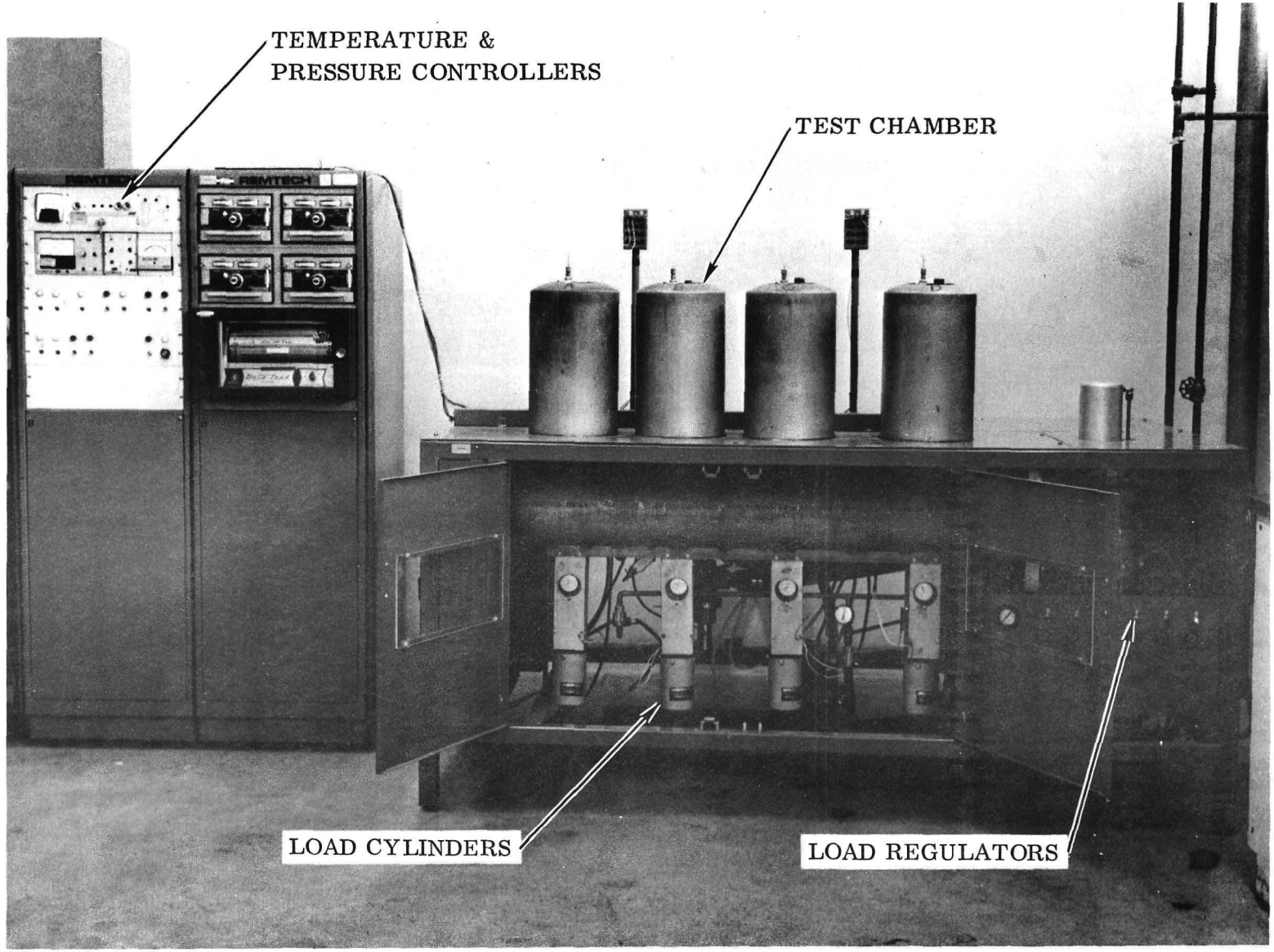


Figure 4-8. Flight Simulation Facility (Photo 117204B)

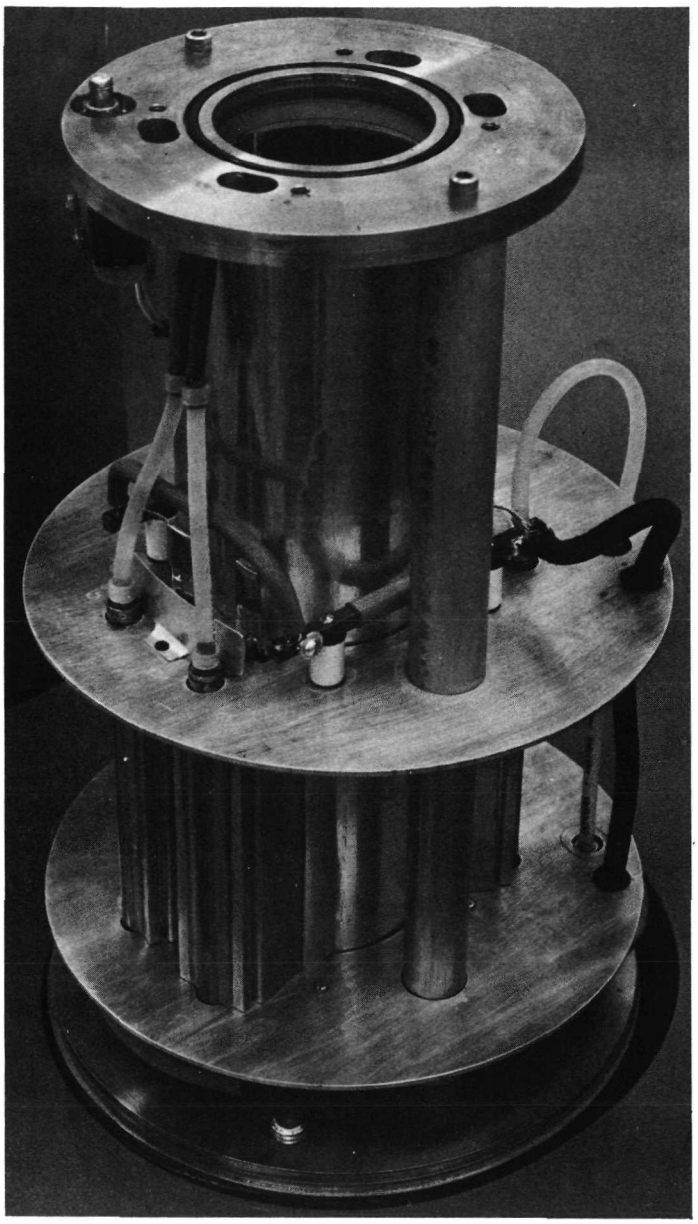

Figure 4-9. Quartz Lamp Furnace Chamber (Photo 111303B)

A furnace chamber with the outer cover removed is shown in Figure 4-9. Each chamber is made up of a rigid support containing an 80-mm-diameter quartz tube, vacuum sealed at both ends with O-rings. The specimens (Figure 4-10), held in pin-and-clevis-type fixtures, are each heated with four 1200-watt quartz lamps (partially visible in Figure 4-9) mounted in eliptical aluminum relfectors around the periphery of the quartz tube, To increase the radiant heating efficiency, the quartz tube is enclosed by an Alzak electrobrightened aluminum reflector slotted to accept the four quartz lamps. The end supports and the four lamp reflectors are water cooled. Additional cooling is provided by a blower that forces air at a high flow rate into the lower end support plate, past the lamps, reflectors, and quartz tube and out the top between the upper end plate and the outer cover.

The furnaces are operated by four Research Inc. Thermac temperature controllers and Phaser proportional power regulators. A single Data-trak programmer is utilized to provide the desired thermal profile for the four chambers. The Thermac temperature controllers employ a closed-loop servo technique to control the temperature of the specimens during exposure testing. A Pt/Pt + 13 percent Rh thermocouple mounted on each of the specimens provides a feedback voltage proportional to specimen temperature. This voltage is compared at the Thermac input to a command signal generated by an analog function generator. The command signal may be varied as a function of time according to a pre-plotted program chart mounted in the Data-trak.

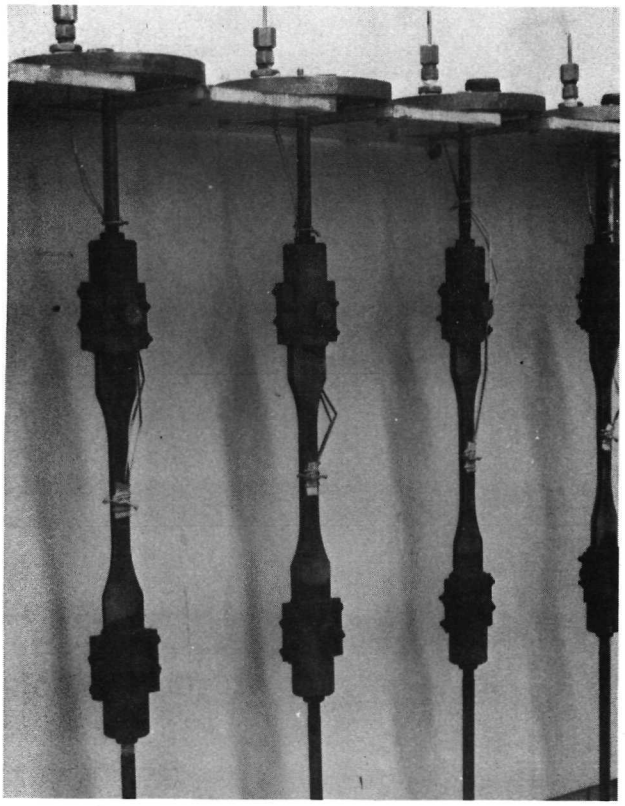

Figure 4-10. Flight Simulation Specimens Mounted in Test Fixtures (Photo 118930B)

During exposure testing, temperature was continuously monitored by a strip-chart recorder connected to the four control thermocouples through a selector switch. Frequent temperature surveys of the four specimens were made during flight simulation testing. Special care was taken in attaching the thermocouples to ensure the measurement of true specimen temperature. To prevent radiation of the quartz lamps directly onto the thermocouple, and to eliminate errors in measurement as a result of differences in emittance between thermocouples and specimens, the following technique was used. The thermocouples were enclosed in Irish Refrasil sleeving and attached, one to each specimen with Irish Refrasil cord. Irish Refrasil, produced by HITCO, was chosen because of its ability to retain soft, flexible characteristics during high-temperature exposures and its compatibility with the silicide coatings. With the thermocouples shielded in this manner, errors in temperature measurement were minimized, while response to temperature change was rapid.

A series of tests was made to determine the temperature uniformity along a 2 inch (5.08 cm) gage section of a specimen in each of the chambers. Checks were made at 500 (533), 1000 (811), 1500 (1089), 2000 (1366), and 2500°F (1644°K). Temperature variations were held to ±20°F (±11°K) or better for all temperatures in each of the chambers. One additional test was made to compare (1) the temperature as measured by a Pt/Pt + 13 percent Rh thermocouple tied to a superalloy specimen in a manner identical to that used during exposure testing with (2) the temperature measured by a chromel-alumel thermocouple spotwelded to the specimen. Comparisons were made at five temperatures between 900° and 1725°F (755° and 1214°K). The two sets of temperature readings agreed within 10°F (6°K). All temperature measurements performed during these calibration procedures were made after the specimens had reached equilibrium. With the furnace chambers used in this program a steady state condition could be reached in a minute or less.

During simulation testing, temperature control was very good, with variations from the desired levels for the four specimens normally held to less than ±10° F (±6° K).

Load application is accomplished by pneumatic force cylinders located immediately below each chamber (Figure 4-11). The cylinders, manufactured by Bellofram, are a low-friction diaphragm type. The lower pullrods on the specimens pass through the common vacuum manifold, through low-friction rubber vacuum seals, and are pinned to the force cylinders as shown in Figure 4-11. Loads are applied by activating any of a series of solenoid operated valves connected to preset pressure regulators. The four

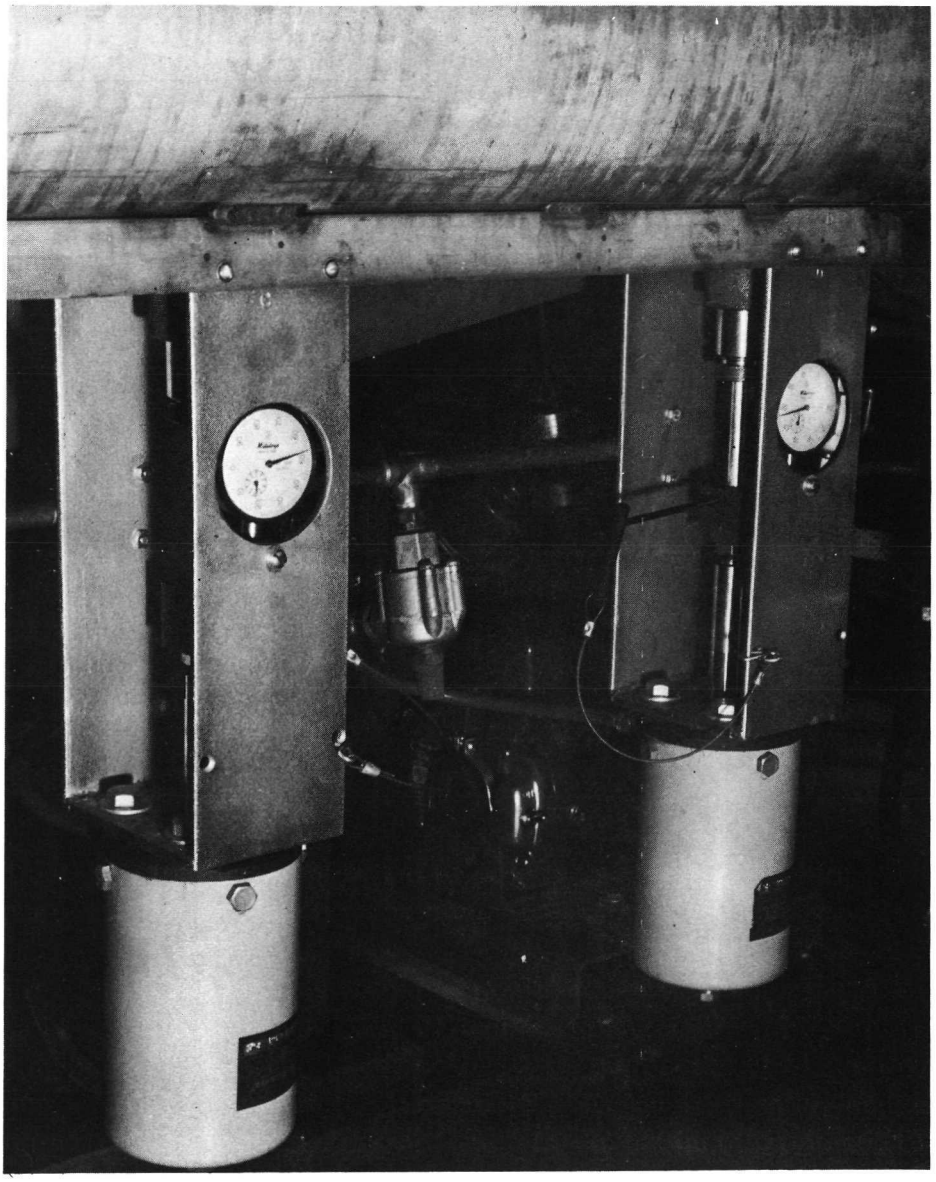

Figure 4-11. Force Cylinders for Load Application (Photo 111304B)

cylinders are connected in parallel so that all specimens are loaded equally. Six independent pressure regulators are utilized — thus allowing the selection of six different load levels during a flight simulation cycle. Each cylinder can operate in the range from 0 to 500 lb (0 to 2220 N).

Programming of the load profile is accomplished with the same Data-trak used for temperature. Load levels are preset with the six numbered regulators, which can be programmed to operate at any time during an exposure cycle. The loads can be applied for any desired duration, in any order, and as often as desired. The programmer uses a binary code system with three photodiodes operating a series of logic relays. The photodiodes are activated or deactivated by light or dark tapes placed on the Data-trak chart.

The following technique is used to preset the desired load levels for the simulation cycle. A calibrated load link is mounted in the system in the same position as a test specimen. The load link, shown in Figure 4-12, was made by attaching four strain gages to a dummy specimen of 0.026 inch (0.066 cm) thick, extra-full-hard type 301 stainless steel. Calibration of the load link was by deadweight loading in the range 0 to 20 lb (0 to 89 N) and with a Baldwin-Emergy SR-4 testing machine for higher loads. After mounting in the simulator, the system is evacuated and the six regulators adjusted to give the proper readout on the SR-4 portable strain indicator (Figure 4-12). Once the six regulators are properly set for one chamber, the load link is moved in turn to the remaining three chambers to determine the variations in loads among the four chambers. This calibration procedure was repeated frequently during the test program, and loads were readjusted as necessary. Deviations from the required loads from chamber to chamber and from week to week were generally less than one pound (4.4 N) for loads less than 30 pounds (130 N) and less than five pounds (22 N) for loads greater than 30 pounds (130 N).

The environmental simulator is capable of operation in the pressure range from ambient to $2 \times 10^{-7}$ psi (1.4 mN/m$^2$). The four chambers are connected through a common manifold to a vacuum pumping station consisting of a Welch mechanical pump and a CVC oil diffusion pump. Chamber pressure can be controlled to ±0.025 psi (±340 N/m$^2$) in the region from 0 to 7.4 psi (0 to 51 kN/m$^2$) by means of a solenoid operated leak valve operating against an independent pressure recovery pump. The leak valve is operated by a Bristol pressure controller (Figure 4-13). A precut cam on the Bristol unit was used to program the desired pressure profile.

During the reentry portion of the flight simulation cycle, the Bristol unit was used, as described above, for obtaining the desired pressure profile (Figure 4-5). A different technique was necessary for obtaining the boost profile because of the wide pressure range required. During boost, the system was pumped down to its ultimate pressure as fast as possible and held constant until the beginning of reentry. The

difference between the predicted and test pressure profiles (Figure 4-5) is small, and because of the relatively low temperatures during boost, this difference is believed to be of no consequence.

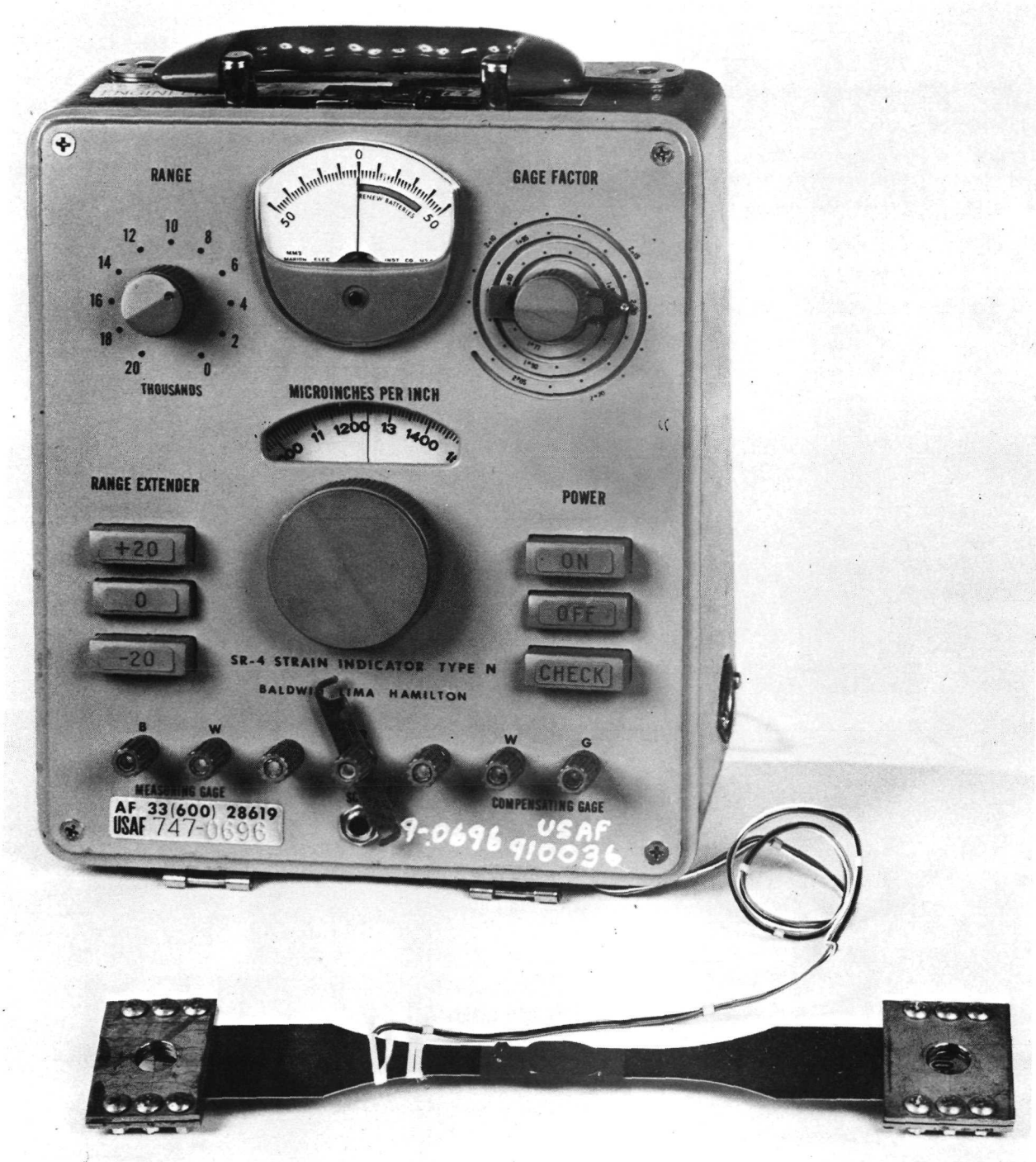


Figure 4-12. Load Link and Portable Strain Indicator (Photo 34174B)

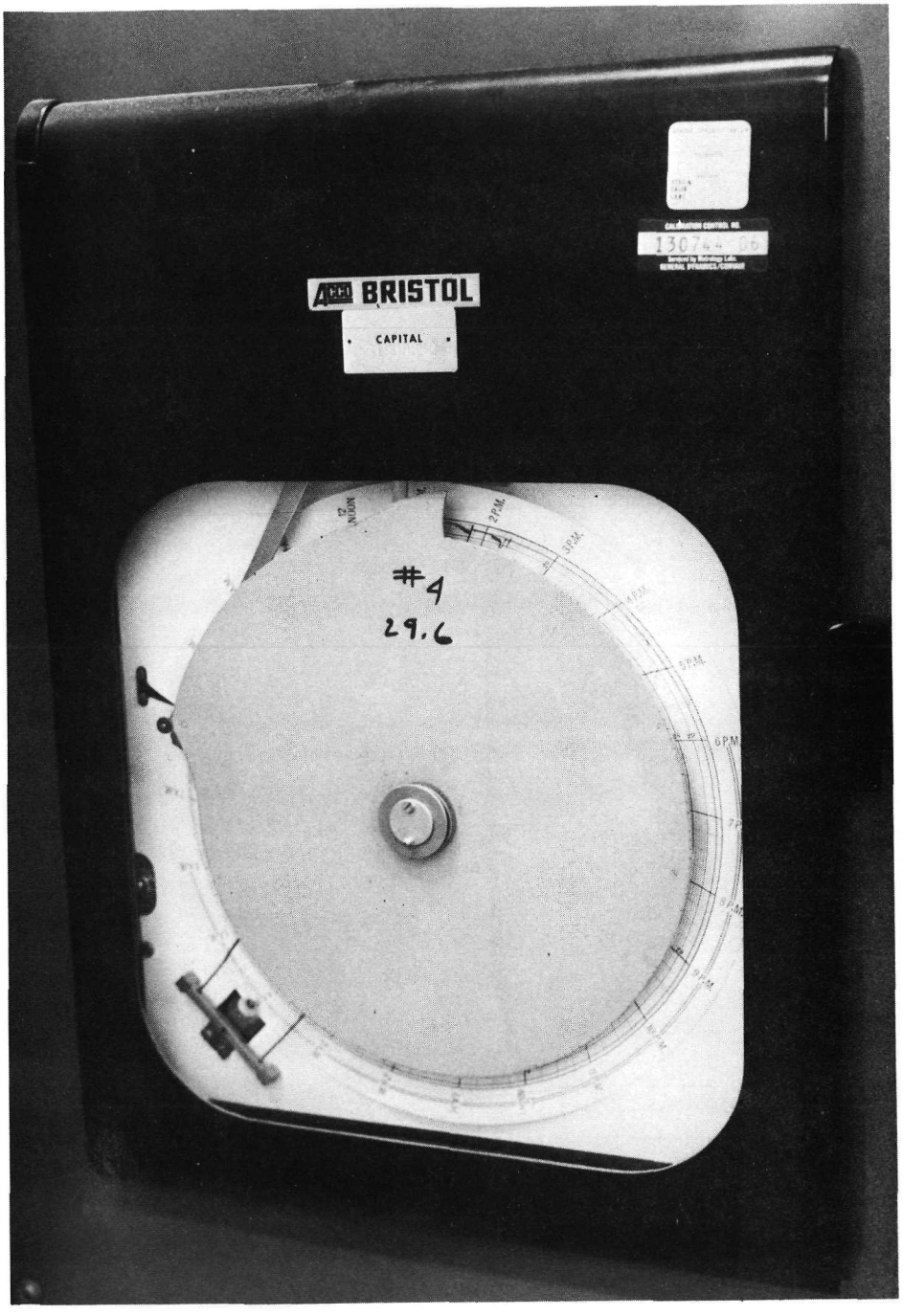


Figure 4-13. Bristol Pressure Programmer (Photo 117206B)

4.2.3.2 Creep measurements: Cyclic creep measurements were performed concurrently with the flight simulation testing. Permanent creep extension was determined periodically during the 100 flight cycles for all parent metal and electron beam welded specimens and selected diffusion bonded specimens. The technique used was to (1) suitably mark the specimens, (2) expose for about 10 flight cycles, (3) remove from the simulator and measurement separation of the fiducial marks, and (4) repeat measurements after approximately every 10 cycles.

The major difficulty was in obtaining a stable set of fiducial marks within the gage section of the specimens. These gage marks must survive the high-temperature exposure conditions and not degrade either the oxidation resistance of the coating or the strength of the substrate. Several techniques were tried. Spot welded iridium wires and high-temperature cements (Sauereisen No. 8 and Synar) did not adhere to the specimens under thermal cycling. Hardness indentations fell into two categories: those large enough to be visible severely cracked the coating, while those that didn't crack the coating were not clearly visible. The best marking method found was to use light scratches and hard (6H) pencil lines. The scratches were preferred, but generally didn't last as long as the pencil marks. Both types of marks tended to be removed by coating spalling. However, it was generally possible to re-mark the specimens (pencil only) during the 10-cycle examinations and, thereby, obtain a complete record of the creep strain. As an added precaution, gage marks were placed on both sides of each specimen. All specimens had at least two sets of gage marks, and many had three sets. Because of the difficulty in retaining fiducial marks and measuring them, a good deal of personal judgement was required in performing the measurements. At the end of 100 cycles (or failure) the data for each specimen were carefully examined along with notes and comments made from personal observations at the time of the measurements. The set of data points that was considered to be the most representative, based on engineering judgement, was then used to determine the individual creep curves.

Measurements of extension were made with a Gaertner cathetometer that, with careful use, could be read to 0.0025 cm. For the 5 cm gage section utilized in the tests, this allowed creep values to be recorded to 0.05 percent. Because of the finite thickness of the fiducial marks as well as changes in appearance during cycling (due to coating oxidation and spalling) the reproducibility of the optical creep measurements was found to be of the order of 0.005 cm or 0.1 percent.

4.2.4 Test procedure. — The following is a step-by-step description of the procedure used to perform the flight simulation exposures and concurrent cyclic creep measurements:

(1) Gage mark a set of four specimens and measure initial gage length.

(2) Attach upper and lower pullrods, tie on Pt/Pt+ 13 Rh thermocouple and load specimens into simulator.

(3) Pin lower pullrods to pneumatic force cylinders.

(4) Initiate flight cycle by starting Data-trak and pump down system. High-vacuum valve to diffusion pump will automatically open when chamber pressure reaches 50 microns (6.7 $N/m^2$).

(5) At completion of boost portion of cycle, manually close high-vacuum valve and initiate reentry rise by activating Bristol programmer.

(6) During exposure, rotate thermocouple selector switch through its four positions at each temperature plateau to record the temperatures of the four specimens.

(7) At the end of the cycle, open the system to atmospheric pressure, reset the Data-trak and Bristol programmers, and begin next cycle.

(8) At 10-cycle intervals, remove and visually examine specimens for evidence of coating spallation or failure, and any subsequent substrate attack. Measure creep extension and submit to NDE laboratory for examination and photography.

4.2.5 Test results and discussion. —

4.2.5.1 Material system evaluation: A total of 72 specimens (2 alloys, 2 coatings, 3 conditions, 6 replicates) were exposure tested in the flight simulation portion of the test program. The results are summarized in Table 4-3. These specimens received 6324 total cycles with 39 completing 100 cycles and 33 failing in from 42 to 97 cycles. The term "failure" as used for these tests denotes complete specimen fracture.

Table 4-3. Flight Simulation Test Results

| Alloy | Coating | Condition | Test Sets | Cycles |
|---|---|---|---|---|
| Cb-752 | Sylvania | Parent | D, K | 100, 100, 100, 100, 100, 100 |
| Cb-752 | Sylvania | EB Weld | A, F | 100, 100, 100, 100, 100, 97* |
| Cb-752 | Sylvania | Diff. Bond | J, M | 100, 100, 100, 100, 100, 100 |
| Cb-752 | Vac-Hyd | Parent | C, K | 89*, 85*, 84*, 83*, 69*, 42* |
| Cb-752 | Vac-Hyd | EB Weld | B, F | 65*, 61*, 61*, 57*, 50*, 49* |
| Cb-752 | Vac-Hyd | Diff. Bond | N, P | 75*, 69*, 61*, 58*, 55*, 44* |
| C-129Y | Sylvania | Parent | D, L | 100, 100, 100, 100, 100, 100 |
| C-129Y | Sylvania | EB Weld | G, M | 100, 100, 100, 100, 100, 100 |
| C-129Y | Sylvania | Diff. Bond | H | 100, 100, 100, 100, 100, 100 |
| C-129Y | Vac-Hyd | Parent | C, O | 100, 100, 100, 91*, 86*, 78* |
| C-129Y | Vac-Hyd | EB Weld | G, P | 100, 94*, 90*, 89*, 79*, 62* |
| C-129Y | Vac-Hyd | Diff. Bond | E | 96*, 89*, 88*, 80*, 74*, 74* |

Note: * Indicates failure  Total cycles: 6324

During exposure testing, the specimens were removed from the simulator at 10 to 15 cycle intervals for visual examination, and, in addition, photographs were taken to retain a permanent record of any coating changes. The following is a description of the simulation results based on these visual observations for each group of specimens (alloy/coating/ condition). Typical photographs (black and white) showing the changes in coating appearance with cycling are also included. Finally, color photographs of the specimens at the completion of 100 cycles or failure were taken to document typical post-cycling coloration.

Group 1, Cb-752/R-512E, parent: During the first 10 cycles, the light gray metallic color of the as-coated specimens changed to a dark grey on one side and a light yellow-green-brown on the other. The difference in appearance of the two sides arises from the coating process. During firing, the specimens were placed on a silica support with one surface in contact with the silica, and the other surface untouched. Why this would affect the initial color changes during simulation testing was not determined. In addition to the color changes, a light surface and edge spall occurred as cycling progressed. Spalling of the dark side was generally heavier and revealed a light underlayer similar in color to the light side. After about 50 cycles, the two sides were similar in color. During the last 50 cycles, light spalling of the surface continued, and the center portions (both sides) darkened in color. This center darkening is believed to have been the result of the Irish Refrasil used for attaching the thermocouples. All six specimens survived 100 cycles in very good condition. The only coating failure observed was in a loading pin hole in the grip end of one specimen. Severe attack and considerable substrate consumption occurred. The reason for the failure was most likely accidential chipping of the coating around the hole during loading of the specimen into the simulator pullrod rather than a coating defect. A typical specimen as it appeared at various stages during the 100 simulation cycles is shown in Figures 4-14 and 4-15. Four of the specimens at the completion of 100 cycles are shown in Figure 4-16.

Group 2, Cb-752/R-512E, electron beam weld: The specimens in this group behaved very much like those in group 1 with the exception of one that failed during the ninety-seventh cycle. Failure occurred about 3/8 inch (0.95 cm) from the weld and did not appear to have been caused by oxidation. Figure 4-17 shows the specimen after 94 cycles and after failure (97 cycles). An enlargement of one of the failed ends is presented in Figure 4-18. No evidence of coating failure or severe oxidation is visible in either figure. The typical coating spall can be seen along with what appears to be some transverse coating cracks. The five specimens that survived 100 cycles exhibited slight coating spall and color changes very similar to those in group 1. The weld areas did not appear to have been affected any differently than the adjacent material, which gives an indication of the suitability of electron beam welds for this application. As was the case in the previous group, one specimen had a small area of coating failure at one of the loading pin holes. Photographs of a typical specimen as it progresses through the 100 cycles are shown in Figures 4-19 and 4-20. Figure 4-21 shows three of the specimens after the completion of 100 cycles.

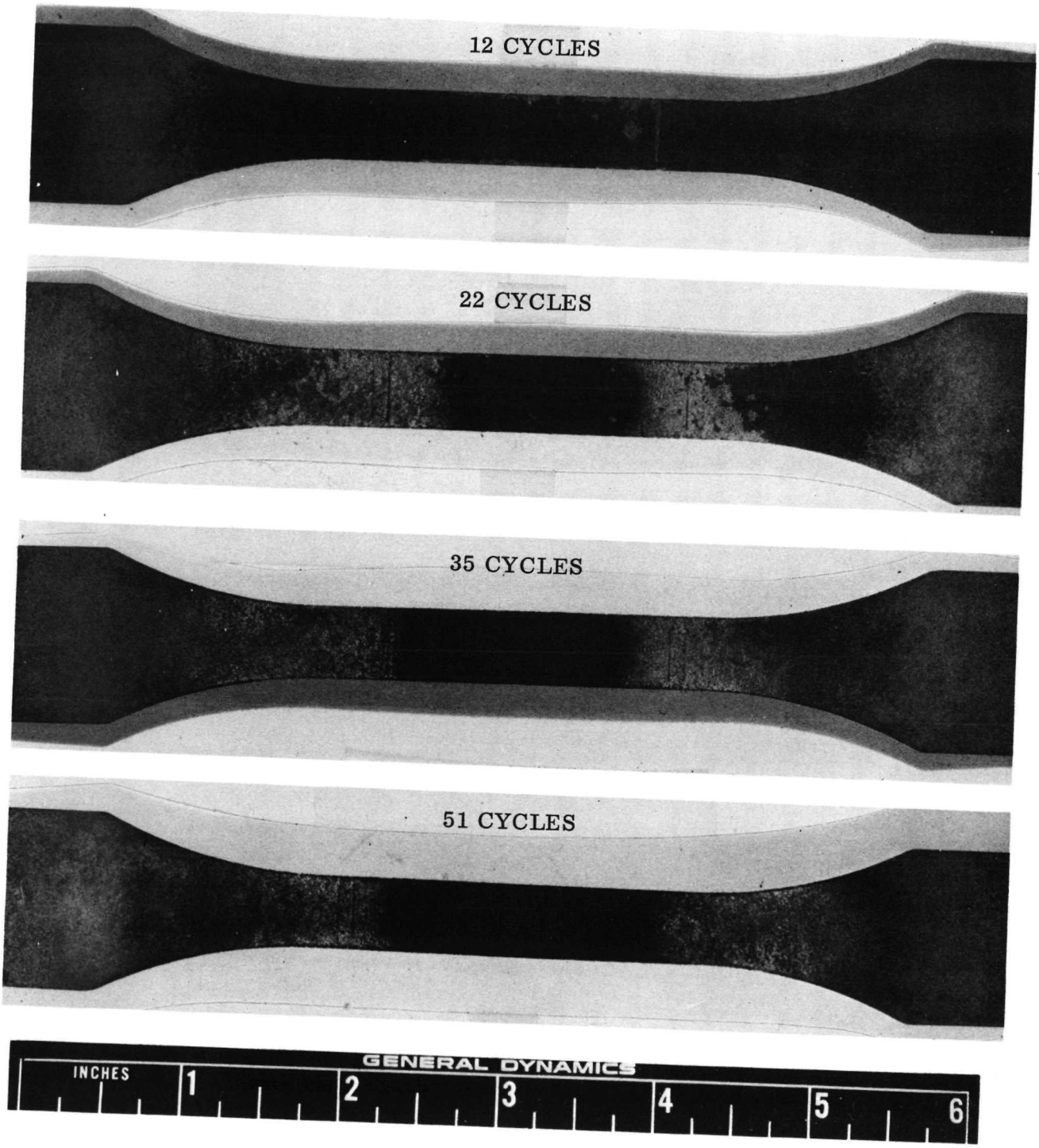


Figure 4-14. Cb-752/R-512E After Flight Simulation Exposure — Specimen BSP-4

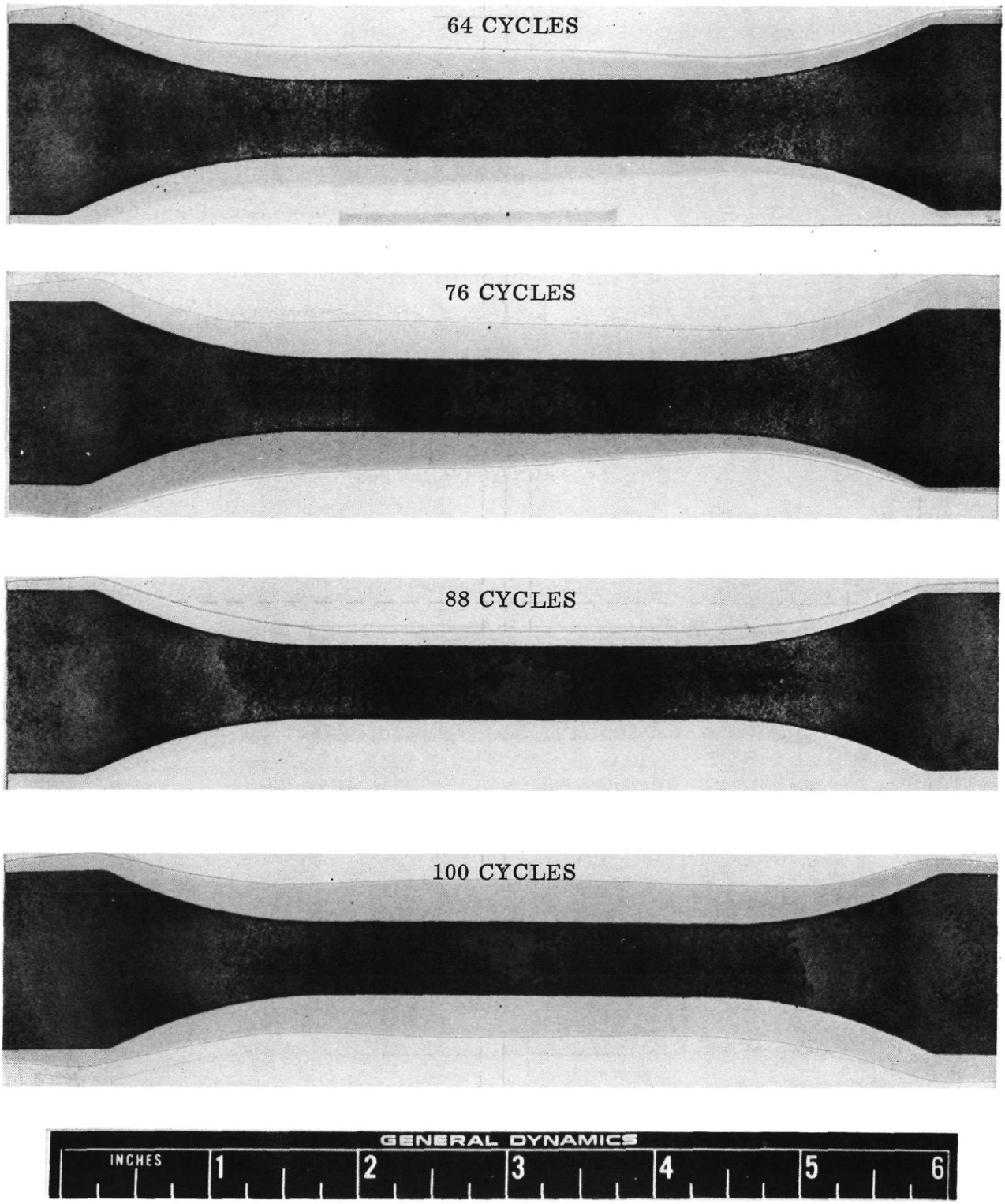


Figure 4-15. Cb-752/R-512E After Flight Simulation Exposure — Specimen BSP-4

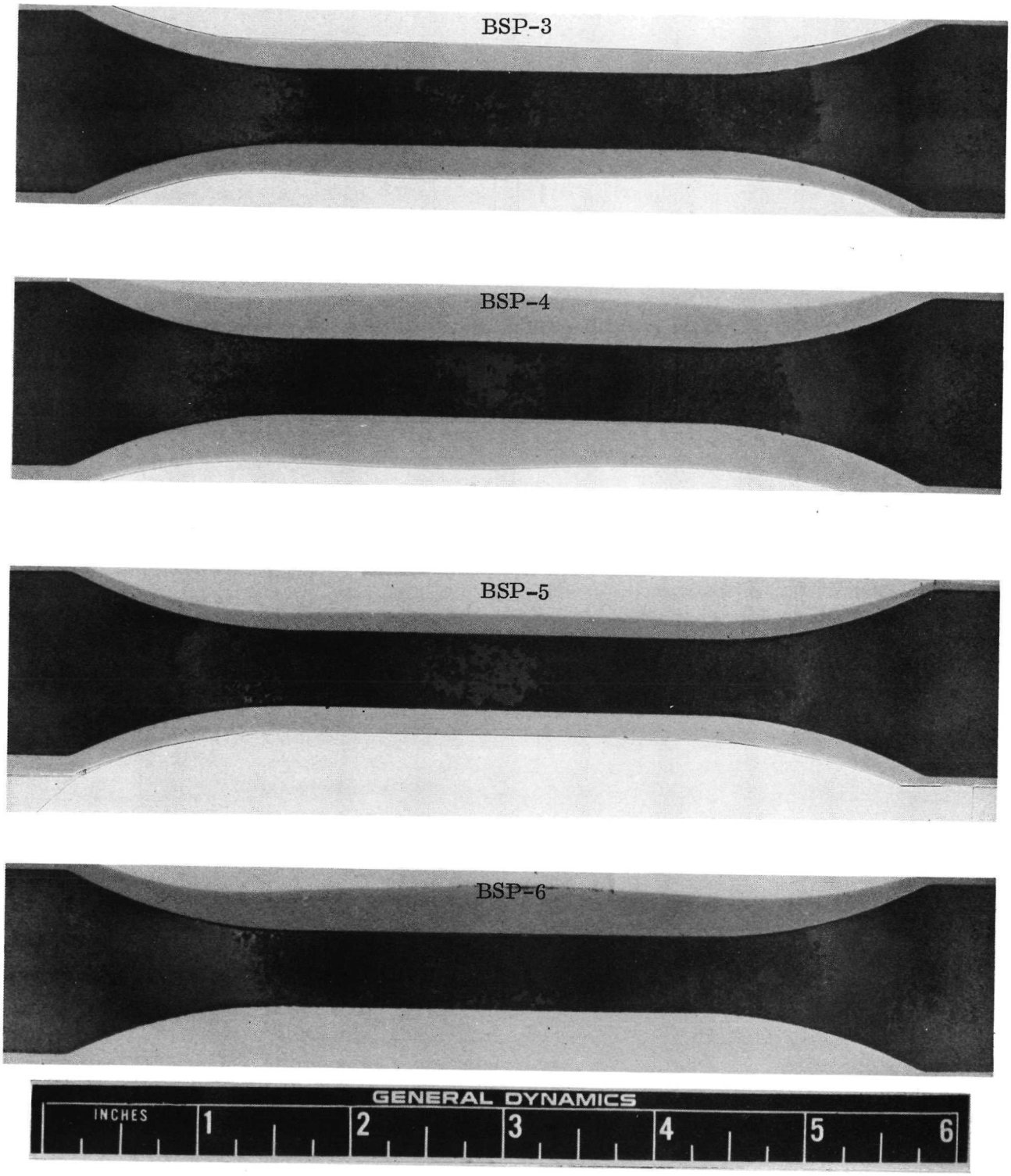


Figure 4-16. Cb-752/R-512E Parent Specimens After 100 Flight Simulation Exposure Cycles

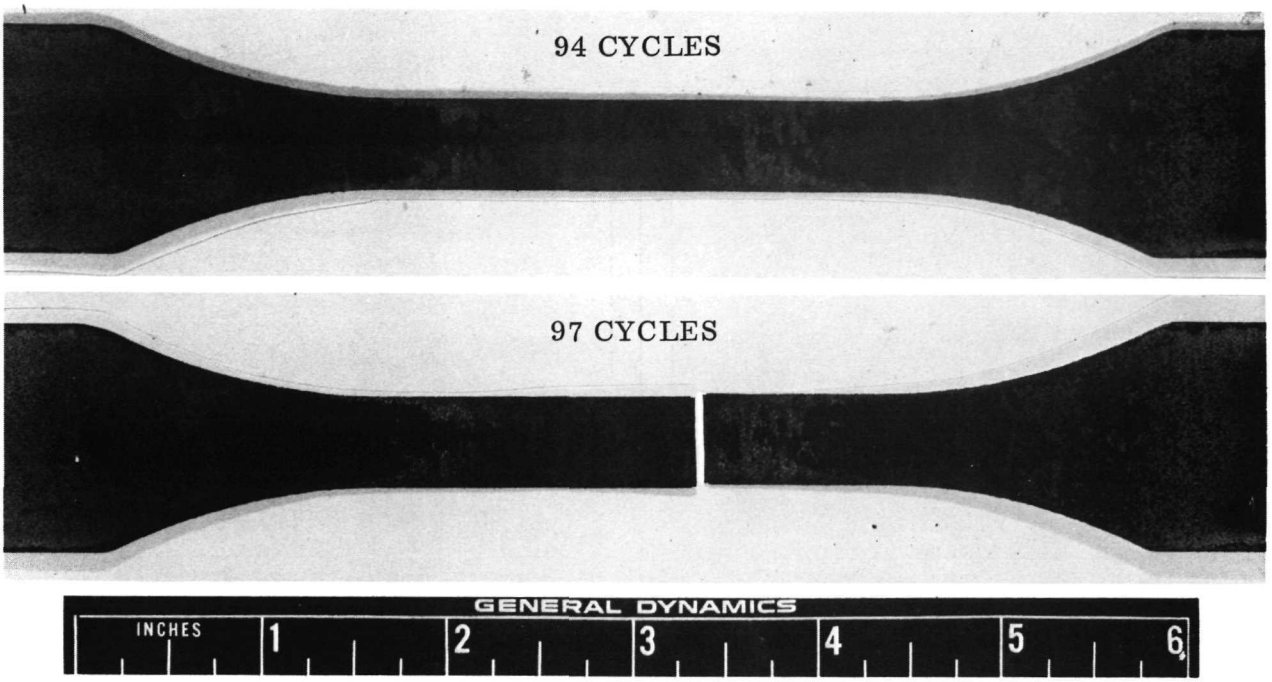


Figure 4-17. Cb-752/R-512E After Flight Simulation Exposure — Specimen BSE-10

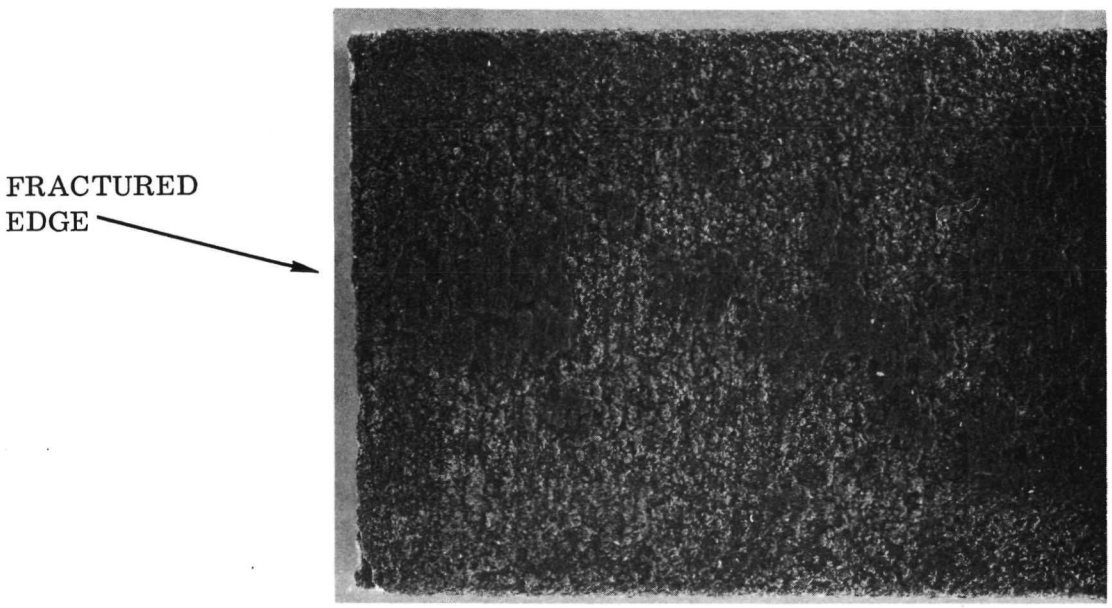


Figure 4-18. Enlargement of Fractured End — Specimen BSE-10 After 97 Flight Simulation Cycles (6X) (Photo D-920)

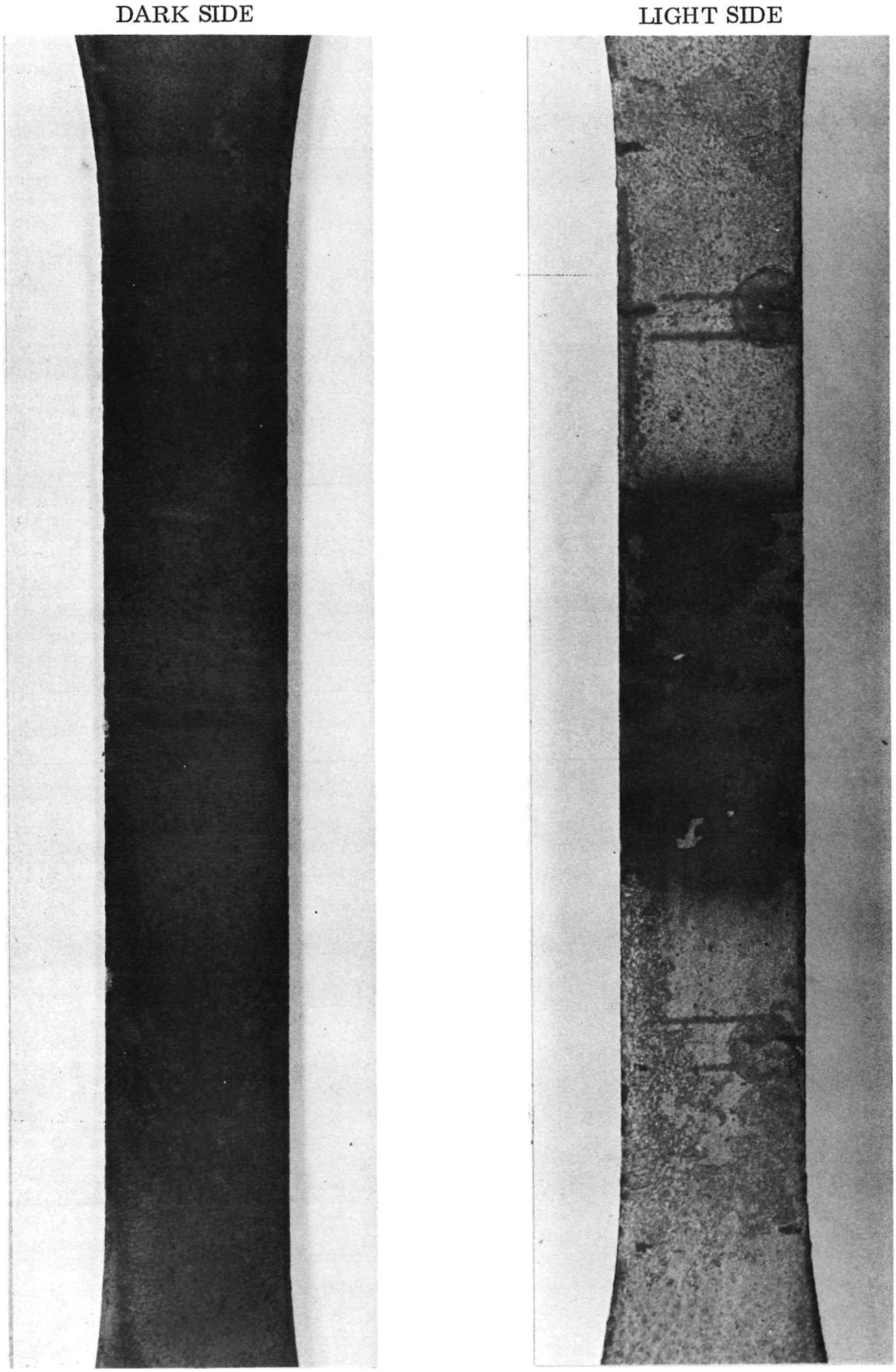


Figure 4-19. Cb-752/R-512E After 20 Flight Simulation Exposure — Specimen BSE-5

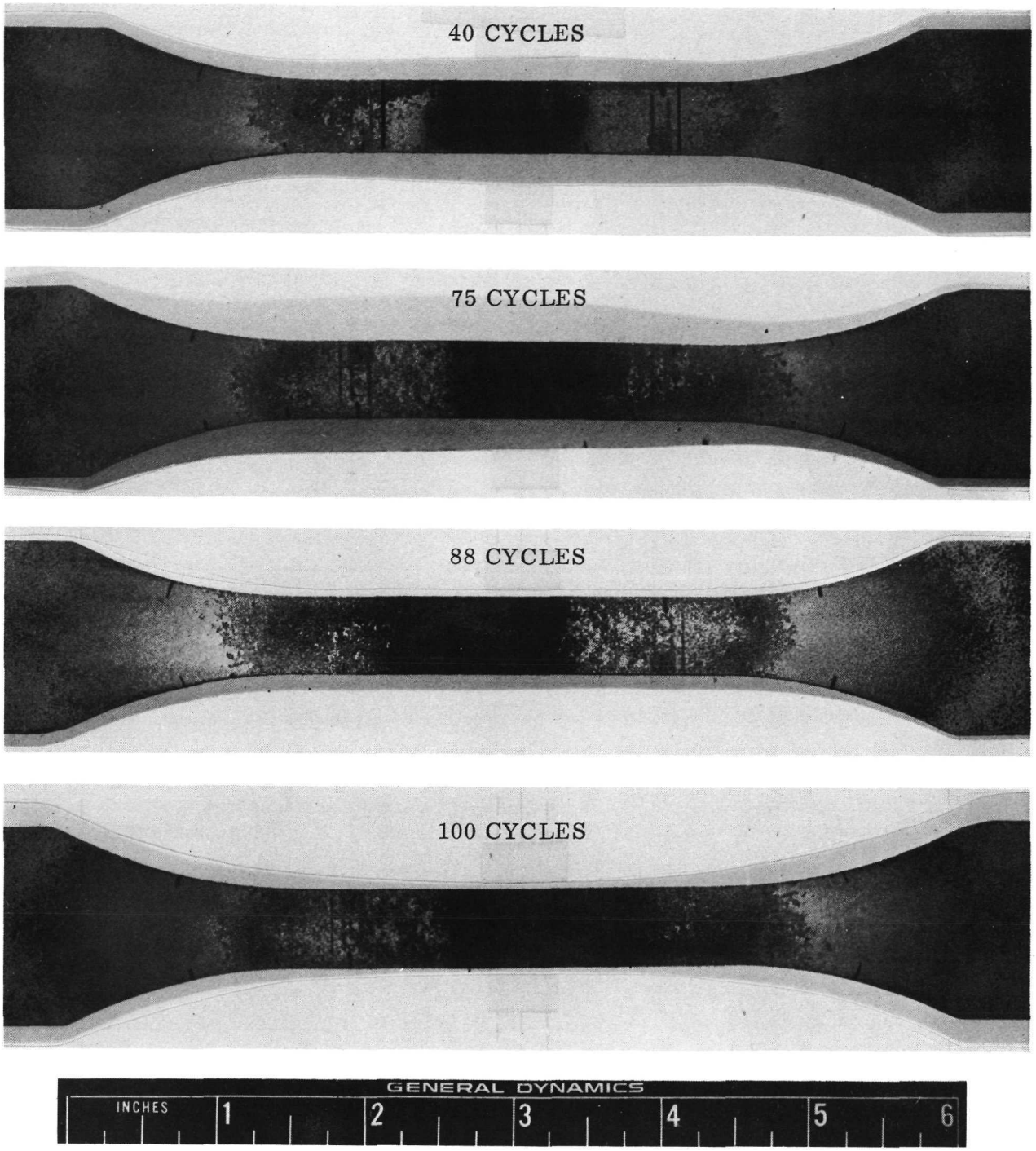


Figure 4-20. Cb-752/R-512E After Flight Simulation Exposure — Specimen BSE-5

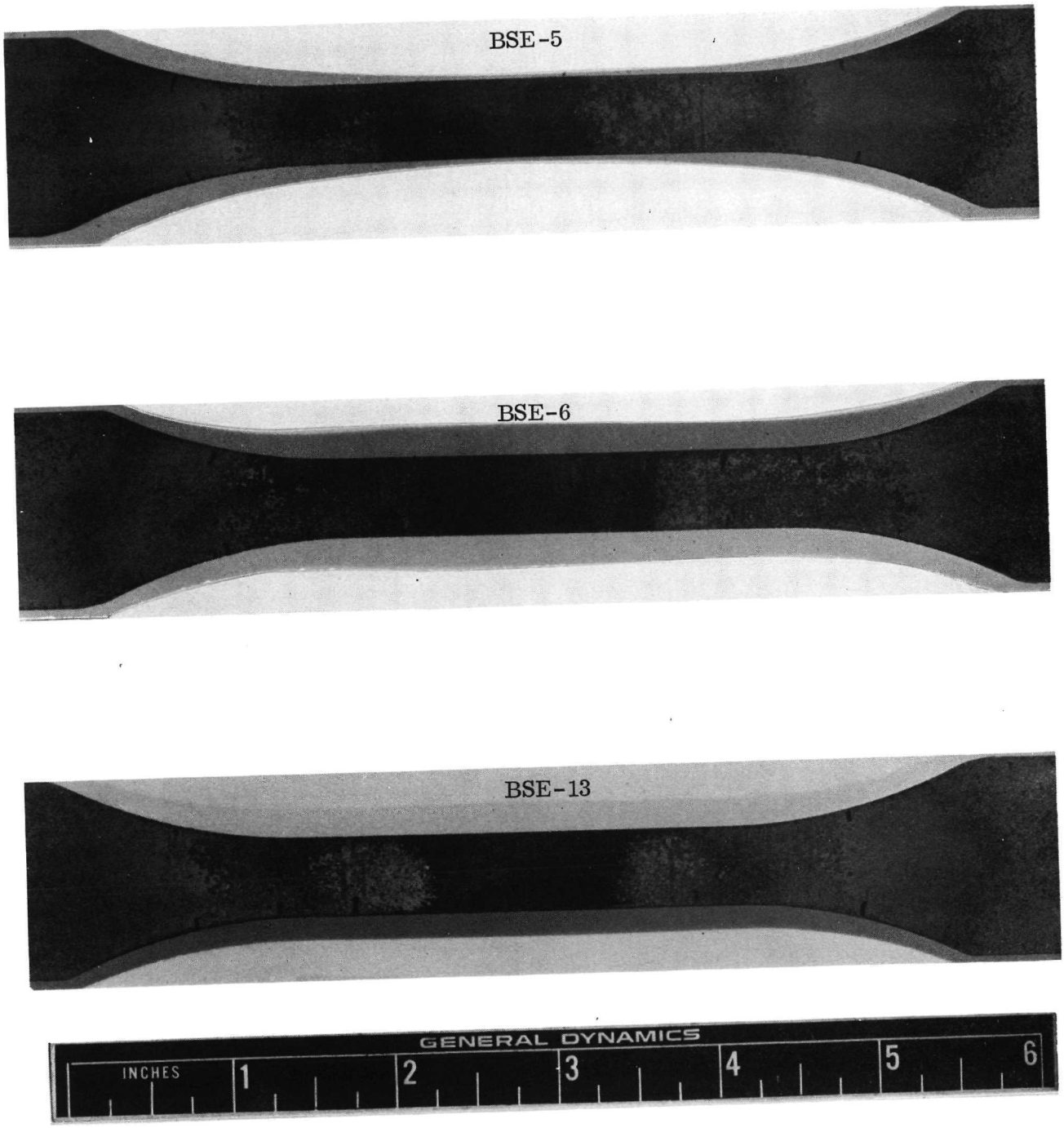


Figure 4-21. Cb-752/R-512E Electron Beam Weld Specimens After 100 Flight Simulation Exposure Cycles

Group 3, Cb-752/R-512E, diffusion bond: There was little difference in the behavior of this group from the previous ones. Color changes and light coating spall were the only visible effects of flight simulation testing with all six specimens surviving 100 cycles. In the early stages of exposure, light and dark sides were again observed on the specimens. Initially, in contrast to the first two groups, spalling was more prevalent on the lighter colored of the two sides. As cycling progressed (after 30 cycles), however, the darker sides showed more coating spall. In both cases, a lighter colored underlayer was revealed. During the last 50 simulation cycles, the center portions of the specimens darkened in color. No unusual behavior was observed in the 1/2-inch (1.27 cm) bond area. Figures 4-22 and 4-23 show a typical specimen as it proceeds through cycling, and Figure 4-24 shows four specimens at the end of test.

Group 4, Cb-752/VH-109, parent: During the first 10 cycles, the metallic color of the as-coated specimens changed to a light brown-grey with a small amount of green. Both sides were similar in appearance. A slight coating spall was present at the edges. Heavy surface spall occurred as early as 21 cycles on one specimen, and by 42 cycles was severe enough to cause failure. By the end of 50 cycles, all the remaining specimens showed heavy coating spall at both surfaces and edges. This surface attack increased in severity and by the eighty-ninth, all specimens had failed. Failures occurred during the high loads early in the boost portion of the flight cycle. While a great amount of coating spalled from the specimens, there appeared to be no consumption or erosion of substrate from either the surface or edges. The appearance and increase in severity of the coating attack is shown in Figures 4-25 and 4-26 as cycling progresses. Figure 4-27 shows four of the failed specimens. An enlargement of an area of severe spallation is found in Figure 4-28.

Group 5, Cb-752/VH-109, electron beam weld: The performance of these specimens, like the previous group, was very poor. All failed during test with cycle lives of between 49 and 65. Five of the six specimens failed early in the boost portion of the exposure cycle, while the sixth failed early in the entry portion at 2400°F (1589°K). All fractures were well away from the weld-affected zones. The behavior of these specimens was considerably different than those of group 4, however. After only 10 cycles, severe edge failure with the beginning of substrate attack had occurred as shown in Figure 4-29. By 20 cycles, edge failures were prevalent on all specimens, both in the reduced section and the cooler grip ends. This edge attack increased with cycling with as much as 0.10 inch (0.25 cm) of material completely consumed in the worst cases. For several specimens this severe edge attack occurred on only one side. After approximately 40 cycles severe surface spall, similar to that found in the previous group, was observed. Both surface and edge attack continued until all specimens had failed. Figure 4-30 illustrates how the coating attack progressed during cycling. A photograph of four failed specimens is presented in Figure 4-31. Portions of specimen BVE-15 had previously been removed for metallographic examination.

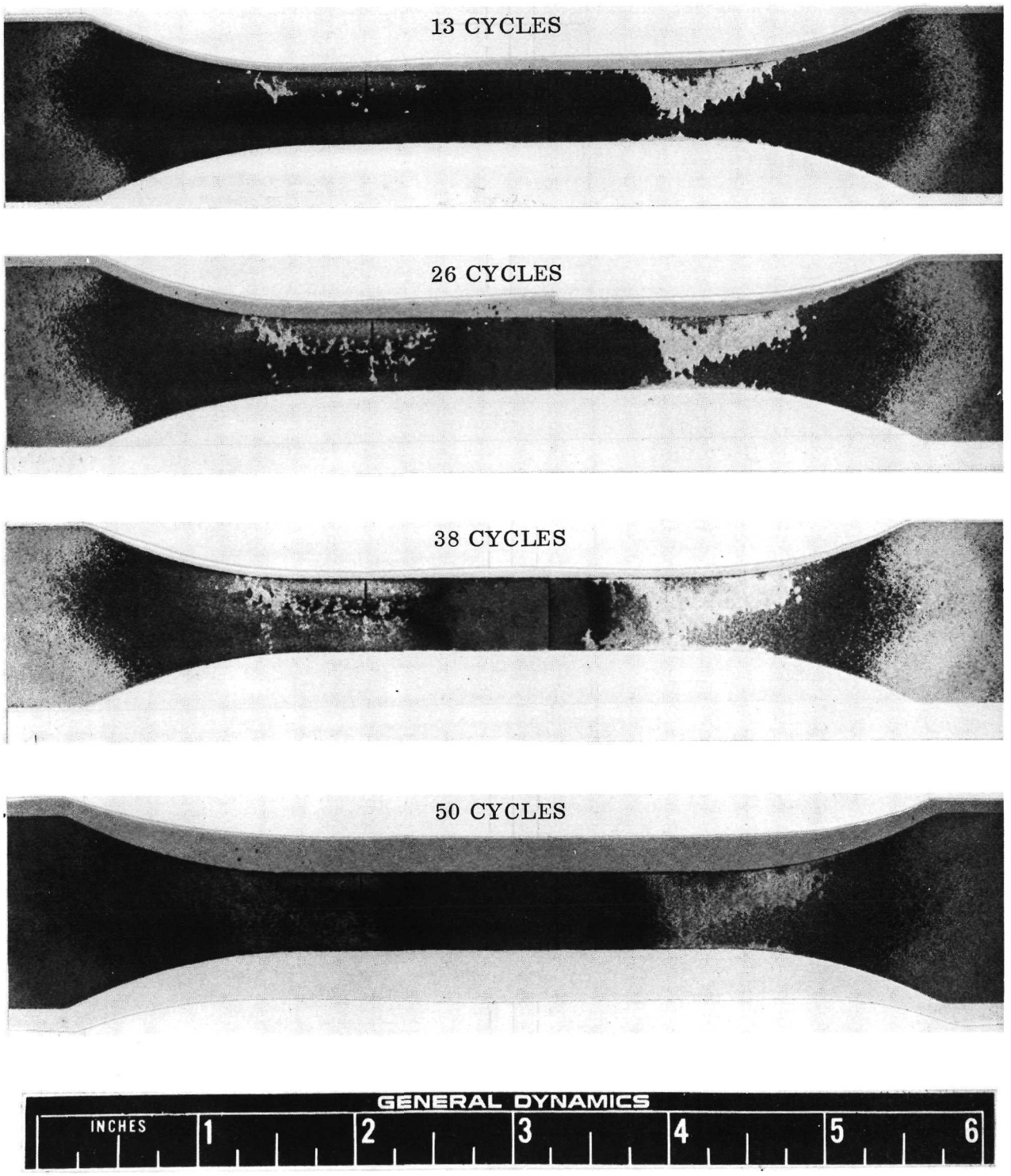


Figure 4-22. Cb-752/R-512E After Flight Simulation Exposure — Specimen BSD-5

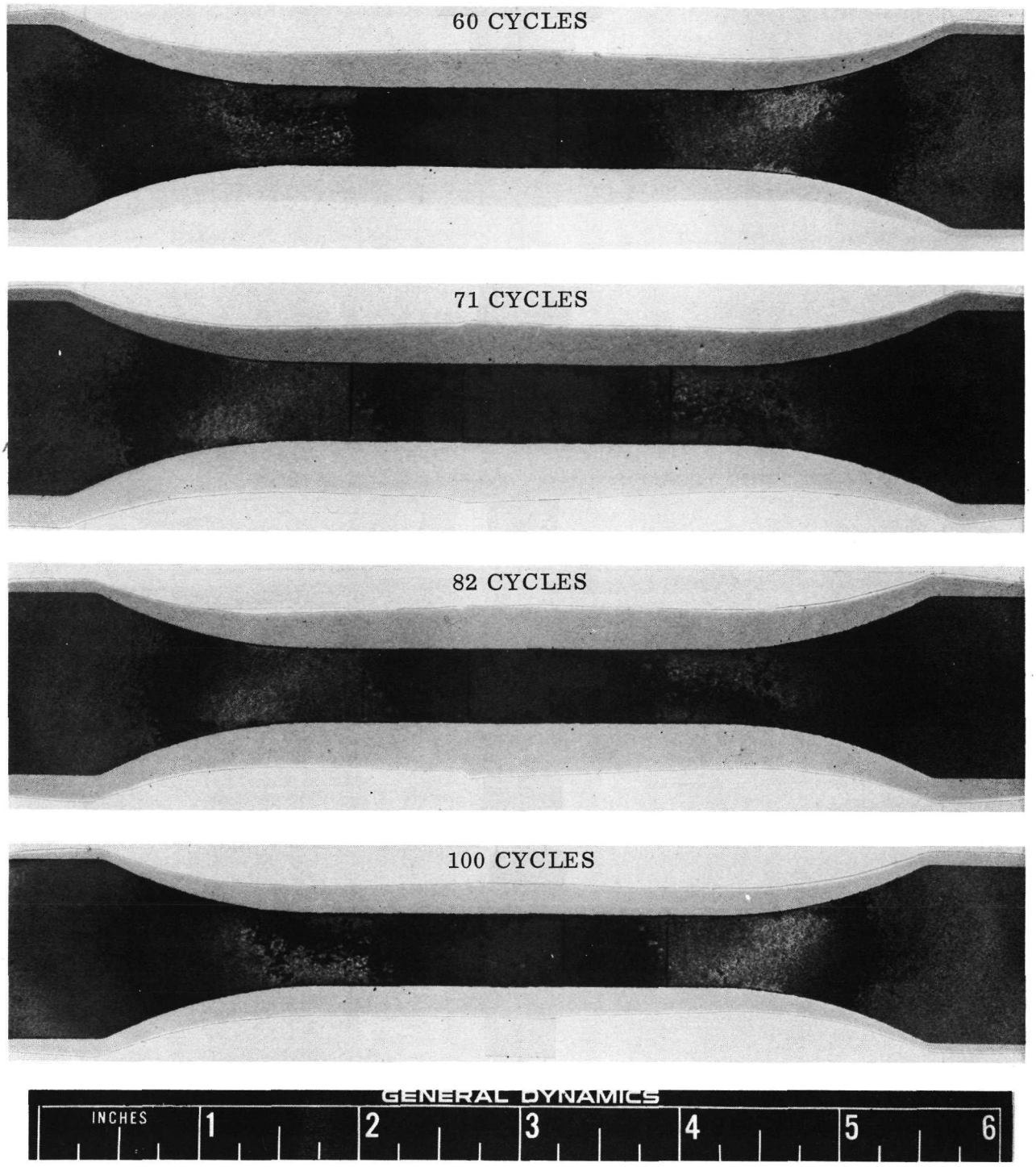


Figure 4-23. Cb-752/R-512E After Flight Simulation Exposure — Specimen BSD-5

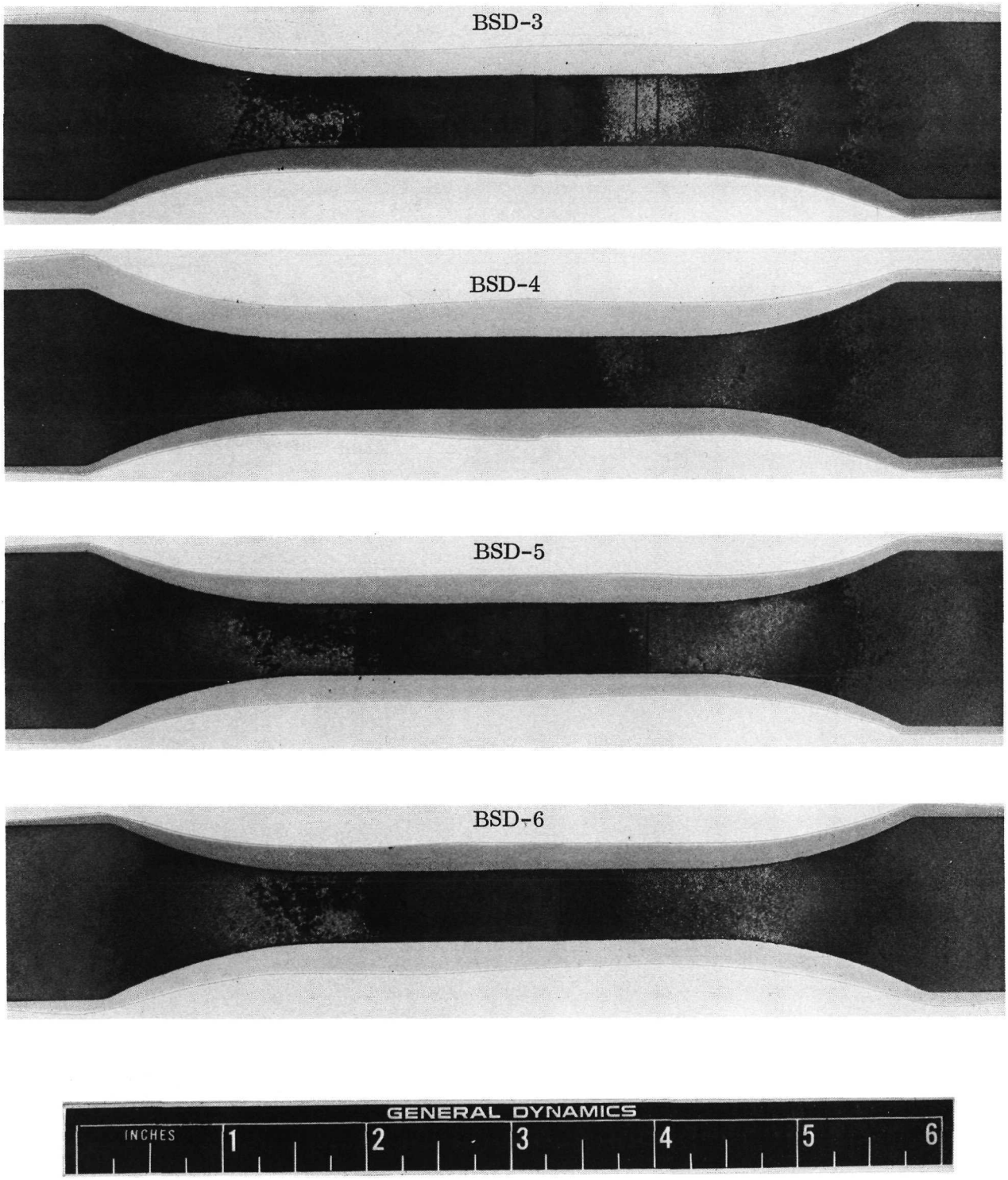


Figure 4-24. Cb-752/R-512E Diffusion Bond Specimens After 100 Flight Simulation Exposure Cycles

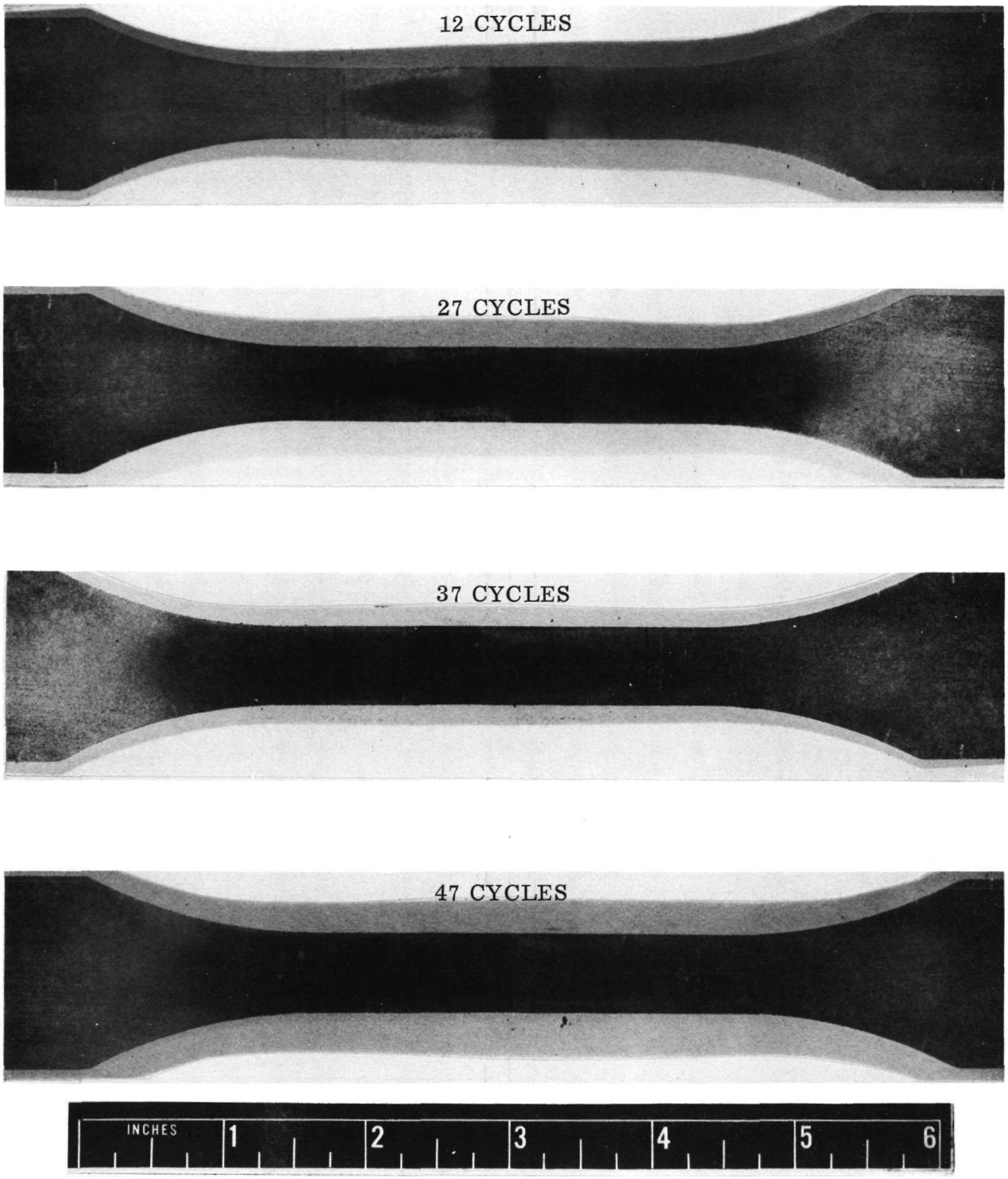


Figure 4-25. Cb-752/VH-109 After Flight Simulation Exposure — Specimen BVP-6

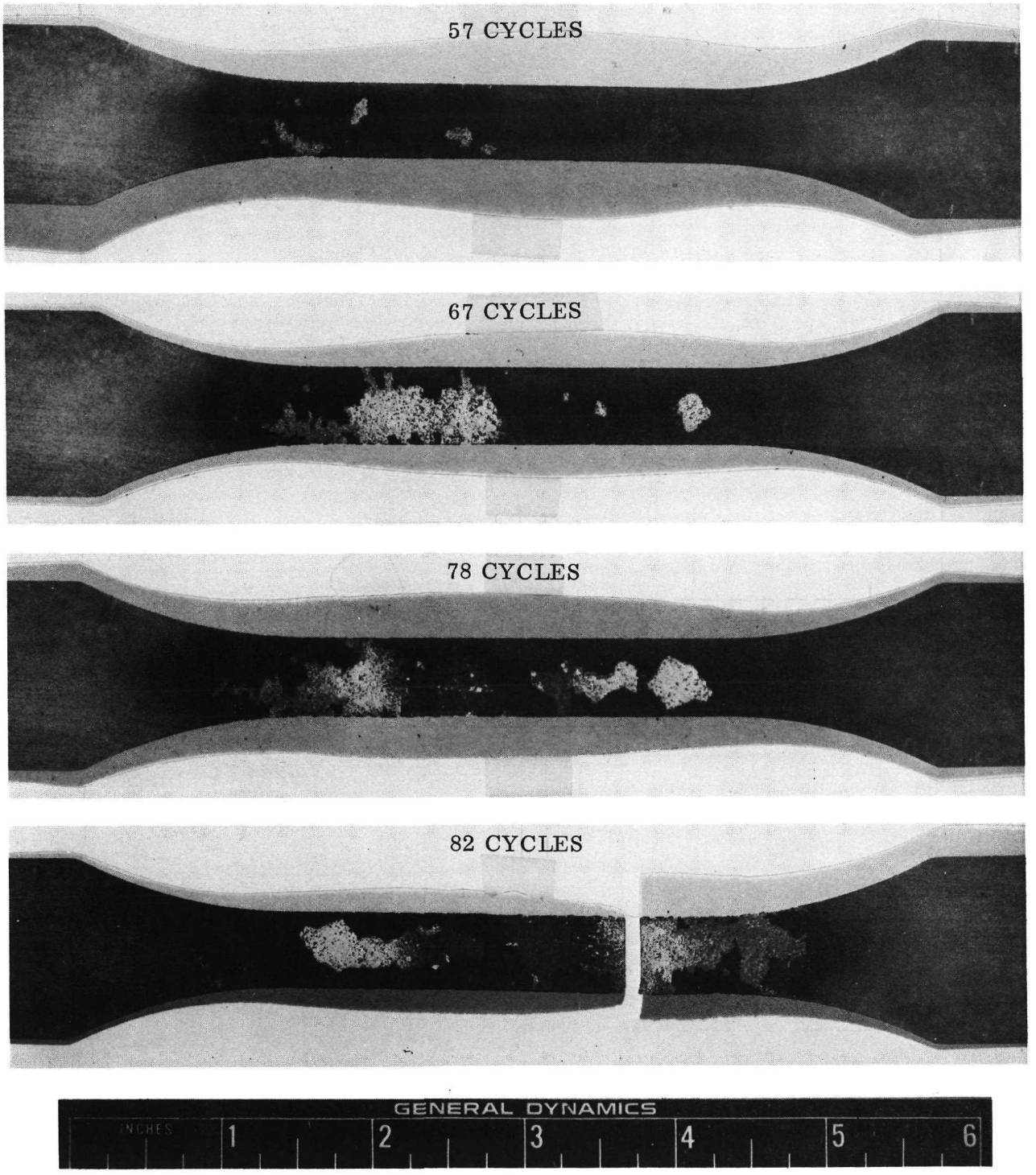


Figure 4-26. Cb-752/VH-109 After Flight Simulation Exposure — Specimen BVP-6

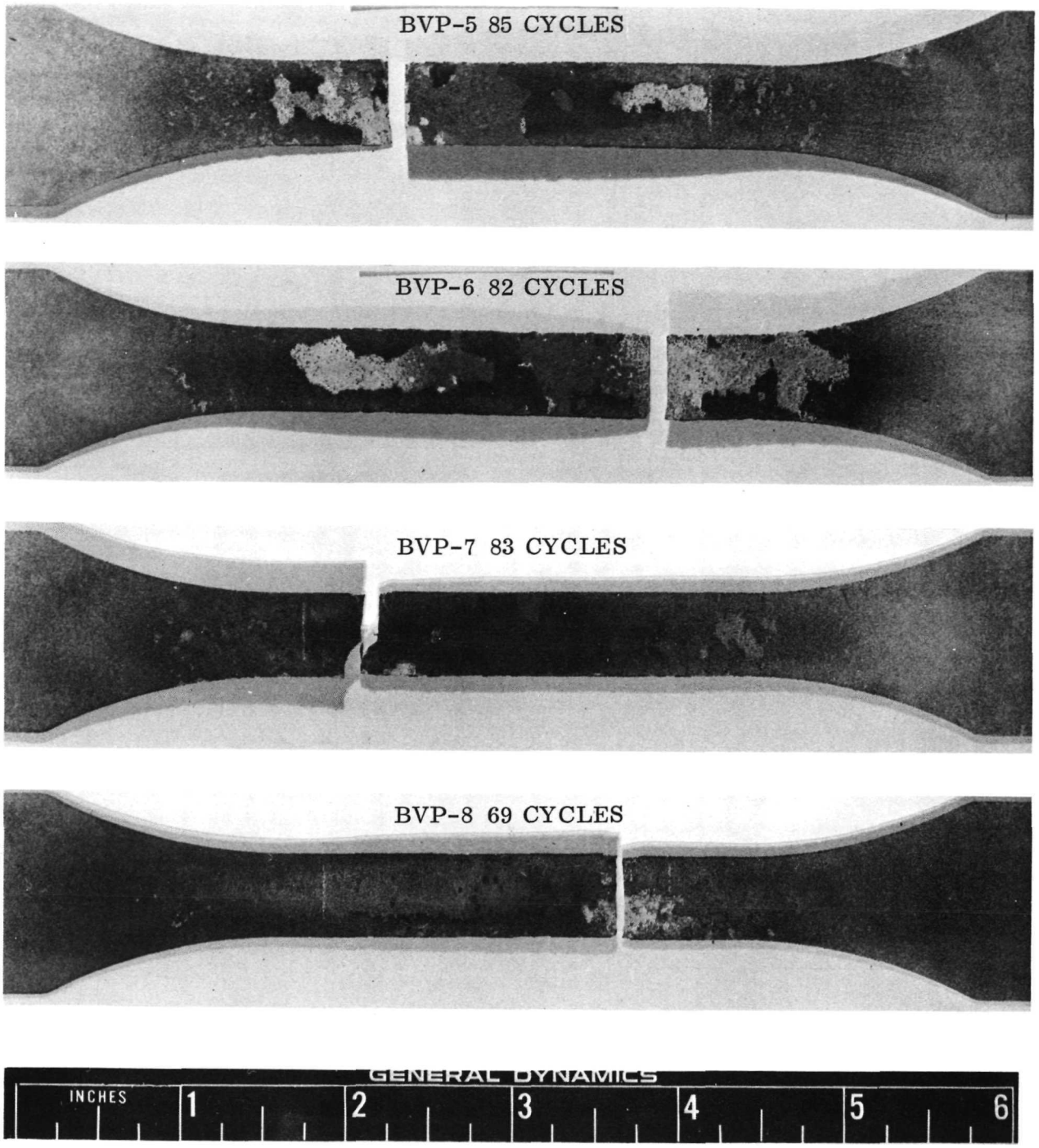


Figure 4-27. Cb-752/VH-109 Parent Specimens After Flight Simulation Exposure

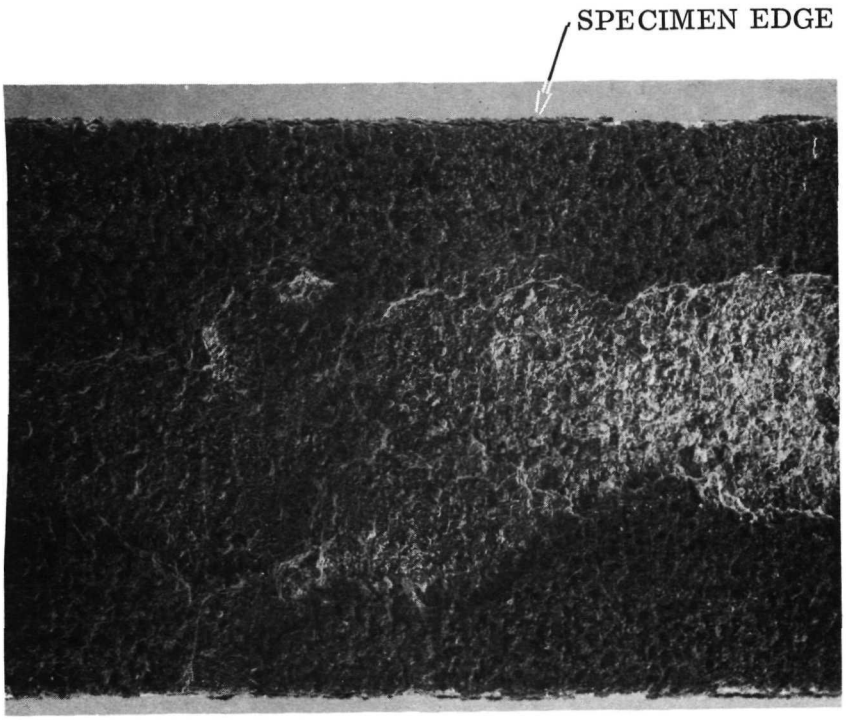


Figure 4-28. Enlargement of Spall Area — Specimen BVP-6 After 82 Flight Simulation Cycles (6X) (Photo D-924)

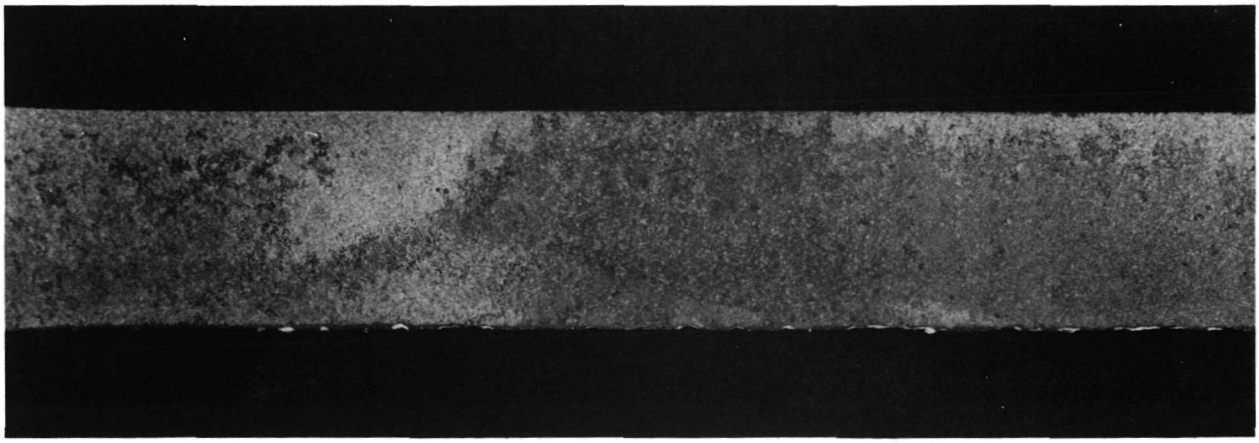

Figure 4-29. Cb-752/VH-109 After 10 Flight Simulation Exposure Cycles – Specimen BVE-13 (Photo C-9533)

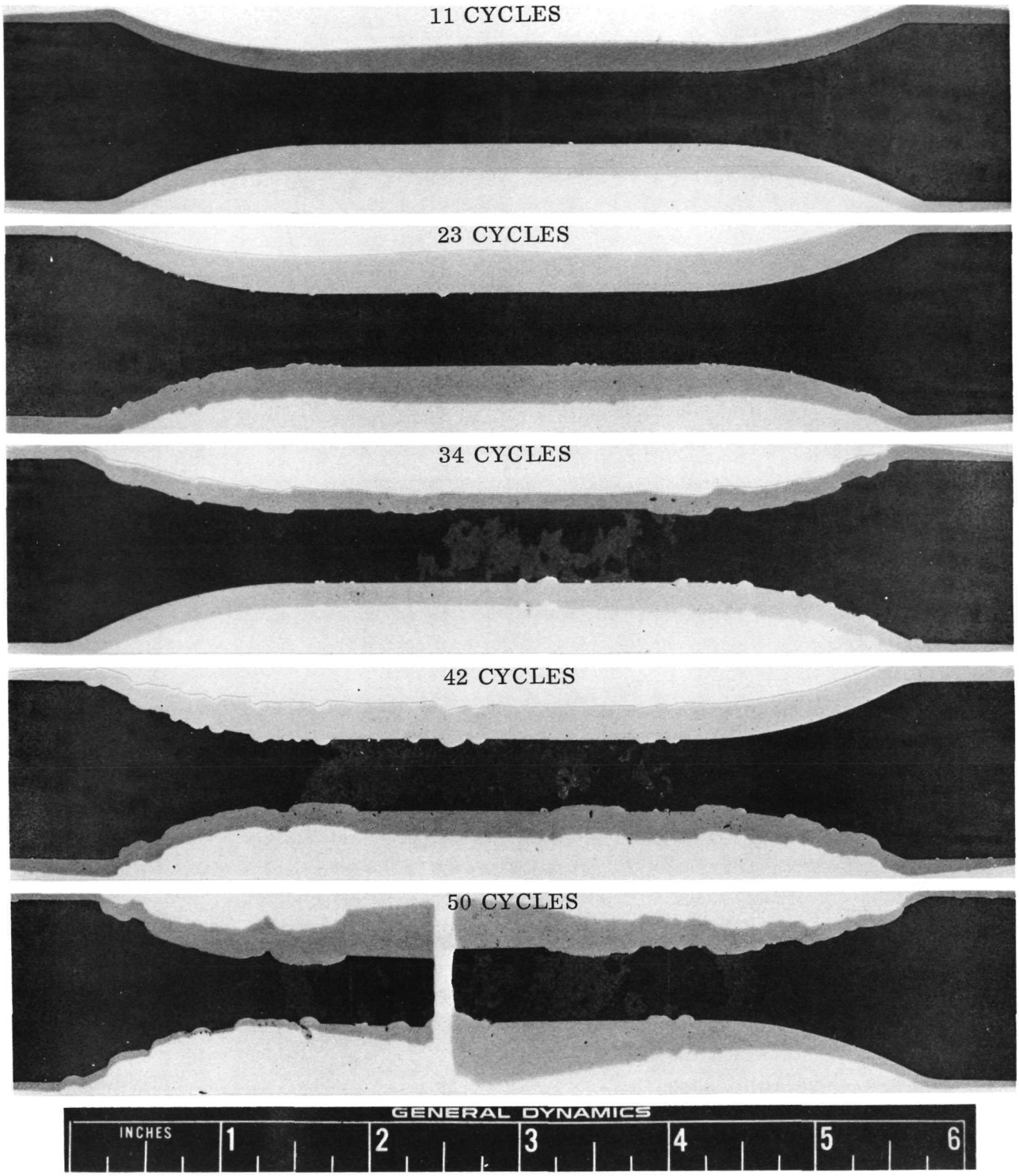


Figure 4-30. Cb-752/VH-109 After Flight Simulation Exposure — Specimen BVE-4

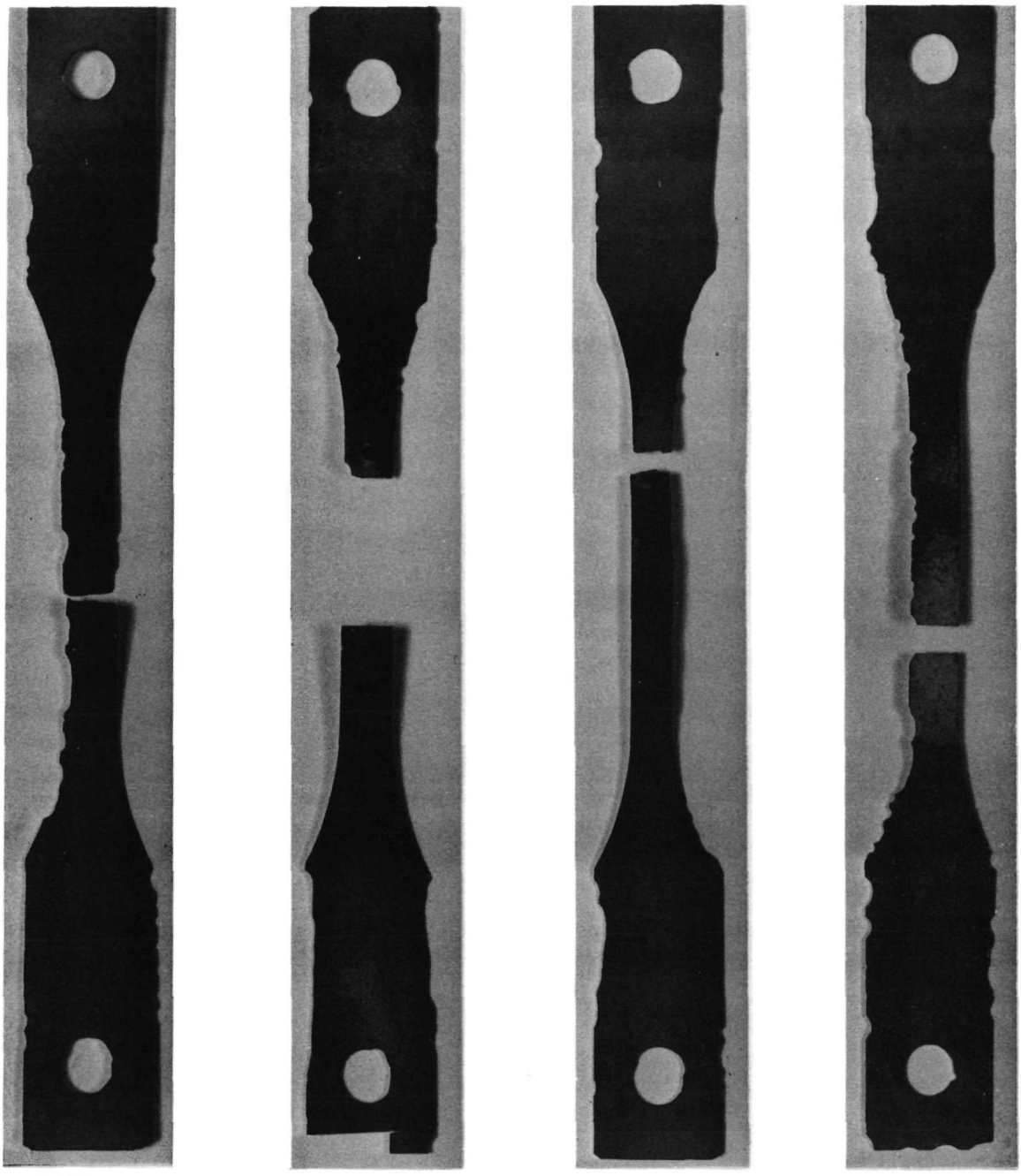

BVD-6
49 CYCLES

BVE-15*
56 CYCLES

BVE-13
61 CYCLES

BVE-14
61 CYCLES

*Sectioned for metallographic examination.

Figure 4-31. Cb-752/VH-109 Electron Beam Weld Specimens After Flight Simulation Exposure

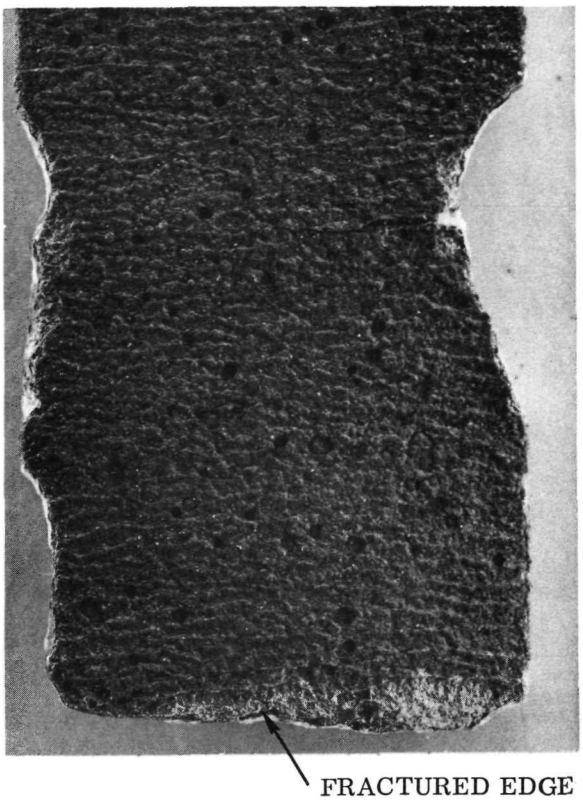


Figure 4-32. Enlargement of Fractured End — Specimen BVE-6 (Electron-Beam-Welded Cb-752/VH-109) After 49 Flight Simulation Cycles (6X) (Photo D-923)

An enlargement of one of the specimens to show the edge erosion more clearly is presented in Figure 4-32. A rather large crack that has initiated from an attack site is visible. Final specimen failure generally occurred at locations of this type.

Group 6, Cb-752/VH-109, diffusion bond: The specimens of this group reacted in a manner similar to those of group 4, but with a somehwat lower average lifetime, 60 versus 75 cycles. Also, the color changes were slightly different. The initial color after 10 cycles was a dark green-brown with some trace of yellow, as opposed to the much smaller amount of green in group 4. Some light-to-moderate surface spall occurred during the early cycles. The first severe attack was visible at 33 cycles, and increased rapidly thereafter. As was the case with group 4, and in contrast to group 5, no substrate consumption or erosion at the edges was observed. Failure in all specimens initiated in areas of severe coating spall well away from the bond areas. Generally, the 1/2 inch (1.27 cm) overlap bond areas were free of surface spall. Because of the double thickness of material in these sections, stresses are cut in half and creep elongations would be well below those in the remainder of the gage section. The creep deformation is apparently responsible, in part, for the severe surface spallation. Figures 4-33 and 4-34 depict a typical specimen of this group as it progresses through flight simulation testing. Four of the completed specimens are shown in Figure 4-35.

Group 7, C-129Y/R-512E, parent: During the first 10 cycles, the as-coated metallic color of these specimens changed to a dark grey on one side, and a medium brown-yellow on the other. All specimens survived 100 exposure cycles with only light-to-moderate coating spall. Two specimens did show a few local failure sites on the edges, but they were very shallow and did not appear to extend to the substrate.

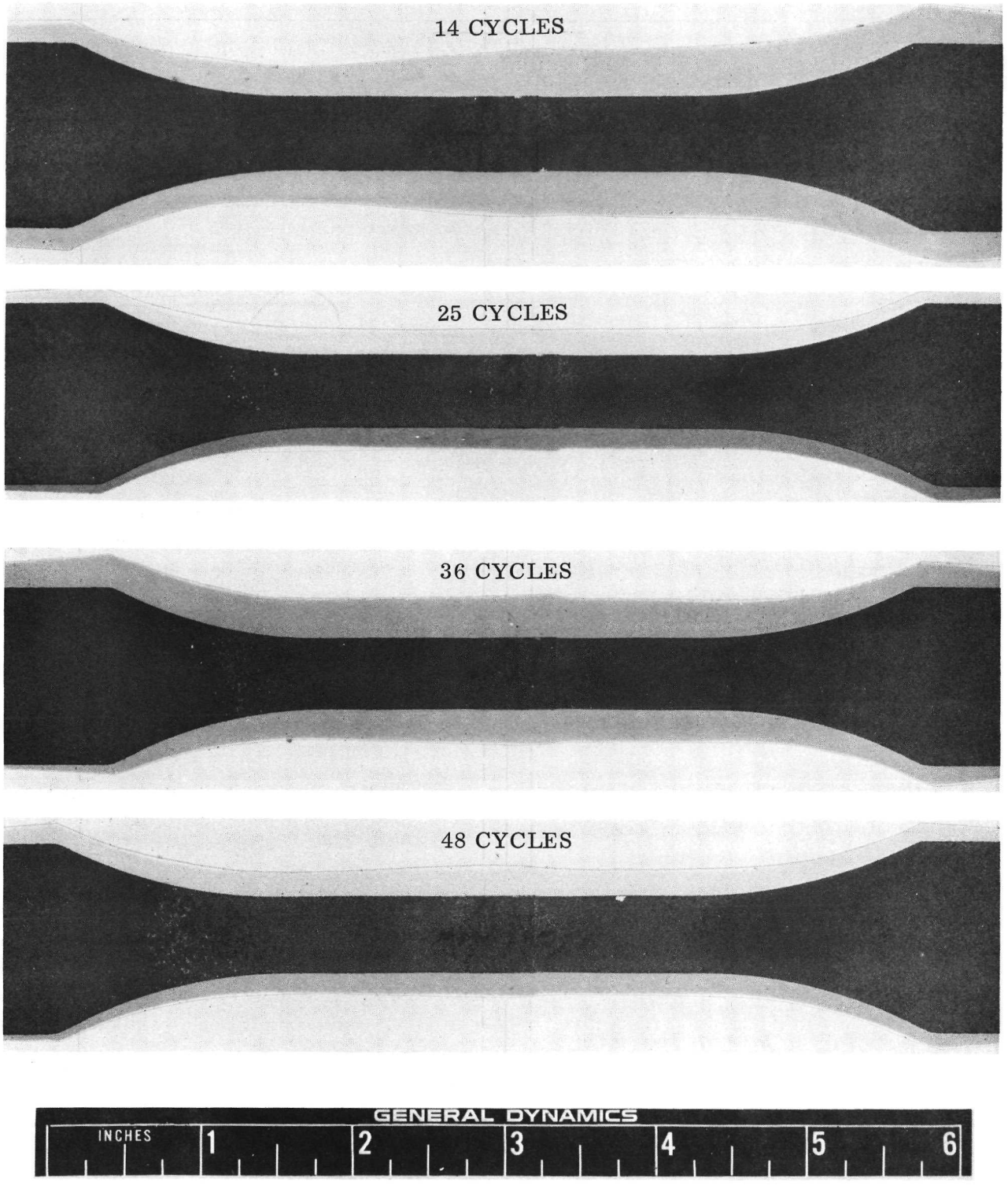


Figure 4-33. Cb-752/VH-109 After Flight Simulation Exposure — Specimen BVD-4

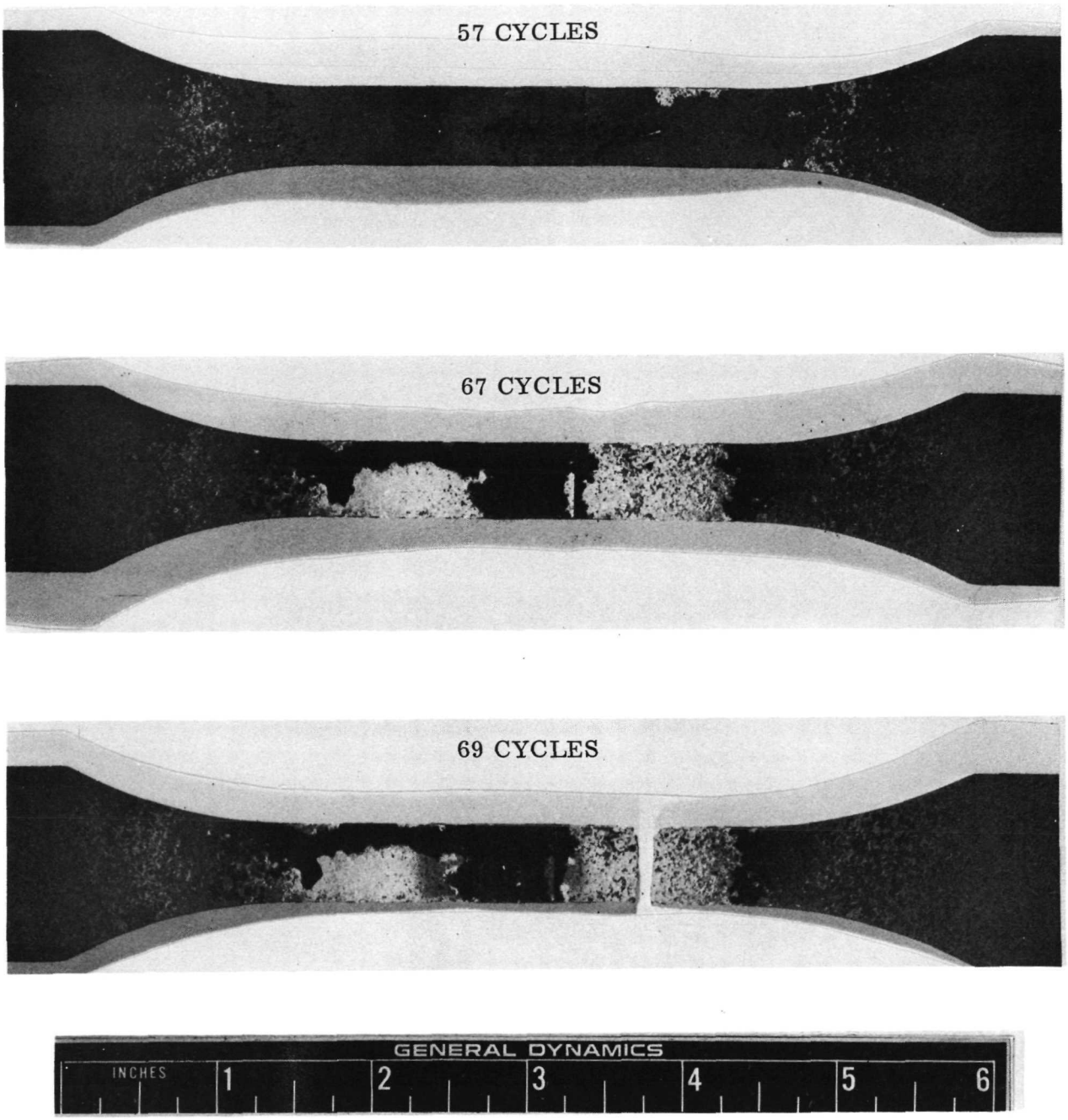


Figure 4-34. Cb-752/VH-109 After Flight Simulation Exposure — Specimen BVD-4

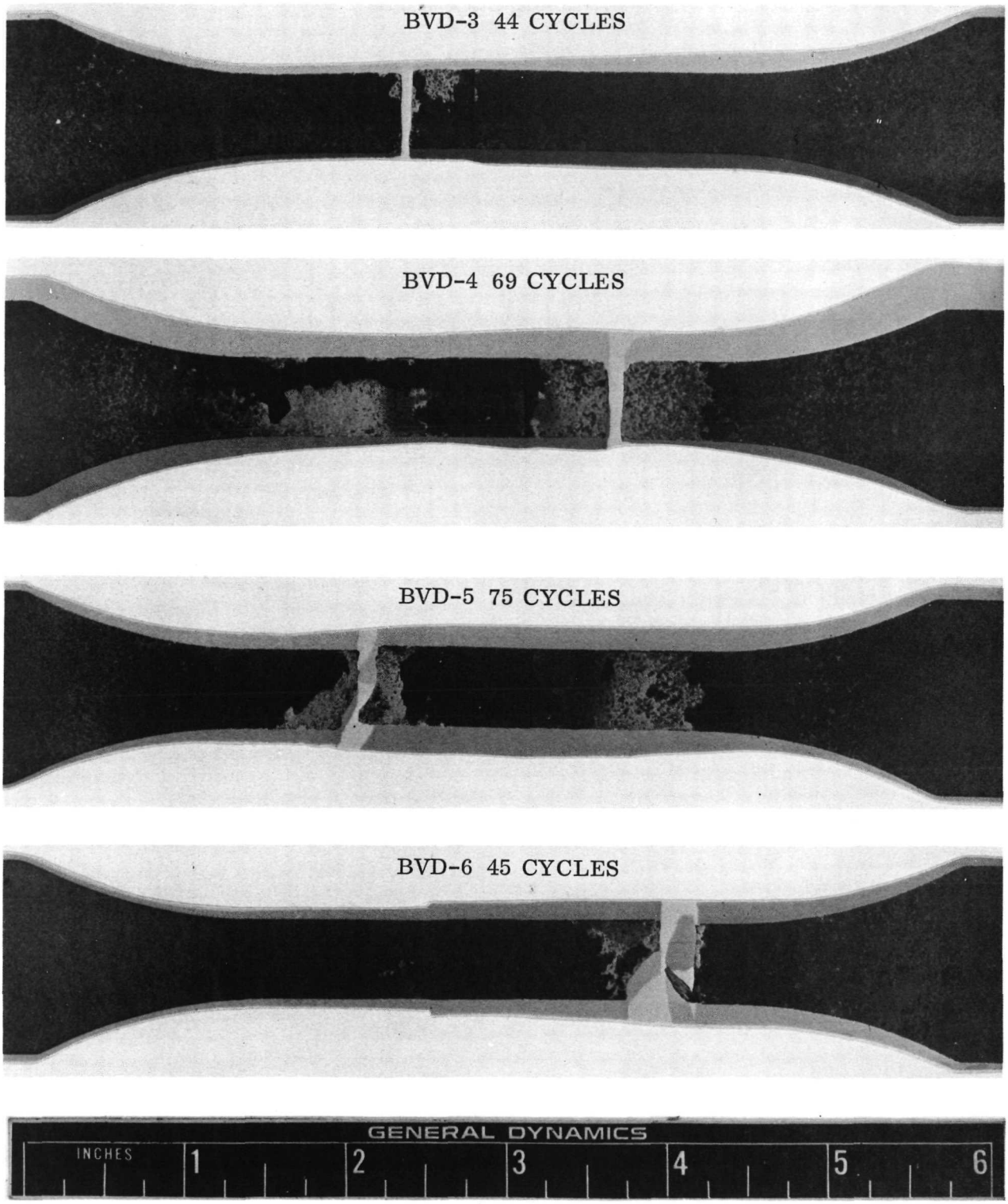


Figure 4-35. Cb-752/VH-109 Diffusion Bond Specimens After Flight Simulation Exposure

These attack sites were observed after about 80 cycles. One specimen suffered severe attack with substrate consumption at a loading pin hole, but, again, this was probably caused by accidental chipping during loading. Figures 4-36 and 4-37 show a typical specimen at various stages of exposure. Four completed specimens are shown in Figure 4-38.

Group 8, C-129Y/R-512E, electron beam weld: These specimens behaved much like the previous group for the first 80 flight simulation cycles. The initial color change was to dark grey on one side, and a lighter grey with some yellow and green on the other. During cycling, the dark sides were nearly unchanged while the light sides darkened gradually in the center sections. Other than a slight coating spall, the specimens survived the first 60 to 80 cycles extremely well. At 60 cycles, however, one specimen developed an edge-type coating failure that extended to the substrate. The other five specimens experienced the same type of attack during the last 20 cycles. While all specimens survived 100 cycles, four showed severe edge attack with substrate erosion ranging from 0.03 to 0.10 inch (0.08 to 0.25 cm), and two had coating failures just to the substrate. No failure sites were located within the weld affected zones, again indicating the apparently good resistance of a coated electron beam weld to flight simulation exposure. Photographs of a typical specimen as it progresses through cycling are presented in Figures 4-39 and 4-40. Four specimens after 100 cycles are shown in Figure 4-41. Figure 4-42 is an enlargement of one of the areas of severe attack showing several failure sites.

Group 9, C-129Y/R-512E, diffusion bond: Flight simulation results from these specimens were very similar to those of the two preceding groups. Color changes, a light-to-moderate coating spall, and resistance to coating failure for about 80 cycles were the same. In like manner, all six specimens survived 100 cycles. Of the six, two experienced severe edge failures and substrate erosion, and two others had small failures that extended just to the substrate. No failures were located in the bond areas. Figures 4-43 to 4-45 show typical specimens during cycling, and after completion of 100 cycles.

Group 10, C-129Y/VH-109, parent: During the initial exposure cycles, the specimens of this group took on a light brown-grey color with a small amount of green. Except for some darkening in the center sections, little color change occurred with increased cycling. In the first 50 cycles, light-to-moderate coating spall was observed. At this point, the surface of some of the specimens began to show a spongy, porous appearance and developed small areas of severe coating spall. In addition, some edge failures and the beginning of substrate oxidation and erosion were noted. As cycling progressed, all specimens but one developed severe surface spall, and/or edge attack. Three specimens failed between 78-91 cycles in areas of severe surface attack. Of the three that survived 100 cycles, two were in very poor condition with considerable

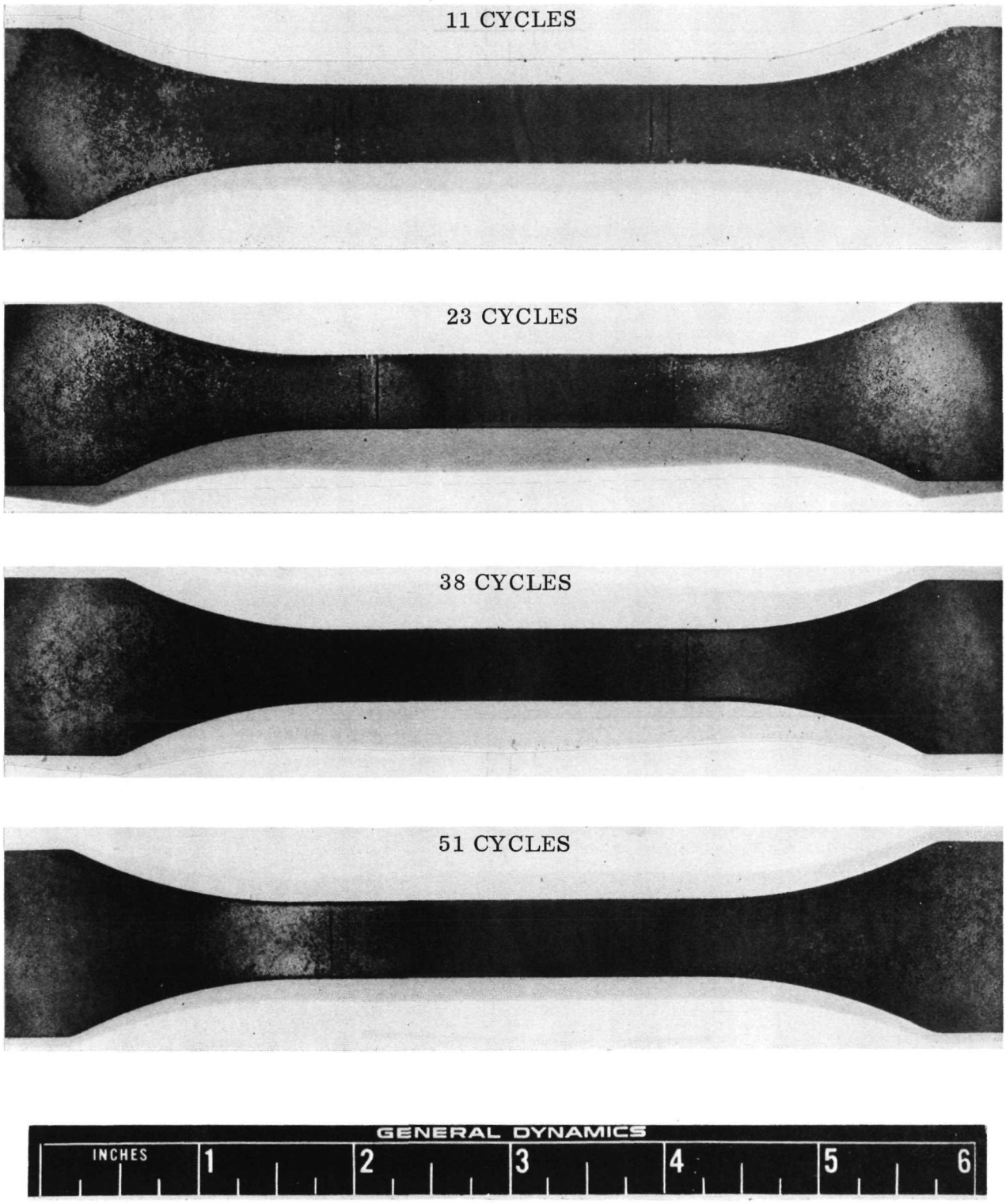


Figure 4-36. C-129Y/R-512E After Flight Simulation Exposure — Specimen YSP-3

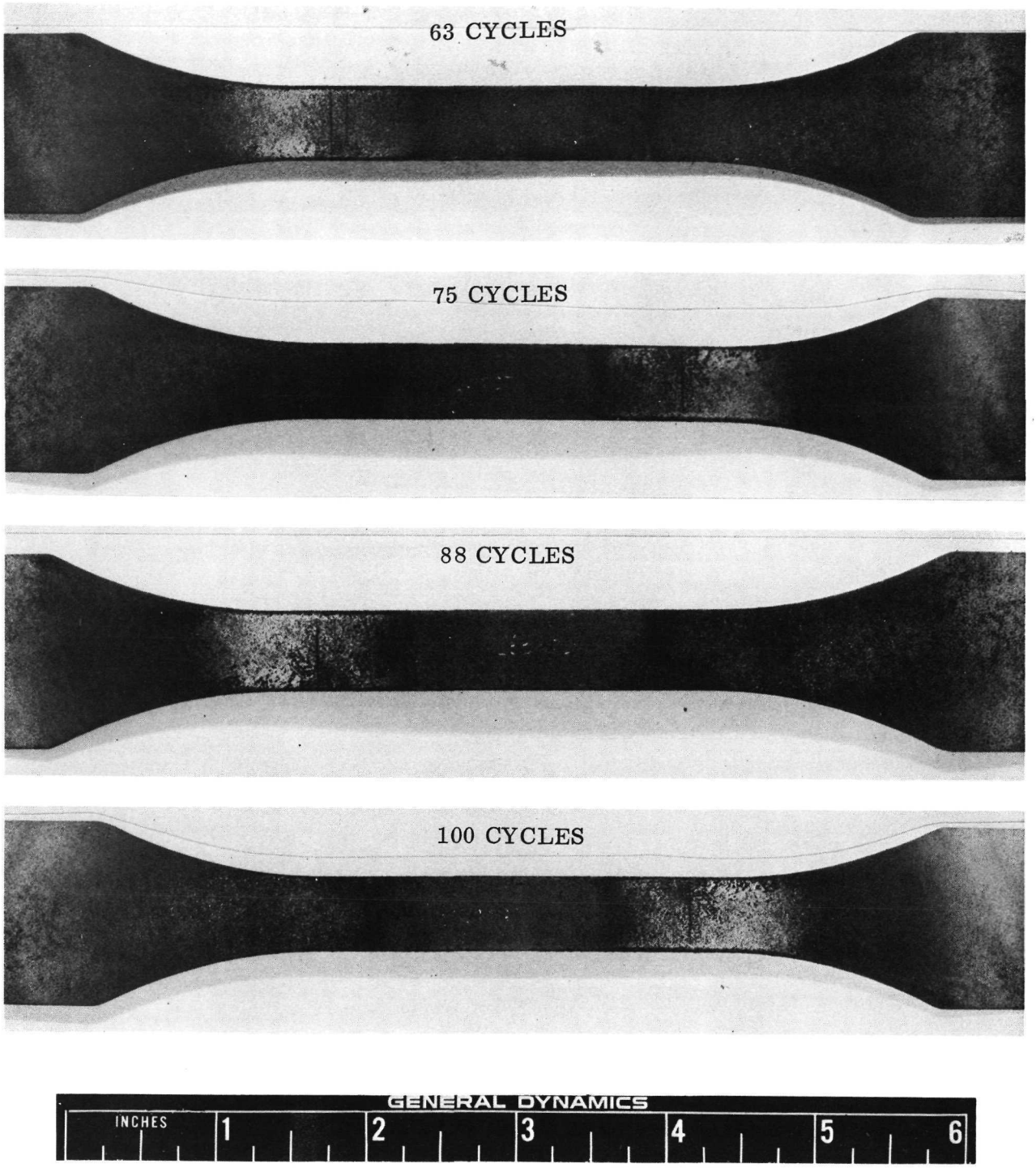


Figure 4-37. C-129Y/R-512E After Flight Simulation Exposure — Specimen YSP-3

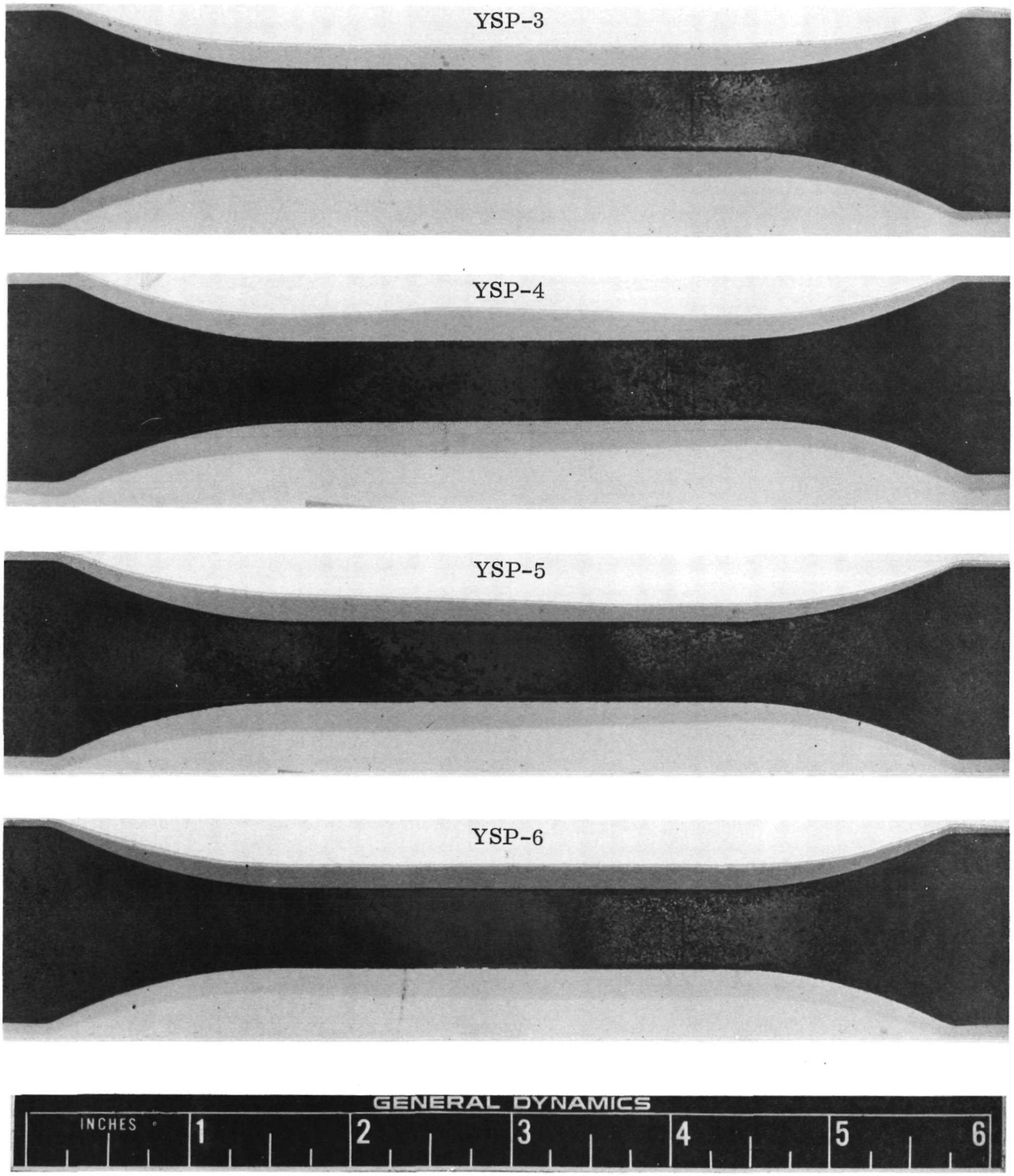


Figure 4-38. C-129Y/R-512E Parent Specimens After 100 Flight Simulation Exposure Cycles

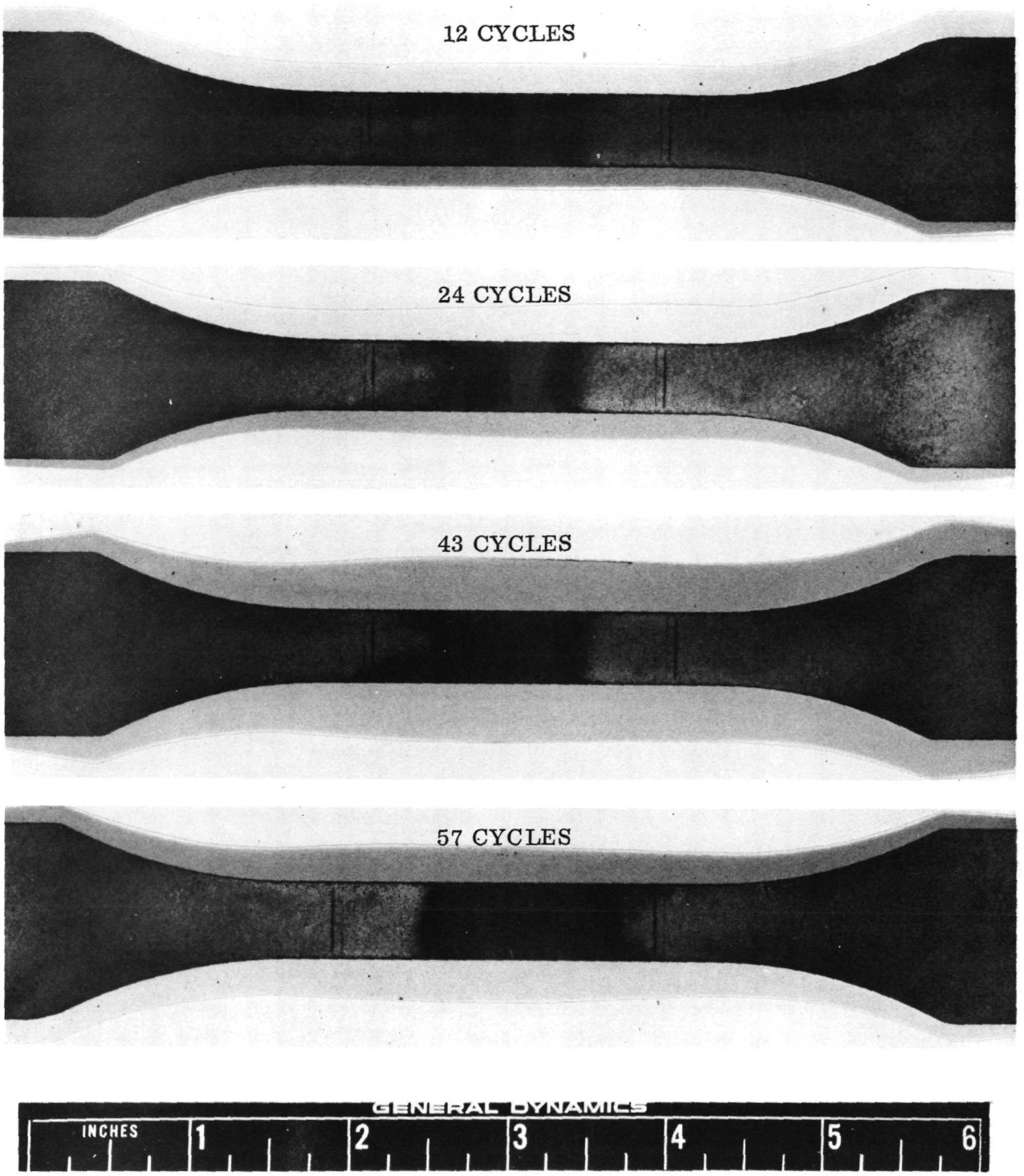


Figure 4-39. C-129Y/R-512E After Flight Simulation Exposure — Specimen YSE-14

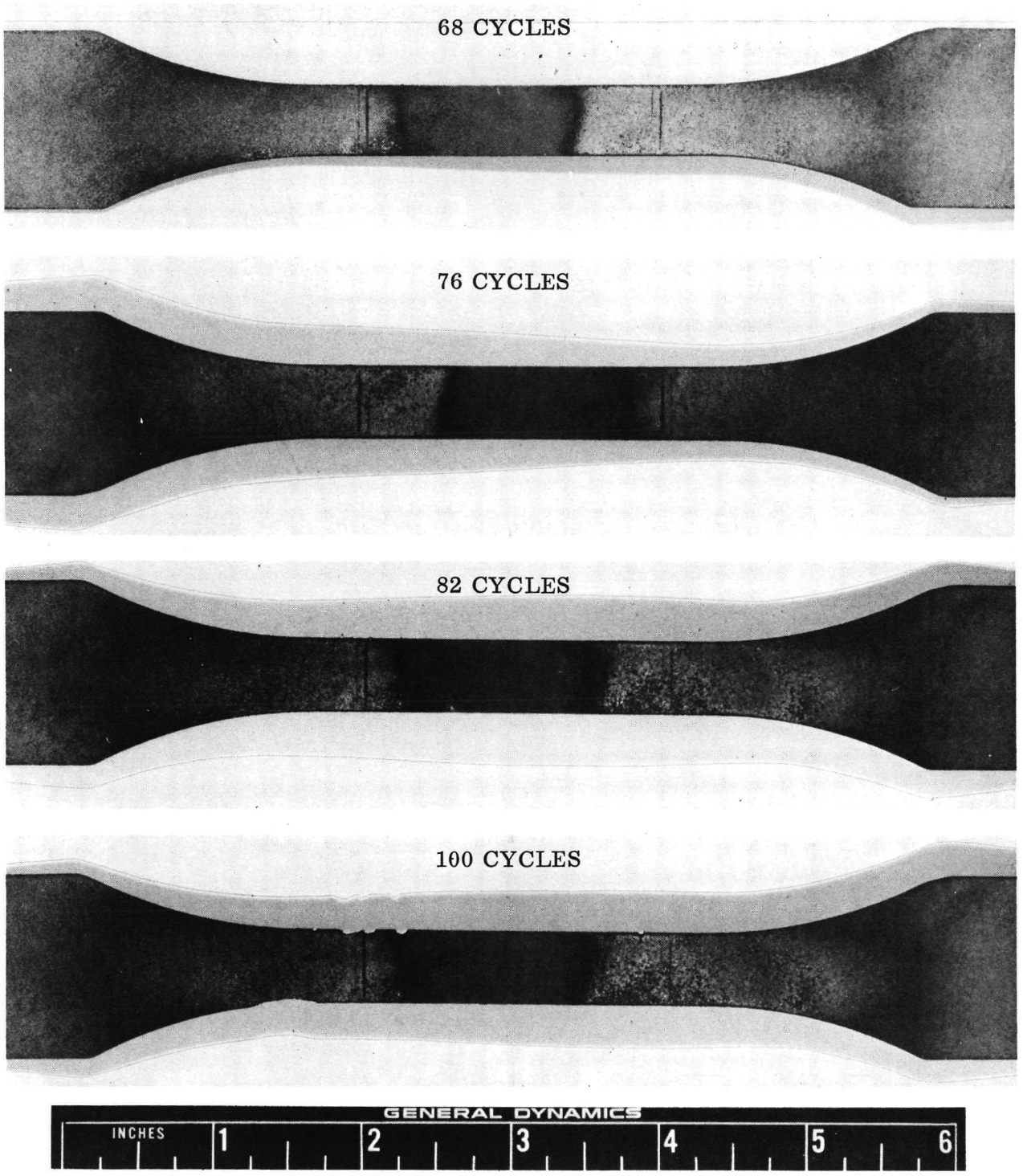


Figure 4-40. C-129Y/R-512E After Flight Simulation Exposure — Specimen YSE-14

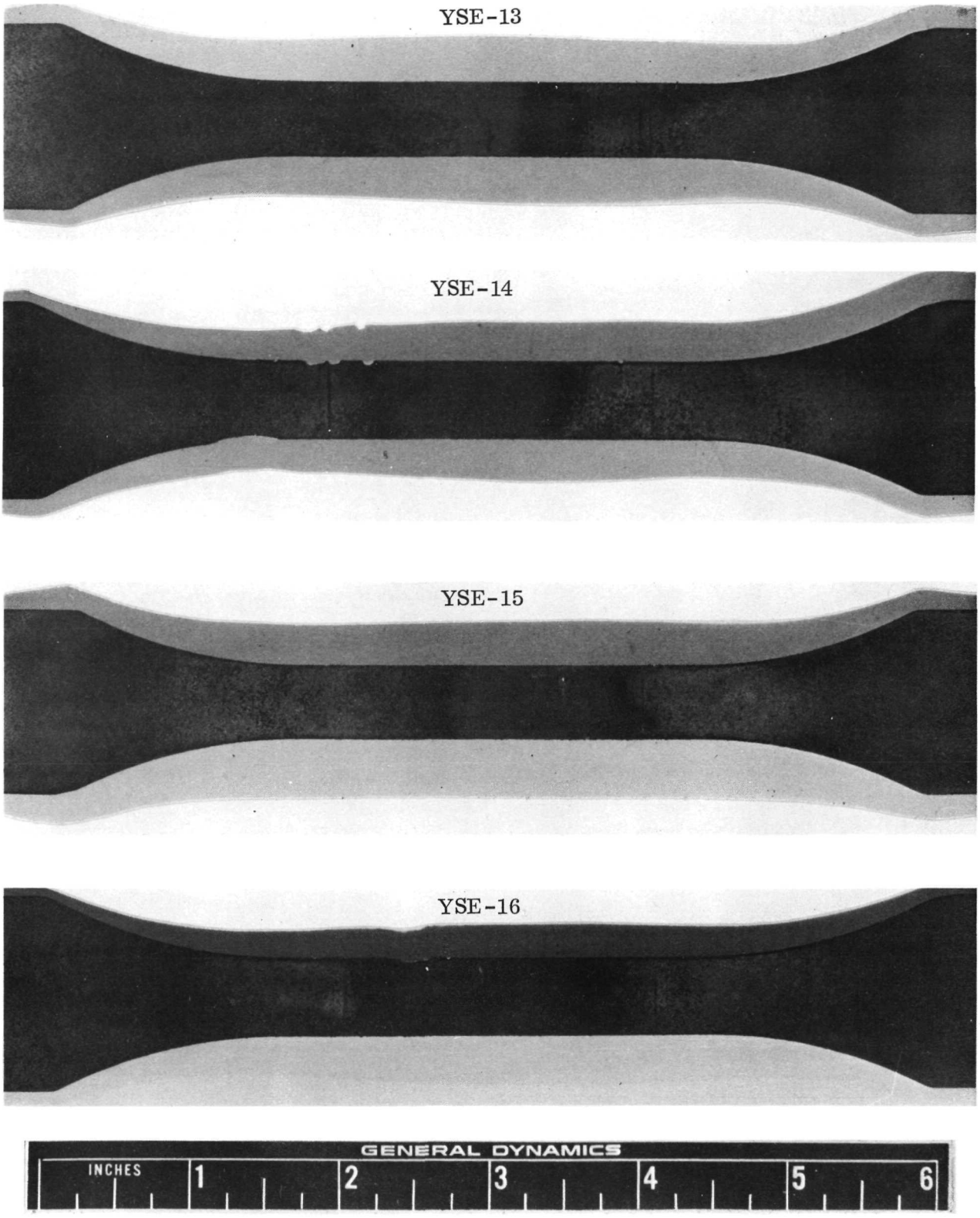


Figure 4-41. C-129Y/R-512E Electron Beam Weld Specimens After 100 Flight Simulation Exposure Cycles

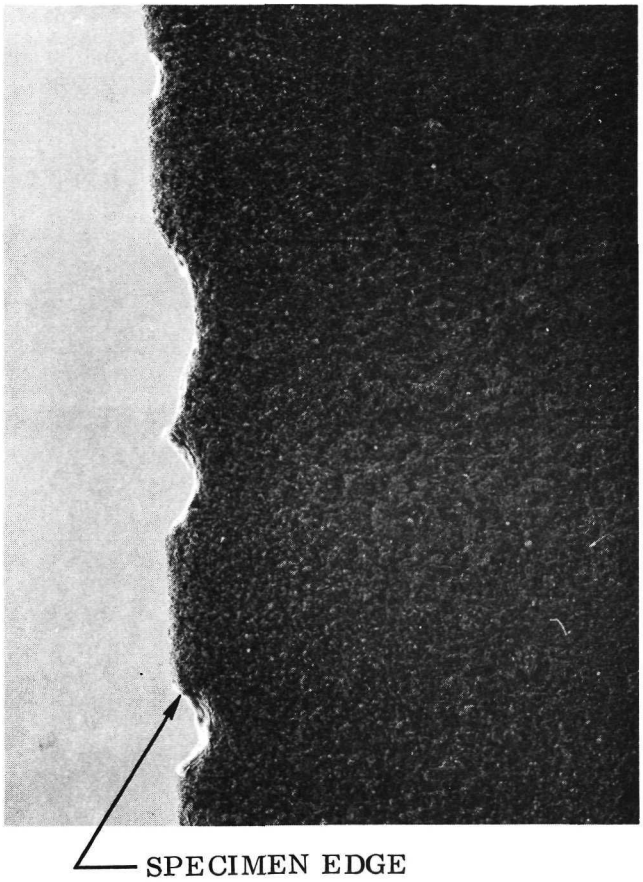


Figure 4-42. Enlargement of Severe Edge Attack Region — Specimen YSE-14 After 100 Flight Simulation Cycles (6X) (Photo D-921)

edge erosion. In contrast to the others, one specimen showed no visible signs of coating failure after the 100 cycles. Figure 4-46 shows this specimen and three others for comparison after the completion of flight simulation testing. A typical specimen at various stages of exposure is presented in Figures 4-47 and 4-48.

Group 11, C-129Y/VH-109, electron beam weld: These specimens differed in color somewhat from the previous group. They changed to a darker brown with much more green. Their behavior during cycling was similar, however, although only one specimen completed 100 cycles. In the first 70 cycles only one specimen experienced anything more than slight coating spall. At this time the remaining specimens developed a spongy appearance and began to experience heavy surface spall in these areas. Fracture occurred in these regions of severe spall and, in all cases, away from the welds or heat-affected zones. The specimens failed between 62 and 94 cycles at the high tensile loads early in the boost portion of the flight cycle. The one specimen that survived 100 cycles was severely spalled, and also contained a deep pit within the spalled region. Failure occurred at this location during post-exposure tensile testing (Section 4.4). Photographs of specimens during the course of exposure testing and at completion are given in Figures 4-49 to 4-51.

Group 12, C-129Y/VH-109, diffusion bond: None of these specimens lasted 100 cycles. Failures were observed between 74 and 96 cycles. Color changes closely matched those of group 11, rather than 10 with the heavier green shades. The failure mode was the same as that of groups 10 and 11, i.e., light spall during the first 50 to 70 cycles, appearance of a porous spongy surface, severe spall of these regions, followed by eventual fracture within one of these coating failure regions. No fractures occurred within 1/8 inch (0.32 cm) of the diffusion bonded regions. In one specimen, local oxidation attack was sufficient to create a hole completely through the specimen.

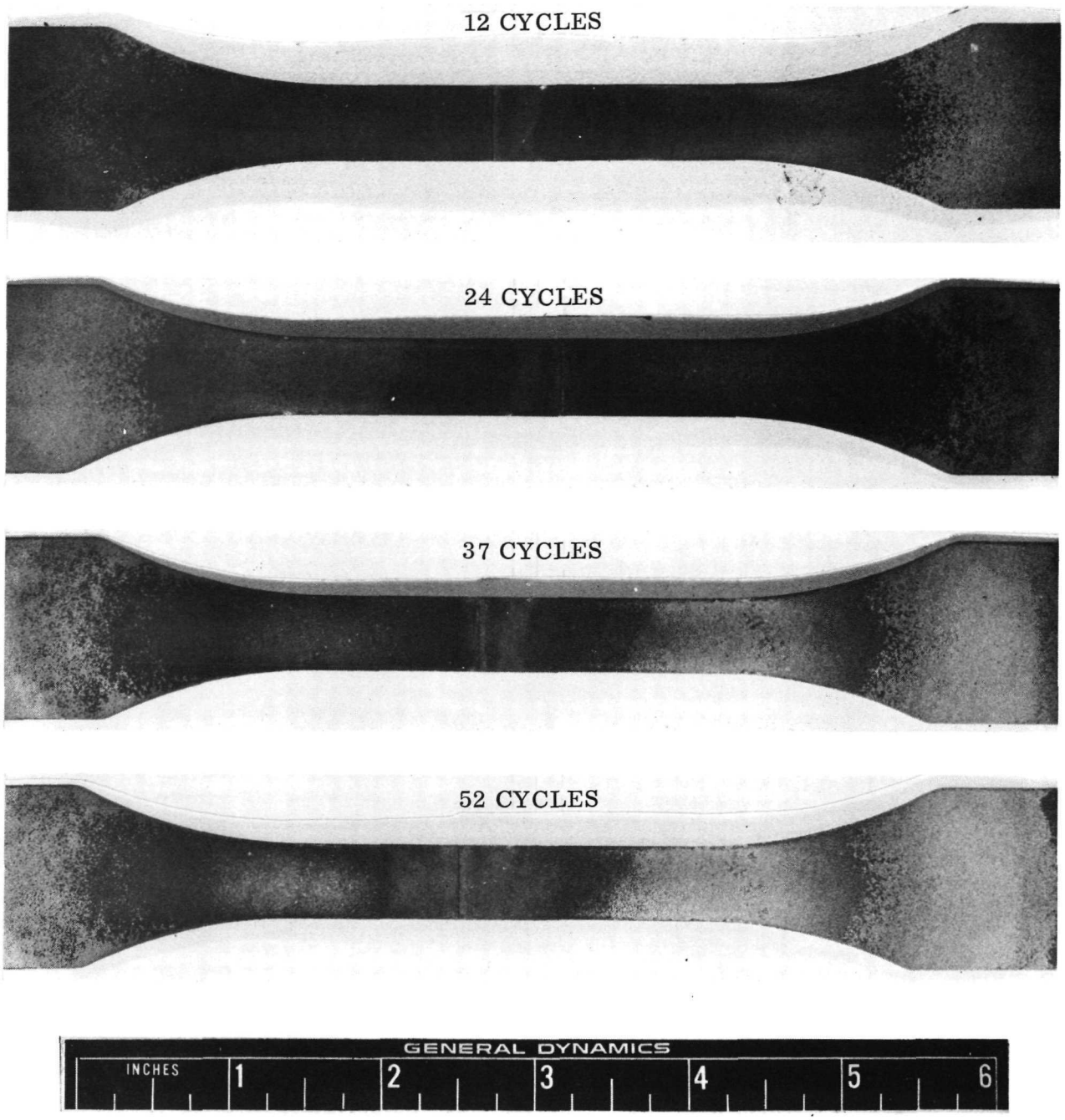


Figure 4-43. C-129Y/R-512E After Flight Simulation Exposure — Specimen YSD-6

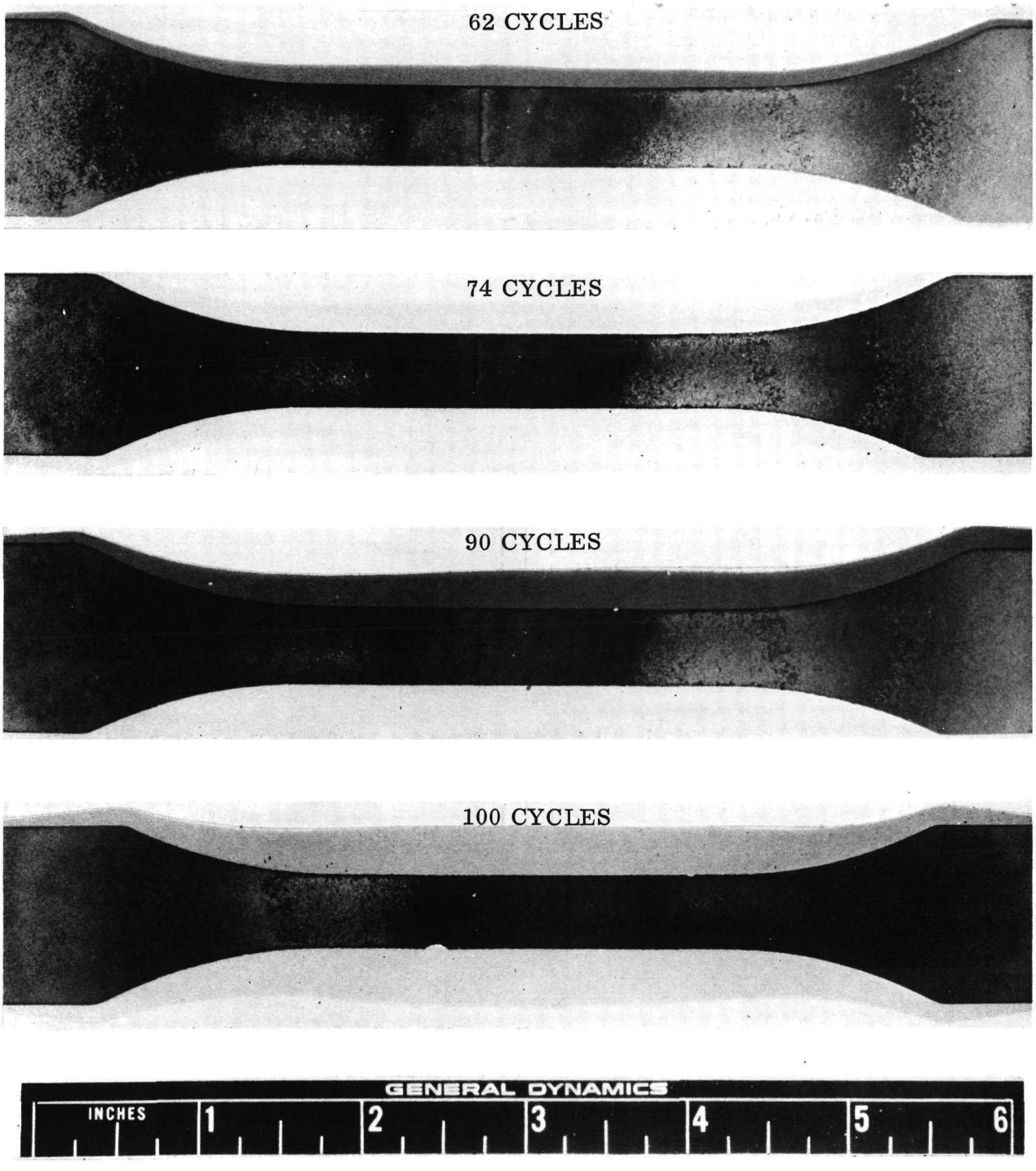


Figure 4-44. C-129Y/R-512E After Flight Simulation Exposure — Specimen YSD-6

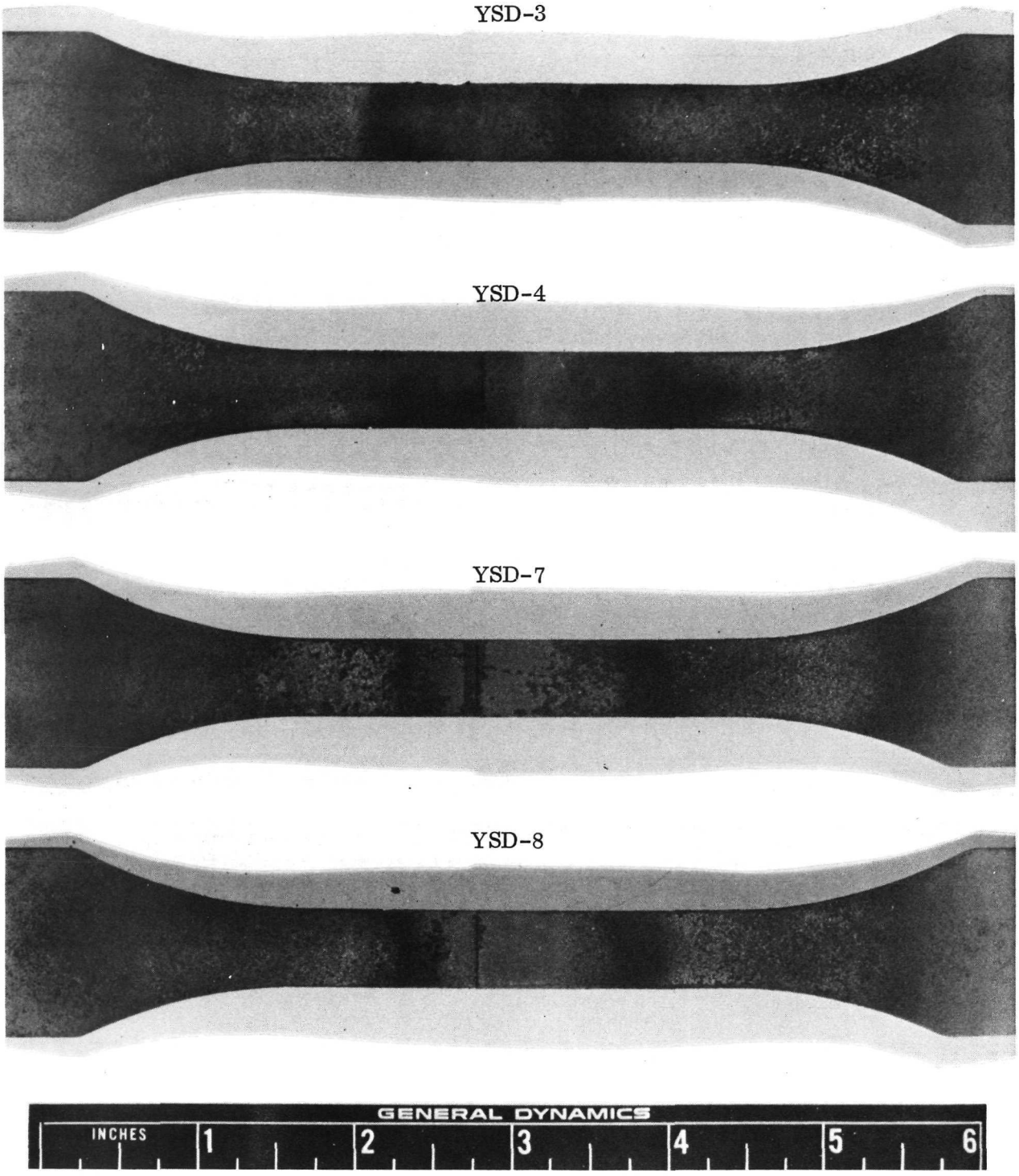


Figure 4-45. C-129Y/R-512E Diffusion Bond Specimens After 100 Flight Simulation Exposure Cycles

Failure did not occur at this location, however. Figures 4-52 and 4-53 show a typical specimen at various intervals during flight simulation exposure. The six specimens of this group at the completion of cycling are pictured in Figure 4-54. Sections of specimen YVD-14 had been removed for metallographic examination. A closeup of one of the specimens, YVD-4, showing the porous surface spall and the underlying region is presented in Figure 4-55.

Test analysis: The results of the flight simulation exposures (Table 4-3 and the preceeding discussion) clearly indicate the superiority of the Sylvania R-512E coating over the Vac-Hyd VH-109 coating. Of the 36 R-512E coated specimens, 35 survived 100 cycles, while only 4 of the 36 VH-109 specimens completed 100 cycles. No visible coating failures were observed in the R-512E coated Cb-752 specimens. The R-512E specimen that did not complete 100 exposures appeared to have failed because of mechanical loading rather than by gross oxidation. Fracture may have resulted from changes in substrate properties caused by oxygen contamination. Though no coating failures were visible with the unaided eye, evidence of contamination was found during subsequent metallographic examination. This particular specimen also had the smallest uncoated cross-sectional area [0.0060 $in^2$ (0.0387 $cm^2$) as compared to an average of 0.0068 $in^2$ (0.0439 $cm^2$)] of all the specimens in test. Twelve of the 18 R-512E coated C-129Y specimens, on the other hand, while completing 100 exposure cycles, exhibited edge-type coating erosion. This erosion becomes visible after about 80 cycles. Six of the specimens were severely attacked [0.03 to 0.10 inch (0.09 to 0.25 cm) of substrate oxidized away at one or more sites], and the other six showed moderate edge attack (substrate exposed).

The four VH-109 coated specimens that survived 100 flight cycles were all C-129Y alloy. This alloy was considerably better than the Cb-752 alloy as a substrate for the VH-109 coating. This is shown clearly in Table 4-4, which lists the average cyclic lifetimes for the six VH-109 coated groups. It is interesting to note that the R-512E coating performed better on the Cb-752 alloy, for which it was originally developed,

Table 4-4. Average Cyclic Lifetimes for Vac-Hyd VH-109 Coated Specimens

| Alloy | Condition | Average Cyclic Lifetime | |
|---|---|---|---|
| Cb-752 | Parent | 75 | |
| Cb-752 | EB weld | 57 | 64 |
| Cb-752 | Diff. bond | 60 | |
| C-129Y | Parent | 92 | |
| C-129Y | EB weld | 86 | 87 |
| C-129Y | Diff. bond | 84 | |

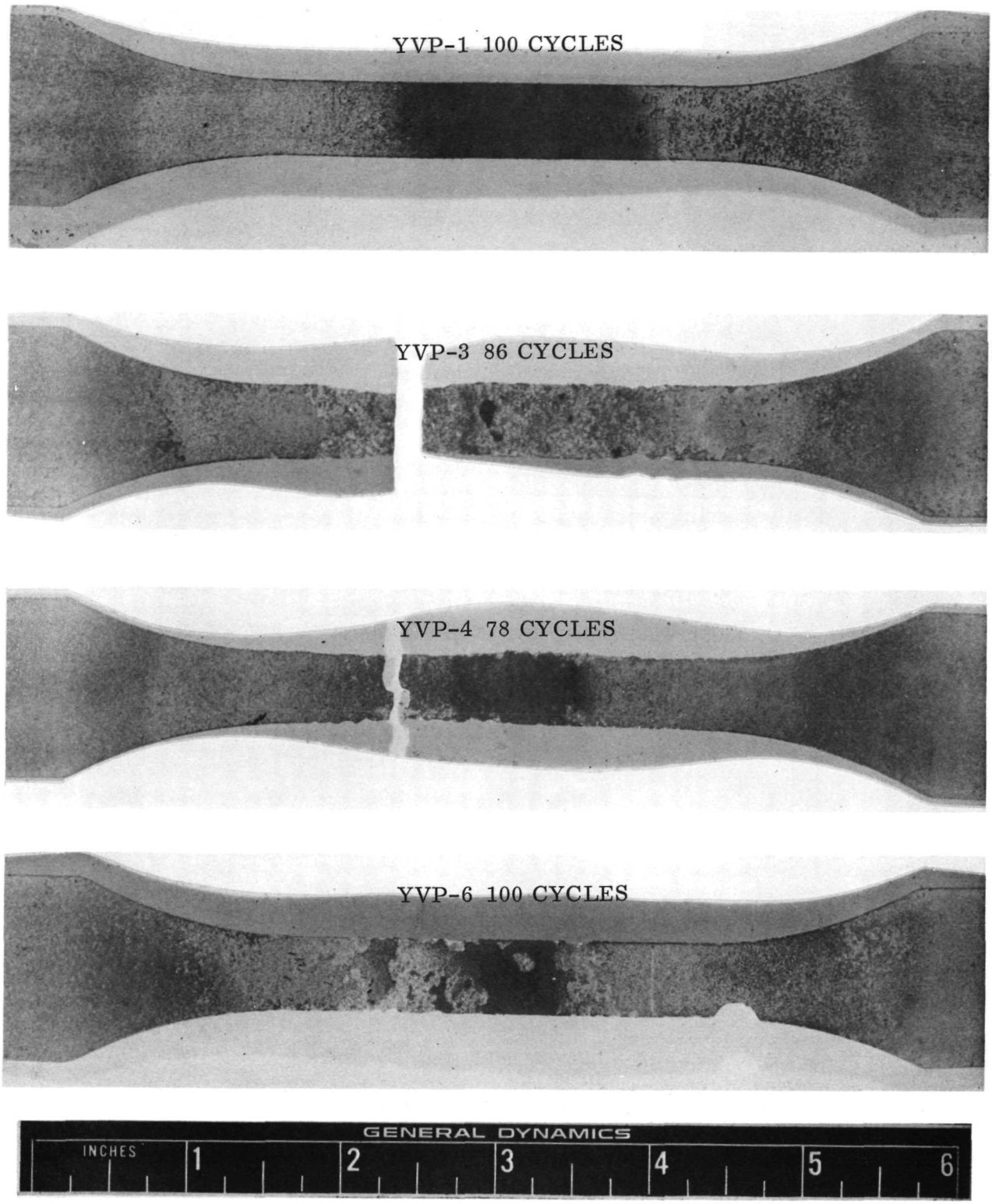


Figure 4-46. C-129Y/VH-109 Parent Specimens After Flight Simulation Exposure

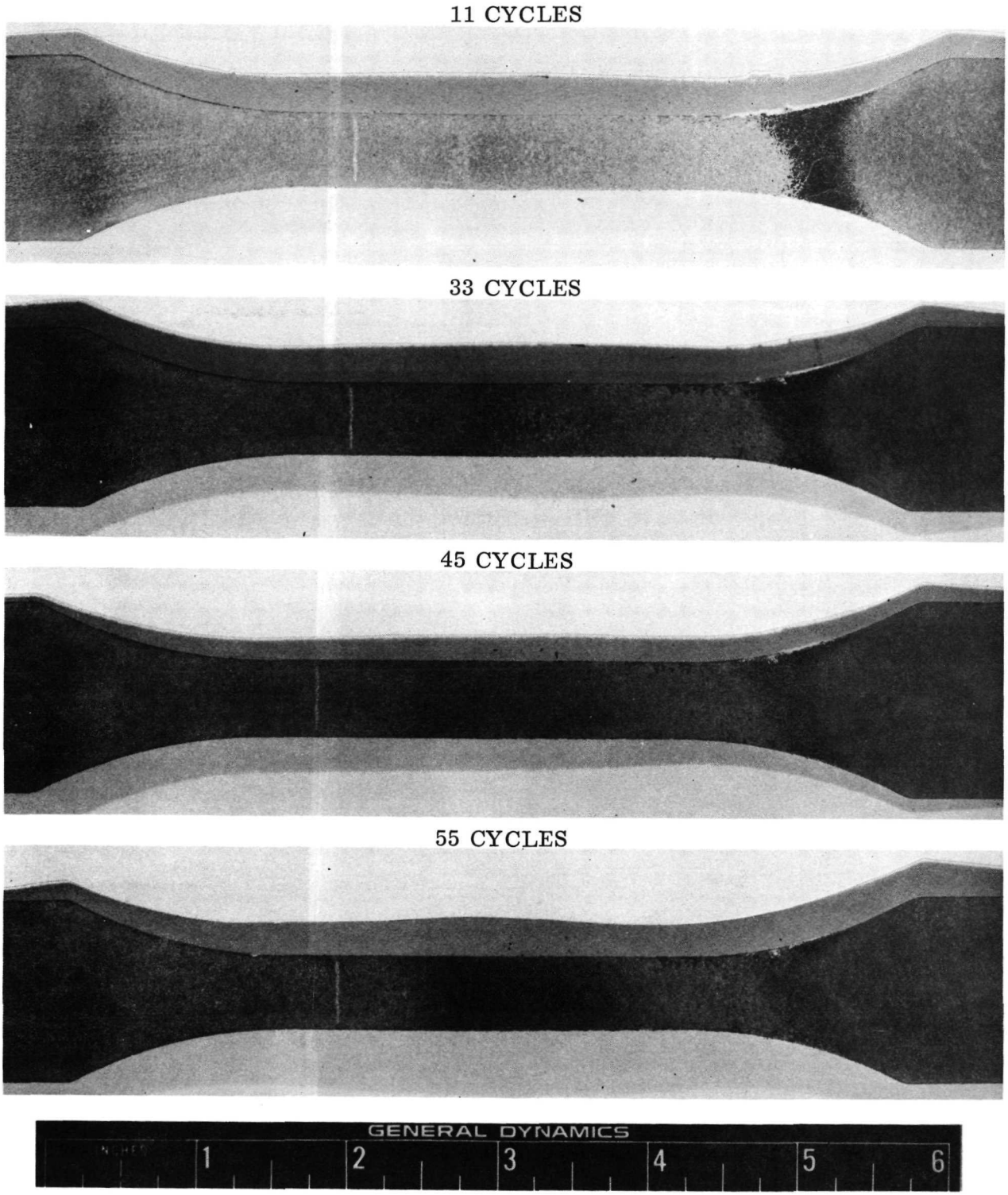


Figure 4-47. C-129Y/VH-109 After Flight Simulation Exposure — Specimen YVP-6

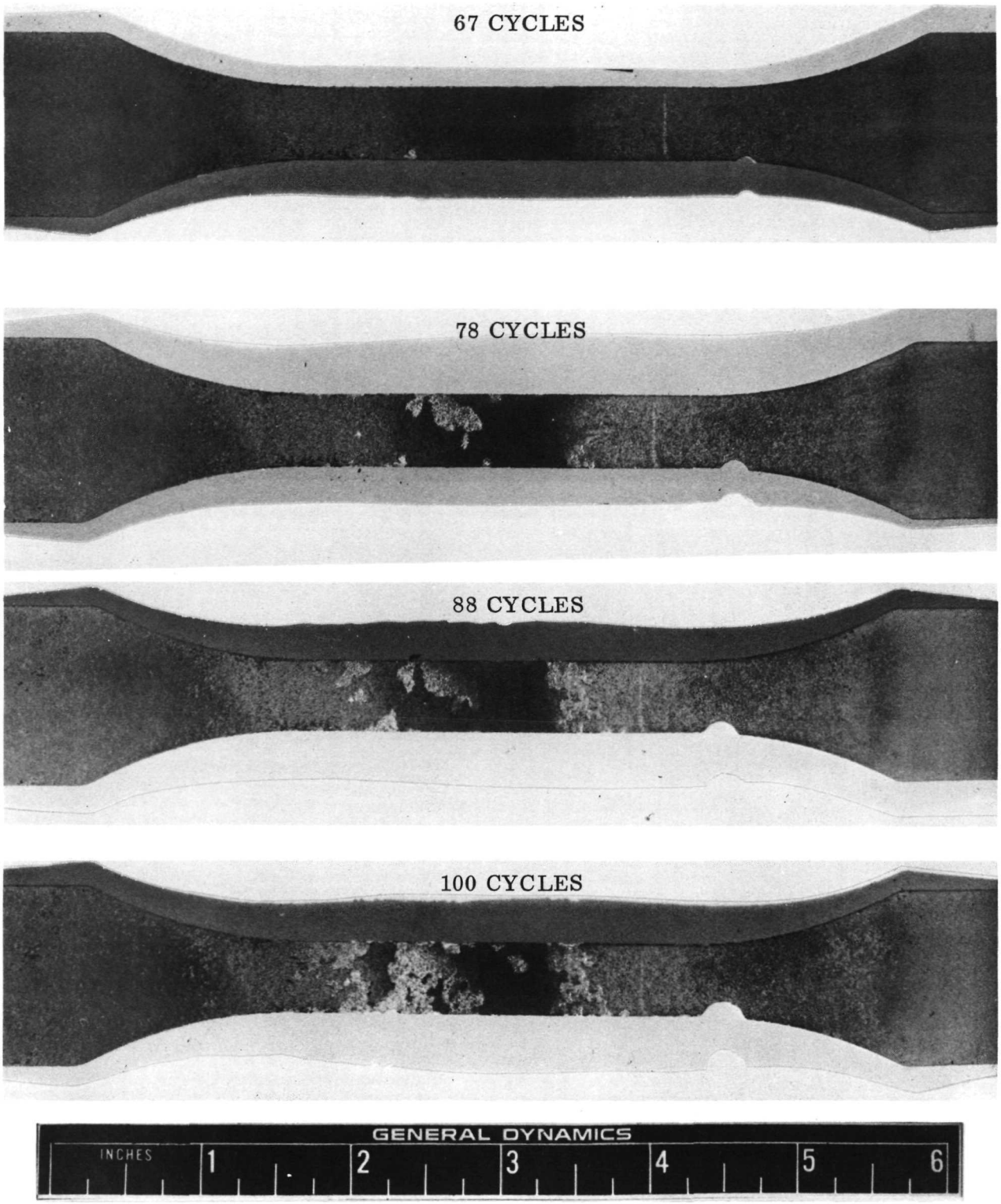


Figure 4-48. C-129Y/VH-109 After Flight Simulation Exposure — Specimen YVP-6

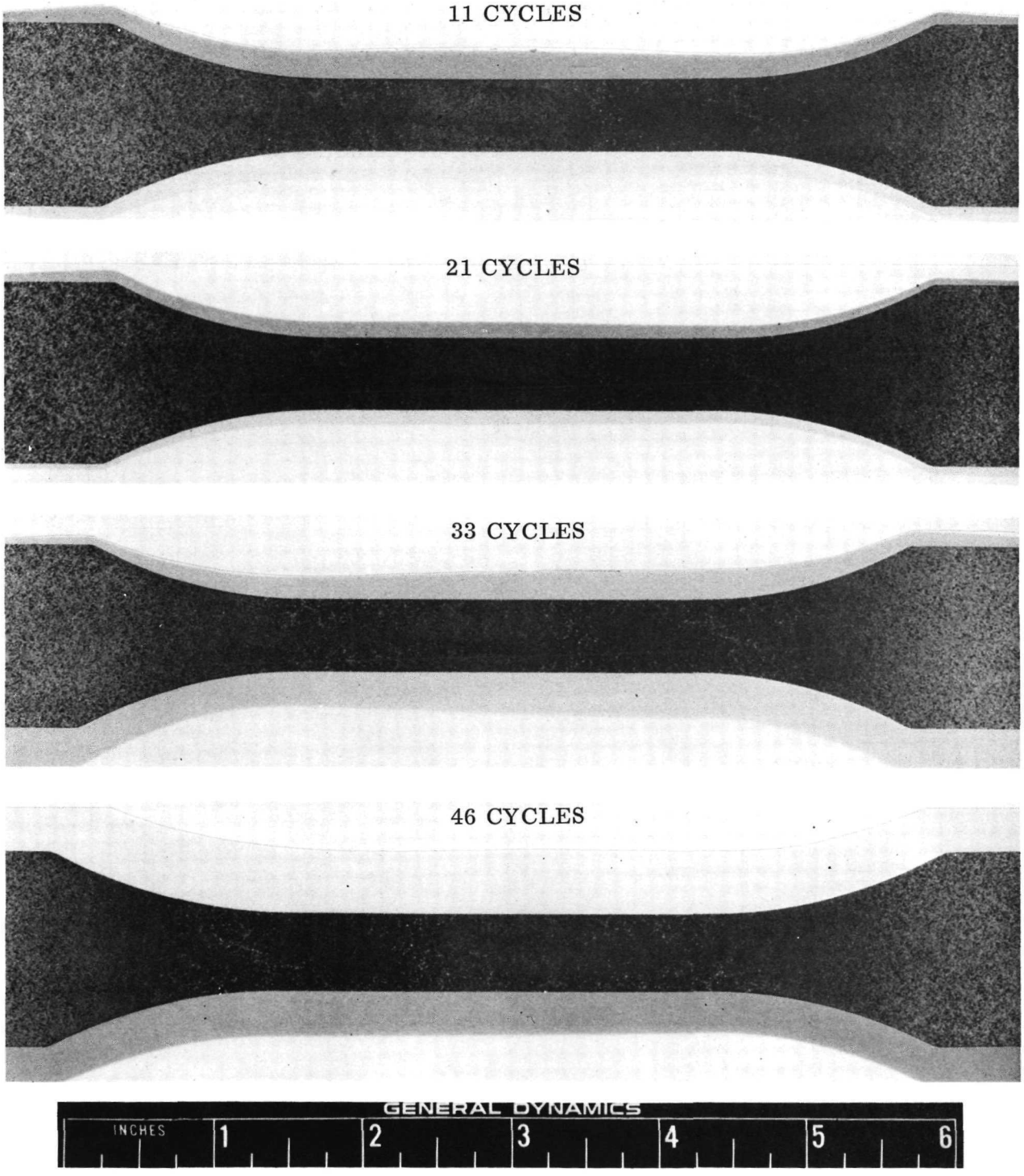


Figure 4-49. C-129Y/VH-109 After Flight Simulation Exposure — Specimen YVE-8

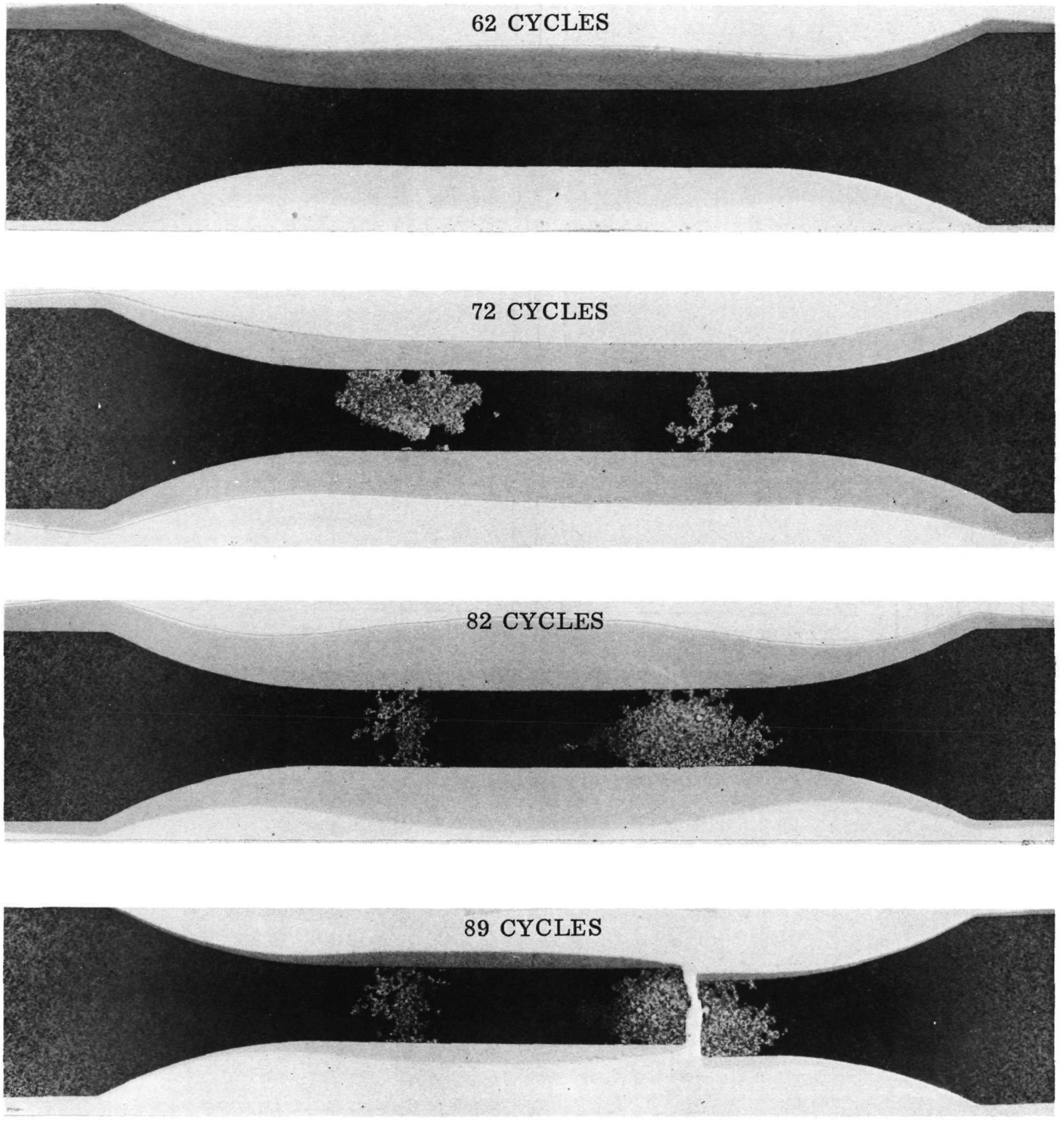


Figure 4-50. C-129Y/VH-109 After Flight Simulation Exposure — Specimen YVE-8

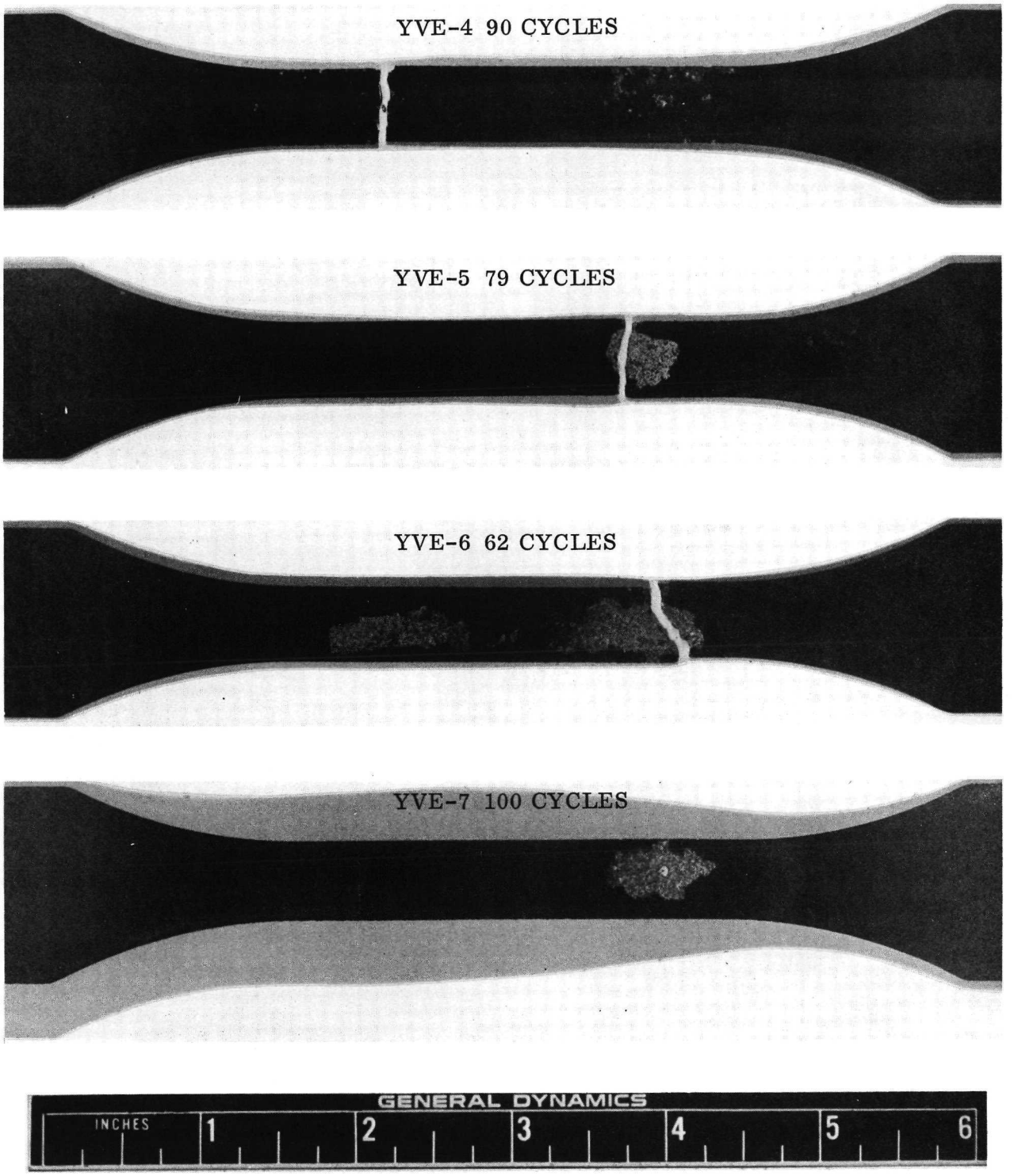


Figure 4-51. C-129Y/VH-109 Electron Beam Weld Specimens After Flight Simulation Exposure

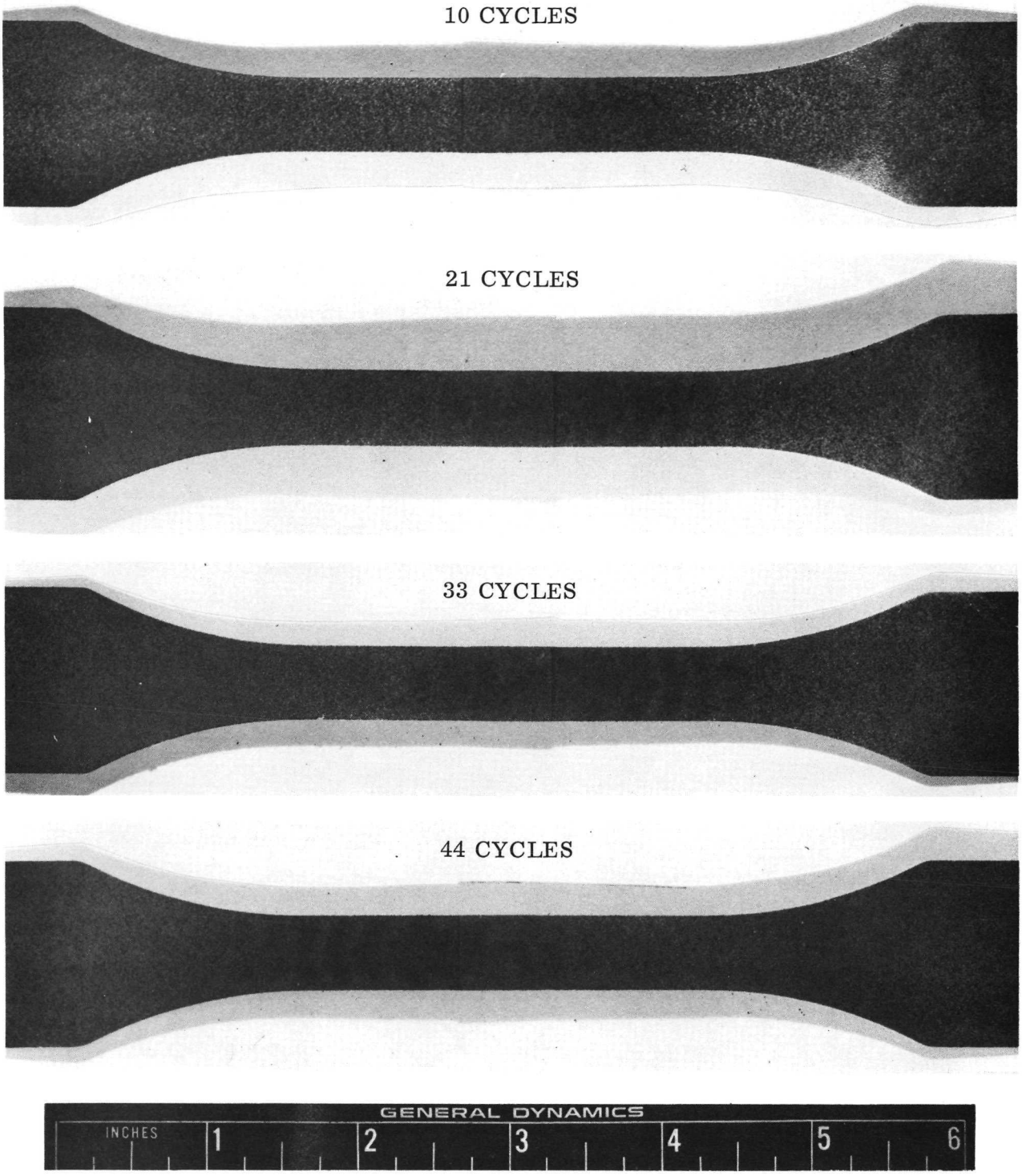


Figure 4-52. C-129Y/VH-109 After Flight Simulation Exposure — Specimen YVD-4

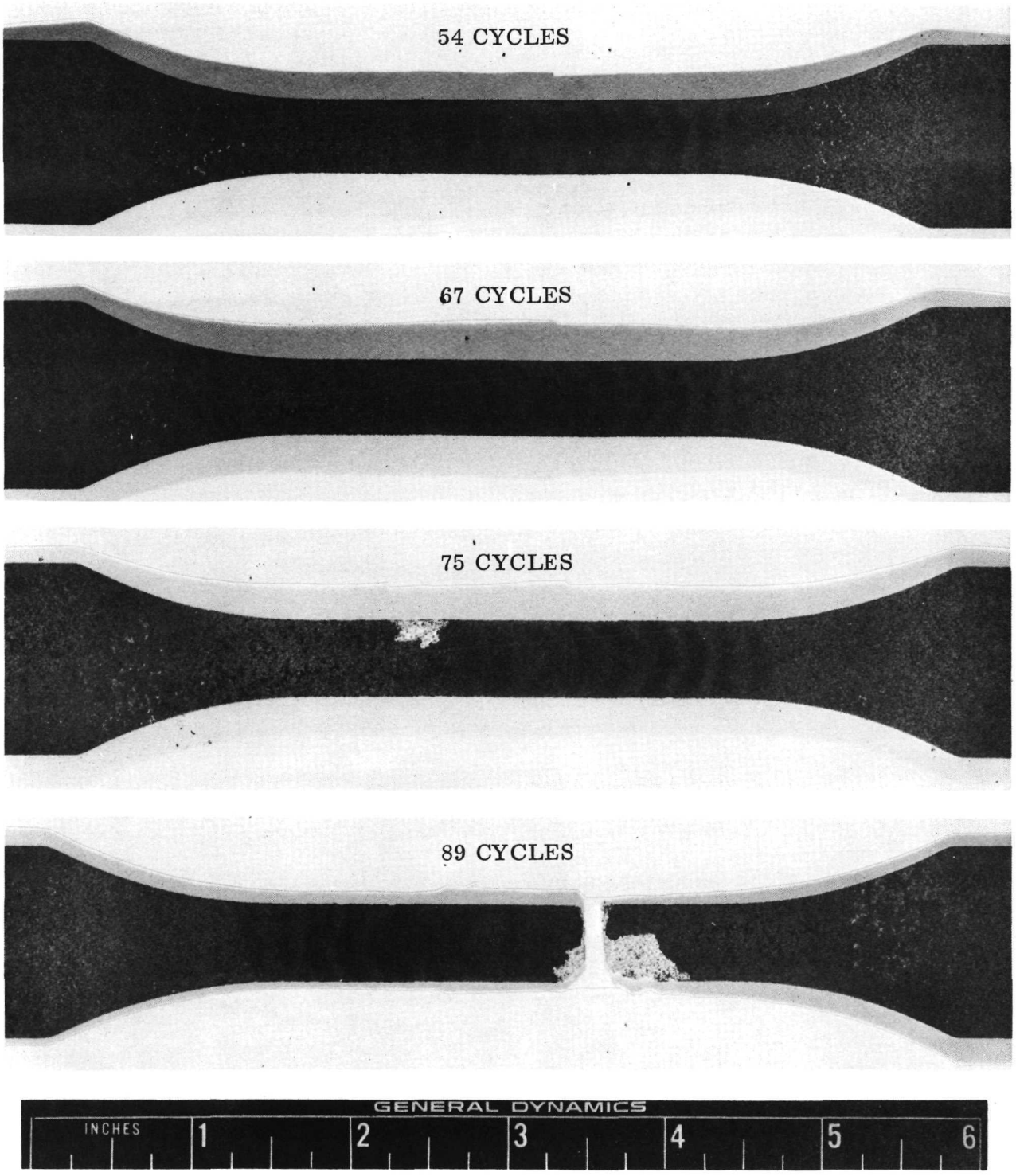


Figure 4-53. C-129Y/VH-109 After Flight Simulation Exposure — Specimen YVD-4

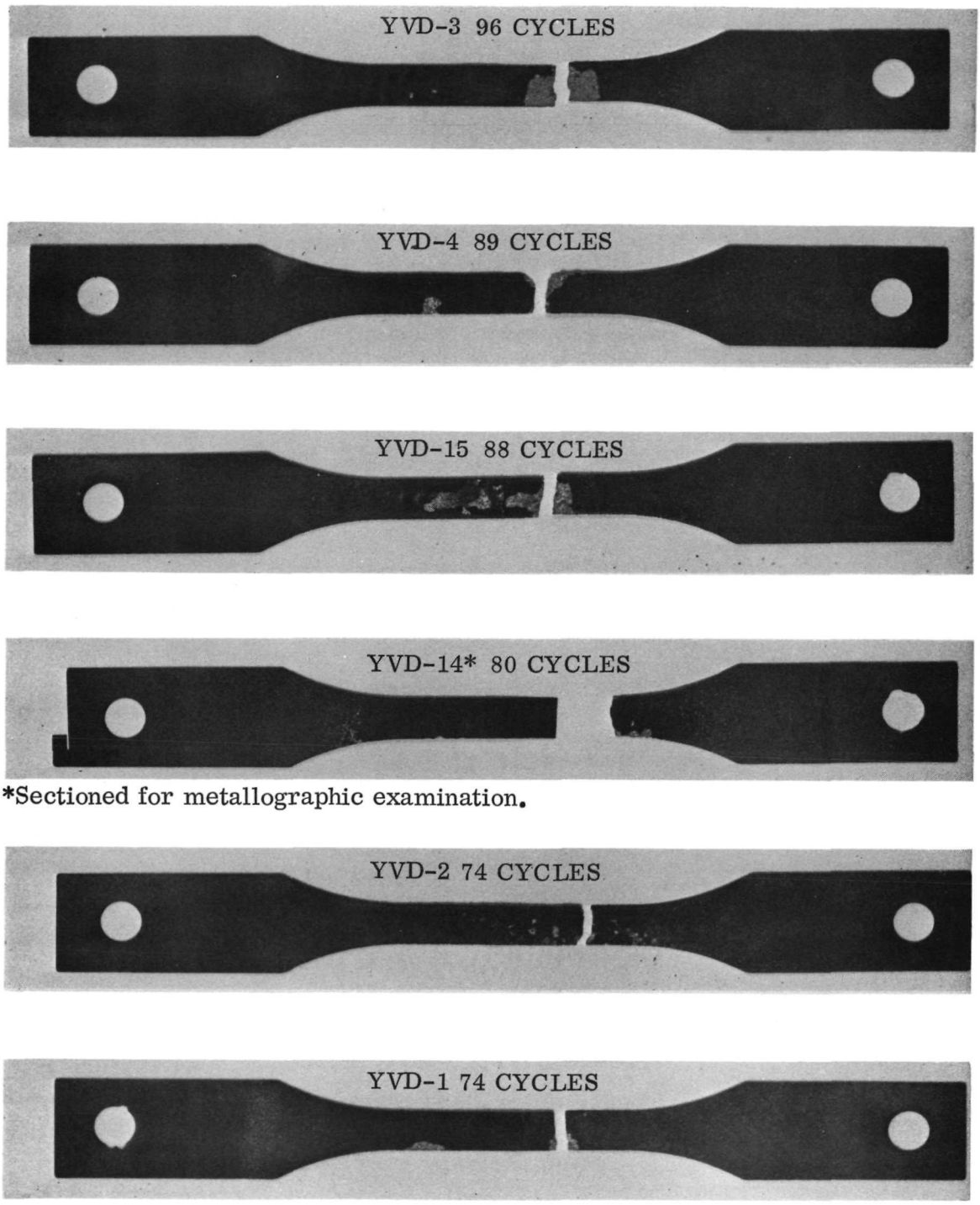


*Sectioned for metallographic examination.

Figure 4-54. C-129Y/VH-109 Diffusion Bond Specimens After Flight Simulation Exposure

while the VH-109 coating performed better on the C-129Y alloy, for which it was originally developed. It should be noted that the Sylvania coating technique has had a standard of high quality and performance for many years. It was believed, and since verified (Reference 22), that a key factor in the performance of Vac-Hyd's duplex coating processes was in the area of quality control. By using more standard NDE techniques the green state coating uniformity could be determined and controlled. In addition, it is believed that a thixotropic agent modification was necessary to maintain the VH-109 heavy modifiers, i.e., hafnium and tantalum, in the proper dispersed suspension.

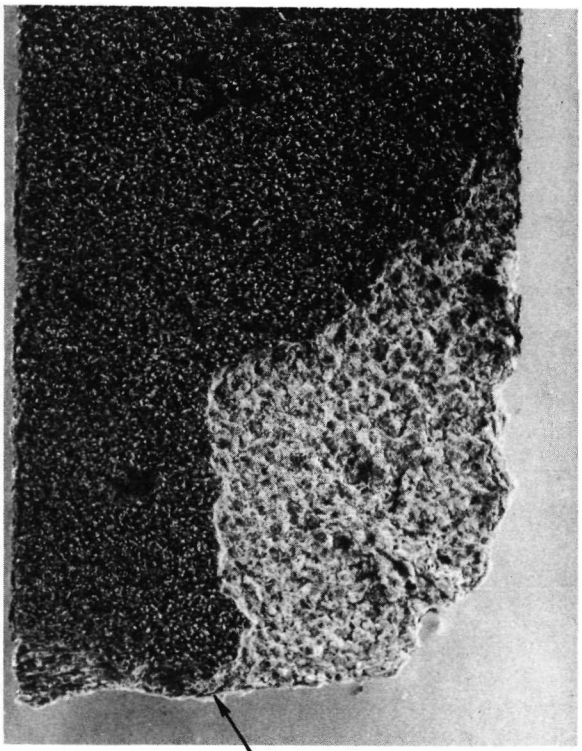


Figure 4-55. Enlargement of Spall Area — Specimen YVD-4 After 89 Flight Simulation Cycles (6X) (Photo D-922)

The failure mechanism for the R-512E coating (observed on the C-129Y alloy only) was the formation of a small defect at the edge of the specimen — leading to the breakdown of the coating. The substrate was then exposed and eroded away as oxidation proceeded as discussed below. The nonadherent oxide offered little resistance to further oxidation, and gradual consumption of the specimen occurred as cycling progressed.

The VH-109 coated specimens experienced two distinct failure mechanisms. The first, common to all groups of specimens, was a surface phenomenon in which large, rather thick, portions of the coating spalled from the surface. While the substrate was generally not exposed, the remaining coating and oxide offered little resistance to oxygen penetration, and failure rapidly followed. For the C-129Y alloy, spallation of the coating was preceded by the formation of a porous, spongy surface layer. The second mechanism was the edge attack and erosion type observed for the R-512E coating (C-129Y alloy). This edge erosion was very severe on the VH-109 coated Cb-752 weld specimens, and to a lesser degree on the VH-109 coated C-129Y parent metal specimens.

For the edge erosion type of failure, rough measurements were made of the rate at which the material was consumed on two of the C-129Y specimens, one with the

R-512E coating, and one with the VH-109 coating. Plotted in Figure 4-56 is the amount of substrate consumption (measured at an edge) as a function of flight simulation cycles. Initial coating failures were visible at 55 and 58 cycles, respectively, for the two specimens. These measurements were not intended to be very precise; hence, the exact shape of the curve cannot be determined. A straight line appears to fit the data quite well giving a linear rate of edge erosion of about 0.0025 inch (0.0064 cm) per cycle for both systems. For a system with an adherent oxide one would expect a parabolic rate of substrate oxidation typical of a diffusion controlled process. On the other hand, for a system in which the oxidation products offered no resistance to further oxidation a

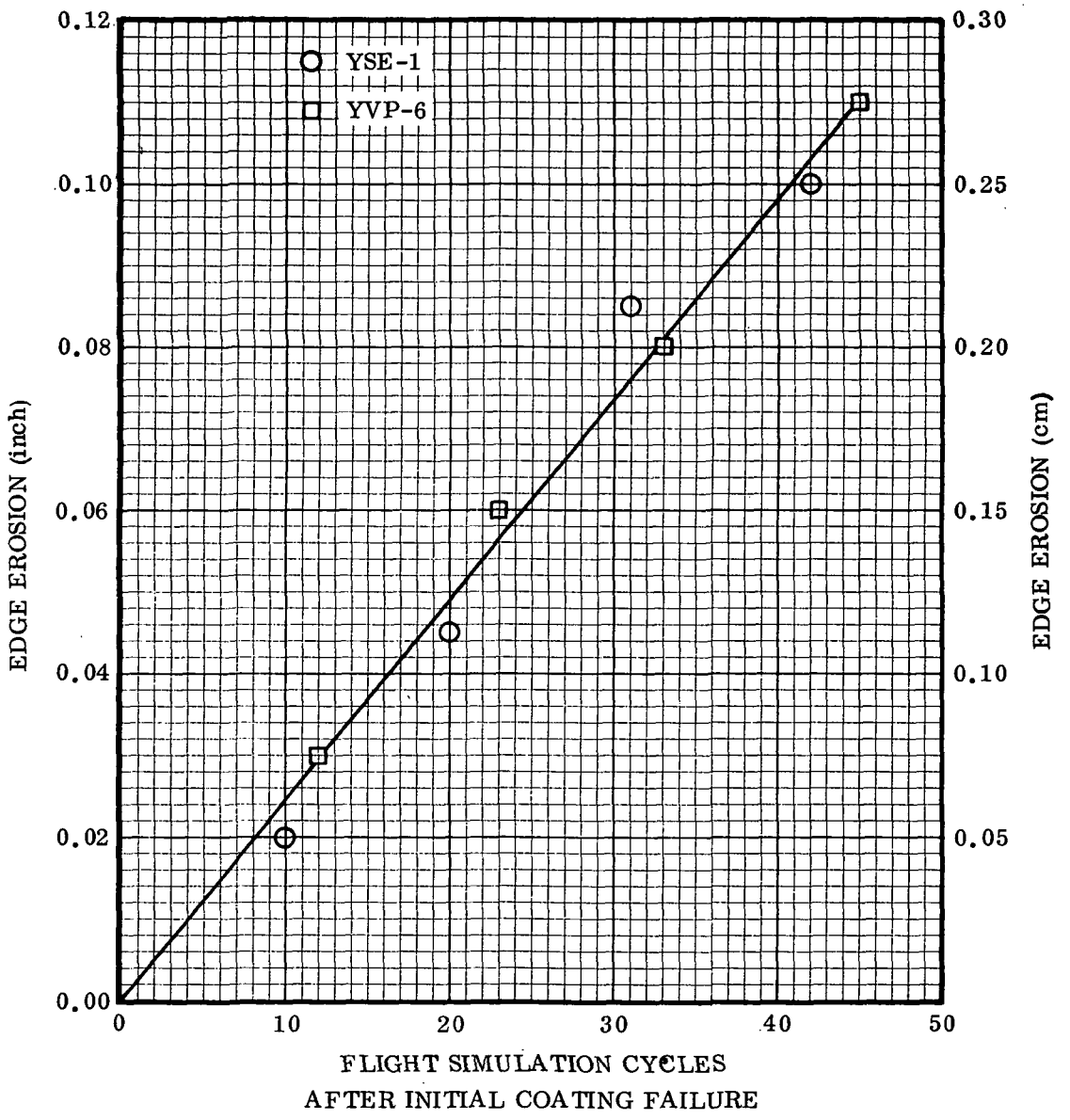


Figure 4-56. Edge Erosion as a Function of Flight Simulation Cycles

linear reaction rate would be expected. While the silicide coated columbium alloy system doesn't exactly meet this latter criterion the data would indicate that it is nearly so, once initial coating failure has occurred.

The resistance of electron beam welds and diffusion bonds to flight simulation exposure was found to be excellent. No failures were observed in the joint regions for either type of specimen. In addition, coating spall was generally less severe, and in most cases, nonexistent at the diffusion bonded overlap areas.

Based on the visual observations of coating behavior during cyclic flight simulation testing as described in this section, the four material systems can be rated as follows:

1. Cb-752/R-512E
2. C-129Y/R-512E
3. C-129Y/VH-109
4. Cb-752/VH-109

4.2.5.2 Cyclic creep: At 10 to 15 cycle intervals the flight simulation specimens were removed from the exposure apparatus for measurement of creep extension. These cyclic creep data were obtained for parent metal and electron beam welded specimens of both alloys with both coatings. A limited number of diffusion bonded specimens were measured along the bond areas to determine if any shear deformation occurred during exposure. In addition, one group of diffusion bonded specimens was measured using a 2-inch (5.08 cm) gage length.

The results have been listed in Tables 4-5 and 4-6 showing total creep extension for individual specimens. Several of the specimens are not included because of incomplete creep data. This was generally caused by loss of the fiducial marks early in the exposure. In addition, only three of the 24 diffusion bonded specimens were included in the cyclic creep measurement program. For specimens that did not survive 100 cycles, the last measurement prior to failure was used. The individual data points are plotted for each specimen as a function of flight simulation cycles in Figures 4-57 to 4-65. No attempt has been made to draw curves through the data points because of the scatter in the measurements. However, a least squares curve fit for each of the parent specimens is included in Appendix B. Included in Figures 4-57, 4-60, 4-62, and 4-64 are the predicted scatter bands for cumulative creep through 100 cycles. As previously discussed in Section 4.2.2, the applied loads were based on nominal specimens with a base metal thickness of 0.011 inch (0.028 cm) after coating and after 100 cycles. The band for each of the parent specimens is plotted using the actual minimum and maximum specimen thicknesses with the assumed base metal diffusion and with an added factor of a uniform 10 percent load increase.

Table 4-5. Cyclic Creep Data – Sylvania R-512E Coated Specimens

| Specimen Number | Alloy | Specimen Type | Cycles | Percent Creep |
|---|---|---|---|---|
| BSP-1 | Cb-752 | Parent | 100 | 2.07 |
| BSP-2 | Cb-752 | Parent | 100 | 2.07 |
| BSP-3 | Cb-752 | Parent | 100 | 2.27 |
| BSP-4 | Cb-752 | Parent | 100 | 2.27 |
| BSP-6 | Cb-752 | Parent | 100 | 2.17 |
| | | | | Avg. 2.17 |
| BSE-6 | Cb-752 | EB weld | 100 | 3.16 |
| BSE-10 | Cb-752 | EB weld | 94* | 2.65 |
| BSE-13 | Cb-752 | EB weld | 100 | 2.36 |
| | | | | Avg. 2.76 |
| BSD-3 | Cb-752 | Diff. bond | 100 | 1.38 |
| BSD-5 | Cb-752 | Diff. bond | 100 | 1.67 |
| BSD-6 | Cb-752 | Diff. bond | 100 | 1.91 |
| | | | | Avg. 1.65 |
| YSP-1 | C-129Y | Parent | 100 | 1.58 |
| YSP-2 | C-129Y | Parent | 100 | 1.88 |
| YSP-3 | C-129Y | Parent | 100 | 1.67 |
| YSP-4 | C-129Y | Parent | 100 | 1.87 |
| YSP-5 | C-129Y | Parent | 100 | 1.88 |
| YSP-6 | C-129Y | Parent | 100 | 1.67 |
| | | | | Avg. 1.76 |
| YSE-1 | C-129Y | EB weld | 100 | 2.07 |
| YSE-2 | C-129Y | EB weld | 100 | 2.16 |
| YSE-13 | C-129Y | EB weld | 100 | 2.27 |
| YSE-14 | C-129Y | EB weld | 100 | 2.56 |
| YSE-15 | C-129Y | EB weld | 100 | 2.37 |
| YSE-16 | C-129Y | EB weld | 100 | 2.17 |
| | | | | Avg. 2.27 |

*Specimen failed during ninety-seventh cycle.

The method, as discussed in Appendix B, was a first-cut approach to predict data scatter. Obviously, as indicated by the four aforementioned figures, the method, assumptions, and basic material property data need considerable refining. However, in examining Figures 4-57, 4-60, 4-62, and 4-64 several observations can be made. First, the fit for the VH-109 coated specimens for both Cb-752 and C-129Y is considerably better than for the R-512E coated specimens. Second, primary creep was ignored in the prediction method. And third, the assumed linear rate of diffusion was incorrect. In fact, for R-512E both the linearity and the rate were incorrect. This function for Cb-752 was later confirmed in Reference 20. Considerable work must yet be done not only to isolate the driving parameters but to generate better baseline material data.

Table 4-6. Cyclic Creep Data — Vac-Hyd VH-109 Coated Specimens

| Specimen Number | Alloy | Specimen Type | Cycles at Last Reading | Cycles to Failure | Percent Creep |
|---|---|---|---|---|---|
| BVP-3 | Cb-752 | Parent | 79 | 89 | 1.18 |
| BVP-4 | Cb-752 | Parent | 32 | 42 | 0.69 |
| BVP-5 | Cb-752 | Parent | 80 | 85 | 1.18 |
| BVP-6 | Cb-752 | Parent | 57 | 83 | 1.28 |
| BVP-7 | Cb-752 | Parent | 78 | 84 | 1.48 |
| BVP-8 | Cb-752 | Parent | 69 | 69 | 1.48 |
| BVE-3 | Cb-752 | EB weld | 55 | 65 | 0.98 |
| BVE-4 | Cb-752 | EB weld | 42 | 50 | 0.79 |
| BVE-6 | Cb-752 | EB weld | 42 | 49 | 0.89 |
| BVE-13 | Cb-752 | EB weld | 58 | 61 | 1.78 |
| BVE-14 | Cb-752 | EB weld | 45 | 61 | 0.79 |
| BVE-15 | Cb-752 | EB weld | 55 | 57 | 1.28 |
| YVP-1 | C-129Y | Parent | 100 | * | 1.97 |
| YVP-2 | C-129Y | Parent | 89 | 91 | 1.87 |
| YVP-3 | C-129Y | Parent | 81 | 86 | 1.28 |
| YVP-4 | C-129Y | Parent | 58 | 78 | 0.89 |
| YVP-5 | C-129Y | Parent | 100 | * | 1.67 |
| YVP-6 | C-129Y | Parent | 100 | * | 1.28 |
| YVE-3 | C-129Y | EB weld | 88 | 94 | 2.07 |
| YVE-4 | C-129Y | EB weld | 80 | 90 | 1.67 |
| YVE-6 | C-129Y | EB weld | 56 | 62 | 1.38 |
| YVE-7 | C-129Y | EB weld | 100 | * | 1.76 |

* Completed 100 cycles.

The scatter in the data arose from several sources. The largest contribution was probably caused by fluctuations in the load levels during simulation testing. A variation of one pound would cause an error of 14 percent in the load level at 2400°F (1589°K). It was during this portion of the flight simulation cycle that the major portion of the creep extension occurred. Other sources of scatter were temperature variations, particularly at 2400°F (1589°K), errors in optical creep measurements, differences in specimen cross-sections, and coating failures. Temperature fluctuations were generally held to ±5°F (± 3°K), but occasionally reached ± 10°F (± 6°K). Errors in optical measurements arose from two sources. The first was the result of limitations of the cathetometer and the finite width of the gage marks. The second was the difficulty of retaining the fiducial marks on many of the specimens because of coating spall. The only system in which coating spall was not a problem was the C-129Y/R-512E. While the thickness of the spall on the Cb-752/R-512E specimens was too small to seriously affect the flight simulation performance, it greatly hampered the creep measurements. New marks could be added from time to time, but the more frequently these were required, the greater became the potential error. The reason for this is that for any set

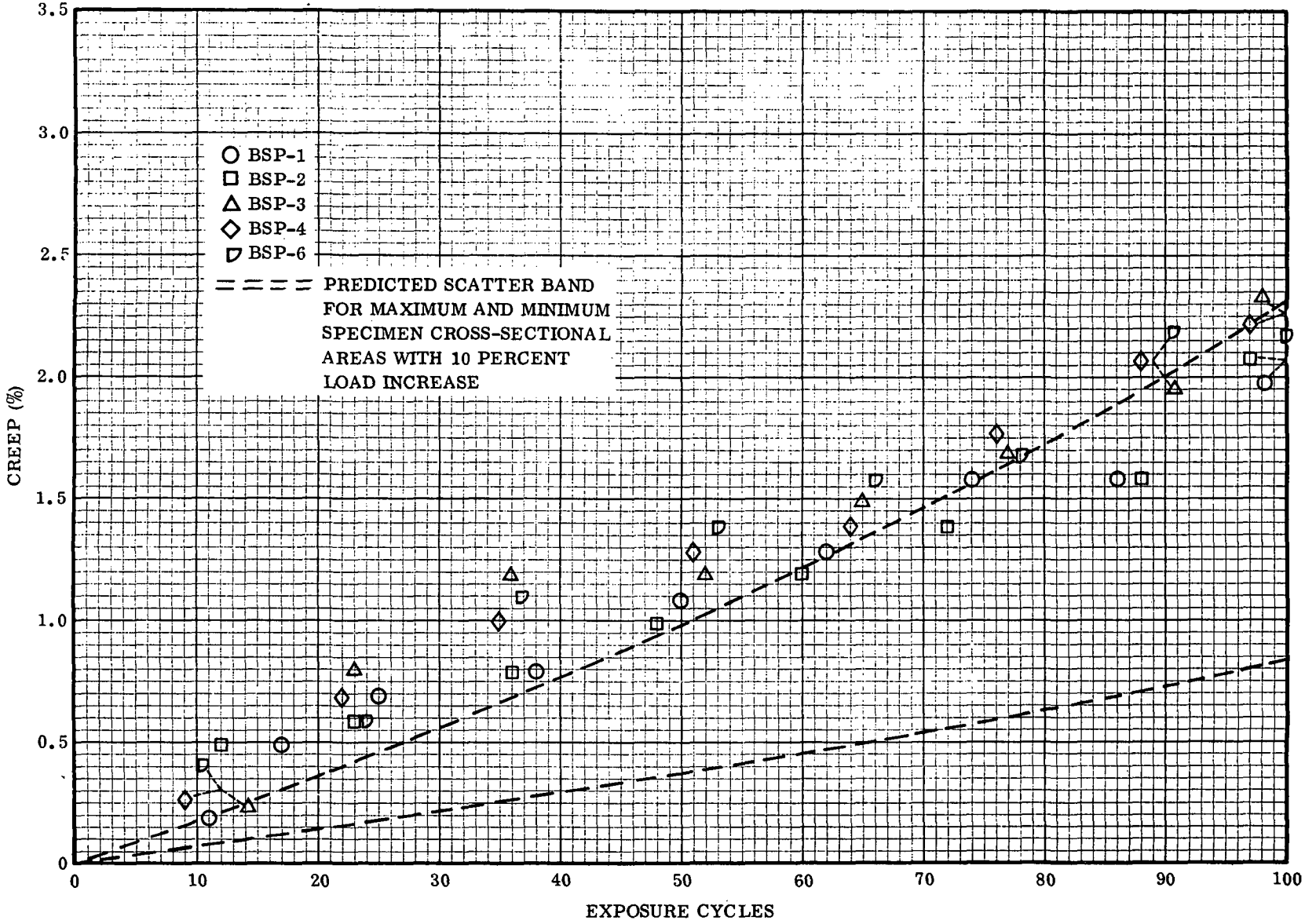


Figure 4-57. Cyclic Creep Data for Cb-752/R-512E Parent Specimens

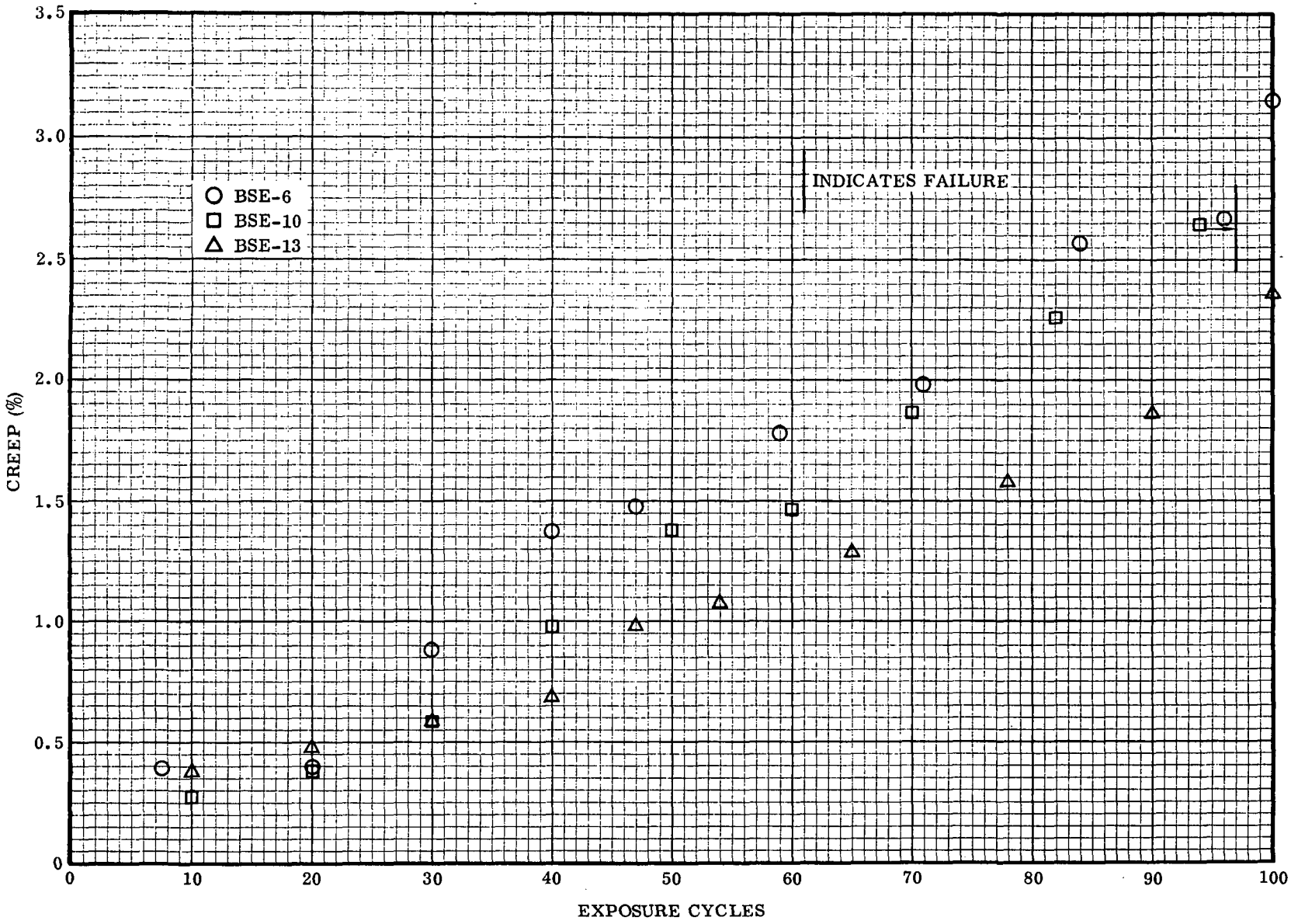


Figure 4-58. Cyclic Creep Data for Cb-752/R-512E Electron Beam Weld Specimens

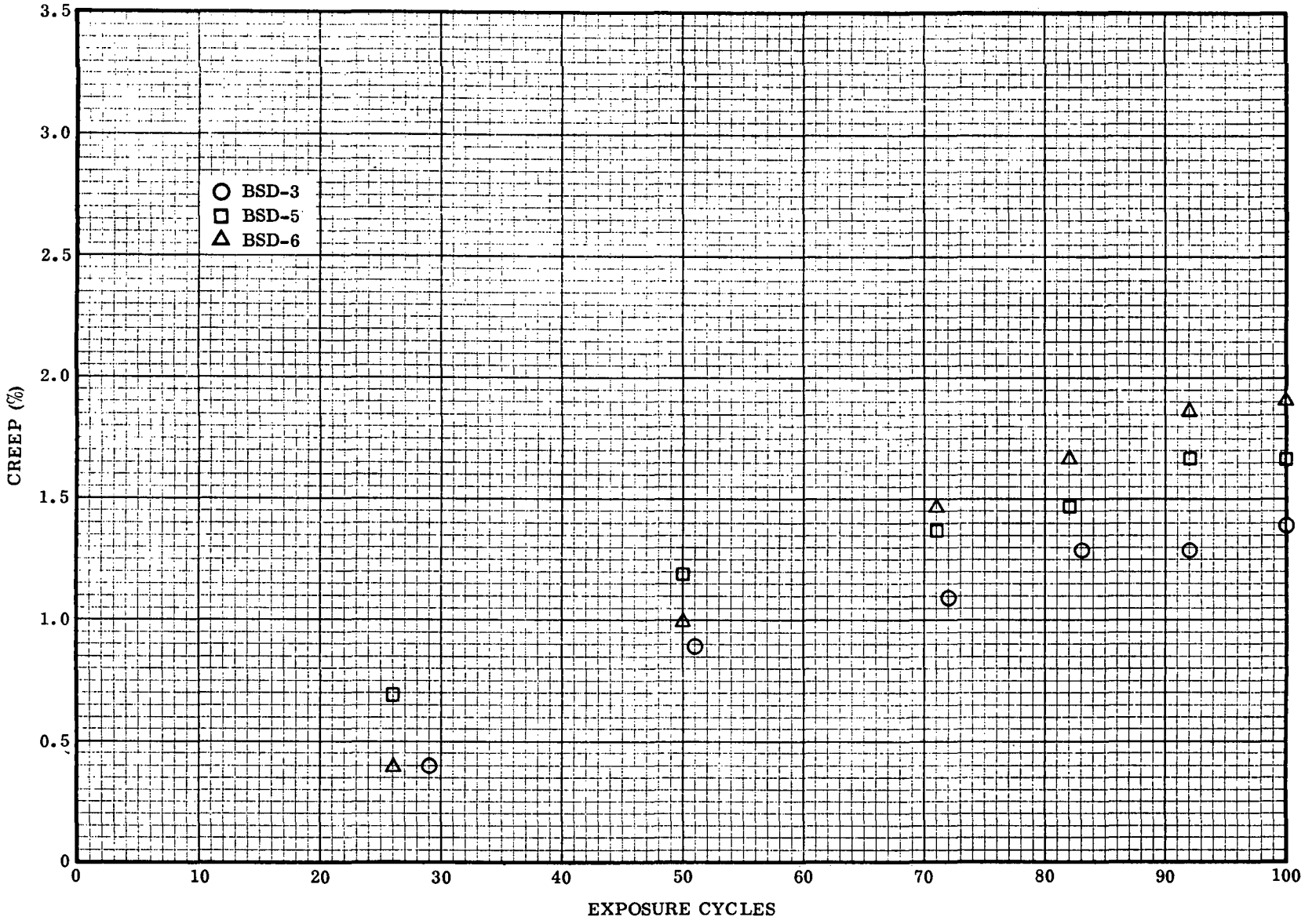


Figure 4-59. Cyclic Creep Data for Cb-752/R-512E Diffusion Bond Specimens

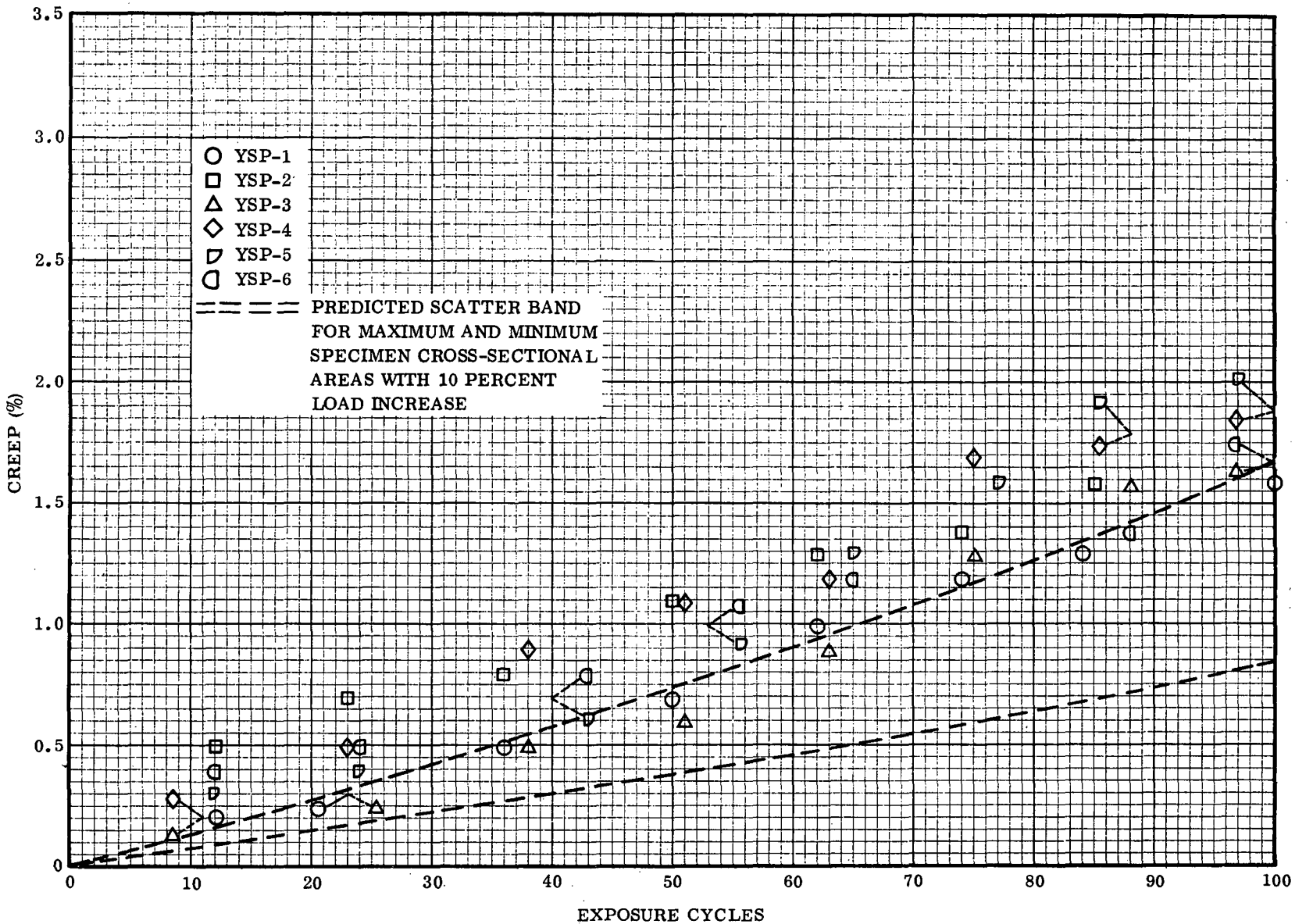


Figure 4-60. Cyclic Creep Data for C-129Y/R-512E Parent Specimens

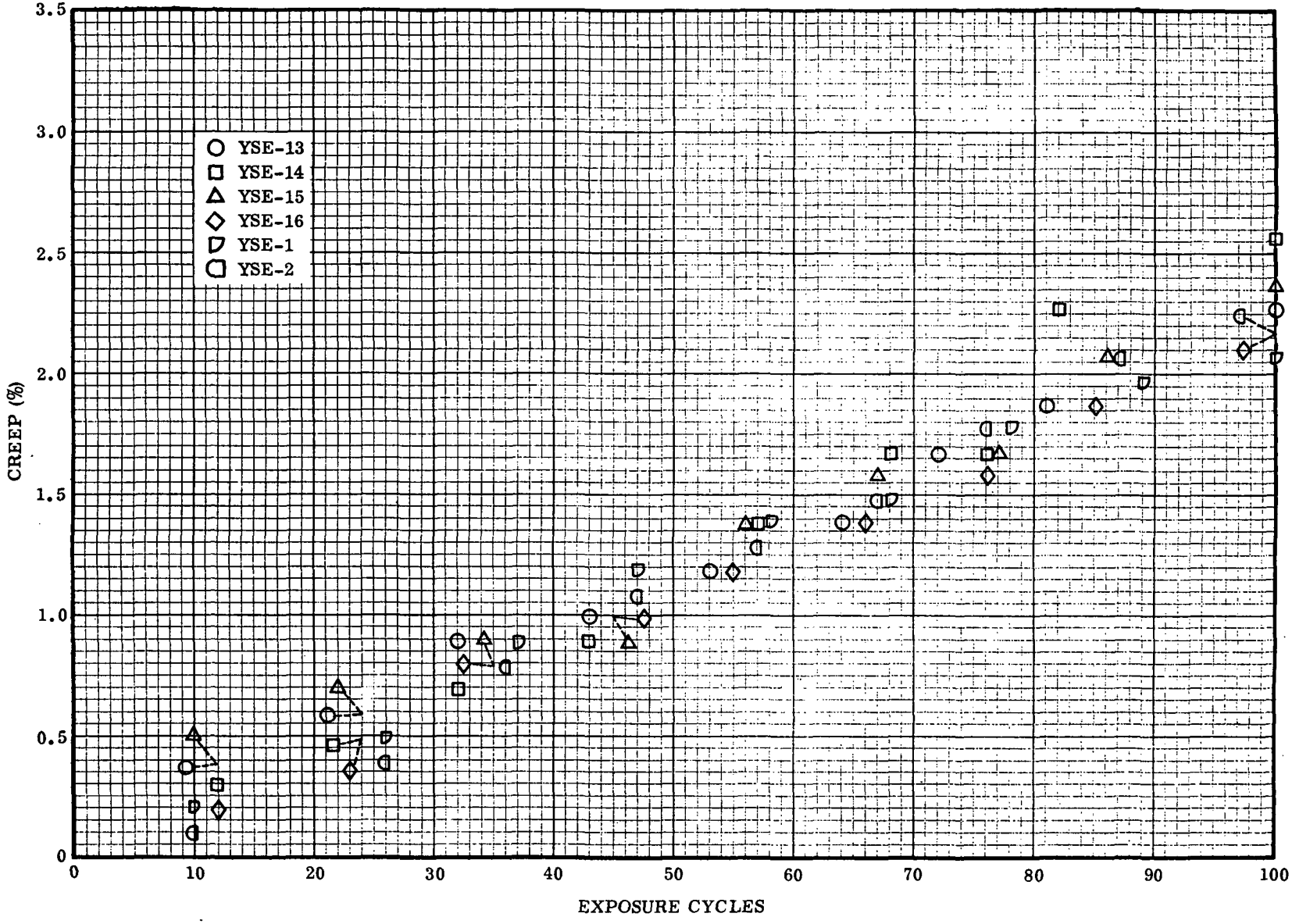


Figure 4-61. Cyclic Creep Data for C-129Y/R-512E Electron Beam Weld Specimens

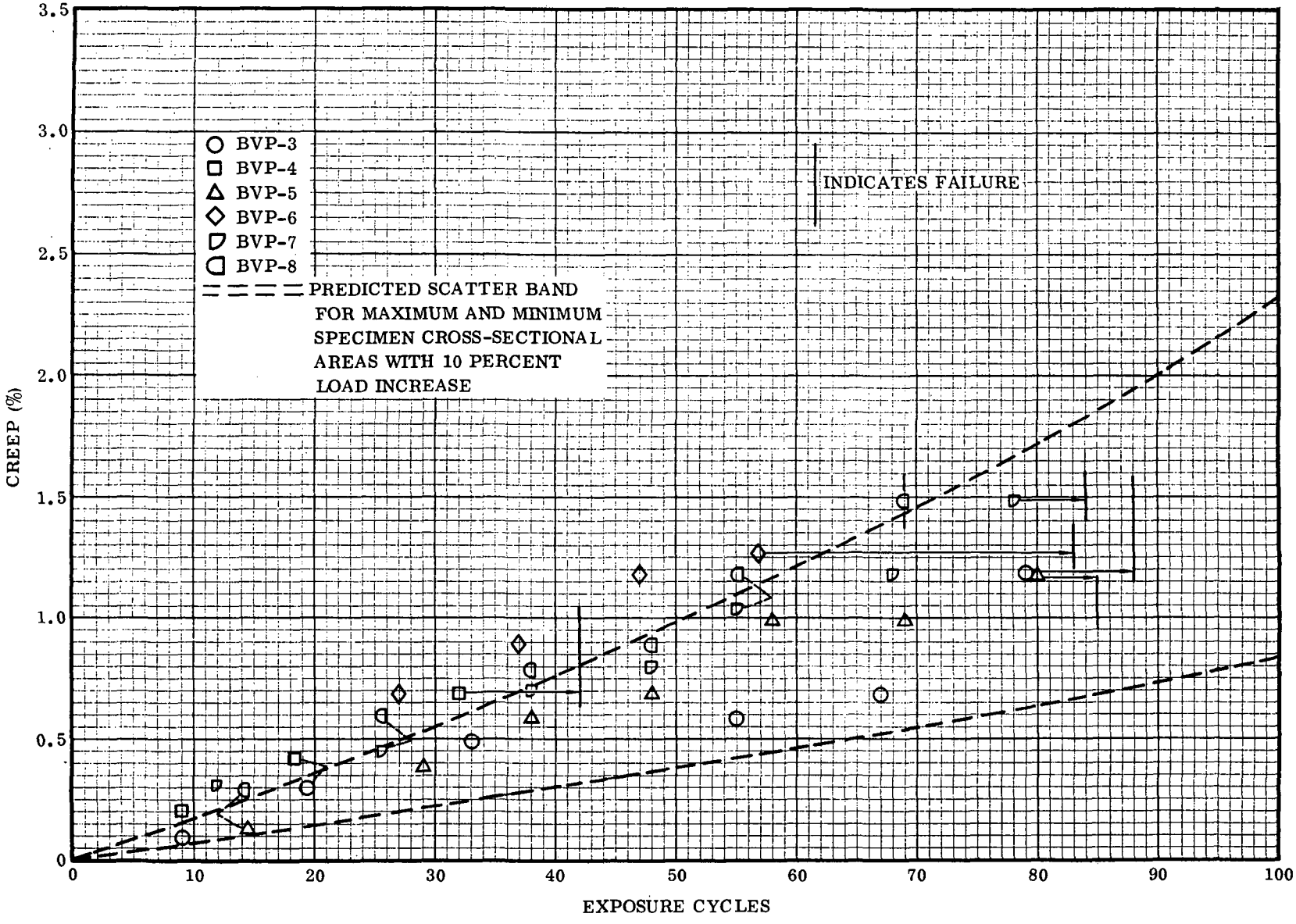


Figure 4-62. Cyclic Creep Data for Cb-752/VH-109 Parent Specimens

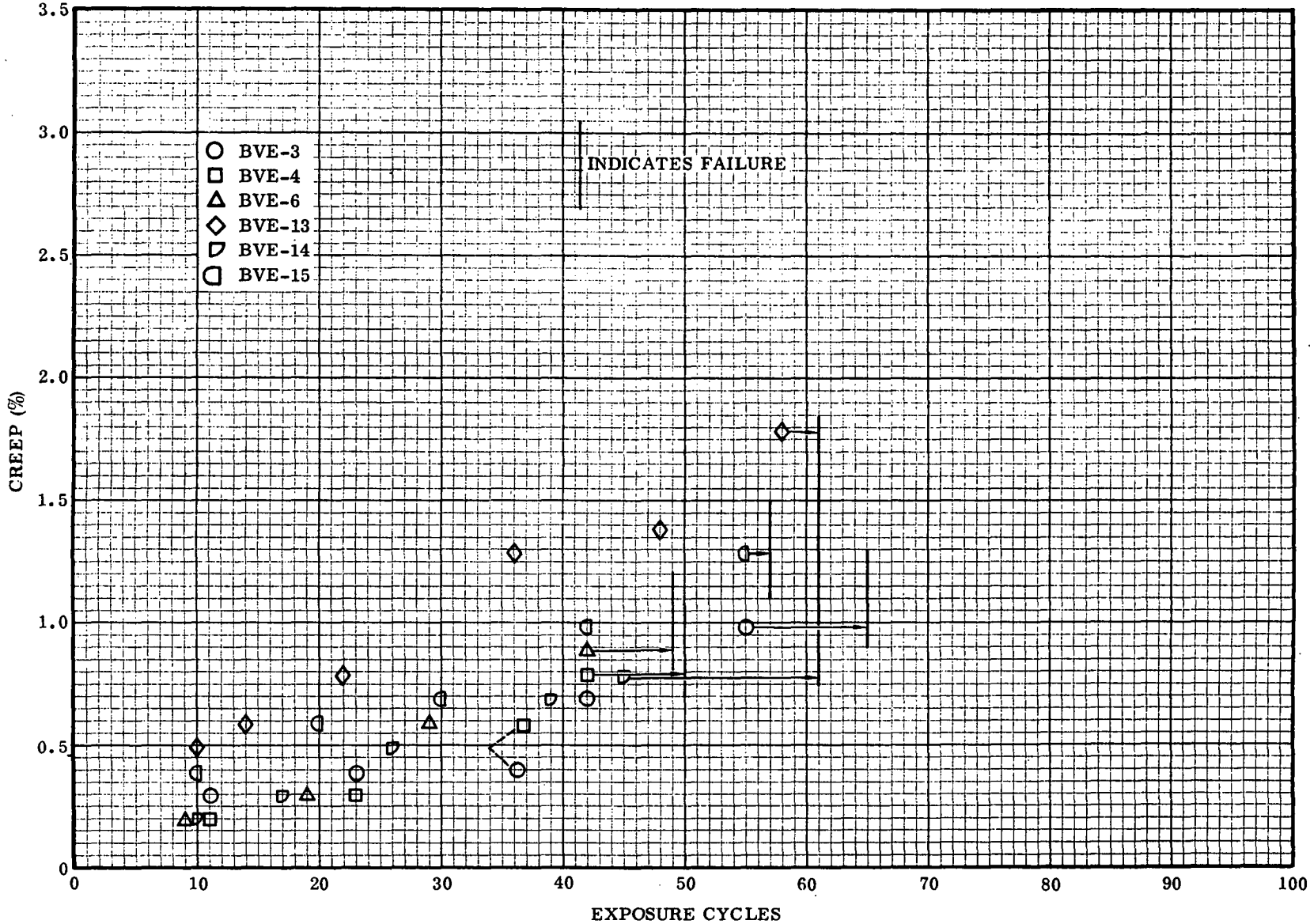


Figure 4-63. Cyclic Creep Data for Cb-752/VH-109 Electron Beam Weld Specimens

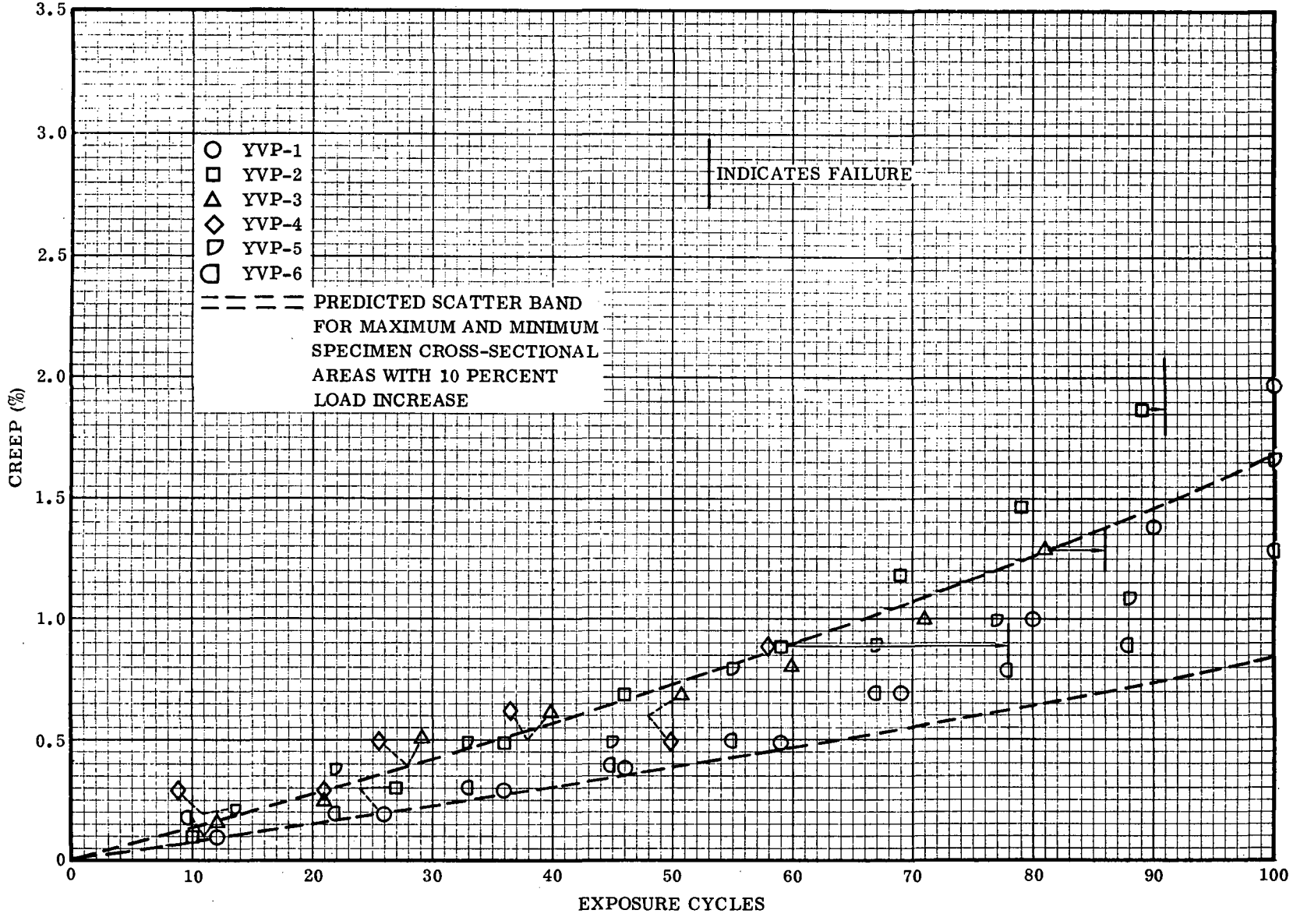


Figure 4-64. Cyclic Creep Data for C-129Y/VH-109 Parent Specimens

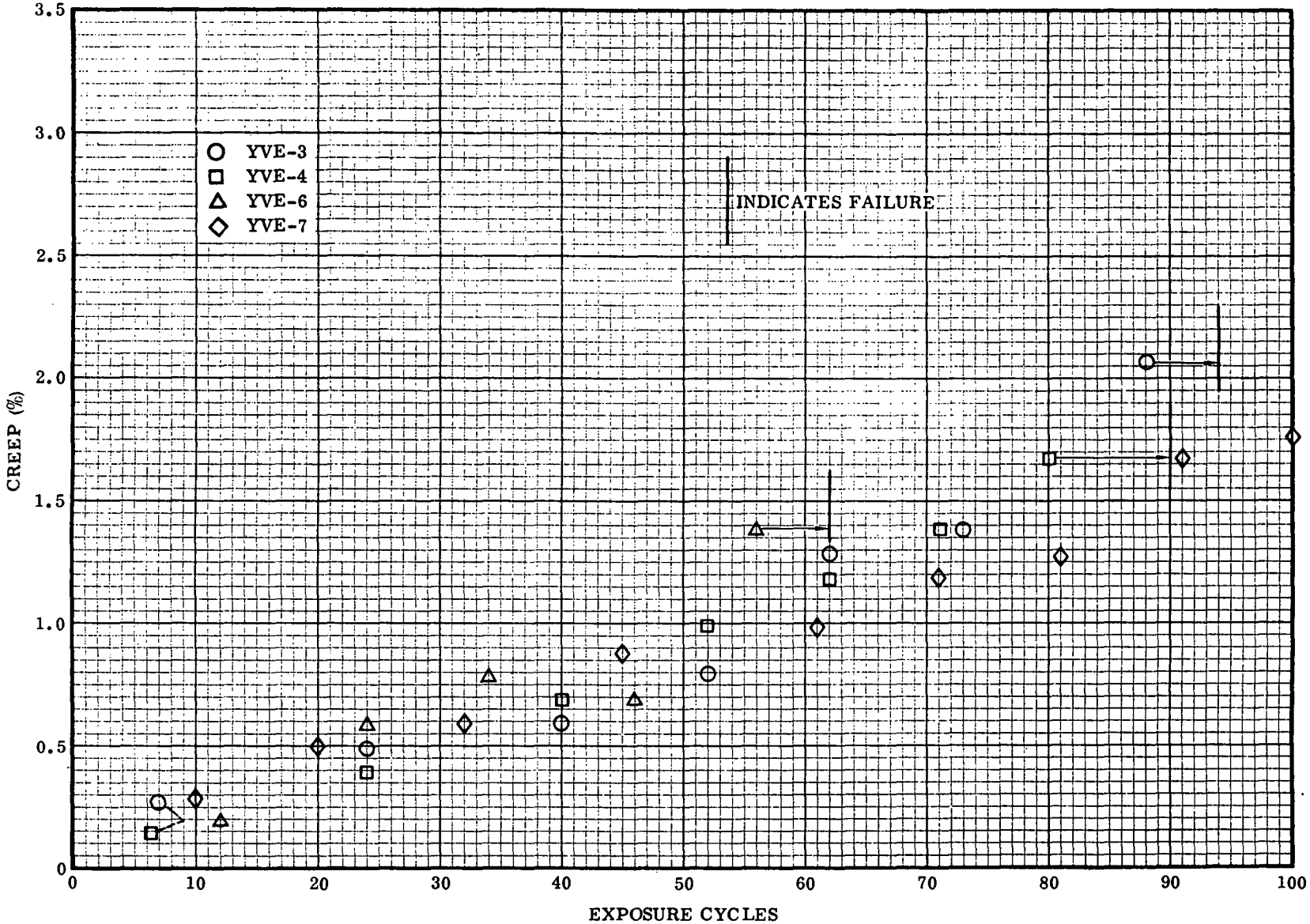


Figure 4-65. Cyclic Creep Data for C-129Y/VH-109 Electron Beam Weld Specimens

of readings there is a maximum potential error of 0.010 cm, i.e., reproducibility in reading the upper gage mark is ±0.005 cm and ±0.005 cm for the lower gage mark. These potential errors (the 0.010 cm) are not additive for each consecutive set of readings unless the fiducial marks are changed. However, whenever a new set of marks is required another potential error of 0.010 cm is introduced. All exposures were made with the same load settings so that differences in cross-sectional areas among the specimens would cause differences in the applied stress levels. With one exception these size differences were small. Table 4-7 gives the maximum, minimum, and average cross-sectional areas of the specimens in each group. These are uncoated areas. The actual calculated areas can be found in Appendix B. As-coated substrate dimensions were not obtained so that any differences in substrate loss during coating was a potential and unknown cause of error. The final source of scatter in the data was the result of coating failures and subsequent loss of substrate during simulation testing. Scatter of this nature was more prevalent in the VH-109 coated specimens as nearly all VH-109 specimens experienced coating failure and substrate loss while only a few R-512E specimens were so affected.

Table 4-7. Cross-Sectional Areas Before Coating

| | | | Area | | | | | |
|---|---|---|---|---|---|---|---|---|
| | | | $in^2$ | | | $cm^2$ | | |
| Alloy | Coating | Specimen Type | Minimum | Maximum | Average | Minimum | Maximum | Average |
| Cb-752 | R-512E | Parent | 0.0073 | 0.0073 | 0.0073 | 0.0478 | 0.0478 | 0.0478 |
| Cb-752 | R-512E | EB weld | 0.0060 | 0.0065 | 0.0063 | 0.0393 | 0.0425 | 0.0412 |
| Cb-752 | R-512E | Diff. bond | 0.0068 | 0.0072 | 0.0070 | 0.0445 | 0.0471 | 0.0458 |
| C-129Y | R-512E | Parent | 0.0068 | 0.0071 | 0.0070 | 0.0445 | 0.0464 | 0.0458 |
| C-129Y | R-512E | EB weld | 0.0068 | 0.0069 | 0.0068 | 0.0445 | 0.0451 | 0.0445 |
| C-129Y | R-512E | Diff. bond | 0.0067 | 0.0068 | 0.0068 | 0.0438 | 0.0445 | 0.0445 |
| Cb-752 | VH-109 | Parent | 0.0070 | 0.0071 | 0.0070 | 0.0458 | 0.0464 | 0.0458 |
| Cb-752 | VH-109 | EB weld | 0.0066 | 0.0067 | 0.0067 | 0.0432 | 0.0438 | 0.0438 |
| Cb-752 | VH-109 | Diff. bond | 0.0066 | 0.0069 | 0.0068 | 0.0432 | 0.0451 | 0.0445 |
| C-129Y | VH-109 | Parent | 0.0068 | 0.0072 | 0.0069 | 0.0445 | 0.0471 | 0.0451 |
| C-129Y | VH-109 | EB weld | 0.0066 | 0.0068 | 0.0067 | 0.0432 | 0.0445 | 0.0438 |
| C-129Y | VH-109 | Diff. bond | 0.0067 | 0.0068 | 0.0068 | 0.0438 | 0.0445 | 0.0445 |

From a study of Figures 4-57 to 4-65, several observations can be made about the cyclic creep properties of these systems. The amount of cyclic creep strain was slightly higher for the Cb-752 alloy than for the C-129Y alloy. This is clearly shown for the Sylvania coating were complete 100 cycle data are available. This is in contrast to the static creep tests where the Cb-752 alloy was found to have a slightly higher creep strength than the C-129Y alloy (see Section 4.5).

A study of the data also reveals that the cyclic creep strain was higher for the electron beam weld specimens than the unwelded material. This would appear to indicate that the welded material possessed a lower creep strength than the unwelded material. However, based on the similarity of the tensile properties of the specimens after flight simulation exposure this is thought to be unlikely. A more logical explanation for the apparent difference in creep strengths is the difference in specimen dimensions. The uncoated cross-sectional areas of the weld specimens were less than that of the parent specimens in every case (Table 4-7). For the system showing the greatest difference in creep strain between welded and unwelded specimens (Cb-752/R-512E), a difference of about 15 percent existed in the uncoated cross-sectional areas. The large difference in creep strain between parent metal and weld specimens of the C-129Y/R-512E system may be partially explained by the higher susceptibility of the weld specimens to edge type coating failures (see Section 4.2.5.1).

Two sets of diffusion bonded specimens were checked for creep extension. In the first, measurements were made using the 1/2-inch (1.27 cm) bond overlap as the gage length to determine if any shear deformation took place during exposure. Within the accuracy of the measurements, 0.05 to 0.10 percent creep, there was no slippage taking place. These measurements were discontinued after 50 cycles. The second set of specimens was measured in the normal manner using a 2-inch (5.08 cm) gage section that included the 1/2-inch (1.27 cm) bond. The data are plotted in Figure 4-59. While the scatter of the data is quite large, the average creep strain after 100 cycles is very nearly 75 percent of that for the parent metal specimens of the same group. This would be expected, assuming little creep to occur in the bond region where the stresses are half of those in the adjacent areas.

A comparison of the static creep data (Section 4.5) with the cyclic creep data reveals a considerably increased creep rate for the cyclic tests. For example, for C-129Y/R-512E at 2400°F (1589°K) and 1 ksi (6.89 $MN/m^2$), 2 percent creep occurs in 86 hours, while for the cyclic tests 2 percent creep (approximately) occurs in 100 cycles. Assuming that the flight simulation cycle is equivalent to 15 minutes at 2400°F (1589°K) with a 1 ksi (6.89 $MN/m^2$) stress, the time for 100 cycles is about 25 hours as compared to 86 hours for the static test. The difference for the Cb-752/R-512E system is even greater — 25 hours compared to just over 200 hours.

As a check on the high creep rates observed during the flight simulation exposures, an additional set of specimens was introduced into the test program. These extra specimens included the following systems: C-129Y/R-512E, parent; C-129Y/R-512E, electron beam weld; and Cb-752/R-512E, electron beam weld. The same temperature and pressure conditions were retained, but the load profile was reduced about 64 percent of the standard load in an attempt to hold the total creep strain to about 1 percent after 100 cycles. The 2400°F (1589°K) load was 4.5 lb (20 N) as compared to the 7 lb (31 N) used in the original exposures.

The data are plotted in Figure 4-66 for the three material systems. The total creep strain for the three specimens falls between 1 and 1.5 percent. These values are in fair agreement with the previous results for the Cb-752 specimens (considering the difference in load profiles), but somewhat high for the C-129Y alloy. It is interesting to note that the Cb-752 alloy ranked slightly higher in creep resistance in these tests, in agreement with the static creep tests. Table 4-8 summarizes the cyclic and static creep results for the C-129Y/R-512E system.

Table 4-8. Cyclic and Static Creep Properties of C-129Y/R-512E

| Test | Stress | Total Creep (%) | Time |
|---|---|---|---|
| Cyclic | | | |
| Normal load profile | 1 ksi* (6.89 $MN/m^2$) | 2.0** | 100 cycles |
| Reduced load profile | 0.64* (4.41 $MN/m^2$) | 1.3** | 100 cycles |
| Static | | | |
| 2400°F (1589°K) | 1 ksi (6.89 $MN/m^2$) | 2.0 | 86 hours |
| 2400°F (1589°K) | 0.64 ksi (4.41 $MN/m^2$) | 1.0 | 86 hours |

* Stress during 2400°F (1589°K) portion of flight cycle.

** Average of parent and weld specimens.

4.2.5.3 Metallography: An extensive metallographic study was conducted during the course of the flight simulation test program. Specimens from the 12 exposure groups (alloy/coating, condition) were examined both before and after flight simulation exposure. While not a part of the flight simulation test program, the plasma arc metallographic group is also included in this section.

4.2.5.3.1 Flight simulation exposure: Results of the flight simulation metallographic study presented in the following discussion are divided into four sections by material system, i.e., alloy/coating. This was done because of the similarity in the behavior of the parent metal, electron beam weld, and diffusion bond specimens of the same system. Specimens were examined at the locations shown in Figure 4-67, in both the as-coated condition and after exposure. The as-coated specimens had previously been tensile tested while the exposed specimens had either failed during simulation testing, or were tensile tested after 100 cycles. As a result, considerable cracking of the brittle coating with some loss was evident in many of the polished sections. A typical specimen from each exposure group was chosen for examination according to the plan illustrated in Figure 4-67. In addition, a second specimen was generally selected from each group to study some special effect, e.g., a site of severe coating

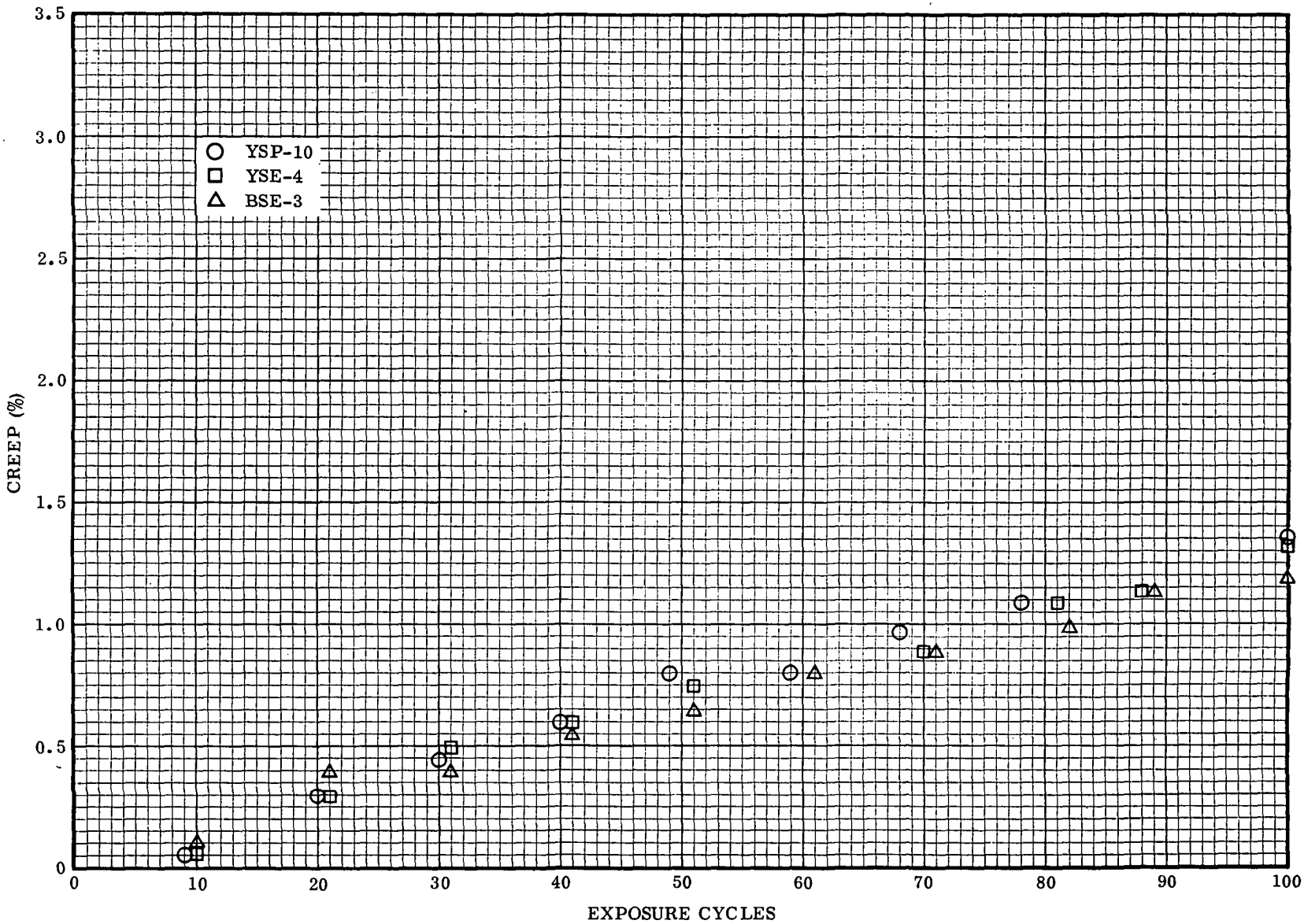


Figure 4-66. Cyclic Creep Data for Flight Simulation Tests with Reduced Load Profile

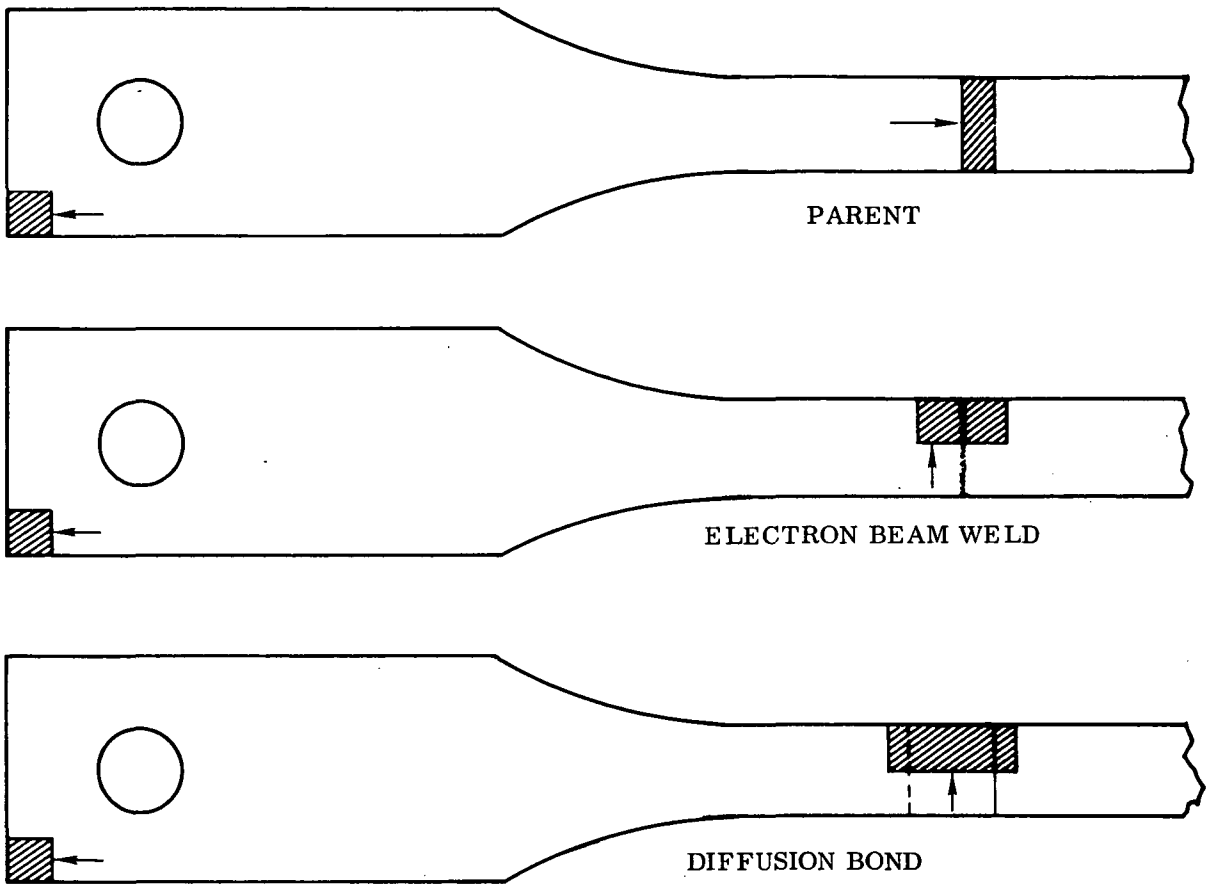


Figure 4-67. Location of Sections for Metallographic Examinations

spall or edge attack. The normal procedure for preparing the metallographic specimens was to use a very light etch ($HF-HNO_3-H_2O$) to bring out the details in the coating and diffusion zone. In addition, the as-coated samples were later re-etched for a longer period of time to show the grain structure of the substrate and details of the joints. Several of the specimens were also etched by an anodizing technique developed by Wah Chang Albany. This method was particularly useful for revealing areas of oxygen contamination. Photomicrographs of these specimens were taken in color to more clearly illustrate the regions of contamination.

System 1, Cb-752/R-512E: Photomicrographs for this system are shown in Figures 4-68 to 4-73 for parent specimens, Figures 4-74 to 4-80 for weld specimens, and Figures 4-81 to 4-84 for diffusion bond specimens. The as-coated specimens are shown after a light etch to highlight the coating and diffusion zone, and again after a longer etch to show the grain structure of the substrate and the details of the joint specimens. The light etch used in Figures 4-68, 4-74, and 4-81 reveals the various coating layers and numerous fine cracks typical of a silicide coating. The cracks are larger and increased in number in the weld and diffusion bond specimens as these

sections were cut from the gage sections of tensile tested specimens. The parent metal sample, on the other hand, was cut from the less deformed shoulder portion of the specimen. Higher magnification views of the coating/substrate interface are shown in Figures 4-70 and 4-76. The absence of subsurface cracks parallel to the coating/substrate interface as well as voids or porosity is an indication of good coating adherence. No evidence of substrate contamination or formation of second phase particles is visible in the substrate at these magnifications. The coating is composed of layers or zones (as many as seven can be distinguished) of disilicides and subsilicides, primarily $MSi_2$ in the outer layer, and $M_5Si_3$ in the inner layers, where M=(Cb, Cr, Fe) (Reference 23). The difference in crack size between the parent and weld samples is readily apparent at the higher magnification. These cracks, which are always present in silicide coatings, arise either during the coating process as a result of residual compressive stresses because of the large difference in specific volume of the substrate and the coating, or during cooldown after coating because of tensile stresses generated by thermal expansion mismatch between coating and substrate. They generally terminate in the diffusion zone, but many have extended to the substrate as a result of tensile testing and the polishing operation.

Figures 4-69, 4-75, and 4-84 show the more heavily etched parent, weld, and bond specimens prior to exposure. The longer etch has removed much of the detail of the coating and greatly increased the crack size by chemical attack. The grain structure is generally equiax although not particularly uniform — with the bond sample having a slightly larger grain size. A narrow [0.040 inch (0.102 cm)] trapezoidal shaped weldment is visible in Figure 4-75. The weld appears to be free of cracks, porosity, or gross contamination. The diffusion bond sample, Figure 4-84, shows coating penetration at the lap joint corner with some type of interaction at the titanium inner layer. This is not surprising as titanium reacts readily during the formation of the silicide coating.

During the bonding and coating processes the 0.001 inch (0.003 cm) titanium foil and the columbium alloy sheet have interdiffused to form a solid solution zone about 0.002 inch (0.005 cm) thick. Some fine cracks, porosity, and inclusions are visible within the diffusion zone, but the interfaces appear to be free from defects. The origin of the microcracks is unknown although not uncommon for this joining process (Reference 24). It has been pointed out previously (Reference 24) that because they are parallel to any load across the bond, they appear to be harmless. The porosity, primarily aligned in two parallel rows, is believed to have originated at the former titanium foil surface. The rows have a spacing of about 0.0006 inch (0.0015 cm) rather than the initial foil thickness of 0.001 inch (0.003 cm). Movement of the voids toward the center of the titanium foil could be the result of the Kirkendall effect if the titanium were the faster diffusing constituent. Sufficient diffusion data were not available to verify this, however.

The effect of flight simulation cycling on coating performance and tensile properties of the parent, weld, and bond specimens of Cb-752/R-512E was very similar. Metallographic examination of these specimens, however, revealed a striking difference between the welds and the other two groups. Considerable substrate contamination as a result of oxygen penetration was visible in the weld samples, whereas none was found in the parent or bond samples. Figures 4-77 to 4-80 were taken from two specimens of the weld group. While no substrate contamination is visible in the weld zone, Figure 4-77, evidence of substrate attack can be seen at the bottom of several coating cracks. Similar attack, along with contamination, is shown in Figure 4-78 taken a short distance from the weld of Figure 4-77. An enlargement of one of these coating cracks is presented in Figure 4-79. Oxidation at the root of this crack has consumed about 0.0005 inch (0.0013 cm) of the substrate and left the grey oxide visible in the photograph. No unusual effects were noted in the weld itself, another indication of the suitability of electron beam welds to simulated flight exposure cycling. Figure 4-80 was taken near the fracture site of specimen BSE-10, the only R-512E coated specimen that did not complete 100 flight simulation cycles. While no evidence of coating failure was observed from a macroscopic examination of the specimen, the photomicrograph in Figure 4-80 shows considerable substrate contamination.

In contrast to the weld samples, the exposed parent metal specimens, Figures 4-71 to 4-73, and diffusion bond specimens, Figures 4-82 and 4-83, show no evidence of coating failure or substrate contamination. This is clearly shown in Figure 4-73, a photo of an anodized parent metal specimen. After 100 flight cycles, the coating cracks have enlarged and filled with a grey oxide but have not penetrated through the diffusion zone into the alloy substrate. Figures 4-71 and 4-72 are taken from the gage section and the grip of an exposed parent specimen. Because of the steep temperature gradient in the simulator, the grip section remained relatively cool during cycling and showed almost no effect from the 100 cycles. From a comparison of thicknesses in the two figures, a substrate consumption by diffusion zone growth of about 0.0005 inch (0.0013 cm) per side in 100 cycles was determined.

The final two photomicrographs of this section, Figures 4-82 and 4-83, were taken from two exposed bond specimens. Again, no substrate contamination was found, but numerous coating cracks have penetrated the diffusion zone and substrate oxidation appears imminent. The effect of 100 flight cycles on the appearance of the bond was limited to a slight increase in the titanium/coating interaction at the bond edges, Figure 4-83. No effect on coating performance was observed.

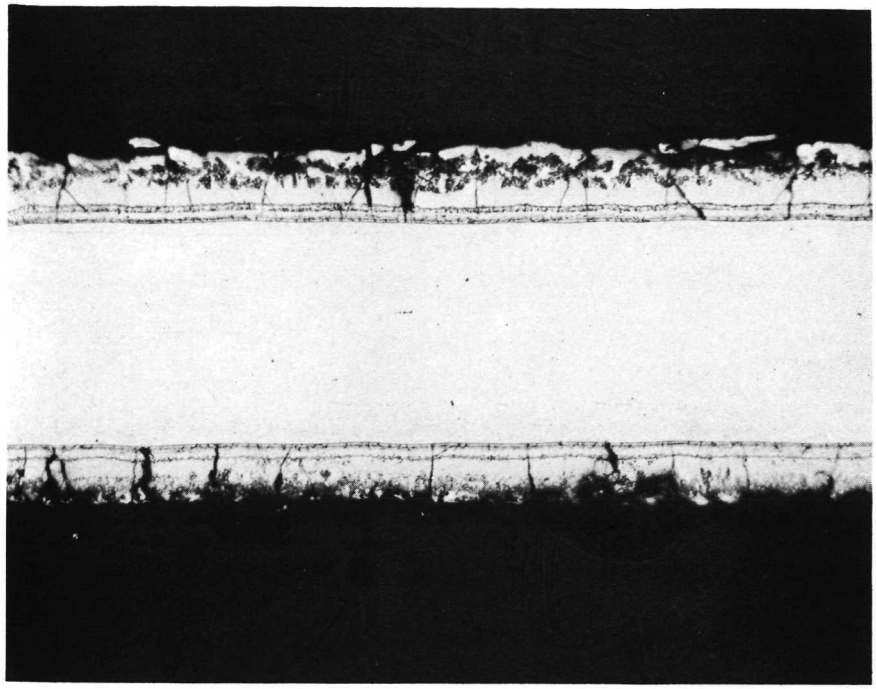

Magnification: 100X
Etch: Light
Specimen No.: BSP-21
Flight Cycles: 0
Negative No.: D-1143
Mount No.: 94-0

Figure 4-68. Microstructure of Unexposed Cb-752/R-512E Parent Specimen — Gage Section

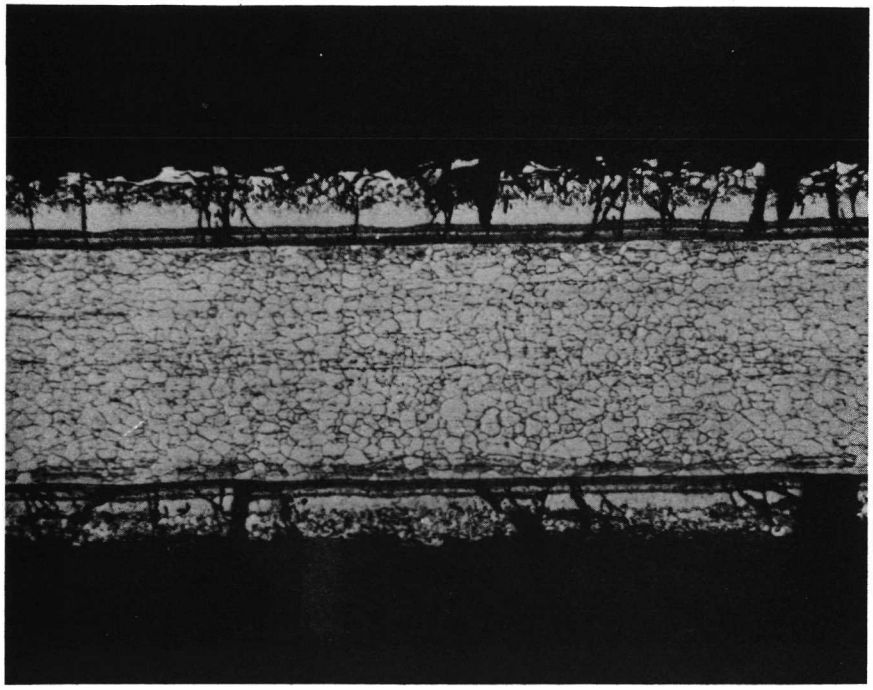

Magnification: 100X
Etch: Heavy
Specimen No.: BSP-21
Flight Cycles: 0
Negative No.: C-9699
Mount No.: 94-0

Figure 4-69. Microstructure of Unexposed Cb-752/R-512E Parent Specimen — Gage Section

| | |
|---|---|
| Magnification: | 500X |
| Etch: | Light |
| Specimen No.: | BSP-21 |
| Flight Cycles: | 0 |
| Negative No.: | D-1144 |
| Mount No.: | 94-0 |

Figure 4-70. Microstructure of Unexposed Cb-752/R-512E Parent Specimen — Gage Section

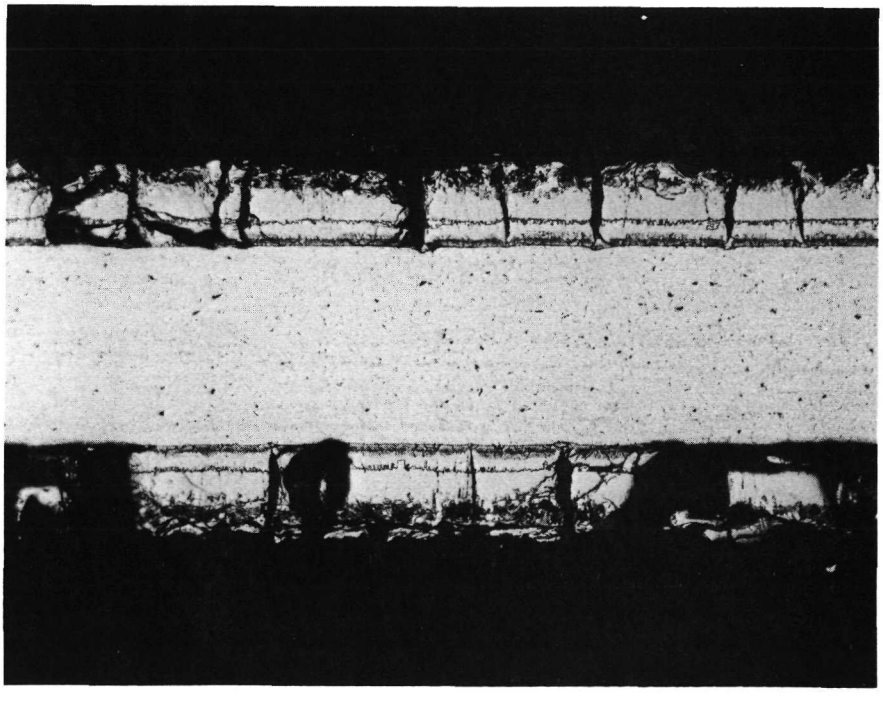

| | |
|---|---|
| Magnification: | 100X |
| Etch: | Light |
| Specimen No.: | BSP-2 |
| Flight Cycles: | 100 |
| Negative No.: | D-506 |
| Mount No.: | 432-0 |

Figure 4-71. Microstructure of Exposed Cb-752/R-512E Parent Specimen — Gage Section

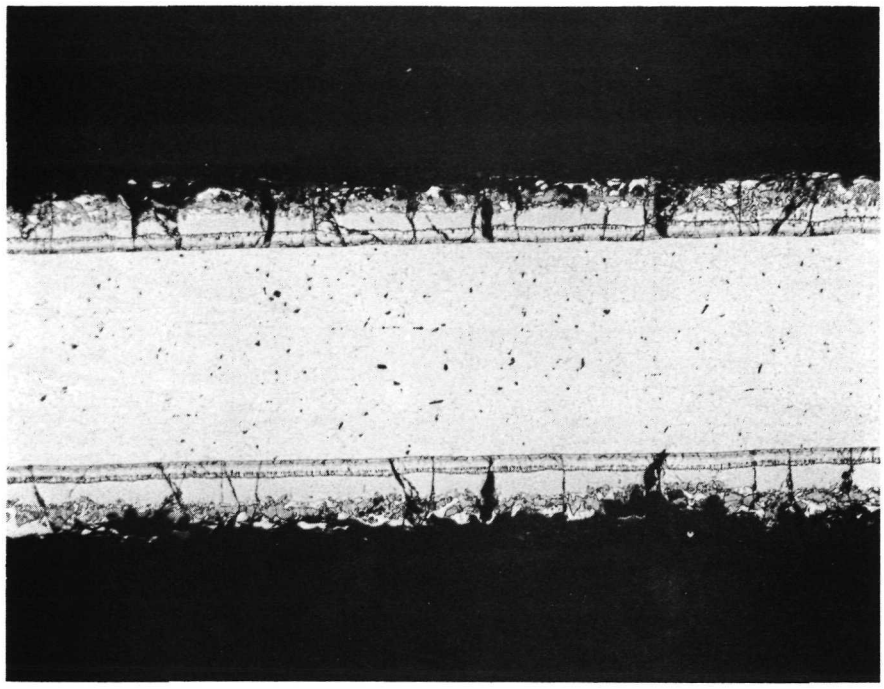

Magnification: 100X
Etch: Light
Specimen No.: BSP-2
Flight Cycles: 100
Negative No.: D-507
Mount No.: 432-0

Figure 4-72. Microstructure of Exposed Cb-752/R-512 Parent Specimen — Grip Section

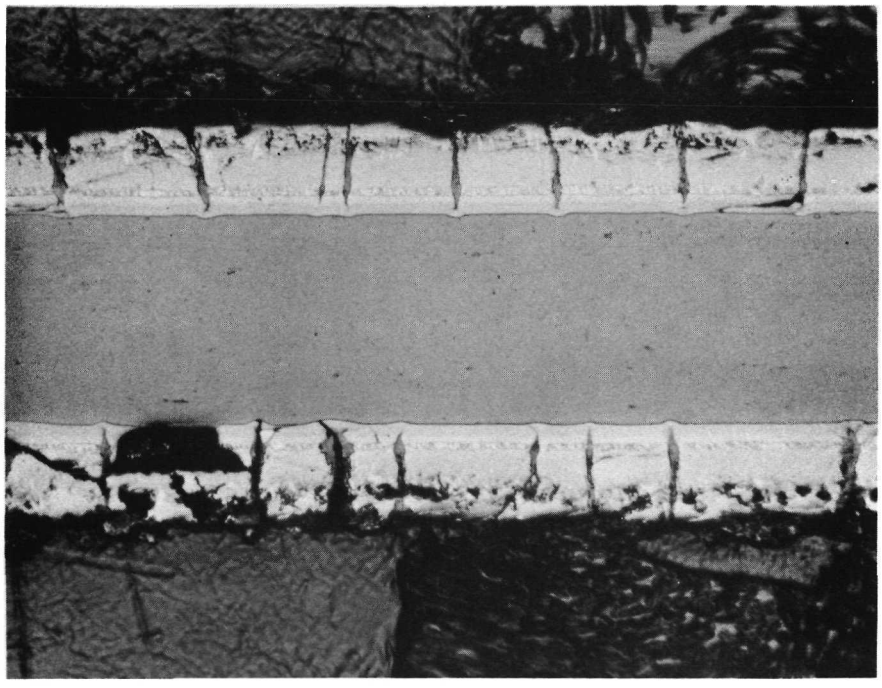

Magnification: 100X
Etch: Anodized
Specimen No.: BSP-5
Flight Cycles: 100
Negative No.: D-800
Mount No.: 506-0

Figure 4-73. Microstructure of Exposed Cb-752/R-512E Parent Specimen — Gage Section

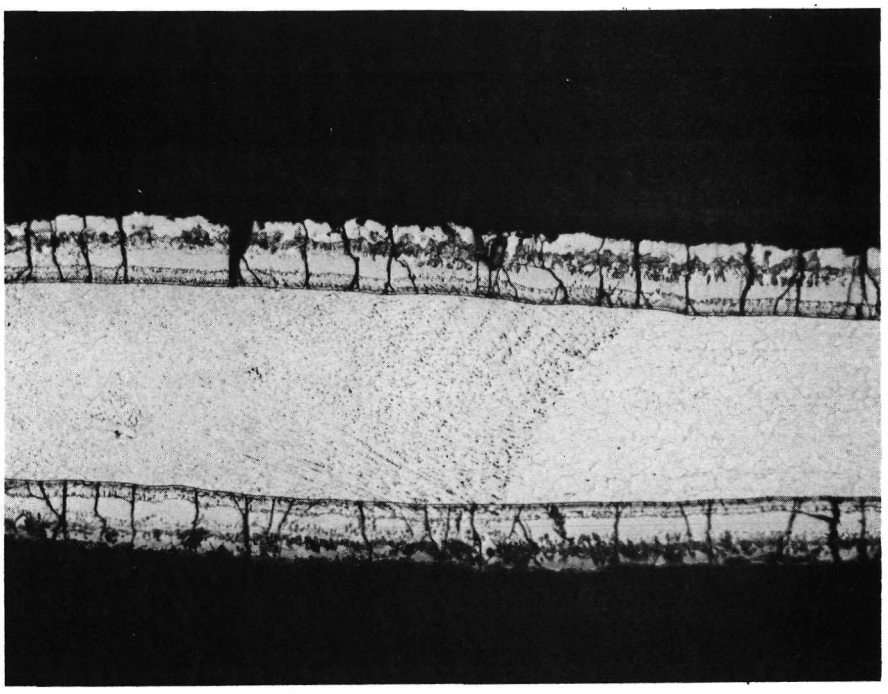

| | |
|---|---|
| Magnification: | 100X |
| Etch: | Light |
| Specimen No.: | BSP-18 |
| Flight Cycles: | 0 |
| Negative No.: | D-1135 |
| Mount No.: | 93-0 |

Figure 4-74. Microstructure of Unexposed Cb-752/R-512E Electron Beam Weld Specimen – Gage Section

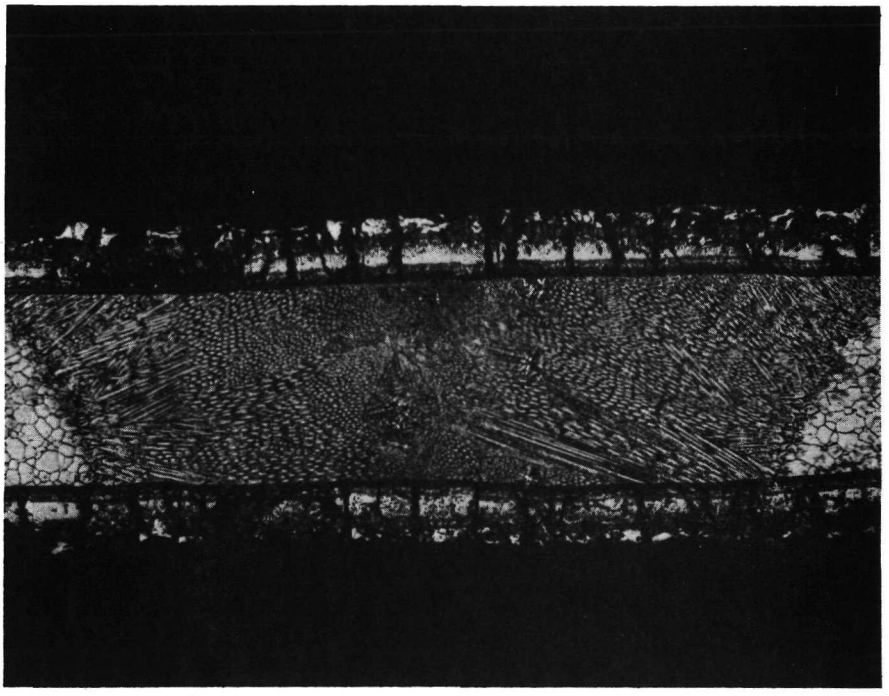

| | |
|---|---|
| Magnification: | 100X |
| Etch: | Heavy |
| Specimen No.: | BSE-18 |
| Flight Cycles: | 0 |
| Negative No.: | C-9702 |
| Mount No.: | 93-0 |

Figure 4-75. Microstructure of Unexposed Cb-752/R-512E Electron Beam Weld Specimen – Gage Section

Magnification: 500X
Etch: Light
Specimen No.: BSE-18
Flight Cycles: 0
Negative No.: D-1136
Mount No.: 93-0

Figure 4-76. Microstructure of Unexposed Cb-752/R-512E Electron Beam Weld Specimen – Gage Section

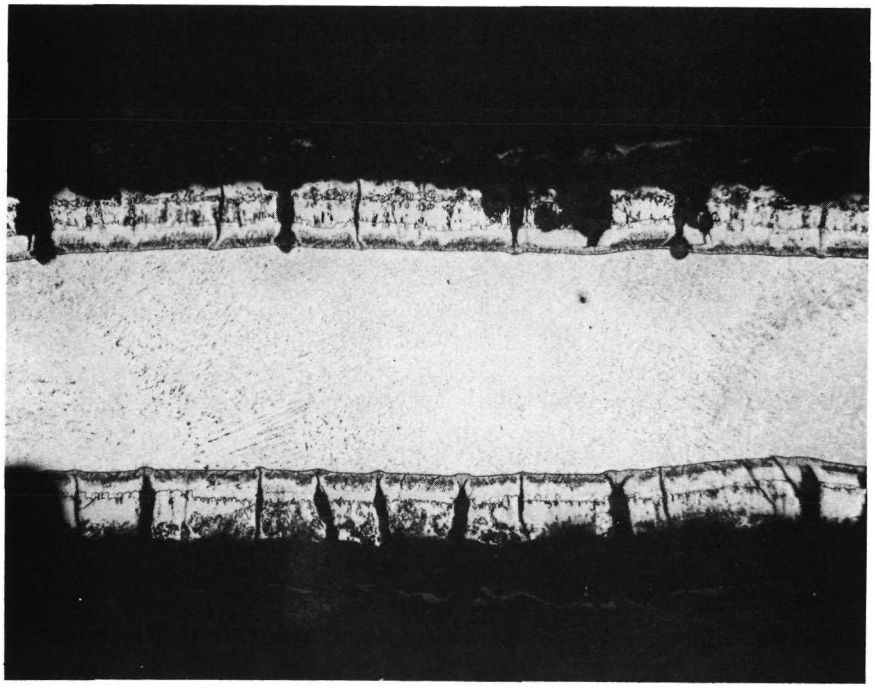

Magnification: 100X
Etch: Light
Specimen No.: BSE-6
Flight Cycles: 100
Negative No.: D-1213
Mount No.: 299-0

Figure 4-77. Microstructure of Exposed Cb-752/R-512E Electron Beam Weld Specimen – Gage Section

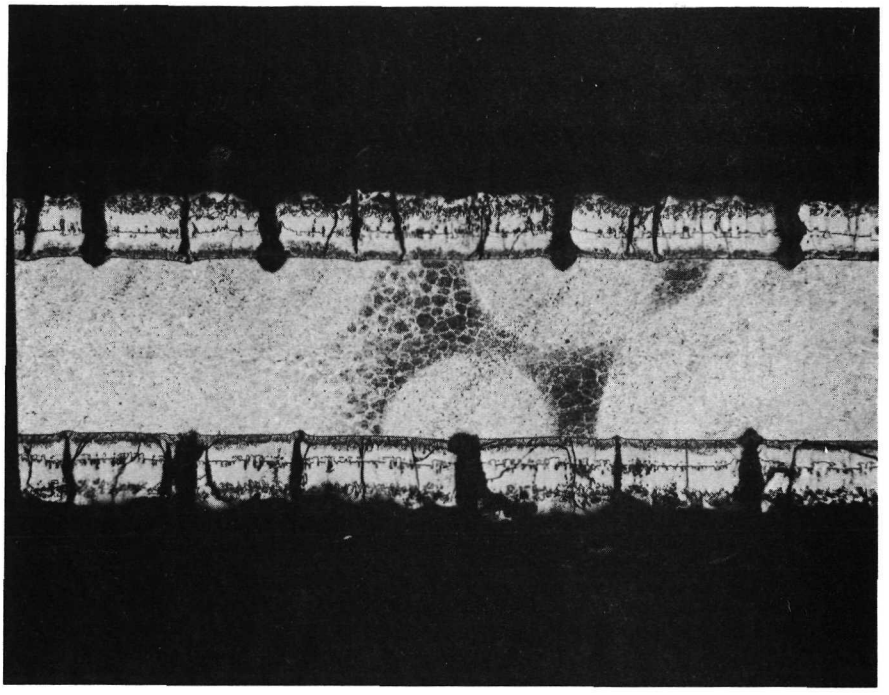

| | |
|---|---|
| Magnification: | 100X |
| Etch: | Light |
| Specimen No.: | BSE-6 |
| Flight Cycles: | 100 |
| Negative No.: | D-1214 |
| Mount No.: | 299-0 |

Figure 4-78. Microstructure of Exposed Cb-752/R-512E Electron Beam Weld Specimen – Gage Section

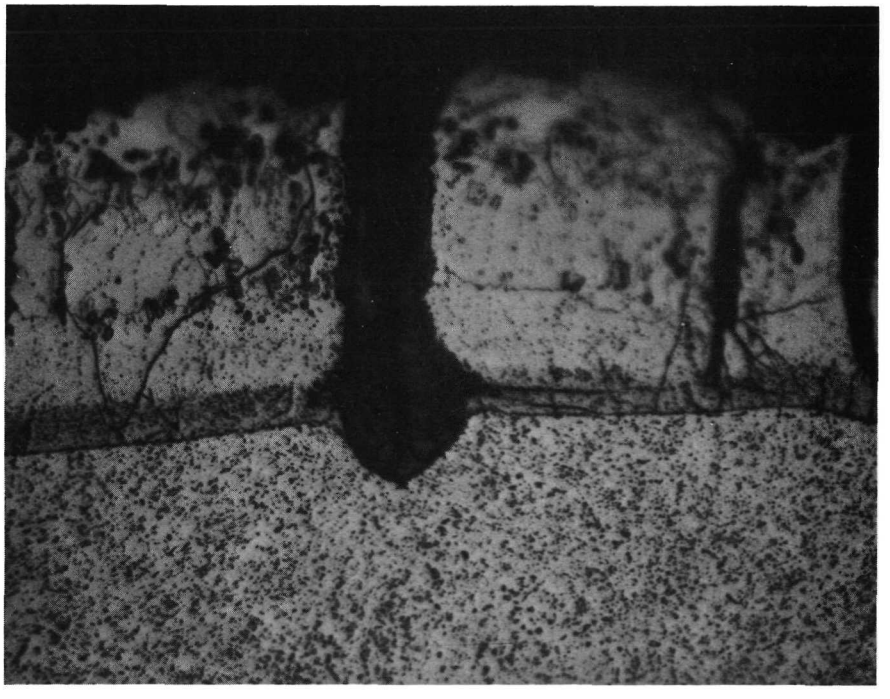

| | |
|---|---|
| Magnification: | 500X |
| Etch: | Light |
| Specimen No.: | BSE-6 |
| Flight Cycles: | 100 |
| Negative No.: | D-1217 |
| Mount No.: | 299-0 |

Figure 4-79. Microstructure of Exposed Cb-752/R-512E Electron Beam Weld Specimen – Gage Section

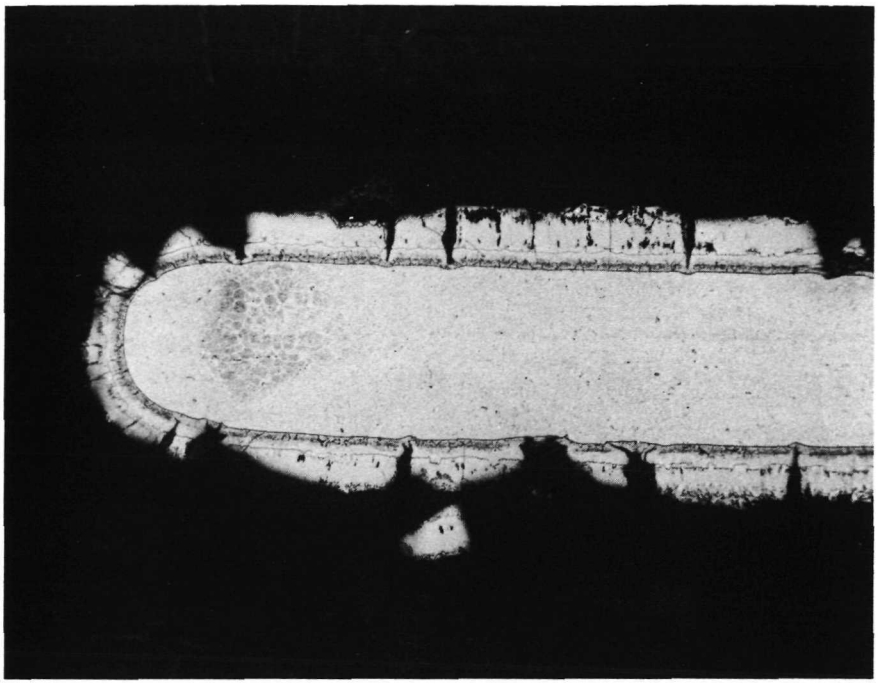

| | |
|---|---|
| Magnification: | 100X |
| Etch: | Light |
| Specimen No.: | BSE-10 |
| Flight Cycles: | 97 |
| Negative No.: | D-1215 |
| Mount No.: | 327-0 |

Figure 4-80. Microstructure of Exposed Cb-752/R-512E Electron Beam Weld Specimen – Gage Section

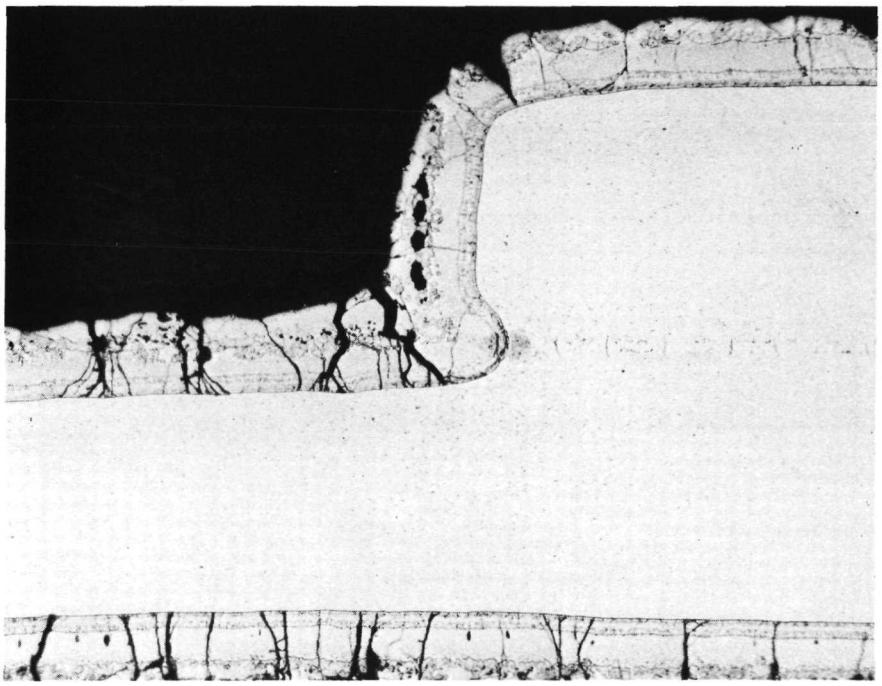

| | |
|---|---|
| Magnification: | 100X |
| Etch: | Light |
| Specimen No.: | BSD-23 |
| Flight Cycles: | 0 |
| Negative No.: | D-1152 |
| Mount No.: | 181-0 |

Figure 4-81. Microstructure of Unexposed Cb-752/R-512E Diffusion Bond Specimen – Gage Section

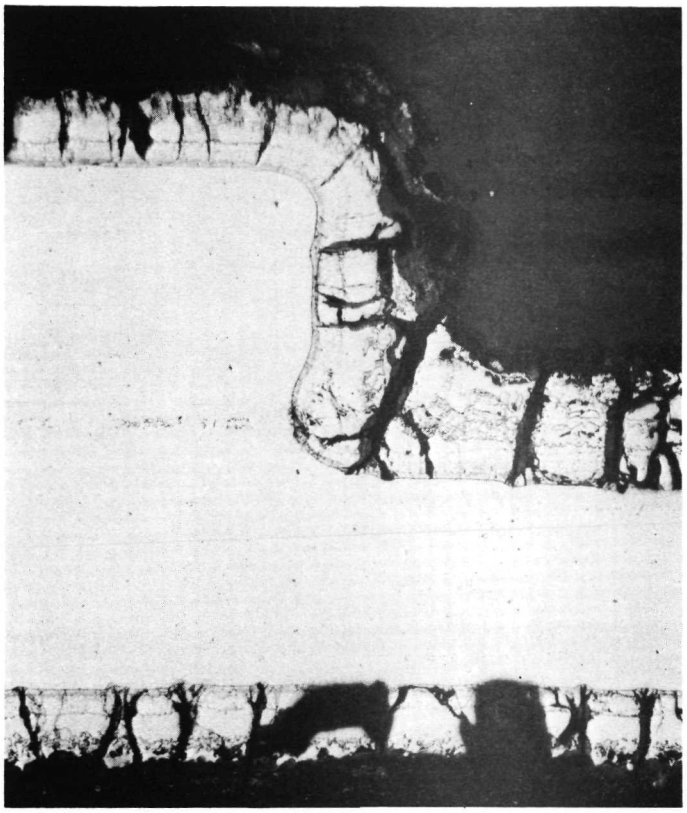

Magnification: 100X
Etch: Light
Specimen No.: BSD-3
Flight Cycles: 100
Negative No.: D-884
Mount No.: 596-0

**Figure 4-82.** Microstructure of Exposed Cb-752/R-512E Diffusion Bond Specimen — Gage Section

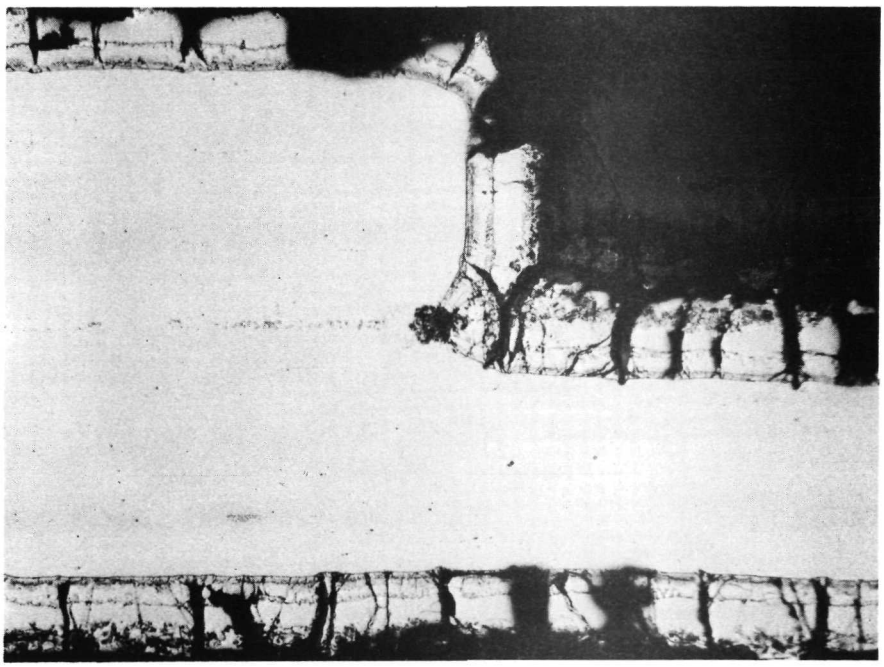

Magnification: 100X
Etch: Light
Specimen No.: BSD-10
Flight Cycles: 100
Negative No.: D-886
Mount No.: 596-0

**Figure 4-83.** Microstructure of Exposed Cb-752/R-512E Diffusion Bond Specimen — Gage Section

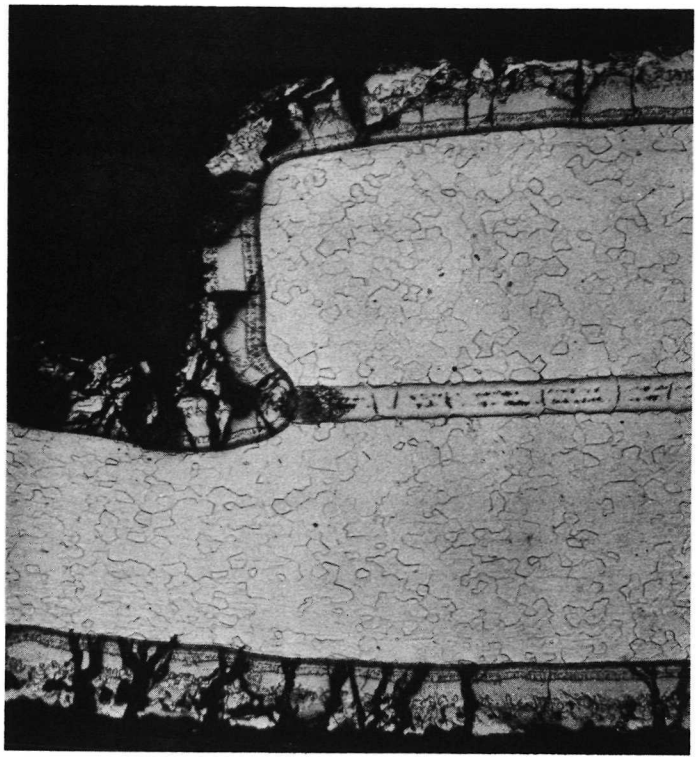

| | |
|---|---|
| Magnification: | 100X |
| Etch: | Heavy |
| Specimen No.: | BSD-23 |
| Flight Cycles: | 0 |
| Negative No.: | C-9736 |
| Mount No.: | 181-0 |

Figure 4-84. Microstructure of Unexposed Cb-752/R-512E Diffusion Bond Specimen — Gage Section

System 2, Cb-752/VH-109. Photomicrographs for this system are presented in Figures 4-85 to 4-90 for parent specimens, Figures 4-91 to 4-95 for weld specimens, and Figures 4-96 to 4-101 for the bond specimens.

Examination of the as-coated samples, Figures 4-85, 4-91, and 4-96, revealed a significant difference in coating uniformity between the VH-109 specimens and the R-512E specimens. During firing of the coatings, approximately 0.001 inch (0.003 cm) of substrate per side is consumed. For the R-512E specimens, this loss of material was very uniform. The VH-109 specimens, on the other hand, showed many small regions of excessive substrate loss. While the effect was more prevalent for the weld specimens, see for example Figure 4-91, it was also observed to some degree in the parent and bond specimens. Irregularities of this nature are thought to result from the application of nonuniform slurry compositions.

The structure of the VH-109 coating was somewhat similar to the R-512E coating, (compare Figures 4-87 and 4-93 to Figures 4-70 and 4-76), except for having fewer distinct layers. The as-coated grain structure of the three types of specimens was also the same for the two coatings, Figures 4-86, 4-92, and 4-97, with the diffusion bonds again having a slightly large size. The weld and bond specimens were

affected about the same by the VH-109 coating as by the R-512E except for an increased coating penetration at the lap joint corners of several of the VH-109 diffusion bond specimens.

Samples of exposed parent metal specimens are shown in Figures 4-88 to 4-90. Each specimen has a thick oxide layer with very little coating remaining. Several areas of complete coating failure with oxide extending to the substrate can be seen. In Figure 4-90, etching was long enough to show the oxygen contamination within the alloy. Measurements on Figures 4-88 and 4-89 reveal a loss of substrate during the 88 flight cycles of about 0.0005 inch (0.0013 cm) per side.

Very similar structures were observed in exposed weld specimens, Figures 4-94 and 4-95. The reason for the significantly lower average exposure lifetimes of the weld specimens compared to the parent specimens was not apparent from these figures. One might suggest that the uneven coating, more prevalent in the welds, might be the answer. However, in these small areas of excessive substrate loss, the coating has generally been retained more effectively than in the other regions. Coating failures and substrate contamination can be seen in both figures.

Photomicrographs of two exposed bond specimens are presented in Figures 4-98 to 4-101. The first, BVD-9, shows considerable coating loss and substrate contamination. One bond corner has been severely undercut during the coating operation and appears to have some interaction at the coating/titanium innerlayer interface. The other specimen, Figures 4-100 and 4-101, has been etched lighter and shows less oxygen contamination but clearly shows the outer oxide layer and several sites of oxide penetration to the substrate.

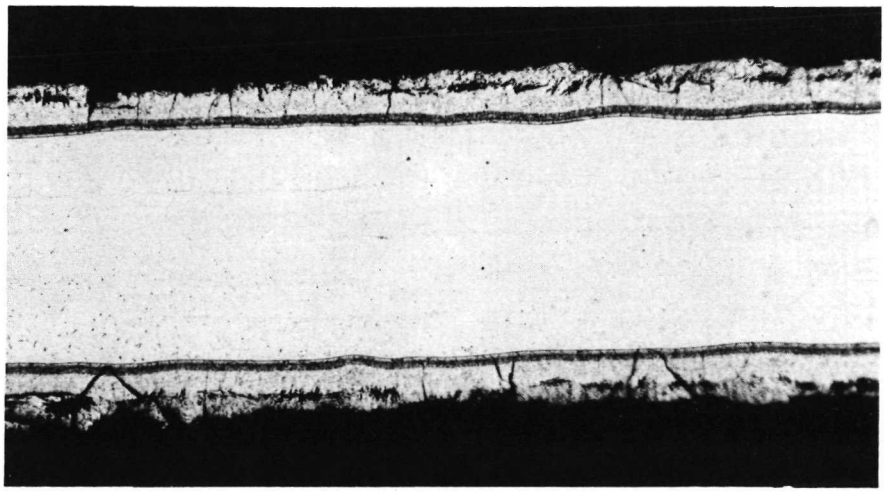

| | |
|---|---|
| Magnification: | 100X |
| Etch: | Light |
| Specimen No.: | BVP-20 |
| Flight Cycles: | 0 |
| Negative No.: | D-1141 |
| Mount No.: | 94-0 |

Figure 4-85. Microstructure of Unexposed Cb-752/VH-109 Parent Specimen — Gage Section

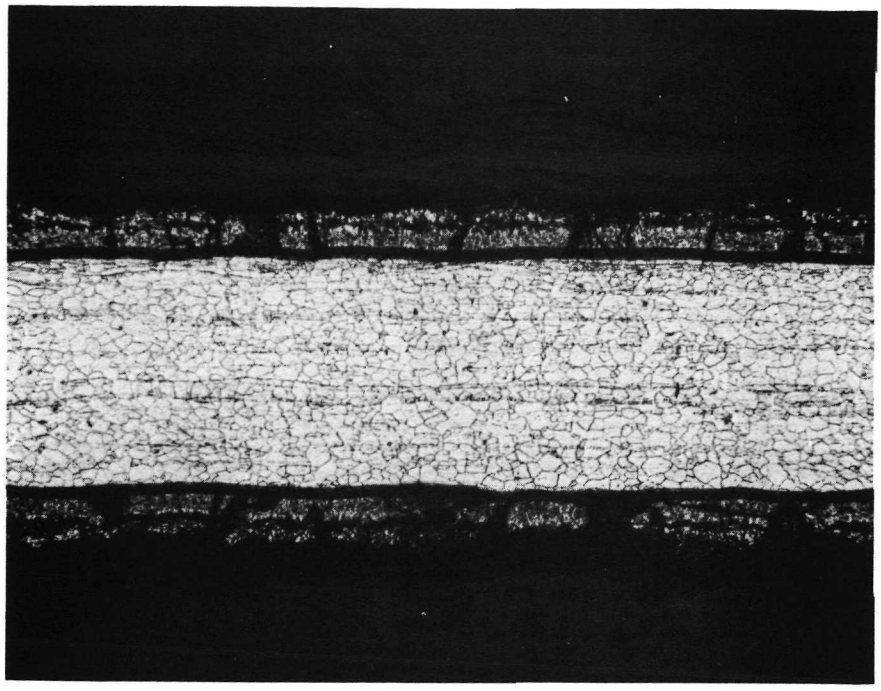

Magnification: 100X
Etch: Heavy
Specimen No.: BVP-20
Flight Cycles: 0
Negative No.: C-9698
Mount No.: 94-0

Figure 4-86. Microstructure of Unexposed Cb-752/VH-109 Parent Specimen — Gage Section

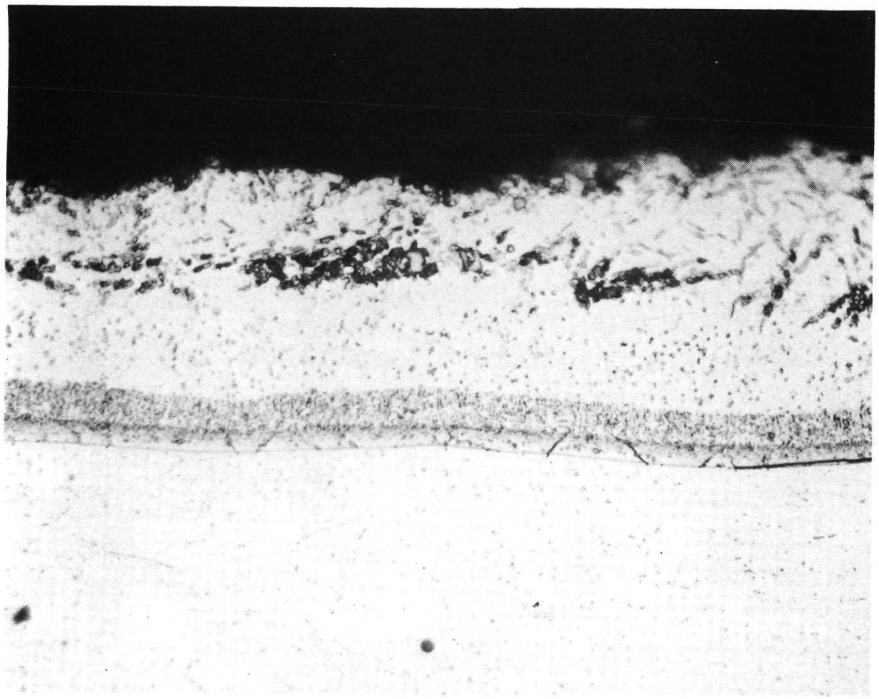

Magnification: 500X
Etch: Light
Specimen No.: BVP-20
Flight Cycles: 0
Negative No.: D-1142
Mount No.: 94-0

Figure 4-87. Microstructure of Unexposed Cb-752/VH-109 Parent Specimen — Gage Section

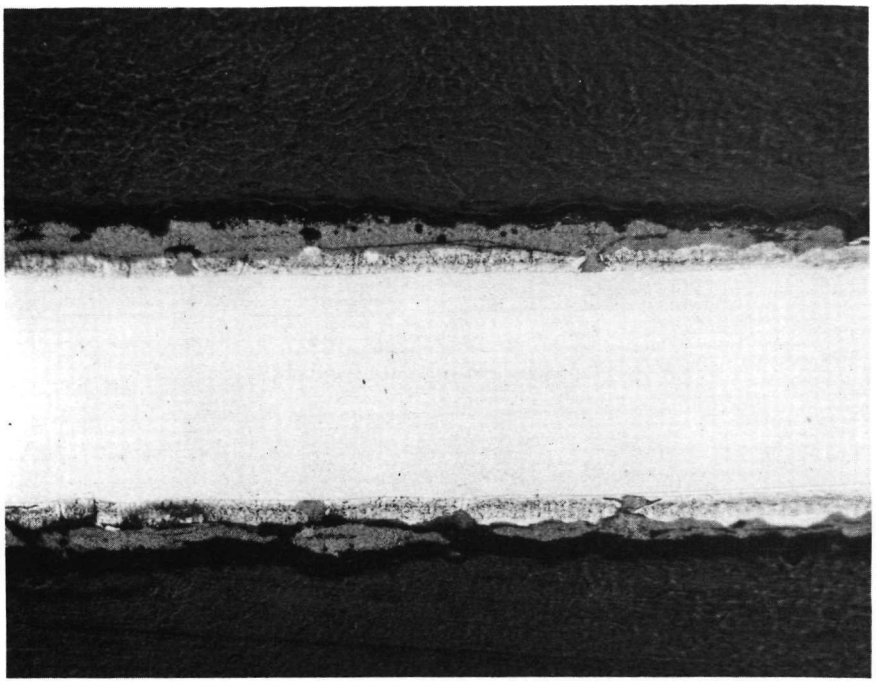

Magnification: 100X
Etch: Light
Specimen No.: BVP-3
Flight Cycles: 88
Negative No.: D-881
Mount No.: 595-0

Figure 4-88. Microstructure of Exposed Cb-752/VH-109 Parent Specimen — Gage Section

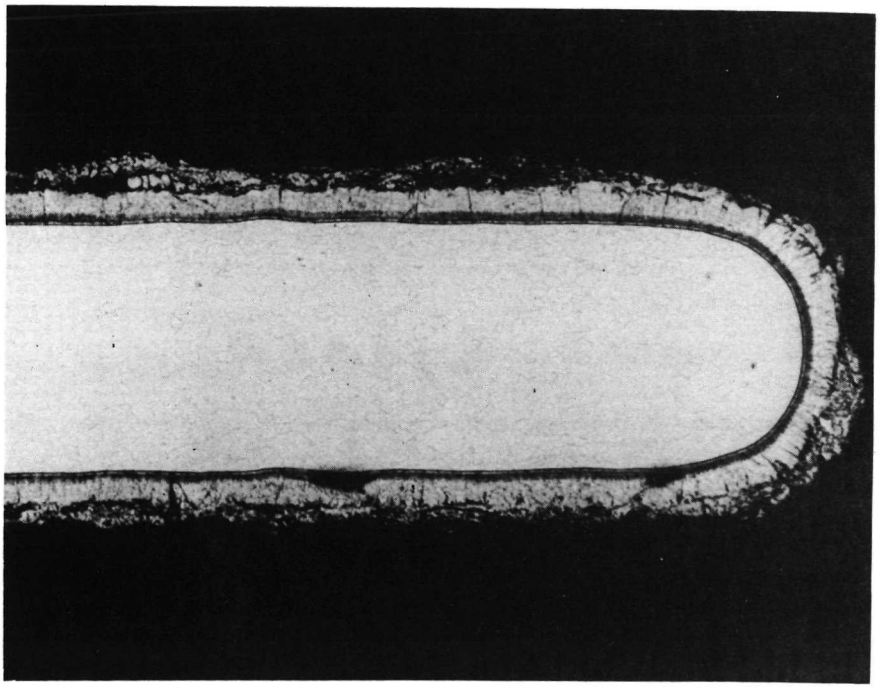

Magnification: 100X
Etch: Light
Specimen No.: BVP-3
Flight Cycles: 88
Negative No.: D-882
Mount No.: 595-0

Figure 4-89. Microstructure of Exposed Cb-752/VH-109 Parent Specimen — Grip Section

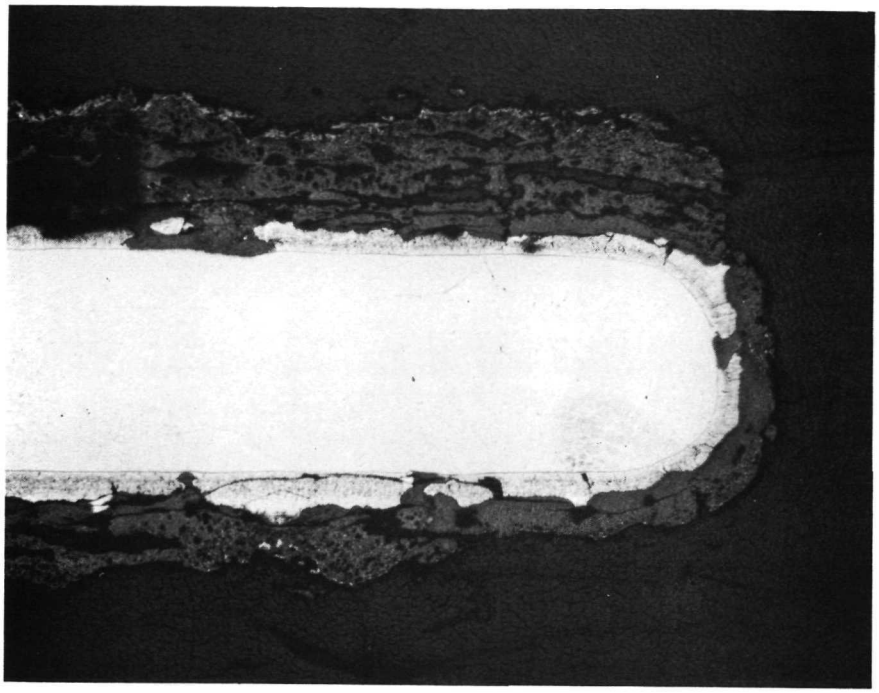

| | |
|---|---|
| Magnification: | 100X |
| Etch: | Light |
| Specimen No.: | BVP-7 |
| Flight Cycles: | 83 |
| Negative No.: | D-893 |
| Mount No.: | 627-0 |

Figure 4-90. Microstructure of Exposed Cb-752/VH-109 Parent Specimen — Gage Section

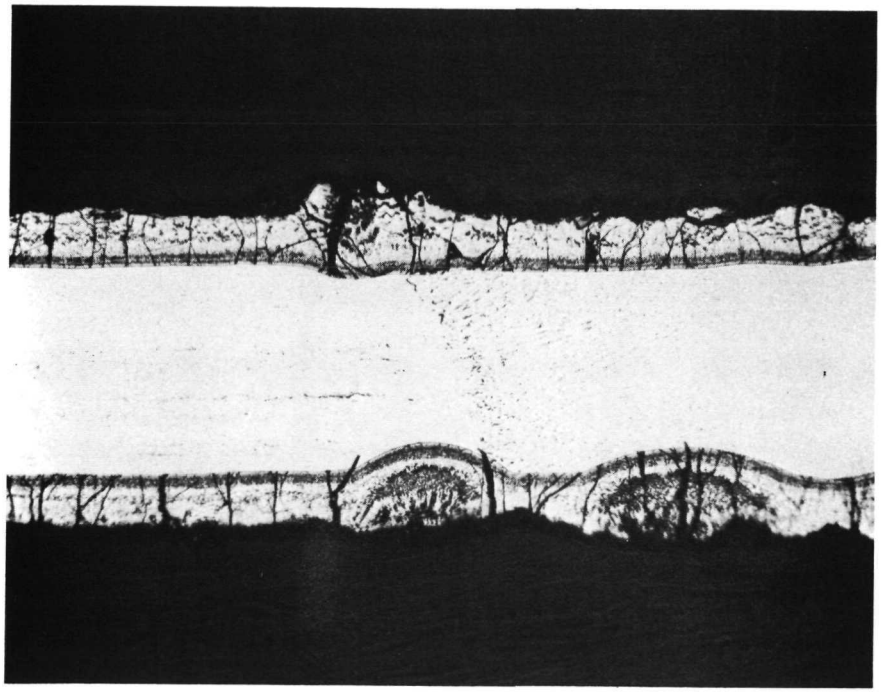

| | |
|---|---|
| Magnification: | 100X |
| Etch: | Light |
| Specimen No.: | BVE-18 |
| Flight Cycles: | 0 |
| Negative No.: | D-1137 |
| Mount No.: | 93-0 |

Figure 4-91. Microstructure of Unexposed Cb-752/VH-109 Electron Beam Weld Specimen — Gage Section

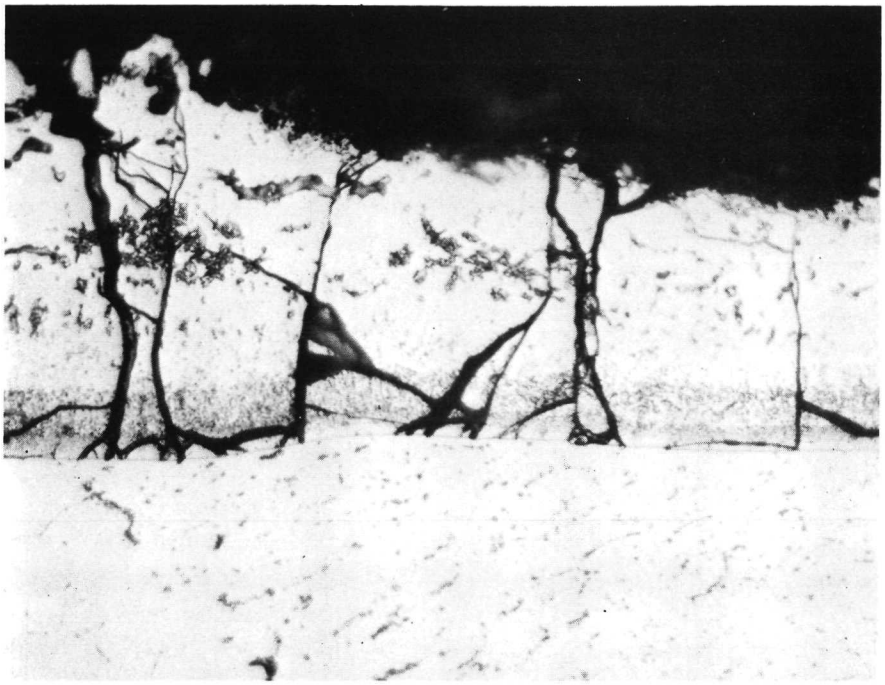

Magnification: 100X
Etch: Heavy
Specimen No.: BVE-18
Flight Cycles: 0
Negative No.: C-9703
Mount No.: 93-0

Figure 4-92. Microstructure of Unexposed Cb-752/VH-109 Electron Beam Weld Specimen – Gage Section

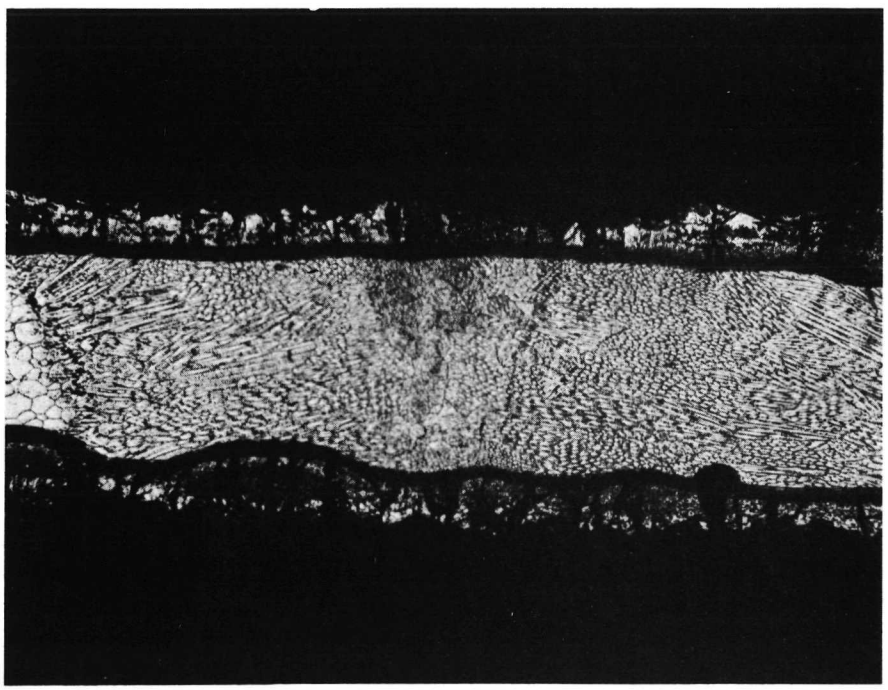

Magnification: 500X
Etch: Light
Specimen No.: BVE-18
Flight Cycles: 0
Negative No.: D-1138
Mount No.: 93-0

Figure 4-93. Microstructure of Unexposed Cb-752/VH-109 Electron Beam Weld Specimen – Gage Section

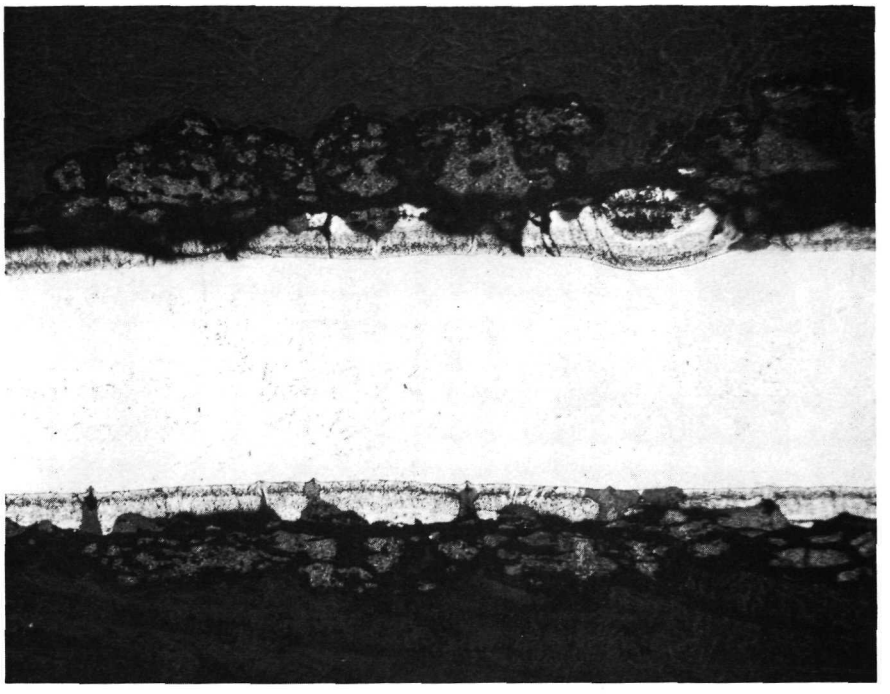

Magnification: 100X
Etch: Light
Specimen No.: BVE-14
Flight Cycles: 61
Negative No.: D-883
Mount No.: 595-0

Figure 4-94. Microstructure of Exposed Cb-752/VH-109 Electron Beam Weld Specimen – Gage Section

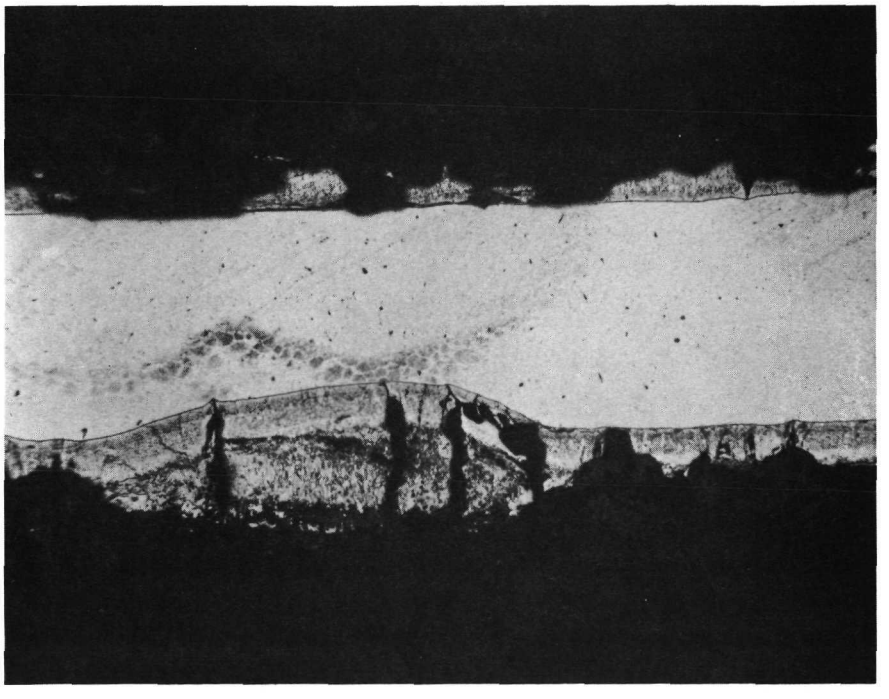

Magnification: 100X
Etch: Light
Specimen No.: BVE-15
Flight Cycles: 57
Negative No.: D-140
Mount No.: 320-0

Figure 4-95. Microstructure of Exposed Cb-752/VH-109 Electron Beam Weld Specimen – Gage Section

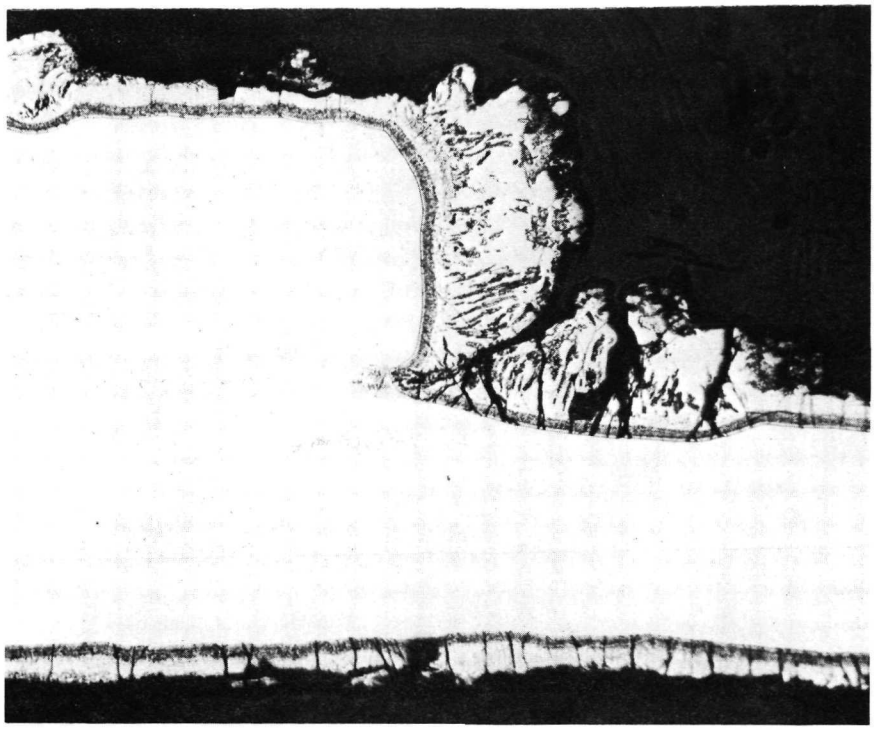

Magnification: 100X
Etch: Light
Specimen No.: BVD-18
Flight Cycles: 0
Negative No.: D-1139
Mount No.: 93-0

Figure 4-96. Microstructure of Unexposed Cb-752/VH-109 Diffusion Bond Specimen – Gage Section

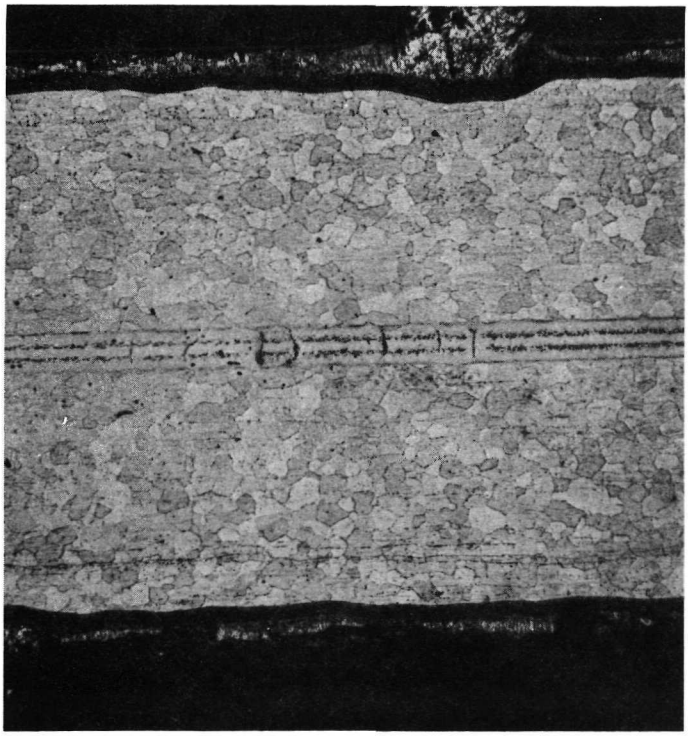

Magnification: 100X
Etch: Heavy
Specimen No.: BVD-18
Flight Cycles: 0
Negative No.: C-9704
Mount No.: 93-0

Figure 4-97. Microstructure of Unexposed Cb-752/VH-109 Diffusion Bond Specimen – Gage Section

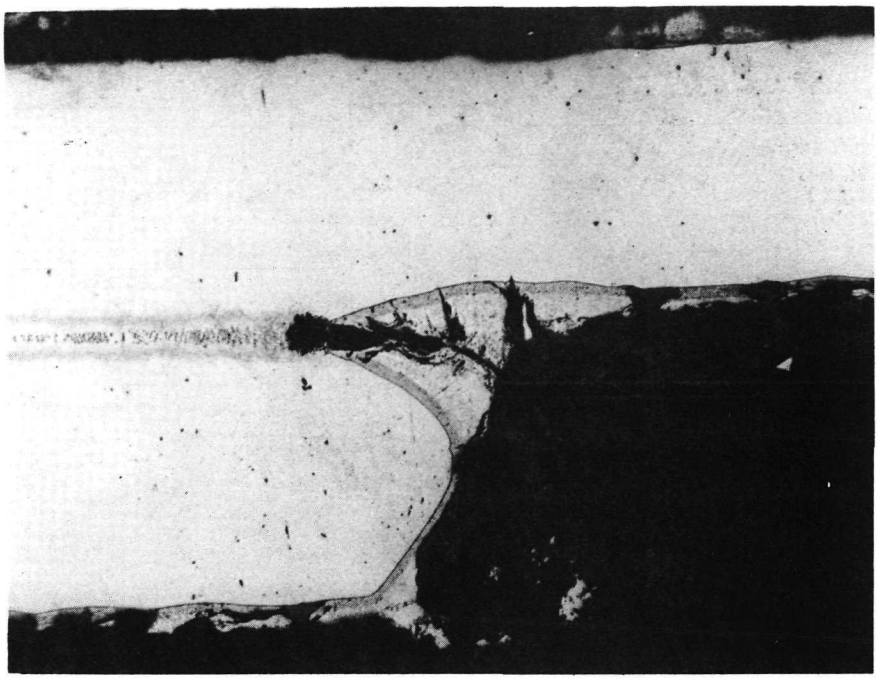

Magnification: 100X
Etch: Light
Specimen No.: BVD-9
Flight Cycles: 61
Negative No.: D-950
Mount No.: 655-0

**Figure 4-98. Microstructure of Exposed Cb-752/VH-109 Diffusion Bond Specimen – Gage Section**

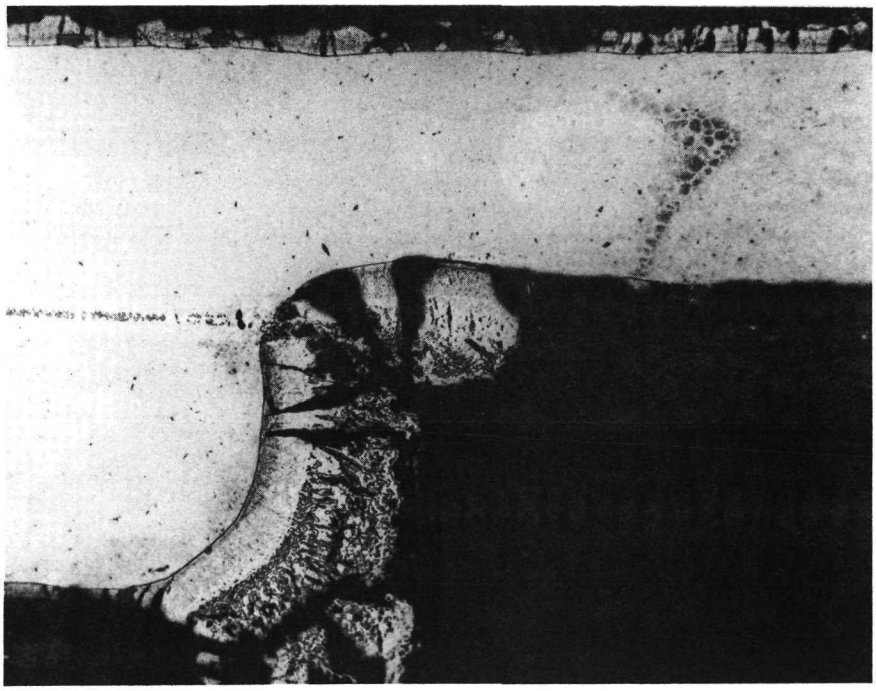

Magnification: 100X
Etch: Light
Specimen No.: BVD-9
Flight Cycles: 61
Negative No.: D-952
Mount No.: 655-0

**Figure 4-99. Microstructure of Exposed Cb-752/VH-109 Diffusion Bond Specimen — Gage Section**

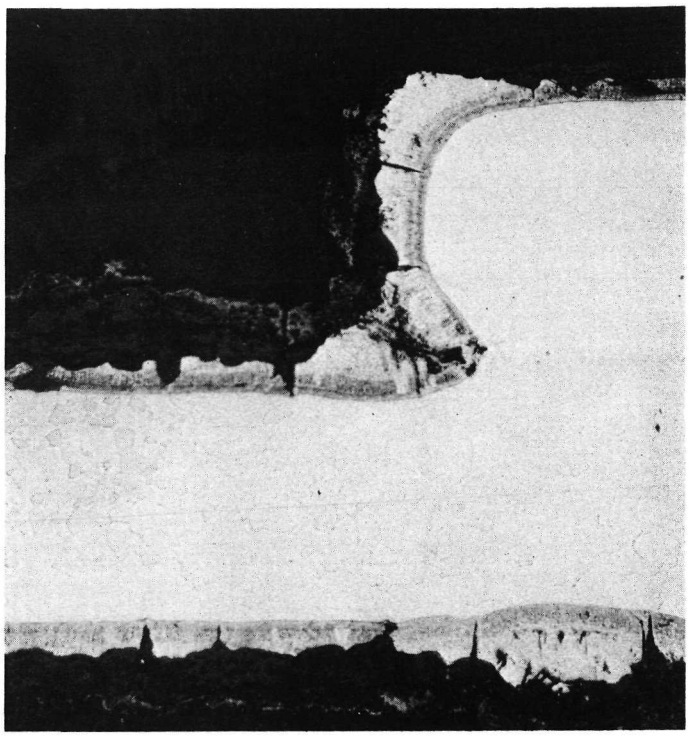

Magnification: 100X
Etch: Light
Specimen No.: BVD-4
Flight Cycles: 69
Negative No.: D-911
Mount No.: 627-0

Figure 4-100. **Microstructure of Exposed Cb-752/VH-109 Diffusion Bond Specimen — Gage Section**

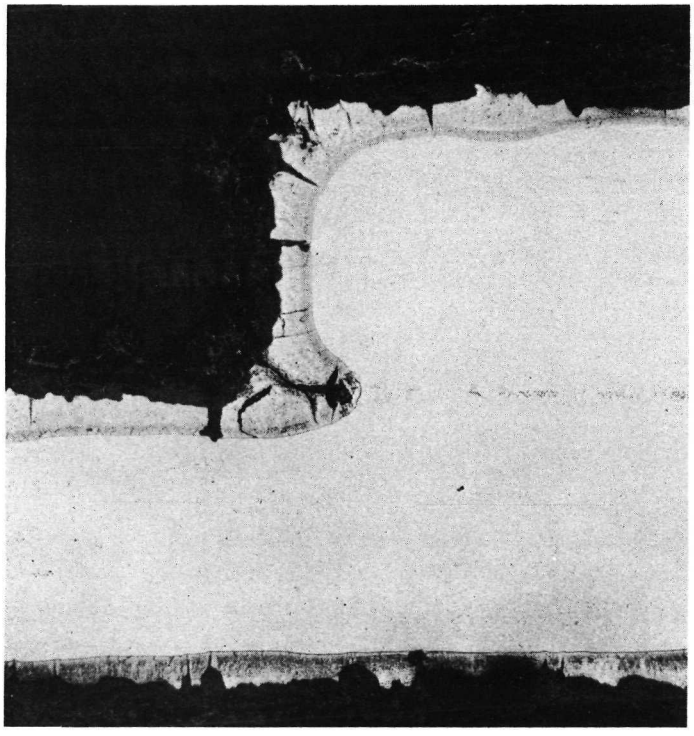

Magnification: 100X
Etch: Light
Specimen No.: BVD-4
Flight Cycles: 69
Negative No.: D-910
Mount No.: 627-0

Figure 4-101. **Microstructure of Exposed Cb-752/VH-109 Diffusion Bond Specimen — Gage Section**

System 3, C-129Y/R-512E: Photomicrographs of this system are presented in Figures 4-102 to 4-106 for the parent specimens, Figures 4-107 to 4-114 for the welds, and Figures 4-115 to 4-121 for the diffusion bonds. The same type of examination of the as-coated specimens as used on the Cb-752 alloy was employed with this system, and the results were very nearly the same. The lightly etched samples, Figures 4-102, 4-107, and 4-115, show the same coating uniformity found in the Cb-752 specimens. Under high magnification, the details of the coating on the C-129Y alloy, Figures 4-104 and 4-109, and the Cb-752 alloy, Figures 4-70 and 4-76, are almost identical. Similar comparisons hold for the more heavily etched structures, Figures 4-103, 4-108, and 4-116, except that the slight increase in grain size of the bond specimens over the parents and welds observed in the Cb-752 alloy was not found in this system.

Figures 4-105 and 4-106 were taken from an exposed parent metal specimen. No contamination of the alloy is visible, although several coating cracks have penetrated very close to the substrate. Measurements from the gage section and the cooler grip section gave a loss of substrate by diffusion zone growth of about 0.0006 inch (0.0015 cm) per side in 100 cycles. One region of uneven coating application is visible in Figure 4-106. These regions, which were quite common to the VH-109 coating, were rarely observed in the R-512E coated specimens, and then only in the grip sections.

Photomicrographs of the exposed electron beam weld specimens are shown in Figures 4-110 to 4-114. The weld region of Figure 4-110 is similar to the parent specimen of this system. Many coating cracks, extending just to the substrate, are visible, but no contamination of the alloy is apparent, and no detrimental effects can be seen in the weld or heat-affected zone. One localized site of coating failure was found in this same specimen, however, when given an anodized etch. This is shown in Figure 4-111, taken in a region adjacent to the weld. Figure 4-112 is an enlargement of the crack showing the contamination of the substrate more clearly.

Figures 4-113 and 4-114 are from a specimen that was too badly oxidized (edge attack) after 100 flight simulation cycles to warrant tensile testing. For this reason, the number and size of coating cracks is somewhat reduced. Figure 4-113 shows a region of severe coating failure with consumption of the substrate along with considerable evidence of contamination of the alloy. Figure 4-114 was taken from the grip portion of the specimen and shows another example of the uneven coating occasionally found in the R-512E coated specimens. The origin of these uneven regions is not definitely known. Two possibilities exist. They could develop during coating formation as a result of nonuniform slurry composition as postulated previously for the VH-109 coating, or they could be the result of an uneven surface on the uncoated specimens. The difference in coating appearance at these locations as compared to the uniform areas is quite large for the VH-109 coating, e.g., see Figure 4-91, while little or no difference can be seen in the R-512E coating, Figure 4-114. This observation plus the

frequency of occurrence leads one to suggest that the effect arises from slurry inhomogeneities for the VH-109 specimens and surface irregularities prior to coating in the R-512E specimens.

An exposed diffusion bond specimen is pictured in Figures 4-117 to 4-121. The two lap joint corners in Figures 4-117 and 4-118 show the typical oxide filled coating cracks extending, in many cases, to the substrate. A careful examination of Figure 4-117 reveals some sign of contamination at the root of several of these cracks. A better indication is given in Figure 4-119 taken after anodizing the specimen. The oxygen contaminated region revealed by the etching treatment has extended radially from the crack tip for a distance of about 0.0025 inch (0.0064 cm). The remaining two photos, Figures 4-120 and 4-121, also with the anodized etch, show the difference between the two bond corners. In one, an interaction between the titanium innerlayer and the silicide coating is clearly visible. The other corner, Figure 4-121, shows no interaction, but what appears to be porosity can be seen in the titanium innerlayer. The porosity is common to both alloys. In the unexposed specimens, it is aligned in two rows within the titanium inner layer, e.g., see Figures 4-82, 4-97, 4-116, and 4-133. After exposure, these rows have often joined to form a single band. Again, movement of these voids is toward the center of the titanium foil.

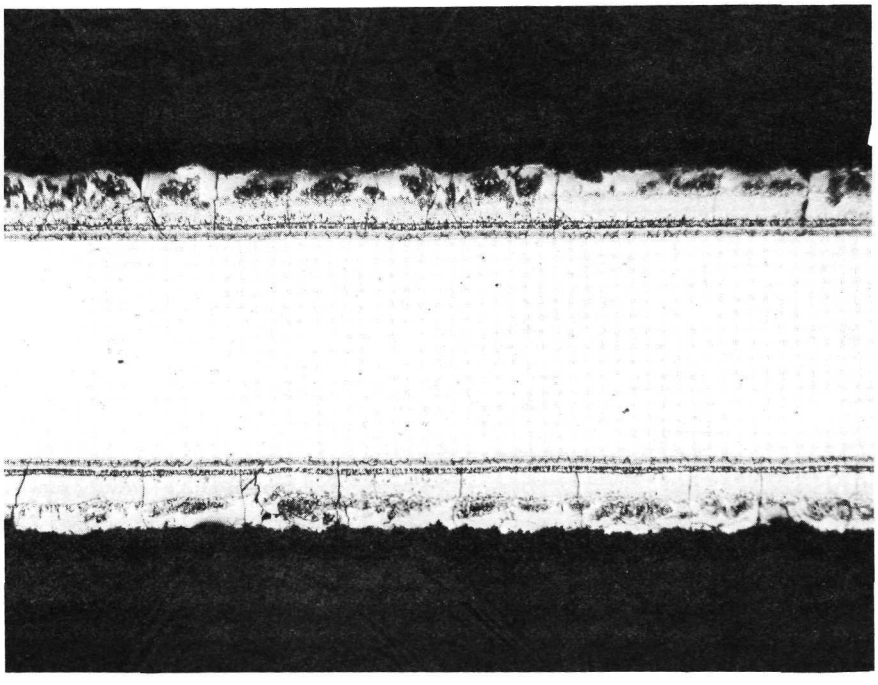

Magnification: 100X
Etch: Light
Specimen No.: YSP-20
Flight Cycles: 0
Negative No.: D-1133
Mount No.: 42-0

Figure 4-102. Microstructure of Unexposed C-129Y/R-512E Parent Specimen — Gage Section

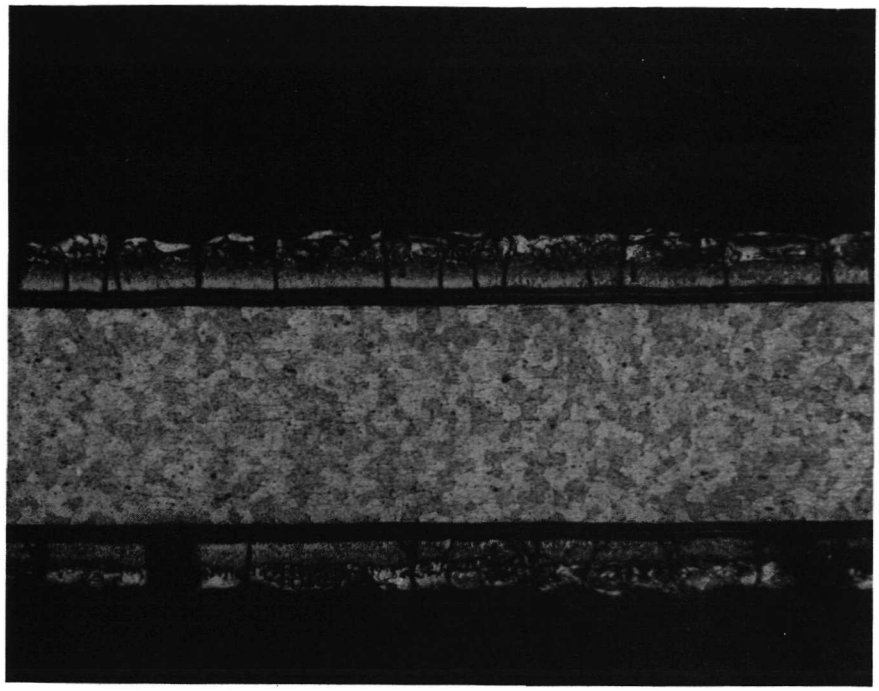

| | |
|---|---|
| Magnification: | 100X |
| Etch: | Heavy |
| Specimen No.: | YSP-20 |
| Flight Cycles: | 0 |
| Negative No.: | C-9744 |
| Mount No.: | 42-0 |

Figure 4-103. Microstructure of Unexposed C-129Y/R-512E Parent Specimen — Gage Section

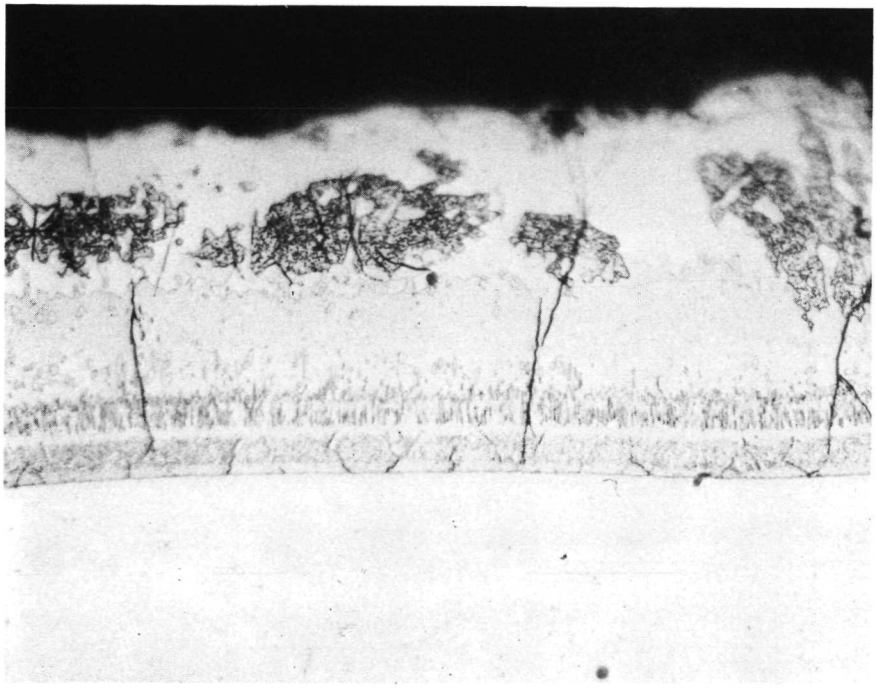

| | |
|---|---|
| Magnification: | 500X |
| Etch: | Light |
| Specimen No.: | YSP-20 |
| Flight Cycles: | 0 |
| Negative No.: | D-1134 |
| Mount No.: | 42-0 |

Figure 4-104. Microstructure of Unexposed C-129Y/R-512E Parent Specimen — Gage Section

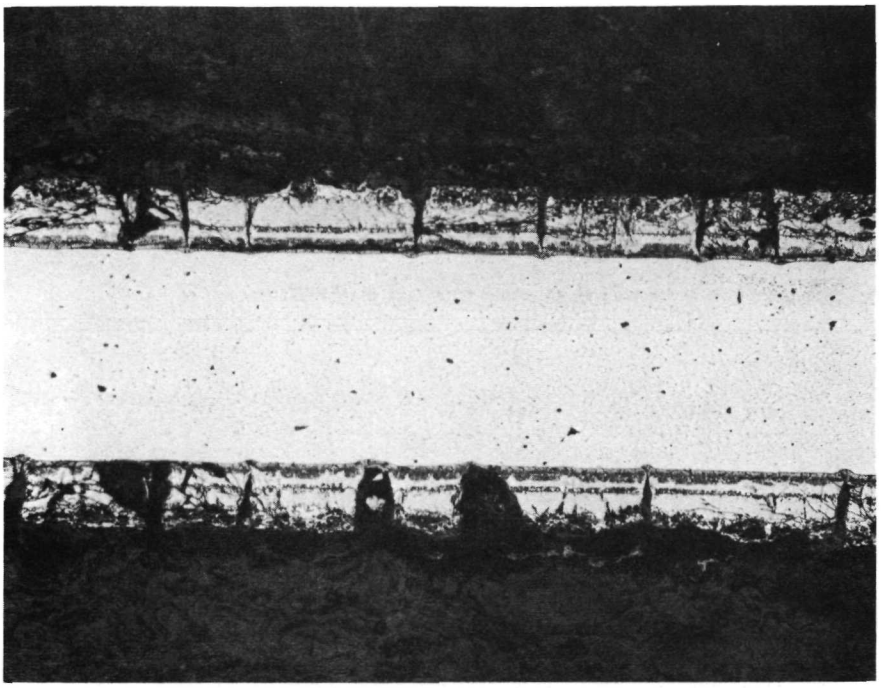

Magnification: 100X
Etch: Light
Specimen No.: YSP-1
Flight Cycles: 100
Negative No.: D-509
Mount No.: 508-0

Figure 4-105. Microstructure of Exposed C-129Y/R-512E Parent Specimen — Gage Section

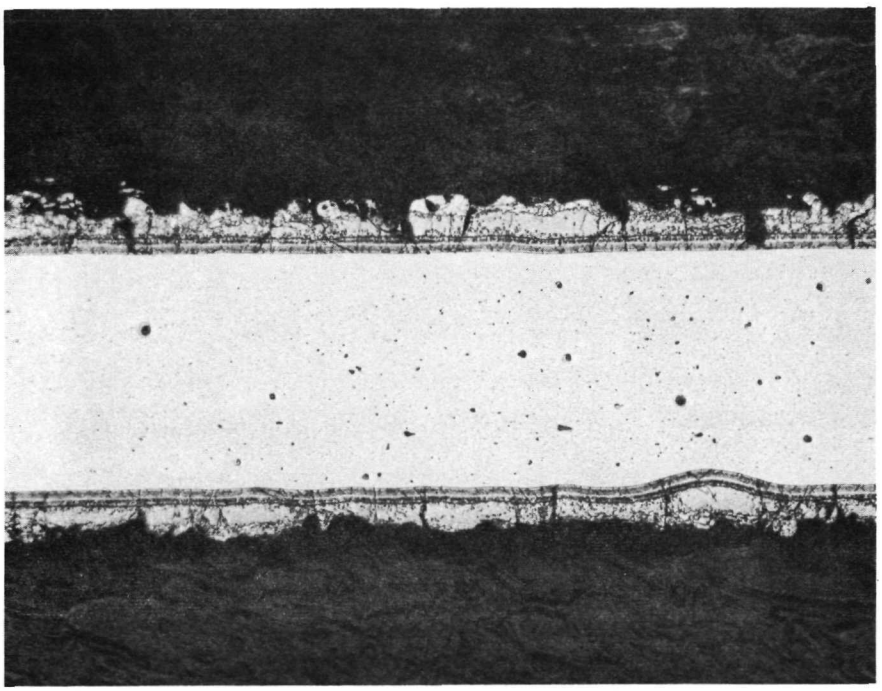

Magnification: 100X
Etch: Light
Specimen No.: YSP-1
Flight Cycles: 100
Negative No.: D-510
Mount No.: 508-0

Figure 4-106. Microstructure of Exposed C-129Y/R-512E Parent Specimen — Grip Section

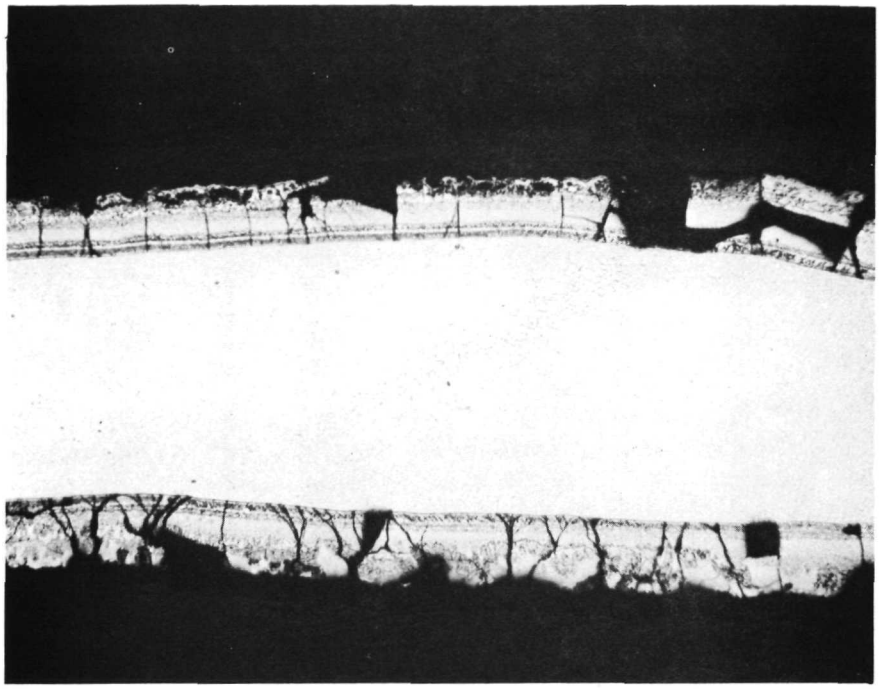

| | |
|---|---|
| Magnification: | 100X |
| Etch: | Light |
| Specimen No.: | YSE-18 |
| Flight Cycles: | 0 |
| Negative No.: | D-1145 |
| Mount No.: | 95-0 |

Figure 4-107. Microstructure of Unexposed C-129Y/R-512E Electron Beam Weld Specimen — Gage Section

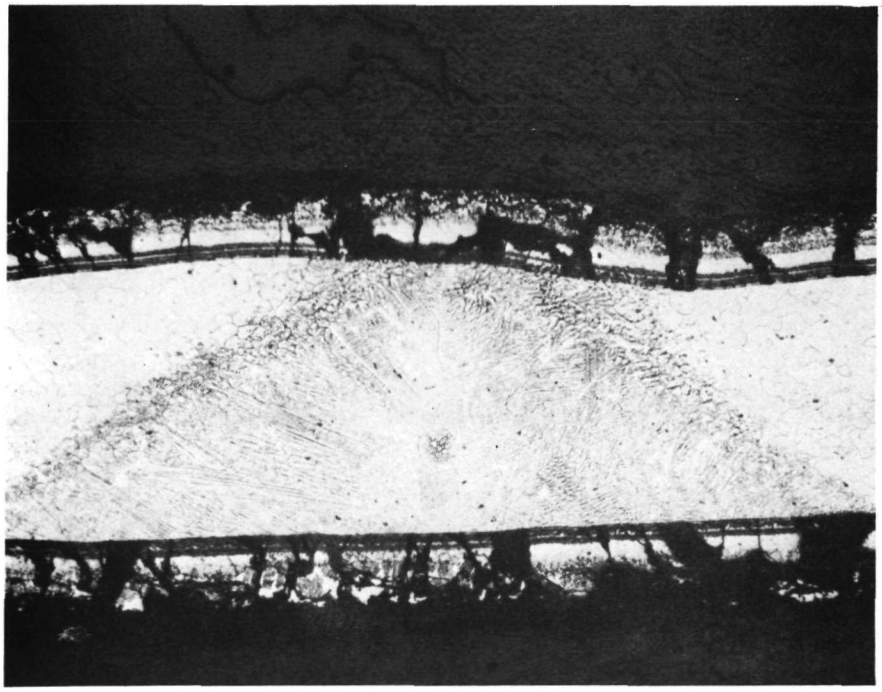

| | |
|---|---|
| Magnification: | 100X |
| Etch: | Heavy |
| Specimen No.: | YSE-18 |
| Flight Cycles: | 0 |
| Negative No.: | C-9700 |
| Mount No.: | 95-0 |

Figure 4-108. Microstructure of Unexposed C-129Y/R-512E Electron Beam Weld Specimen – Gage Section

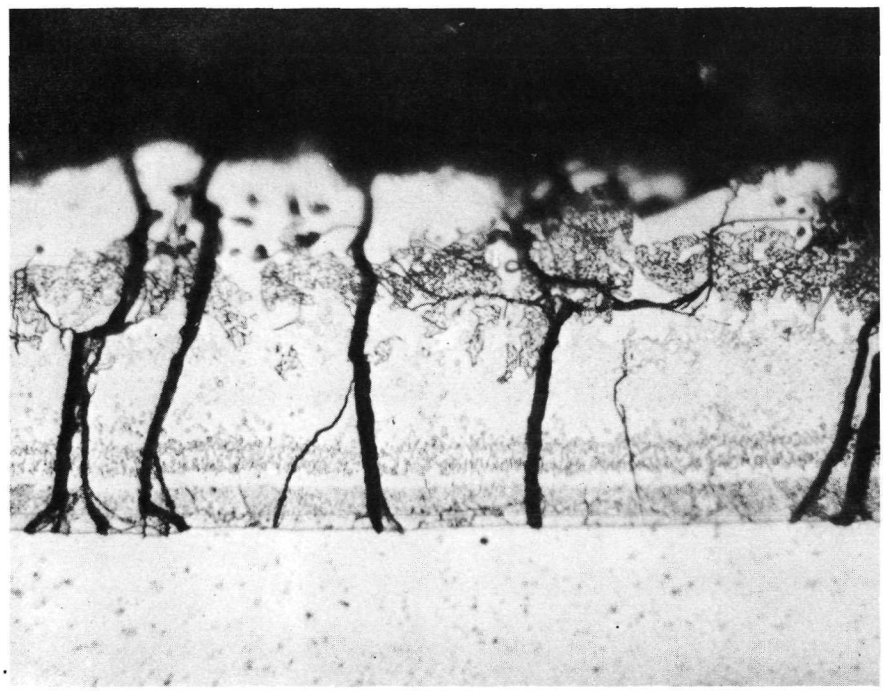

Magnification: 500X
Etch: Light
Specimen No.: YSE-18
Flight Cycles: 0
Negative No.: D-1147
Mount No.: 95-0

Figure 4-109. Microstructure of Unexposed C-129Y/R-512E Electron Beam Weld Specimen – Gage Section

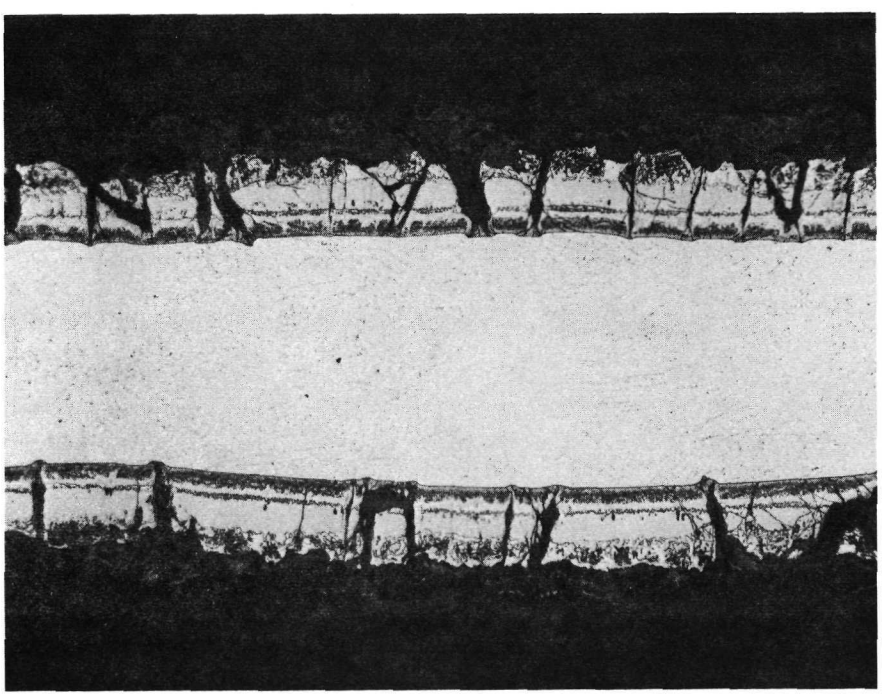

Magnification: 100X
Etch: Light
Specimen No.: YSE-13
Flight Cycles: 100
Negative No.: D-512
Mount No.: 505-0

Figure 4-110. Microstructure of Exposed C-129Y/R-512E Electron Beam Weld Specimen – Gage Section

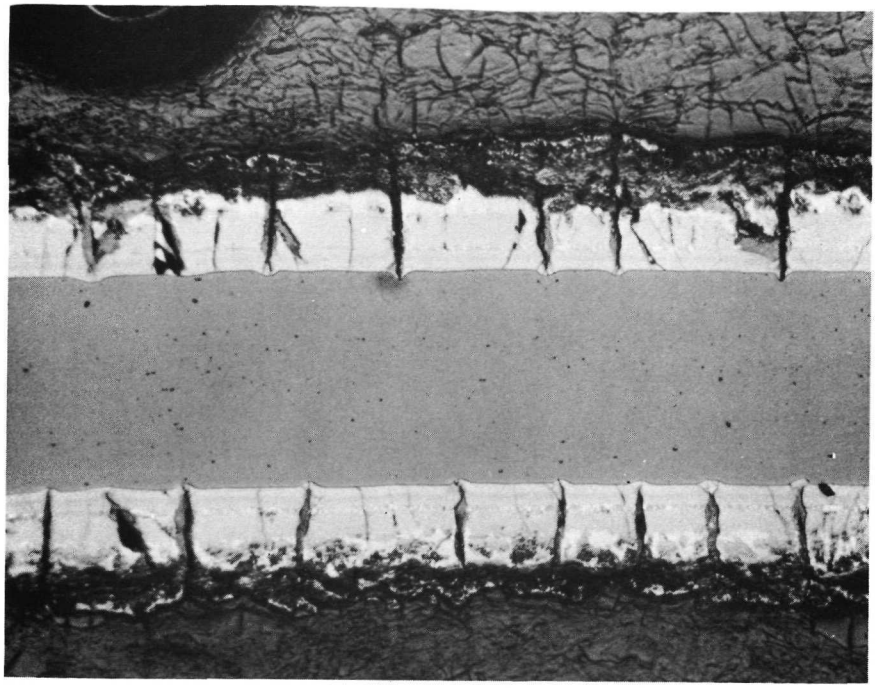

Magnification: 100X
Etch: Anodized
Specimen No.: YSE-13
Flight Cycles: 100
Negative No.: D-797
Mount No.: 505-0

Figure 4-111. Microstructure of Exposed C-129Y/R-512E Electron Beam Weld Specimen – Gage Section

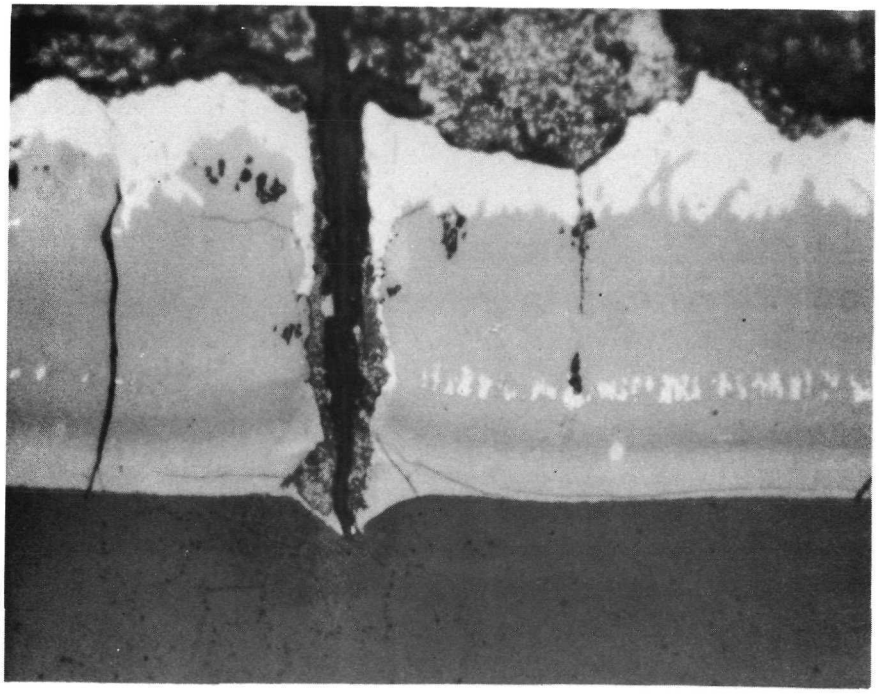

Magnification: 500X
Etch: Anodized
Specimen No.: YSE-13
Flight Cycles: 100
Negative No.: D-803
Mount No.: 505-0

Figure 4-112. Microstructure of Exposed C-129Y/R-512E Electron Beam Weld Specimen – Gage Section

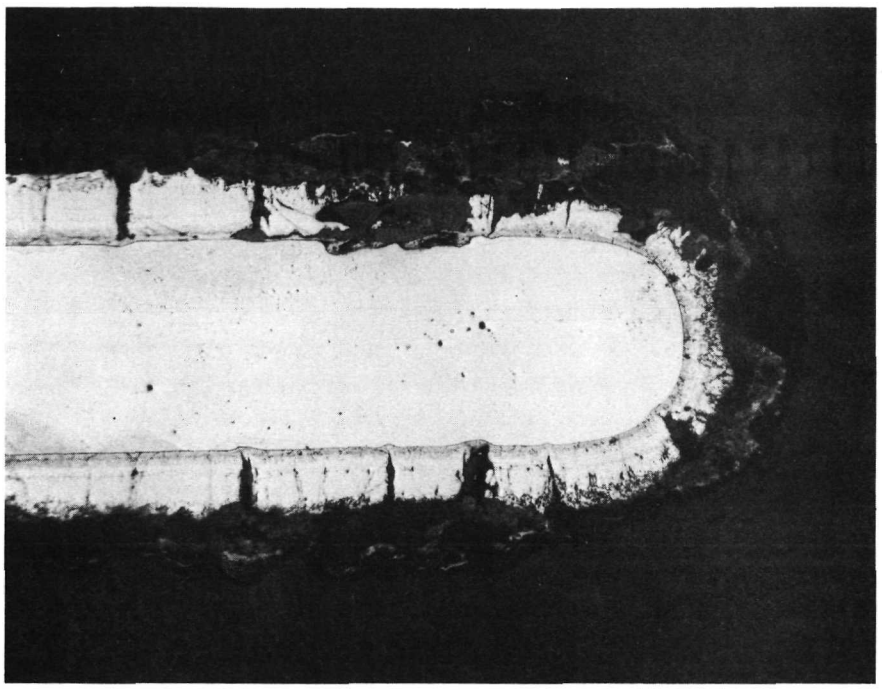

Magnification: 100X
Etch: Light
Specimen No.: YSE-14
Flight Cycles: 100
Negative No.: D-889
Mount No.: 626-0

Figure 4-113. Microstructure of Exposed C-129Y/R-512E Electron Beam Weld Specimen – Gage Section

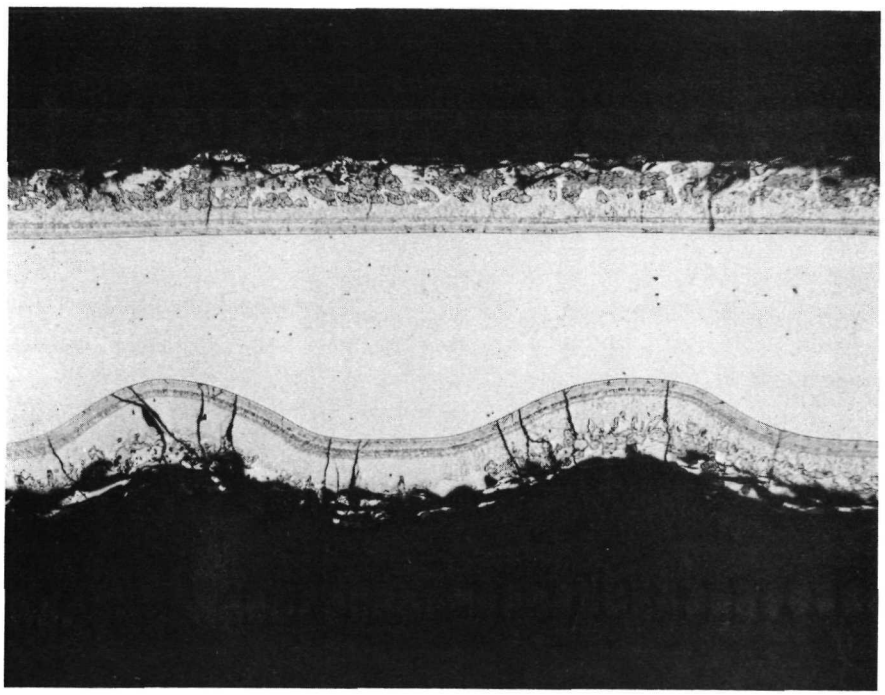

Magnification: 100X
Etch: Light
Specimen No.: YSE-14
Flight Cycles: 100
Negative No.: D-891
Mount No.: 626-0

Figure 4-114. Microstructure of Exposed C-129Y/R-512E Electron Beam Weld Specimen – Grip Section

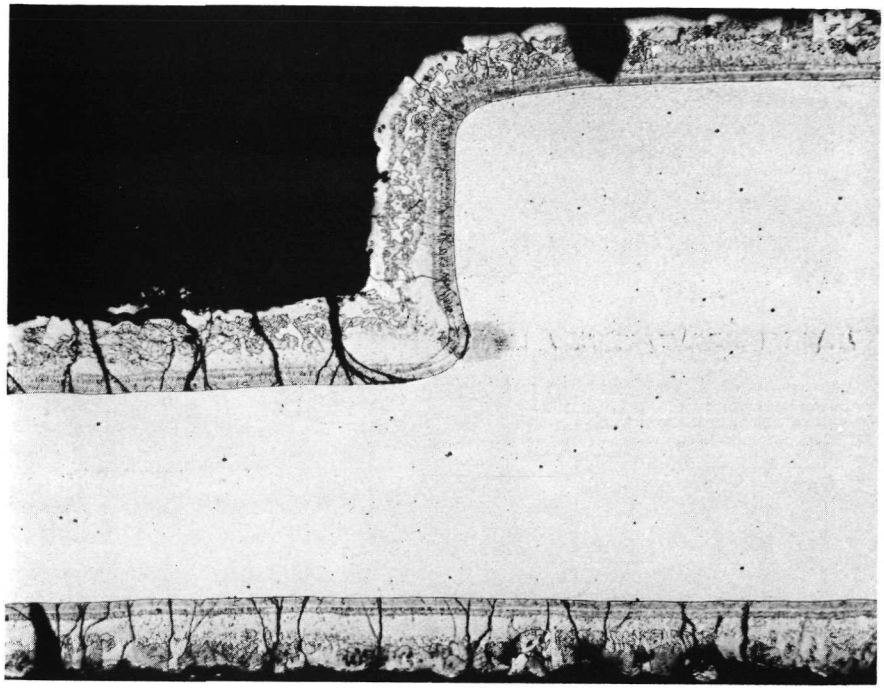

| | |
|---|---|
| Magnification: | 100X |
| Etch: | Light |
| Specimen No.: | YSD-9 |
| Flight Cycles: | 0 |
| Negative No.: | D-1150 |
| Mount No.: | 181-0 |

Figure 4-115. Microstructure of Unexposed C-129Y/R-512E Diffusion Bond Specimen — Gage Section

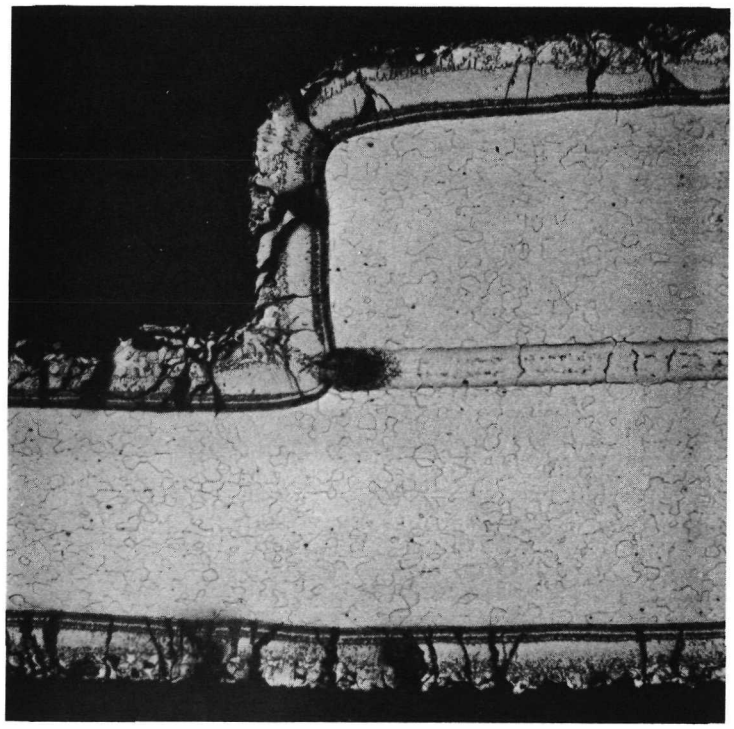

| | |
|---|---|
| Magnification: | 100X |
| Etch: | Heavy |
| Specimen No.: | YSD-9 |
| Flight Cycles: | 0 |
| Negative No.: | C-9735 |
| Mount No.: | 181-0 |

Figure 4-116. Microstructure of Unexposed C-129Y/R-512E Diffusion Bond Specimen — Gage Section

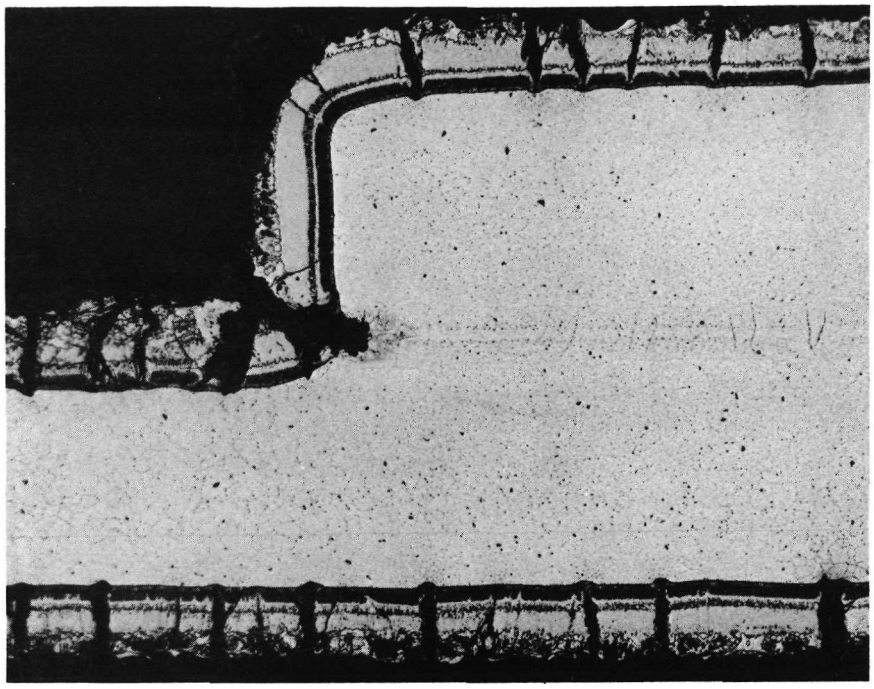

Magnification: 100X
Etch: Light
Specimen No.: YSD-7
Flight Cycles: 100
Negative No.: D-513
Mount No.: 507-0

Figure 4-117. Microstructure of Exposed C-129Y/R-512E Diffusion Bond Specimen — Gage Section

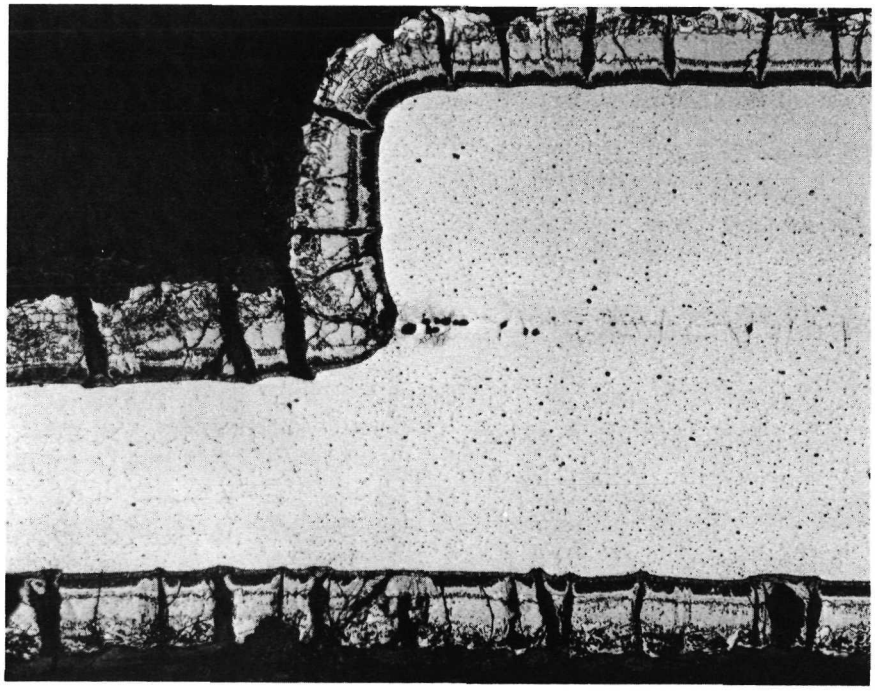

Magnification: 100X
Etch: Light
Specimen No.: YSD-7
Flight Cycles: 100
Negative No.: D-514
Mount No.: 507-0

Figure 4-118. Microstructure of Exposed C-129Y/R-512E Diffusion Bond Specimen — Gage Section

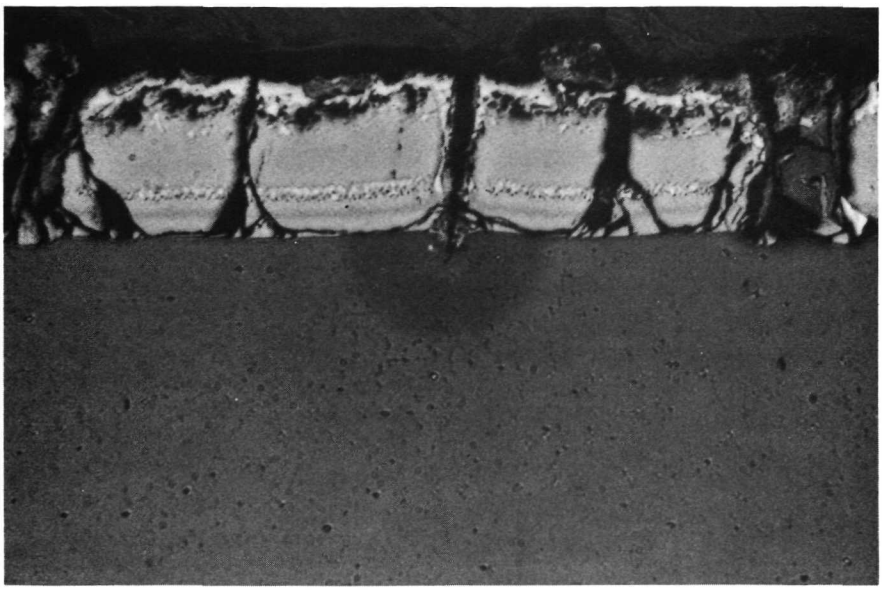

Magnification: 200X
Etch: Anodized
Specimen No.: YSD-7
Flight Cycles: 100
Negative No.: 2-N-4
Mount No.: 507-0

Figure 4-119. Microstructure of Exposed C-129Y/R-512E Diffusion Bond Specimen — Gage Section

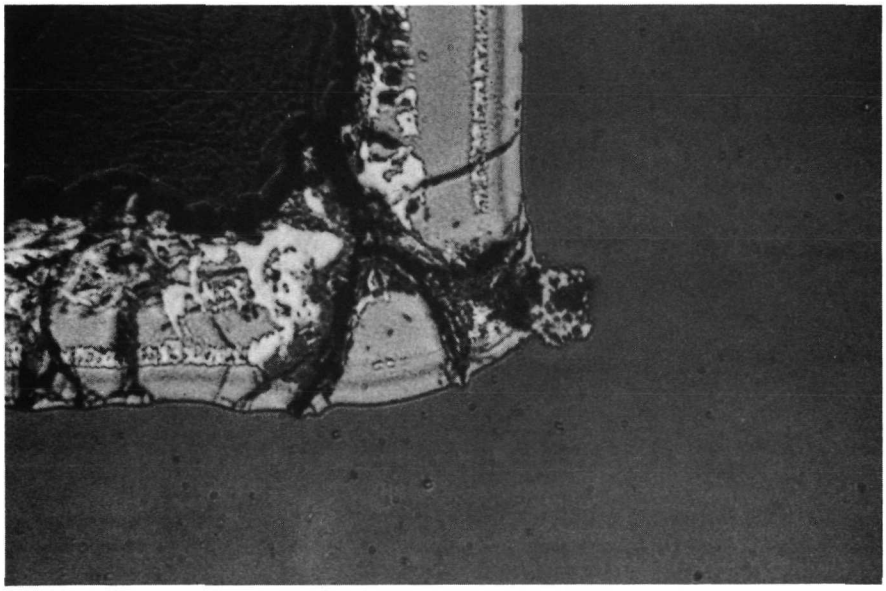

Magnification: 200X
Etch: Anodized
Specimen No.: YSD-7
Flight Cycles: 100
Negative No.: 2-N-3
Mount No.: 507-0

Figure 4-120. Microstructure of Exposed C-129Y/R-512E Diffusion Bond Specimen – Gage Section

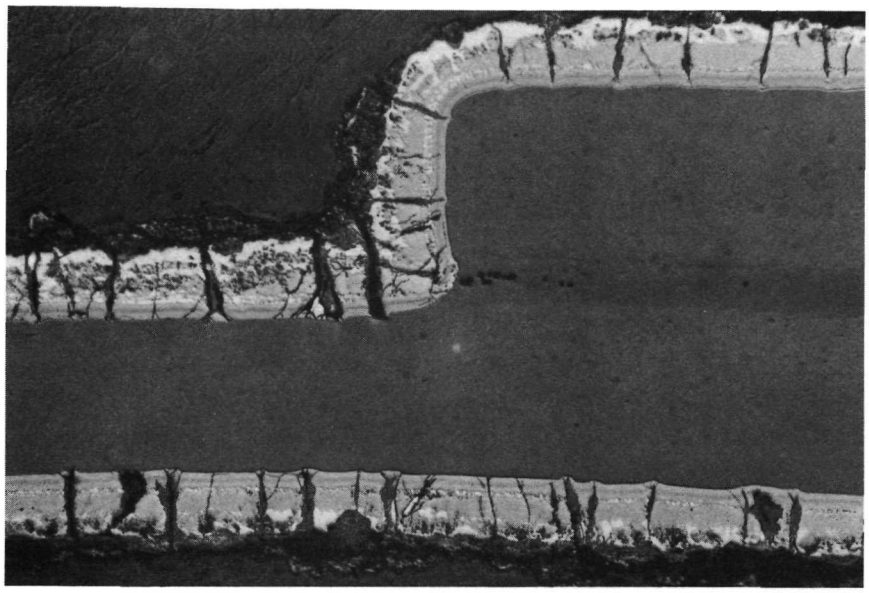

Magnification: 80X
Etch: Anodized
Specimen No.: YSD-7
Flight Cycles: 100
Negative No.: 2-N-6
Mount No.: 507-0

Figure 4-121. Microstructure of Exposed C-129Y/R-512E Diffusion Bond Specimen — Gage Section

System 4, C-129Y/VH-109: Photomicrographs for this system are shown in Figures 4-122 to 4-128 for parent specimens, Figures 4-129 to 4-133 for weld specimens, and Figures 4-134 to 4-138 for the bond specimens.

The uniformity of the VH-109 coating on the C-129Y specimens was much improved over the Cb-752 specimens. Some slight irregularities were found, but generally the as-coated specimens, Figures 4-122, 4-129, and 4-134, compared favorably with R-512E coated specimens. The more heavily etched samples, Figures 4-123, 4-130, and 4-135, again showed an equiax grain structure in the three types of specimens. The weld showed no adverse effects from the coating process, but some undercutting or coating penetration was observed at the diffusion bond corner, Figure 4-135.

The coating in the low-magnification photos of the parent specimen, Figures 4-122 and 4-123, appears to contain extensive subsurface cracks parallel to the coating/substrate interface. Examination at higher magnification, Figures 4-124, reveals, however, that these are one of the coating layers or zones, rather than cracks.

Two exposed parent metal specimens were examined, YVP-1, which survived 100 flight cycles, with no visible signs of coating failure, and YVP-4, which failed in 78 cycles with severe surface attack and edge erosion. Figure 4-125 taken from YVP-1 shows one of many areas of substrate contamination where coating failure occurred. The photo shows considerable loss of coating thickness as a result of oxidation. A comparison of this figure with Figure 4-126, taken from the grip portion of

the specimen, shows a loss of substrate by diffusion zone growth of about 0.0007 inch (0.0018 cm) per side in 100 cycles. Figures 4-127 and 4-128, taken from specimen YVP-4, reveal severe substrate contamination much worse than in YVP-1, and areas of total coating oxidation with thick oxide buildup. Figure 4-127, viewing the edge of the specimen, shows the complete loss of coating and subsequent oxidation of the columbium alloy (light grey oxide). Another region of substrate oxidation can be seen in Figure 4-128 in an area where the coating and its oxides have completely spalled from the specimen. An intergranular crack is also present in the microstructure.

Exposed weld specimens are shown in Figures 4-131 to 4-133. Figure 4-131, a section through the weld, contains several locations of coating failure with evidence of oxygen contamination of the substrate. The specimen in Figure 4-132 has survived more cycles, 94 as compared to 62, and is more heavily contaminated. The figure shows the small amount of coating remaining and the very thick oxide scale which has formed. A photograph from the same specimen after the anodizing etch is presented in Figure 4-133. Several sites of coating failure, substrate contamination, and the thick oxide scale are clearly visible.

Figures 4-136 to 4-138 are sections of a diffusion bond specimen that failed in 88 cycles with considerable coating spall. Contamination of the substrate is very severe, and several cracks are visible. Little of the coating remains, and in several locations oxidation of the substrate has occurred. These are the lighter grey areas in Figure 4-136.

Test analysis: The results of the metallographic examination again demonstrated the clear superiority of the Sylvania R-512E coating over the Vac-Hyd VH-109 coating. In like manner the metallographic results are consistent with the observations of

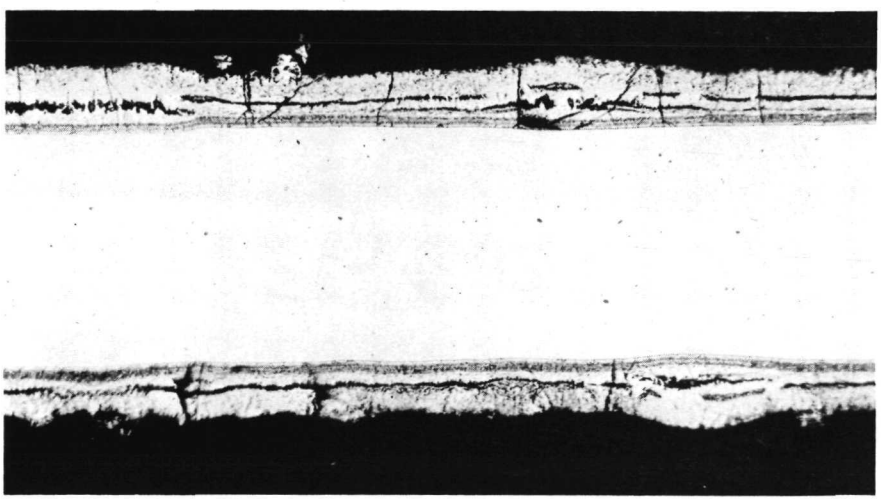

| | |
|---|---|
| Magnification: | 100X |
| Etch: | Light |
| Specimen No.: | YVP-21 |
| Flight Cycles: | 0 |
| Negative No.: | D-1129 |
| Mount No.: | 41-0 |

Figure 4-122. Microstructure of Unexposed C-129Y/VH-109 Parent Specimen — Gage Section

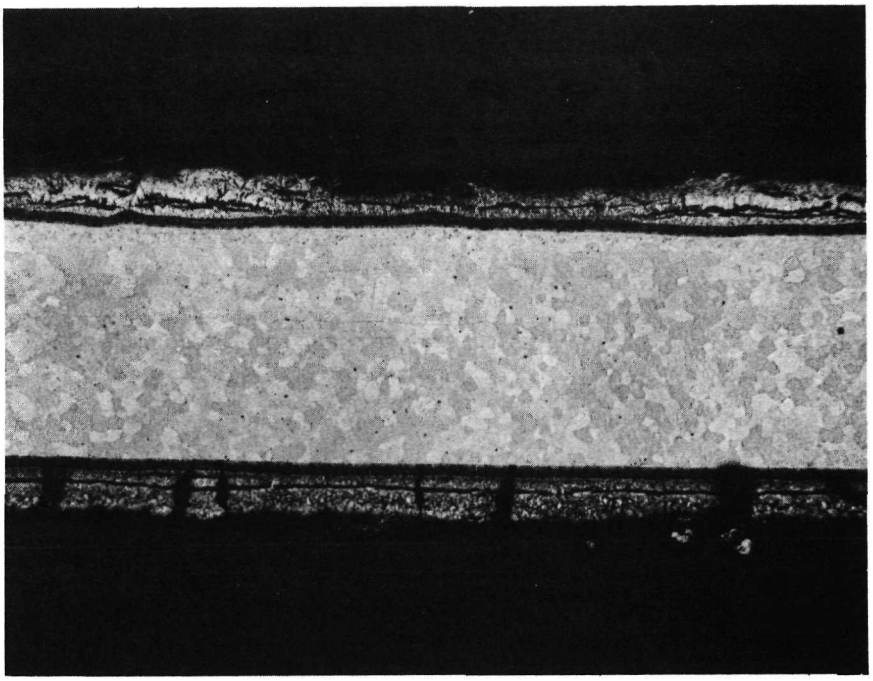

| | |
|---|---|
| Magnification: | 100X |
| Etch: | Heavy |
| Specimen No.: | YVP-21 |
| Flight Cycles: | 0 |
| Negative No.: | C-9740 |
| Mount No.: | 41-0 |

Figure 4-123. Microstructure of Unexposed C-129Y/VH-109 Parent Specimen — Gage Section

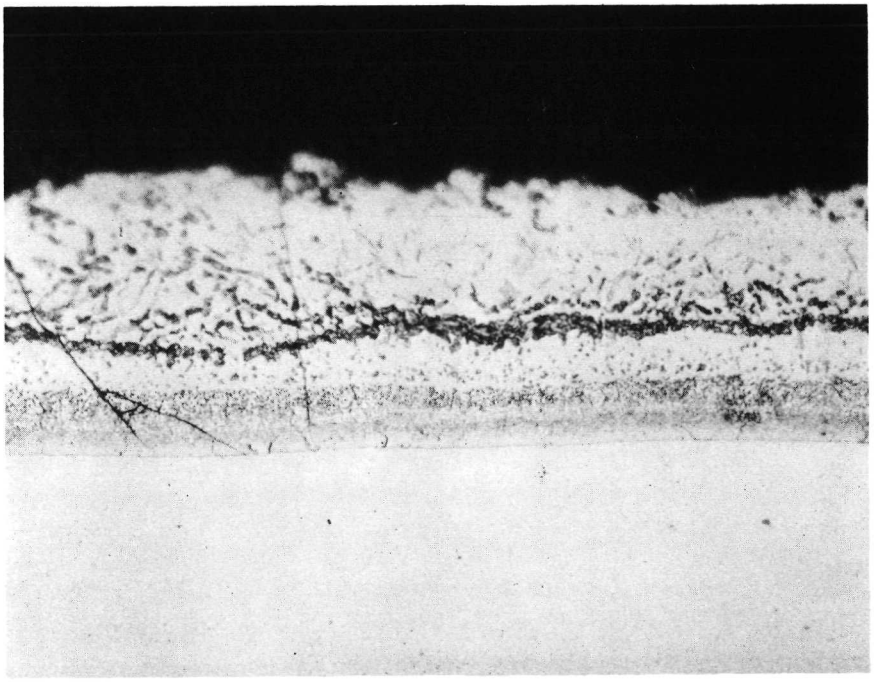

| | |
|---|---|
| Magnification: | 500X |
| Etch: | Light |
| Specimen No.: | YVP-21 |
| Flight Cycles: | 0 |
| Negative No.: | D-1130 |
| Mount No.: | 41-0 |

Figure 4-124. Microstructure of Unexposed C-129Y/VH-109 Parent Specimen — Gage Section

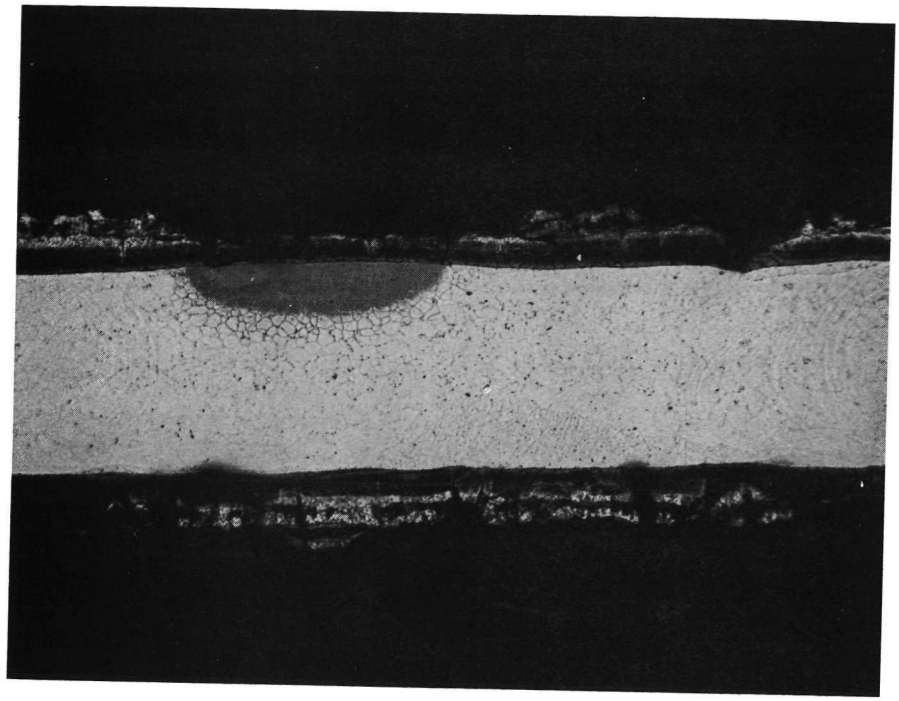

Magnification: 100X
Etch: Light
Specimen No.: YVP-1
Flight Cycles: 100
Negative No.: D-1330
Mount No.: 653-0

Figure 4-125. Microstructure of Exposed C-129Y/VH-109 Parent Specimen — Gage Section

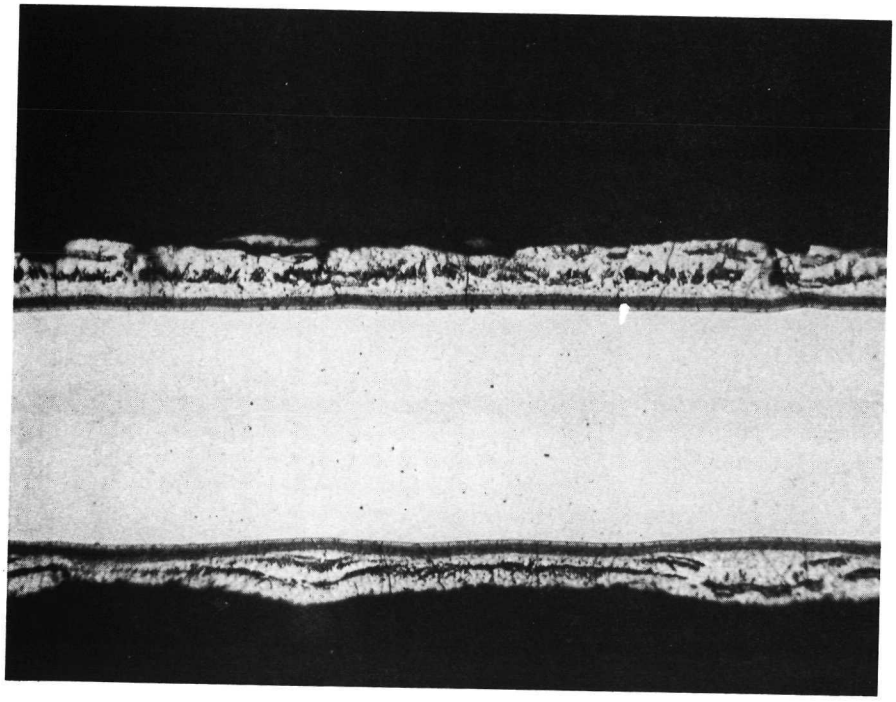

Magnification: 100X
Etch: Light
Specimen No.: YVP-1
Flight Cycles: 100
Negative No.: D-1332
Mount No.: 653-0

Figure 4-126. Microstructure of Exposed C-129Y/VH-109 Parent Specimen — Grip Section

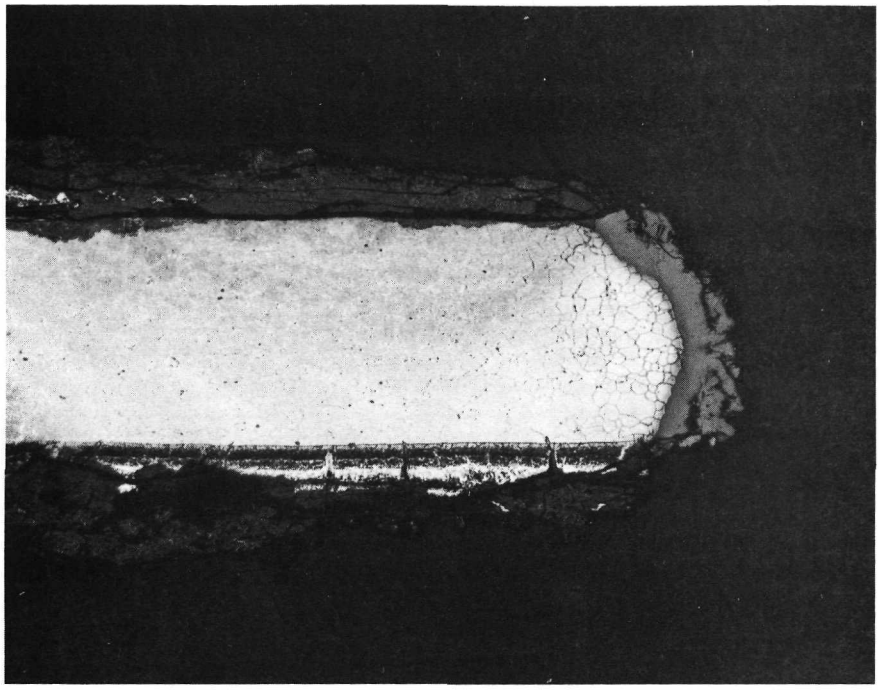

Magnification: 100X
Etch: Light
Specimen No.: YSP-4
Flight Cycles: 78
Negative No.: D-1335
Mount No.: 654-0

Figure 4-127. Microstructure of Exposed C-129Y/VH-109 Parent Specimen — Gage Section

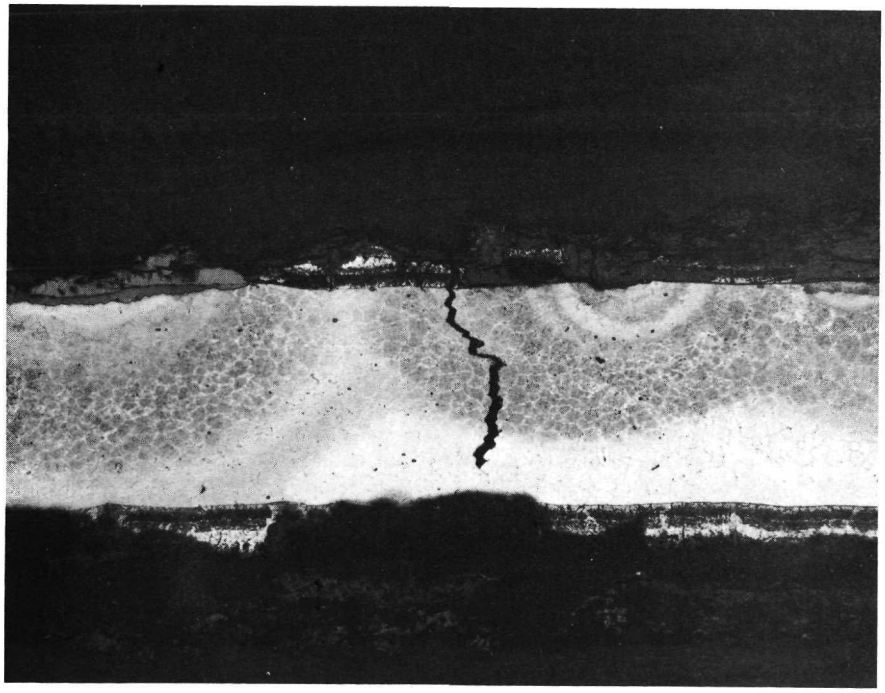

Magnification: 100X
Etch: Light
Specimen No.: YVP-4
Flight Cycles: 78
Negative No.: D-1334
Mount No.: 654-0

Figure 4-128. Microstructure of Exposed C-129Y/VH-109 Parent Specimen — Gage Section

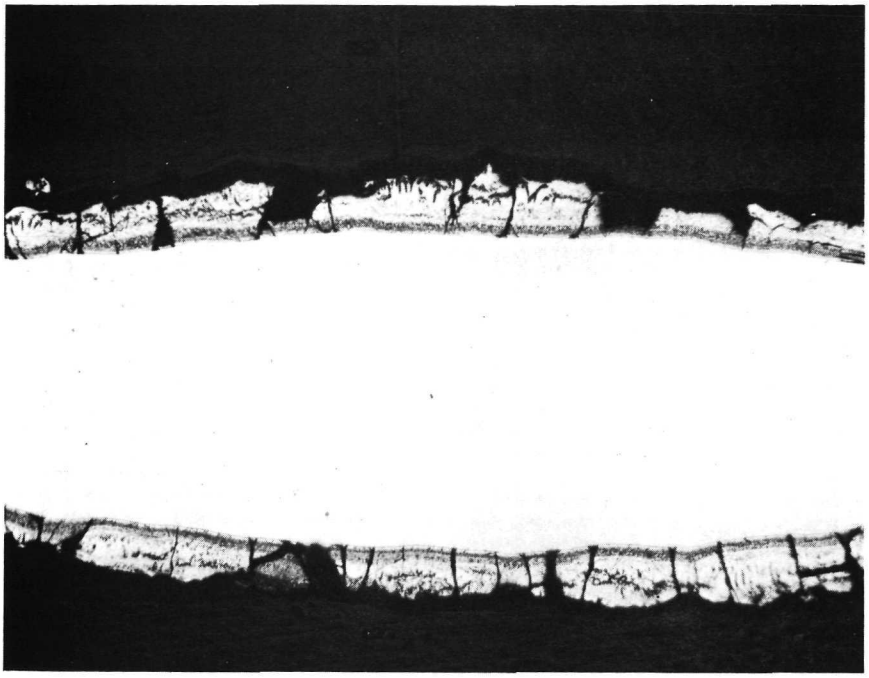

Magnification: 100X
Etch: Light
Specimen No.: YVE-20
Flight Cycles: 0
Negative No.: D-1131
Mount No.: 41-0

Figure 4-129. Microstructure of Unexposed C-129Y/VH-109 Electron Beam Weld Specimen – Gage Section

Magnification: 100X
Etch: Heavy
Specimen No.: YVE-20
Flight Cycles: 0
Negative No.: C-9739
Mount No.: 41-0

Figure 4-130. Microstructure of Unexposed C-129Y/VH-109 Electron Beam Weld Specimen — Gage Section

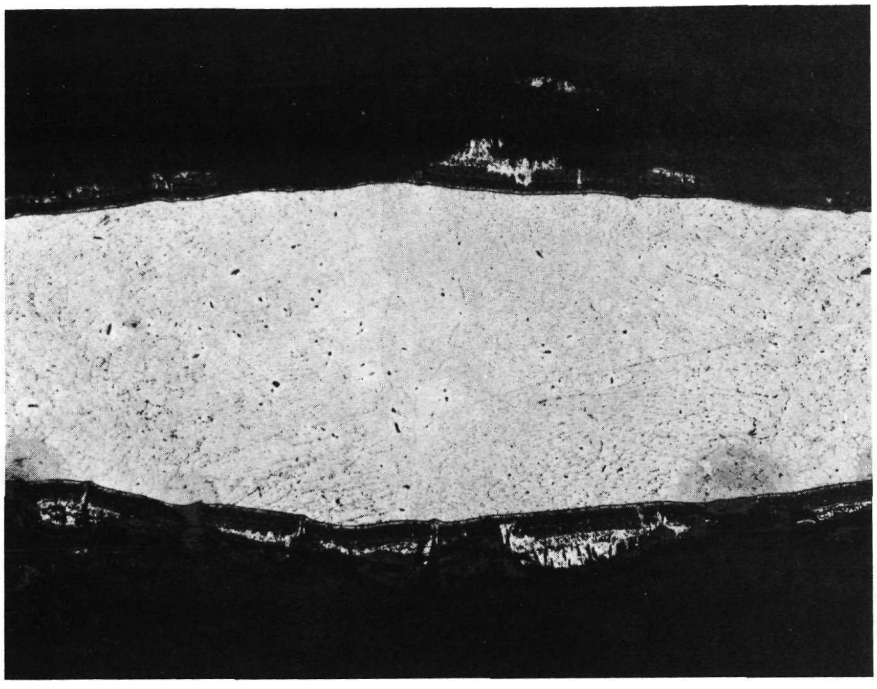

| | |
|---|---|
| Magnification: | 100X |
| Etch: | Light |
| Specimen No.: | YVE-6 |
| Flight Cycles: | 62 |
| Negative No.: | D-515 |
| Mount No.: | 433-0 |

Figure 4-131. Microstructure of Exposed C-129Y/VH-109 Electron Beam Weld Specimen — Gage Section

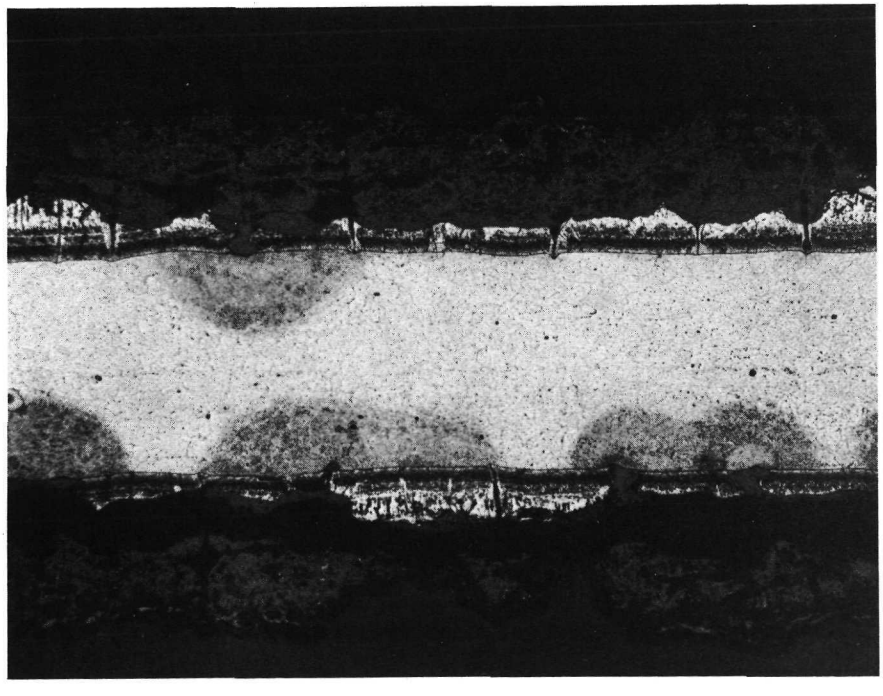

| | |
|---|---|
| Magnification: | 100X |
| Etch: | Light |
| Specimen No.: | YVE-3 |
| Flight Cycles: | 94 |
| Negative No.: | D-517 |
| Mount No.: | 431-0 |

Figure 4-132. Microstructure of Exposed C-129Y/VH-109 Electron Beam Weld Specimen — Gage Section

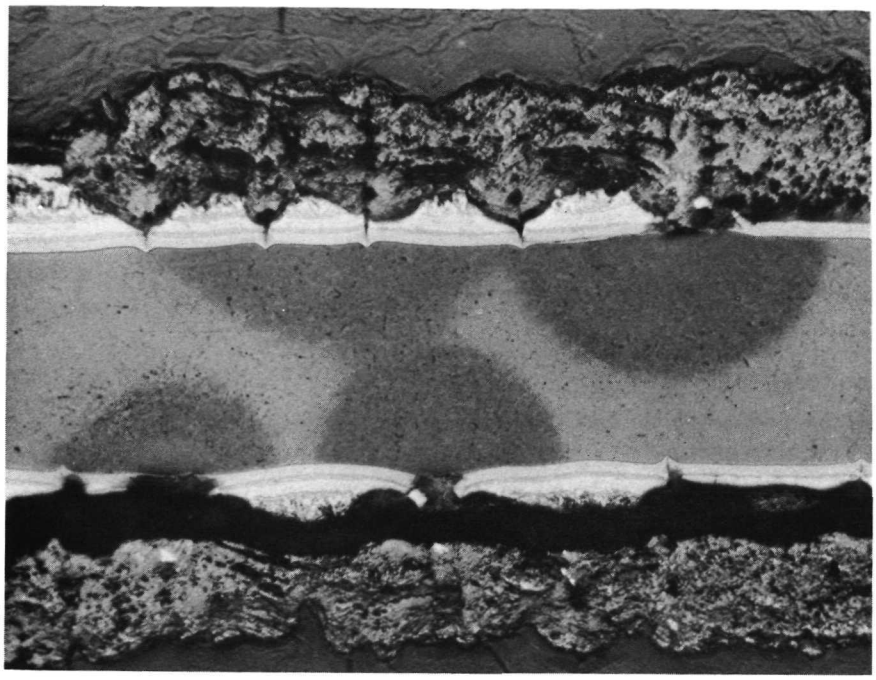

Magnification: 100X
Etch: Anodized
Specimen No.: YVE-3
Flight Cycles: 94
Negative No.: D-796
Mount No.: 431-0

Figure 4-133. Microstructure of Exposed C-129Y/VH-109 Electron Beam Weld Specimen — Gage Section

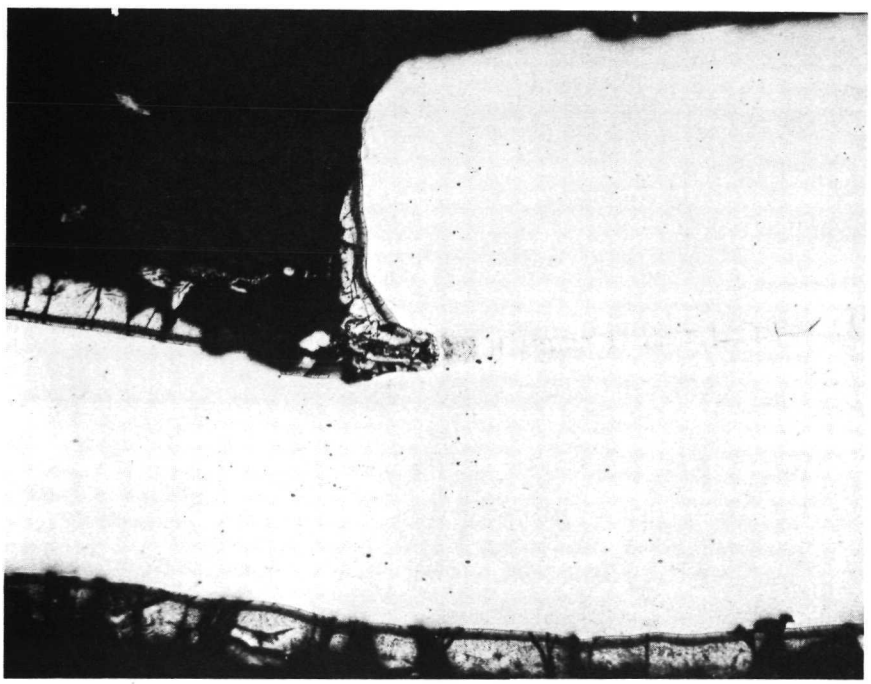

Magnification: 100X
Etch: Light
Specimen No.: YVD-22
Flight Cycles: 0
Negative No.: D-1149
Mount No.: 95-0

Figure 4-134. Microstructure of Unexposed C-129Y/VH-109 Diffusion Bond Specimen — Gage Section

| | |
|---|---|
| Magnification: | 100X |
| Etch: | Heavy |
| Specimen No.: | YVE-22 |
| Flight Cycles: | 0 |
| Negative No.: | C-9701 |
| Mount No.: | 95-0 |

Figure 4-135. Microstructure of Unexposed C-129Y/VH-109 Diffusion Bond Specimen — Gage Section

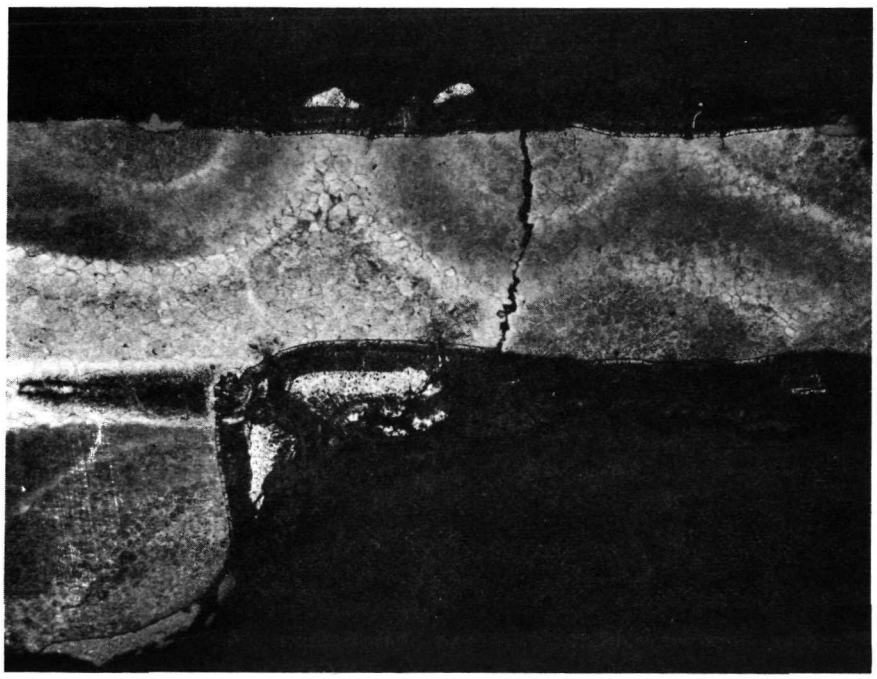

| | |
|---|---|
| Magnification: | 100X |
| Etch: | Light |
| Specimen No.: | YVD-15 |
| Flight Cycles: | 88 |
| Negative No.: | D-519 |
| Mount No.: | 430-0 |

Figure 4-136. Microstructure of Exposed C-129Y/VH-109 Diffusion Bond Specimen — Gage Section

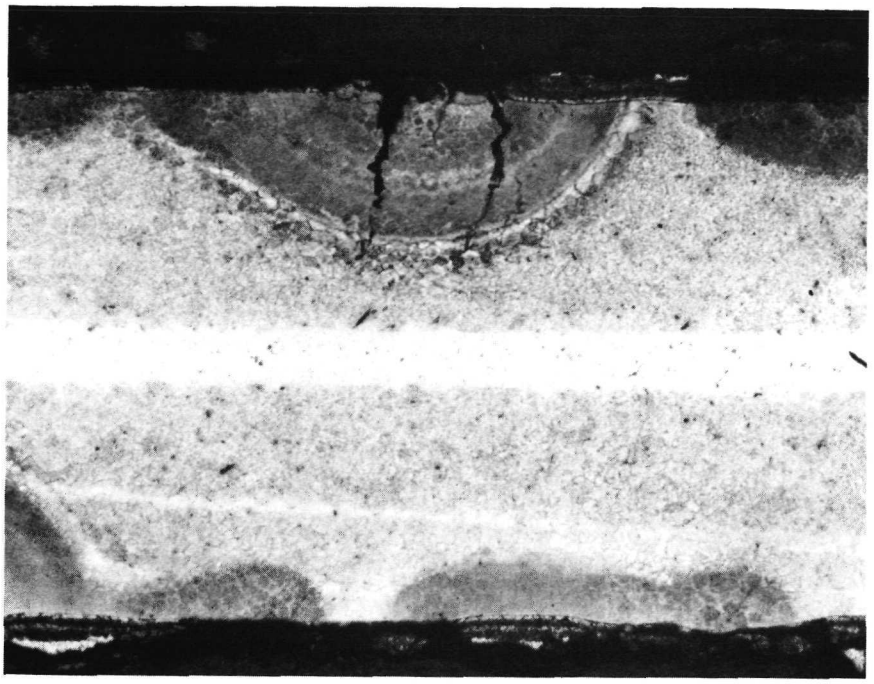

Magnification: 100X
Etch: Light
Specimen No.: YVD-15
Flight Cycles: 88
Negative No.: D-518
Mount No.: 430-0

Figure 4-137. Microstructure of Exposed C-129Y/VH-109 Diffusion Bond Specimen — Gage Section

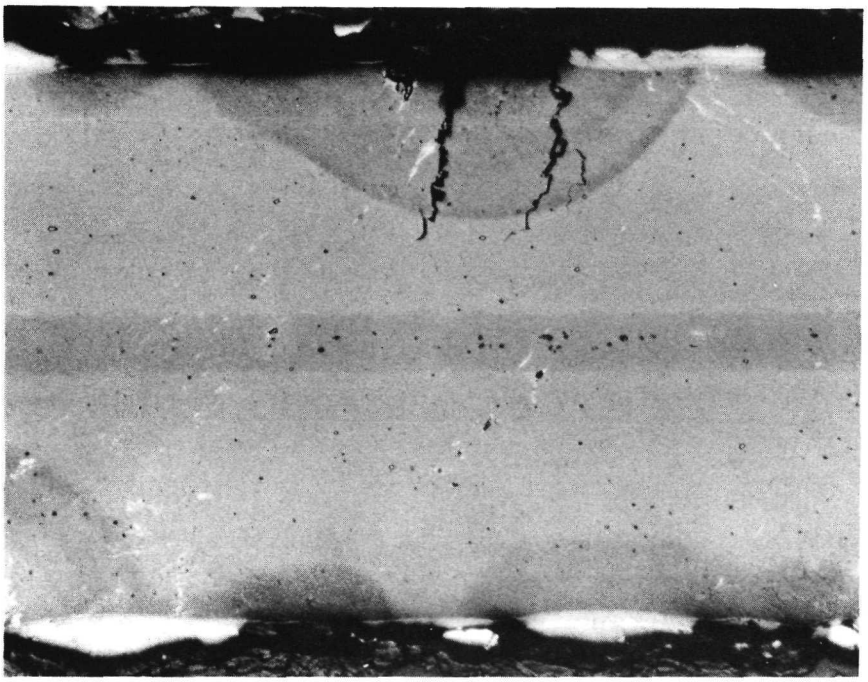

Magnification: 100X
Etch: Anodized
Specimen No.: YVD-15
Flight Cycles: 88
Negative No.: D-794
Mount No.: 430-0

Figure 4-138. Microstructure of Exposed C-129Y/VH-109 Diffusion Bond Specimen — Gage Section

Section 4.2.5.1 that with the R-512E coating the Cb-752 alloy exhibited better resistance to flight simulation exposure than the C-129Y alloy. For the Cb-752/R-512E system, oxygen contamination of the substrate was found only in the weld specimens. The other three systems, on the other hand, showed contamination in parent, weld, and diffusion bond specimens. For both of the VH-109 coated alloys this contamination was very severe. Several examples of intergranular cracking were also noted in the C-129Y/VH-109 specimens. After 100 flight cycles the thickness of the R-512E coating had not changed significantly, while that of the VH-109 coating was drastically reduced. Substrate consumption during these 100 cycles was about 0.0005 inch (0.0013 cm) per side for the Cb-752 alloy with both coatings and slightly higher, 0.0006 to 0.0007 inch (0.0015 to 0.0018 cm) per side for the C-129Y alloy. These values are in reasonably good agreement with similar measurements made on static creep specimens (Section 4.5) — assuming as before (Section 4.2.5.2) that one flight simulation cycle was equivalent to 15 minutes at 2400°F (1589°K). Resistance of joints to flight simulation exposure was excellent in all four systems. Some coating penetration at lap joint corners and slight interaction between the titanium innerlayer and the silicide coating were noted in the diffusion bonds, but these effects appeared to have no influence on performance. No adverse effects were observed in any of the weld areas. Coating uniformity was generally good for all systems except the Cb-752/VH-109. Irregularities in both coating thickness and composition were prevalent for these specimens, particularly the electron beam weld samples. As previously stated (Section 4.2.5.1) improvements were made by Vac-Hyd to better control the coating uniformity (Reference 22). However, additional testing of specimens coated with Vac-Hyd's later processes were not within the constraints of this program.

4.2.5.3.2 Plasma arc exposure: Seven of the 12 plasma arc specimens were selected for metallographic examination after tensile testing. Of these, four showed visual signs of coating failure with substrate erosion. These specimens were sectioned in the region of the coating failures, while the three undamaged specimens were sectioned near the center of the gage length. All sections were taken transverse to the long direction of the specimens. Both the standard $HF-HNO_3-H_2O$ etch and the anodizing treatment were used to detect any evidence of substrate contamination.

The first four photomicrographs, Figures 4-139 to 4-142, were taken from R-512E coated specimens of Cb-752 and C-129Y. The condition of the specimen after plasma arc exposure is noted on each figure. The principal difference in the photomicrographs between the specimens with and without coating failure and substrate erosion during exposure is the condition of the coating. During tensile testing, considerable cracking of the coating occurred in the specimens that were undamaged during plasma arc exposure and retained good ductility. The specimens with coating failure and substrate attack, on the other hand, fractured at this notch with essentially no elongation. As a result, little damage to the coating occurred during the tensile test.

All four R-512E coated specimens show very little coating loss as a result of the 40 exposure cycles. The normal coating cracks had increased in size somewhat, but none had penetrated to the substrate and allowed oxygen contamination of the alloys. The only substrate contamination found was at the edge of the specimen where coating failure and attack of the substrate had occurred. This is in contrast to the flight simulation tests where substrate contamination in areas where no visual coating failure was observed was quite common. The absence of contamination is not surprising, however, since the plasma arc tests were limited to 40 cycles as compared to 100 for the flight simulation tests.

One of the VH-109 coated specimens, YVE-9, survived 40 exposure cycles with no apparent damage. During tensile testing, however, a brittle failure with no measurable elongation was obtained. Examination of the microstructure, Figure 4-143, revealed no evidence of contamination. Because of the brittle failure, the coating was not damaged during tensile testing. The amount of coating loss in 40 cycles appears to be somewhat greater for the VH-109 specimens than for the R-512E specimens. A thicker oxide buildup was also common for the VH-109 coating. The thick oxide scale was found on the side facing the plasma arc.

The remaining two VH-109 specimens, Figures 4-144 and 4-145, both experienced considerable edge attack during exposure. Again, however, no substrate contamination was found except at the specimen edges where total coating loss occurred in the plasma tests. In regions removed from the coating failure, these two specimens could not be distinguished from the VH-109 specimen that completed 40 cycles without a coating failure. Figure 4-144, taken near a failure site in a C-129Y specimen, shows a portion of the contaminated region (the dark area). A Cb-752 specimen photographed in a region well removed from a failure site and showing no contamination is presented in Figure 4-145. Again the heavy buildup of oxide on one side can be seen.

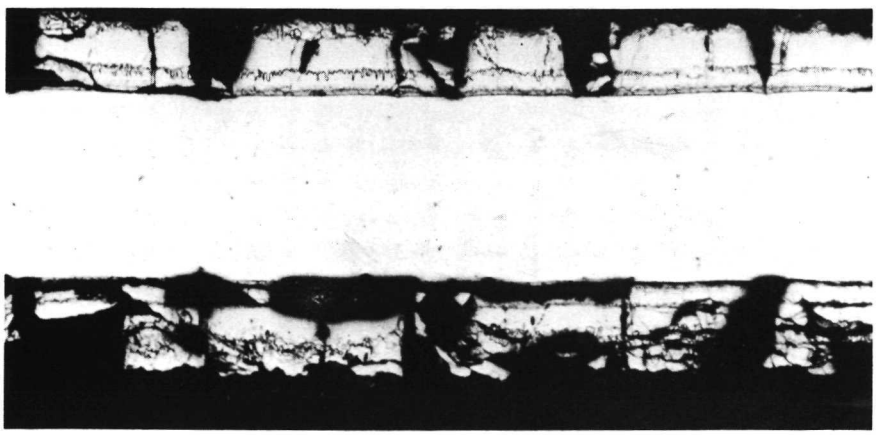

| | |
|---|---|
| Magnification: | 100X |
| Etch: | Light |
| Specimen No.: | BSP-16 |
| Flight Cycles: | 40 |
| % Edge Erosion: | 0 |
| Negative No.: | D-1336 |
| Mount No.: | 599-0 |

Figure 4-139. Microstructure of Plasma Arc Exposed Cb-752/R-512E Specimen – Gage Section

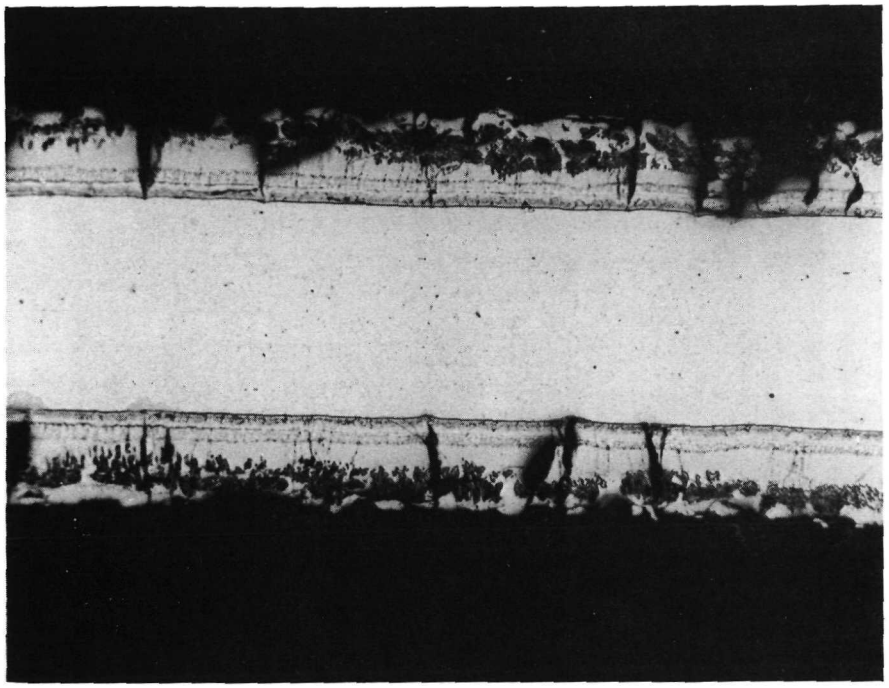

Magnification: 100X
Etch: Light
Specimen No.: BSP-20
Flight Cycles: 40
% Edge Erosion: 18
Negative No.: D-949
Mount No.: 599-0

Figure 4-140. Microstructure of Plasma Arc Exposed Cb-752/R-512E Specimen – Gage Section

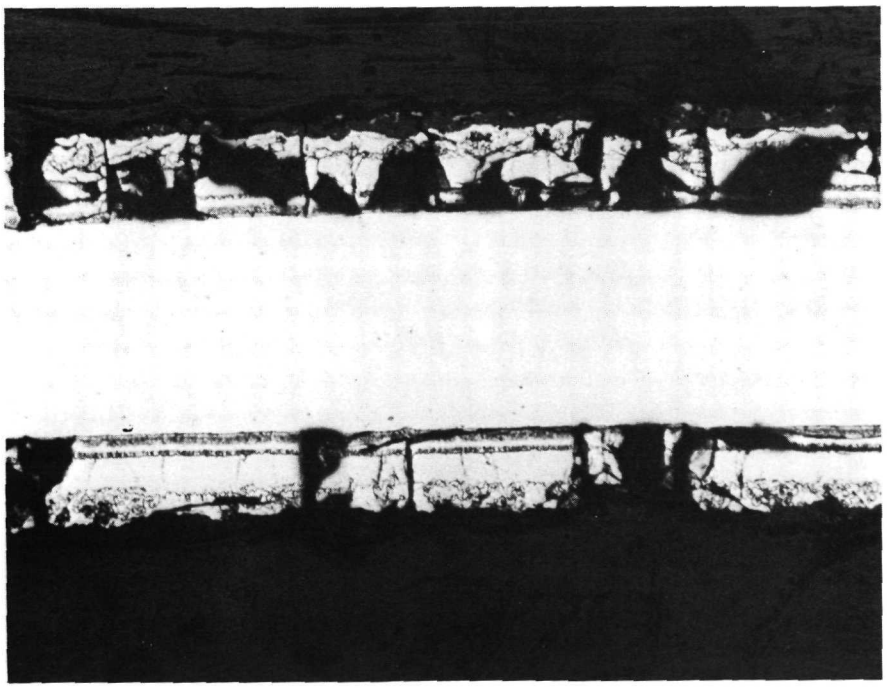

Magnification: 100X
Etch: Light
Specimen No.: YSP-16
Flight Cycles: 40
% Edge Erosion: 0
Negative No.: D-1338
Mount No.: 598-0

Figure 4-141. Microstructure of Plasma Arc Exposed C-129Y/R-512E Specimen – Gage Section

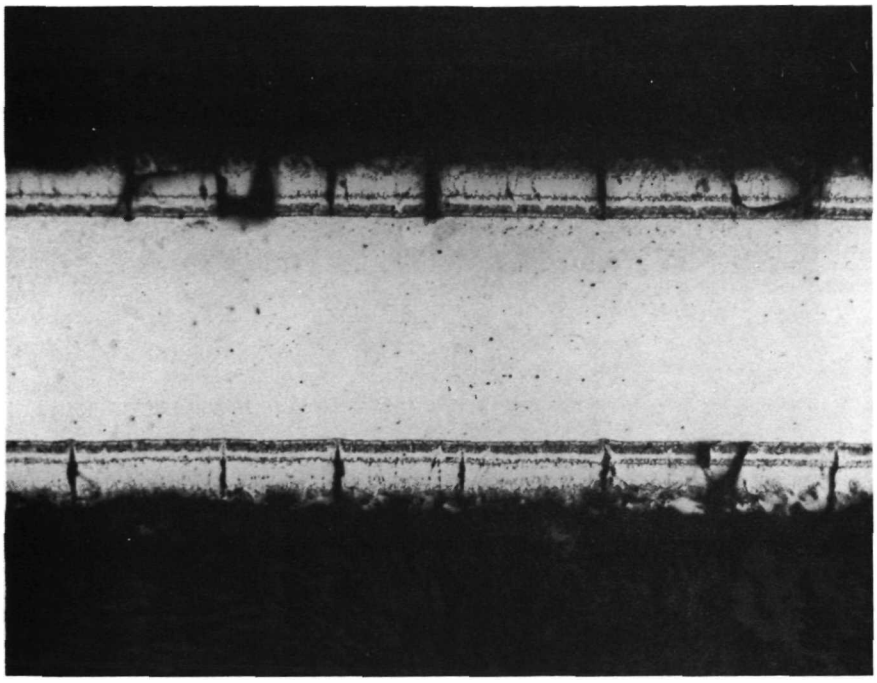

Magnification: 100X
Etch: Light
Specimen No.: YSE-5
Flight Cycles: 30
% Edge Erosion: 46
Negative No.: D-955
Mount No.: 598-0

Figure 4-142. Microstructure of Plasma Arc Exposed C-129Y/R-512E Specimen – Gage Section

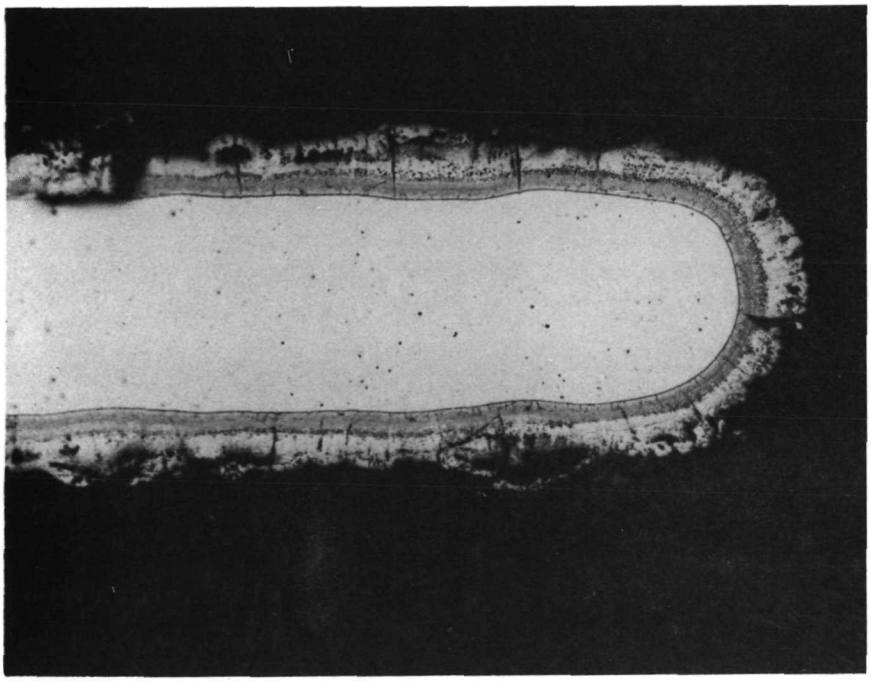

Magnification: 100X
Etch: Light
Specimen No.: YVE-9
Flight Cycles: 40
% Edge Erosion: 0
Negative No.: D-953
Mount No.: 600-0

Figure 4-143.. Microstructure of Plasma Arc Exposed C-129Y/VH-109 Specimen – Gage Section

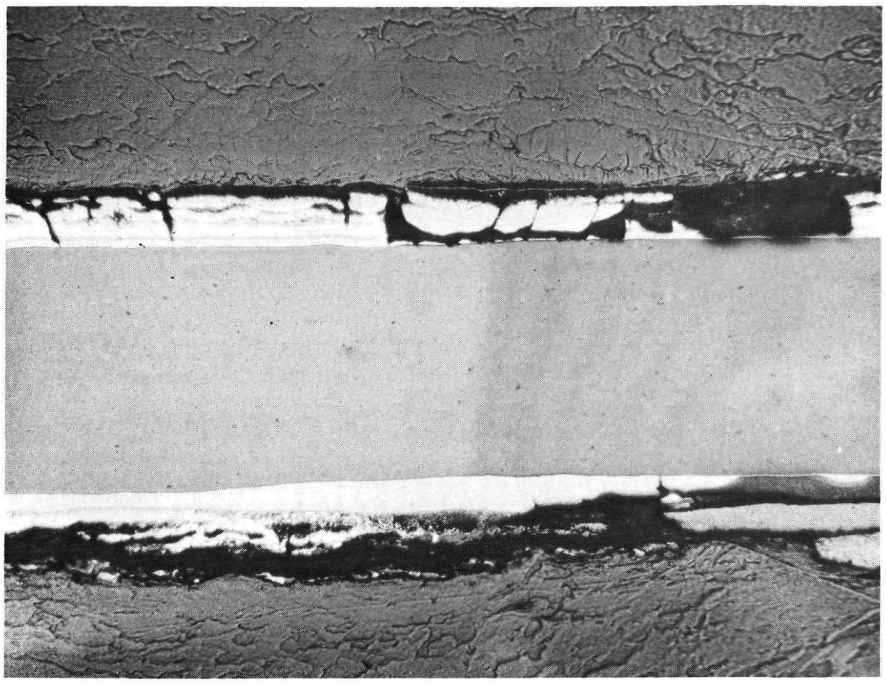

Magnification: 100X
Etch: Anodized
Specimen No.: YVP-16
Flight Cycles: 30
% Edge Erosion: 50
Negative No.: D-1981
Mount No.: 600-0

Figure 4-144. Microstructure of Plasma Arc Exposed C-129Y/VH-109 Specimen — Gage Section

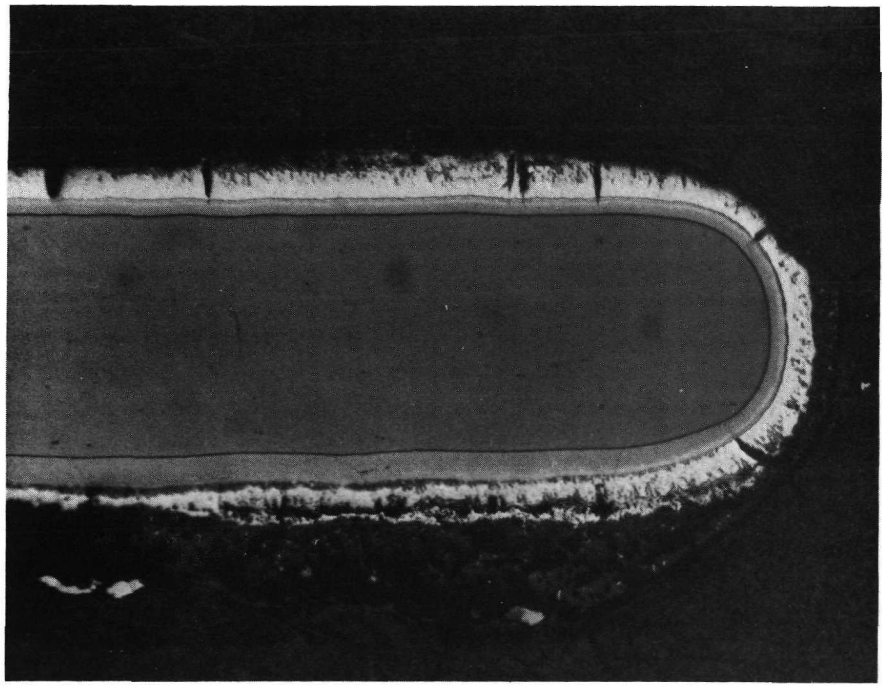

Magnification: 100X
Etch: Light
Specimen No.: BVP-2
Flight Cycles: 40
% Edge Erosion: 24
Negative No.: D-1232
Mount No.: 601-0

Figure 4-145. Microstructure of Plasma Arc Exposed Cb-752/VH-109 Specimen – Gage Section

## 4.3 Plasma Arc Testing

4.3.1 Test plan.— The primary objective of the plasma arc test series was to determine the comparative effects of high-velocity convective-air heating on various columbium alloy/coating combinations. A time-temperature profile similar to that used for the flight simulation tests was used so that the results of the two test techniques could be compared. A static-in-plane load of seven pounds (0.32 kg) was applied to each specimen throughout the test. This load was consistent with the maximum applied load during the flight simulation tests at the peak temperature.

4.3.2 Test specimen description. — Twelve test specimens were introduced into plasma arc testing. The specimens were of the same type as that used for flight simulation tests, that is, flat standard tensile specimens, 11 inches (27.94 cm) in length by 1.25 inches (3.18 cm) wide at the grips. The gage section was reduced to 0.50 inch (1.27 cm) in width. The nominal specimen thickness was 0.015 inch (0.038 cm) before coating. The types and number of specimens were:

| Alloy/Coating | Vac-Hyd VH-109 | Sylvania R-512E |
|---|---|---|
| Cb-752 | 2 | 2 |
| C-129Y | 2 | 2 |
| C-129Y (EB welded) | 2 | 2 |

4.3.3 Test equipment. — The test setup consisted of a metal support fixture for holding the specimens and an electric plasma arc generator with supersonic (M = 3.3) nozzle. The test apparatus was operated in a water-cooled, evacuated test chamber. The metal support fixture was designed with a water-cooled leading edge and also contained an insulated surface consisting of Dyna-Flex covered with Refrasil cloth, over which the gage area of the test specimen was placed. The test setup is shown in Figure 4-146.

The plasma arc generator was mounted on the chamber bulkhead where the necessary instrumentation and water feedthroughs were also installed. A large window in the chamber opposite the test zone permitted time-lapse motion pictures to be taken of the specimens during the test. Automatic optical pyrometers were positioned to view the specimens through the window for temperature measurement and control.

Infrared Industries model TD9 and a model TD9FH optical pyrometers were used. Both instruments operated by detecting emitted infrared radiation in the 0.75 to 0.90 micron wavelength range. The TD9F, which was used for temperature control, has an operating range from 1400° to 8300° F (1033° to 4867° K) with a 0.5-degree view angle of four manual-switch-selected ranges. The TD9FH was used for surveying uniformity at the higher temperatures. It has an operating range from 1840° to 8300° F (1278° to

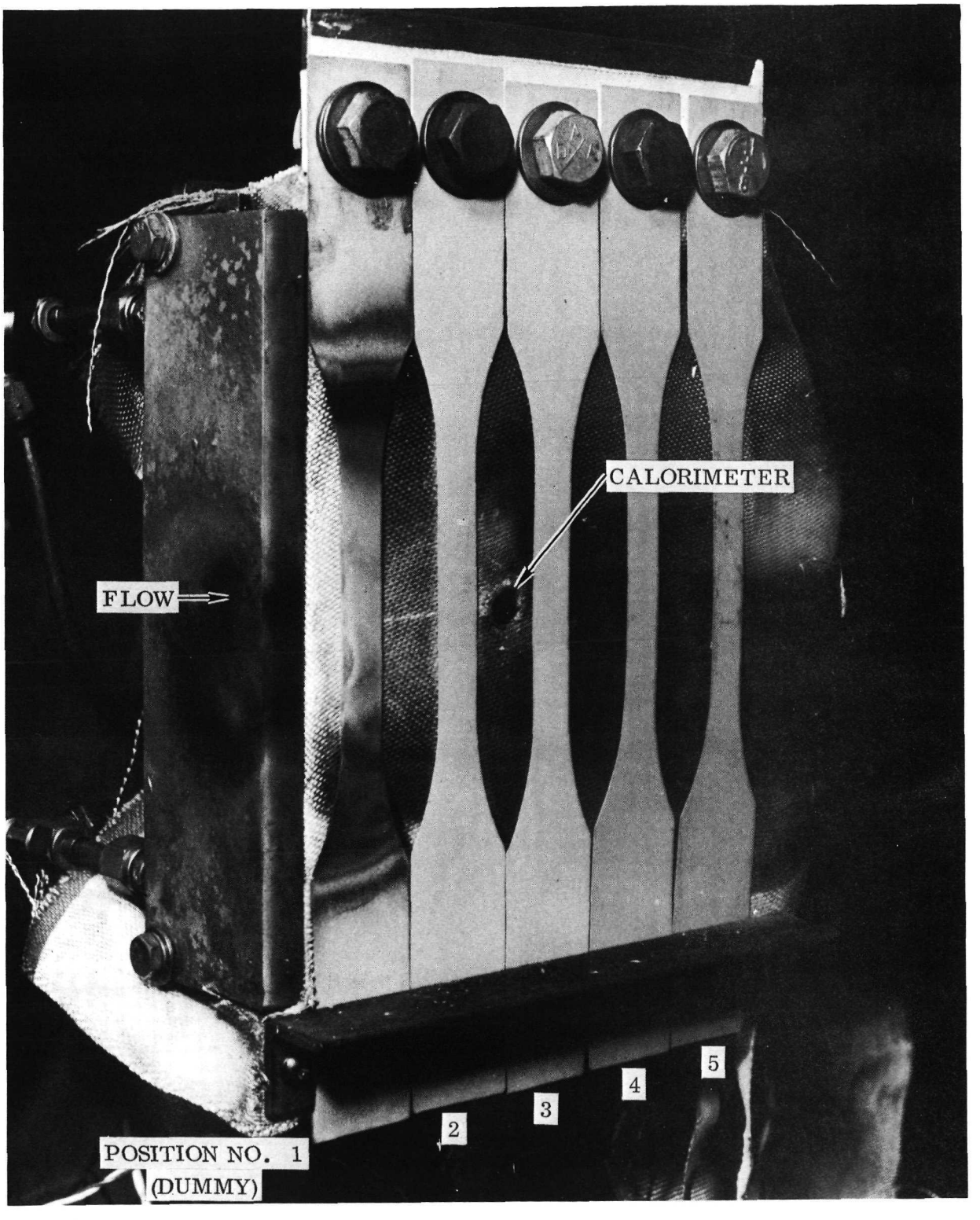


Figure 4-146. Plasma Arc Test Specimen Arrangement

4867° K) with a 0.17-degree view angle in three manual-switch-selected ranges. Each unit is also provided with an emittance control, which was set at 0.85. During the initial testing, thermocouples were also used in an attempt to measure and control specimen temperature. Thermocouples were installed by spot welding Pt/Pt + 13 percent Rh and chromel/alumel thermocouple pairs to 0.003-inch (0.076 mm) thick rhodium foil tabs. The tabs were positioned between the test specimen and the insulation layer in the gage section.

Primary temperature control was achieved through the use of a closed-loop, temperature-feedback servo system. The desired temperature versus time profile, shown in Figure 4-147, was prepared in a curve-following function generator. The

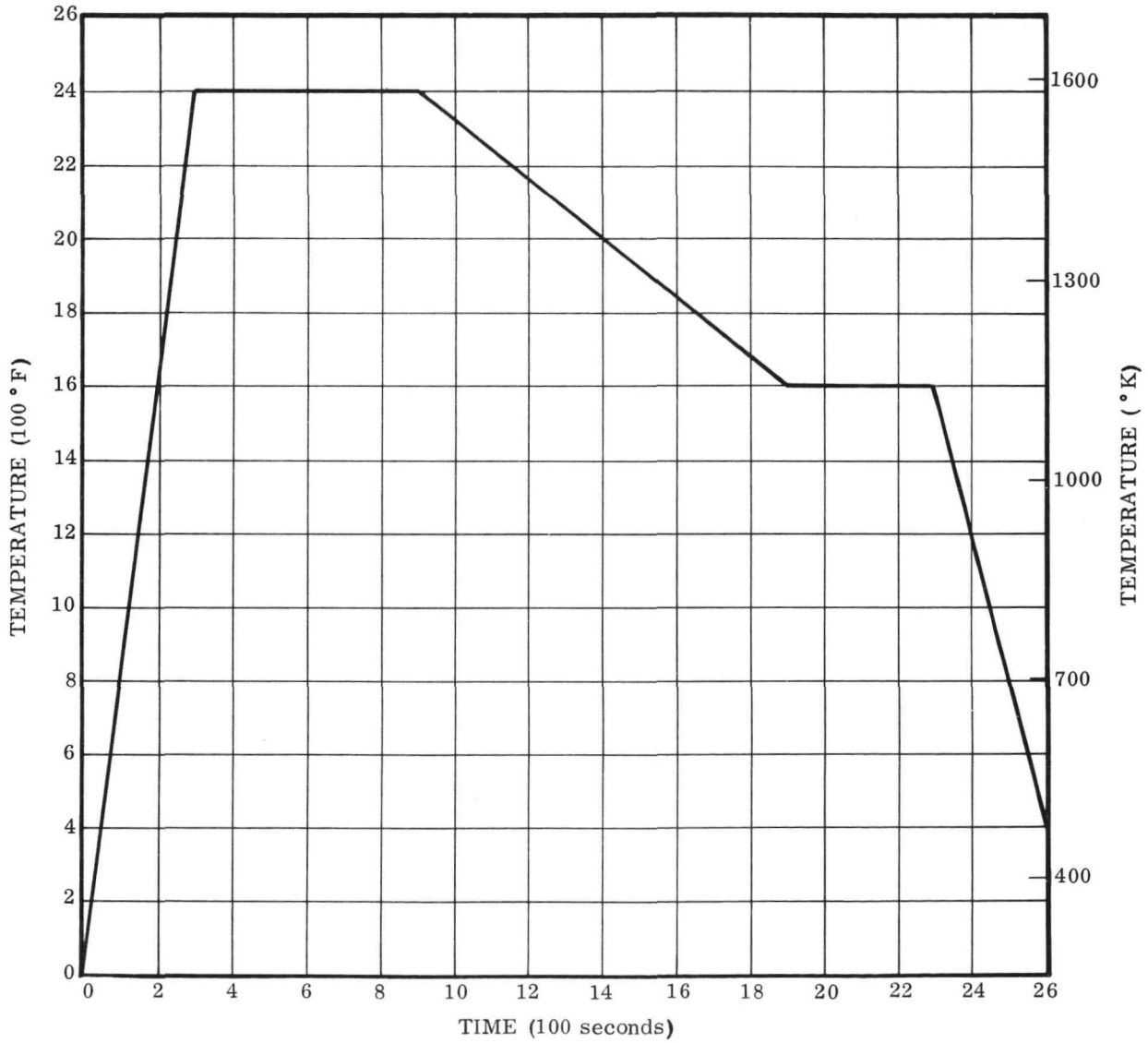


Figure 4-147. Plasma-Arc Test Temperature Profile

desired temperature was automatically compared with that sensed by the optical pyrometer. The error signal was in turn used to regulate the control voltage signal applied to the plasma arc power supplies. More or less electrical power to the plasma arc generator results in higher or lower specimen temperatures. To facilitate the wide range of electrical operating conditions required for this program, individual plasma arc power supplies were manually switched on or off as required at discrete points during the simulated entry temperature profile.

The plasma arc generator was operated with nitrogen gas for the primary flow through the arc chamber. Oxygen gas was mixed with the heated nitrogen in a mixing chamber ahead of the nozzle to form a 21% $O_2$, 79% $N_2$ air composition. The total gas flow was held constant during the temperature cycle at 0.0025 lb/sec (1.1 gm/sec).

4.3.4 Test procedure. — The metal support fixture and insulation assembly was prepared by installing a calorimeter between positions 2 and 3 and installing three Pt/Pt + 13 percent Rh and two chromel/alumel thermocouples as previously described. An automatic optical pyrometer was also positioned to view the specimens. A spare specimen, not a part of the test group, was installed in the number one position. Test specimens identified as Group 1 were installed and positioned as follows:

| Position | 1 | 2 | 3 | 4 | 5 |
|---|---|---|---|---|---|
| Specimen | Spare | BVP-1 | BVP-2 | YVP-16 | YVP-20 |

The specimens were each loaded with a seven-pound (0.32 kg) weight attached to the lower specimen mounting hole. The plasma generator with its supersonic nozzle was positioned so that the hot gas issuing from it would flow over the surface of the center of the test specimen in the gage area. Preliminary test runs of short duration were performed on the Group 1 specimens to determine the adequacy of the test setup to meet the program objectives. Following the evaluation test runs, automatically temperature controlled, full-duration test runs were initiated.

A typical test sequence was performed as follows:

(1) Evacuate test chamber to approximately 1.0 torr (133.32 $N/m^2$) pressure.

(2) Turn on time-lapse motion picture camera.

(3) Initiate nitrogen gas flow at approximately 0.0005 lb/sec (0.23 gm/sec).

(4) Start data recording equipment.

(5) Start plasma arc on manual power at minimum power.

(6) Simultaneously increase nitrogen and oxygen gas to 0.001975 lb/sec (0.90 gm/sec) and 0.000525 lb/sec (0.24 gm/sec).

(7) Adjust chamber pressure to 4.0 torr (533.29 $N/m^2$).

(8) Verify control pyrometer optical system is on target.

(9) Transfer plasma arc control from manual to automatic and begin temperature program.

(10) Adjust chamber pressure as may be required to obtain best temperature distribution.

(11) When temperature cycle has been completed, start another temperature cycle without turning plasma jet off.

(12) Shut test system down at the end of each 10 complete cycles and rotate specimens, e.g., Position 2 to Position 5, Position 3 to Position 2, etc.

4.3.5 Test results and discussion. — During the evaluation test runs it was found that the thermocouple temperature measurements were unreliable due to poor or inconsistent contact resistance between the thermocouple sensing area and the specimen surface. A pressure plate had been installed to overcome the Dyna-Flex shrinkage, but did not provide sufficient reaction. Optical pyrometry provided a stable temperature signal suitable for automatic temperature programming and was therefore used for the remainder of the test program. Thermocouple temperatures continued to be recorded until it was necessary to replace the insulation layer into which they were installed.

As previously stated, the 12 test specimens were tested in three groups of four specimens each. After each group completed 10 cycles, their positions were rotated. The temperature uniformity over each of the four specimens per group was considered to be good, varying within 100° F (55°K). It was attempted to minimize this variance by rotating positions. A tabular presentation of the test run chronology and specimen position is given in Table 4-9.

Specimen BVP-1 broke at 320 seconds into cycle 8. Specimen YVP-20 developed a 0.06 inch (1.52 mm) notch on the leading edge on the first run, but had grown only to nearly 0.12 inch (3.04 mm) by the end of cycle 20. Specimen YVP-16 began to develop a notch on the leading edge during cycle 11 and continued to grow to 0.19 inch (4.82 mm) deep by the end of cycle 20.

Table 4-9. Test Run Chronology

| | Cycle 1 - 10 | Cycle 11 - 20 | Cycle 21 - 30 | Cycle 31 - 40 |
|---|---|---|---|---|
| Group 1 | BVP-1, BVP-2, YVP-16, YVP-20 | YVP-20, BVP-2, YVP-16* | YVP-16, YVP-20, BVP-2 | |
| Group 2 | YSE-5, YSE-6, BSP-16, BSP-20 | BSP-20, YSE-5, YSE-6, BSP-16 | BSP-16, BSP-20, YSE-5, YSE-6 | YSE-6, BSP-16, BSP-20, BVP-2** |
| Group 3 | YVE-9, YVE-1, YSP-16, YSP-13 | YSP-13, YVE-9, YVE-1, YSP-16 | YSP-16, YSP-13, YVE-1 | YVE-1, YSP-16, YSP-13, YVE-9 |

*Specimens not reordered till cycle 14.
**YSE-5 taken out of Group 2 and replaced with BVP-2 from Group 1

During the initial testing it was observed that there was a strong shock wave causing local heating of the Refrasil cloth between positions 1 and 2. With the failure of BVP-1 at cycle 8 it was suspected that it may have contributed to an early failure through excessive temperature on the leading edge of the specimen. Attempts were made to remedy the situation. It was found that slight alteration of the operating pressure [i.e., raising from 5.0 to 5.8 torr (667 to 773 $N/m^2$)] could shift the shock wave forward closer to the dummy specimen located in position 1. This, however, resulted in rapid failure of the dummy specimen. No additional edge failures were noted on position 2 specimens using this technique; however, the shock wave soon began to erode the Refasil cloth at position 1. To correct this, a piece of fused silica "Glass-rock" was inlayed into position 1. This extended the life of the insulation back-up layer, but eventually the Refrasil developed a hole between position 2 and 3, thus suggesting the existence of a second weaker shock wave striking that location. Upon closer observation it was noted that the second shock was more apparent at the lower test temperatures, and undesirable heating effects from that wave could be reduced by dropping the chamber static pressure to 4.0 torr (533 $N/m^2$). One additional significant failure occurred in group 1 on specimen YVP-20 during cycle 26. At the end of 30 cycles specimen YVP-16 from group 1 was dropped from further testing due to excessive reduction in cross section. Figure 4-148 shows the group 1 specimens after completion of testing.

Although most of the anomalies that occurred during group 1 testing had been eliminated, shock wave attachment between positions 1 and 2 continued to be a problem during the first 10 cycles of group 2 testing. Leading edge failure was initiated during cycle 9 on specimen YSE-5. Since coating breakdown had occurred, gradual erosion of the substrate continued until at the end of cycle 30, when the notch had grown to 0.23 inch (5.84 mm), the specimen was removed from further testing.

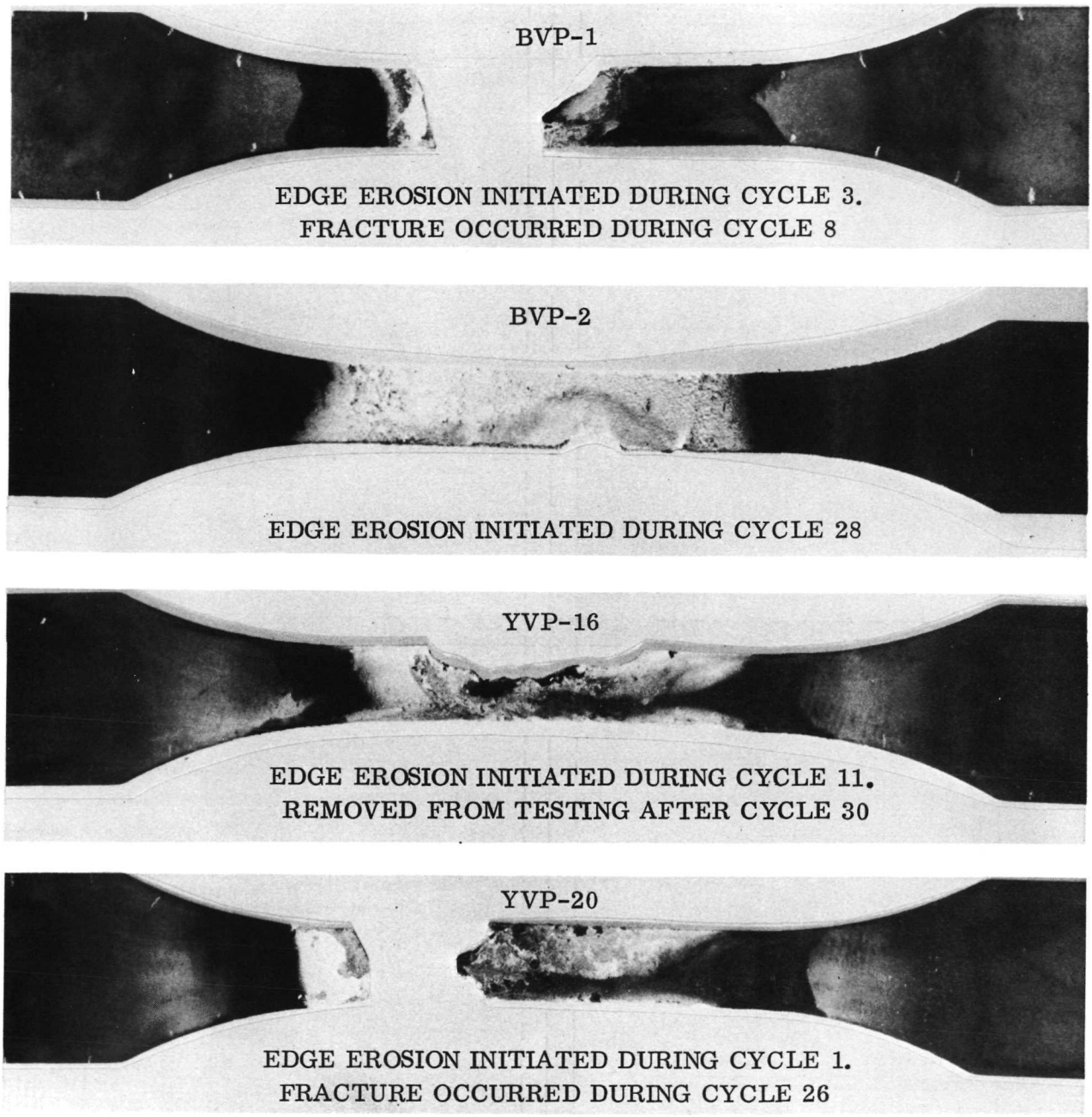


Figure 4-148. Plasma Arc Specimens — VH-109 Coated C-129Y and Cb-752 (Group 1)

A notch developed on the leading edge of specimen BSP-20 during cycle 29. Erosion of the substrate again was gradual. The notch had progressed to 0.09 inch (2.29 mm) when the tests were completed at the end of 40 cycles. The other two specimens in this group, YSE-6 and BSP-16, sustained no visible failures during the 40 cycles. Figure 4-149 shows the specimens at test completion.

The specimens of group 3, consisting of two VH-109 and two R-512E coated C-129Y, sustained the least damage of any group. Leading edge attack on specimen YVE-1 was initiated during cycle 38 and progressed to a depth of 0.14 inch (3.56 mm) at the end of 40 cycles. Leading edge attack on specimen YSP-13 was initiated during cycle 35 and progressed to a depth of 0.07 inch (1.78 mm) at the end of 40 cycles. The group 3 specimens are shown in Figure 4-150 after test completion.

Conclusions based on such a limited number of specimens are difficult, especially since one group of specimens representing one-third of the total was used to establish test procedures. However, the following observations can be made and opinions expressed.

- Each of the failure sites was at the location of a shock wave attachment. Each failure was initiated at a thin edge, i.e., a known problem area for coated refactory metals. Therefore, thin edges must be avoided in the design of leading edges, heat shields, and heat shield components.
- Coated columbium alloys appear to be good candidate material systems for temperature applications up to 2400°F (1589°K) in vehicle regions not affected by direct shock wave impingement.
- There is a decided difference between the performance of a damage site under static conditions and high mass flow air environments. The rate of edge erosion during the static air tests (Section 4.2) was 0.0025 inch (0.0064 cm) per cycle. The rate of edge erosion during the plasma arc tests was between 0.005 inch (0.127 mm) and 0.021 inch (0.535 mm) per cycle, depending on the shock intensity at the initiation of coating breakdown.
- Coating defects or damage sites do not result in catastrophic failure (i.e., rapid oxidation resulting in specimen fracture) of the substrate of tensile specimens under in-plane loads representative of flight hardware. The ability of the tensile loaded specimens to sustain more than one simulated entry cycle after initial coating breakdown was clearly demonstrated.

## 4.4 Tensile Testing

4.4.1 Test plan. — Three sets of tensile tests were carried out during the course of the investigation. In the first, room temperature tests were performed on uncoated Cb-752 and C-129Y, R-512E coated Cb-752 and C-129Y, and VH-109 coated Cb-752 and C-129Y; and 2400°F (1589°K) tests were performed on R-512E coated Cb-752 and C-129Y. Additional characterization tests were made at 1400°F (1033°K), and 2000°F

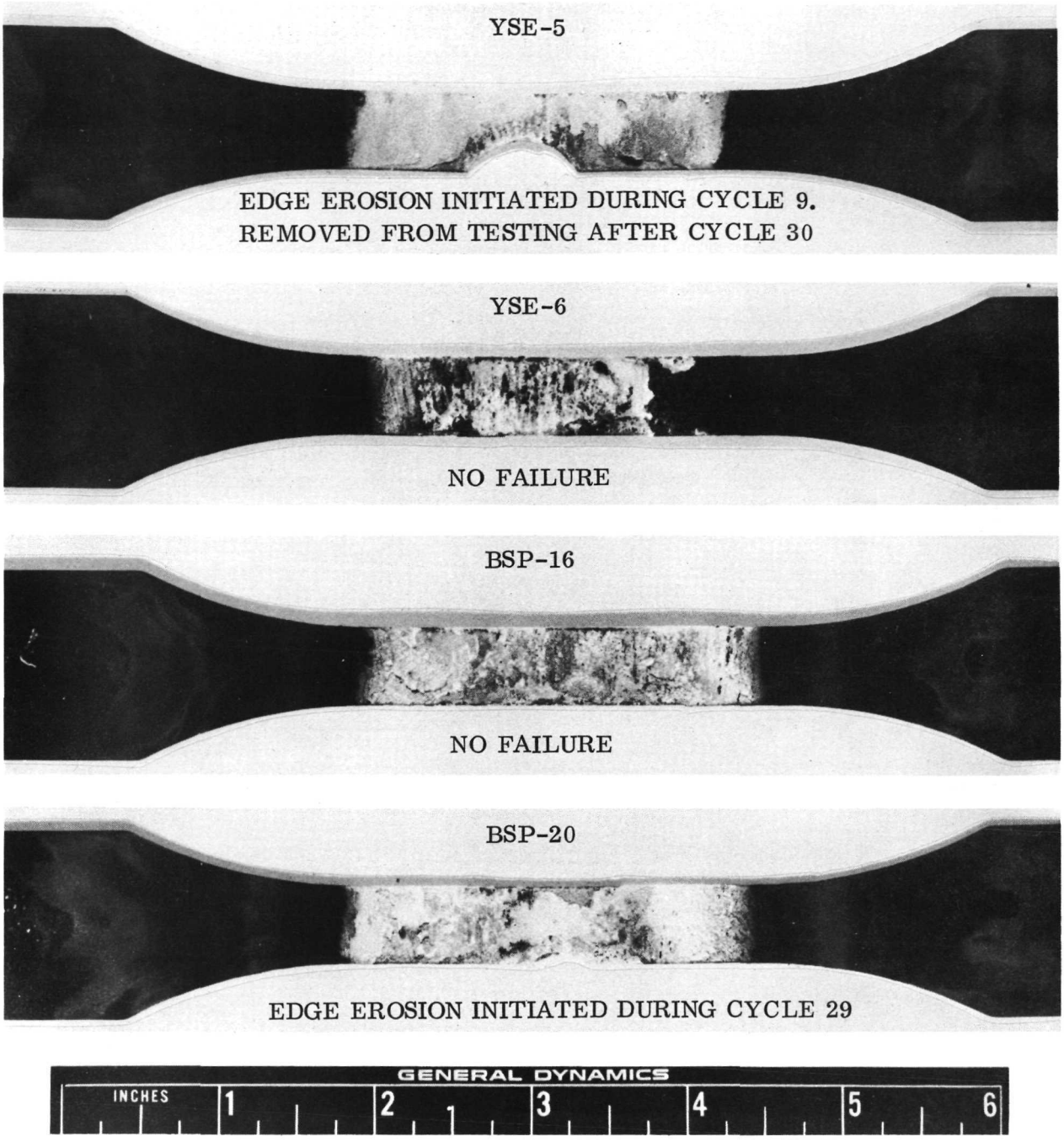


Figure 4-149. Plasma Arc Test Specimens — R-512E Coated C-129Y and Cb-752 (Group 2)

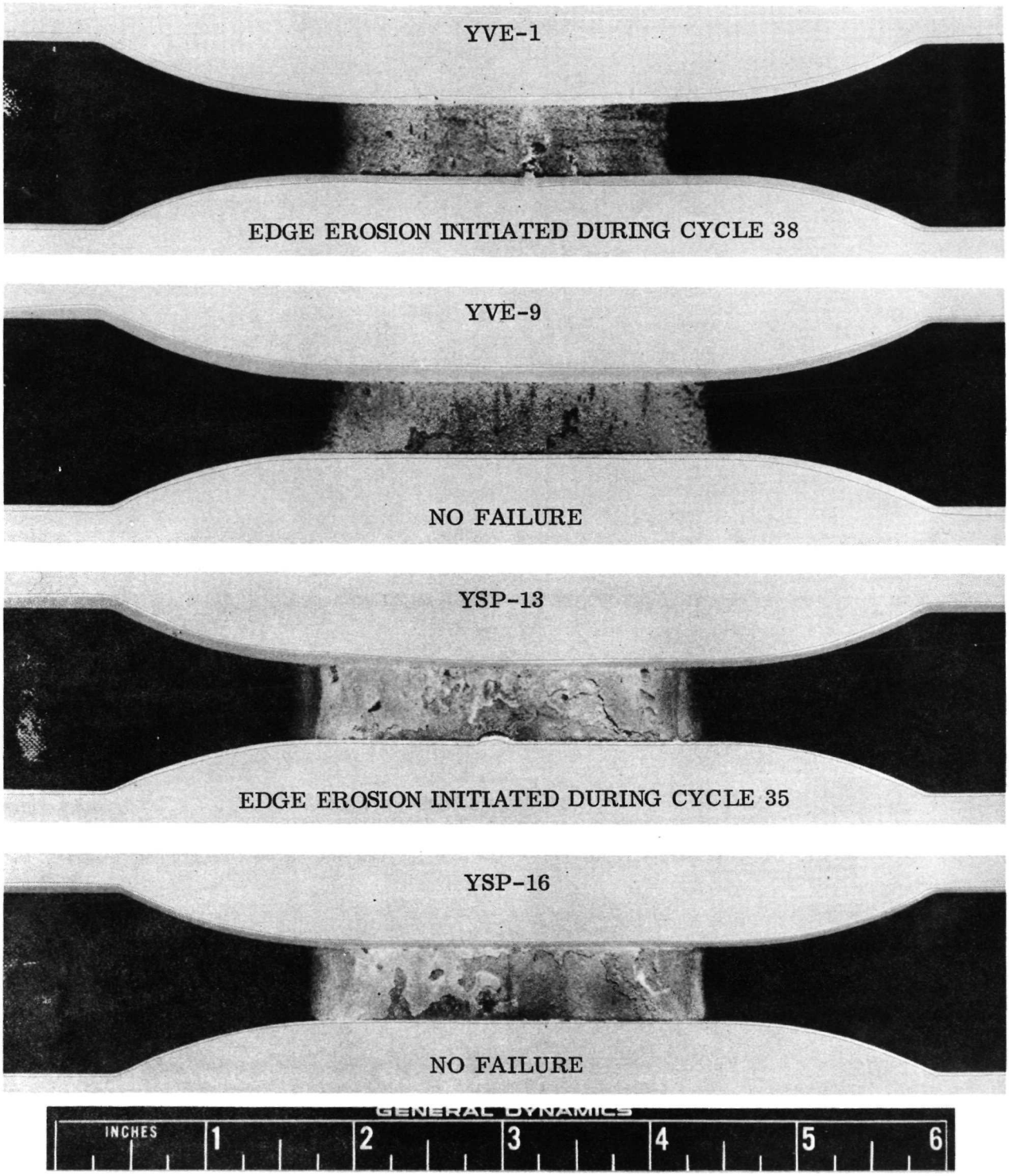


Figure 4-150. Plasma Arc Specimens — VH-109 and R-512E Coated C-129Y (Group 3)

(1366°K) on the two R-512E coated alloys that were selected for further evaluation in Phase II. All tests were run in triplicate.

The second set of tensile tests were those performed on the specimens that survived 100 flight simulation cycles. For each group of six exposed specimens, three each were to be tested at room temperature and 2400° F (1589° K). In cases where less than six specimens survived or severe oxidation attack had occurred, the three best specimens were to be tested at room temperature. The reasons for this decision were:

(1) Room temperature test results are more sensitive to changes in mechanical properties resulting from exposure cycling. This is particularly true for elongation changes.

(2) Test results generally show less scatter at lower temperatures, hence, greater assurance of obtaining reliable information.

(3) There was less likelihood of testing malfunctions occurring during a room temperature test than at 2400° F (1589° K).

(4) Several specimens had coating failures with varying degrees of substrate consumption in the area of the pin holes. Specimens of this type were less likely to give grip failures in 2400° F (1589° K) tests than at room temperature because of the temperature gradients in the furnace that tend to keep the grip ends cooler and, hence, stronger than the reduced section.

The third set of tensile tests consisted of 10 plasma arc specimens that had survived the 40 exposure cycles. These tests were all conducted at room temperature.

Room temperature, 1400° F (1033° K), and 2000° F (1366° K) tests were performed at Convair Aerospace and 2400° F (1589° K) tests at North American Rockwell Space Division.

4.4.2 Test equipment and procedure. — All testing was performed with specimens that were 11 inches (27.94 cm) long, 1.25 inches (3.18 cm) wide with a 0.50 inch (1.27 cm) reduced section, and a 2 inch (5.08 cm) gage length. Room temperature tensile tests were conducted with an Instron Universal Testing Instrument, Model TTCM1. Strain was measured with a Baldwin-Lima-Hamilton Corporation Model PS-5M separable averaging extensometer of the microformer type. No special techniques were required for the room temperature tensile tests except that care was required in attaching the extensometer to prevent damage to the brittle silicide coating prior to testing. Test procedures agreed as closely as possible with those recommended

by the Refractory Metals Sheet Rolling Panel of the Materials Advisory Board (Reference 24). A strain rate of 0.005 ± 0.002 inch per inch (0.013 ± 0.005 cm/cm) per minute was used to 0.6 percent offset. Beyond 0.6 percent offset, a strain rate of 0.05 ±0.02 inch per inch (0.13 ± 0.05 cm/cm) per minute was used to fracture.

Materials Advisory Board, ASTM, and AIA procedures and recommended practices (References 25 to 27) were adhered to as closely as possible in conducting the 1400° F (1033°K) and 2000° F (1366°K) tests. The major difficulty in these tests was the measurement of gage section strain.

The extensometer used in these measurements was specially built by Convair Aerospace to function at these high temperatures. Since the tests were conducted in air the choice of materials for the extension arms was limited. TD Nickel was selected because of its good stability and oxidation resistance in the 2000° to 2400° F (1366° to 1589° K) range. The major deficiency of TD Nickel is its poor weld joint efficiency (40 to 60 percent), and, while welding was required in fabrication of the extensometer, the operating stresses were so low that no problems were encountered. Pointed TD Nickel screws were initially tried as the attachment points. Better results were obtained, however, with knife edges running the width of the specimen, and this method was used for the actual measurements. A close-up view of the extension rods attached to a specimen is shown in Figure 4-151. The pin and clevis grips and pullrods were made from Nicrotung, a nickel base alloy suitable for use to 1900° F (1311° K). Because of the temperature gradient in the furnace, grip temperatures were below 1900° F (1311° K) for specimen gage section temperatures of 2000° F (1366°K).

Testing was carried out with a Baldwin-Emery SR-4 Testing machine, Model FGT. A platinum wound resistance furnace capable of temperatures to 2600° F (1700° K) was used. An overall view of the testing setup with a specimen ready for loading into the

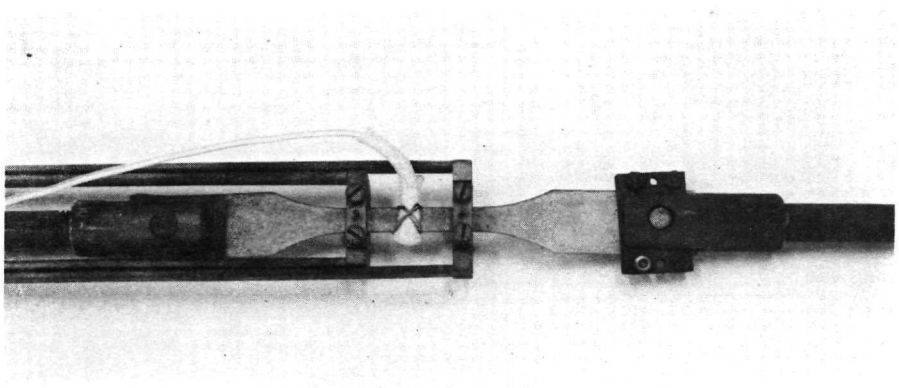

Figure 4-151. Extension Rods of TD Nickel Extensometer Attached to Tensile Specimen (Photo 91361B)

furnace is shown in Figure 4-152. Temperature was measured with a Cr-Al thermocouple wired to the gage section as shown in Figure 4-151.

Prior to testing, the temperature gradient along the gage section of a practice specimen was checked at several temperatures between room temperature and 2200° F (1478° K). It was found to be well within the Material Advisory Board permissible variation of ± 10° F (±11° K) below 1800° F (1255° K) and ±20° F (±22° K) above 1800° F (1255° K) (Reference 25). Temperature variations at a single location on the specimen during the time period required for conducting the tests were also within these limitations.

The extensometer was calibrated at room temperature with a Boekeler calibration instrument and found to meet the ASTM specifications for a Class B-2 extensometer (Reference 28). This class is suitable for use in determining 0.2 percent offset yield strength but not of sufficient accuracy for elastic modulus determinations.

The strain rate for the 1400° F (1033° K) tests was 0.005 ± 0.002 inch per inch (0.013 ± 0.005 cm/cm) per minute to 0.6 percent offset and then 0.05 ± 0.02 inch per inch (0.13 ±0.05 cm/cm) per minute to fracture. The 2200° F (1478° K) tests were run at 0.05 ±0.02 inch per inch (0.13 ±0.05 cm/cm) per minute from zero strain to fracture.

Testing at 2400° F (1589° K) was subcontracted to the Laboratories and Test Group of North American Rockwell Space Division. The tensile tests were conducted in the L&T designed and fabricated 2600° F (1700° K) air test system shown in Figures 4-153 and 4-154. The furnace is equipped with silicon carbide heating elements and operates in two positions, stand-by and test. In the stand-by position the specimen and instrumentation are readied for testing while the furnace is heated (Figure 4-153). The split shell configuration of the furnace permits it to be hydraulically actuated to the test position enveloping the specimen. Specimen heating rates can be controlled to some degree by the speed that the furnace is moved into the test position. For these tests the most rapid heating rates possible were employed.

The furnace has three independently controlled heating zones to control thermal gradients. The test zone is 2 inches (5.08 cm) wide by 2.5 inches (6.35 cm) deep by 4 inches (10.2 cm) high. Three Research Incorporated Thermac and Ignition power regulator systems in conjunction with a Bristol strip chart controller are used to control the test furnace temperatures. The controller can be operated with a programmed input, or manually.

Temperature was measured at four locations. A Pt/Pt + 13 percent Rh thermocouple measured and recorded temperature in the heat zone. This thermocouple also was used as feedback to the power controller. Three chromel/alumel thermocouples

Figure 4-152. High Temperature Tensile Testing Equipment (Photo 91360B)

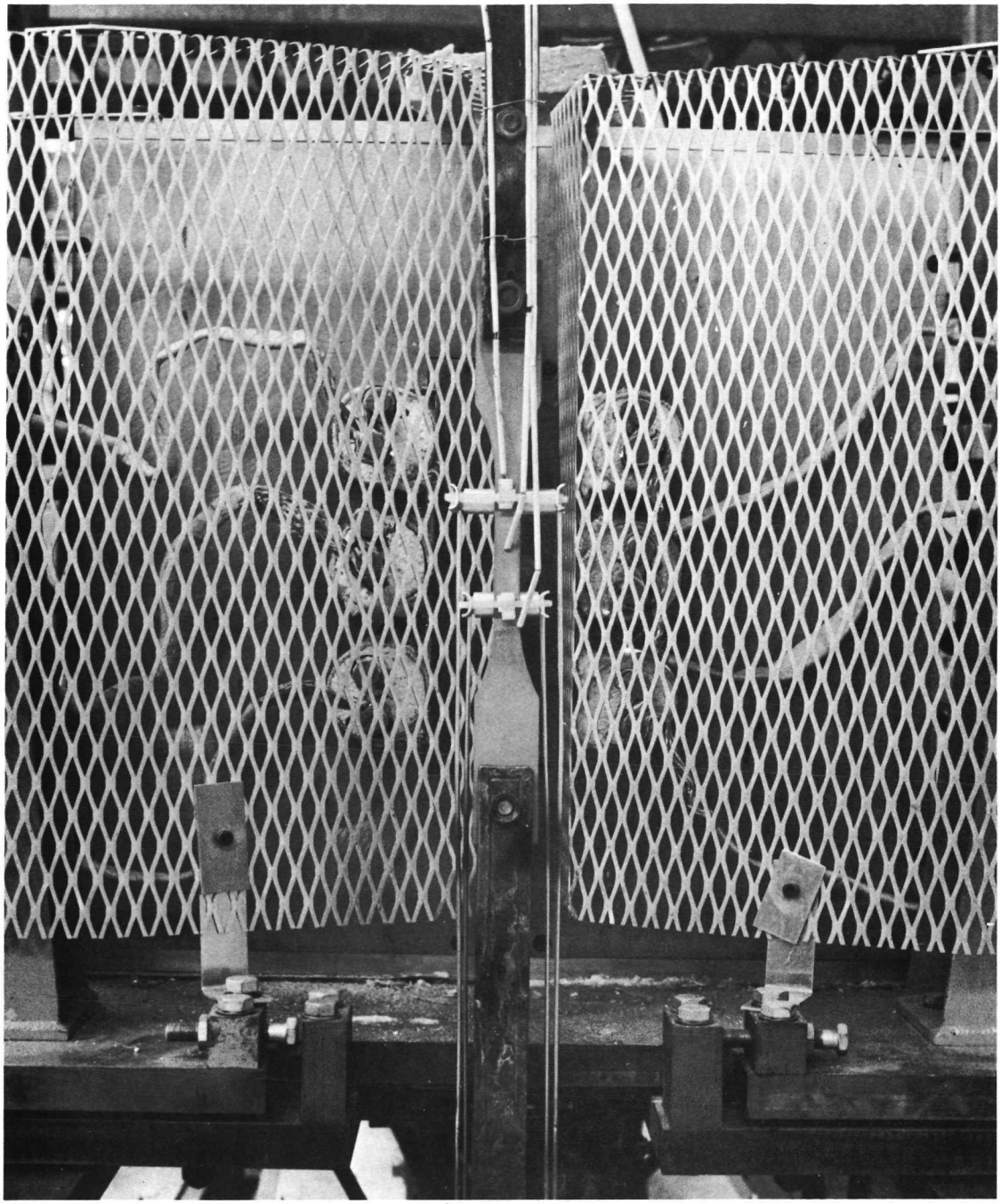

Figure 4-153. Tensile Specimen in Test-Ready Position

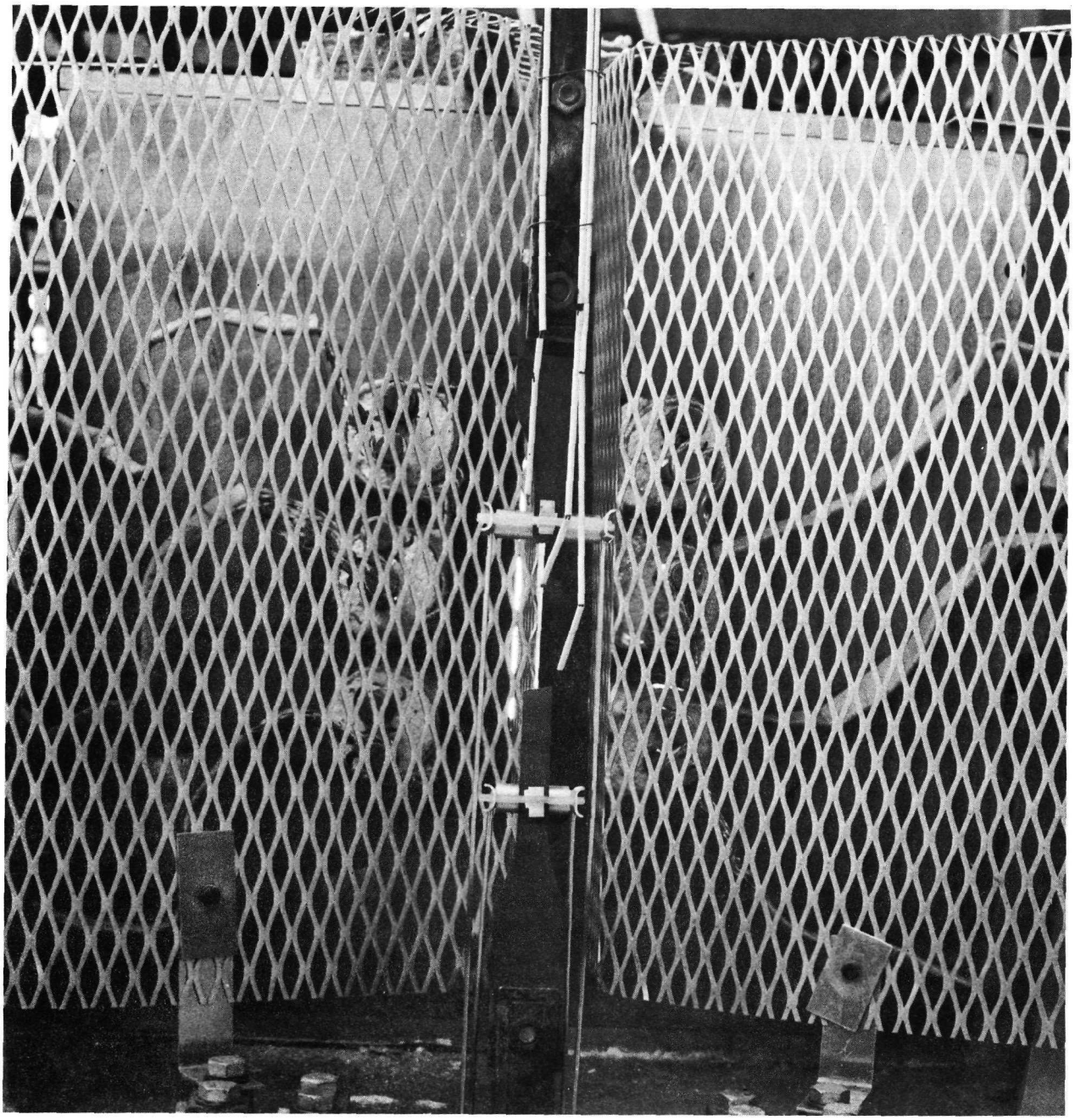

Figure 4-154. Tensile Specimen after Failure

were positioned along the specimen's gage length to indicate the temperature gradient. The gradient was not allowed to exceed ± 25° F (± 14° K) at 2400° F (1489° K). The temperature in the center of the test zone was also kept within 25° F (14° K) of 2400° F (1589° K). The three thermocouples adjacent to the specimen were replaced after every two tests to avoid erroneous readings due to oxidation.

Specimen loading was applied with a hydraulic actuator in an MTS closed-loop servo system with load mode controls. Loads were measured with a 2000 pound (908 kg) Ormond load cell. Strain was measured with a platiumum sapphire hang-down extensometer. A Peters microformer transducer was used in conjunction with an MTS ac transducer module and a Mosely X-Y recorder for autographic load-strain recording. Water-cooled load straps were used to pin the specimens into the test load train. The use of water-cooled load straps eliminates high-temperature material compatibility problems and the need for grip-end reinforcement for carrying load.

4.4.3 Test results and discussion. — In an attempt to maintain an orderly presentation of the large amount of tensile test data, the results have been divided into three sections. The first, Flight Simulation, includes uncoated specimens tested at room temperature; coated but unexposed specimens tested at room temperature and 2400° F (1589° K); and coated specimens exposed for 100 cycles and tested at room temperature and 2400° F (1589° K). The second, Materials Characterization, consists of tests at 1400° F (1033° K) and 2000° F (1366° K) on unexposed Cb-752 and C-129Y alloys with the Sylvania R-512E coating. The third section, Plasma Arc, presents the tensile results from the plasma arc exposed specimens. All strength values for coated specimens were calculated using the original uncoated cross-sectional areas.

4.4.3.1 Flight simulation: The data for the R-512E coated specimens are presented in Tables 4-10 through 4-15. The results are broken down into groups in the same manner as used in the discussion of the flight simulation coating evaluation, i.e., alloy, coating, specimen type. Because of the small number of VH-109 coated specimens that survived 100 cycles and because no 2400° F (1589° K) testw were made, the data for the VH-109 specimens were combined into two tables, one for each alloy. These are Tables 4-16 and 4-17.

Room temperature tensile properties of the columbium alloys were decreased by the application of the coatings. For the R-512E coating, both alloys suffered a drop of about 15 percent in ultimate strength, 17 percent in yield strength, and 20 percent in elastic modulus. These decreases were similar for parent metal, weld, and diffusion bonded specimens. For the VH-109 coated specimens, strength and modulus decreases were generally less than the R-512E coated specimens. The changes were not consistent, however, between the two alloys and among the three types of specimens. This may indicate a lack of quality control in processing of the

Table 4-10. Tensile Test Data — Cb-752/R-512E, Parent

| Specimen No. | Condition | Exposure Cycles | Test Temperature °F | Test Temperature (°K) | $F_{TU}$† ksi | $F_{TU}$† ($MN/m^2$) | $F_{TY}$† ksi | $F_{TY}$† ($MN/m^2$) | Elongation (%) | E† psi × $10^6$ | E† ($GN/m^2$) |
|---|---|---|---|---|---|---|---|---|---|---|---|
| 6-A-1 | Bare | 0 | 75 | 297 | 80.0 | 551.6 | 61.8 | 426.1 | 28.5 | — | — |
| 6-A-2 | Bare | 0 | 75 | 297 | 79.8 | 550.2 | 63.2 | 435.8 | 30.0 | 17.3 | 119.3 |
| 6-B-1 | Bare | 0 | 75 | 297 | 80.3 | 553.7 | 63.3 | 436.5 | 25.0 | — | — |
| 6-B-2 | Bare | 0 | 75 | 297 | 81.9 | 564.7 | 64.4 | 444.0 | 25.0 | — | — |
| 7-A-1 | Bare | 0 | 75 | 297 | 79.4 | 547.5 | 62.7 | 432.3 | 28.5 | 16.7 | 115.1 |
| 7-A-2 | Bare | 0 | 75 | 297 | 80.1 | 552.3 | 63.6 | 438.5 | 27.0 | — | — |
| 7-B-1 | Bare | 0 | 75 | 297 | 80.5 | 555.1 | 62.9 | 633.7 | 23.5 | — | — |
| 7-B-2 | Bare | 0 | 75 | 297 | 78.1 | 538.5 | 61.0 | 420.6 | 26.0 | 16.7 | 115.1 |
| 8-B-1 | Bare | 0 | 75 | 297 | 80.8 | 557.1 | 63.5 | 437.8 | 25.5 | — | — |
| 9-B-1 | Bare | 0 | 75 | 297 | 81.8 | 564.0 | 64.8 | 446.8 | 26.0 | 17.4 | 120.0 |
| 10-B-1 | Bare | 0 | 75 | 297 | 80.6 | 555.7 | 64.1 | 442.0 | 26.0 | 18.1 | 124.8 |
| Average | | | | | 80.3 | 553.7 | 63.2 | 435.8 | 26.5 | 17.2 | 118.6 |
| BSP-21 | Coated | 0 | 75 | 297 | 67.1 | 462.7 | 50.7 | 349.6 | 13.0 | 12.8 | 88.3 |
| BSP-22 | Coated | 0 | 75 | 297 | 67.4 | 464.7 | 50.6 | 348.9 | 12.0* | 11.5 | 79.3 |
| BSP-23 | Coated | 0 | 75 | 297 | 67.4 | 464.7 | 50.4 | 347.5 | 13.5* | 12.3 | 84.8 |
| BSP-1 | Coated | 100 | 75 | 297 | 59.1 | 407.5 | 45.0 | 310.3 | 2.5 | 13.2 | 91.0 |
| BSP-2 | Coated | 100 | 75 | 297 | 59.2 | 408.2 | 44.9 | 309.6 | 2.5 | 13.6 | 93.8 |
| BSP-5 | Coated | 100 | 75 | 297 | 56.0 | 386.1 | 46.4 | 319.9 | 2.5* | 16.6 | 114.5 |
| BSP-13 | Coated | 0 | 2400 | 1589 | 25.1 | 173.1 | 17.3 | 119.3 | 7.0** | 9.5 | 65.5 |
| BSP-14 | Coated | 0 | 2400 | 1589 | 25.6 | 176.5 | 18.2 | 125.5 | 12.5 | 8.9 | 61.4 |
| BSP-15 | Coated | 0 | 2400 | 1589 | 25.7 | 177.2 | 18.2 | 125.5 | 12.0 | 9.2 | 63.4 |
| BSP-3 | Coated | 100 | 2400 | 1589 | 25.8 | 177.9 | 20.7 | 142.7 | 3.0* | 9.9 | 68.3 |
| BSP-4 | Coated | 100 | 2400 | 1589 | 26.3 | 181.3 | 20.7 | 142.7 | 4.0 | 9.6 | 66.2 |
| BSP-6 | Coated | 100 | 2400 | 1589 | 25.5 | 175.8 | 20.6 | 142.0 | 2.5 | 11.1 | 76.5 |

†Values based on original uncoated cross-sections.

* Failed out of gage section.

** Failed at extensometer attachment point.

Table 4-11. Tensile Test Data — Cb-752/R-512E, Electron Beam Weld

| Specimen No. | Condition | Exposure Cycles | Test Temperature | | $F_{TU}$ † | | $F_{TY}$ † | | Elongation (%) | E † | |
|---|---|---|---|---|---|---|---|---|---|---|---|
| | | | °F | (°K) | ksi | ($MN/m^2$) | ksi | ($MN/m^2$) | | psi × $10^6$ | ($GN/m^2$) |
| BSE-16 | Bare | 0 | 75 | 297 | 80.9 | 557.8 | 64.1 | 442.0 | 21.0 | 14.8 | 102.0 |
| BVE-16 | Bare | 0 | 75 | 297 | 80.8 | 557.1 | 63.5 | 437.8 | 20.5 | 14.6 | 100.7 |
| BVE-17 | Bare | 0 | 75 | 297 | 80.8 | 557.1 | 63.8 | 439.9 | 20.5 | 15.1 | 104.1 |
| BSE-18 | Coated | 0 | 75 | 297 | 67.0 | 462.0 | 51.0 | 351.6 | 10.0 | 11.3 | 77.9 |
| BSE-19 | Coated | 0 | 75 | 297 | 69.6 | 479.9 | 52.5 | 362.0 | 11.0 | 11.6 | 80.0 |
| BSE-20 | Coated | 0 | 75 | 297 | 68.0 | 468.9 | 50.9 | 351.0 | 11.0 | 11.8 | 81.4 |
| BSE-5 | Coated | 100 | 75 | 297 | 56.6 | 390.3 | 45.1 | 311.0 | 3.0 | 8.5 | 58.6 |
| BSE-6 | Coated | 100 | 75 | 297 | 59.2 | 408.2 | 42.4 | 292.3 | 4.0* | 8.5 | 58.6 |
| BSE-11 | Coated | 100 | 75 | 297 | 59.5 | 410.3 | 48.8 | 336.5 | 5.5 | 14.6 | 100.7 |
| BSE-8 | Coated | 0 | 2400 | 1589 | 25.7 | 177.2 | 18.9 | 130.3 | 6.0** | 9.3 | 64.1 |
| BSE-17 | Coated | 0 | 2400 | 1589 | 24.8 | 171.0 | 18.9 | 130.3 | 5.0 | 8.7 | 60.0 |
| BSE-22 | Coated | 0 | 2400 | 1589 | 24.8 | 171.0 | 16.7 | 115.1 | 8.5 | 6.9 | 47.6 |
| BSE-7 | Coated | 100 | 2400 | 1589 | 27.9 | 192.4 | 22.4 | 154.4 | 2.0 | 9.1 | 62.7 |
| BSE-13 | Coated | 100 | 2400 | 1589 | 23.8 | 164.1 | ‡ | | 10.0 | 7.4 | 51.0 |
| BSE-10 | Coated | 97 | *** | — | — | — | — | — | — | — | — |

† Values based on original uncoated cross-sections.

‡ Extensometer malfunction.

* Failed out of gage section.

** Failed at extensometer attachment point.

*** Failed during flight simulation exposure testing.

Table 4-12. Tensile Test Data — Cb-752/R-512E, Diffusion Bond

| Specimen No. | Condition | Exposure Cycles | Test Temperature | | $F_{TU}$† | | $F_{TY}$† | | Elongation (%) | E† | |
|---|---|---|---|---|---|---|---|---|---|---|---|
| | | | °F | (°K) | ksi | ($MN/m^2$) | ksi | ($MN/m^2$) | | psi × $10^6$ | ($GN/m^2$) |
| BSD-24 | Bare | 0 | 75 | 297 | 83.4 | 575.0 | 62.4 | 430.2 | 17.0 | 16.7 | 115.1 |
| BVD-23 | Bare | 0 | 75 | 297 | 82.4 | 568.1 | 62.3 | 429.6 | 16.0 | 16.9 | 116.5 |
| BVD-24 | Bare | 0 | 75 | 297 | 83.9 | 578.5 | 63.7 | 439.2 | 15.0 | 17.0 | 117.2 |
| BSD-16 | Coated | 0 | 75 | 297 | 68.2 | 470.2 | 51.7 | 356.5 | 13.5 | 15.2 | 104.8 |
| BSD-17 | Coated | 0 | 75 | 297 | 70.0 | 482.7 | 52.1 | 359.2 | 13.5 | 15.3 | 105.5 |
| BSD-23 | Coated | 0 | 75 | 297 | 71.0 | 489.5 | 53.0 | 365.4 | 12.0 | 13.9 | 95.8 |
| BSD-3 | Coated | 100 | 75 | 297 | 61.3 | 422.7 | 49.7 | 342.7 | 5.0* | 14.6 | 100.7 |
| BSD-4 | Coated | 100 | 75 | 297 | 57.9 | 399.2 | 44.8 | 308.9 | 5.0 | 15.7 | 108.3 |
| BSD-10 | Coated | 100 | 75 | 297 | 60.5 | 417.1 | 47.9 | 330.3 | 7.0 | 15.5 | 106.9 |
| BSD-20 | Coated | 0 | 2400 | 1589 | 24.5 | 168.9 | — | — | 9 0 | — | — |
| BSD-21 | Coated | 0 | 2400 | 1589 | 27.1 | 186.9 | — | — | 5.5 | — | — |
| BSD-22 | Coated | 0 | 2400 | 1589 | 23.4 | 161.3 | — | — | 12.0 | — | — |
| BSD-5 | Coated | 100 | 2400 | 1589 | 25.8 | 177.9 | — | — | 2.0* | — | — |
| BSD-6 | Coated | 100 | 2400 | 1589 | 24.6 | 169.6 | — | — | 2.5 | — | — |
| BSD-9 | Coated | 100 | 2400 | 1589 | 25.9 | 178.6 | — | — | 4.5 | — | — |

† Values based on original uncoated cross-sections.

* Failed out of gage section.

Table 4-13. Tensile Test Data - C-129Y/R-512E, Parent

| Specimen No. | Condition | Exposure Cycles | Test Temperature °F | Test Temperature (°K) | $F_{TU}$ † ksi | $F_{TU}$ † ($MN/m^2$) | $F_{TY}$ † ksi | $F_{TY}$ † ($MN/m^2$) | Elongation (%) | E † psi x $10^6$ | E † ($GN/m^2$) |
|---|---|---|---|---|---|---|---|---|---|---|---|
| 1-A-1 | Bare | 0 | 75 | 297 | 85.1 | 586.8 | 68.4 | 471.6 | 25.0 | — | — |
| 1-A-2 | Bare | 0 | 75 | 297 | 84.8 | 584.7 | 66.2 | 456.4 | 23.5 | — | — |
| 5-A-1 | Bare | 0 | 75 | 297 | 83.9 | 578.5 | 68.4 | 471.6 | 17.0* | 15.1 | 104.1 |
| 5-A-2 | Bare | 0 | 75 | 297 | 84.4 | 581.9 | 68.4 | 471.6 | 20.0* | 16.3 | 112.4 |
| 5-B-1 | Bare | 0 | 75 | 297 | 83.3 | 574.4 | 68.3 | 470.9 | 27.0 | 15.0 | 103.4 |
| 5-B-2 | Bare | 0 | 75 | 297 | 85.2 | 587.5 | 68.2 | 470.2 | 21.0* | 15.5 | 106.9 |
| V-19 | Bare | 0 | 75 | 297 | 84.9 | 585.4 | 67.8 | 467.5 | 26.0 | — | — |
| S-19 | Bare | 0 | 75 | 297 | 84.2 | 580.6 | 67.2 | 463.3 | 26.0 | — | — |
| Average | | | | | 84.5 | 582.6 | 67.9 | 468.2 | 23.2 | 15.5 | 106.9 |
| YSP-20 | Coated | 0 | 75 | 297 | 69.0 | 475.8 | 54.5 | 375.8 | 13.0* | 12.3 | 84.8 |
| YSP-21 | Coated | 0 | 75 | 297 | 70.2 | 484.0 | 54.7 | 377.2 | 16.0 | 12.2 | 84.1 |
| YSP-22 | Coated | 0 | 75 | 297 | 70.0 | 482.7 | 54.9 | 378.5 | 16.5 | 12.4 | 85.5 |
| YSP-1 | Cozted | 100 | 75 | 297 | 65.9 | 454.4 | 57.9 | 399.2 | 5.0 | 13.5 | 93.1 |
| YSP-3 | Coated | 100 | 75 | 297 | 64.2 | 442.7 | 57.4 | 395.8 | 4.5 | 14.0 | 96.5 |
| YSP-4 | Coated | 100*** | 75 | 297 | 61.3 | 422.7 | 55.4 | 382.0 | 5.0 | 13.5 | 93.1 |
| YSP-15 | Coated | 0 | 2400 | 1589 | 25.1 | 173.1 | 17.9 | 123.4 | 6.0** | 8.6 | 59.3 |
| YSP-17 | Coated | 0 | 2400 | 1589 | 24.2 | 166.9 | 18.1 | 124.8 | 6.5 | 8.6 | 59.3 |
| YSP-18 | Coated | 0 | 2400 | 1589 | 25.3 | 174.4 | 18.4 | 126.9 | 8.5 | 7.5 | 51.7 |
| YSP-2 | Coated | 100 | 2400 | 1589 | 27.9 | 192.4 | 22.0 | 151.7 | 4.5 | 10.0 | 69.0 |
| YSP-5 | Coated | 100 | 2400 | 1589 | 29.1 | 200.6 | 22.7 | 156.5 | 4.0* | 10.9 | 75.2 |
| YSP-6 | Coated | 100*** | 2400 | 1589 | 28.4 | 195.8 | 23.6 | 162.7 | 5.0* | 13.2 | 91.0 |

† Values based on original uncoated cross-sections.

* Failed out of gage section.

** Failed at extensometer attachment point.

***Evidence of edge erosion.

Table 4-14. Tensile Test Data — C-129Y/R-512E, Electron Beam Weld

| Specimen No. | Condition | Exposure Cycles | Test Temperature | | $F_{TU}$ † | | $F_{TY}$ † | | Elongation (%) | E † | |
|---|---|---|---|---|---|---|---|---|---|---|---|
| | | | °F | (°K) | ksi | ($MN/m^2$) | ksi | ($MN/m^2$) | | psi × $10^6$ | ($GN/m^2$) |
| YSE-20 | Bare | 0 | 75 | 297 | 82.8 | 570.9 | 66.9 | 461.3 | 14.0* | 15.0 | 103.4 |
| YVE-21 | Bare | 0 | 75 | 297 | 86.8 | 598.5 | 69.6 | 479.9 | 19.0 | 15.4 | 106.2 |
| YVE-22 | Bare | 0 | 75 | 297 | 86.8 | 598.5 | 69.8 | 481.3 | 21.0 | 15.5 | 106.9 |
| YSE-18 | Coated | 0 | 75 | 297 | 76.8 | 529.5 | 59.4 | 409.6 | 11.0* | 12.5 | 86.2 |
| YSE-19 | Coated | 0 | 75 | 297 | 75.5 | 520.6 | 58.8 | 405.4 | 8.0* | 12.1 | 83.4 |
| YSE-21 | Coated | 0 | 75 | 297 | 75.9 | 523.3 | 59.1 | 407.5 | 8.0* | 12.2 | 84.1 |
| YSE-2 | Coated | 100**** | 75 | 297 | 56.1‡ | 386.8 | 54.9 | 378.5 | 2.0 | 14.1 | 97.2 |
| YSE-13 | Coated | 100**** | 75 | 297 | 64.6 | 445.4 | 57.3 | 395.1 | 2.0 | 13.5 | 93.1 |
| YSE-15 | Coated | 100**** | 75 | 297 | 57.9‡ | 399.2 | 57.3 | 395.1 | 1.5 | 14.0 | 96.5 |
| YSE-17 | Coated | 0 | 2400 | 1589 | 26.7 | 184.1 | †† | — | 11.0 | 7.9 | 54.5 |
| YSE-22 | Coated | 0 | 2400 | 1589 | 27.4 | 188.9 | 18.3 | 126.2 | 13.0 | 7.8 | 53.8 |
| YSE-23 | Coated | 0 | 2400 | 1589 | 26.7 | 184.1 | 18.2 | 125.5 | 5.0** | 8.9 | 61.4 |
| YSE-16 | Coated | 100**** | 2400 | 1589 | 25.5‡ | 175.8 | 22.9 | 157.9 | 2 | 8.7 | 60.0 |
| YSE-1 | Coated | 100**** | *** | — | — | — | — | — | — | — | — |
| YSE-14 | Coated | 100**** | *** | — | — | — | — | — | — | — | — |

† Values based on original uncoated cross-sections.

‡ Fracture occurred at site of previous coating failure.

†† Extensometer malfunction.

* Failed out of gage section.

** Failed at extensometer attachment point.

*** Too badly erroded during exposure to warrant testing.

****Evidence of edge erosion.

Table 4-15. Tensile Test Data — C-129Y/R-512E, Diffusion Bond

| Specimen No. | Condition | Exposure Cycles | Test Temperature | | $F_{TU}$† | | $F_{TY}$† | | Elongation (%) | E† | |
|---|---|---|---|---|---|---|---|---|---|---|---|
| | | | °F | (°K) | ksi | ($MN/m^2$) | ksi | ($MN/m^2$) | | psi × $10^6$ | ($GN/m^2$) |
| YSD-18 | Bare | 0 | 75 | 297 | 87.6 | 604.0 | 67.1 | 462.7 | 10.5* | 18.5 | 127.6 |
| YVD-18 | Bare | 0 | 75 | 297 | 86.4 | 595.7 | 66.6 | 459.2 | 11.0* | 18.8 | 129.6 |
| YSD-9 | Coated | 0 | 75 | 297 | 75.4 | 519.9 | 58.4 | 402.7 | 7.0* | 14.6 | 100.7 |
| YSD-19 | Coated | 0 | 75 | 297 | 74.4 | 513.0 | 57.3 | 395.1 | 13.0 | 14.7 | 101.4 |
| YSD-24 | Coated | 0 | 75 | 297 | 70.3 | 484.7 | 55.1 | 379.9 | 7.5 | 13.8 | 95.2 |
| YSD-4 | Coated | 100** | 75 | 297 | 57.2‡ | 394.4 | 56.8 | 391.6 | 1.5 | 15.3 | 105.5 |
| YSD-5 | Coated | 100 | 75 | 297 | 62.2 | 428.9 | 57.1 | 393.7 | 2.0 | 15.9 | 109.6 |
| YSD-7 | Coated | 100 | 75 | 297 | 65.3 | 450.2 | 56.8 | 391.6 | 3.0 | 16.2 | 111.7 |
| YSD-21 | Coated | 0 | 2400 | 1589 | 23.8 | 164.1 | — | — | 4.0 | — | — |
| YSD-22 | Coated | 0 | 2400 | 1589 | 26.7 | 184.1 | — | — | 3.5 | — | — |
| YSD-23 | Coated | 0 | 2400 | 1589 | 25.7 | 177.2 | — | — | 3.5 | — | — |
| YSD-3 | Coated | 100** | 2400 | 1589 | 24.8‡ | 171.0 | — | — | 1.0 | — | — |
| YSD-6 | Coated | 100** | 2400 | 1589 | 23.5‡ | 162.0 | — | — | 1.5 | — | — |
| YSD-8 | Coated | 100** | 2400 | 1589 | 26.3‡ | 181.3 | — | — | 2.0 | — | — |

† Values based on original uncoated cross-sections.

‡ Fracture occurred at site of previous coating failure.

* Failed out of gage section.

**Evidence of edge erosion.

Table 4-16. Room Temperature Tensile Test Data — C-129Y/VH-109

| Specimen No. | Specimen Type | Condition | Exposure Cycles | $F_{TU}$† | | $F_{TY}$† | | Elongation (%) | E† | |
|---|---|---|---|---|---|---|---|---|---|---|
| | | | | ksi | ($MN/m^2$) | ksi | ($MN/m^2$) | | psi × $10^6$ | ($GN/m^2$) |
| ‡ | Parent | Bare | 0 | 84.5 | 582.6 | 67.9 | 468.2 | 23.2 | 15.5 | 106.9 |
| YVP-21 | Parent | Coated | 0 | 72.2 | 532.3 | 60.2 | 415.1 | 14.0* | 13.3 | 91.7 |
| YVP-22 | Parent | Coated | 0 | 75.6 | 521.3 | 58.6 | 404.1 | 17.0 | 13.3 | 91.7 |
| YVP-23 | Parent | Coated | 0 | 75.6 | 521.3 | 59.2 | 408.2 | 14.0 | 13.8 | 95.2 |
| YVP-1 | Parent | Coated | 100*** | 69.2 | 477.1 | 58.8 | 405.4 | 6.5 | 14.7 | 101.4 |
| YVP-5 | Parent | Coated | 100*** | 11.4†† | 78.6 | ** | — | 0 | 11.3 | 77.9 |
| YVP-6 | Parent | Coated | 100 | 39.8†† | 274.4 | ** | — | 1.0 | 11.9 | 82.1 |
| YVE-21 | EB weld | Bare | 0 | 86.8 | 598.5 | 69.6 | 479.9 | 19.0 | 15.4 | 106.2 |
| YVE-22 | EB weld | Bare | 0 | 86.8 | 598.5 | 69.8 | 481.3 | 21.0 | 15.5 | 106.9 |
| YSE-20 | EB weld | Bare | 0 | 82.8 | 570.9 | 66.9 | 461.3 | 14.0* | 15.0 | 103.4 |
| YVE-18 | EB weld | Coated | 0 | 82.0 | 565.4 | 64.9 | 447.5 | 13.0 | 13.9 | 95.8 |
| YVE-19 | EB weld | Coated | 0 | 81.3 | 560.6 | 65.4 | 450.9 | 11.0* | 14.0 | 96.5 |
| YVE-20 | EB weld | Coated | 0 | 82.5 | 568.8 | 65.8 | 453.7 | 10.0* | 14.1 | 97.2 |
| YVE-7 | EB weld | Coated | 100*** | 21.3†† | 146.9 | ** | — | 0 | 18.2 | 125.5 |
| YVD-18 | Diff. bond | Bare | 0 | 86.4 | 595.7 | 66.6 | 459.2 | 11.0* | 18.8 | 129.6 |
| YSD-18 | Diff. bond | Bare | 0 | 87.6 | 604.0 | 67.1 | 462.7 | 10.5* | 18.5 | 127.6 |
| YVD-22 | Diff. bond | Coated | 0 | 83.8 | 577.8 | 67.3 | 464.0 | 10.0* | 15.5 | 106.9 |
| YVD-23 | Diff. bond | Coated | 0 | 83.8 | 577.8 | 67.5 | 465.4 | 8.5* | 15.1 | 104.1 |
| YVD-24 | Diff. bond | Coated | 0 | 82.5 | 568.8 | 66.2 | 456.4 | 10.0* | 16.2 | 111.7 |

† Values based on original uncoated cross-sections.

‡ Average of 8 specimens (see Table 4-13).

†† Fracture occurred at site of previous coating failure.

* Failed out of gage section.

** Failed before yield.

***Evidence of edge erosion.

Table 4-17. Room Temperature Tensile Data — Unexposed Cb-752/VH-109

| Specimen No. | Specimen Type | Condition | $F_{TU}$ † | | $F_{TY}$ † | | Elongation (%) | E † | |
|---|---|---|---|---|---|---|---|---|---|
| | | | ksi | ($MN/m^2$) | ksi | ($MN/m^2$) | | psi $\times 10^6$ | ($GN/m^2$) |
| ‡ | Parent | Bare | 80.3 | 553.7 | 63.2 | 435.8 | 26.5 | 17.2 | 118.6 |
| BVP-20 | Parent | Coated | 73.8 | 508.9 | 57.6 | 397.2 | 11.0* | 12.9 | 88.9 |
| BVP-21 | Parent | Coated | 72.7 | 501.3 | 56.1 | 386.8 | 11.5* | 12.9 | 88.9 |
| BVP-22 | Parent | Coated | 73.8 | 508.9 | 57.0 | 393.0 | 13.0* | 12.7 | 87.6 |
| BVE-16 | EB weld | Bare | 80.8 | 557.1 | 63.5 | 437.8 | 20.5 | 14.6 | 100.7 |
| BVE-17 | EB weld | Bare | 80.8 | 557.1 | 63.8 | 439.9 | 20.5 | 15.1 | 104.1 |
| BSE-16 | EB weld | Bare | 80.9 | 557.8 | 64.1 | 442.0 | 21.0 | 14.8 | 102.0 |
| BVE-18 | EB weld | Coated | 72.1 | 497.1 | 57.4 | 395.8 | 7.0* | 12.3 | 84.8 |
| BVE-19 | EB weld | Coated | 71.3 | 491.6 | 57.1 | 393.7 | 5.5* | 13.9 | 95.8 |
| BVE-20 | EB weld | Coated | 72.2 | 497.8 | 58.4 | 402.7 | 7.5 | 16.2 | 111.7 |
| BVD-23 | Diff. bond | Bare | 82.4 | 568.1 | 62.3 | 429.6 | 16.0 | 16.9 | 116.5 |
| BVD-24 | Diff. bond | Bare | 83.9 | 578.5 | 63.7 | 439.2 | 15.0 | 17.0 | 117.2 |
| BSD-24 | Diff. bond | Bare | 83.4 | 575.7 | 62.4 | 430.2 | 17.0 | 16.7 | 115.1 |
| BVD-17 | Diff. bond | Coated | 76.1 | 524.7 | 59.6 | 410.9 | 10.0* | 15.3 | 105.5 |
| BVD-18 | Diff. bond | Coated | 75.6 | 521.3 | 59.3 | 408.9 | 7.5* | 15.4 | 106.2 |
| BVD-19 | Diff. bond | Coated | 79.3 | 546.8 | 62.4 | 430.2 | 10.0 | 15.4 | 106.2 |

† Values based on original uncoated cross-sections.

‡ Average of 11 specimens (see Table 4-10).

* Failed out of gage section.

VH-109 coating, since the decrease in properties is primarily the result of the loss of substrate during the coating process.

The major effect of coating (both R-512E and VH-109) was a drastic reduction in room temperature ductility. Decreases in elongation of between 30 and 50 percent were obtained from parent metal and electron beam weld samples of both alloys with both coatings. The elongation values of the coated diffusion bonded specimens agreed closely with the parent metal and weld specimens.

There was no adverse effect of coating on the electron beam welds or diffusion bonds. Both were 100 percent joint efficient in the room temperature tensile tests. Of the 24 specimens tested, all but one failed well away from either the weld or bond areas. The one exception (specimen BVE-20 in the heat-affected zone) had properties comparable to those of the same group that failed in the base metal.

The unexposed 2400° F (1589° K) tensile results are discussed in section 4.4.3.2

The effect of flight simulation testing on tensile properties at room temperature and 2400° F (1589° K) can be found in Tables 4-10 through 4-17. The data are not complete because of the failure of many of the specimens (primarily VH-109 coated) to complete 100 flight cycles. In addition, several specimens, while surviving the 100 exposure cycles, were defected as a result of coating failure at the edges. Oxygen contamination and, in many cases, severe substrate erosion by oxidation occurred at these failure sites. These defects acted as stress raisers and often led to premature failure during tensile testing.

The best results were obtained from the R-512E coated Cb-752 specimens (Tables 4-10 through 4-12). The parent, weld, and diffusion bonded specimens gave very nearly the same results when tested at room temperature. All experienced decreases in ultimate strength of about 10 to 15 percent after exposure. This decrease is readily accounted for by the loss in substrate as a result of diffusion zone growth during cycling. Strength values were calculated by using the original uncoated cross-sectional areas. It should be observed that while the intrinsic strengths of the specimens had not changed significantly, their load carrying ability was reduced by 10 to 15 percent. Yield strength values generally showed less of an effect of the thermal cycling. The elongation values, on the other hand, were greatly reduced. Decreases of 50 to 80 percent of the unexposed values were measured. The exposed specimens became severly notched by the presence of numerous coating cracks that enlarge during cycling and, in many cases, extended into the substrate. Any oxygen contamination of the substrate also acts to reduce the ductility.

The ability of R-512E coated Cb-752 electron beam welds and diffusion bonds to withstand flight simulation exposure was again demonstrated by the room temperature

tensile test results. Mechanical property changes were very similar to those of the parent material. No failures occurred in the vicinity of either type of joint.

The exposed specimens tensile tested at 2400° F (1589° K) gave some rather unexpected results. Although the alloy cross-section had been reduced about 10 percent by diffusion zone growth during flight simulation cycling, no decrease in ultimate strength (based on uncoated area) was obtained. The yield strengths were slightly higher, while the elongations behaved as expected and showed significant decreases.

For columbium alloys, the decrease in strength after coating is not generally as pronounced at elevated temperatures as at room temperature. The reason for this might well be that at the higher temperatures the coating, with increased ductility, can now support a portion of the applied load. If this were true, the conversion of alloy substrate to diffusion zone during flight simulation cycling would have little effect on the net cross-section of the coating/alloy composite and, hence, on the elevated temperature ultimate strength.

In like manner to the room temperature tests, the exposed joint specimens tested at 2400° F (1580° K) gave tensile results very similar to the parent specimens. Again, no failures occurred in the vicinity of either type of joint.

The tensile data for the R-512E coated C-129Y alloy are presented in Tables 4-12 through 4-15. For specimens that survived the 100 flight simulation cycles with no visible coating failures, the room temperature tensile strengths and elongation values showed decreases similar to those of the R-512E coated Cb-752 specimens. Yield strengths were generally not affected as much and, in one case (parent metal), were higher after exposure. Three of the room temperature test specimens (two welds and one diffusion bond) had edge-type coating failures. These specimens possessed lower tensile strengths and all fractured at the coating failure sites with 1.5 to 2 percent elongation. The weld and diffusion bond areas did not appear to have been affected any differently than the base material by the exposure cycling. One diffusion bonded specimen (YSD-5) did fail at the edge of the bond overlap, but its properties were not significantly different from the other specimens.

The exposed R-512E coated C-129Y specimens tested at 2400° F (1589° K) were similar to the Cb-752 specimens in that no decrease in tensile strength was found. Strength properties of the parent specimens were slightly higher after cycling, while those of the joint specimens were essentially unchanged. The elongation values decreased slightly for the parent specimens. All the joint specimens failed at sites of previous coating failures with elongation of two percent or less. None of the failure sites was located near a weld or bond area.

Only four VH-109 coated specimens survived 100 flight simulation cycles. All were of the C-129Y alloy, three parent metal and one electron beam weld specimens. The post exposure tensile test data, room temperature only, are presented in Table 4-16. Three of these specimens suffered severe coating failure during exposure testing with considerable edge erosion or surface attack. These specimens all failed at an attack site with almost zero elongation and greatly reduced tensile strength. The fourth specimen, YVP-1, was the only one of the 36 VH-109 coated specimens that survived flight simulation testing with no visible sign of coating failure. This specimen also retained very good tensile properties. The decrease, after 100 flight cycles, compared favorably with the R-512E coated specimens. This one specimen shows that with the proper processing the VH-109 coating can compete equally with the R-512E coating under cyclic flight simulation testing. The overall results, however, greatly favor the Sylvania coating at this time.

4.4.3.2 Materials characterization: Based on the results of the flight simulation study, two of the materials systems were selected for further evaluation in Phase II of the contract. The two substrate/coating materials systems chosen were Cb-752/R-512E and C-129Y/R-512E. As a part of the Phase I characterization of these materials, additional tensile tests were performed at 1400° F (1033° K) and 2000° F (1366°K). Parent metal, electron beam weld, and diffusion bonded specimens were included in this task. The results are presented in Tables 4-18 and 4-19. The data along with that from the room temperature and 2400° F (1589° K) tests are plotted in Figures 4-155 and 4-156 for the parent metal specimens. No curves are presented for the electron beam welds or the diffusion bonds as they closely parallel the parent metal results. Figures 4-155 and 4-156 show the typical decrease in tensile properties with temperature. One point of interest is the similarity in properties at 1400° F (1033° K) and 2000° F (1366°K). In this region, elongation values have dropped to very low levels. The intermediate temperature embrittlement is typical of silicide coated columbium alloys (References 29 through 32). At 2400° F (1589°K) strength values have dropped sharply, while elongation has increased.

The electron beam weld and diffusion bond specimens possessed tensile properties equal to those of the parent metal specimens. With one exception (YSE-7), all specimens tested at 1400° F (1033° K) and 2000° F (1366°K) failed in the base metal. At 2400° F (1589° K) no weld failures were observed, but five of the six diffusion bond specimens failed at the edge of the bond area. Tensile properties were comparable to parent specimens, however. Because of the geometry of the diffusion bonded specimens, slight bending moments are applied at the two bond edges. These moments generally caused a slight permanent bend in each half of the specimens on the sides opposite the bond edges. With the exception of the 2400° F (1589° K) tests, failure did not occur at these locations, however. During the 2400° F (1589° K) tests, steep temperature gradients exist along the specimens on either side of the bond. The

Table 4-18. 1400°F (1033°K) and 2000°F (1366°K) Tensile Test Data — Unexposed Cb-752/R-512E

| Specimen No. | Specimen Type | Test Temperature | | $F_{TU}$† | | $F_{TY}$† | | Elongation (%) |
|---|---|---|---|---|---|---|---|---|
| | | °F | (°K) | ksi | ($MN/m^2$) | ksi | ($MN/m^2$) | |
| BSP-7 | Parent | 1400 | 1033 | 30.8 | 212.4 | ‡ | — | 1.0* |
| BSP-8 | Parent | 1400 | 1033 | 30.6 | 211.0 | 30.4 | 209.6 | 2.0 |
| BSP-9 | Parent | 1400 | 1033 | 30.3 | 208.9 | 29.4 | 202.7 | 1.5 |
| BSP-10 | Parent | 2000 | 1366 | 32.0 | 220.6 | 29.0 | 200.0 | 1.0†† |
| BSP-11 | Parent | 2000 | 1366 | ** | — | 28.3 | 195.1 | ** |
| BSP-12 | Parent | 2000 | 1366 | 32.7 | 225.5 | 28.9 | 199.3 | 1.0* |
| BSE-1 | EB weld | 1400 | 1033 | 32.7 | 225.5 | 32.2 | 222.7 | 0.5 |
| BSE-21 | EB weld | 1400 | 1033 | 29.2 | 201.3 | ‡ | — | 1.0* |
| BSE-4 | EB weld | 2000 | 1366 | 29.3 | 202.0 | 28.2 | 194.4 | 2.0 |
| BSE-9 | EB weld | 2000 | 1366 | 34.4 | 237.2 | 32.0 | 220.6 | 1.0* |
| BSE-12 | EB weld | 2000 | 1366 | 31.9 | 220.0 | ‡ | — | 3.0 |
| BSD-13 | Diff. bond | 1400 | 1033 | 31.4 | 216.5 | — | — | 1.0 |
| BSD-14 | Diff. bond | 1400 | 1033 | 30.2 | 208.2 | — | — | 1.5 |
| BSD-15 | Diff. bond | 1400 | 1033 | ** | — | — | — | ** |
| BSD-12 | Diff. bond | 2000 | 1366 | 32.2 | 222.0 | — | — | 1.5 |
| BSD-18 | Diff. bond | 2000 | 1366 | 32.4 | 223.4 | — | — | 1.5 |
| BSD-19 | Diff. bond | 2000 | 1366 | 32.6 | 224.8 | — | — | 2.0 |

† Strength values based on original uncoated cross-sections.

‡ Extensometer malfunction.

†† Failed at extensometer attachment point.

* Failed out of gage section.

** Failed in grip.

Table 4-19. 1400°F (1033°K) and 2000°F (1366°K) Tensile Test Data — Unexposed C-129Y/R-512E

| Specimen No. | Specimen Type | Test Temperature | | $F_{TU}$† | | $F_{TY}$† | | Elongation (%) |
|---|---|---|---|---|---|---|---|---|
| | | °F | (°K) | ksi | ($MN/m^2$) | ksi | ($MN/m^2$) | |
| YSP-7 | Parent | 1400 | 1033 | 35.2 | 242.7 | 34.9 | 240.6 | 1.0 |
| YSP-8 | Parent | 1400 | 1033 | 34.7 | 239.3 | 34.3 | 236.5 | 2.5 |
| YSP-11 | Parent | 1400 | 1033 | 34.4 | 237.2 | 33.7 | 232.4 | 1.5‡ |
| YSP-9 | Parent | 2000 | 1366 | ** | — | 33.0 | 227.5 | ** |
| YSP-12 | Parent | 2000 | 1366 | 36.7 | 253.0 | 34.1 | 235.1 | 2.0 |
| YSP-19 | Parent | 2000 | 1366 | 36.6 | 252.4 | 32.2 | 222.0 | 2.0 |
| YSE-7 | EB weld | 1400 | 1033 | 35.2 | 242.7 | 35.2 | 242.7 | 1.0 |
| YSE-8 | EB weld | 1400 | 1033 | 36.3 | 250.3 | 36.3 | 250.3 | 1.5* |
| YSE-9 | EB weld | 1400 | 1033 | 36.6 | 252.4 | 35.4 | 244.1 | 2.0‡ |
| YSE-10 | EB weld | 2000 | 1366 | ** | — | ** | — | ** |
| YSE-11 | EB weld | 2000 | 1366 | 39.4 | 271.7 | 35.7 | 246.2 | 3.0 |
| YSE-12 | EB weld | 2000 | 1366 | 38.1 | 262.7 | 35.6 | 245.5 | 2.0 |
| YSD-13 | Diff. bond | 1400 | 1033 | 35.2 | 242.7 | — | — | 1.0 |
| YSD-14 | Diff. bond | 1400 | 1033 | 35.3 | 243.4 | — | — | 1.5* |
| YSD-15 | Diff. bond | 1400 | 1033 | 34.3 | 236.5 | — | — | 1.0 |
| YSD-16 | Diff. bond | 2000 | 1366 | 38.6 | 273.0 | — | — | 2.0 |
| YSD-17 | Diff. bond | 2000 | 1366 | 34.0 | 234.4 | — | — | 1.5 |
| YSD-20 | Diff. bond | 2000 | 1366 | 32.2 | 222.0 | — | — | 2.0 |

† Strength values based on original uncoated cross-sections.

‡ Failed at extensometer attachment point.

* Failed out of gage section.

** Failed in grip.

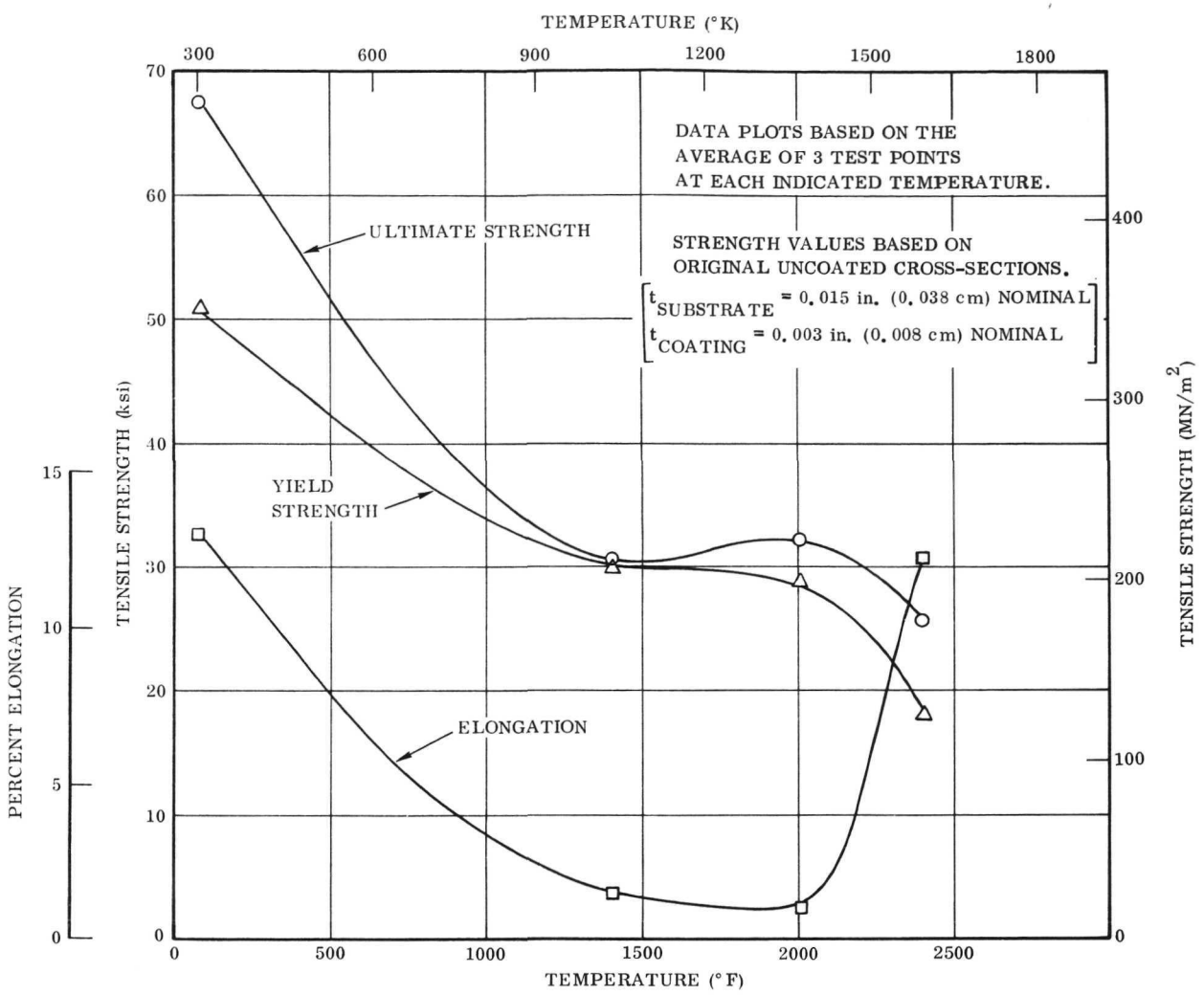


Figure 4-155. Tensile Properties of Cb-752/R-512E

change in strength with temperature is greater at 2400° F (1589° K) than at the intermediate temperatures (see Figures 4-155 and 4-156). This would tend to concentrate the bend deformation to a smaller region and in turn increase the stress concentration. An effect of this nature may account for the bond edge failure locations at the higher temperature.

4.4.3.3 Plasma arc exposure: Twelve specimens were submitted to plasma arc exposure for an intended 40 cycles. Of these, eight survived 40 cycles, two were removed after 30 cycles, and two failed during test. The 10 unfailed specimens were tensile tested at room temperature, and the results are listed in Table 4-20. Six of the specimens suffered severe coating failure and substrate attack during the plasma arc exposures. As would be expected, these samples failed prematurely during tensile

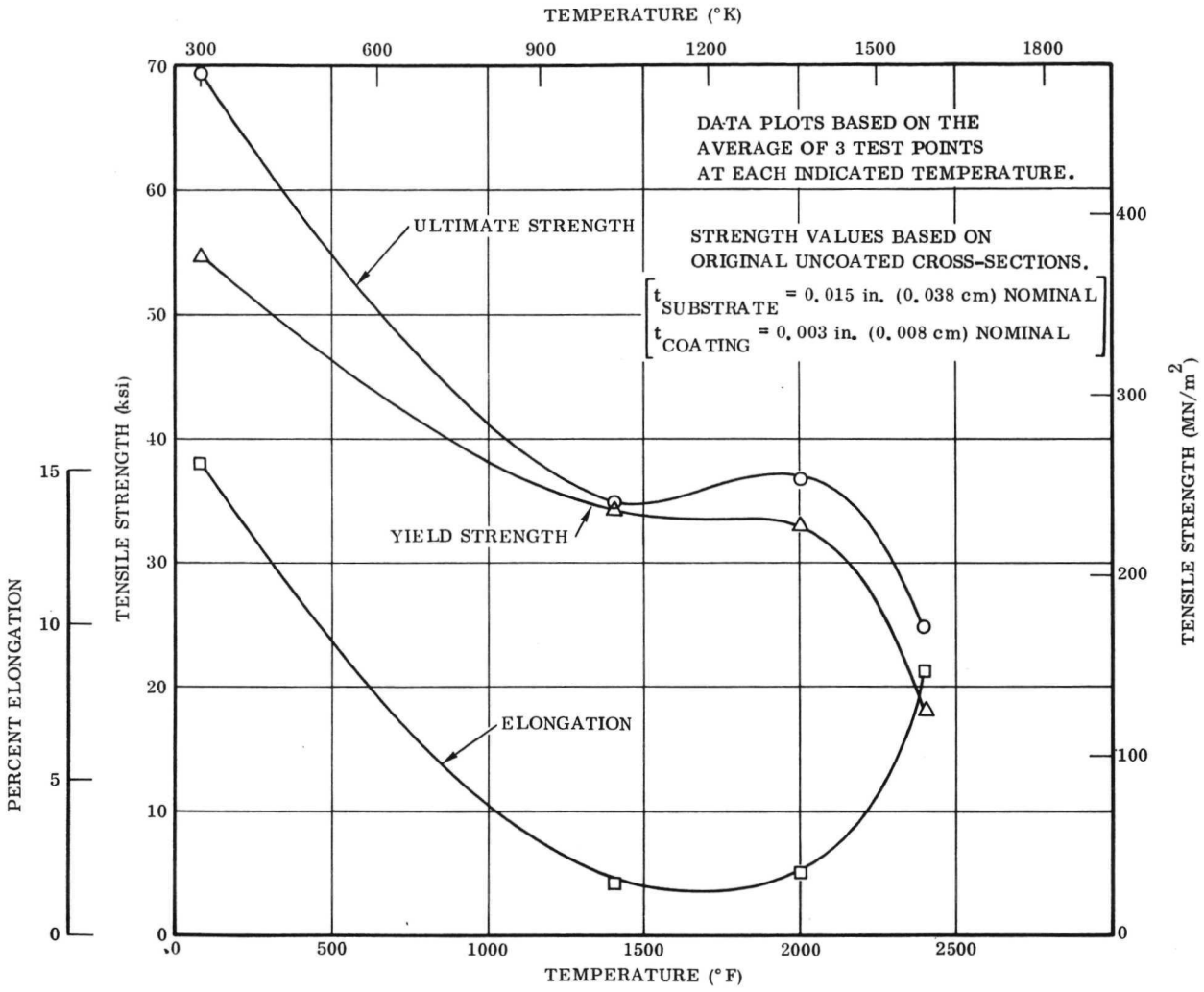


Figure 4-156. Tensile Properties of C-129Y/R-512E

testing with almost no elongation. The three R-512E coated specimens that survived the 40 plasma arc exposure cycles without visible coating failure showed almost no degradation in tensile and yield strengths and retained good elongation. The one surviving VH-109 coated specimen suffered a 25 percent decrease in strength and failed with no measurable elongation.

With the R-152E coating, the two alloys gave very nearly equal results. One-half of the Cb-752 and one-half of the C-129Y specimens survived the 40 plasma arc simulation cycles with no visible coating failure. While the R-512E coating again appears superior to the VH-109 coating, the limited number of specimens prevents a choice between the Cb-752 or C-129Y alloys.

Table 4-20. Room Temperature Tensile Test Data — Plasma Arc Specimens

| Specimen No. | Specimen Type | Exposure Cycles | $F_{TU}$† | | $F_{TY}$† | | Elongation (%) | E† | | Remarks |
|---|---|---|---|---|---|---|---|---|---|---|
| | | | ksi | ($MN/m^2$) | ksi | ($MN/m^2$) | | psi x $10^6$ | ($GN/m^2$) | |
| YSP-16 | Parent | 40 | 68.6 | 473.0 | 55.7 | 384.1 | 13.5 | 14.1 | 97.2 | No attack |
| YSP-13 | Parent | 40 | 43.1 | 297.2 | 42.6 | 293.7 | 1.0 | 13.7 | 94.5 | Edge attack (14%) |
| YSE-6 | EB weld | 40 | 74.6 | 514.4 | 60.4 | 416.5 | 13.0 | 14.0 | 96.5 | No attack |
| YSE-5 | EB weld | 30 | 31.9 | 220.0 | 29.2 | 201.3 | 1.5 | 12.7 | 87.6 | Edge attack (46%) |
| BSP-16 | Parent | 40 | 63.1 | 435.1 | 49.4 | 340.6 | 13.5* | 15.4 | 106.2 | No attack |
| BSP-20 | Parent | 40 | 39.5 | 272.4 | 39.0 | 268.9 | 1.0 | 15.5 | 106.9 | Edge attack (18%) |
| YVP-16 | Parent | 30 | 28.5 | 196.5 | 26.6 | 183.4 | 1.0 | 10.9 | 75.2 | Edge attack (50%) |
| YVP-20 | Parent | 26 | — | — | — | — | — | — | — | Failed 26 cycle |
| YVE-9 | EB weld | 40 | 61.2 | 422.0 | 61.2 | 422.0 | 0* | 18.2 | 125.5 | No attack |
| YVE-1 | EB weld | 40 | 35.5 | 244.8 | ** | — | 0 | ** | — | Edge attack (28%) |
| BVP-1 | Parent | 8 | — | — | — | — | — | — | — | Failed 8 cycle |
| BVP-2 | Parent | 40 | 23.2 | 160.0 | ** | — | 0 | 12.4 | 85.5 | Edge attack (24%) |

† Values based on original uncoated cross-sections.

* Failed out of gage section.

** Failed before yield.

Coating failures that occurred during plasma arc exposure generally initiated at an edge and were followed by gradual erosion of the substrate. The percentage of the specimen width that was consumed by oxidation is listed in Table 4-20 in the Remarks column. For the 0.5 inch (1.27 cm) specimens used in this program, the material lost varied from 0.07 to 0.25 inch (0.02 to 0.64 cm) across the width.

## 4.5 Static Creep Testing

Creep data spanning the time period and elevated-temperature range expected during Space Shuttle vehicle performance are required for design evaluation of the coated columbium alloy TPS. The principal candidate columbium alloy/coating systems in the Phase I studies were: C-129Y/R-512E, Cb-752/R-512E, C-129Y/VH-109, and Cb-752/VH-109. Investigation disclosed that suitable creep data for these material systems were not available. A static creep test program was undertaken to determine the creep properties of the most promising material systems. Creep tests were conducted for C-129Y/R-512E and Cb-752/R-512E systems at temperatures from 2000° F (1366° K) to 2400° F (1589° K).

4.5.1 Test plan. — Three temperatures and three stress levels were selected for the creep tests as defined in Table 4-21. The same stress levels were specified for both material systems since the two columbium alloy substrates have similar strength properties in the uncoated condition, and the coating was not expected to have a major effect on elevated-temperature strength. Selection of the stress levels was based on available creep data for uncoated columbium alloys with appropriate allowance for base metal consumed during coating application. The target was to provide stress levels covering the range of 10 to 100 hours for one percent creep. The stress levels were calculated on the basis of the original metal thickness prior to coating. However, provision was also made to determine and express the stress levels on the basis of substrate thickness remaining after coating.

4.5.2 Test equipment. — The creep tests were conducted with a 20,000-lb (9080 kg) capacity Arcweld Creep Machine, Model EE, and an Astro Model 1000T high temperature furnace. The creep test facility is shown in Figure 4-157. The Astro furnace is radiant heated with graphite heating elements that operate in an argon atmosphere and are protected from the test atmosphere by a ceramic muffle tube. The muffle tube material is alumina, and the maximum operating temperature of the furnace with the alumina tube is 3362° F (2123° K). The furnace is equiped with four viewing ports for optical measurements. The muffle tube contains four holes that are aligned with the four sight ports. A continuous protective argon flow is maintained around the graphite element, and the gas exhausts through the holes in the muffle tube and out the top of the

Table 4-21. Test Plan for Creep Tests of C-129Y/R-512E and Cb-752/R-512E Coated Columbium Alloys

| Test Temperature °F (°K) | Stress Levels | | |
|---|---|---|---|
| | $S_1$ psi ($MN/m^2$) | $S_2$ psi ($MN/m^2$) | $S_3$ psi ($MN/m^2$) |
| 2000 (1366) | 8,500 (58.7) | 10,000 (69.0) | 12,500 (86.2) |
| 2200 (1478) | 3,000 (20.7) | 4,000 (27.6) | 5,000 (34.5) |
| 2400 (1589) | 1,000 ( 6.9) | 1,500 (10.3) | 2,000 (13.8) |

Duplicate specimens for each test condition
Duration of test — 100 hours or 2% creep
Stress levels based on original metal thickness prior to coating
Nominal sheet thickness — 0.015 inch (0.381 mm)
Nominal coating thickness — 0.003 inch (0.076 mm)

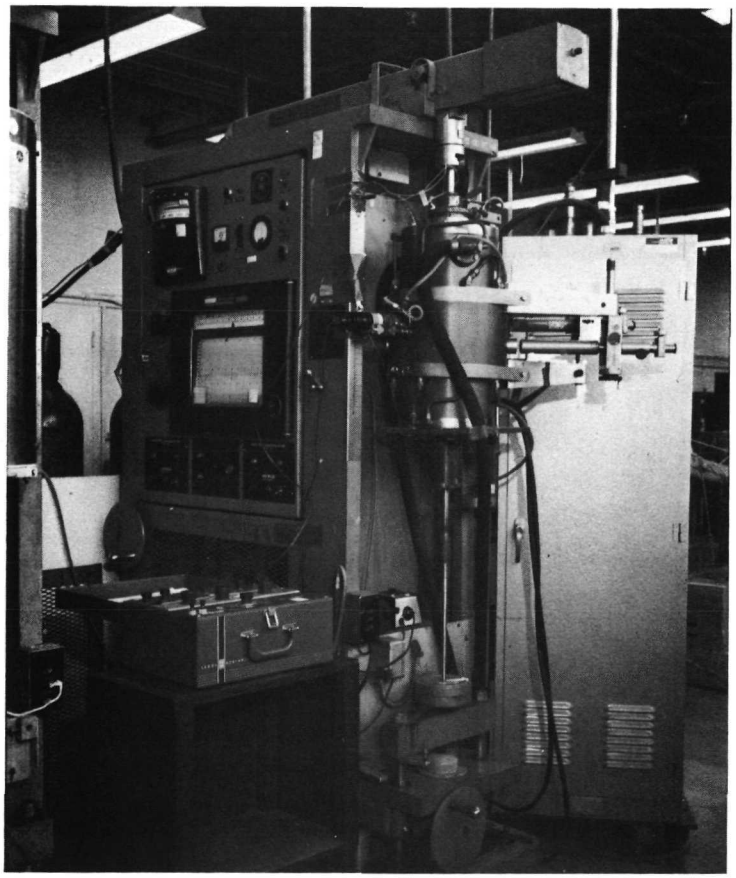

Figure 4-157. Creep Test Facility — Astro Furnace and Arcweld Creep Test Machine (Photo 119963B)

furnace. Openings are provided at the top and bottom of the furnace for the pull rods. The muffle tube is open to the atmosphere from the clearance gap around the pull rods.

Temperature control for the furnace is provided by a Honeywell controller-recorder using a molybdenum sheathed W-5 percent Re/W-26 percent Re thermocouple. The thermocouple is inserted through the heating element so that it is in contact with the outside of the muffle tube. The test temperature is measured with a Pt/Pt-13 percent Rh thermocouple tied to the gage section of the test specimen with Irish Refrasil cord. A sheath of Irish Refrasil cloth is used to prevent reaction between the thermocouple and the coated specimen.

Strain measurement is made with an optical method using markers either attached to or machined into the test specimens. The optical equipment consists of two Gaertner filar micrometer 50X magnification microscopes mounted on the Astro furnace to sight through two of the viewing ports. Illumination of the markers is provided by lamps at the two opposite viewing ports.

Calibration and certification was performed for the creep machine, loading weights, micrometer microscopes, and temperature controller-recorder. The creep machine loading system was calibrated with load cells. It was found necessary to prepare a calibration curve and make a correction for loads under 200 pounds (90.8 kg). The micrometer microscopes were calibrated with a stage micrometer. The microscopes can be read to an accuracy of one division, which is equal to 0.00002 inches (5.08 μm).

4.5.3 Test procedures. —

4.5.3.1 Specimen preparation: The configuration of the creep specimen is shown in Figure 4-2. The specimen is quite long; consequently, the grip ends are well out of the hot zone and gripping problems are minimized. Previous work (Reference 33) with this type of specimen (with integral tabs) has indicated a tendency toward low values of ultimate strength and total elongation in a room temperature test. The yield strength, however, was not affected. As the creep tests involve low values of strain (creep design data is normally less than two percent), the notch effect of the tabs is not believed to be significant.

The specimens were vibratory finished to provide edge and corner radii necessary to achieve good coating reliability. The nominal thickness of the columbium alloy sheet material was 0.015 inch (0.381 mm), and the nominal coating thickness specified to the coating suppliers was 3.0 mils (0.076 mm).

4.5.3.2 Strain measurement: The major difficulty encountered in creep testing of coated columbium alloy specimens is the measurement of strain. The optical technique was selected for this program to minimize the difficulty in accurate measurement of

creep (strain versus time). The preliminary creep tests conducted with the integral tab specimen disclosed an unanticipated problem with alignment in the Astro furnace. The view ports are located to sight directly through the center of the furnace. Vertically the two sets of viewing ports are two inches (5.09 cm) apart, but are located radially 20° apart to provide clearance between the two microscopes. The combination of offset tabs and microscope angle prevented good illumination of the tabs even with the specimen rotated. The result was poor accuracy in measurement of the movement of the tabs. In retrospect, the difficulty could have been avoided by bending the tabs to an angle of 60 to 90° from the plane of the specimen. However, bending of the tabs had to be accomplished prior to coating application to prevent damage to the coating. Since the creep specimens were already coated, another solution had to be found for specimen alignment. The problem was solved with the use of iridium wire markers cemented to the tabs as shown in Figure 4-158. The iridium markers were made from 0.020-inch (0.508 mm) wire formed to make an angle with 0.2 inch (5.08 mm) long legs. The iridium markers were bonded to the specimen with a refractory cement composed of molybdenum disilicide and colloidal silica. The cement was air dried and then fired for one-half hour at 1850°F (1283°K) in argon.

Strain measurement with the iridium markers gave more accurate and reliable results. It was found easier to make the readings from the bottom edge of the wire markers because deposited material gradually built up on the top of the wire.

No failures of the cemented markers occurred during the creep tests. However, occasionally the cemented markers would spall from the coating surface after completion of the test. This took place simultaneously with the spalling of an oxide layer from the specimen surface during the rapid cooling after removal from the furnace.

The optical readings were generally taken at intervals of 15 to 30 minutes for the first several hours, after which readings were taken at intervals of one to three hours. Some longer intervals between readings occurred at night and when the tests were continued over a weekend.

The total strain for each specimen was also determined by measurement of the wire markers and both sets of integral tabs with a cathotometer before and after the creep test. These measurements were used to verify the strain measurements made during the test.

4.5.3.3 Load application: The Arcweld Creep Machine features a 20 to 1 ratio loading arm with automatic leveling of the loading arm. The automatic leveling maintains the specimen centered in the hot zone of the furnace. The accuracy of load application for the 20,000-lb (9,080 kg) capacity machine was found to be reduced for very small loads. Significant load variations also were introduced with small loads

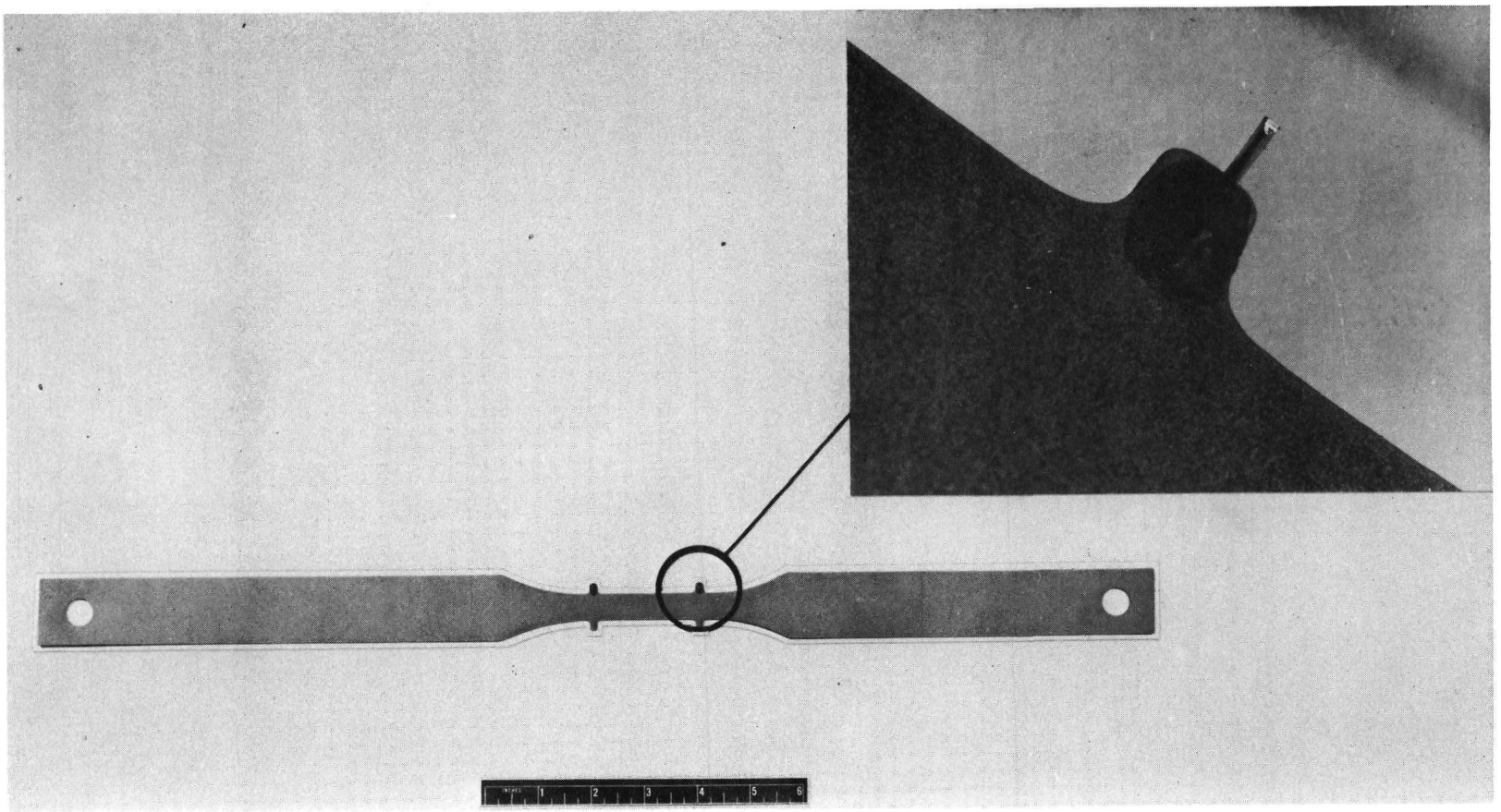

Figure 4-158. Coated Columbium Creep Test Specimen (Photo 05950M)

during automatic leveling of the loading arm. One of the changes in test procedures found necessary was the adoption of dead weight loading for creep tests conducted at loads of less than 50 pounds (22.7 kg). For the nominal 0.5-inch (12.7 mm) by 0.015-inch (0.38 mm) gage section, a 50 pound (22.7 kb) load applies a stress of approximately 8 ksi (55.2 $MN/m^2$). Therefore, all creep tests at 2200° F (1478° K) and 2400° F (1589°K) were conducted using the dead weight loading technique, and the 2000° F (1366° K) tests were conducted using the automatic leveling. The sequence of starting the test was to apply a small load to the specimen initially while the temperature was being stabilized and the microscopes were being aligned. Then the full load was applied and strain measurements were begun immediately. The elapsed time between the initial small load application and the full load application was approximately one-half hour for most tests. In a few cases, the elapsed time was as much as one hour to achieve proper alignment and temperature stabilization. The difference in measurements between initial and full load is due to elastic strain, and this was not included in strain measurements reported.

4.5.3.4 Furnace atmosphere: The tests were conducted in an atmosphere that was essentially argon with a slight contamination of air. A flow rate of 3 cfph (0.085 $m^3/hr$) of argon was introduced through the graphite element chamber into the muffle tube. This flow rate is equivalent to 72 volume changes per hour under standard conditions for the 2.25 inch (5.72 cm) i.d., by 19.38 inch (49.21 cm) long alumina muffle tube. Clearance for the pull rods at the bottom of the furnace permitted some leakage of air into the muffle tube as evidenced by specimen surface oxidation and some coating failures. The composition of the furnace atmosphere was checked several times by gas analysis. During creep tests at 2400° F (1589°K), the furnace atmosphere was found to contain 0.2 percent $O_2$ and 0.8 percent $N_2$ indicating a mixture of approximately 1 percent air and 99 percent argon. For a 2000° F (1366° K) creep test, the furnace atmosphere was found to contain 0.15 percent $O_2$ and 0.58 percent $N_2$. The higher temperature would tend to increase the chimney effect in the muffle tube, which may account for a greater amount of air leakage into the furnace atmosphere at 2400° F (1489° K).

The Astro furnace has provisions for sealing around the pull rods using Viton O-rings, thus enabling testing in oxidizing, inert, or reducing atmospheres. Creep testing of coated columbium alloys for 100 hours in a severely oxidizing atmosphere generally would not be desirable due to the high probability of coating and specimen failures.

Prior to selection of the slightly oxidizing atmosphere for the creep test program, several preliminary tests were made with a more severely oxidizing environment. A bottled gas mixture, consisting of 2.4 percent oxygen and the balance argon, was introduced at a controlled flow rate into the muffle tube at the bottom of the furnace. Two detrimental effects were observed, which made use of this severely oxidizing atmosphere unsuitable for measurement of long-time creep. First, coating edge

failures were encountered, which resulted in severe substrate contamination and embrittlement. Secondly, the flowing oxygen-argon mixture penetrated into the heating element chamber and caused severe oxidation of the graphite elements with a resultant short service life.

4.5.3.5 Thickness measurements: Thickness measurements of the coated columbium alloy creep specimens were made by three methods: micrometer, eddy current, and metallographic cross-section. The gage section of each specimen was measured before and after coating using a micrometer with flat anvils. These measurements provided part growth due to formation of the coating. The relationship of part growth to coating thickness and substrate consumption was established by metallographic examination, and the part growth data was converted to coating thickness and remaining substrate thickness for each specimen. These results provided information to convert the creep stress level based on original metal thickness prior to coating to the stress level based on remaining substrate after coating.

Information was also desired on the uniformity of the coating for both sides as well as for the gage section and grip ends. The Dermitron eddy current instrument with the C-probe was used for these measurements. Initial calibration of the Dermitron instrument was accomplished with one to six layers of 0.001-inch (0.0254 mm) thick Mylar film placed on bare columbium alloy. Metallographic measurements of coating thickness were subsequently used to prepare calibration curves for each substrate/coating material system. The latter calibration curves were used to convert Dermitron readings to coating thickness.

Dermitron readings were made on three locations in the gage section and two locations on the grip (one at each end) for both sides, giving a total of 10 Dermitron readings for each creep specimen. The average reading in the center of the gage section was used to determine the coating thickness for comparison to the thickness measurements made with a micrometer.

4.5.4 Test results and discussion. —

4.5.4.1 C-129Y/R-512E creep data: Results of creep testing of C-129Y/R-512E system at 2000°F (1366°K), 2200°F (1478°K), and 2400°F (1589°K) are presented in Table 4-22. Data are reported for 23 creep specimens.

Creep curves are presented in Figures 4-159 and 4-160 for 2000°F (1366°K), in Figures 4-161 and 4-162 for 2200°F (1478°K), and in Figures 4-163 and 4-164 for 2400°F (1589°K). The 2000°F (1366°K) and 2200°F (1478°K) curves show essentially linear creep with the exception of a small amount of primary creep exhibited by some of the specimens. The 2400°F (1589°K) curves show two types of creep behavior. The

Table 4-22. Summary of Creep Test Results for C-129Y/R-512E

| Specimen No. | Test Temperature °F | Test Temperature (°K) | Stress ksi† | Stress ($MN/m^2$) | Hours to Creep (0.5%) | Hours to Creep (1.0%) | Hours to Creep (2.0%) | Creep Rate (% per hr‡) | Total Test Time (hr) | Total Creep (%) Optical Extensometer | Total Creep (%) Before/After Measurement |
|---|---|---|---|---|---|---|---|---|---|---|---|
| YSC-19 | 2400 | 1589 | 1.0 | 6.9 | 20.5 | 40.5 | 81* | 0.025 | 74 | 1.82 | 2.0 |
| YSC-23 | 2400 | 1589 | 1.0 | 6.9 | 19.0 | 36.5 | 73 | 0.027 | 69 | 1.88 | 1.8 |
| YSC-18 | 2400 | 1589 | 1.5 | 10.3 | 13.5 | 27.0 | 54* | 0.036 | 85 | 2.06 | 2.3 |
| YSC-13 | 2400 | 1589 | 1.5 | 10.3 | 9.5 | 19.0 | 38* | 0.053 | 55 | 2.38 | 2.5 |
| YSC-8 | 2400 | 1589 | 1.5 | 10.3 | 8.5 | 20.0 | 68.5 | 0.050 | 69 | 2.01 | 2.0 |
| YSC-17 | 2400 | 1589 | 2.0 | 13.8 | 5.8 | 12.5 | 25* | 0.080 | 45 | 2.65 | 2.9 |
| YSC-12 | 2400 | 1589 | 2.0 | 13.8 | 7.5 | 15.0 | 30 | 0.067 | 41 | 2.75 | 2.7 |
| YSC-7 | 2200 | 1478 | 3.0 | 20.7 | ** | - | - | - | 70 | ** | 1.4 |
| YSC-2 | 2200 | 1478 | 3.0 | 20.7 | 26 | 45 | 83* | 0.022 | 80 | 1.92 | 2.0 |
| YSC-25 | 2200 | 1478 | 3.0 | 20.7 | 29 | 61 | 127 | 0.016 | 97 | 1.51 | 1.3 |
| YSC-15 | 2200 | 1478 | 3.0 | 20.7 | 26 | 51.5 | 103 | 0.019 | 118 | 2.12 | 2.1 |
| YSC-21 | 2200 | 1478 | 4.0 | 27.6 | 20 | 43.5 | 90* | 0.023 | 71 | 1.55 | 1.7 |
| YSC-20 | 2200 | 1478 | 4.0 | 27.6 | 24 | 48 | 96 | 0.022 | 97 | 2.00 | 2.1 |
| YSC-30 | 2200 | 1478 | 5.0 | 34.5 | 12.2 | 24.4 | 48.6 | 0.041 | 65 | 2.67 | 2.6 |
| YSC-16 | 2200 | 1478 | 5.0 | 34.5 | 14 | 28.5 | 54 | 0.035 | 72 | 2.75 | 3.1 |
| YSC-24 | 2000 | 1366 | 8.5 | 58.6 | >100 | - | - | 0.003 | 102 | 0.30 | 0.6 |
| YSC-9 | 2000 | 1366 | 8.5 | 58.6 | 60 | >100 | - | 0.008 | 118 | 0.98 | 1.1 |
| YSC-27 | 2000 | 1366 | 10.0 | 69 | 40 | 90.5 | >100 | 0.011 | 136 | 1.79 | 1.8 |
| YSC-10 | 2000 | 1366 | 10.0 | 69 | 47.5 | 95 | >100 | 0.011 | 112.5 | 1.26 | 1.2 |
| YSC-14 | 2000 | 1366 | 12.5 | 86.2 | 29 | 56.5 | 105* | 0.018 | 100 | 1.90 | 2.1 |
| YSC-11 | 2000 | 1366 | 12.5 | 86.2 | 27 | 49 | 82.5 | 0.020 | 115.5 | 3.47 | 3.8 |
| YSC-6 | 2000 | 1366 | 15.0 | 103.4 | 9.5 | 18.5 | 33.5 | 0.054 | 55.5 | 4.28 | 4.3 |
| YSC-4 | 2000 | 1366 | 15.0 | 103.4 | 7.5 | 17 | 31.5 | 0.059 | 50.7 | 3.39 | 3.7 |

† Stress based on original metal thickness before coating.

‡ Average creep rate during first 1% creep.

* Extrapolated values.

** Test terminated at 70 hours due to vaporization of iridium marker. No valid readings after 14.5 hours.

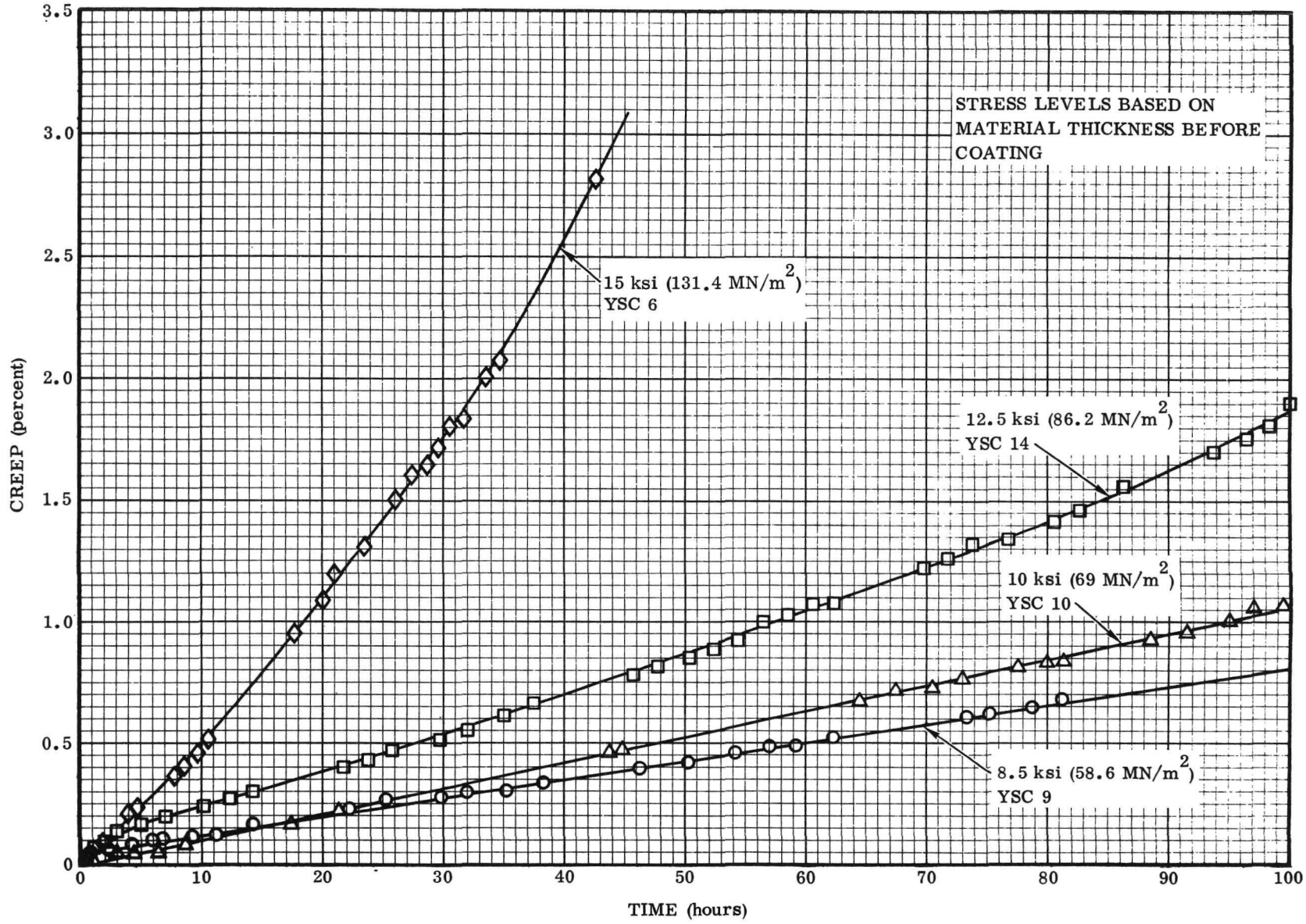


Figure 4-159. Creep Strain for C-129Y/R-512E at 2000° F (1366° K)

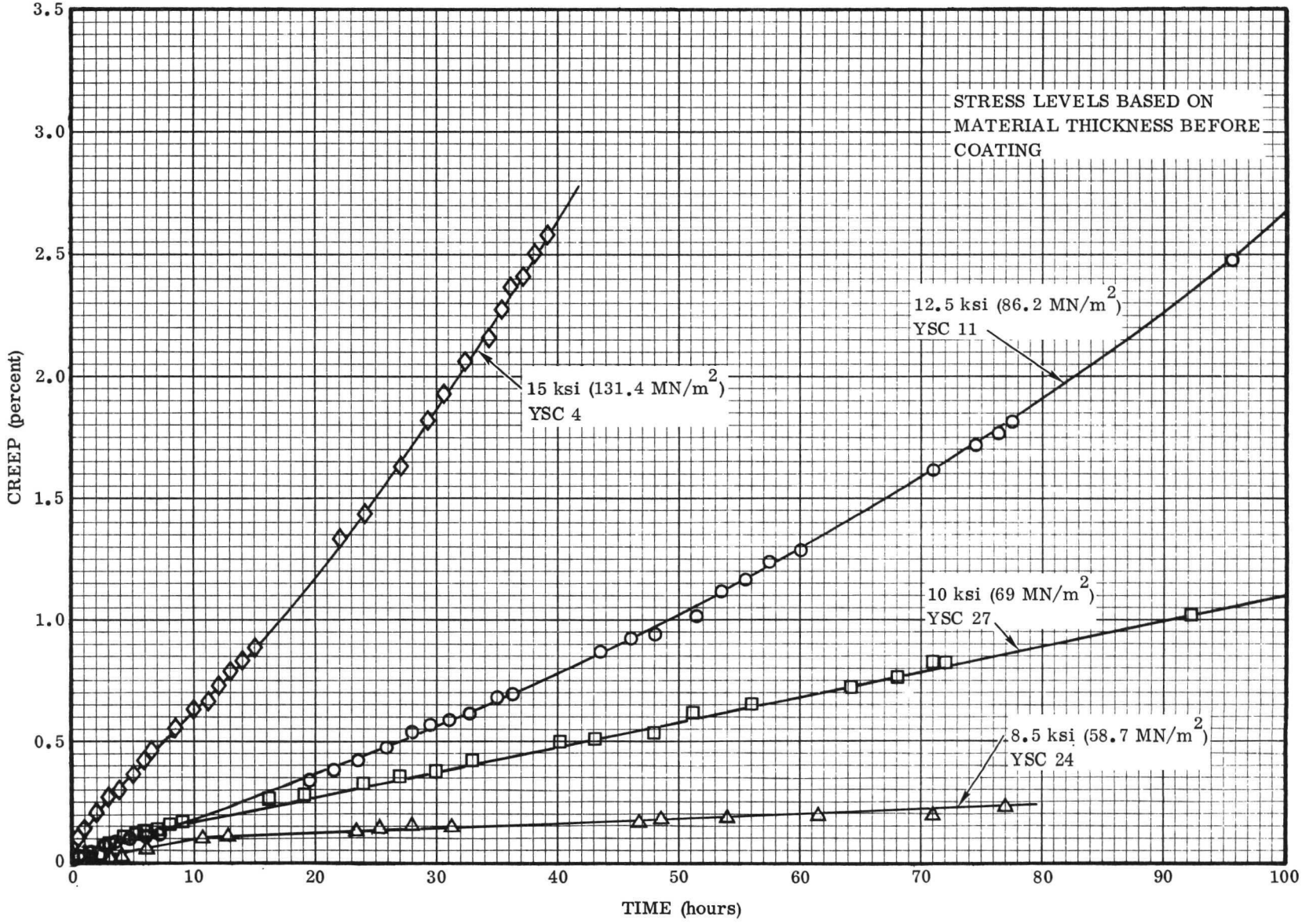


Figure 4-160. Creep Strain for C-129Y/R-512E at 2000° F (1366°K)

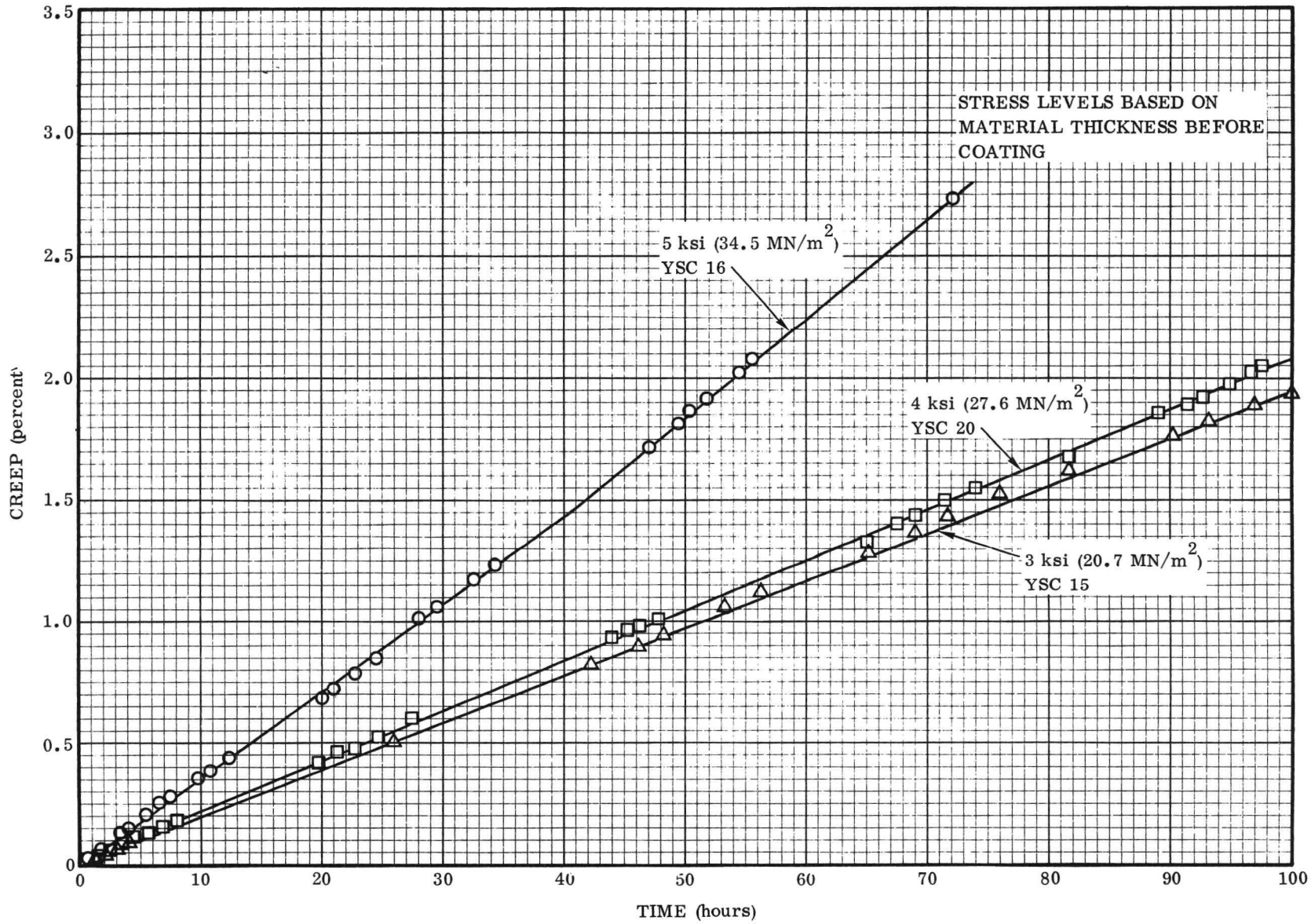


Figure 4-161. Creep Strain for C-129Y/R-512E at 2200° F (1478° K)

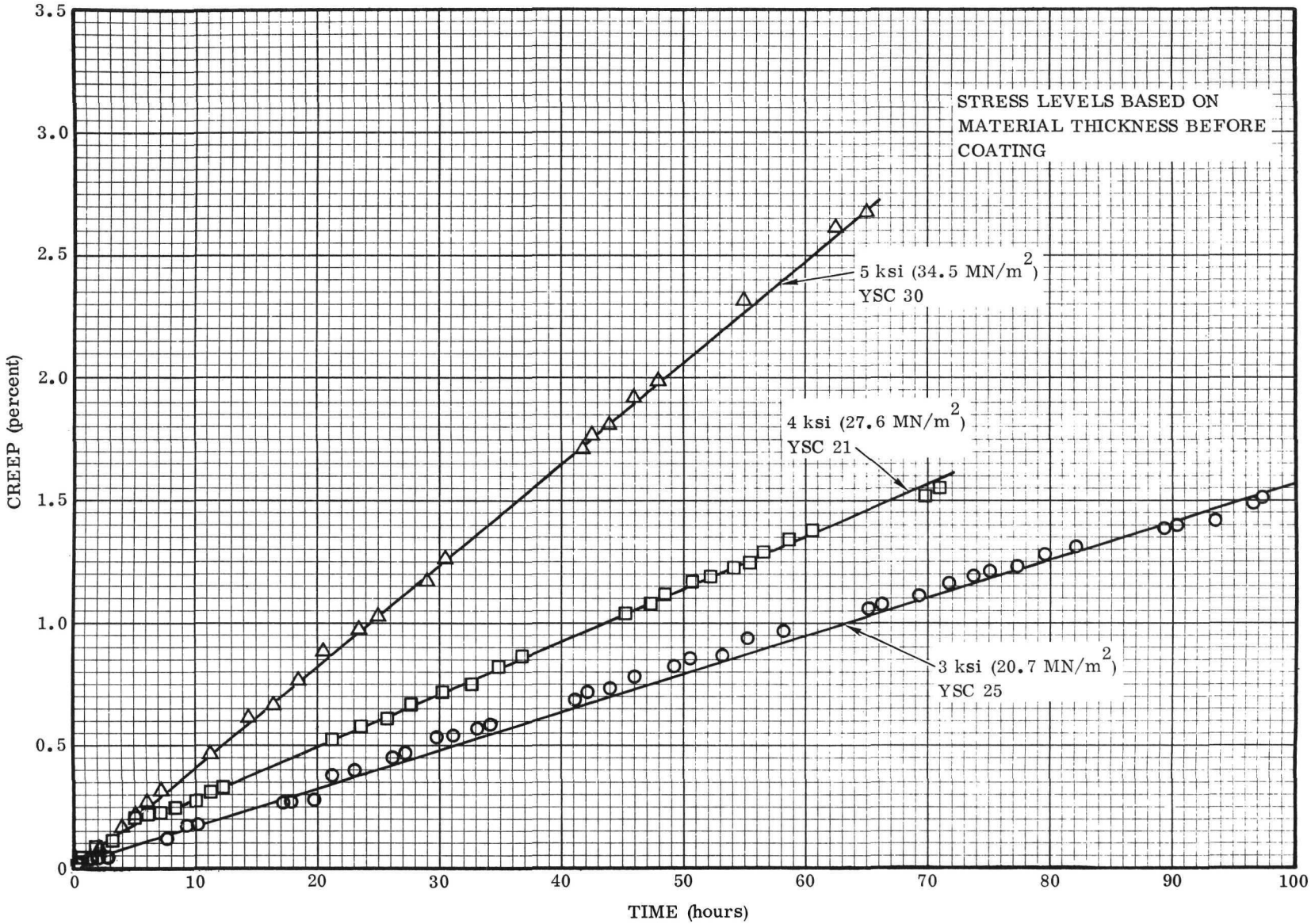


Figure 4-162. Creep Strain for C-129Y/R-512E at 2200°F (1478°K)

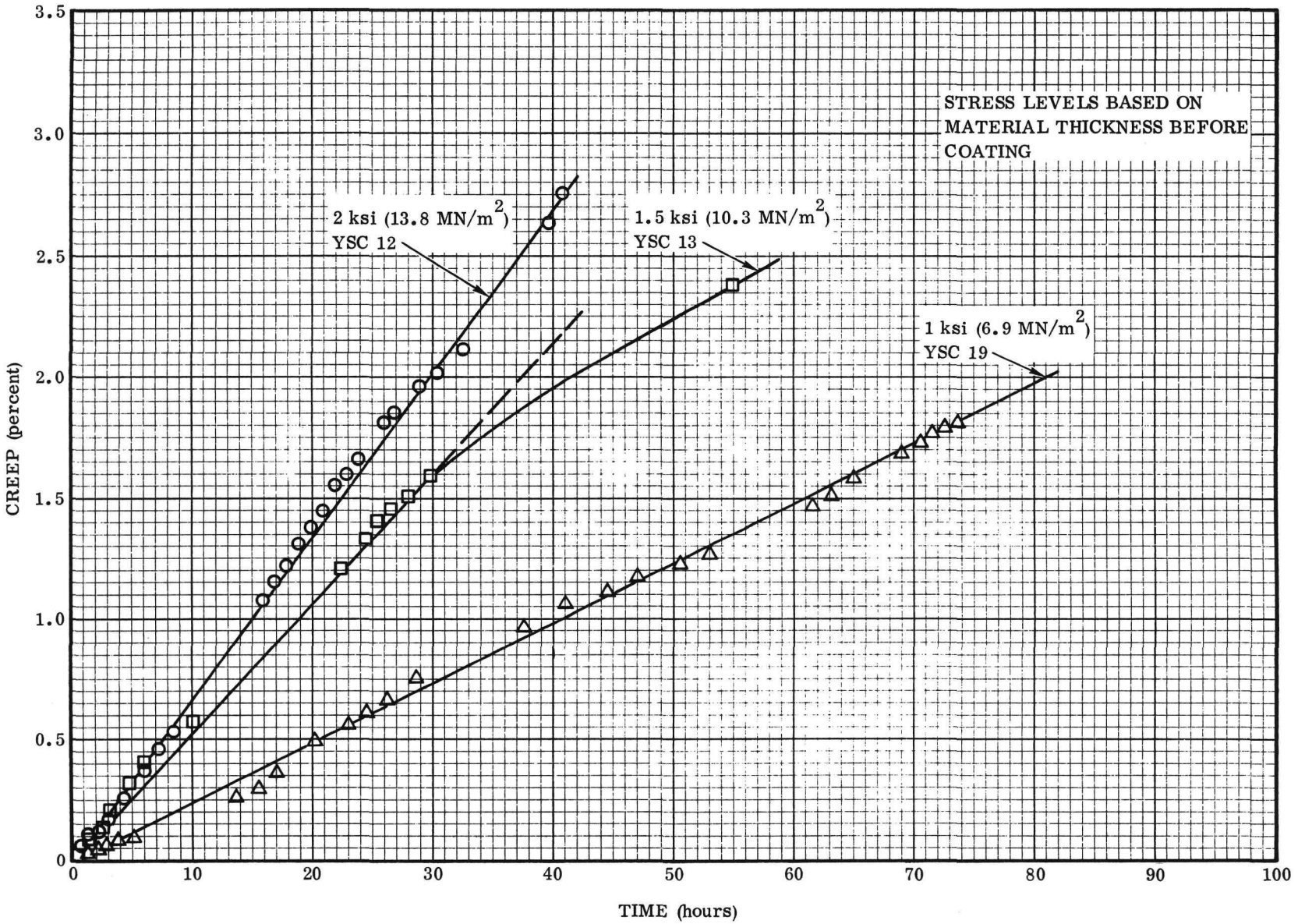


Figure 4-163. Creep Strain for C-129Y/R-512E at 2400° F (1589° K)

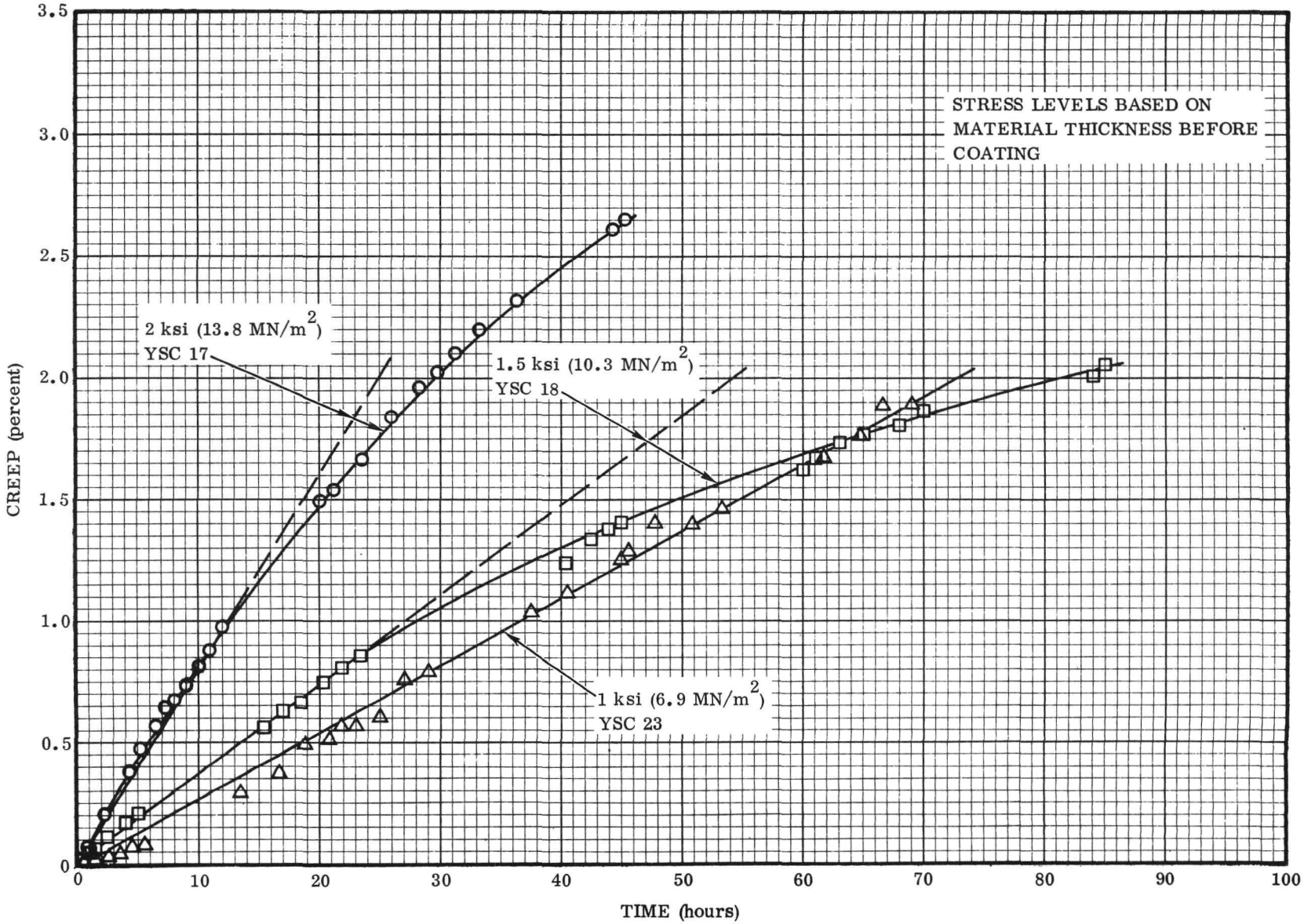


Figure 4-164. Creep Strain for C-129Y/R-512E at 2400°F (1589°K)

specimens show essentially linear creep as illustrated by the 1 ksi (6.9 $MN/m^2$) and 2 ksi (13.8 $MN/m^2$) curves in Figure 4-163. However, about one-third of the specimens tested at 2400° F (1589° K) show linear creep for about the first 30 hours (and at least 1 percent creep) followed by a decreasing creep rate as illustrated by the 1.5 ksi (10.3 $MN/m^2$) curve in Figure 4-163. Investigation of this creep behavior has led to the conclusion that the decreasing creep rate is caused by the strengthening effect of oxygen contamination from localized coating failures at the edges. In some cases, the coating failures are not evident by visual examination — possibly due to the heavy oxide layer that forms on the specimen. This is disucssed in section 4.5.4.4 on results of metallographic examination.

Since it is believed that the decreasing creep rate for the 2400° F (1589° K) tests is the result of coating breakdown, the creep curves exhibiting this behavior have been extrapolated as shown by the dashed line in Figure 4-163 to obtain the two percent creep data.

Average creep data for each temperature and stress level are summarized in Table 4-23. Composite creep curves for 0.5, 1.0, and 2.0 percent creep in C-129Y/R-512E prepared from the data in Table 4-23 are presented in Figure 4-165.

Table 4-23. Average Creep Data for C-129Y/R-512E Coated Columbium Alloy[1]

| Test Temperature | | Stress[2] | Hours to Creep | | | Creep Rate | Recalculated Stress[4] |
|---|---|---|---|---|---|---|---|
| °F | (°K) | ksi ($MN/m^2$) | 0.5% | 1% | 2% | % per hr[3] | ksi ($MN/m^2$) |
| 2400 | (1589) | 1.0 ( 6.9) | 19.8 | 38.5 | 77 | 0.026 | 1.27 ( 8.8) |
| | | 1.5 (10.3) | 10.5 | 22 | 56.8 | 0.048 | 1.90 (13.1) |
| | | 2.0 (13.8) | 6.6 | 13.8 | 27.5 | 0.072 | 2.54 (17.5) |
| 2200 | (1478) | 3.0 (20.7) | 27 | 52.5 | 104.3 | 0.019 | 3.81 (26.3) |
| | | 4.0 (27.6) | 22 | 45.8 | 93 | 0.022 | 5.08 (35.0) |
| | | 5.0 (34.5) | 13.1 | 26.4 | 51.3 | 0.038 | 6.35 (43.8) |
| 2000 | (1366) | 8.5 (58.6) | 80 | >100 | | 0.006 | 10.80 (69.5) |
| | | 10.0 (69 ) | 43.8 | 92.8 | >100 | 0.011 | 12.70 (87.6) |
| | | 12.5 (86.2) | 28 | 52.8 | 93.8 | 0.019 | 15.90 (109.6) |
| | | 15.0 (103.4) | 8.5 | 17.8 | 32.5 | 0.057 | 19.06 (131.4) |

1. Average creep data for two test specimens.
2. Stress based on original metal thickness before coating.
3. Average creep rate during first 1 percent creep.
4. Stress recalculated based on estimated thickness of substrate remaining after coating.

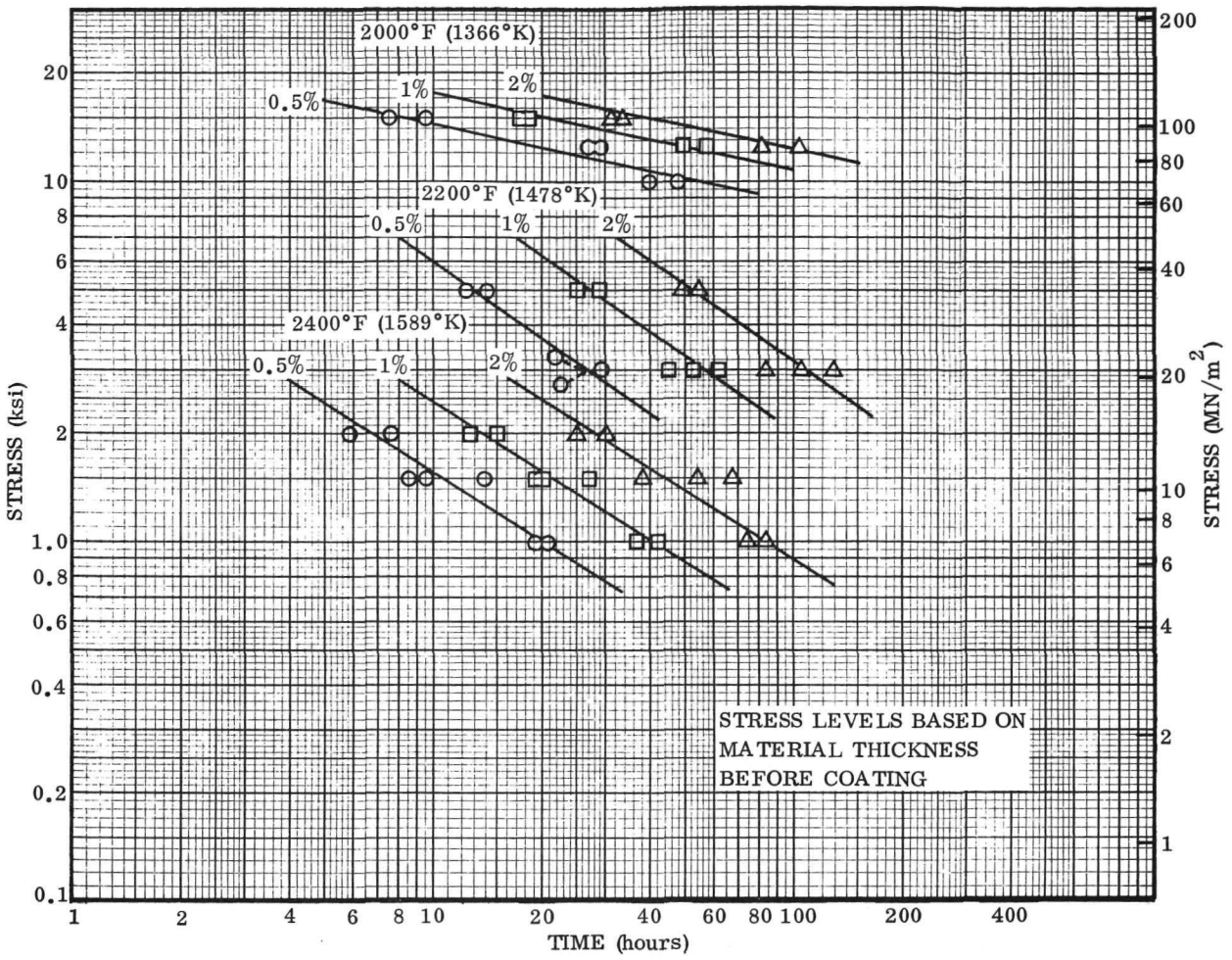


Figure 4-165. Creep Properties of C-129Y/R-512E at 2000° F (1366° K), 2200° F (1478° K), and 2400° F (1589° K)

The C-129Y/R-512E creep specimens are shown in Figure 4-166. Although several of the specimens have coating edge failures in the gage section, these failures have not grown large enough to be readily visible in the photograph. However, coating failures can be observed in the grip area for two specimens (YSC 13 and YSC 22). The larger size of the defects in the grips can be attributed to a thinner, less reliable coating compared to the gage section as discussed in section 4.5.4.3.

Figure 4-167 illustrates the oxide formation and spalling behavior of creep specimens tested at the three different temperatures. At 2000° F (1366° K), the oxide is thin and severe spalling takes place after removal from the furnace. At 2200° F (1478° K), the oxide is moderately thick, but usually only slight spalling occurs. The 2400° F (1589° K) specimen shows heavy oxide and severe spalling of the outer layer of oxide.

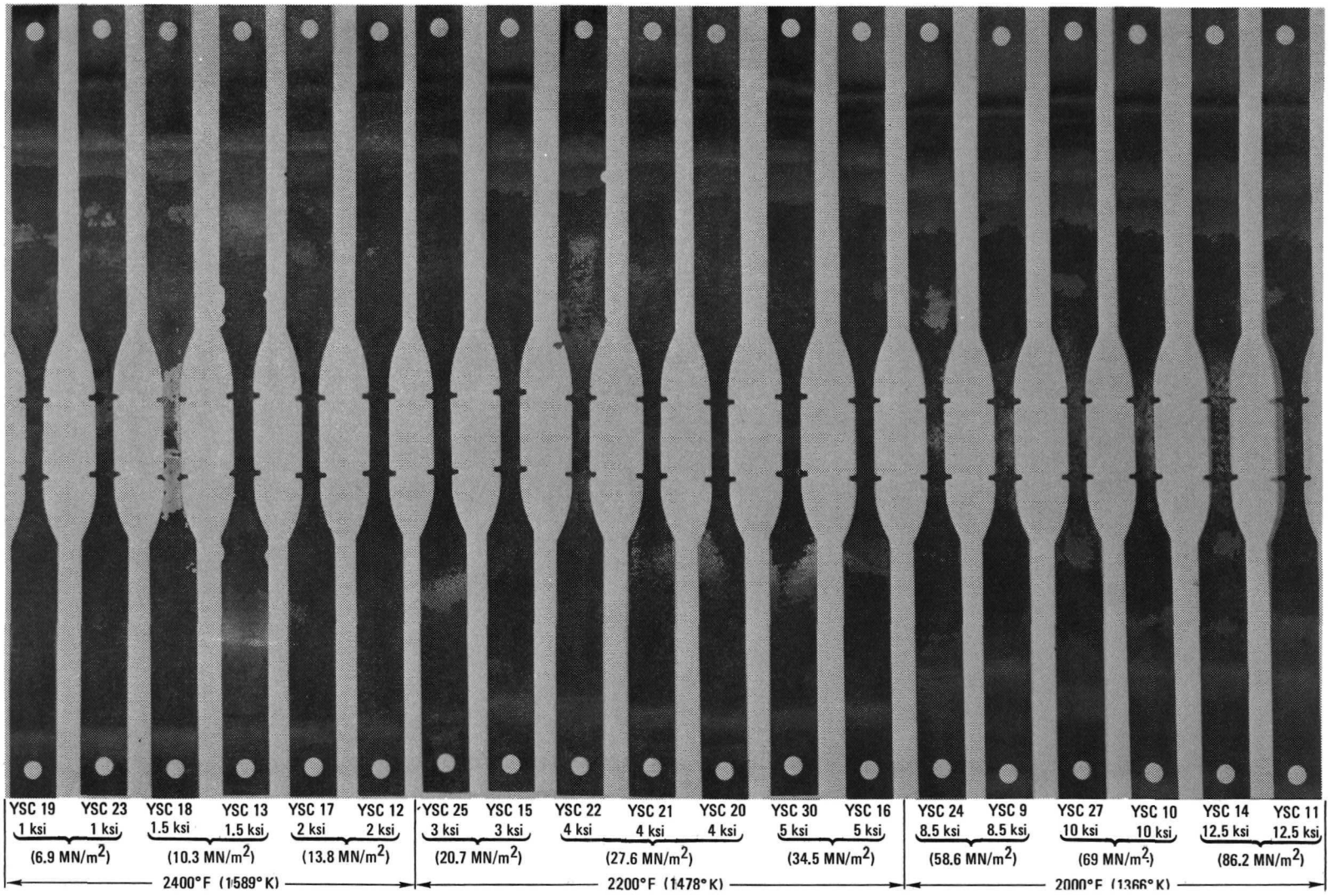


Figure 4-166. C-129Y/R-512E Creep Test Specimens (Photo 118779B)

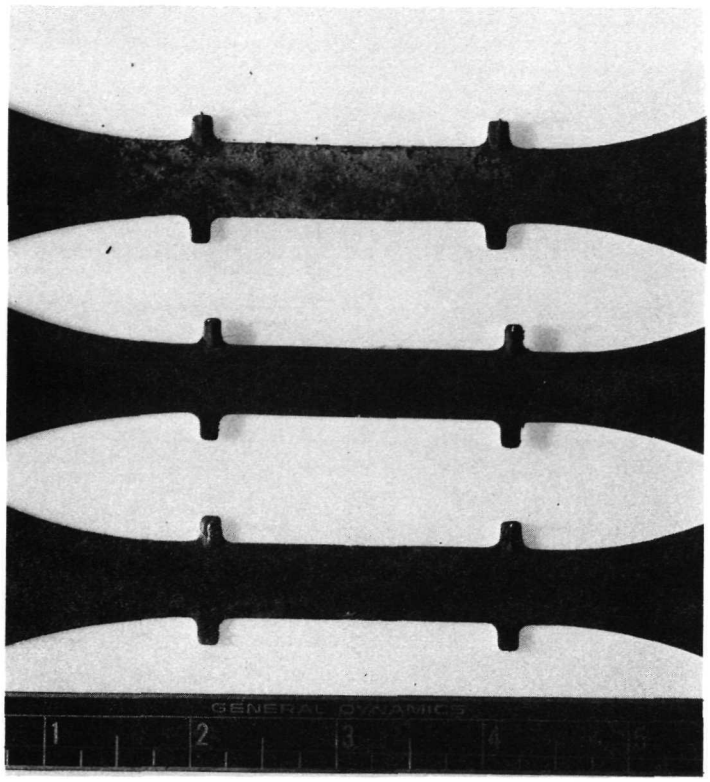


Figure 4-167. Oxide Spalling of C-129Y/R-512E Creep Test Specimens (Photo 118780B)

Comparison of the creep data for C-129Y/R-512E with the limited published data available on coated and uncoated C-129Y alloy is shown in Figure 4-168 for 2000°F (1366°K) and 2200°F (1478°K) (also see References 34 and 35). Suitable data for properties comparison at 2400°F (1589°K) are not available.

4.5.4.2 Cb-752/R-512E creep data: Test results for 22 creep specimens of Cb-752/R-512E tested at 2000°F (1366°K), 2200°F (1478°K), and 2400°F (1589°K) are listed in Table 4-24. The test plan given in Table 4-21 was followed with one exception; a 15 ksi (103.5 $MN/m^2$) stress level at 2000°F (1366°K) was added and the 8.5 ksi (58.7 $MN/m^2$) stress level was deleted. This change was made because the creep resistance of Cb-752/R-512E at 2000°F (1366°K) was somewhat higher than anticipated.

Creep curves are presented in Figures 4-169 and 4-170 for 2000°F (1366°K), in Figures 4-171 and 4-172 for 2200°F (1478°K), and in Figures 4-173 and 4-174 for 2400°F (1589°K). The curves are quite similar to those for C-129Y/R-512E, with

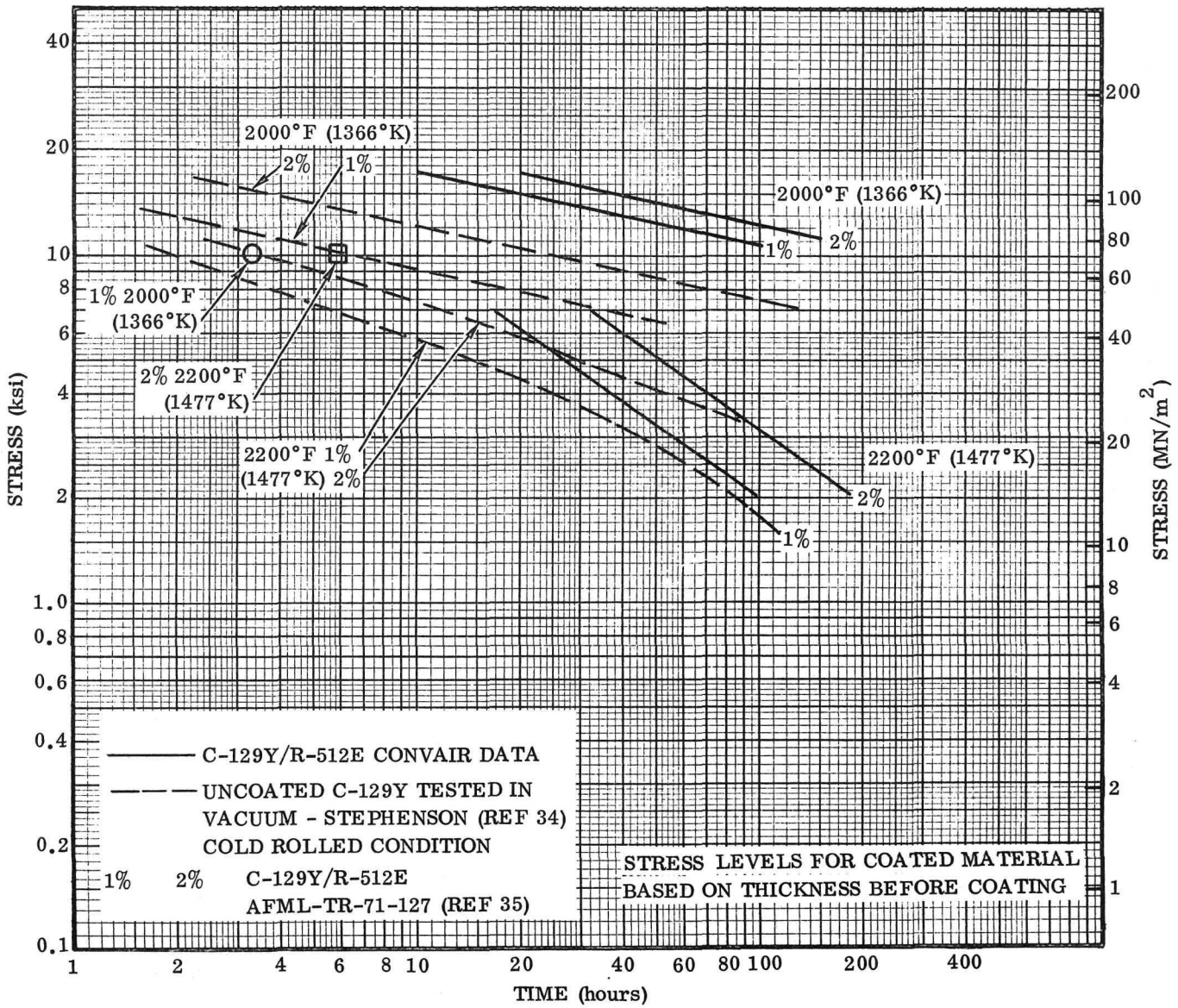


Figure 4-168. Comparison of Creep Properties of C-129Y/R-512E with Coated and Uncoated C-129Y at 2000° F (1366° K) and 2200° F (1478° K)

Table 4-24. Summary of Creep Test Results for Cb-752/R-512E

| Specimen No. | Test Temperature °F | Test Temperature (°K) | Stress ksi† | Stress ($MN/m^2$) | Hours to Creep (0.5%) | Hours to Creep (1.0%) | Hours to Creep (2.0%) | Creep Rate (% per hr‡) | Total Test Time (hr) | Total Creep (%) Optical Extensometer | Total Creep (%) Before/After Measurement |
|---|---|---|---|---|---|---|---|---|---|---|---|
| BSC-2 | 2400 | 1589 | 1.0 | 6.9 | 46* | ** | - | 0.011 | ** | ** | 0.9 |
| BSC-22 | 2400 | 1589 | 1.0 | 6.9 | ** | - | - | 0.019 | 15.9 | 0.29 | 0.3 |
| BSC-9 | 2400 | 1589 | 1.0 | 6.9 | 49 | 103 | - | 0.010 | 118 | 1.12 | 1.1 |
| BSC-24 | 2400 | 1589 | 1.0 | 6.9 | 58 | >100 | - | 0.007 | 116 | 0.80 | 0.9 |
| BSC-1 | 2400 | 1589 | 1.5 | 10.3 | 29 | 56 | 110 | 0.018 | 93 | 1.53 | 1.6 |
| BSC-10 | 2400 | 1589 | 1.5 | 10.3 | 19 | 33.5 | 62* | 0.030 | 114 | 1.98 | 2.0 |
| BSC-25 | 2400 | 1589 | 1.5 | 10.3 | 20 | ** | - | 0.023 | 27.2 | 0.62 | 0.7 |
| BSC-5 | 2400 | 1589 | 2.0 | 13.8 | 11 | 23.5 | 49* | 0.043 | 44 | 1.61 | 1.7 |
| BSC-8 | 2400 | 1589 | 2.0 | 13.8 | 12.5 | 25.5 | 51.5* | 0.039 | 72 | 2.32 | 2.4 |
| BSC-7 | 2200 | 1478 | 3.0 | 20.7 | 36 | 85 | >100 | 0.012 | 94 | 1.09 | 1.2 |
| BSC-20 | 2200 | 1478 | 3.0 | 20.7 | 47.5 | 97.5 | >100 | 0.010 | 100 | 1.04 | 1.2 |
| BSC-4 | 2200 | 1478 | 4.0 | 27.6 | 29.5 | 58.5 | 116* | 0.017 | 90 | 1.46 | 1.5 |
| BSC-21 | 2200 | 1478 | 4.0 | 27.6 | 28 | 59 | 120* | 0.017 | 101 | 1.75 | 1.8 |
| BSC-3 | 2200 | 1478 | 5.0 | 34.5 | 21.5 | 43 | 80* | 0.023 | 75 | 1.84 | 1.8 |
| BSC-18 | 2200 | 1478 | 5.0 | 34.5 | 24.5 | 49 | 102* | 0.020 | 74.5 | 1.54 | 1.7 |
| BSC-13 | 2000 | 1366 | 10.0 | 69 | 69 | 130 | - | 0.008 | 137.5 | 1.05 | 1.4 |
| BSC-17 | 2000 | 1366 | 10.0 | 69 | 80 | >100 | - | 0.006 | 98 | 0.63 | 0.7 |
| BSC-11 | 2000 | 1366 | 12.5 | 86.2 | 29.5 | 53.5 | 91 | 0.019 | 92.7 | 2.05 | 2.2 |
| BSC-15 | 2000 | 1366 | 12.5 | 86.2 | 18.5 | 38.5 | 73.5 | 0.026 | 97.5 | 2.72 | 3.1 |
| BSC-26 | 2000 | 1366 | 12.5 | 86.2 | 29.5 | 53.5 | 96 | 0.019 | 141 | ✱ | 5.0 |
| BSC-16 | 2000 | 1366 | 15.0 | 103.5 | 11 | 22 | 40 | 0.045 | 45 | 2.33 | 2.4 |
| BSC-14 | 2000 | 1366 | 15.0 | 103.5 | 9.5 | 19 | 34.5 | 0.053 | 47.1 | 2.81 | 3.1 |

† Stress based on original metal thickness before coating.

‡ Average creep rate during first 1% creep.

* Extrapolated values.

** Not determined — test aborted due to furnace failure.

✱ No valid data after 98 hours.

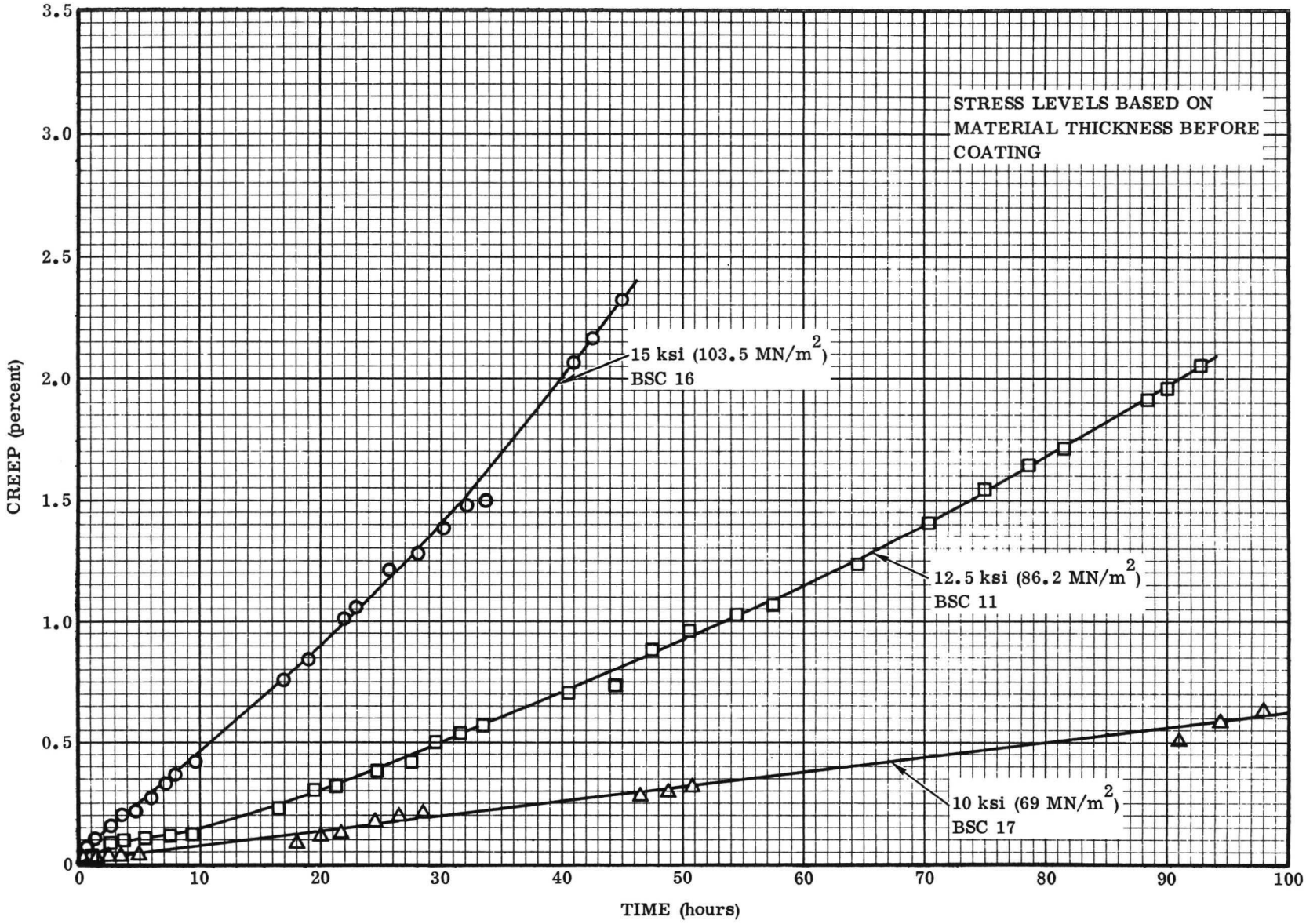


Figure 4-169. Creep Strain for Cb-752/R-512E at 2000° F (1366° K)

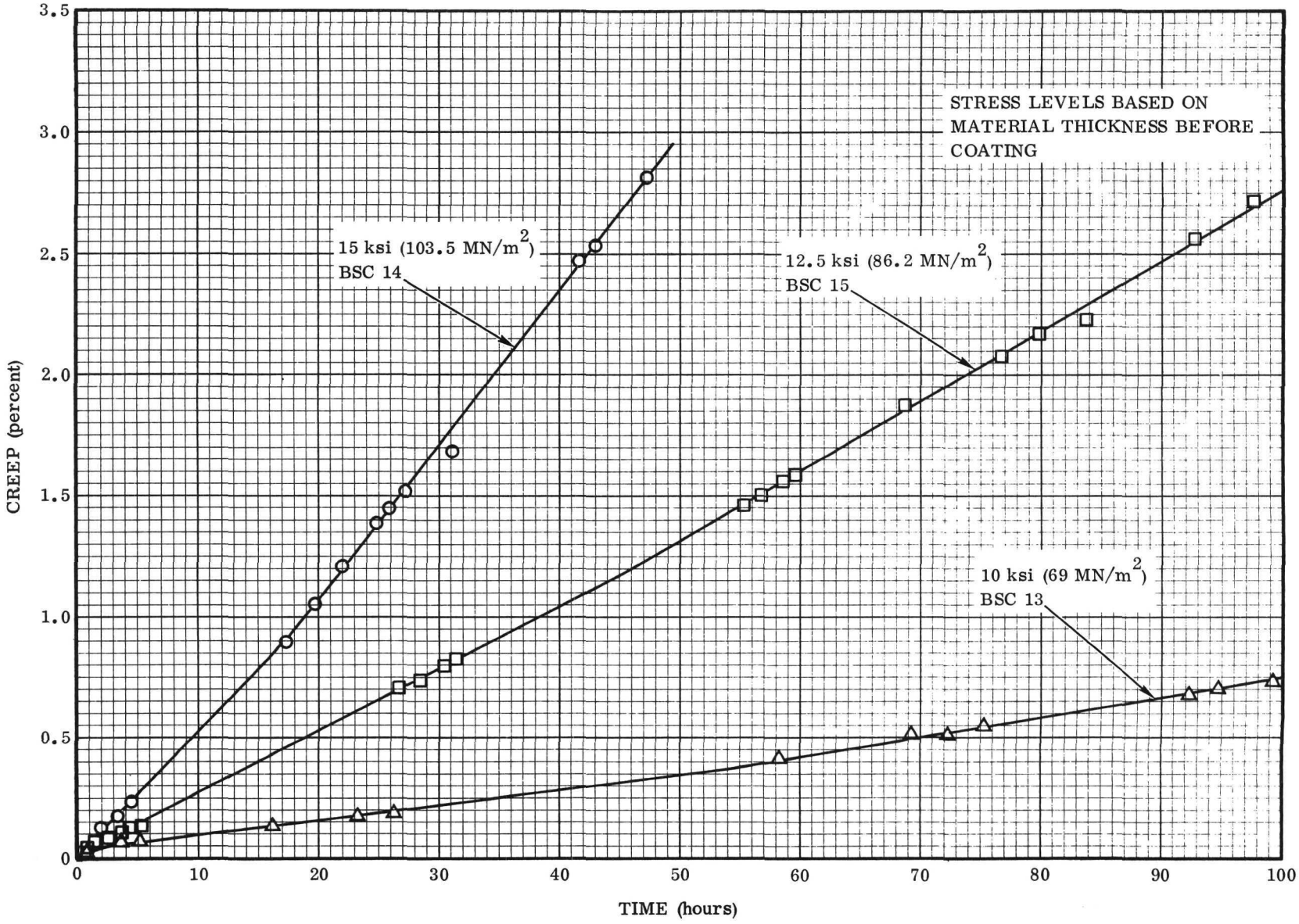


Figure 4-170. Creep Strain for Cb-752/R-512E at 2000° F (1366°K)

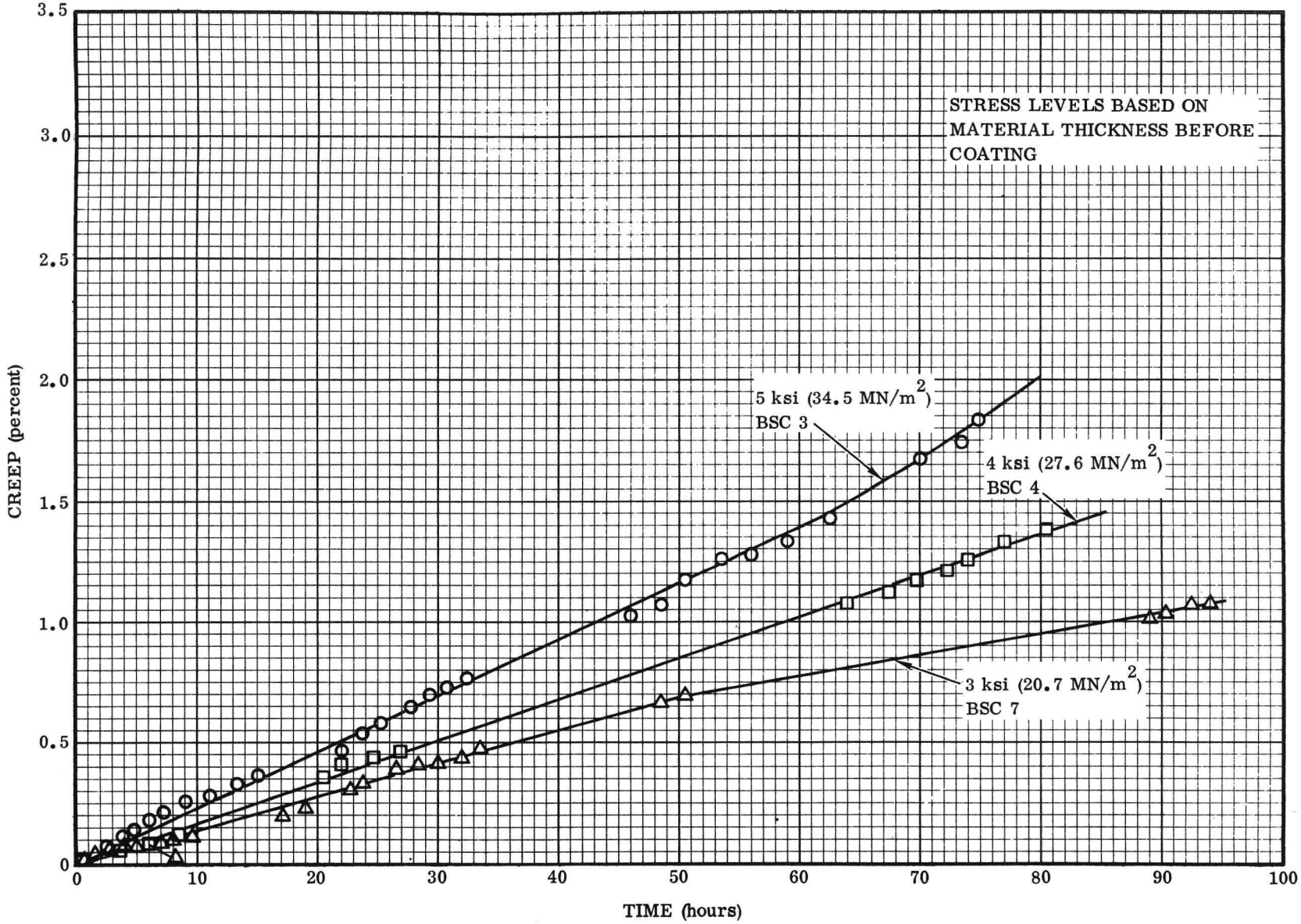


Figure 4-171. Creep Strain for Cb-752/R-512E at 2200° F (1478° K)

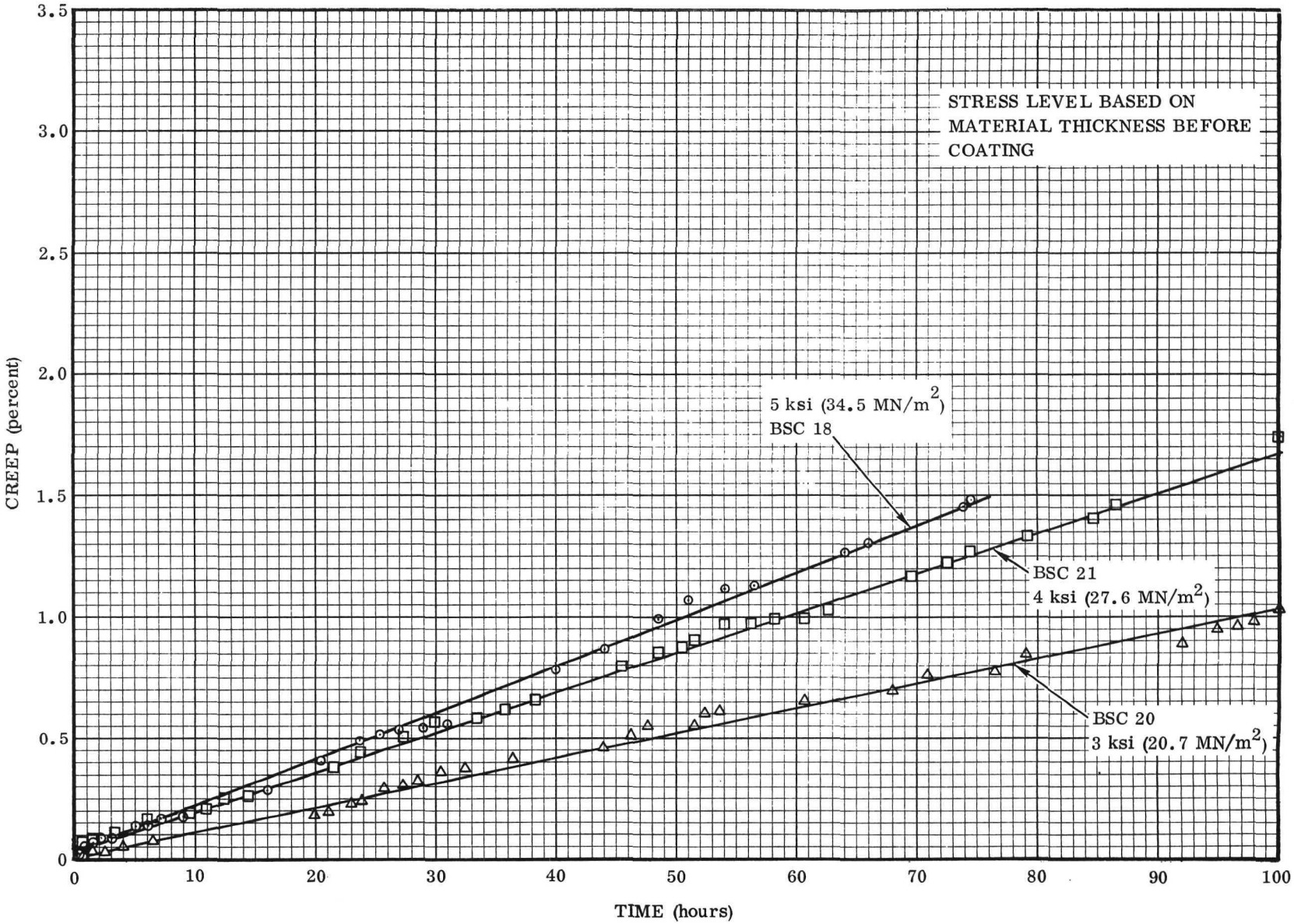


Figure 4-172. Creep Strain for Cb-752/R-512E at 2200°F (1478°K)

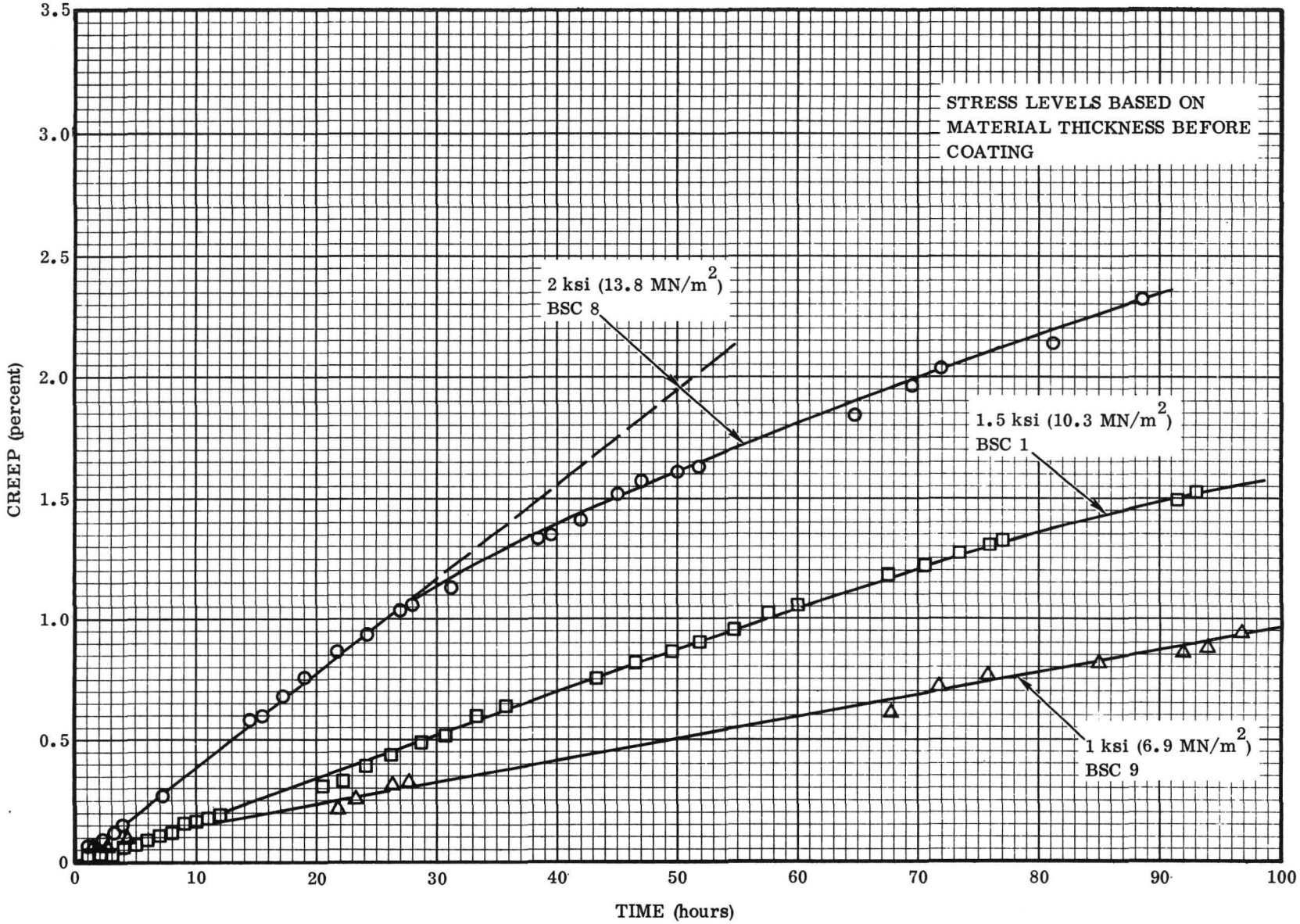


Figure 4-173. Creep Strain for Cb-752/R-512E at 2400° F (1589° K)

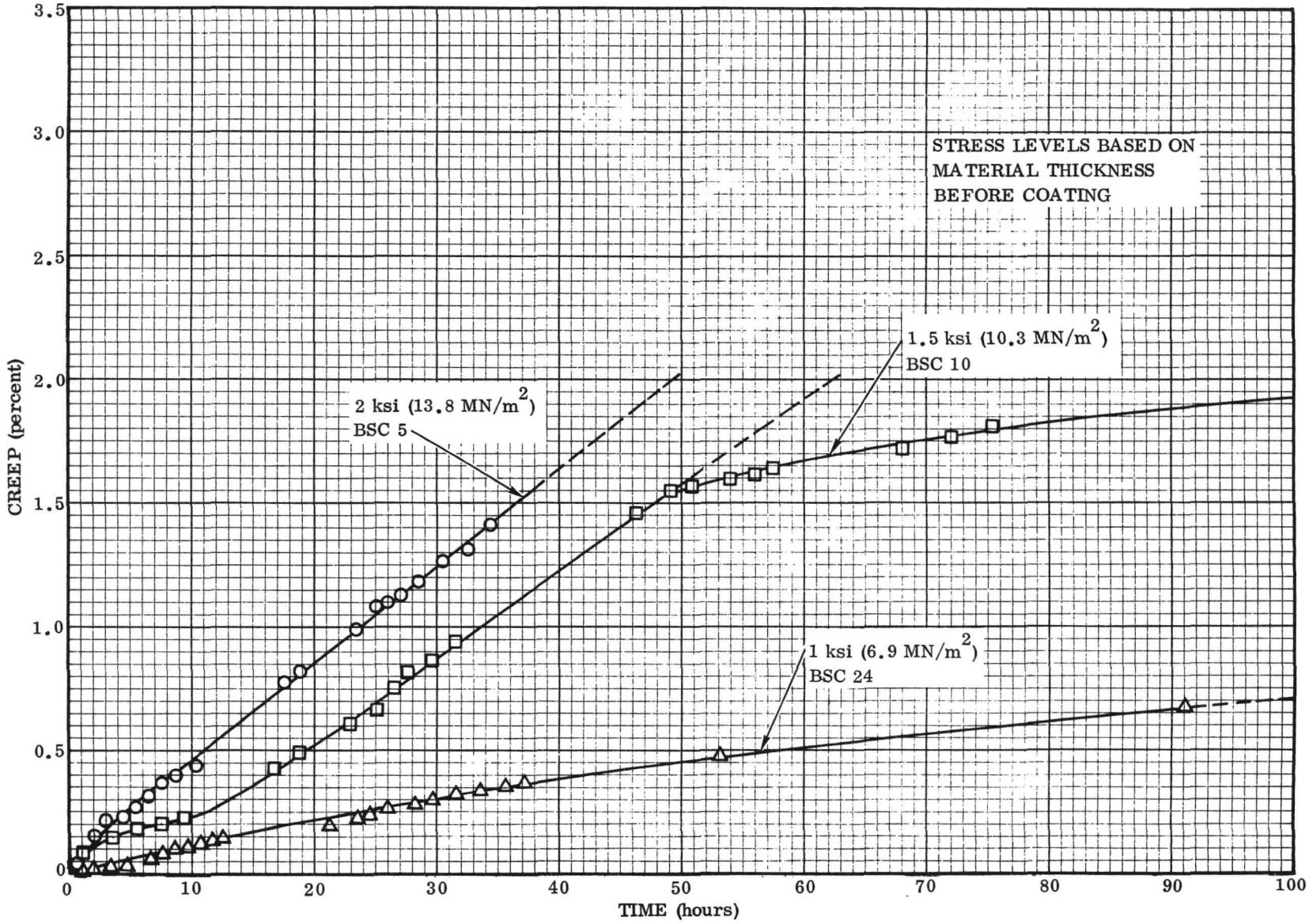


Figure 4-174. Creep Strain for Cb-752/R-512E at 2400° F (1589° K)

some curves showing slight primary creep, followed by essentially linear creep. The 2400°F (1589°K) curves show a decreasing creep rate after about 30 hours, which is attributed to substrate strengthening from oxygen diffusion. The average creep data for Cb-752/R-512E are summarized in Table 4-25, and composite creep curves for 0.5, 1.0, and 2.0 percent creep are presented in Figure 4-175.

The creep strengths of Cb-752/R-512E and C-129Y/R-512E are compared in Figure 4-176 for one percent creep. Cb-752/R-512E shows slightly higher creep strength at all three test temperatures. This is not in agreement with the cyclic creep data from the flight simulation tests, which indicated slightly higher creep strength for C-129Y/R-512E. The reason for this apparent discrepancy between constant exposure and cyclic creep is not known at present.

Comparison of the creep test results from Cb-752/R-512E with published data on coated and uncoated Cb-752 is shown in Figure 4-177 to 4-179 (also see References 36, 37, 38, and 39).

Table 4-25. Average Creep Data for Cb-752/R-512E Coated Columbium Alloy[1]

| Test Temperature | | Stress[2] | | Hours to Creep | | | Creep Rate | Recalculated Stress[4] | |
|---|---|---|---|---|---|---|---|---|---|
| °F | (°K) | ksi | ($MN/m^2$) | 0.5% | 1% | 2% | % per hr[3] | ksi | ($MN/m^2$) |
| 2400 | (1589) | 1.0 | ( 6.9) | 51 | >100 | | 0.012 | 1.27 | ( 8.8) |
| | | 1.5 | (10.3) | 22.7 | 44.2 | 86 | 0.027 | 1.90 | ( 13.1) |
| | | 2.0 | (13.8) | 11.8 | 24.5 | 50.2 | 0.041 | 2.54 | ( 17.5) |
| 2200 | (1478) | 3.0 | (20.7) | 41.7 | 91.2 | >100 | 0.011 | 3.81 | ( 26.3) |
| | | 4.0 | (27.6) | 28.7 | 58.7 | 118 | 0.017 | 5.08 | ( 35.0) |
| | | 5.0 | (34.5) | 23 | 46 | 91 | 0.022 | 6.35 | ( 43.8) |
| 2000 | (1366) | 10.0 | (58.7) | 74.8 | 145 | | 0.007 | 12.70 | ( 87.6) |
| | | 12.5 | (69) | 25.8 | 48.5 | 86.8 | 0.021 | 15.90 | (109.6) |
| | | 15.0 | (86.2) | 10.2 | 20.5 | 37.2 | 0.049 | 19.00 | (131.4) |

1. Average creep data for two test specimens except as noted.
2. Stress based on original metal thickness before coating.
3. Average creep rate during first 1 percent creep.
4. Stress recalculated based on estimated thickness of substrate remaining after coating.

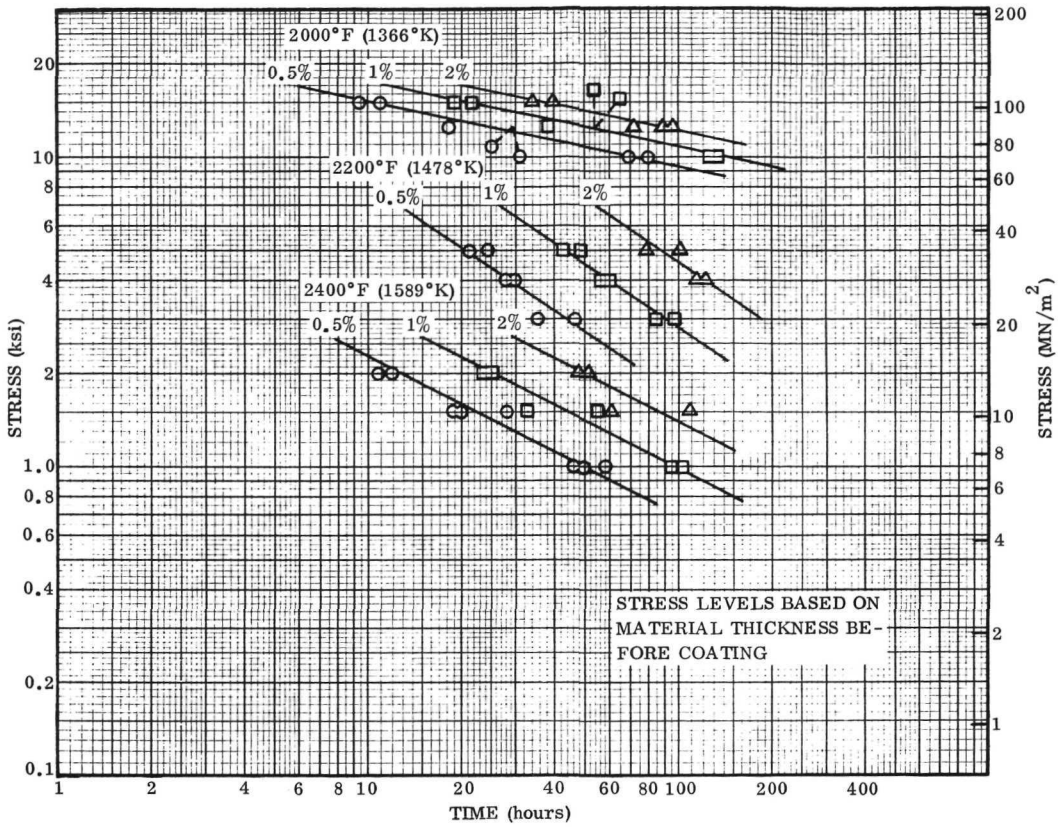


Figure 4-175. Creep Properties of Cb-752/R-512E at 2000°F (1366°K), 2200°F (1478°K), and 2400°F (1589°K)

The creep results are compared in Figure 4-178 with some recent creep data on Cb-752/R-512E developed by North American Rockwell at 2000°F (1366°K), 2250°F (1505°K), and 2500°F (1644°K). The agreement is very good at 2000°F (1366°K). However, it is difficult to correlate the 2250°F (1505°K) and 2500°F (1644°K) data due to the different in test temperature and the limited data points.

Figure 4-179 compares data from another source (Reference 14) for both coated and uncoated Cb-752 at 2400°F (1589°K). Remarkably good agreement is shown, particularly in view of the significant differences in test procedures. However, data for 0.5 and 1 percent creep were not available from these tests, which would have provided a more useful comparison.

The oxide growth and spalling for Cb-752/R-512E are very similar to that described for C-129Y/R-512E. Typical creep test specimens for Cb-752/R-512E are shown in Figure 4-180.

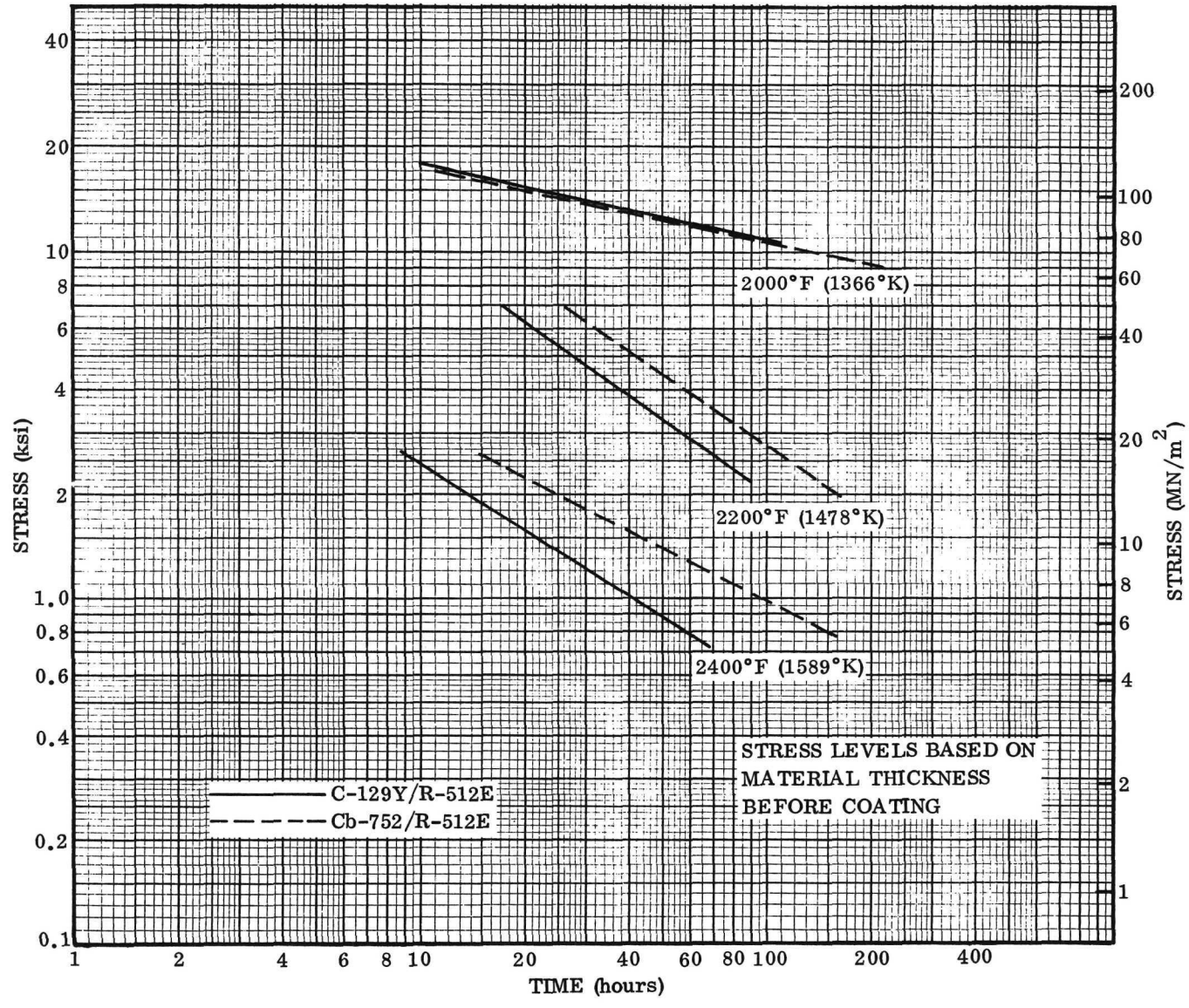


Figure 4-176. Comparison of Creep Properties of C-129Y/R-512E and Cb-752/R-512E for 1 Percent Creep

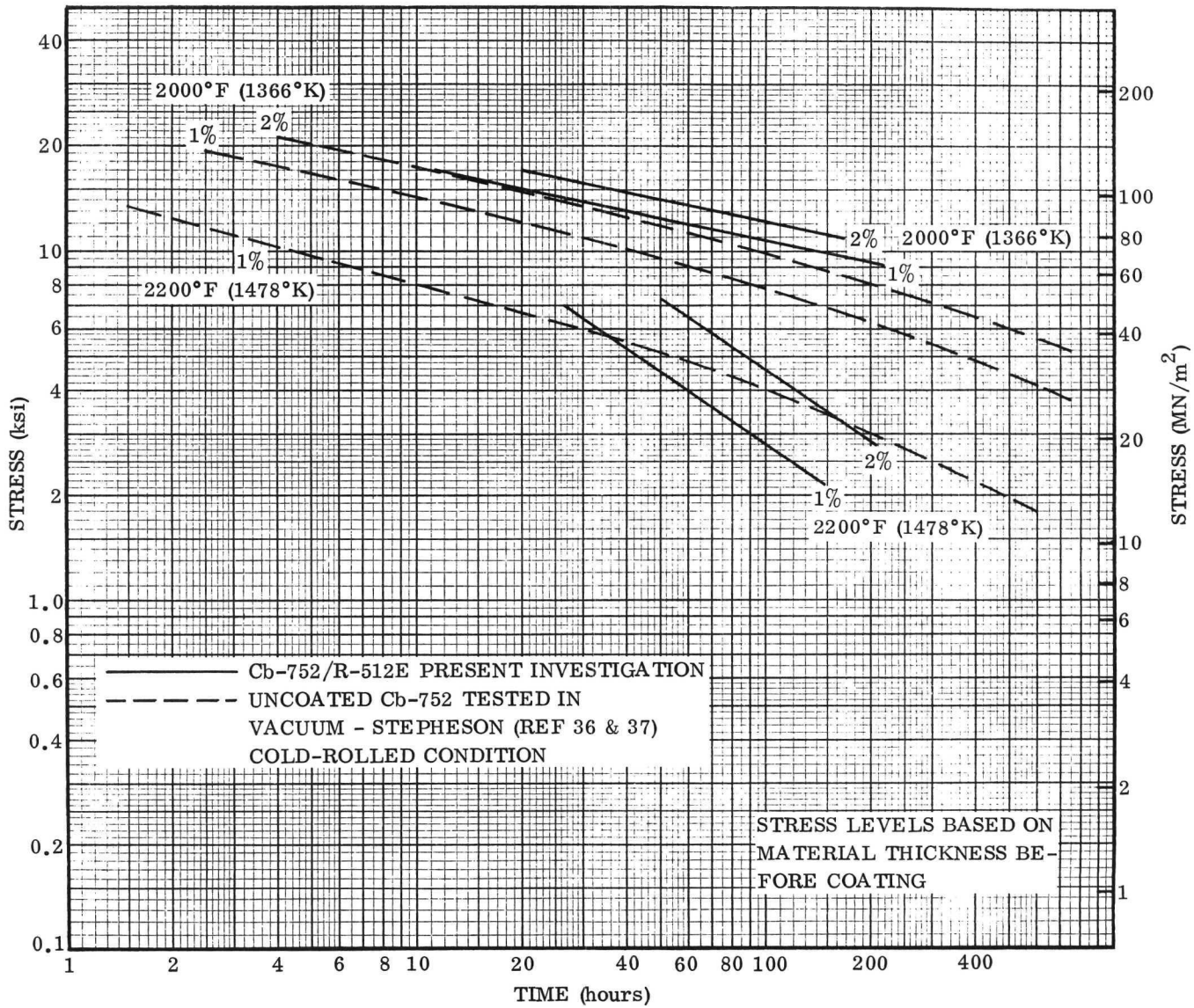


Figure 4-177. Comparison of Creep Properties of Cb-752/R-512E with Uncoated Cb-752 at 2000° F (1366° K) and 2200° F (1478° K)

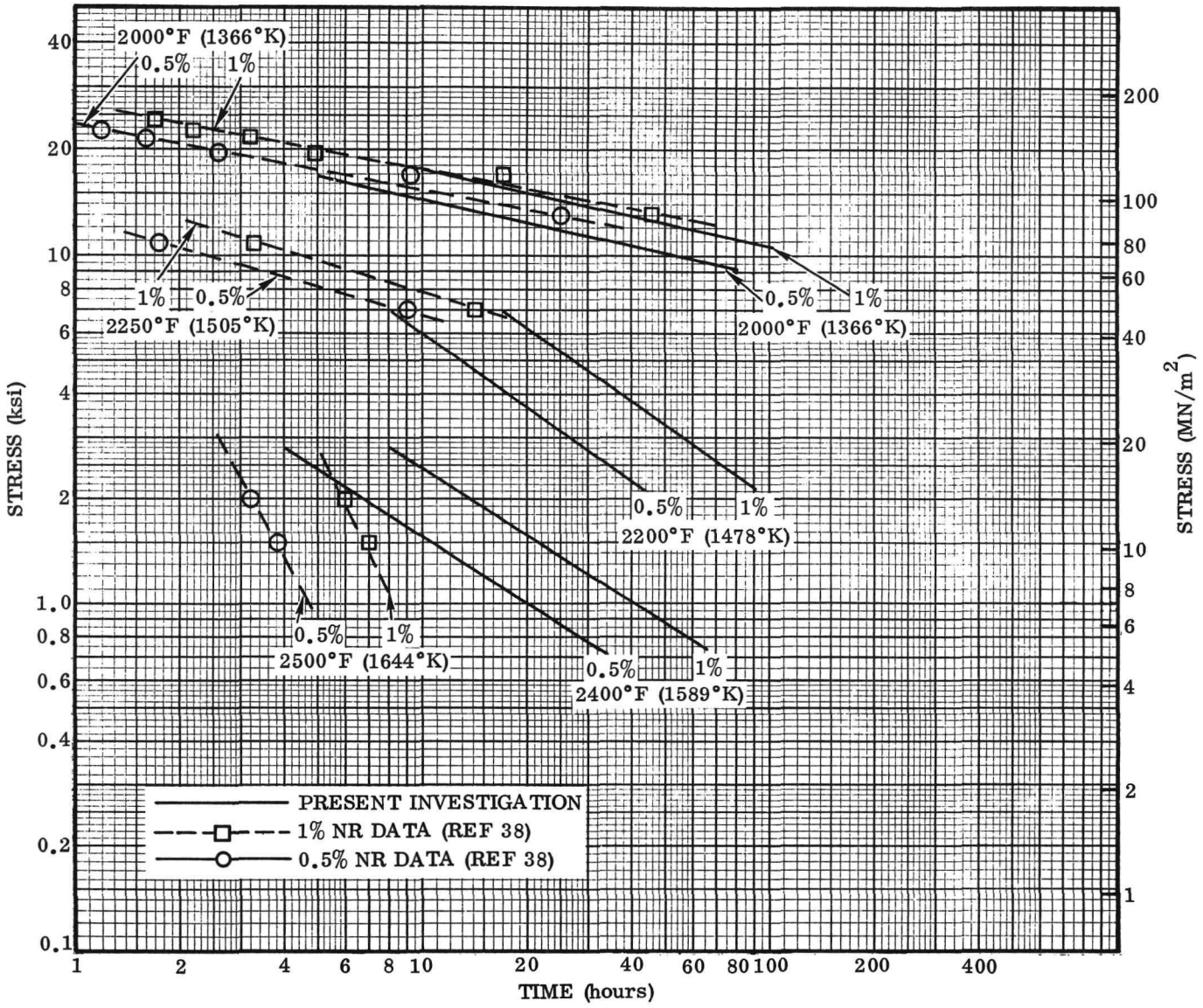


Figure 4-178. Comparison of Creep Properties of Cb-752/R-512E with Creep Test Results Reported by North American Rockwell

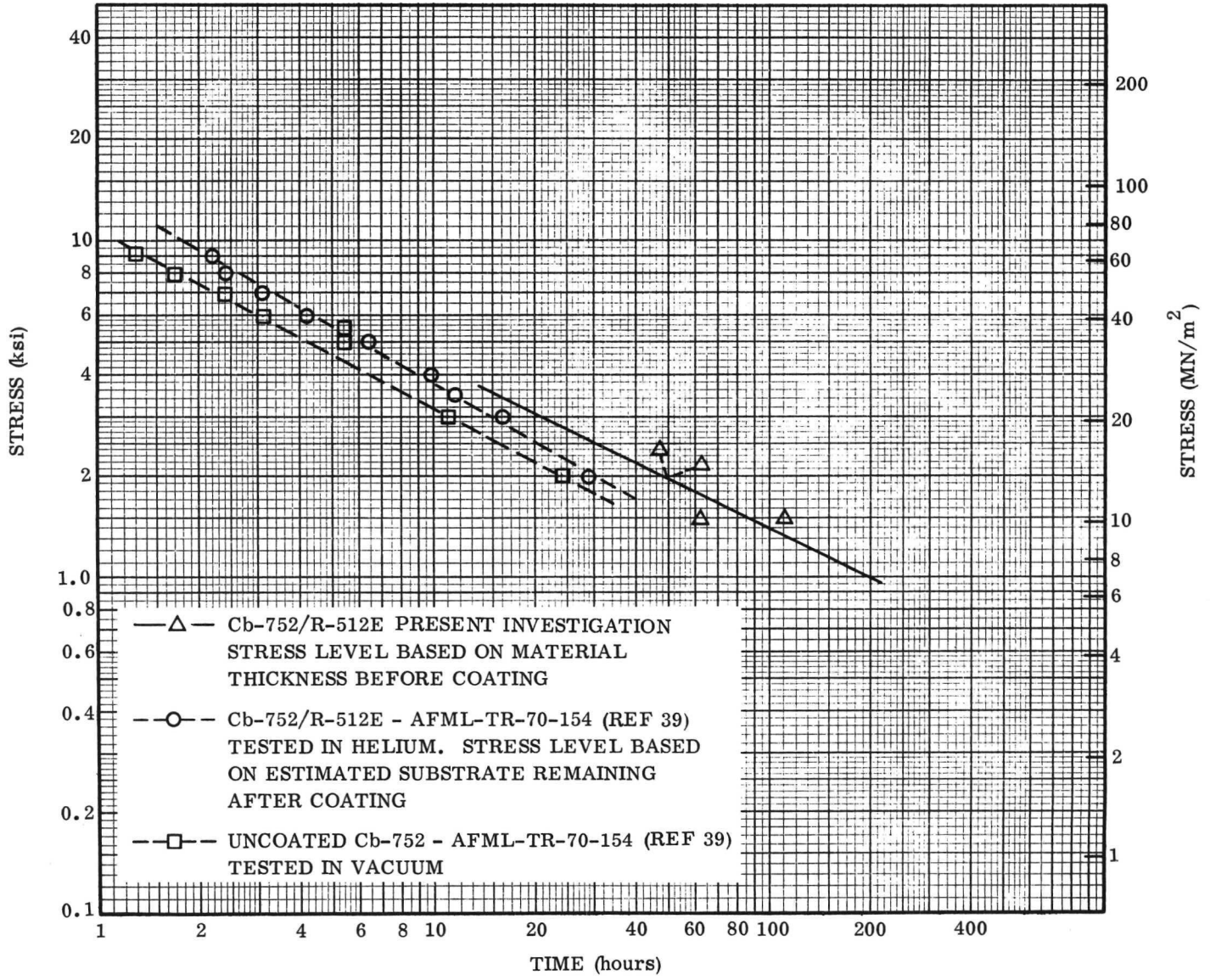


Figure 4-179. Comparison of Creep Properties of Cb-752/R-512E with Coated and Uncoated Cb-752 for Two Percent Creep at 2400° F (1589° K)

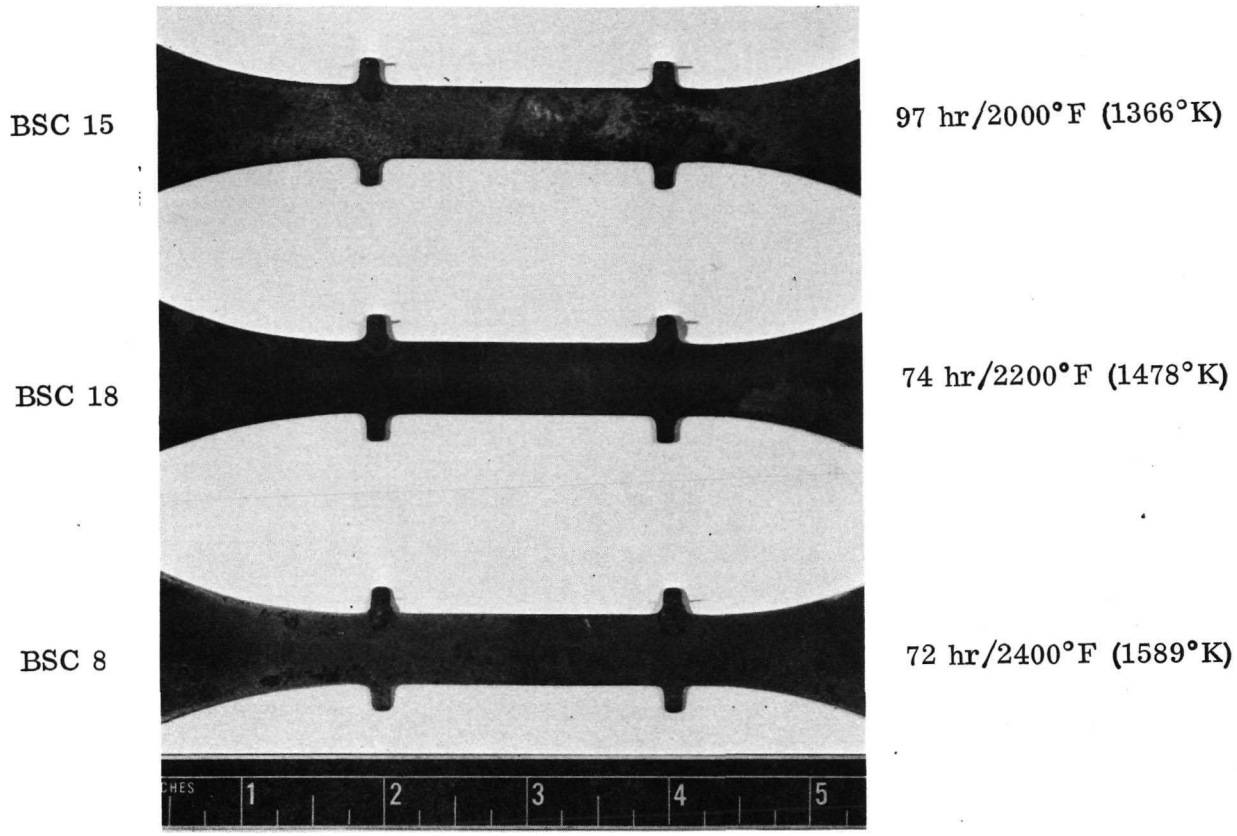


Figure 4-180. Typical Cb-752/R-512E Creep Test Specimens Showing Oxide Spalling (Photo 120247B)

4.5.4.3 Thickness measurements: Figure 4-181 shows the relationship of substrate consumption to coating part growth as established by metallographic examination. A slight difference in substrate consumption was indicated between the C-129Y/R-512E and Cb-752/R-512E material systems, but this was within the limit of experimental error. The substrate consumption is equivalent to approximately 33 percent of the total coating thickness.

The metallographic examinations used to establish substrate consumption and also to establish the Dermitron calibration curves were made using a very limited number of creep specimens in the as-coated condition. The destructive testing of creep specimens was necessary because the test coupons that accompanied the creep specimens to the coating vendor were inadvertently left out when the specimens were coated. Furthermore, provision was not made to obtain coupons with a range of coating thicknesses to be used as standards for preparation of Dermitron calibration curves.

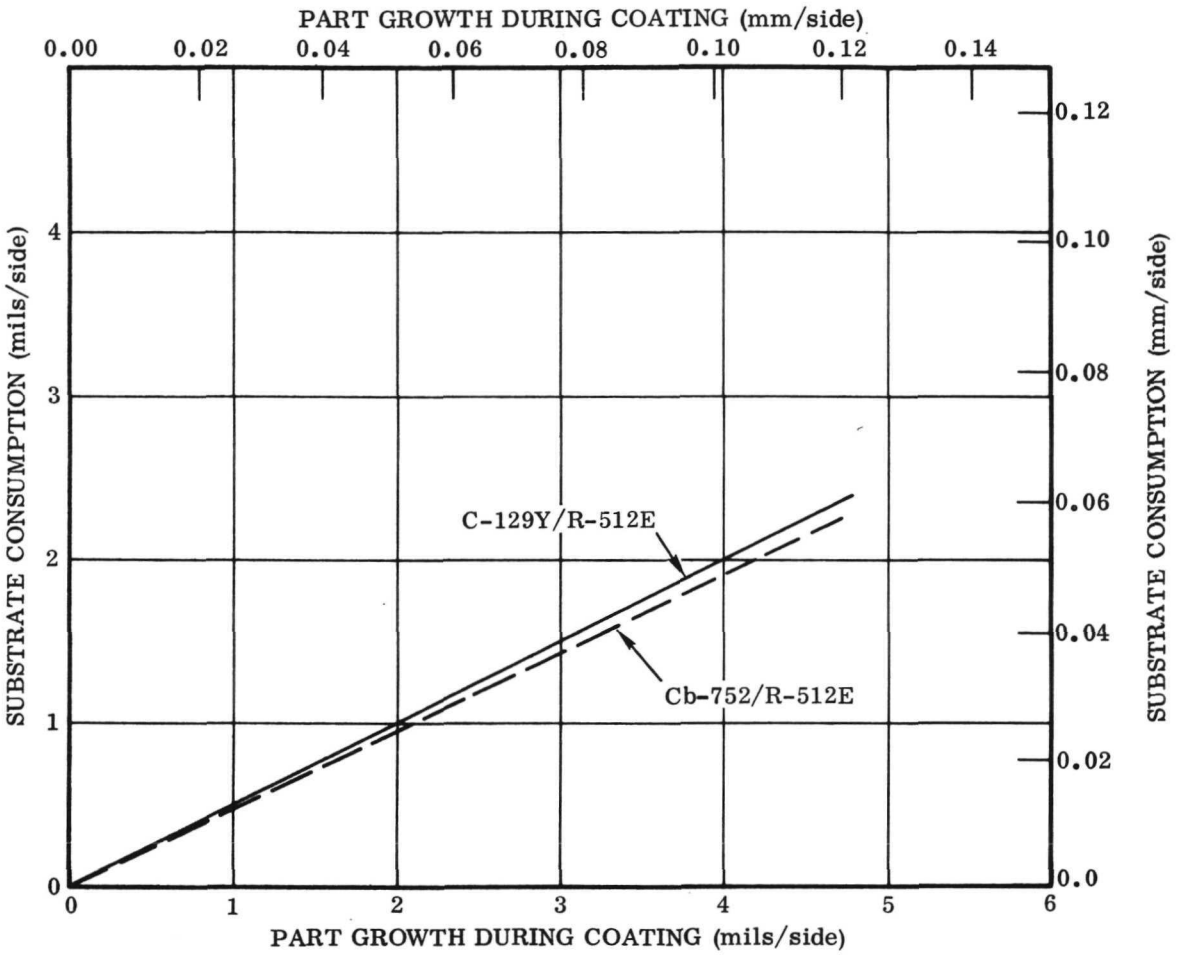


Figure 4-181. Substrate Consumption Versus Coating Part Growth for C-129Y/R-512E and Cb-752/R-512E

Coating and substrate thickness measurements of the creep specimens are summarized in Table 4-26 for C-129Y/R-512E and in Table 4-27 for Cb-752/R-512E. The coating thickness, remaining substrate thickness, and loss of substrate during coating were determined from micrometer measurements using the relationship established in Figure 4-181.

Tables 4-26 and 4-27 also list average Dermitron readings in the gage section and coating thicknesses determined from these readings using a Dermitron calibration curve. The Dermitron calibration is shown in Figure 4-182 with one curve for Mylar film and one curve for each of the two coated columbium alloy material systems. Metallographic examination resulted in the slightly different calibration curves for C-129Y/R-512E and Cb-752/R-512E. However, it is believed that this difference is less than the range of experimental error, which might be introduced with the limited number of specimens and coating thickness range examined.

# Table 4-26. Summary of Measurement Data for C-129Y/R-512E Creep Specimens

| Specimen No. | Bare Thickness | | Coated Thickness | | Part Growth | | Determined From Micrometer Measurements | | | | | | | Dermitron Measurements | | |
|---|---|---|---|---|---|---|---|---|---|---|---|---|---|---|---|---|
| | | | | | | | Coating Thickness | | Substrate Consumption | | Remaining Substrate | | Loss of Substrate Thickness During Coating(%) | Average Reading | Coating Thickness | |
| | in. | (mm) | in. | (mm) | mils/side | (mm/side) | mils/side | (mm/side) | mils/side | (mm/side) | in. | (mm) | | | mils/side | (mm/side) |
| YSC-1 | 0.0137 | 0.348 | 0.0188 | 0.478 | 2.5 | 0.064 | 3.7 | 0.094 | 1.25 | 0.032 | 0.0112 | 0.284 | 19 | 42 | 4.9 | 0.124 |
| YSC-2 | 0.0142 | 0.361 | 0.0195 | 0.495 | 2.6 | 0.066 | 3.9 | 0.099 | 1.3 | 0.033 | 0.0116 | 0.295 | 19 | 39 | 4.5 | 0.114 |
| YSC-3 | 0.0141 | 0.358 | 0.0193 | 0.490 | 2.6 | 0.066 | 3.9 | 0.099 | 1.3 | 0.033 | 0.0115 | 0.292 | 18 | 37 | 4.3 | 0.109 |
| YSC-4 | 0.0142 | 0.361 | 0.0198 | 0.503 | 2.8 | 0.071 | 4.2 | 0.107 | 1.4 | 0.036 | 0.0114 | 0.290 | 20 | 37 | 4.3 | 0.109 |
| YSC-5* | 0.0141 | 0.358 | 0.0201 | 0.511 | 3.0 | 0.076 | 4.5 | 0.114 | 1.5 | 0.038 | 0.0111 | 0.282 | 22 | 40 | 4.7 | 0.119 |
| YSC-6 | 0.0140 | 0.356 | 0.0198 | 0.503 | 2.9 | 0.074 | 4.3 | 0.109 | 1.45 | 0.037 | 0.0111 | 0.282 | 21 | 38 | 4.4 | 0.112 |
| YSC-7 | 0.0132 | 0.335 | 0.0198 | 0.503 | 3.1 | 0.079 | 4.6 | 0.117 | 1.5 | 0.038 | 0.0101 | 0.257 | 24 | 40 | 4.7 | 0.119 |
| YSC-8 | 0.0140 | 0.356 | 0.0198 | 0.503 | 2.9 | 0.074 | 4.3 | 0.109 | 1.45 | 0.037 | 0.0111 | 0.282 | 21 | 39 | 4.5 | 0.114 |
| YSC-9 | 0.0141 | 0.358 | 0.0198 | 0.503 | 2.8 | 0.071 | 4.2 | 0.107 | 1.4 | 0.036 | 0.0113 | 0.287 | 20 | 36 | 4.2 | 0.107 |
| YSC-10 | 0.0140 | 0.356 | 0.0205 | 0.521 | 3.2 | 0.081 | 4.8 | 0.122 | 1.6 | 0.041 | 0.0108 | 0.274 | 23 | 42 | 4.9 | 0.124 |
| YSC-11 | 0.0143 | 0.363 | 0.0206 | 0.523 | 3.1 | 0.079 | 4.6 | 0.117 | 1.55 | 0.039 | 0.0112 | 0.284 | 22 | 41 | 4.8 | 0.122 |
| YSC-12 | 0.0147 | 0.373 | 0.0213 | 0.541 | 3.3 | 0.084 | 4.9 | 0.124 | 1.65 | 0.042 | 0.0114 | 0.290 | 23 | 42 | 4.9 | 0.124 |
| YSC-13 | 0.0146 | 0.371 | 0.0212 | 0.538 | 3.3 | 0.084 | 4.9 | 0.124 | 1.65 | 0.042 | 0.0113 | 0.287 | 22 | 41 | 4.8 | 0.122 |
| YSC-14 | 0.0146 | 0.371 | 0.0212 | 0.538 | 3.3 | 0.084 | 4.9 | 0.124 | 1.65 | 0.042 | 0.0113 | 0.287 | 23 | 40 | 4.7 | 0.119 |
| YSC-15 | 0.0147 | 0.373 | 0.0216 | 0.549 | 3.4 | 0.086 | 5.1 | 0.130 | 1.7 | 0.043 | 0.0113 | 0.287 | 24 | 40 | 4.7 | 0.119 |
| YSC-16 | 0.0147 | 0.373 | 0.0216 | 0.549 | 3.4 | 0.086 | 5.1 | 0.130 | 1.7 | 0.043 | 0.0113 | 0.287 | 24 | 36 | 4.2 | 0.107 |
| YSC-17 | 0.0153 | 0.389 | 0.0215 | 0.546 | 3.1 | 0.079 | 4.6 | 0.117 | 1.55 | 0.039 | 0.0122 | 0.310 | 21 | 38 | 4.4 | 0.112 |
| YSC-18 | 0.0153 | 0.389 | 0.0212 | 0.538 | 2.9 | 0.074 | 4.3 | 0.109 | 1.45 | 0.037 | 0.0124 | 0.315 | 20 | 39 | 4.5 | 0.114 |
| YSC-19 | 0.0151 | 0.384 | 0.0213 | 0.541 | 3.1 | 0.079 | 4.6 | 0.117 | 1.55 | 0.039 | 0.0120 | 0.305 | 21 | 40 | 4.7 | 0.119 |
| YSC-20 | 0.0153 | 0.389 | 0.0213 | 0.541 | 3.0 | 0.076 | 4.5 | 0.114 | 1.5 | 0.038 | 0.0123 | 0.312 | 20 | 38 | 4.4 | 0.112 |
| YSC-21 | 0.0147 | 0.373 | 0.0207 | 0.526 | 3.0 | 0.076 | 4.5 | 0.114 | 1.5 | 0.038 | 0.0117 | 0.297 | 21 | 39 | 4.5 | 0.114 |
| YSC-22 | 0.0149 | 0.378 | 0.0206 | 0.523 | 2.8 | 0.071 | 4.2 | 0.107 | 1.4 | 0.036 | 0.0121 | 0.307 | 19 | 38 | 4.4 | 0.112 |
| YSC-23 | 0.0147 | 0.373 | 0.0210 | 0.533 | 3.1 | 0.079 | 4.6 | 0.117 | 1.55 | 0.039 | 0.0116 | 0.295 | 21 | 40 | 4.7 | 0.119 |
| YSC-24 | 0.0150 | 0.381 | 0.0211 | 0.536 | 3.0 | 0.076 | 4.5 | 0.114 | 1.5 | 0.038 | 0.0120 | 0.305 | 21 | 40 | 4.7 | 0.119 |
| YSC-25 | 0.0152 | 0.386 | 0.0211 | 0.536 | 3.1 | 0.079 | 4.6 | 0.117 | 1.55 | 0.039 | 0.0121 | 0.307 | 21 | 40 | 4.7 | 0.119 |
| YSC-26 | 0.0152 | 0.386 | 0.0215 | 0.546 | 3.1 | 0.079 | 4.6 | 0.117 | 1.55 | 0.039 | 0.0121 | 0.307 | 21 | 32 | 3.7 | 0.094 |
| YSC-27 | 0.0154 | 0.391 | 0.0216 | 0.549 | 3.1 | 0.079 | 4.6 | 0.117 | 1.55 | 0.039 | 0.0123 | 0.312 | 22 | 32 | 3.7 | 0.094 |
| YSC-28 | 0.0155 | 0.394 | 0.0216 | 0.549 | 3.1 | 0.079 | 4.6 | 0.117 | 1.55 | 0.039 | 0.0124 | 0.315 | 21 | 37 | 4.3 | 0.109 |
| YSC-29 | 0.0155 | 0.394 | 0.0214 | 0.544 | 3.0 | 0.076 | 4.5 | 0.114 | 1.5 | 0.038 | 0.0125 | 0.318 | 20 | 39 | 4.5 | 0.114 |
| YSC-30 | 0.0151 | 0.384 | 0.0211 | 0.536 | 3.0 | 0.076 | 4.5 | 0.114 | 1.5 | 0.038 | 0.0121 | 0.307 | 20 | 41 | 4.8 | 0.122 |

*Used for as-coated metallographic examination

## Table 4-27. Summary of Measurement Data for Cb-752/R-512E Creep Specimens

| Specimen No. | Bare Thickness | | Coated Thickness | | Part Growth | | Determined From Micrometer Measurements | | | | | | | Dermitron Measurements | | |
|---|---|---|---|---|---|---|---|---|---|---|---|---|---|---|---|---|
| | | | | | | | Coating Thickness | | Substrate Consumption | | Remaining Substrate | | Loss of Substrate Thickness During Coating(%) | Average Reading | Coating Thickness | |
| | in. | (mm) | in. | (mm) | mils/side | (mm/side) | mils/side | (mm/side) | mils/side | (mm/side) | in. | (mm) | | | mils/side | (mm/side) |
| BSC-1 | 0.0130 | 0.330 | 0.0189 | 0.480 | 3.0 | 0.076 | 4.4 | 0.112 | 1.4 | 0.036 | 0.0102 | 0.259 | 21 | 38 | 4.3 | 0.109 |
| BSC-2 | 0.0131 | 0.333 | 0.0189 | 0.480 | 2.9 | 0.074 | 4.3 | 0.109 | 1.4 | 0.036 | 0.0103 | 0.262 | 21 | 37 | 4.1 | 0.104 |
| BSC-3 | 0.0131 | 0.333 | 0.0190 | 0.483 | 3.0 | 0.076 | 4.4 | 0.112 | 1.4 | 0.036 | 0.0103 | 0.262 | 21 | 36 | 4.0 | 0.102 |
| BSC-4 | 0.0131 | 0.333 | 0.0204 | 0.518 | 3.6 | 0.091 | 5.3 | 0.135 | 1.7 | 0.043 | 0.0107 | 0.272 | 26 | 44 | 4.9 | 0.124 |
| BSC-5 | 0.0137 | 0.348 | 0.0204 | 0.518 | 3.4 | 0.086 | 5.0 | 0.127 | 1.6 | 0.041 | 0.0105 | 0.267 | 23 | 43 | 4.8 | 0.122 |
| BSC-6* | 0.0137 | 0.348 | 0.0204 | 0.518 | 3.4 | 0.086 | 5.0 | 0.127 | 1.6 | 0.041 | 0.0105 | 0.267 | 23 | 41 | 4.6 | 0.117 |
| BSC-7 | 0.0136 | 0.345 | 0.0204 | 0.518 | 3.4 | 0.086 | 5.0 | 0.127 | 1.6 | 0.041 | 0.0104 | 0.264 | 23 | 40 | 4.5 | 0.114 |
| BSC-8 | 0.0134 | 0.340 | 0.0204 | 0.518 | 3.5 | 0.089 | 5.1 | 0.130 | 1.6 | 0.041 | 0.0102 | 0.259 | 24 | 41 | 4.6 | 0.117 |
| BSC-9 | 0.0135 | 0.343 | 0.0204 | 0.518 | 3.4 | 0.086 | 5.0 | 0.127 | 1.6 | 0.041 | 0.0103 | 0.262 | 24 | 41 | 4.6 | 0.117 |
| BSC-10 | 0.0137 | 0.348 | 0.0199 | 0.505 | 3.1 | 0.079 | 4.5 | 0.114 | 1.4 | 0.036 | 0.0107 | 0.272 | 20 | 39 | 4.4 | 0.112 |
| BSC-11 | 0.0138 | 0.351 | 0.0200 | 0.508 | 3.1 | 0.079 | 4.5 | 0.114 | 1.4 | 0.036 | 0.0110 | 0.279 | 20 | 39 | 4.4 | 0.112 |
| BSC-12 | 0.0138 | 0.351 | 0.0203 | 0.516 | 3.2 | 0.081 | 4.7 | 0.119 | 1.5 | 0.038 | 0.0108 | 0.274 | 22 | 41 | 4.6 | 0.117 |
| BSC-13 | 0.0137 | 0.348 | 0.0200 | 0.508 | 3.2 | 0.081 | 4.7 | 0.119 | 1.5 | 0.038 | 0.0107 | 0.272 | 22 | 40 | 4.5 | 0.114 |
| BSC-14 | 0.0138 | 0.351 | 0.0199 | 0.505 | 3.0 | 0.076 | 4.4 | 0.112 | 1.4 | 0.036 | 0.0110 | 0.279 | 20 | 39 | 4.4 | 0.112 |
| BSC-15 | 0.0138 | 0.351 | 0.0198 | 0.503 | 3.0 | 0.076 | 4.4 | 0.112 | 1.4 | 0.036 | 0.0110 | 0.279 | 20 | 38 | 4.3 | 0.109 |
| BSC-16 | 0.0135 | 0.343 | 0.0201 | 0.511 | 3.3 | 0.084 | 4.8 | 0.122 | 1.5 | 0.038 | 0.0105 | 0.267 | 22 | 40 | 4.5 | 0.114 |
| BSC-17 | 0.0136 | 0.345 | 0.0198 | 0.503 | 3.1 | 0.079 | 4.5 | 0.114 | 1.4 | 0.036 | 0.0108 | 0.274 | 21 | 37 | 4.1 | 0.104 |
| BSC-18 | 0.0138 | 0.351 | 0.0202 | 0.513 | 3.2 | 0.081 | 4.7 | 0.119 | 1.5 | 0.038 | 0.0108 | 0.274 | 22 | 38 | 4.3 | 0.109 |
| BSC-19 | 0.0140 | 0.356 | 0.0202 | 0.513 | 3.1 | 0.079 | 4.6 | 0.117 | 1.4 | 0.036 | 0.0102 | 0.259 | 20 | 37 | 4.1 | 0.104 |
| BSC-20 | 0.0136 | 0.345 | 0.0198 | 0.503 | 3.1 | 0.079 | 4.6 | 0.117 | 1.4 | 0.036 | 0.0108 | 0.274 | 21 | 38 | 4.3 | 0.109 |
| BSC-21 | 0.0137 | 0.348 | 0.0195 | 0.495 | 2.9 | 0.074 | 4.3 | 0.109 | 1.4 | 0.036 | 0.0109 | 0.277 | 20 | 38 | 4.3 | 0.109 |
| BSC-22 | 0.0138 | 0.351 | 0.0195 | 0.495 | 2.8 | 0.071 | 4.1 | 0.104 | 1.3 | 0.033 | 0.0112 | 0.284 | 19 | 36 | 4.0 | 0.102 |
| BSC-23* | 0.0140 | 0.356 | 0.0201 | 0.511 | 3.0 | 0.076 | 4.4 | 0.112 | 1.4 | 0.036 | 0.0112 | 0.284 | 20 | 42 | 4.7 | 0.119 |
| BSC-24 | 0.0140 | 0.356 | 0.0203 | 0.516 | 3.1 | 0.079 | 4.5 | 0.114 | 1.4 | 0.036 | 0.0112 | 0.284 | 20 | 41 | 4.6 | 0.117 |
| BSC-25 | 0.0141 | 0.358 | 0.0200 | 0.508 | 2.9 | 0.074 | 4.3 | 0.109 | 1.4 | 0.036 | 0.0113 | 0.287 | 20 | 38 | 4.3 | 0.109 |
| BSC-26 | 0.0143 | 0.363 | 0.0205 | 0.521 | 3.1 | 0.079 | 4.5 | 0.114 | 1.4 | 0.036 | 0.0115 | 0.292 | 20 | 41 | 4.6 | 0.117 |
| BSC-27 | 0.0144 | 0.366 | 0 0203 | 0.516 | 2.9 | 0.074 | 4.3 | 0.109 | 1.4 | 0.036 | 0.0116 | 0.295 | 19 | 42 | 4.7 | 0.119 |
| BSC-28 | 0.0145 | 0.369 | 0.0211 | 0.536 | 3.3 | 0.084 | 4.8 | 0.122 | 1.5 | 0.038 | 0.0115 | 0.294 | 21 | 39 | 4.4 | 0.112 |

*Used for as-coated metallographic examination.

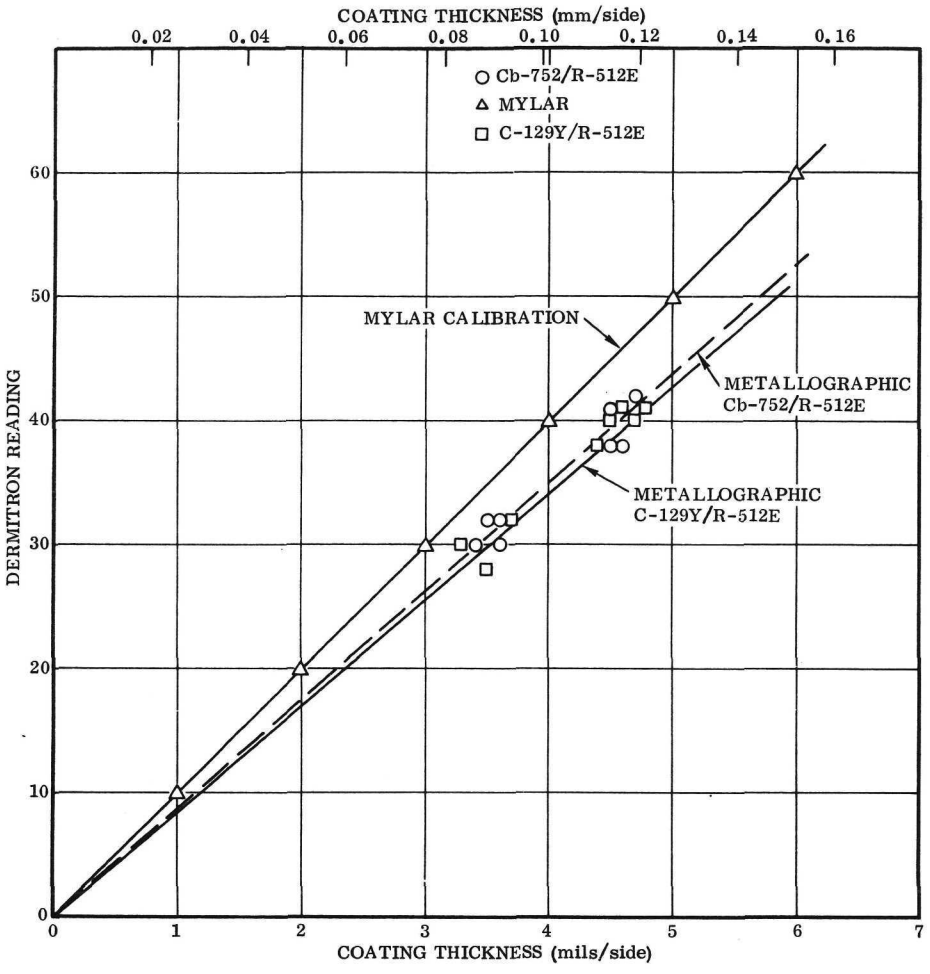


Figure 4-182. Dermitron Reading Versus Coating Thickness for C-129Y/R-512E and Cb-752/R-512E

The average coating thickness for the creep specimens determined by micrometer and Dermitron measurements are compared in Table 4-28. Good agreement is shown for the two techniques. The coating thickness in the gage section is about 1 mil (0.0254 mm)/side thicker than the grip ends for both material systems. The thinner coating on the grip ends was evident from metallographic examination, as well as from micrometer and Dermitron measurements. The data indicate that the gage section was given a double coating application. The gage section and adjacent areas also show visual evidence of an overspray coating on the edges. This is a common practice when the slurry coating is applied by dipping. The grip ends do not show evidence of an overspray coating.

Table 4-29 compares the loss of substrate thickness during the coating process for the C-129Y/R-512E and Cb-752/R-512E systems. The loss of substrate thickness

Table 4-28. Comparison of Coating Thickness Measurements by Micrometer and Dermitron Techniques

| Material System | No. of Specimens | Micrometer Measurement Gage Section | | | | Dermitron Measurements Coating Thickness | | | | | |
|---|---|---|---|---|---|---|---|---|---|---|---|
| | | Part Growth | | Coating Thickness | | Gage Section | | Grip 1 | | Grip 2 | |
| | | mils/side | (mm/side) | mils/side | (mm/side) | mils/side | (mm/side) | mils/side | (mm/side) | mils/side | (mm/side) |
| C-129Y/R-512E | 30 | | | | | | | | | | |
| Range | | 2.5/3.4 | 0.064/0.086 | 3.7/5.4 | 0.094/0.137 | 3.7/4.9 | 0.094/0.124 | 2.9/4.2 | 0.074/0.107 | 2.9/3.8 | 0.074/0.097 |
| Average | | 3.0 | 0.076 | 4.5 | 0.0114 | 4.5 | 0.0114 | 3.5 | 0.089 | 3.5 | 0.089 |
| Cb-752/R-512E | 28 | | | | | | | | | | |
| Range | | 2.8/3.6 | 0.071/0.091 | 4.1/5.3 | 0.104/0.135 | 4.0/4.9 | 0.102/0.124 | 2.9/3.5 | 0.074/0.089 | 2.7/4.0 | 0.086/0.102 |
| Average | | 3.1 | 0.079 | 4.6 | 0.117 | 4.4 | 0.112 | 3.3 | 0.084 | 3.2 | 0.081 |

averages 21 percent for both C-129Y/R-512E and Cb-752/R-512E. Assuming the width lost during coating to be insignificant, this is equivalent to a creep stress increase of 27 percent for the two material systems when stress is calculated on substrate remaining after coating.

At the present time, there is no standard method in general use for determining the thickness of diffusion coatings on columbium alloys. The three techniques used in this program, flat anvil micrometer, Dermitron, and metallographic, show relatively good agreement. However, each technique is subject to judgement and interpretation by the individual making the measurement. For this reason, standardized procedures are needed for measuring and specifying coating thickness for maximum usefulness of data developed by the various users and suppliers of coated columbium hardware.

In the present studies, it was decided to continue with previous Convair practice and use flat micrometers, which measure maximum values for coating thicknesses. The Dermitron calibration and metallographic measurements were also based on the total coating thickness. Other investigators have adopted the use of pointed micrometers, which measure thicknesses that are somewhat similar to average or mean coating thickness on a metallographic cross-section. Each technique has certain advantages and limitations, and comparative results are quite sensitive to variations in coating roughness.

A limited number of measurements were made on the as-coated creep specimens to evaluate the difference between mean coating thickness and maximum thickness values. It was found that the coating thickness was approximately 0.3 mil (0.00254 mm)/side less when measured either with pointed micrometers or metallographically for mean thickness. With this relationship, the calibration curves in Figure 4-182.

Table 4-29. Loss of Substrate Thickness During Coating

| Material System | Number of Specimens | Loss of Substrate Thickness During Coating (%) Range | Average | Creep Stress Increase When Stress is Based on Remaining Substrate After Coating (%) |
|---|---|---|---|---|
| C-129Y/R-512E | 30 | 18/24 | 21 | 27 |
| Cb-752/R-512E | 28 | 19/26 | 21 | 27 |

could be adjusted to reflect mean coating thicknesses for the two material systems. It would be a reasonable approximation to reduce the coating thickness measurements in Tables 4-26 to 4-28 by 0.3 mils (0.0076 mm)/side for comparison with data established on mean coating thickness.

4.5.4.4 Metallographic examination: Typical microstructure of C-129Y/R-512E and Cb-752/R-512E creep specimens in the as-coated condition are presented in Figures 4-183 and 4-184. respectively. The samples were lightly etched with $HNO_3$ - HF-$H_2O$ to develop the coating microstructure with the result that the substrate microstructure is poorly defined.

The microstructure of typical specimens of the two material systems after creep testing are shown in Figures 4-185 and 4-186. Oxide formation in the coating cracks are clearly evident in the microstructure. Penetration of the oxide to the substrate at the edge of the specimen can be observed for the 2000° F (1366° K) creep specimen in Figure 4-185.

The substrate thickness remaining after creep exposure was measured metallographically for the C-129Y/R-512E specimens shown in Figure 4-185. These measurements are compared to substrate thickness after coating to obtain the following indication of substrate consumption for C-129Y/R-512E:

| | | Substrate Thickness mils (mm) | | Substrate Consumption | |
|---|---|---|---|---|---|
| | | As-coated | After Exposure | mils (mm) | mils (mm)/hr |
| YSC12 | 2000° F (1366° K)/112 hr | 11.4 (0.289) | 10.5 (0.267) | 0.9 (0.023) | 0.008 (0.0002) |
| YSC16 | 2200° F (1478° K)/72 hr | 11.3 (0.287) | 9.5 (0.241) | 1.8 (0.046) | 0.025 (0.0006) |
| YSC10 | 2400° F (1589° K)/41 hr | 10.8 (0.274) | 8.9 (0.226) | 1.9 (0.048) | 0.046 (0.0012) |

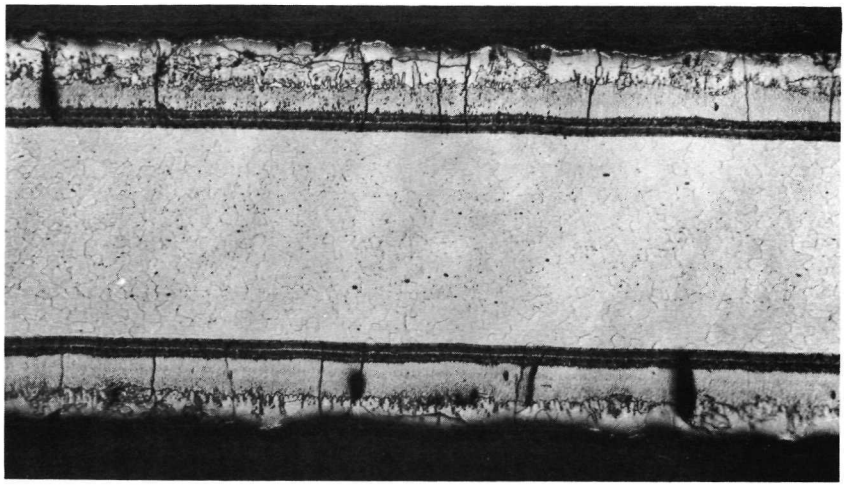

Magnification: 100X

Specimen No.: YSC 5

Section: Gage

Coating: 4.6 mils/side (0.117 mm/side)

Negative No.: D-1094

Mount No.: 671-0

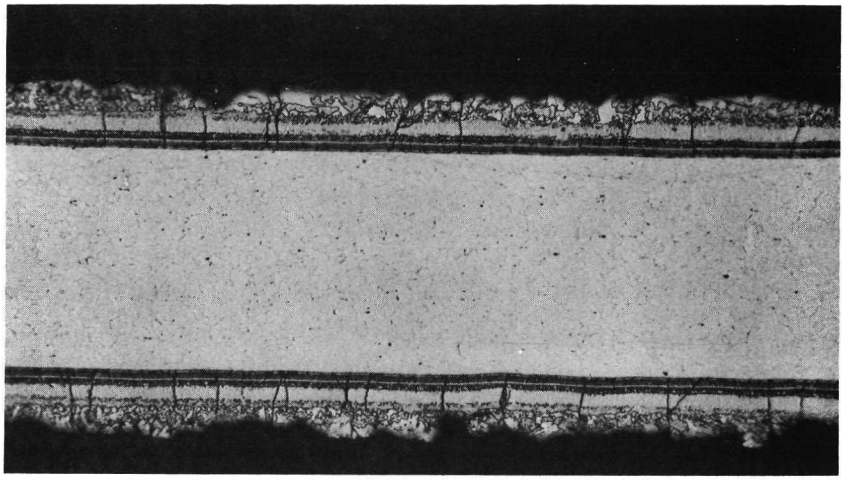

Magnification: 100X

Specimen No.: YSC 5

Section: Grip

Coating: 3.5 mils/side (0.089 mm/side)

Negative No.: D-1097

Mount No.: 671-0

Figure 4-183. Microstructure of C-129Y/R-512E Creep Specimen in As-Coated Condition

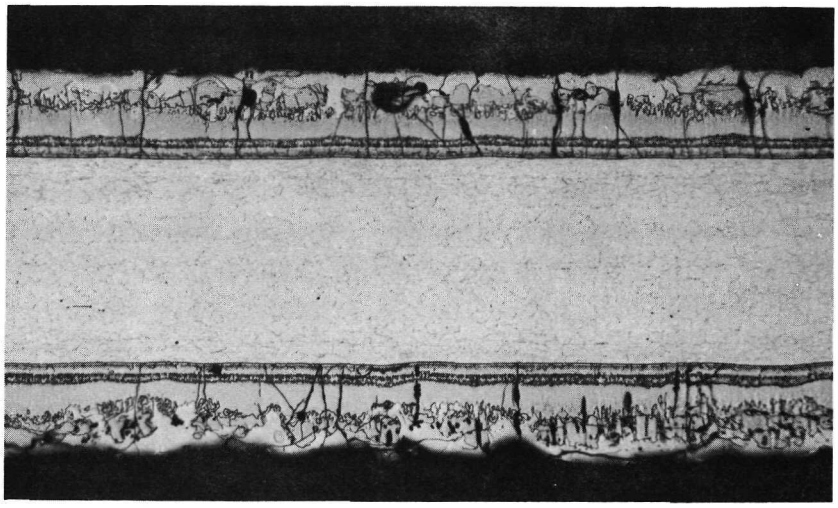

Magnification: 100X

Specimen No.: BSC 6

Section: Gage

Coating: 4.9 mils/side
(0.124 mm/side)

Negative No.: D-1105

Mount No.: 669-0

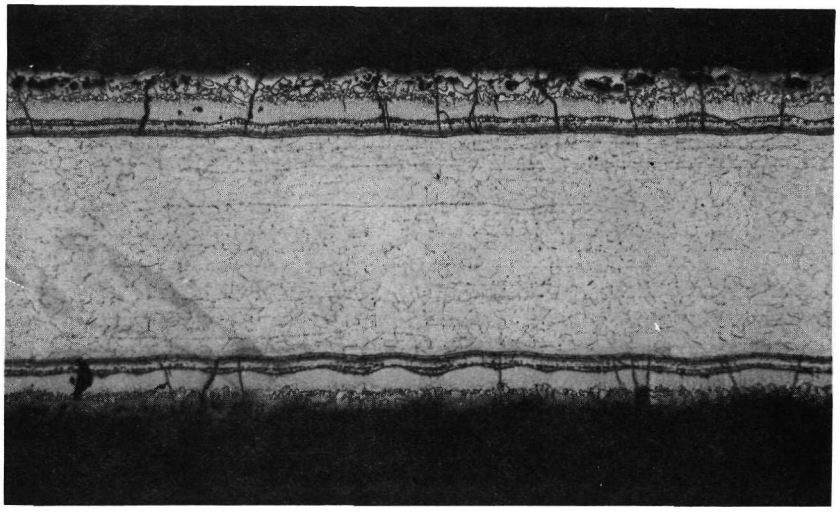

Magnification: 100X

Specimen No.: BSC 6

Section: Grip

Coating: 3.5 mils/side
(0.089 mm/side)

Negative No.: D-1103

Mount No.: 668-0

Figure 4-184. Microstructure of Cb-752/E-512E Creep Specimen in As-Coated Condition

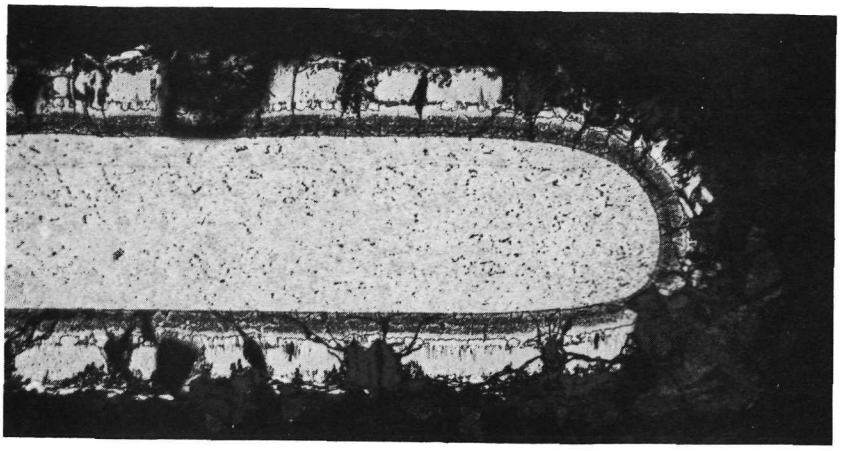

Magnification: 100X
Specimen No.: YSC 10
Temperature: 2000°F (1366°K)
Stress: 10 ksi (69 $MN/m^2$)
Time: 112 hr
Negative No.: D-1119
Mount No.: 689-0

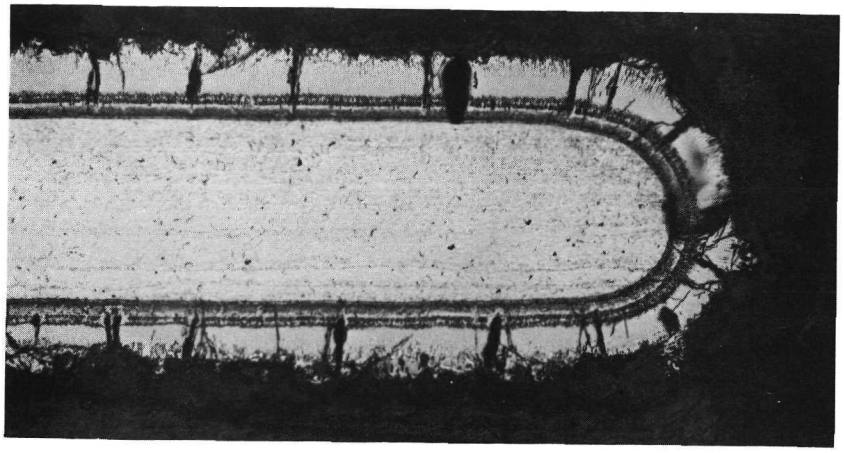

Magnification: 100X
Specimen No.: YSC 16
Temperature: 2200°F (1478°K)
Stress: 5 ksi (34.5 $MN/m^2$)
Time: 72 hr
Negative No.: D-1116
Mount No.: 688-0

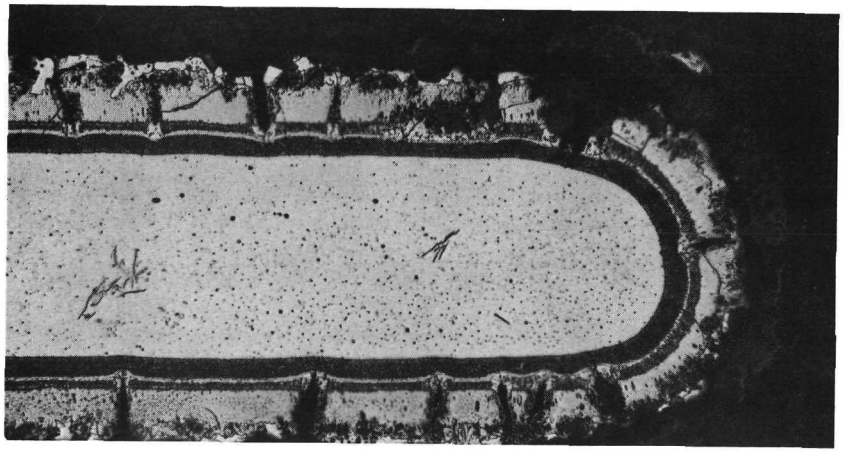

Magnification: 100X
Specimen No.: YSC 12
Temperature: 2400°F (1589°K)
Stress: 2 ksi (13.8 $MN/m^2$)
Time: 41 hr
Negative No.: D-1113
Mount No.: 687-0

Figure 4-185. Microstructure of C-129Y/R-512E Creep Specimens After Testing

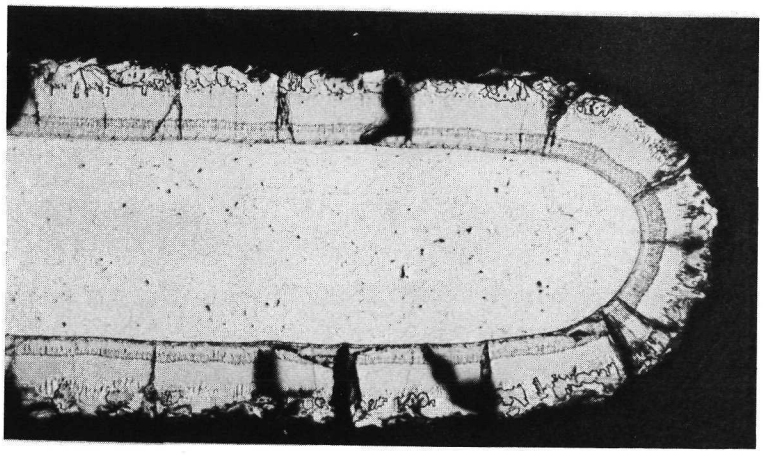

Magnification: 100X
Specimen No.: BSC 15
Temperature: 2000°F (1366°K)
Stress: 12.5 ksi (86.2 $MN/m^2$)
Time: 97 hr
Negative No.: D-1564
Mount No.: 34-P

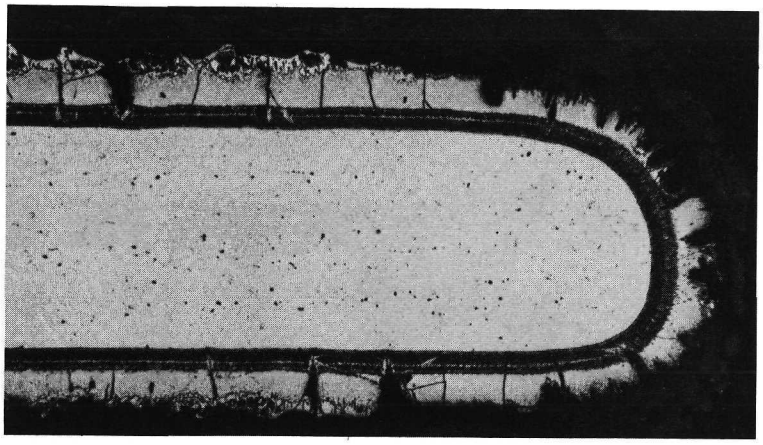

Magnification: 100X
Specimen No.: BSC 4
Temperature: 2200°F (1478°K)
Stress: 4 ksi (27.6 $MN/m^2$)
Time: 90 hr
Negative No.: D-1125
Mount No.: 691-0

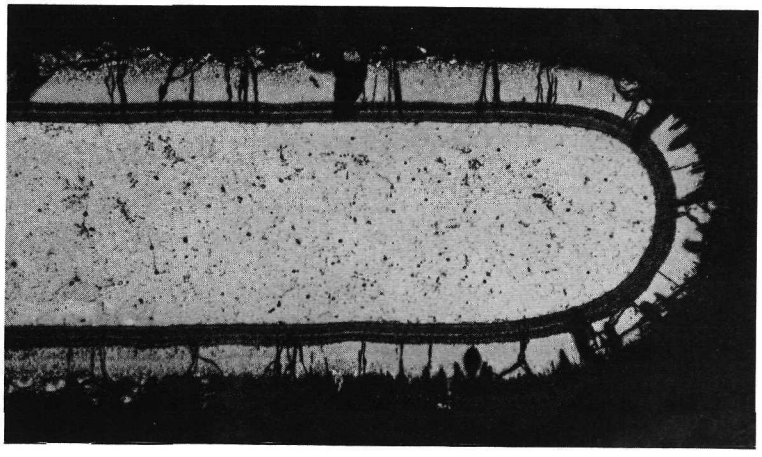

Magnification: 100X
Specimen No.: BSC 1
Temperature: 2400°F (1587°K)
Stress: 1.5 ksi (10.3 $MN/m^2$)
Time: 93 hr
Negative No.: D-1122
Mount No.: 690-0

Figure 4-186. Microstructure of Cb-752/R-512E Creep Specimens After Testing

The rate of substrate consumption with temperature is shown graphically in Figure 4-187. These limited data points appear to indicate a parabolic relationship as would be expected since substrate consumption is a diffusion controlled reaction.

Similar measurements and comparisons for the Cb-752/R-512E specimens showed poor correlation. Several inconsistent results were obtained that will require further studies to resolve. As previously discussed, the availability of test coupons coated in the same coating lot, as well as test coupons with a range of coating thicknesses would greatly assist in preparation of reliable Dermitron and micrometer calibration curves for establishing coating thickness, remaining substrate, and substrate consumption data.

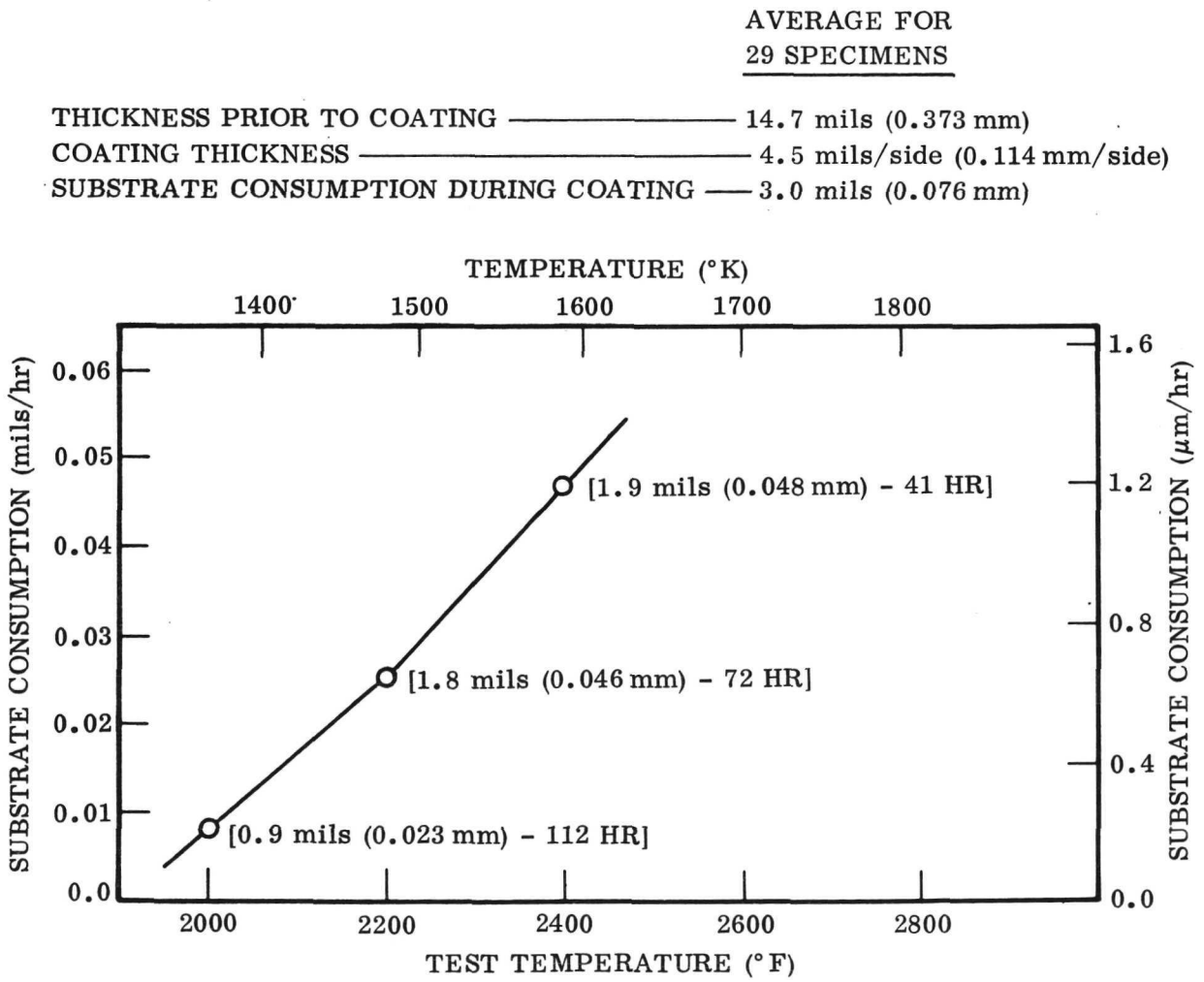


Figure 4-187. Substrate Consumption During Static Creep Testing of C-129Y/R-512E

4.5.4.5 Conclusions:

(1) An optical technique of strain measurement was used successfully to determine constant exposure creep properties for C-129Y/R-512E and Cb-752/R-512E systems at temperatures from 2000° F (1366° K) to 2400° F (1589° K) and times up to 100 hours.

(2) The test atmosphere of approximately 99 percent argon and 1 percent air was sufficiently oxidizing to cause formation of an oxide layer and some coating failures. The coating failures and subsequent oxygen diffusion resulted in substrate strengthening and a decreasing creep rate after about 30 hours at 2400° F (1589° K) for some creep tests. Results for 0.5 percent and 1 percent data were not significantly affected, but extrapolation of some 2400° F (1589° K) creep curves was necessary to obtain realistic 2 percent creep data.

(3) The coating thickness of the C-129Y/R-512E creep specimens was approximately 4.5 mils (0.114 mm)/side in the gage section, and 3.5 mils (0.089 mm)/side in the grips as determined by micrometer, Dermitron, and metallographic measurements. The Cb-752/R-512E specimens had similar coating thicknesses. The specified coating thickness was 3.0 mils (0.076 mm)/side, but the thicker coating on the creep specimens should not have a significant effect on the creep data.

(4) Coating specifications that provide for an optimum coating thickness and standardized procedures for measuring and specifying coating thickness are needed for maximum usefulness of data developed for coated columbium hardware.

(5) Columbium alloy coupons should accompany each coating batch for use in coating qualification, and as standards for calibration of NDT equipment used for determining coating thickness and substrate consumption.

(6) Additional creep testing and metallurgical studies of C-129Y/R-512E and Cb-752/R-512E are needed to provide truly representative creep data and resolve the several data inconsistencies observed in the reported creep tests.

## 4.6 Nondestructive Evaluation (NDE)

4.6.1 Pre-coating. — Ultrasonic C-scan and transmission radiography were used to evaluate all base metal joints in the sheet material prior to the machining of tensile specimens. Specimens were machined from defect-free material based on the indicated uniformity of diffusion bonds and electron beam welds. Areas containing minor defects were reworked for additional specimens.

4.6.2 NDE As-coated. — Thermoelectric testing and stimulated-electron emission radiography were used on all coated specimens for evaluating coating thickness on edges and for determining the uniformity of the coatings respectively. In addition, eddy-current testing was performed on all static creep specimens as a backup to mechanical measurement of coating thickness to assist the analysis of creep data.

4.6.2.1 Thermoelectric testing: A thermoelectric test was devised to measure coating thickness along the edges of the specimens. The test apparatus comprised a 40-watt heating element with a stainless steel tip to which a thermocouple and lead wire were attached by resistance welding. The heating element contained a thermostat with rapid feedback control. Thermocouple wires, inputed to a potentiometer during operation of the device, showed the temperature at the stainless steel tip to be about 617°F (598°K) with regulation within ±1 percent. A wire coil served to radiate the heat from the hot junction to ambient temperature for lead input to a high-impedance microvoltmeter. A second lead wire (cold junction) from the meter input (ground) was connected to a stainless steel plate on which the test specimen was placed. (See Figure 4-188.)

Each coated specimen was stationed at 0.50-inch (1.27 cm) increments around its periphery for evaluation by the thermoelectric test. A numbering system was established using the specimen identification mark as reference for correlating radiographic indications and/or oxidation damage. The thermoelectric response was displayed and simultaneously recorded to provide a permanent record. (See Figure 4-189.)

4.6.2.2 Stimulated electron-emission radiography: Electron-emission radiography (EER) was performed on all flight simulation specimens prior to thermal cycling. The technique employs two single-coated Kodak Type R X-ray films between which the specimens are placed. Electrons ejected from the columbium substrate, and/or the coating itself for the case of the higher average atomic number VH-109 coating, are captured in the film emulsion in proportion to their exit energy. A polyurethane bag is placed around a light-proof envelope (cassette) containing the film/specimen sandwich. Intimate contact between film and specimen is achieved by drawing a vacuum on the envelope.

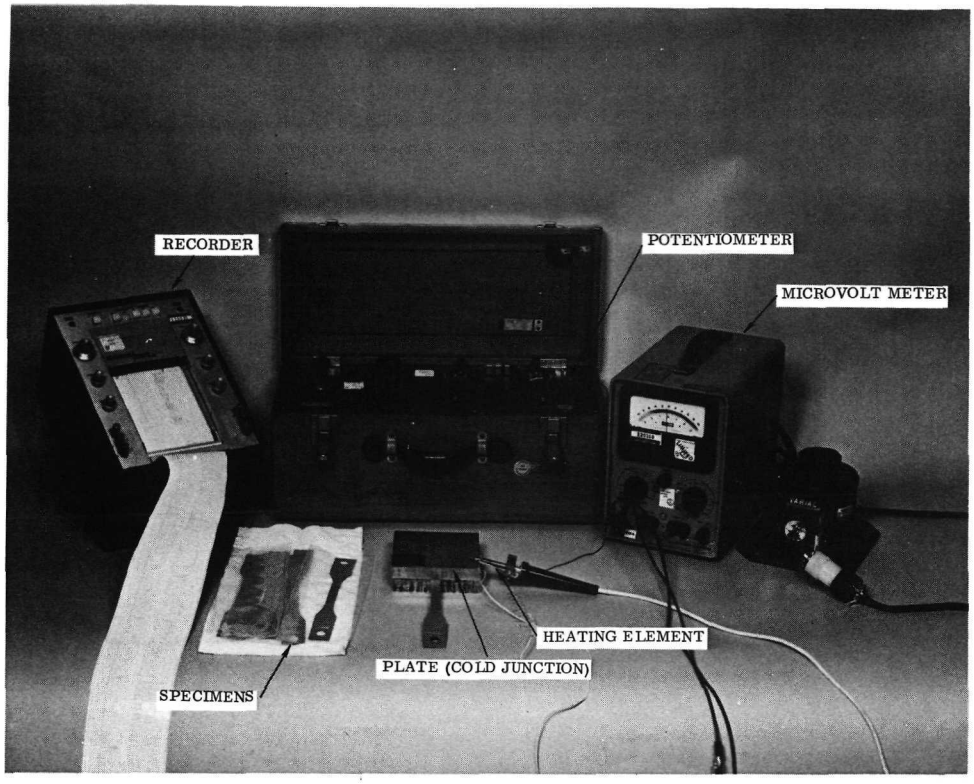


Figure 4-188. Thermoelectric Test Instrumentation

Exposures were made using a bombarding X-ray energy of approximately 0.3 $MeV_{max}$. A 0.010-inch (0.025 cm) lead filter was placed between the specimen and radiation source to reduce the amount of low-energy X-rays to which the film is highly sensitive. Radiographs showing the relative uniformity of the coating were produced using both forward and back-emission electrons captured by the film. (See Figures 4-190 and 4-191.

4.6.2.3 Eddy current (Dermitron): Eddy currents were used for determining as-coated thickness to assist in developing creep stress levels based on metal consumption. Initial calibration of the eddy current instrument was accomplished with one to six layers of 0.001-inch (0.00254 mm) thick Mylar film placed on an uncoated specimen.

Metallographic measurements of coating thickness were used to prepare calibration curves for each substrate/coating material system. The latter calibration curves were used to convert the eddy current readings to coating thickness. Eddy current readings were made at five locations on both sides of each specimen — three readings in the

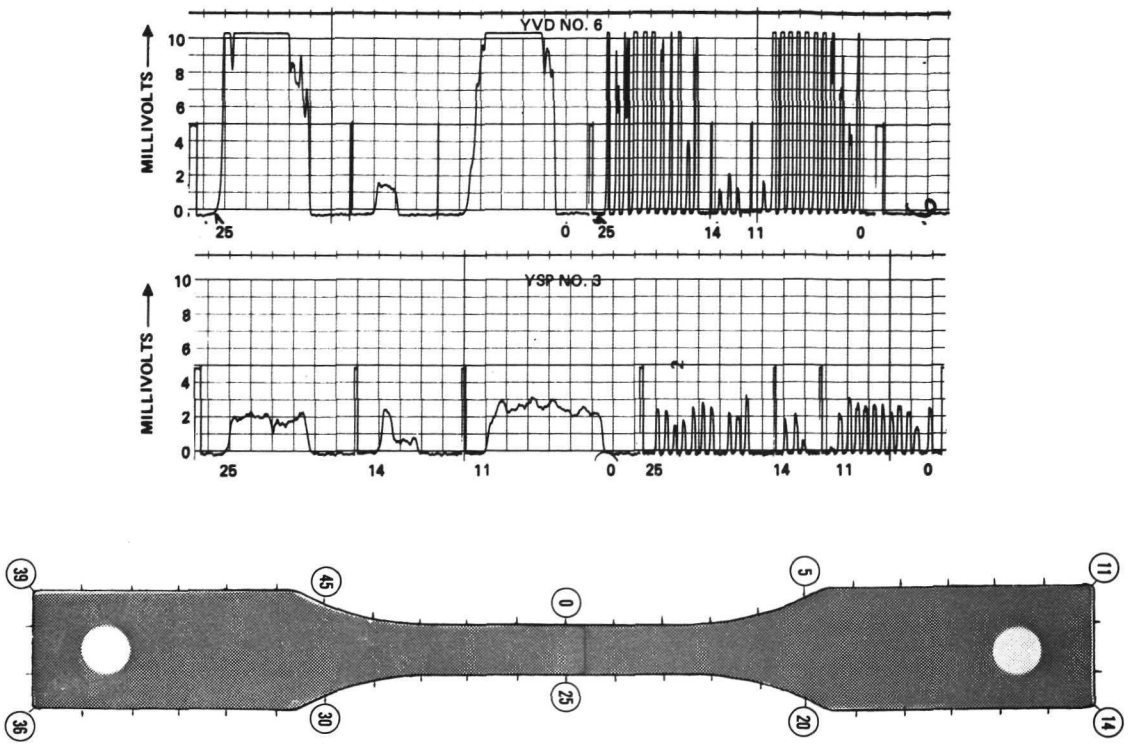


Figure 4-189. Thermoelectric Recordings Showing Coating Variation Between Specimen Lots

gage section and one at each grip end. The average reading in the center of each gage section was compared with the results of micrometer measurements.

4.6.2.4 As-coated NDE summary: Evaluation of the as-coated specimens by EER and thermoelectric testing showed the R-512E coating to be generally more uniform than the VH-109 coating applied during Phase I. A comparison of the data from the two coatings is shown in Figure 4-192. Note the varying film density (mottling) in the EER radiograph and the corresponding erratic thermoelectric reading from the VH-109 coating (right). Poor dispersion of coating modifiers is evident from the gray tones in the radiograph and range of the thermoelectric response (e.m.f.). Electron emission radiographs showing the relative uniformity of typical test specimens are shown in Figures 4-193 through 4-200.

The results of eddy current measurements to assist static creep properties determination are reported in Section 4.5.4.3. While it was not determined to what extent conductivity of the coating would affect the accuracy of the test, the equivalent Mylar thicknesses indicated were within the expected coated thickness range. Although comparison between the eddy current data and the results of thermoelectric tests

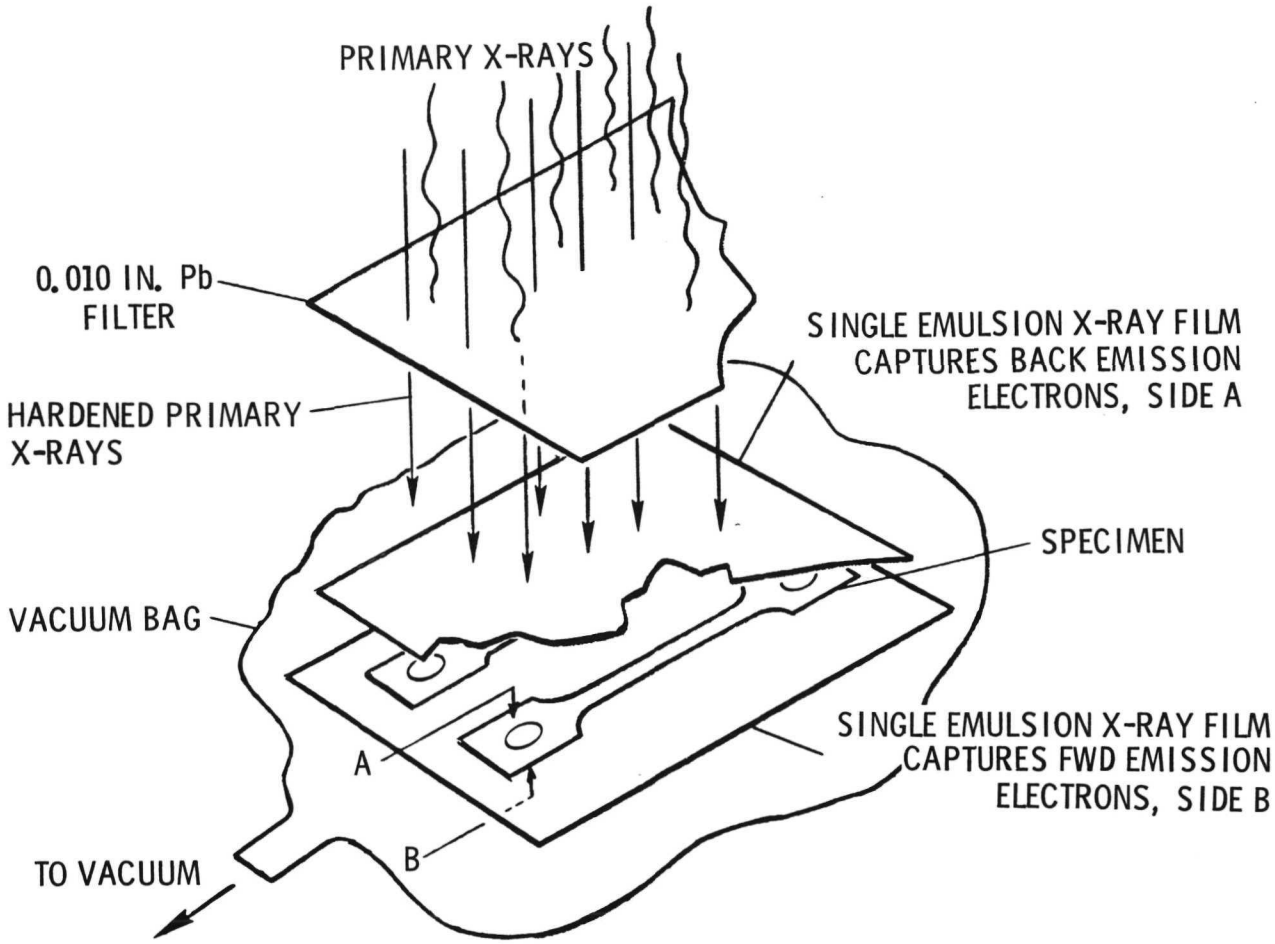


Figure 4-190. Setup for Stimulated Electron-Emission Radiography

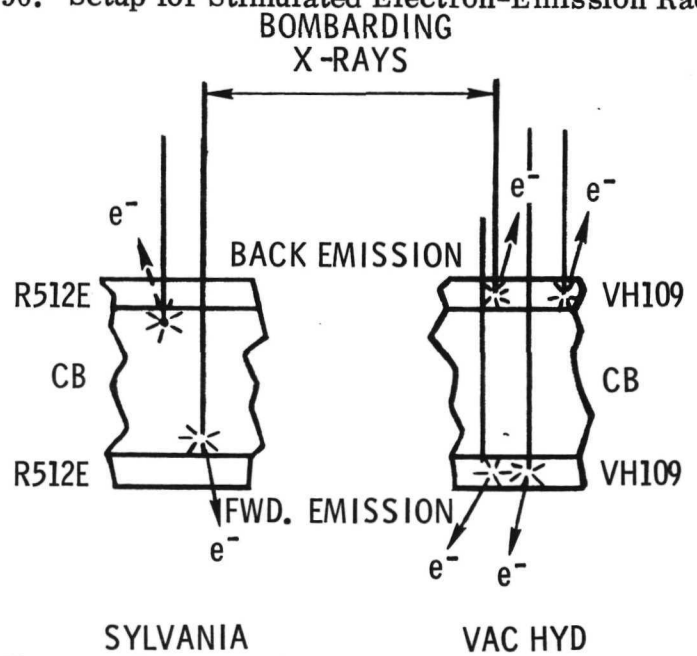


Figure 4-191. Mechanics of Electron Emission

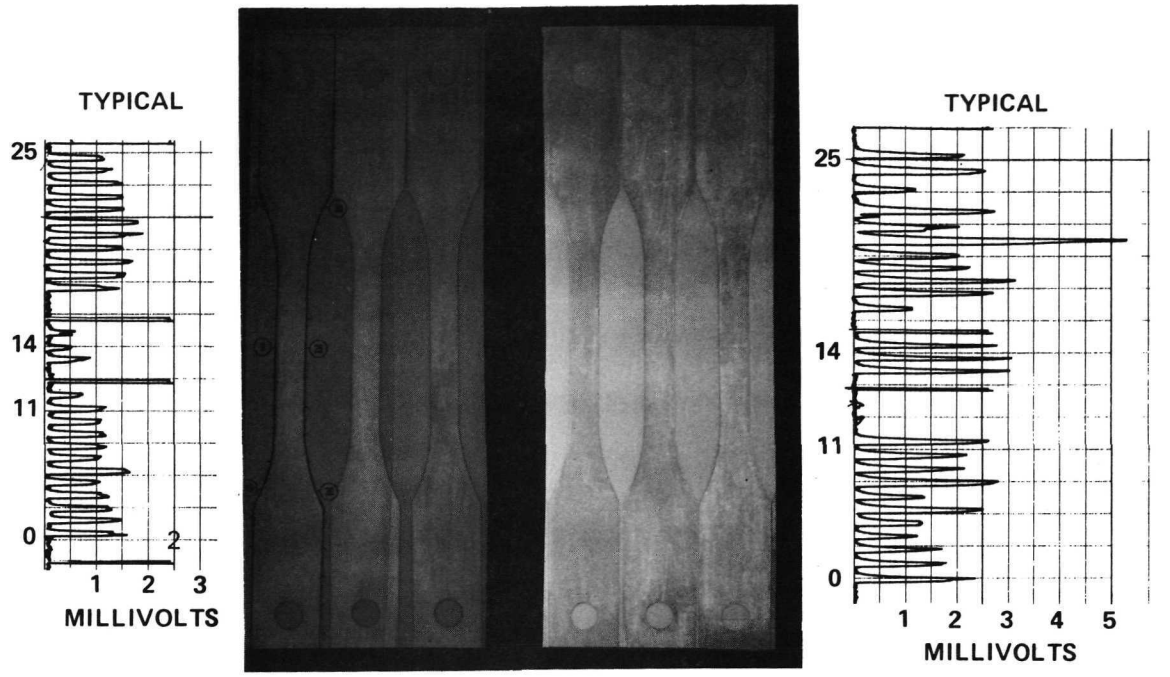


Figure 4-192. Electron-Emission Radiographs and Thermoelectric Recordings Showing Uniformity of Coating Interior and Edges Respectively

(Figure 4-201) shows general agreement between the indicated changes in coating thickness, standards would normally be required for each thickness and type (chemistry) of coating to be tested. The eddy current work done on this program was without the aid of such standards, which are intended only as a backup to direct coating thickness determinations based on the average measured increase in specimen thickness following coating.

4.6.3 Intermediate and postflight simulation test NDE. — Electron-emission radiography was performed on all flight simulation specimens following 10, 20, and 50 cycles and at the completion of thermal cycling. The results were compared with the initial thermoelectric and electron-emission data. Neither thermoelectric nor eddy current testing was performed on the thermally cycled specimens since neither test produces useable data on exposed specimens. (The nonconductive surface oxide prevents application of thermoelectric testing following high-temperature oxidation exposure. Eddy current testing is also affected by oxidation of the coating as well as interdiffusion of coating/substrate constituents; while eddy current testing may be performed following thermal exposure, a technique has not been developed to correct for these effects.)

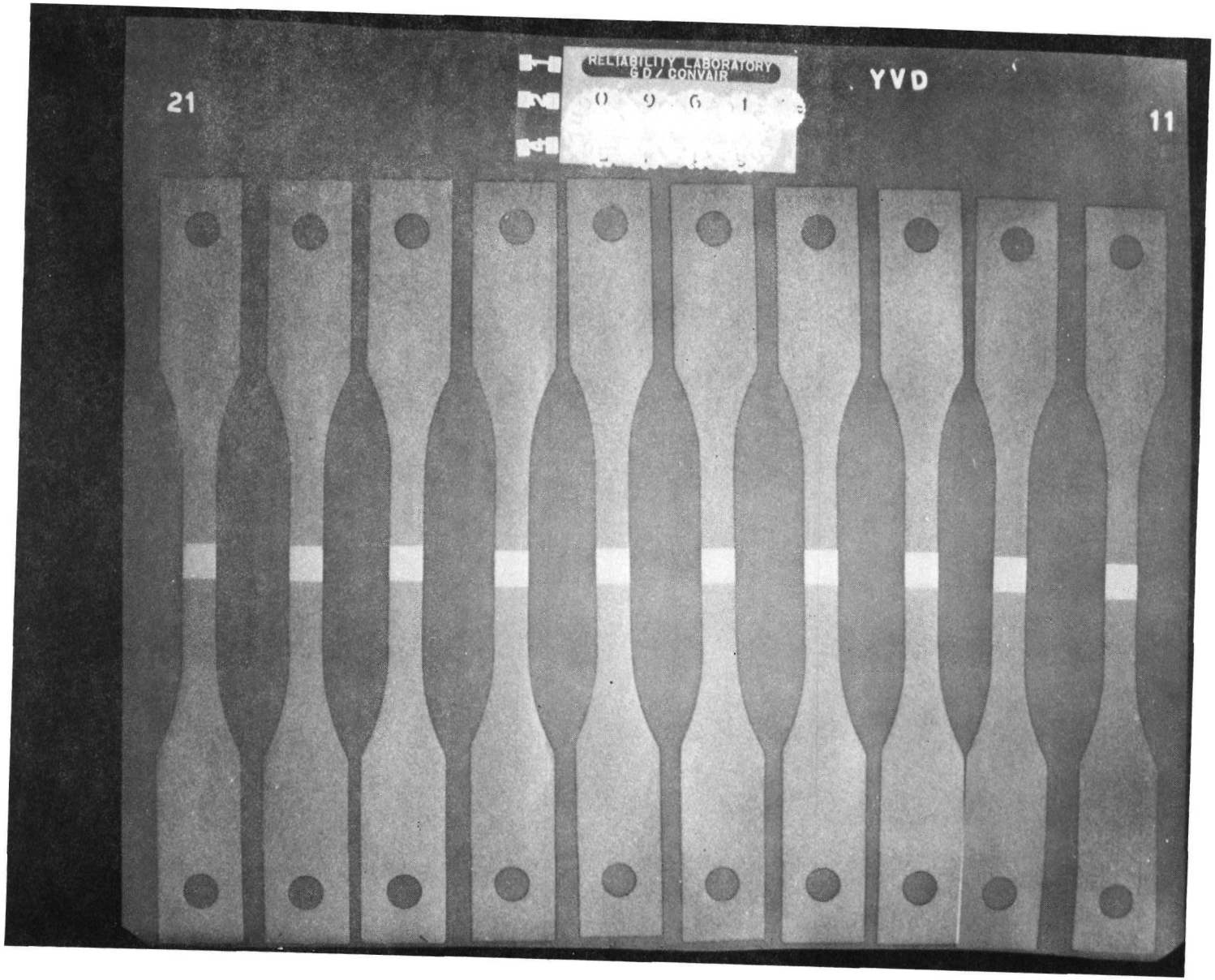


Figure 4-193. Electron Forward-Emission Radiograph, YVD Series

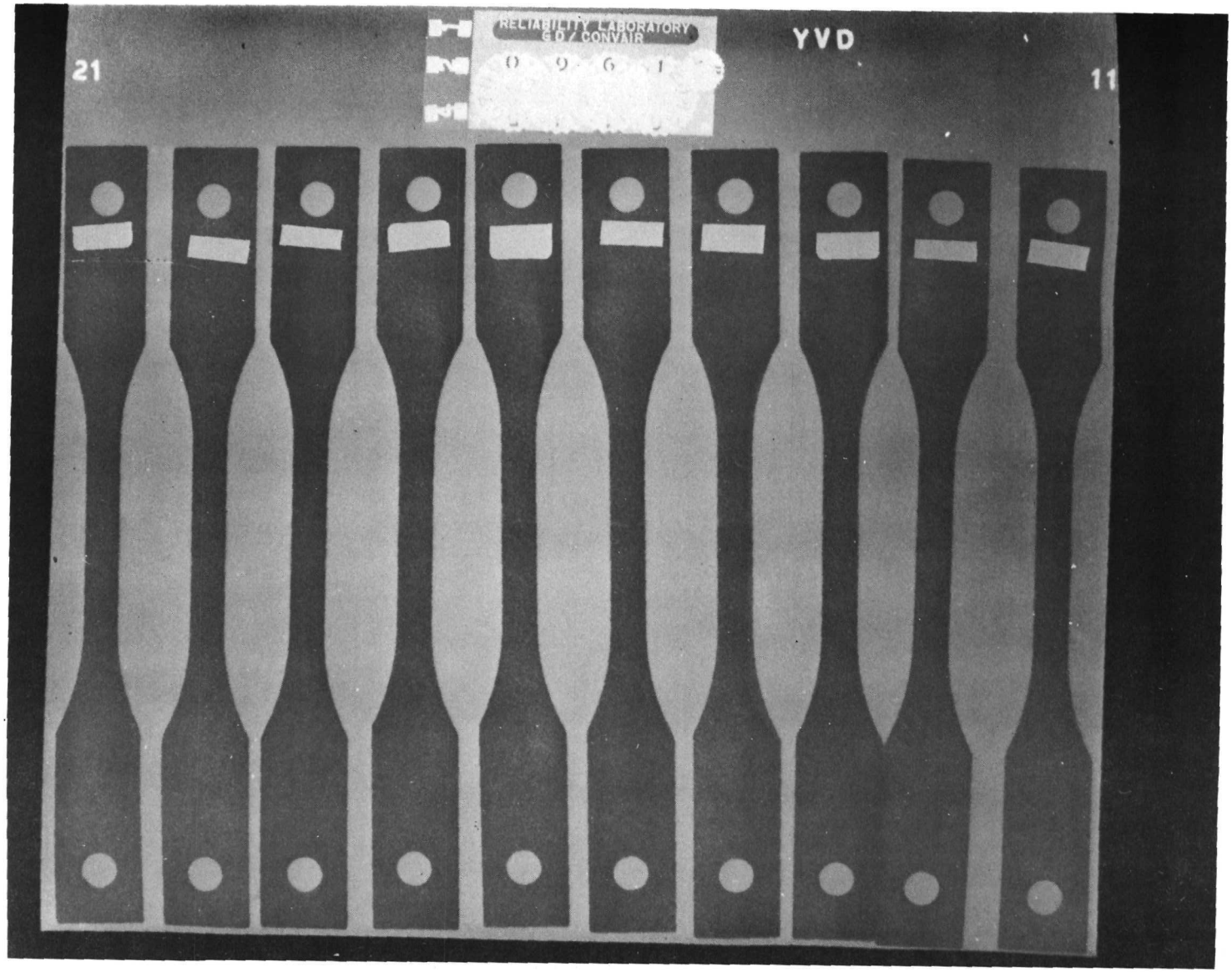


Figure 4-194. Electron Back-Emission Radiograph, YVD Series

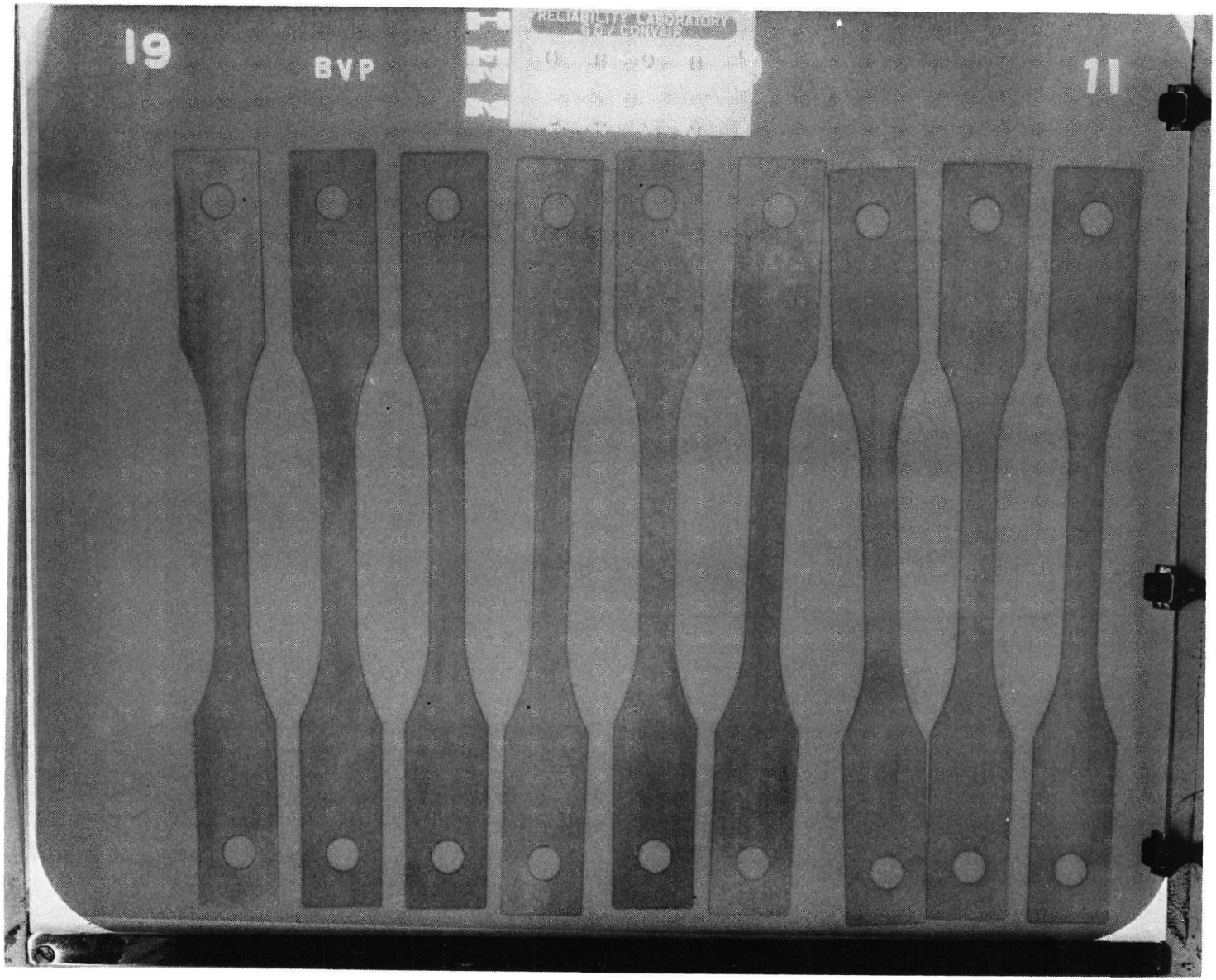


Figure 4-195. Electron Forward-Emission Radiograph, BVP Series

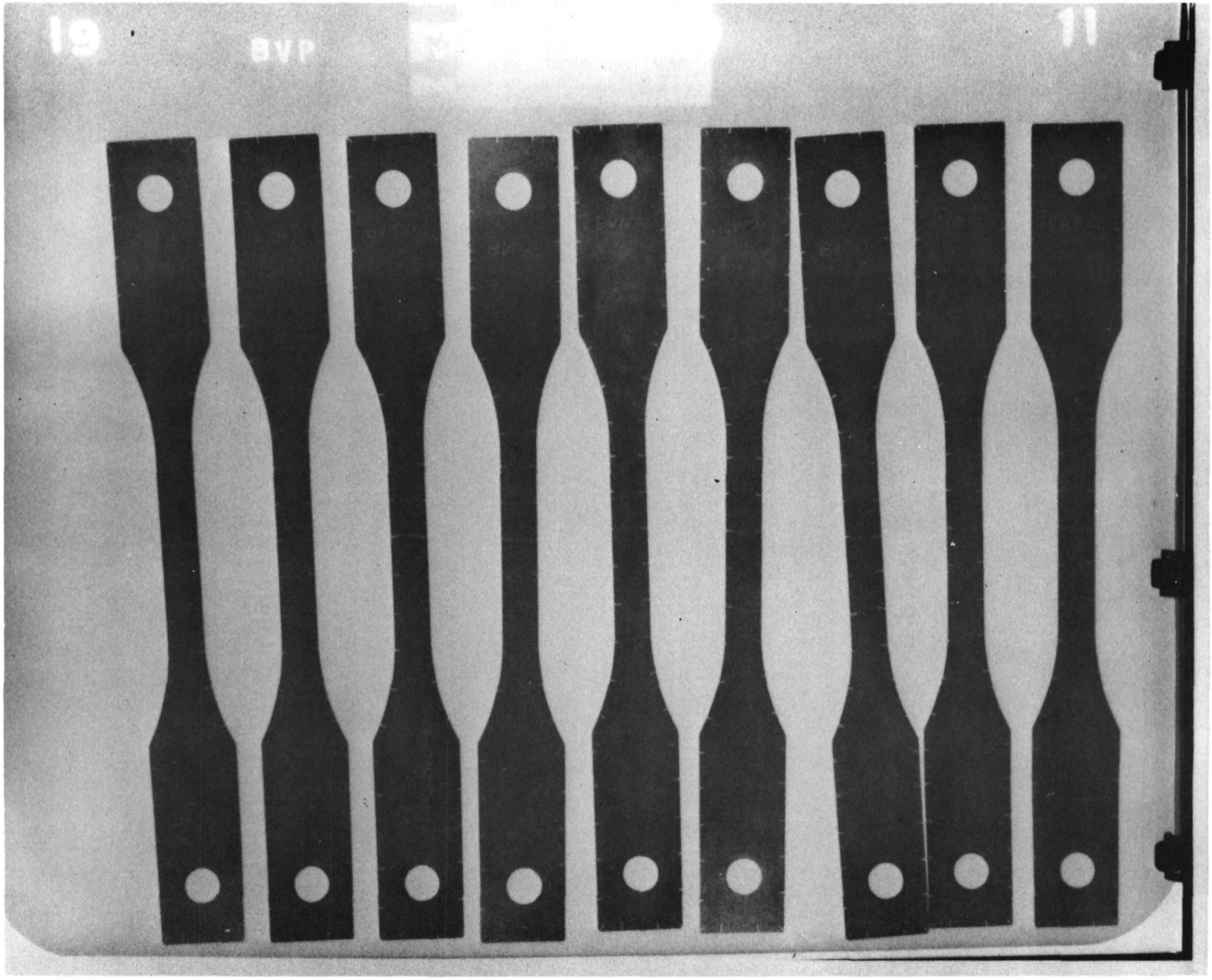


Figure 4-196. Electron Back-Emission Radiograph, BVP Series

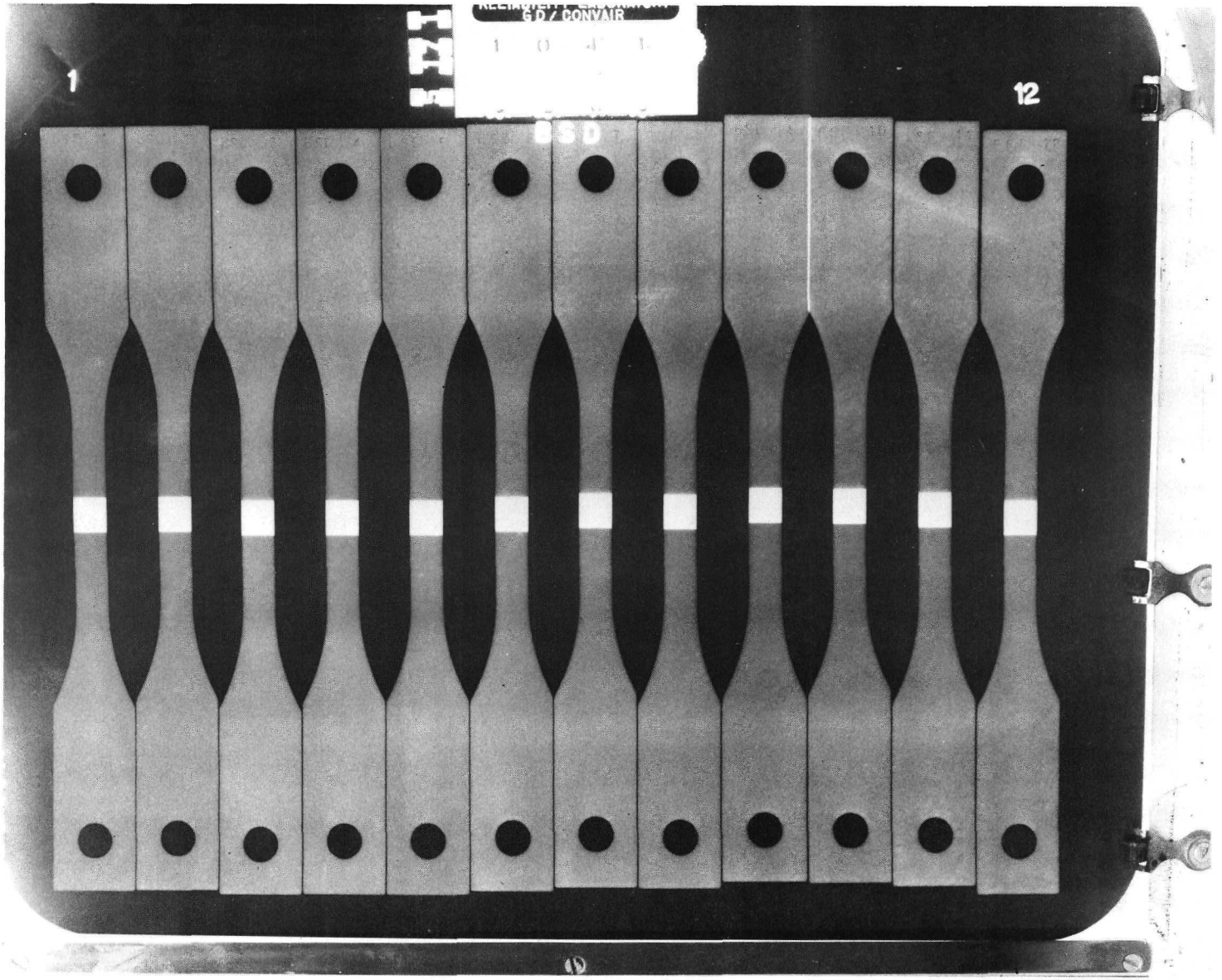


Figure 4-197. Electron Forward-Emission Radiograph, BSD Series

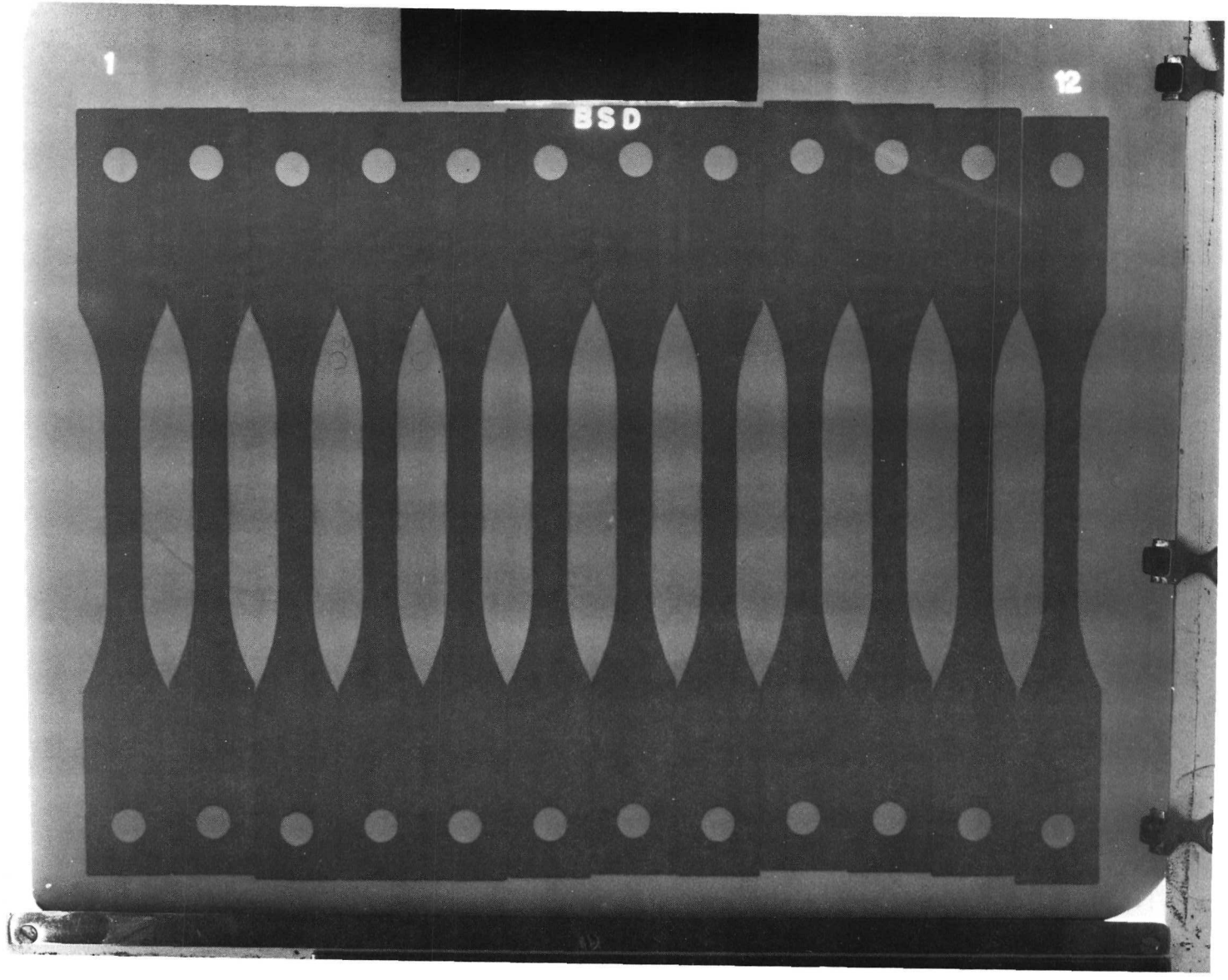


Figure 4-198. Electron Back-Emission Radiograph, BSD Series

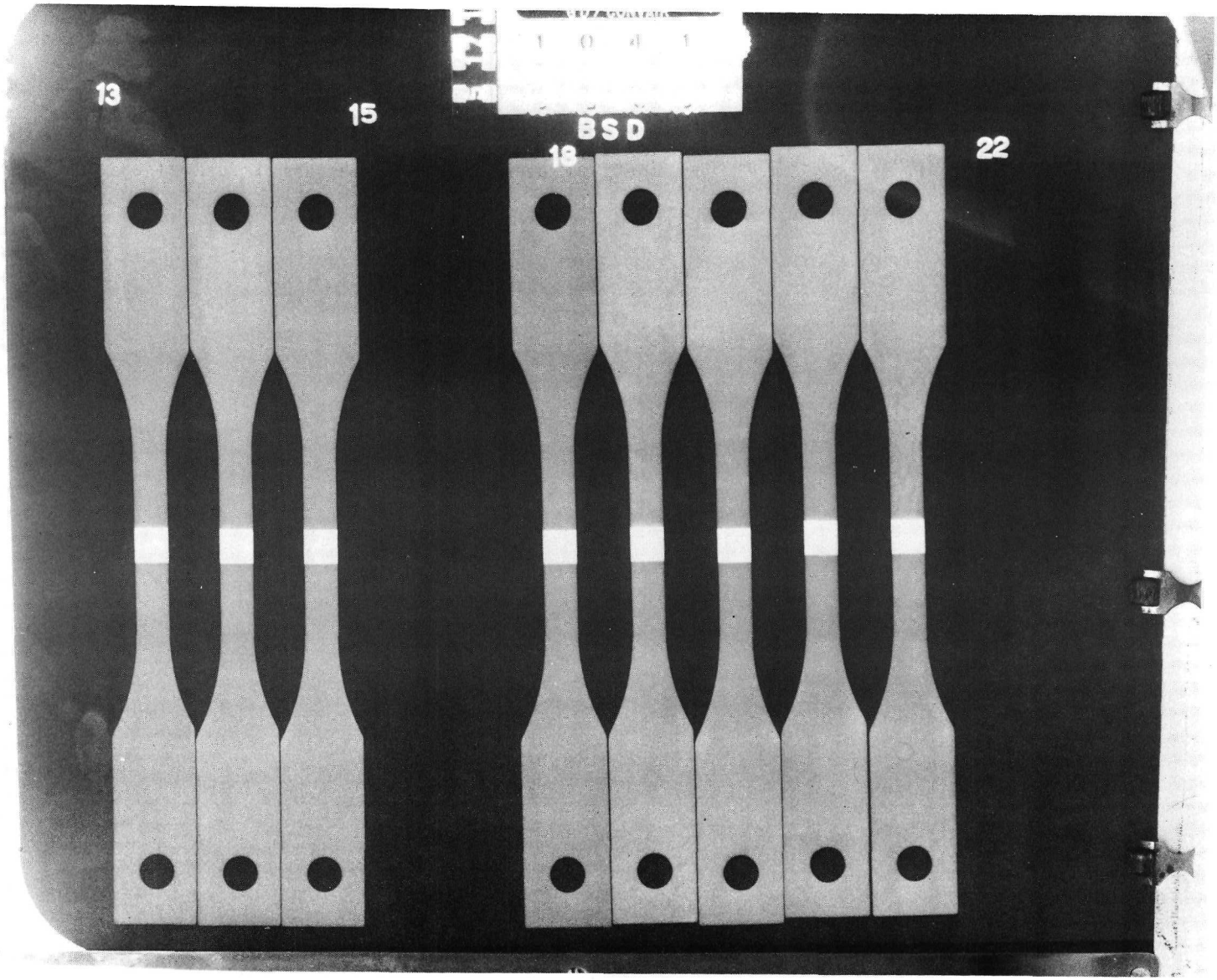


Figure 4-199. Electron Forward-Emission Radiograph, BSD Series

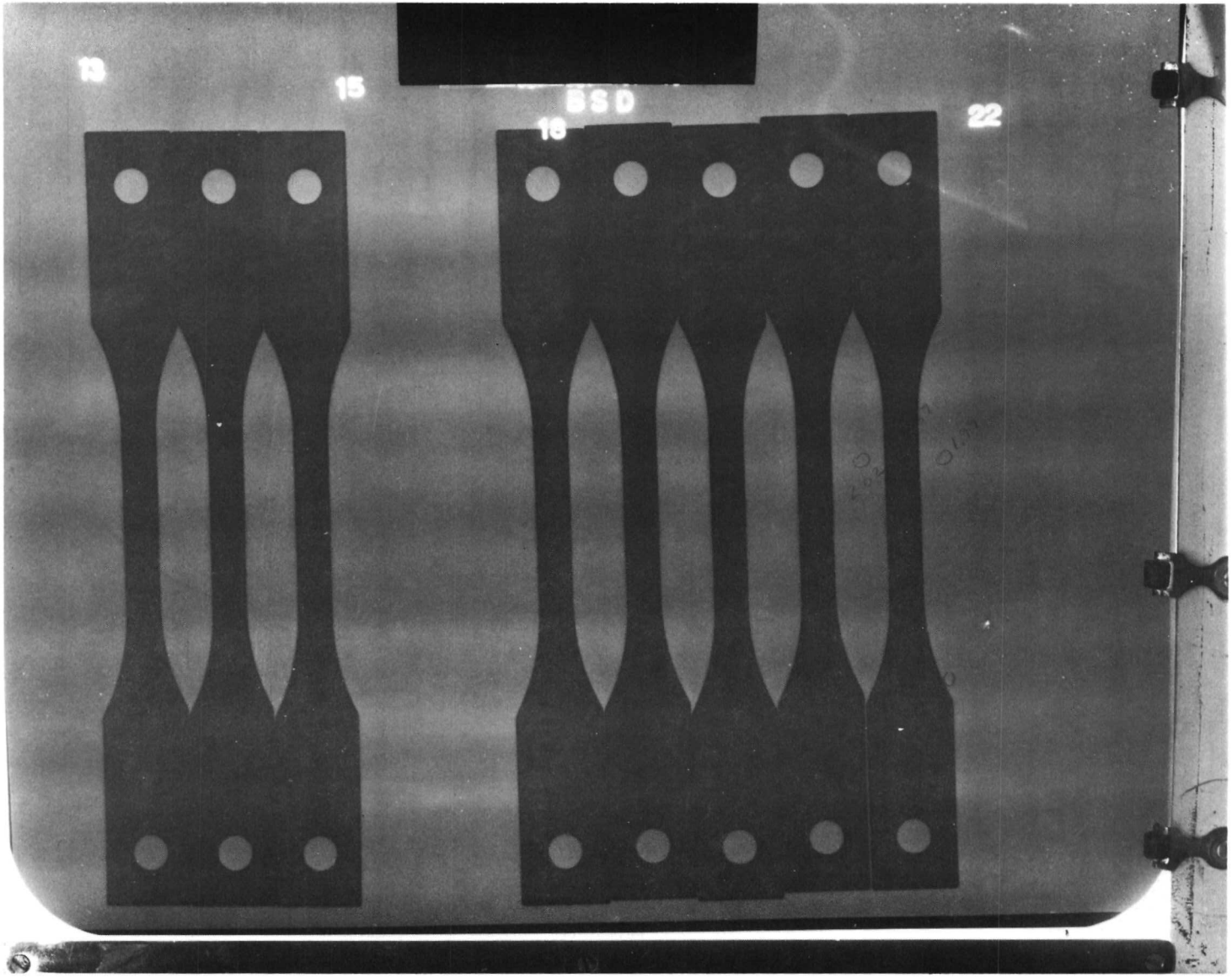


Figure 4-200. Electron Back-Emission Radiograph, BSD Series

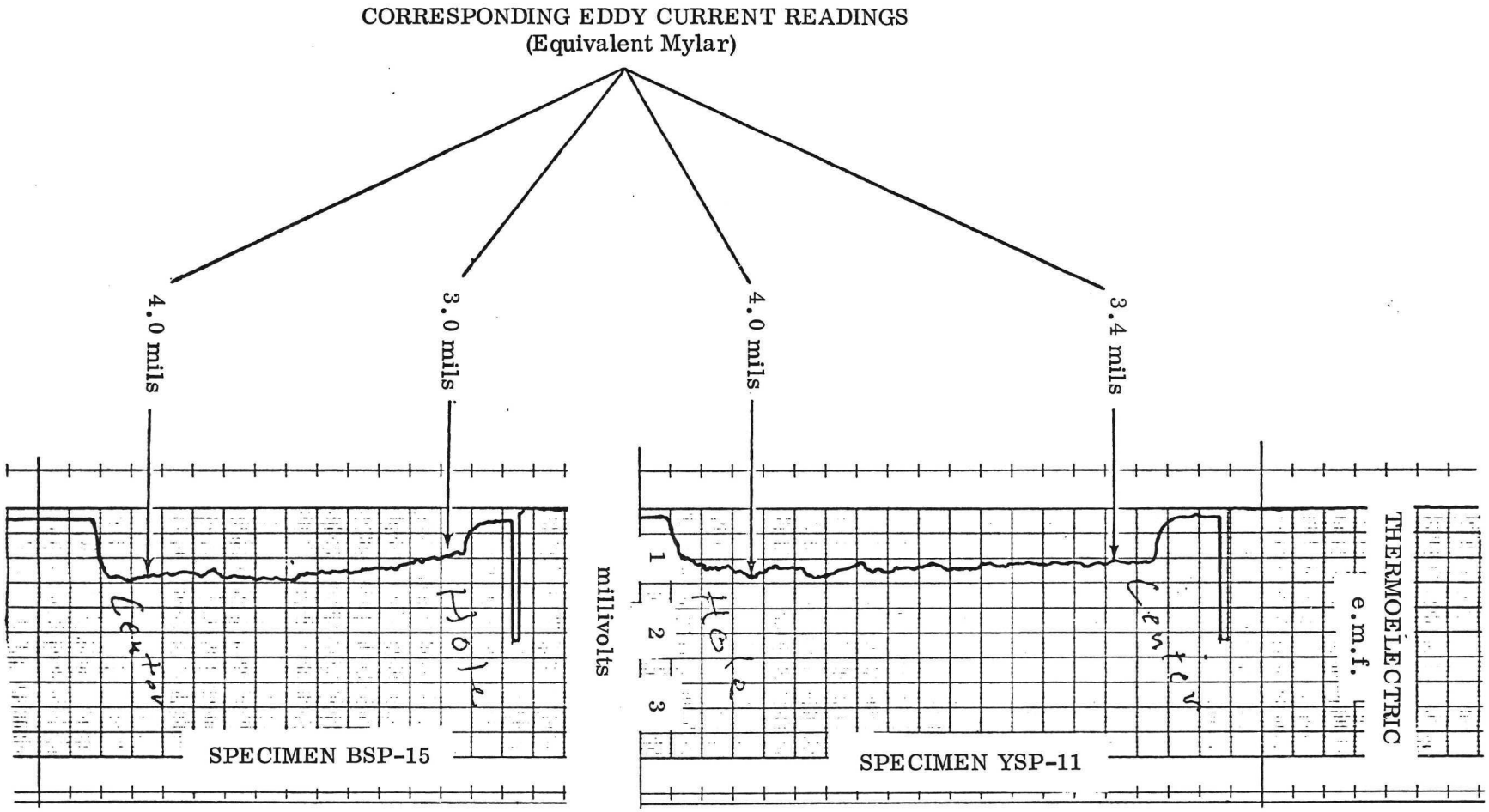


Figure 4-201. Thermoelectric Versus Eddy Current Readings Showing Variation in Coating Thickness

While abnormal or defective coatings were purposely not subjected to flight simulation, local attack frequently occurred without evidence of incipient coating failure. However, a relationship does exist between the general uniformity of the coating and coating life. Figures 4-202 and 4-203, electron-emission and thermoelectric test data, show the coating uniformity of two VH-109 specimens, YVP-1 and BVD-3, which survived 100 and 44 cycles, respectively. For specimen YVP-1, low values of the thermoelectric e.m.f. and uniform darkening of the radiographic image can be observed. The corresponding NDE data from specimen BVD-3 is by comparison erratic and nonuniform.

Electron-emission radiography of the R-512E coated specimens showed light spallation of the coating throughout the test life without consequence. Edge errosion when it occurred was very apparent from the radiographs and the behavior of the coating was easily analyzed. It was observed that spalling of the VH-109 coating resulted in a light image corresponding to the coating remainder whereas the equivalent spall from the R-512E coating produced a dark image. An analysis of the physics associated with the electron image suggested that high atomic number constituents of the VH-109 coating were concentrating at the outer surface of the coating and were progressively spalled as a single layer during cycling. Spectrographic analysis showed the spall material to be hafnium and tantalum; the coating remainder was predominantly silicon.

Figures 4-204 through 4-209 show electron-emission radiographs of selected coated tensile specimens following various cycles of flight simulation. The performance of the coatings is more easily analyzed from the radiographs than by observation of the surface of the coatings using reflected light. A loss of the R-512E coating material, e.g., coating spall, extends the range of photoelectrons otherwise trapped by the coating — resulting in measurable ionization (film blackening) in the X-ray emulsion. For the case of the VH-109 coating, high atomic number modifiers, i.e., hafnium and tantalum, are the primary source of these electrons. Loss of major coating constituents is easily recognized from the electron images produced.

The results of the thermoelectric tests show marked variation in the chemistry of the VH-109 coating system whereas the chemistry of the R-512E coating is consistent and uniform. However, there is no discrete correlation between the thermoelectric readings and the location of edge erosion during thermal cycling. Areas lacking apparent attack in the VH-109 specimens frequently produced identical thermoelectric response as areas exhibiting edge erosion.

4.6.4 Conclusions. — The results of nondestructive evaluation indicate that incipient coating breakdown cannot be detected by conventional NDE techniques. However, uniformity of the coating directly related to coating life is reportable by these

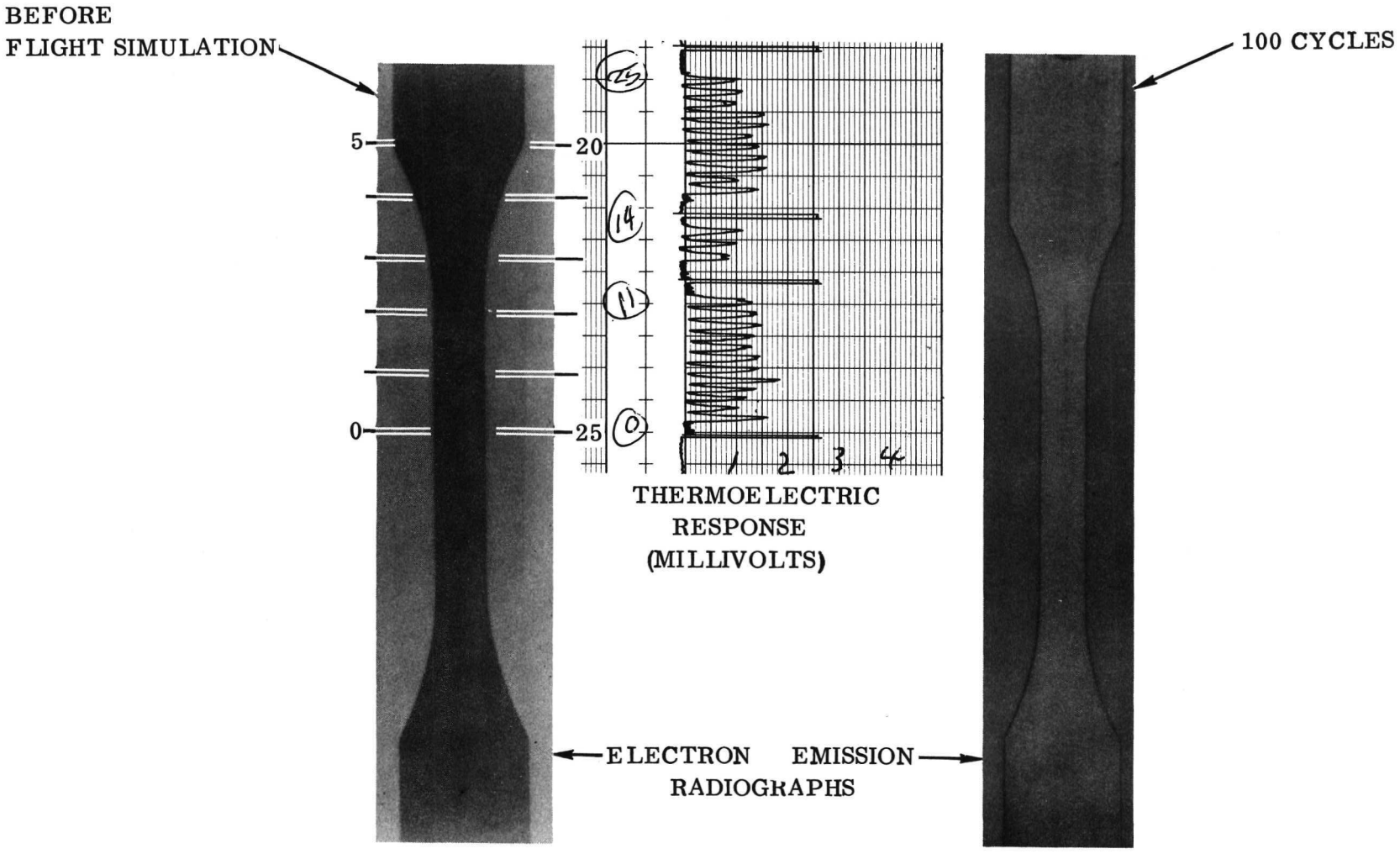


Figure 4-202. Comparison of NDE Data and Coating Performance, Specimen YVP-1

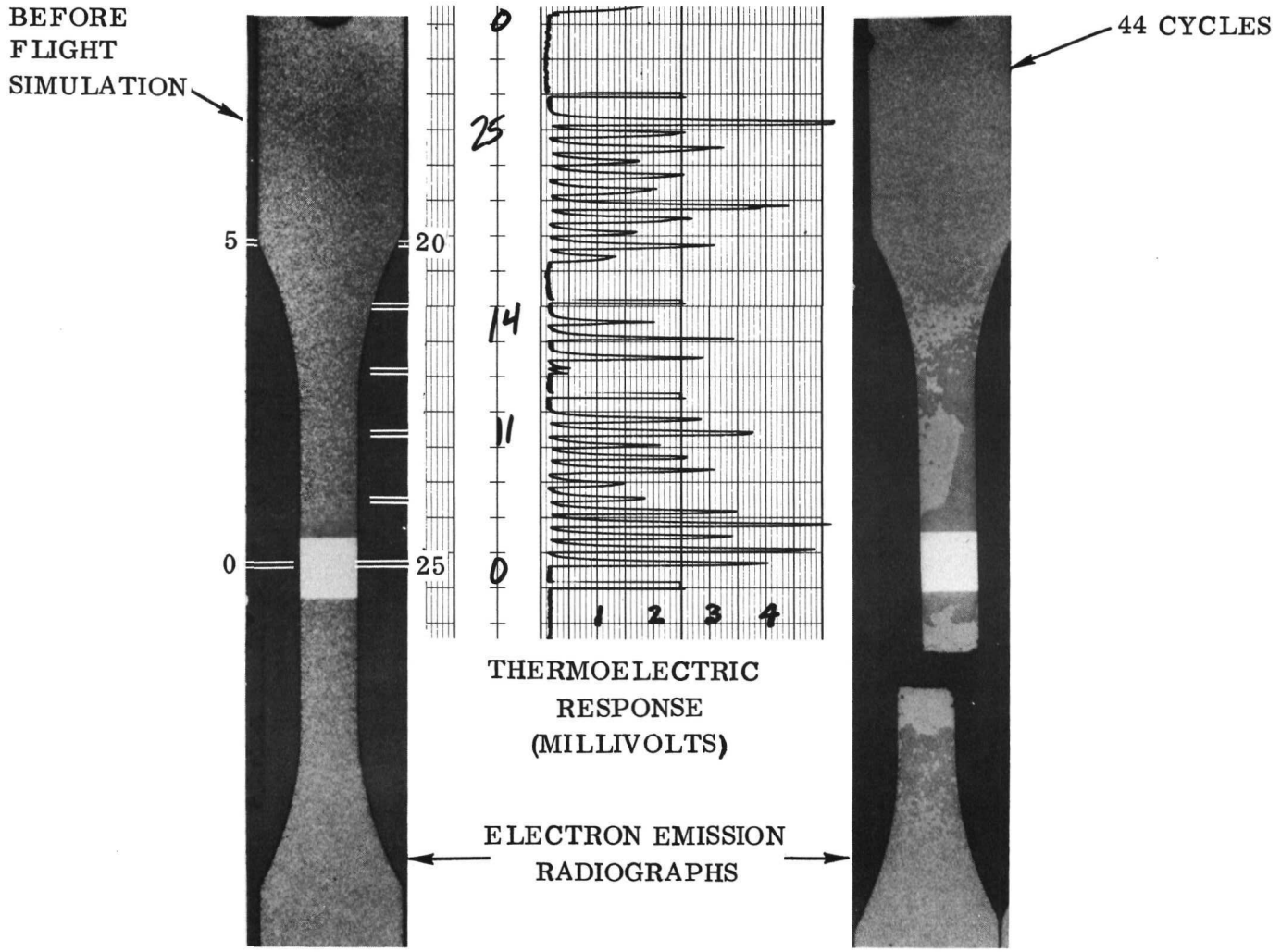


Figure 4-203. Comparison of NDE Data and Coating Performance, Specimen BVD-3

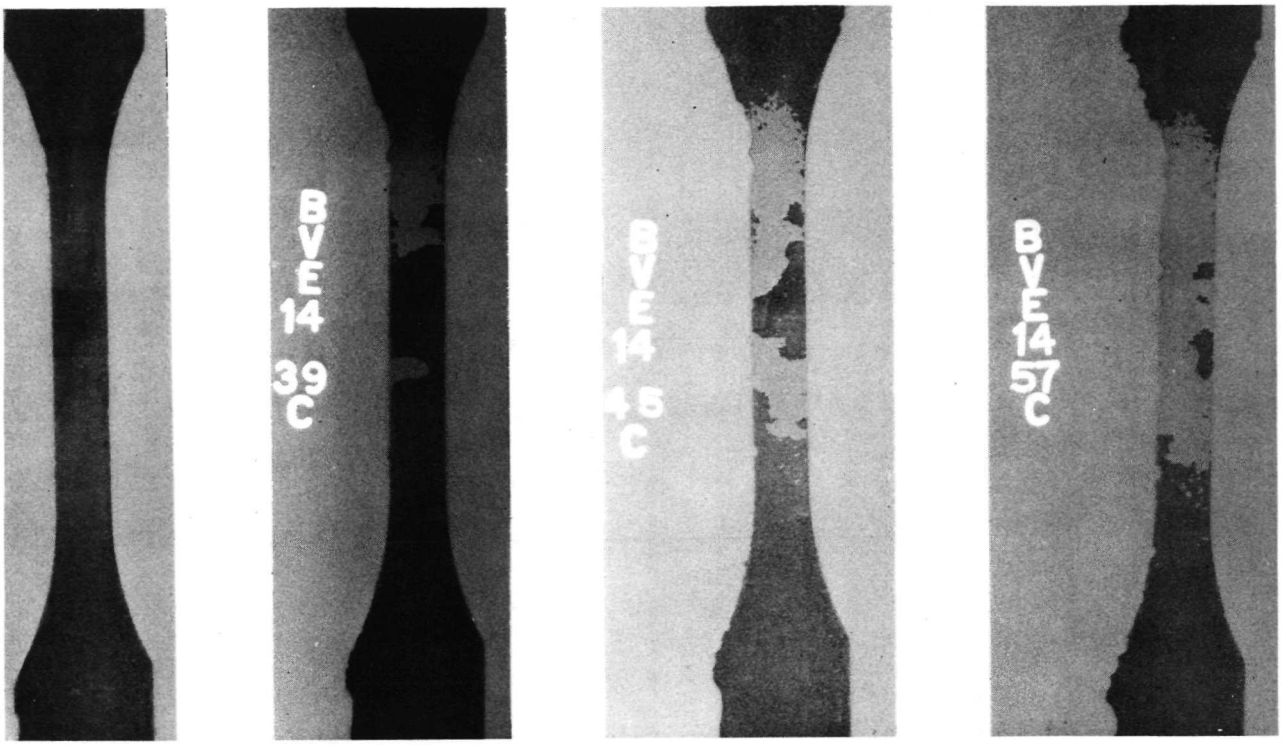


Figure 4-204. Electron-Emission Radiographs Through 57 Flight Simulation Cycles, Specimen BVE-14

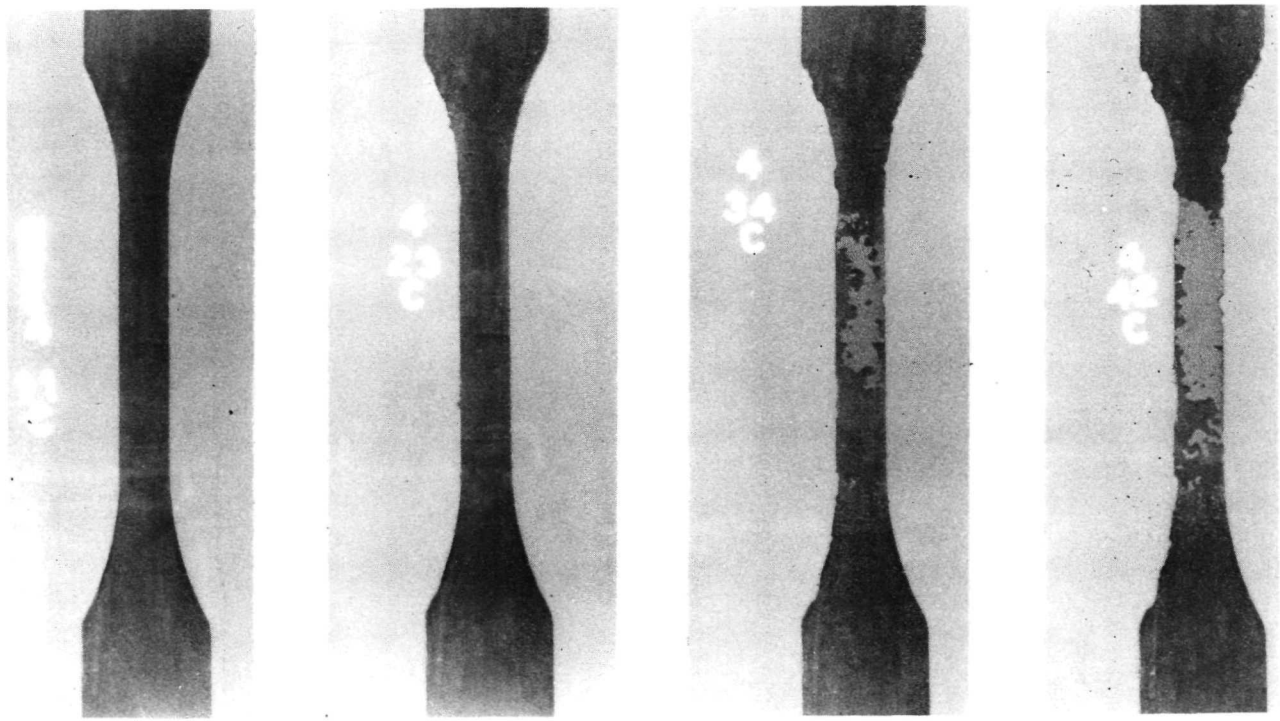

Figure 4-205. Electron-Emission Radiographs Through 42 Flight Simulation Cycles, Specimen BVE-4

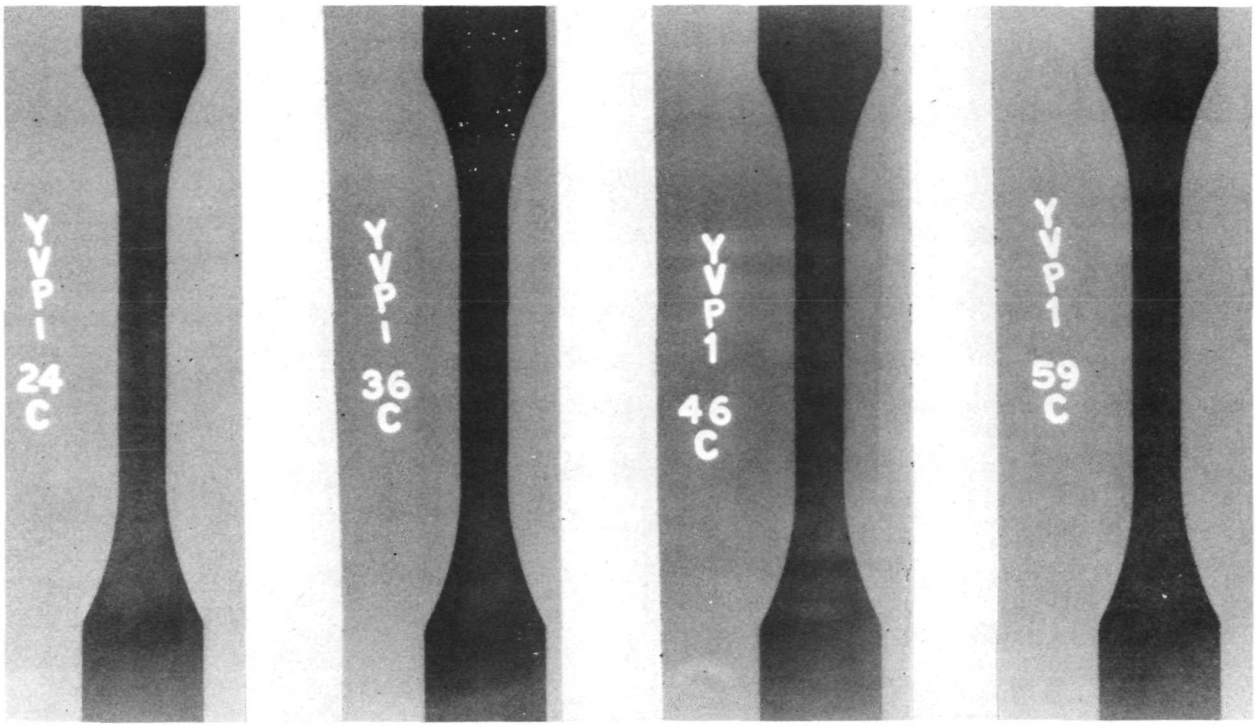


Figure 4-206. Electron-Emission Radiographs Through 59 Flight Simulation Cycles, Specimen YVP-1

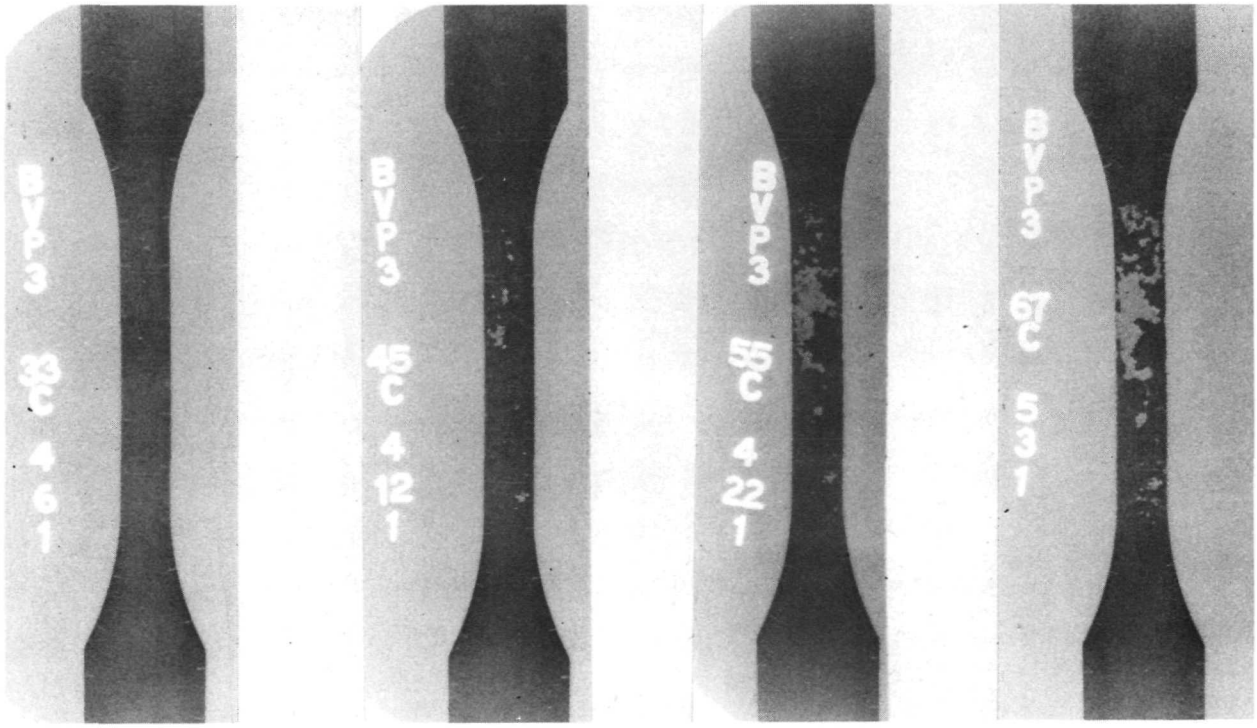


Figure 4-207. Electron-Emission Radiographs Through 67 Flight Simulation Cycles, Specimen BVE-3

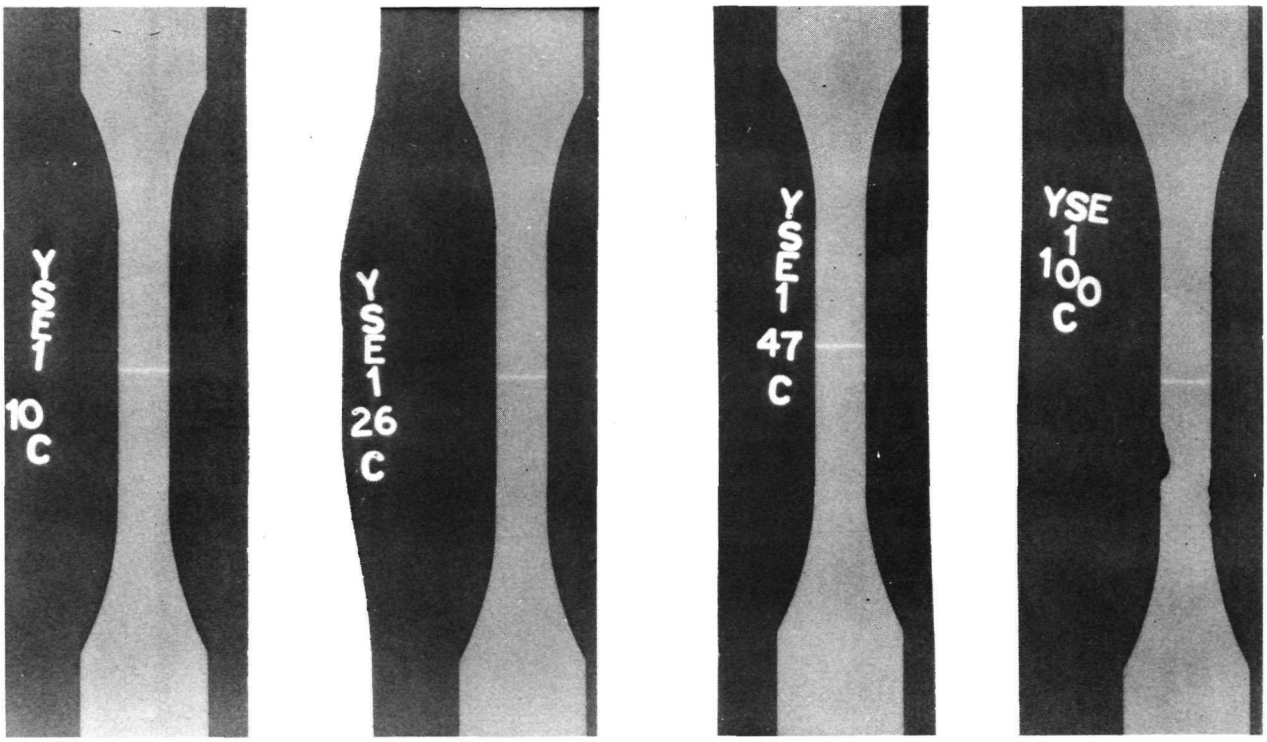


Figure 4-208. Electron-Emission Radiographs Through 100 Flight Simulation Cycles, Specimen YSE-1

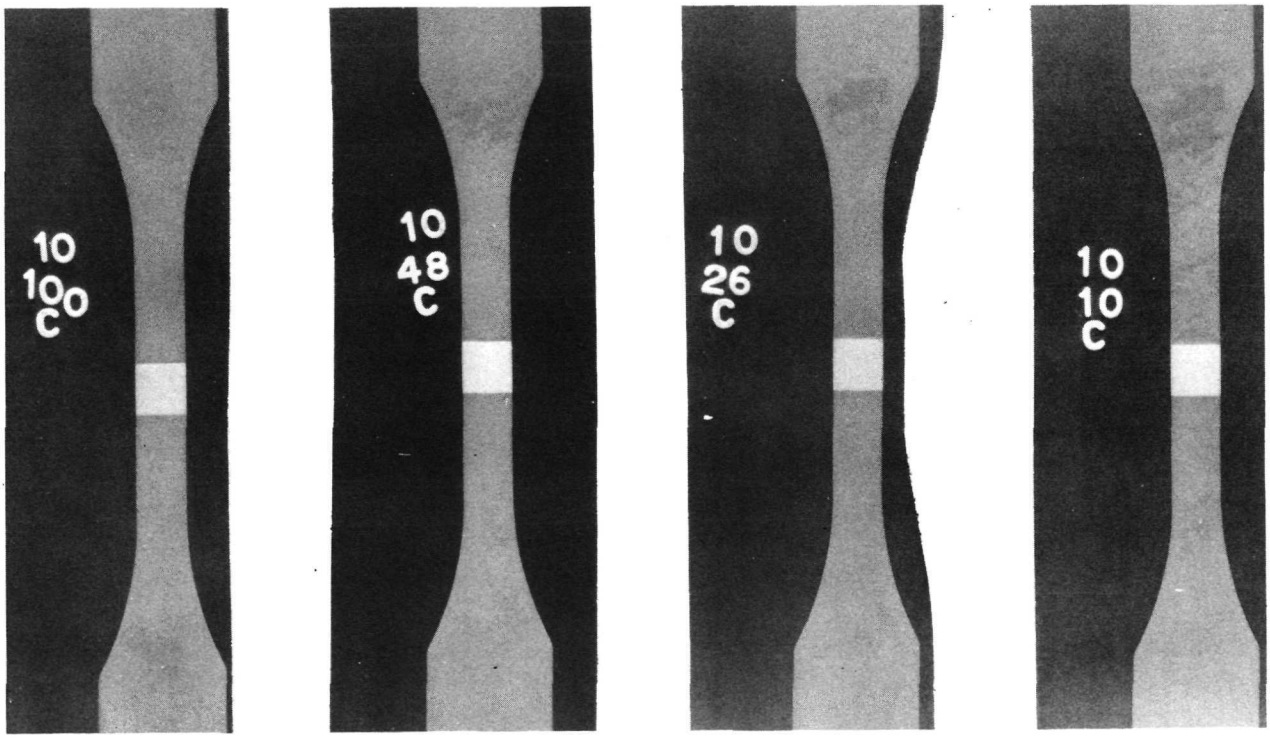


Figure 4-209. Electron-Emission Radiographs Through 100 Flight Simulation Cycles, Specimen BSD-10

methods and is a valuable tool for process control. Despite this general correlation, we are not able with existing NDE technology to predict potential failure sites.

Electron-emission radiography has proved most valuable for assisting the analysis of coating loss and, more particularly, the spallation of heavy metal modifiers from the coating. The information has been useful in attributing coating breakdown and for the analysis of coating variables relating to process control. It is clear that conventional NDE beyond initial inspection checkout is not meaningful for predicting coating life. The value of nondestructive testing as a quality control tool however, is indicated by the superior performance of the R-512E coating, which produced consistent NDE data, versus the relatively poor performance of the VH-109 coating, which produced correspondingly inconsistent data. In the few instances where the VH-109 coating survived 100 cycles, the NDE data showed the coating to be uniform.

It should be pointed out that coatings known to be defective were not selected for flight simulation, as the purpose of NDE during the program was primarily for quality control. While secondary objective included the analysis of conventional NDE methods, the study lacked the statistical data necessary to evaluate the ability of these methods to identify coating defects.

It is apparent from the study that sites of significant edge or surface erosion are readily visible from the time of their initiation, and hence impose a lesser burden on intermediate life NDE. Since the characteristic yellow or white oxide becomes a protuberance (due to its large volumetric condition), little more than a "walk-around" inspection of the vehicle should reveal visible areas of concern. It has also become apparent in this and other programs that catastrophic oxidation of the columbium alloy substrate does not occur at the time coating breakdown is initiated. Providing that these regions are observed while they are relatively small, perhaps 0.25 inch (0.63 cm) in diameter, they can be repaired (Reference 40) and the panel or structure should be serviceable. However, nondestructive testing, e.g., electron-emission radiography, will be performed on a selective basis to assist the analysis of local coating damage and to assess the quality of subsequent repair.

The mechanism of coating failure may be related to variations in the coating process that have heretofore gone undetected. A basic requirement of the process is uniform mixing of coating powders and dispersion of coating constituents in the liquid slurry. Significant variables exist such as particle size and distribution, mixing techniques, time and temperature parameters. While monitoring of such variables may be impractical, their effect may be examined through an analysis of coating kinetics fundamental to understanding, perhaps extending, the service life of the coating. Accordingly, as a supplement to this program, experiments have been made with a radionuclide tagging technique (References 41 and 42) to provide direction for coating

improvement. This technique provides for in situ NDE of the coating to measure coating remainder and uniformity beyond the sensitivity of conventional NDE methods.

On the basis of preliminary tests, which show compatibility between the radionuclide tag and the R-512E coating, it is intended to coat four of the tee-stiffened panels to be evaluated during Phase II with a Sylvania R-512E coating containing a dispersed radionuclide ($^{147}Pm$). It is expected that considerable information regarding coating kinetics will result from the study. Autoradiography and direct radiation counting will provide information relating to coating complex geometries and for evaluating coating loss of refurbishment.

# 5 CONCLUDING REMARKS

The studies presented in this report were directed toward establishing criteria for columbium alloy TPS development, supplementing existing properties data, and, in general, characterizing the candidate material systems for TPS application. These results will be further used in the systematic scaling processes of design, fabrication, and testing to be conducted in the subsequent phases of this program.

The design criteria established would assure guidance toward a fabricable and inspectable system that would provide structural integrity for a 100-mission life. During the test programs the guidelines established for determining failure were reinforced. That is, the mere presence of columbium oxide was no longer a valid reason to terminate a test. Instead, all specimens were taken to structural failure (or 100 cycles). All of the specimens that failed did so by a breakdown of the coating along edges (with one exception). This has been a habitual problem with refractory metals. Even with carefully radiused edges it is necessary to overcoat or structurally thicken edges. By allowing the test specimens to progress to structural failure, it is not implied that a heat shield or structural component would be permitted to do so while on an operational vehicle. A component thus damaged would be replaced or repaired during post-flight inspection or normal maintenance. However, a component with edge or surface coating breakdown would not jeopardize a mission.

All of the six material systems, i.e., Cb-752, C-129Y, and WC-3015, each coated with R-512E and VH-109, were found to have acceptable forming and joining characteristics. Diffusion bonding and electron beam welding were evaluated as methods of joining. Both were found to produce good joints. WC-3015 was found to be the most weldable, followed by C-129Y and Cb-752. However, WC-3015 was found to be the least coatable. The coating process severely distorted the specimens and raised the ductile-to-brittle transition temperature. The net result was to halt the flight simulation evaluation of WC-3015. It is believed that chemistry modifications of this alloy could result in an acceptable sheet alloy for heat shield applications. The important elements to control for maintenance of good ductility are the oxygen and tungsten. It is believed that ductility can be maintained by holding the oxygen to less than 150 ppm and the tungsten to 12 to 14 percent and reduce the titanium content.

Specimens were exposed to boost and reentry temperature, pressure, and loads simulating a Space Shuttle orbiter flight profile. Of the 72 specimens tested (18 each of R-512E-coated Cb-752 and C-129Y and 18 each of VH-109-coated Cb-752 and C-129Y), the Cb-752/R-512E performed as the best system. Although one specimen

of this system sustained structural failure no coating breakdown was exhibited. All of the C-129Y/R-512E specimens completed the required 100 cycles but 12 of 18 sustained various degrees of edge erosion. These sites were observed after 80 cycles. Prior to that time C-129Y/R-512E was clearly the better performer.

Only 4 of the 36 VH-109 coated specimens survived 100 cycles and of these three suffered coating failure. All of these were C-129Y. The average cyclic lifetimes for Vac-Hyd coated specimens were 64 cycles for Cb-752/VH-109 and 87 cycles for C-129Y/VH-109.

Cyclic creep measurements were made throughout the flight simulation testing. The amount of cyclic creep strain was slightly higher for the Cb-752 alloy than for the C-129Y alloy. This is in contrast to the static creep tests. The cyclic creep strain was found to be higher for the electron beam welded material than for the unwelded specimens. However, this difference is questionable since there was a similarity in post-test tensile data, and the uncoated cross-sectional areas of the weld specimens were consistently less than that of the parent metal specimens.

Metallographic examination sustained the opinion of superiority of R-512E over VH-109 on the alloys evaluated. Likewise it was substantiated that Cb-752/R-512E exhibited better performance during the flight simulation exposure than did C-129Y/R-512E. After 100 cycles, substrate consumption was about 0.0005 inch (0.0013 cm) per side for the Cb-752 and slightly higher for the C-129Y. Coating uniformity was generally good for all systems except Cb-752/VH-109. Based on the behavior during flight simulation testing the material systems were rated as follows:

1. Cb-752/R-512E
2. C-129Y/R-512E
3. C-129Y/VH-109
4. Cb-752/VH-109

Plasma arc tests were made using standard tensile specimens and a cyclic thermal profile with an in-plane applied load similar to that of the flight simulation testing. A limited number of specimens (12) were exposed in order to study the comparative effects of the two test techniques. The plasma arc exposure was considerably the more severe of the two. Although shock wave impingement was intended to be avoided, primary and secondary shocks were experienced causing premature edge erosion. The number of specimens was relatively small and the test conditions somewhat varied due to the shock instability problems; therefore, the forming of conclusions seems inappropriate. However, some observations and opinions can be made.

Each failure was initiated at the leading edge of a specimen and resulted from shock wave attachment. Other areas of the specimens appeared unaffected, based on visual observations. Of the eight specimens that sustained attack during the plasma arc tests, the rate of erosion varied from 0.005 inch (0.127 mm) per cycle to 0.021 inch (0.535 mm) per cycle, depending on shock intensity at the initiation of coating breakdown. The rate of edge erosion after coating breakdown did not appear to be affected by either alloy or coating type. The rate of edge erosion during the static air tests was 0.0025 inch (0.0635 mm) per cycle indicating an erosion rate 2 to 12 times as rapid for plasma tests. The initiation and progression of edge erosion was clearly identifiable during the plasma arc tests. In no case did structural failure occur during this initial cycle of coating breakdown. (A minimum of 5 cycles was sustained between the onset of edge erosion and structural failure.) Had it been desirable to do so, coating repair could have been readily effected, which would have completely arrested the oxidation of the columbium substrate. Such repair methods have been developed under Contract NAS 8-26121 (Reference 40).

Room temperature tensile testing was conducted on coated and uncoated Cb-752 and C-129Y before and after exposure. The properties were decreased by the application of the coatings with similar results for both alloys. The decreases were: 15 percent in ultimate strength, 17 percent in yield strength, and 20 percent in modulus of elasticity. The most drastic decrease due to coating was in the ductility, which was reduced between 30 and 50 percent. All types of specimens (parent, electron beam weld, and diffusion bond) behaved in a similar manner.

For the Cb-752/R-512E system tested through flight simulation there was a general decrease of 10 to 15 percent in ultimate strength at room temperature after exposure. This decrease is readily accounted for by the loss in substrate as a result of diffusion zone growth during cycling. Strength values were calculated by using the original uncoated cross-sectional areas. However, while the intrinsic strengths of the specimens had not changed significantly, their load carrying capability was reduced by 10 to 15 percent due to coating diffusion during the 100 cycle exposure. Since oxygen contamination acts to reduce the ductility in addition to the loss due to the presence of cracks in the coating, it was not unusual to experience decreases of 50 to 80 percent in elongation values. Again, there was no significant difference between the joint and parent specimens. All joints were 100 percent efficient in the room temperature tensile testing.

The cycled specimens tensile tested at 2400°F (1589°K) produced no decrease in ultimate strength even though the base metal cross-sectional area had been reduced by approximately 10 percent due to diffusion zone growth. The yield strengths were increased slightly while the elongations were significantly decreased as expected. The strength/stability phenomenon is believed to be the result of the ability of the coating/base metal diffusion layer to support some of the applied load at high temperature.

Based on the results of the flight simulation tests, two material systems were selected for further evaluation: Cb-752/R-512E and C-129Y/R-512E. Added tensile tests at 1400°F (1033°K), 2000°F (1366°K), and 2400°F (1589°K) were performed on unexposed specimens. Decreases in tensile strengths were noted for both systems. The properties at 1400°F (1033°K) and 2000°F (1366°K) were found to be very similar. At these temperatures, the elongation values dropped to levels ranging from 0.5 to 3.0 percent. At 2400°F (1589°K) the tensile strengths dropped sharply while the elongation increased to between 5.5 and 12.5 percent.

Static creep tests were conducted on Cb-752/R-512E and C-129Y/R-512E at 2000°F (1366°K), 2200°F (1478°K), and 2400°F (1589°K), in an atmosphere of 99 percent argon and 1 percent air. Essentially linear creep was found for both systems, with rarely exhibited primary creep at the lower temperatures.

Two types of creep behavior were observed at 2400°F (1589°K). The majority of the data showed linearity. However, approximately one-third of the specimens showed linear creep for the first 30 hours followed by a decreasing creep rate. It was concluded that this behavior was caused by the strengthening effect of oxygen contamination. Linear extrapolations were made whenever this occurrence was evidenced.

In comparing the two material systems it was found that Cb-752/R-512E had slightly higher creep strength at the three test temperatures than did C-129Y/R-512E. These results are not consistent with those of the flight simulation cycling. Although some efforts were made to resolve the apparent discrepency between creep strengths of the material systems and the difference between the cyclic and static creep testing results, the efforts were not conclusive.

The differences could have resulted from variations in specimen thickness, coating thickness (hence, diffusion zone thickness), methods of measuring thickness and creep, or differences in test methods, or a combination of these. The differences between the two alloys is believed to be slight. It is postulated that the cyclic creep strength of the columbium alloys is approximately 60 percent that of the static creep strength. However, additional creep testing and metallurgical studies are needed to provide truly representative design creep data and to resolve the inconsistencies reported herein.

San Diego operation of Convair Aerospace Division,
General Dynamics Corporation
San Diego, California, June 16, 1972

## APPENDIX A

## CONVERSION OF U.S. CUSTOMARY UNITS TO SI UNITS

The International System of Units (designated SI) was adopted by the Eleventh General Conference on Weights and Measures in 1960. The units and conversion factors used in this report are taken from or based on NASA SP-7012, "The International System of Units, Physical Constants and Conversion Factors — Revised, 1969".

The following table expresses the definitions of miscellaneous units of measure as exact numerical multiples of coherent SI units, and provides multiplying factors for converting numbers and miscellaneous units to corresponding new numbers of SI units.

The first two digits of each numerical entry represent a power of 10. An asterisk follows each number that expresses an exact definition. For example, the entry "-02 2.54*" expresses the fact that 1 inch = $2.54 \times 10^{-2}$ meter, exactly, by definition. Most of the definitions are extracted from National Bureau of Standards documents. Numbers not followed by an asterisk are only approximate representations of definitions, or are the results of physical measurements.

### ALPHABETICAL LISTING

| To convert from | to | multiply by | |
|---|---|---|---|
| atmosphere (atm) | newtons/meter$^2$ (N/m$^2$) | +05 | 1.0133* |
| British thermal unit, mean (Btu) | joule (J) | +03 | 1.056 |
| Fahrenheit (F) | kelvin (K) | $t_k = (5/9)(t_f + 459.67)$ | |
| foot (ft) | meter (m) | -01 | 3.048* |
| inch (in.) | meter (m) | -02 | 2.54* |
| mil | meter (m) | -05 | 2.54* |
| millimeter of mercury (mm Hg) | newton/meter$^2$ (N/m$^2$) | +02 | 1.333 |
| nautical mile, U.S. (n.mi.) | meter (m) | +03 | 1.852* |

| To convert from | to | multiply by | |
|---|---|---|---|
| pound force ($lb_f$) | newton (N) | +00 | 4.448* |
| pound mass ($lb_m$) | kilogram (kg) | -01 | 4.536* |
| torr | newton/meter$^2$ ($N/m^2$) | +02 | 1.333 |

## PHYSICAL QUANTITY LISTING

### Acceleration

| | | | |
|---|---|---|---|
| foot/second$^2$ ($ft/sec^2$) | meter/second$^2$ ($m/sec^2$) | -01 | 3.048* |

### Area

| | | | |
|---|---|---|---|
| foot$^2$ ($ft^2$) | meter$^2$ ($m^2$) | -02 | 9.290* |
| inch$^2$ ($in^2$) | meter$^2$ ($m^2$) | -04 | 6.452* |
| inch$^2$ ($in^2$) | centimeter$^2$ ($cm^2$) | +00 | 6.452 |

### Density

| | | | |
|---|---|---|---|
| pound mass/foot$^3$ (pcf, $lb_m/ft^3$) | kilogram/meter$^3$ ($kg/m^3$) | +01 | 1.602 |
| pound mass/inch$^3$ ($lb_m/in^3$) | kilogram/meter$^3$ ($kg/m^3$) | +04 | 2.768 |
| pound mass/inch$^3$ ($lb_m/in^3$) | gram/cm$^3$ (gm/cc) | +01 | 2.768 |

### Energy

| | | | |
|---|---|---|---|
| British thermal unit, mean (Btu) | joule (J) | +03 | 1.056 |

### Energy/Area Time

| | | | |
|---|---|---|---|
| Btu/foot$^2$ second (Btu/$ft^2$ sec) | watt/meter$^2$ ($W/m^2$) | +04 | 1.135 |

### Force

| | | | |
|---|---|---|---|
| kilogram force ($kg_f$) | newton (N) | +00 | 9.807* |
| pound force ($lb_f$) | newton (N) | +00 | 4.448* |

| To convert from | to | multiply by | |
|---|---|---|---|
| | **Length** | | |
| foot (ft) | meter (m) | -01 | 3.048* |
| inch (in.) | meter (m) | -02 | 2.54* |
| micron | meter (m) | -06 | 1.00* |
| mil | meter (m) | -05 | 2.54* |
| mile, U.S. nautical (n.mi.) | meter (m) | +03 | 1.852* |
| | **Mass** | | |
| pound mass ($lb_m$) | kilogram (kg) | -01 | 4.536* |
| | **Pressure** | | |
| atmosphere (atm) | newton/meter$^2$ ($N/m^2$) | +05 | 1.013* |
| millimeter of mercury (mm Hg) | newton/meter$^2$ ($N/m^2$) | +02 | 1.333 |
| pound/foot$^2$ (psf, $lb_f/ft^2$) | newton/meter$^2$ ($N/m^2$) | +01 | 4.788 |
| pound/inch$^2$ (psi, $lb_f/in^2$) | newton/meter$^2$ ($N/m^2$) | +03 | 6.895 |
| | **Temperature** | | |
| Fahrenheit (F) | Kelvin (K) | $t_k = (5/9)(t_f + 459.67)$ | |
| | **Volume** | | |
| foot$^3$ ($ft^3$) | meter$^3$ ($m^3$) | -02 | 2.832* |
| inch$^3$ ($in^3$) | meter$^3$ ($m^3$) | -05 | 1.639* |
| inch$^3$ ($in^3$) | centimeter$^3$ ($cm^3$, cc) | -01 | 1.639 |

## PREFIXES

The names of multiples and submultiples of SI units may be formed by application of the prefixes:

| Multiple | Prefix |
|---|---|
| $10^{-6}$ | micro (μ) |
| $10^{-3}$ | milli (m) |
| $10^{-2}$ | centi (c) |
| $10^{-1}$ | deci (d) |
| $10^{3}$ | kilo (k) |
| $10^{6}$ | mega (M) |
| $10^{9}$ | giga (G) |

## APPENDIX B

## PHASE I TEST LOAD DETERMINATIONS AND CYCLIC CREEP PREDICTIONS

This appendix documents the analytical approach, analysis, and results of analysis for the determination of applied Phase I test loads and predicted creep ranges.

### OBJECT

The object was to test the specimens under conditions of stress and temperature that might be expected in the space shuttle orbiter mission.

### TEMPERATURE PROFILE

The predicted and modified temperature profile for a typical orbiter mission was defined as shown in Figure 4-5. This established the thermal environment.

### STRESS PARAMETERS

The stress level to be experienced in a typical columbium alloy TPS panel was known to be a function of the aerodynamic pressure, the thermal gradients, and its edge restraint. Early temperature studies showed that the panels of interest (which were of thin gages) had small thermal gradients compared to their mean temperatures. Design studies indicated that it would be a requirement to minimize, if not eliminate, any edge restraint since thermal expansion was considerable. These two considerations led to the conclusion that the TPS panel stress would be primarily caused by the pressure differential only. Cyclic creep causing residual stresses was not considered and would not exist in the tensile specimen case.

### AERODYNAMIC LOADS

The definition of aerodynamic pressure depends on location on the orbiter and the mission profile. A worst case pressure differential condition was chosen and is basically as follows:

(1) Up to 3 psi (21 $kN/m^2$) $\Delta p$ might be experienced in the booster launch phase (t = 0 to 170 seconds) when the booster interference effects might be present.

(2) Up to 2 psi (14 $kN/m^2$) $\Delta p$ might be experienced in the orbiter launch phase.

(3) In the entry phase, the pressure differential varies as shown in Figure B-1.

The test apparatus provides for six stepped load inputs; therefore, the pressure profile was simulated with a stepped profile as shown in Figure B-1. The pressure was raised slightly in the last step to account for maneuvers expected in the transition phase from entry to cruise.

## MATERIAL FAILURE MODES

Having a pressure and temperature profile defined, it was then possible to study what stress levels might be seen in a typical design. Three failure modes were considered:

(1) Short time material fracture. The instantaneous stress times an ultimate factor of safety must not exceed the material's ultimate stress at that temperature.

(2) Short time material yield. The instantaneous stress must not exceed the material's yield stress at that temperature.

(3) The accumulative creep of the material after 100 missions would be 1% or less.

## STRESS PREDICTION LOGIC

Regardless of what shape or configuration the TPS panel would take (corrugated, stiffened sheet, etc.) the stress would be proportional to the aerodynamic pressure where

$$f = \frac{Mc}{I} = \frac{\Delta p \ell^2 c}{8I}$$

where

$\ell$ = span of panel

c = extreme fiber displacement from neutral axis

I = moment of inertia of unit width of panel

but for a given design, $\ell$, c, and I are constant and therefore,

$$f = K\Delta p$$

where K is a constant.

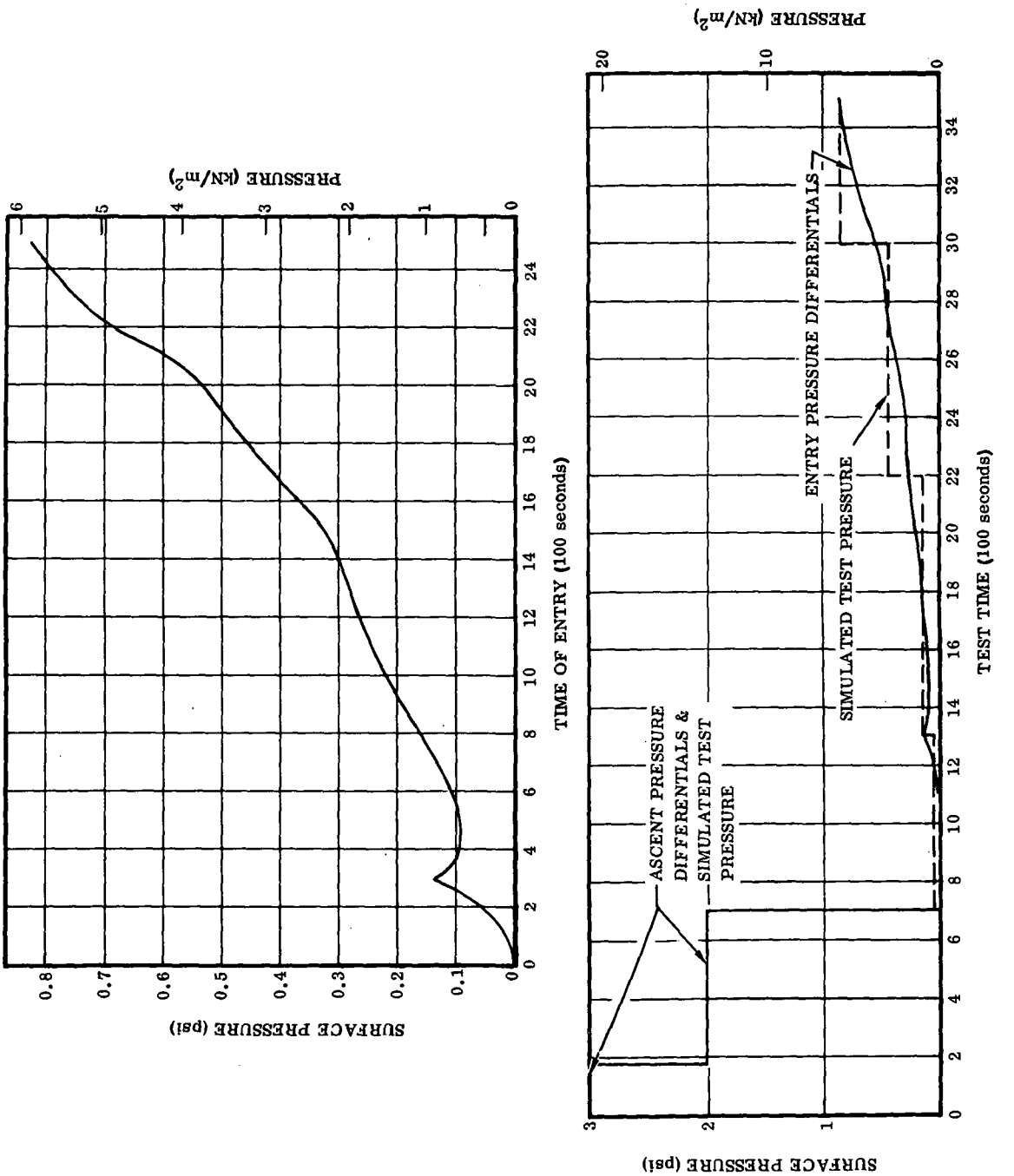


Figure B-1. Surface Pressure on Orbiter TPS Panel Versus Time of Entry and Test Time

Knowing the temperature and pressure, it remains only to evaluate K such that the stress level is low enough to prevent all of the three failure modes.

A computer program was written to make the numeric evaluation of K and thereby evaluate stresses and hence test loads. The program logic is shown in Figure B-2.

## NUMERICAL EVALUATIONS

Two materials were evaluated: a) C-129Y and b) Cb-752.

The results of a numerical evaluation are shown in Figures B-3 and B-4. These results were obtained by the computer program shown in Figure B-2 and subsequently plotted by an IBM 1130. The input temperature versus time data can be seen in Figure B-4. The input of pressure versus time data was taken from Figure B-1.

The input of coefficients to the material strength versus temperature equations are shown in Figures B-5 and B-6. The input of coefficients to the material creep as a function of stress and time are shown in Figures B-7 and B-8.

The indices were input as:

| | | | |
|---|---|---|---|
| Index for output option | NT | = | 2 |
| Number of missions | NLIFE | = | 100 |
| Maximum temperature in material property regime I ($=T_1$)(°F) | ST | = | 1200 |
| Maximum temperature in material property regime II ($=T_2$)(°F) | EN | = | 1600 |
| Unused variable | FTMAX | = | 0 |
| Allowable creep strain (in/in) | CRPAL | = | 0.01 |
| Minimum temperature where creep may be significant (°F) | CRPT | = | 1700 |
| Ultimate factor of safety | UFS | = | 1.5 |

The predicted loads are highly dependent on the specimen thickness; i.e., the limiting stress to prevent the three failure modes is independent of thickness but the test apparatus controlled applied load and therefore was thickness dependent. This presented a problem since there was a wide variation in specimen thickness and coating depths.

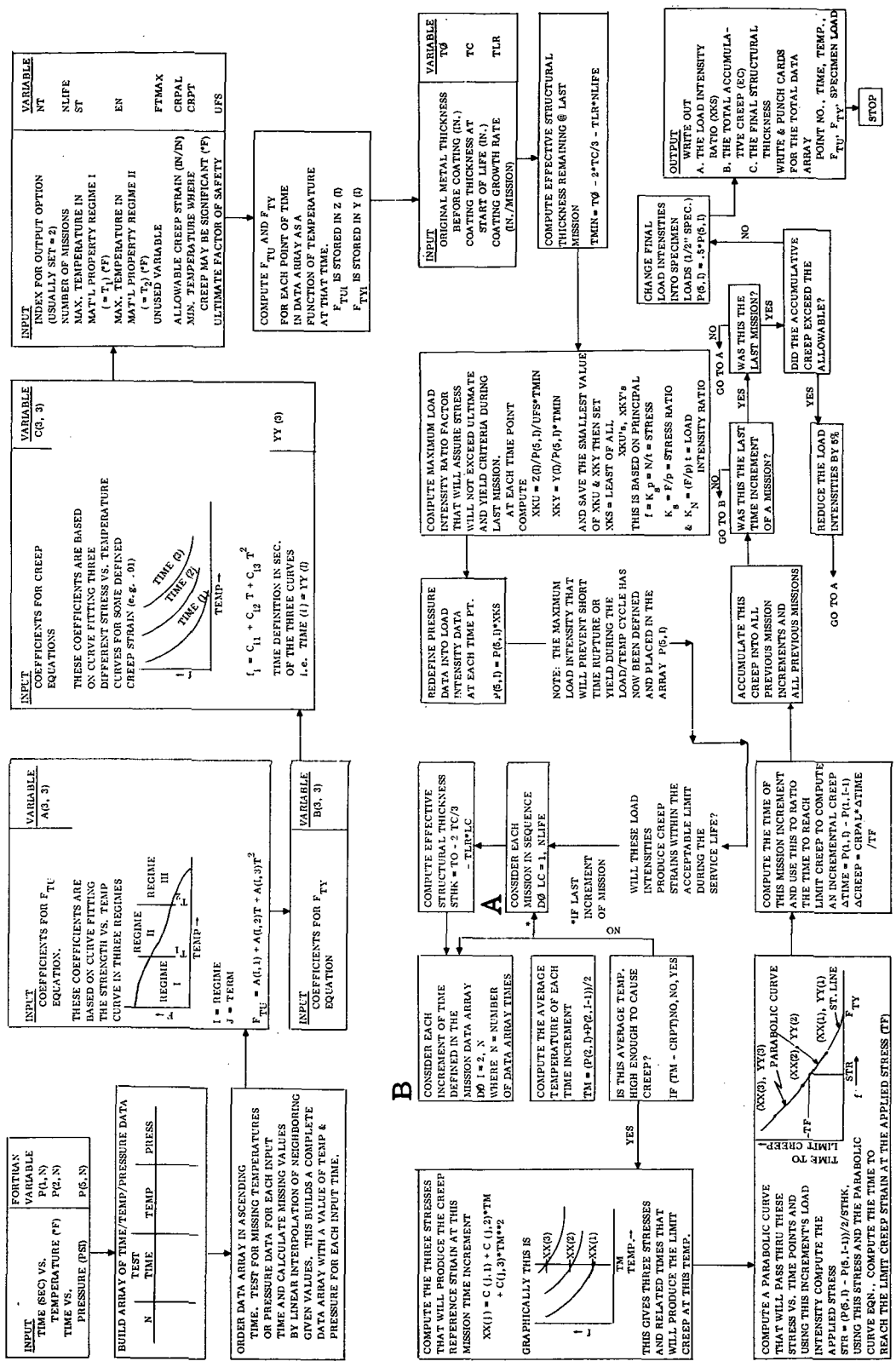


Figure B-2. Flow Diagram for Load Prediction Program

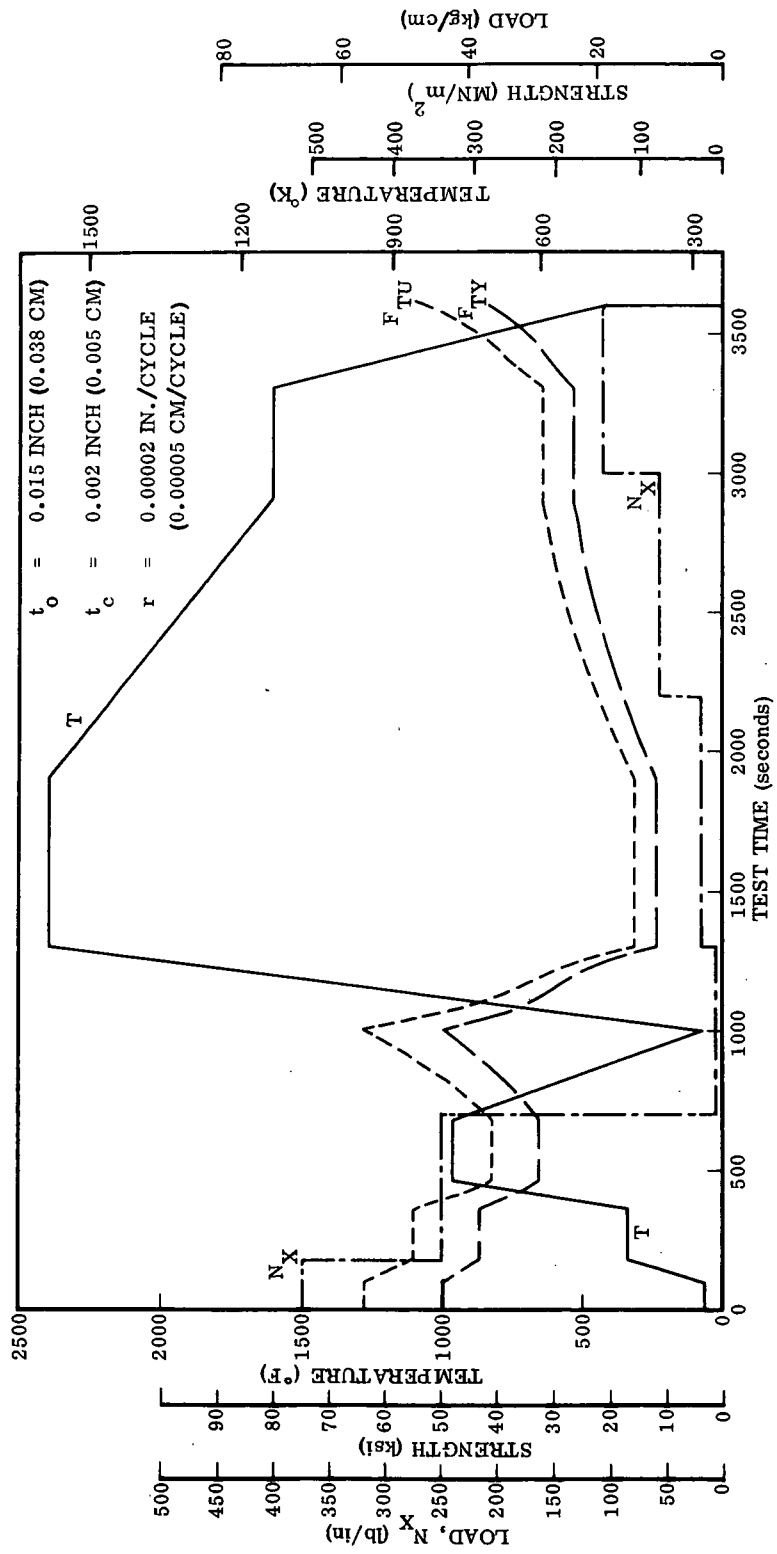


Figure B-3. Sample Results from Test Load Prediction Program for Cb-752

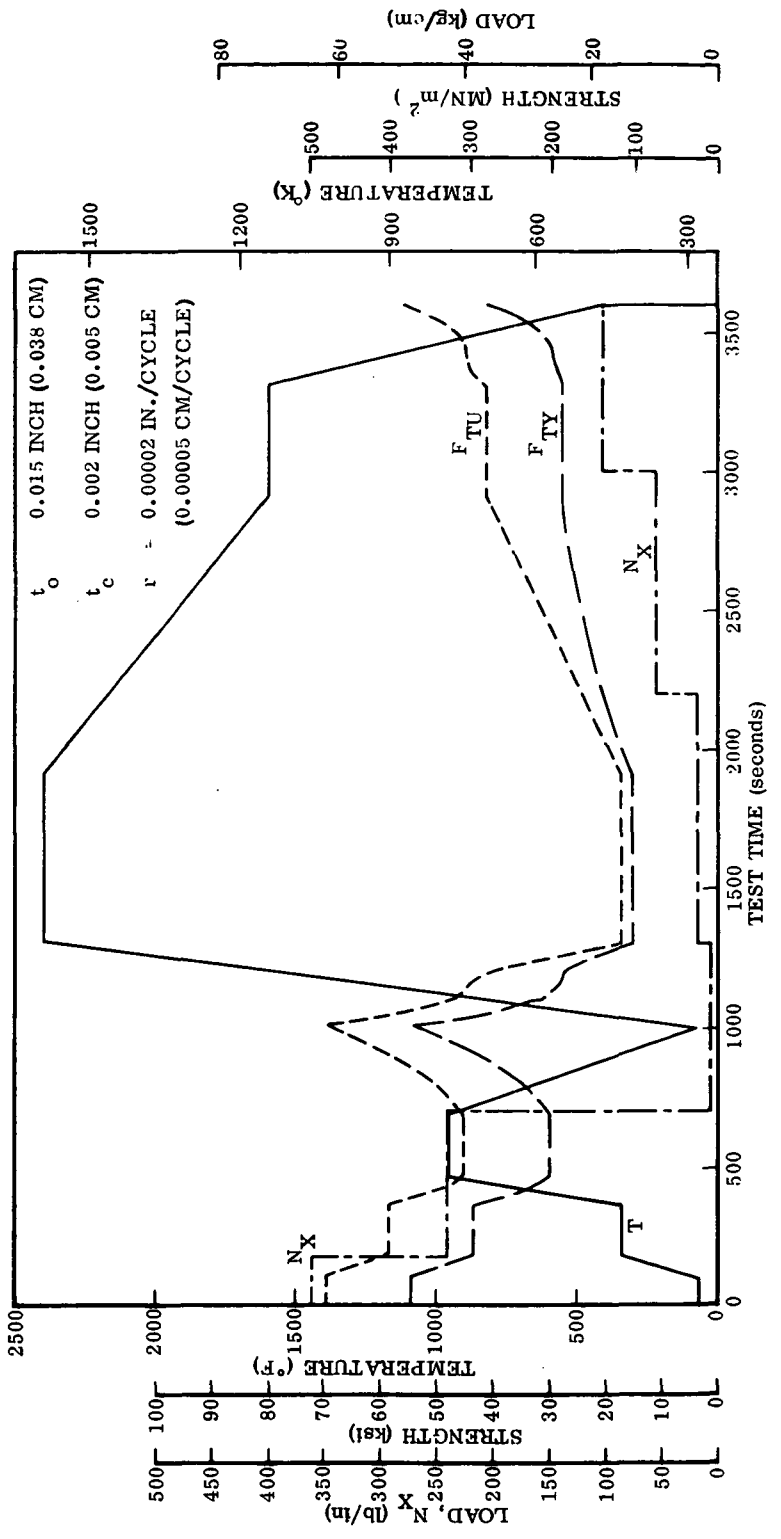


Figure B-4. Sample Results from Test Load Prediction Program for C-129Y

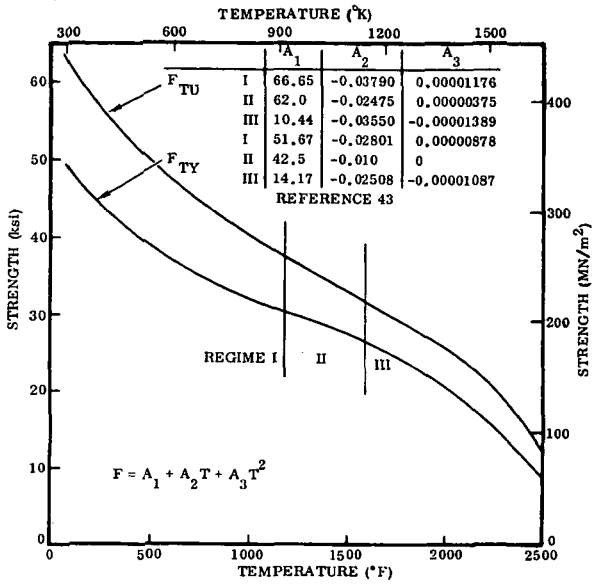


Figure B-5. Curve Fit Equations for Properties of Cb-752

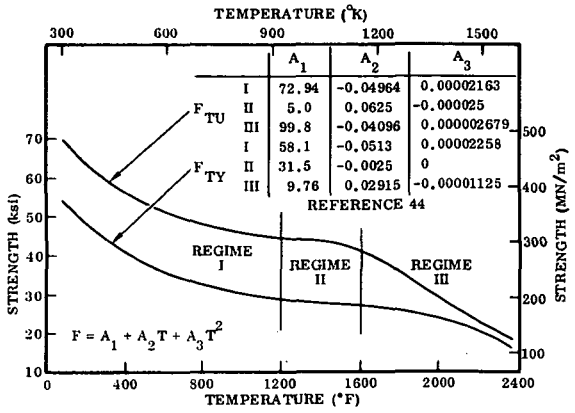


Figure B-6. Curve Fit Equations for Properties of C-129Y

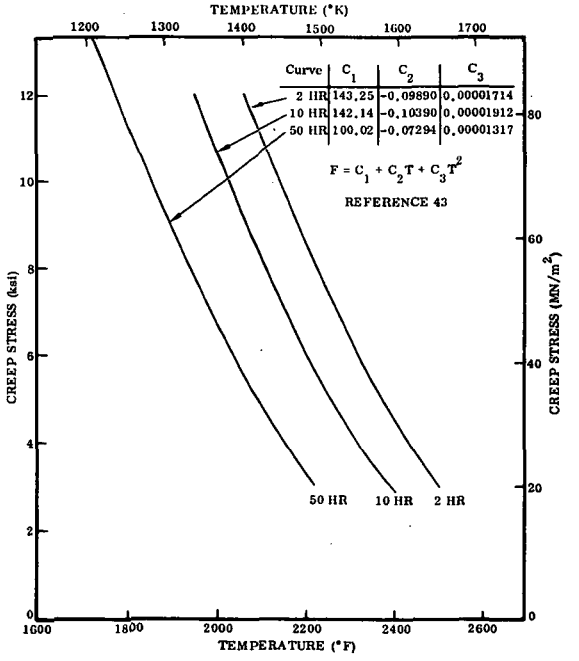


Figure B-7. Curve Fit Equations for Times to Creep 1% for Cb-752

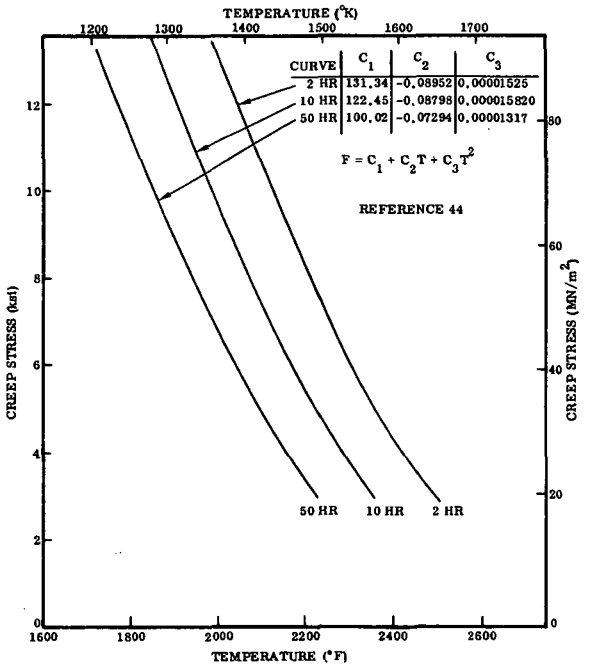


Figure B-8. Curve Fit Equations for Times to Creep 1% for C-129Y

The approach was as follows:

(1) The specimens were divided into 12 categories for each material (three types of specimens — parent material, electron beam welded, diffusion bonded; times two coating types — R-512E and VH-109).

(2) The specimen dimensions in each category were scanned and the specimen with maximum bare and coated thickness was recorded. These data are shown in Table B-1. Also recorded was the specimen with the minimum bare and coated thickness.

The coating thickness was then computed for each data point based on this assumption:

$$t_c = 3\ (t_{oc} - t_o) / 4$$

where variables are as shown in Figure B-9 and

$t_{oc}$ = thickness after coating

$t_o$ = thickness bare

$t_c$ = effective coating thickness

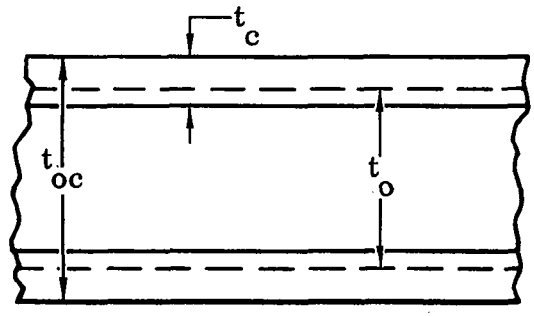


Figure B-9. Thickness Term Nomenclature

The data shown in Table B-1 was plotted and a least-squares line was drawn through the data points. Using the extreme data points to limit the line, the midpoint was then chosen as the design thickness point. This resulted in the values:

For C-129Y: $t_o$ = 0.01415 in. (0.03594 cm) $t_c$ = 0.0045 in. (0.0114 cm)

For Cb-752: $t_o$ = 0.01315 in. (0.03340 cm) $t_c$ = 0.0045 in. (0.0114 cm)

This data was used as input into the load prediction program.

Table B-2 shows the loads predicted by the computer program for the two materials and the test levels finally chosen.

## Table B-1. Specimen Dimension Measurements

| Specimen Number | Alloy | Coating | Specimen Type | Width | | | | Thickness | | | |
|---|---|---|---|---|---|---|---|---|---|---|---|
| | | | | Bare | | Coated | | Bare | | Coated | |
| | | | | inch | (cm) | inch | (cm) | inch | (cm) | inch | (cm) |
| BSP-1 | Cb-752 | R-512E | Parent | 0.4978 | 1.2644 | 0.5030 | 1.2777 | 0.0146 | 0.0371 | 0.0207 | 0.0526 |
| BSP-2 | | | | 0.4980 | 1.2649 | 0.5028 | 1.2771 | 0.0147 | 0.0373 | 0.0208 | 0.0528 |
| BSP-3 | | | | 0.4987 | 1.2667 | 0.5032 | 1.2781 | 0.0147 | 0.0373 | 0.0207 | 0.0526 |
| BSP-4 | | | | 0.4989 | 1.2672 | 0.5032 | 1.2781 | 0.0147 | 0.0373 | 0.0206 | 0.0523 |
| BSP-5 | | | | 0.4988 | 1.2669 | 0.5030 | 1.2777 | 0.0146 | 0.0371 | 0.0207 | 0.0526 |
| BSP-6 | | | | 0.4990 | 1.2675 | 0.5037 | 1.2794 | 0.0146 | 0.0371 | 0.0212 | 0.0538 |
| BSP-7 | | | | 0.4988 | 1.2669 | 0.5032 | 1.2781 | 0.0145 | 0.0368 | 0.0205 | 0.0521 |
| BSP-8 | | | | 0.4989 | 1.2672 | 0.5034 | 1.2786 | 0.0145 | 0.0368 | 0.0208 | 0.0528 |
| BSP-9 | | | | 0.4994 | 1.2685 | 0.5037 | 1.2794 | 0.0145 | 0.0368 | 0.0207 | 0.0526 |
| BSP-10 | | | | 0.4983 | 1.2657 | 0.5040 | 1.2802 | 0.0146 | 0.0371 | 0.0214 | 0.0544 |
| BSE-1 | | | EB Weld | 0.4930 | 1.2522 | 0.4966 | 1.2614 | 0.0131 | 0.0333 | 0.0183 | 0.0465 |
| BSE-2 | | | | 0.4934 | 1.2532 | 0.4970 | 1.2624 | 0.0131 | 0.0333 | 0.0182 | 0.0462 |
| BSE-3 | | | | 0.4940 | 1.2548 | 0.4973 | 1.2631 | 0.0130 | 0.0330 | 0.0180 | 0.0457 |
| BSE-4 | | | | 0.4937 | 1.2540 | 0.4974 | 1.2634 | 0.0130 | 0.0330 | 0.0182 | 0.0462 |
| BSE-5 | | | | 0.4939 | 1.2545 | 0.4979 | 1.2647 | 0.0127 | 0.0323 | 0.0178 | 0.0452 |
| BSE-18 | | | | 0.4999 | 1.2697 | 0.5034 | 1.2786 | 0.0120 | 0.0305 | 0.0162 | 0.0411 |
| BSE-19 | | | | 0.4998 | 1.2695 | 0.5037 | 1.2794 | 0.0115 | 0.0292 | 0.0164 | 0.0417 |
| BSE-20 | | | | 0.5002 | 1.2705 | 0.5042 | 1.2807 | 0.0117 | 0.0297 | 0.0166 | 0.0422 |
| BVP-1 | | VH-109 | Parent | 0.4986 | 1.2664 | 0.5045 | 1.2814 | 0.0147 | 0.0373 | 0.0201 | 0.0511 |
| BVP-2 | | | | 0.5050 | 1.2827 | 0.5085 | 1.2916 | 0.0141 | 0.0358 | 0.0193 | 0.0490 |
| BVP-3 | | | | 0.5044 | 1.2812 | 0.5066 | 1.2868 | 0.0140 | 0.0356 | 0.0186 | 0.0472 |
| BVP-4 | | | | 0.5044 | 1.2812 | 0.5091 | 1.2931 | 0.0139 | 0.0353 | 0.0184 | 0.0467 |
| BVP-5 | | | | 0.5060 | 1.2852 | 0.5081 | 1.2906 | 0.0139 | 0.0353 | 0.0195 | 0.0495 |
| BVP-6 | | | | 0.5047 | 1.2819 | 0.5100 | 1.2954 | 0.0140 | 0.0356 | 0.0188 | 0.0478 |
| BVP-7 | | | | 0.5050 | 1.2827 | 0.5104 | 1.2964 | 0.0139 | 0.0353 | 0.0186 | 0.0472 |
| BVP-8 | | | | 0.5046 | 1.2817 | 0.5088 | 1.2923 | 0.0140 | 0.0356 | 0.0195 | 0.0495 |
| BVP-9 | | | | 0.5044 | 1.2812 | 0.5078 | 1.2898 | 0.0140 | 0.0356 | 0.0183 | 0.0465 |
| BVP-10 | | | | 0.5044 | 1.2812 | 0.5105 | 1.2967 | 0.0140 | 0.0356 | 0.0192 | 0.0488 |
| BVE-1 | | | EB weld | 0.4959 | 1.2596 | 0.4996 | 1.2690 | 0.0137 | 0.0348 | 0.0187 | 0.0475 |
| BVE-2 | | | | 0.4939 | 1.2545 | 0.5025 | 1.2764 | 0.0137 | 0.0348 | 0.0193 | 0.0490 |
| BVE-3 | | | | 0.4941 | 1.2550 | 0.5045 | 1.2814 | 0.0136 | 0.0345 | 0.0199 | 0.0505 |
| BVE-4 | | | | 0.4952 | 1.2578 | 0.4995 | 1.2687 | 0.0136 | 0.0345 | 0.0186 | 0.0472 |
| BVE-5 | | | | 0.4959 | 1.2596 | 0.5014 | 1.2736 | 0.0136 | 0.0345 | 0.0199 | 0.0505 |
| BVE-18 | | | | 0.5007 | 1.2718 | 0.5087 | 1.2921 | 0.0122 | 0.0310 | 0.0175 | 0.0445 |
| BVE-19 | | | | 0.5008 | 1.2720 | 0.5095 | 1.2941 | 0.0121 | 0.0307 | 0.0174 | 0.0442 |
| BVE-20 | | | | 0.5007 | 1.2718 | 0.5051 | 1.2830 | 0.0123 | 0.0312 | 0.0185 | 0.0470 |

## Table B-1. Specimen Dimension Measurements, Contd

| Specimen Number | Alloy | Coating | Specimen Type | Width | | | | Thickness | | | |
|---|---|---|---|---|---|---|---|---|---|---|---|
| | | | | Bare | | Coated | | Bare | | Coated | |
| | | | | inch | (cm) | inch | (cm) | inch | (cm) | inch | (cm) |
| YSP-1 | C-129Y | R-512E | Parent | 0.4984 | 1.2656 | 0.5010 | 1.2725 | 0.0143 | 0.0363 | 0.0192 | 0.0488 |
| YSP-2 | | | | 0.4954 | 1.2583 | 0.4995 | 1.2687 | 0.0144 | 0.0366 | 0.0195 | 0.0495 |
| YSP-3 | | | | 0.5011 | 1.2728 | 0.5042 | 1.2807 | 0.0141 | 0.0358 | 0.0194 | 0.0493 |
| YSP-4 | | | | 0.5004 | 1.2710 | 0.5043 | 1.2809 | 0.0141 | 0.0358 | 0.0195 | 0.0495 |
| YSP-5 | | | | 0.5001 | 1.2703 | 0.5044 | 1.2812 | 0.0137 | 0.0348 | 0.0192 | 0.0488 |
| YSP-6 | | | | 0.5006 | 1.2715 | 0.5040 | 1.2802 | 0.0137 | 0.0348 | 0.0194 | 0.0493 |
| YSP-7 | | | | 0.5010 | 1.2725 | 0.5041 | 1.2804 | 0.0143 | 0.0363 | 0.0194 | 0.0493 |
| YSP-8 | | | | 0.4990 | 1.2675 | 0.5020 | 1.2751 | 0.0143 | 0.0363 | 0.0198 | 0.0503 |
| YSP-9 | | | | 0.5015 | 1.2738 | 0.5048 | 1.2822 | 0.0147 | 0.0373 | 0.0204 | 0.0518 |
| YSP-10 | | | | 0.5014 | 1.2736 | 0.5054 | 1.2837 | 0.0147 | 0.0373 | 0.0201 | 0.0511 |
| YSE-1 | | | EB weld | 0.5044 | 1.2812 | 0.5075 | 1.2891 | 0.0136 | 0.0345 | 0.0187 | 0.0475 |
| YSE-2 | | | | 0.5050 | 1.2827 | 0.5077 | 1.2896 | 0.0137 | 0.0348 | 0.0190 | 0.0483 |
| YSE-3 | | | | 0.5048 | 1.2822 | 0.5086 | 1.2918 | 0.0138 | 0.0351 | 0.0187 | 0.0475 |
| YSE-4 | | | | 0.5057 | 1.2845 | 0.5093 | 1.2936 | 0.0140 | 0.0356 | 0.0191 | 0.0485 |
| YSE-5 | | | | 0.5057 | 1.2845 | 0.5094 | 1.2936 | 0.0140 | 0.0356 | 0.0195 | 0.0495 |
| YSE-18 | | | | 0.4925 | 1.2510 | 0.4956 | 1.2588 | 0.0139 | 0.0353 | 0.0186 | 0.0472 |
| YSE-19 | | | | 0.4922 | 1.2502 | 0.4954 | 1.2583 | 0.0140 | 0.0356 | 0.0186 | 0.0472 |
| YSE-21 | | | | 0.4911 | 1.2474 | 0.4947 | 1.2565 | 0.0137 | 0.0348 | 0.0188 | 0.0478 |
| YVP-1 | | VH-109 | Parent | 0.4868 | 1.2365 | 0.4914 | 1.2482 | 0.0140 | 0.0356 | 0.0198 | 0.0503 |
| YVP-2 | | | | 0.4880 | 1.2395 | 0.4925 | 1.2510 | 0.0147 | 0.0373 | 0.0205 | 0.0521 |
| YVP-3 | | | | 0.4888 | 1.2416 | 0.4940 | 1.2548 | 0.0138 | 0.0351 | 0.0194 | 0.0493 |
| YVP-4 | | | | 0.4886 | 1.2410 | 0.4934 | 1.2532 | 0.0140 | 0.0356 | 0.0203 | 0.0516 |
| YVP-5 | | | | 0.4884 | 1.2405 | 0.4931 | 1.2525 | 0.0145 | 0.0368 | 0.0202 | 0.0513 |
| YVP-6 | | | | 0.4890 | 1.2421 | 0.4930 | 1.2522 | 0.0142 | 0.0361 | 0.0206 | 0.0523 |
| YVP-7 | | | | 0.4893 | 1.2428 | 0.4931 | 1.2525 | 0.0142 | 0.0361 | 0.0192 | 0.0488 |
| YVP-8 | | | | 0.4883 | 1.2403 | 0.4917 | 1.2489 | 0.0141 | 0.0358 | 0.0196 | 0.0498 |
| YVP-9 | | | | 0.4882 | 1.2400 | 0.4910 | 1.2471 | 0.0148 | 0.0376 | 0.0191 | 0.0485 |
| YVP-10 | | | | 0.4882 | 1.2400 | 0.4915 | 1.2484 | 0.0150 | 0.0381 | 0.0203 | 0.0516 |
| YVE-1 | | | EB weld | 0.4868 | 1.2365 | 0.4913 | 1.2479 | 0.0132 | 0.0335 | 0.0184 | 0.0467 |
| YVE-2 | | | | 0.4883 | 1.2403 | 0.4924 | 1.2507 | 0.0133 | 0.0338 | 0.0194 | 0.0493 |
| YVE-3 | | | | 0.4890 | 1.2421 | 0.4943 | 1.2555 | 0.0136 | 0.0345 | 0.0196 | 0.0498 |
| YVE-4 | | | | 0.4878 | 1.2390 | 0.4940 | 1.2548 | 0.0137 | 0.0348 | 0.0201 | 0.0511 |
| YVE-5 | | | | 0.4891 | 1.2423 | 0.4934 | 1.2532 | 0.0137 | 0.0348 | 0.0195 | 0.0495 |
| YVE-18 | | | | 0.4870 | 1.2370 | 0.4926 | 1.2512 | 0.0137 | 0.0348 | 0.0197 | 0.0500 |
| YVE-19 | | | | 0.4840 | 1.2294 | 0.4886 | 1.2410 | 0.0138 | 0.0351 | 0.0197 | 0.0500 |
| YVE-20 | | | | 0.4883 | 1.2403 | 0.4922 | 1.2502 | 0.0139 | 0.0353 | 0.0192 | 0.0488 |

Table B-2. Results of Load Prediction Analysis and Actual Loads Used

| Test Cycle Time (sec) | C-129Y Loads | | Cb-752 Loads | | Actual Test Loads | |
|---|---|---|---|---|---|---|
| | lb | (kg) | lb | (kg) | lb | (kg) |
| 0 - 170 | 141.2 | 64.1 | 130.9 | 59.4 | 140 | 63.6 |
| 170 - 700 | 94.1 | 42.7 | 87.2 | 39.6 | 90 | 40.9 |
| 700 - 1300 | 2.4 | 1.9 | 2.2 | 1.0 | 7 | 3.2 |
| 1300 - 2200 | 7.1 | 3.2 | 6.5 | 3.0 | 7 | 3.2 |
| 2200 - 3000 | 21.2 | 9.6 | 19.6 | 8.9 | 21 | 11.0 |
| 3000 - 3600 | 40.0 | 18.2 | 37.1 | 17.2 | 40 | 18.2 |

## CREEP PREDICTIONS

From the specimen thickness data the maximum and minimum variations were identified (Figure B-9). These values are:

For C-129Y: $t_o$ max = 0.0150 in. (0.0381 cm) $t_c$max = 0.00490 in. (0.01245 cm)

$t_o$ min = 0.0132 in. (0.0335 cm) $t_c$min = 0.00322 in. (0.00818 cm)

For Cb-752: $t_o$ max = 0.0147 in. (0.0373 cm) $t_c$max = 0.00510 in. (0.01295 cm)

$t_o$ min = 0.0115 in. (0.0292 cm) $t_c$min = 0.00315 in. (0.00700 cm)

By modifying the load prediction program (Figure B-2) to accept as input the loads, skipping the strength ratioing steps, and allowing only one pass through the creep analysis section, it was possible to predict the creep that might be seen on a specimen of specified material and thickness.

Three cases of each material were analyzed in this manner. The maximum, nominal and minimum thickness cases were run. The results are shown in Table B-3.

It must be recognized that these creep predictions can be greatly influenced by coating growth rate, peculiarities of cyclic creep over sustained creep, and material properties that change as a function of service cycles experienced. In this analysis the first is assumed and the other two are neglected. The soundness of this approach is open to review and was chosen out of necessity, there being no data on the subject. This could well form the basis for a separate study program.

Table B-3. Creep Predictions Considering Thickness Variations and Nominal Test Loads for 100 Simulated Missions

| Material | Thickness | Predicted Creep (%) |
|---|---|---|
| C-129Y | Maximum | 0.69 |
| | Nominal | 0.93 |
| | Minimum | 1.36 |
| Cb-752 | Maximum | 0.69 |
| | Nominal | 1.05 |
| | Minimum | 1.89 |

Another source of variation in test results and test prediction is the tolerance on the test load. In the test setup the load tolerance was estimated to be ±10% and was in fact approximately 14% at 2400° F (see Section 4.2.5.2).

Assuming the load to be on the high side, the predictions shown in Table B-4 were computed.

Table B-4. Creep Predictions Considering Thickness Variations and Test Loads for 100 Simulated Missions Increased by 10%

| Material | Thickness | Predicted Creep (%) |
|---|---|---|
| C-129Y | Maximum | 0.84 |
| | Nominal | 1.14 |
| | Minimum | 1.67 |
| Cb-752 | Maximum | 0.83 |
| | Nominal | 1.27 |
| | Minimum | 2.32 |

The modified creep predictions were plotted at 10 cycle intervals to compare the predicted scatter band and the actual test data (see Figures 4-57, 4-60, 4-62, and 4-64). In reviewing these figures it can be seen that the cyclic test data is consistently higher than the predictions, especially for the R-512E coated alloys. The initial reaction was to fault the basic creep stress data (Figures B-7 and B-8) and/or the coating diffusion assumptions.

The first corrective approach was to use the latest creep data generated under this program (Section 4.5). The creep data shown in Figures 4-165 and 4-175 were reduced to the three-curve-fit prediction program and are shown in Figures B-10 and B-11. This data was curve fitted and the new coefficients are shown in Figures B-12 and B-13. Using these creep coefficients, the revised creep prediction results are shown in Table B-5.

Table B-5. Creep Predictions Considering Thickness Variation, Load Tolerance (10%), and Present Investigation Creep Data for 100 Simulated Missions

| Material | Thickness | Predicted Creep (%) Nominal Load | Maximum Load |
|---|---|---|---|
| C-129Y | Maximum | 0.56 | 0.66 |
| | Nominal | 0.72 | 0.85 |
| | Minimum | 1.00 | 1.18 |
| Cb-752 | Maximum | 0.28 | 0.35 |
| | Nominal | 0.45 | 0.56 |
| | Minimum | 0.86 | 1.07 |

By comparing the data in Table B-5 with Table B-4, which used the original static creep data, it is obvious that the data source was not responsible for the disparity between cyclic test data and predicted scatter band. In fact, the original creep data resulted in better agreement.

The second empirical corrective approach was to modify the assumptions used for coating diffusion and diffusion rate during exposure. This was done by attempting to match diffusion with residual base metal area that would be necessary to produce the creep strain of the cyclic tests. The results of this approach were unsatisfactory since the computerized conclusion was that the diffusion zone would be approximately 0.006 inch (0.152 mm) per side after 100 cycles or failure for specimens that were nominally 0.014 inch (0.356 mm) thick before coating.

It was, therefore, obvious that a simplistic empirical approach to finding a solution to the static creep versus cyclic creep phenomenon was not to be readily attained. Further studies could not be sustained by this program and will be left to more comprehensive materials studies. To have information available for design, however, a factoring approach will be used for subsequent phases of the program. This, together with recommended mechanical and physical property data, is presented in Appendix C.

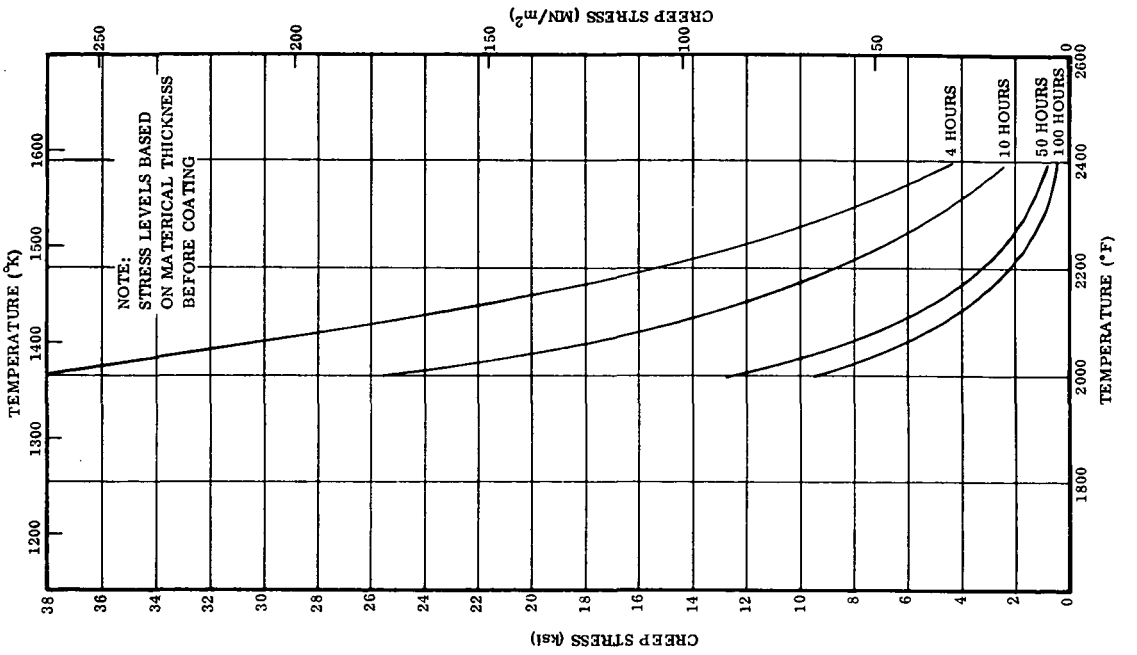


Figure B-11. 1% Creep Properties of C-129Y/ R-512E as Determined Under Present Investigation

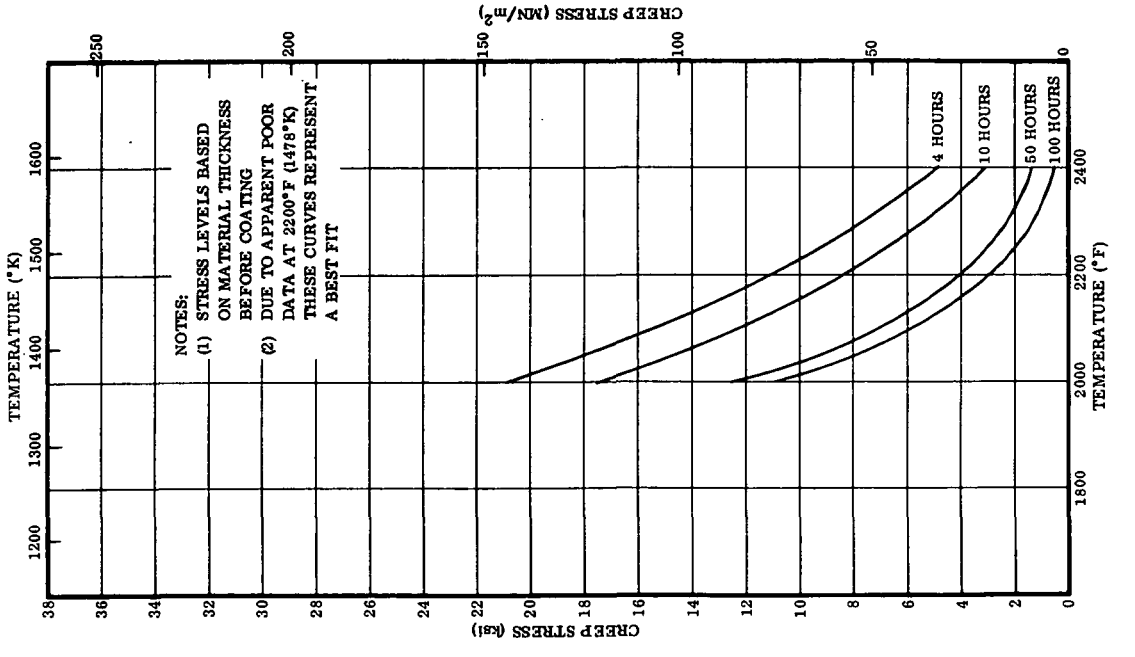


Figure B-10. 1% Creep Properties of Cb-752/ R-512E as Determined Under Present Investigation

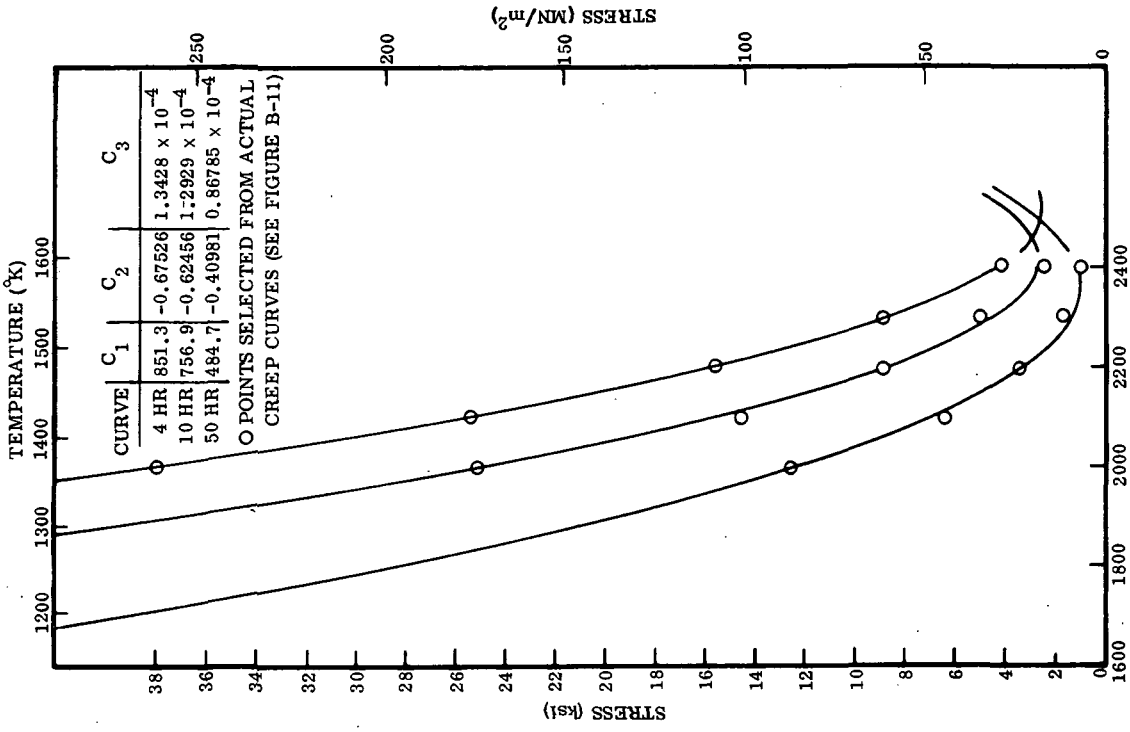


Figure B-13. Curve Fit Equations for C-129Y Using Data Generated Under Present Investigation

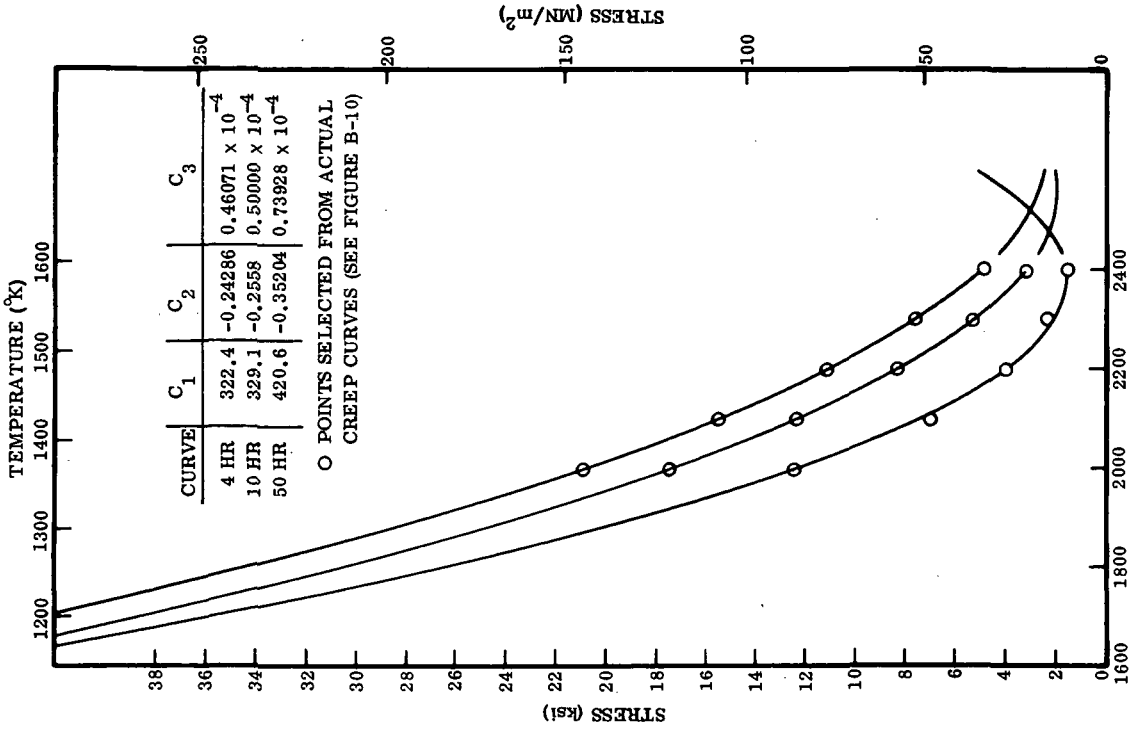


Figure B-12. Curve Fit Equations for Cb-752 Using Data Generated Under Present Investigation

One additional task was performed for the flight simulation test analysis. That was to curve fit by the method of least squares the data for the parent specimens presented in Figures 4-57, 4-60, 4-62, and 4-64. The curve fitted data are shown in Figures B-14 through B-17.

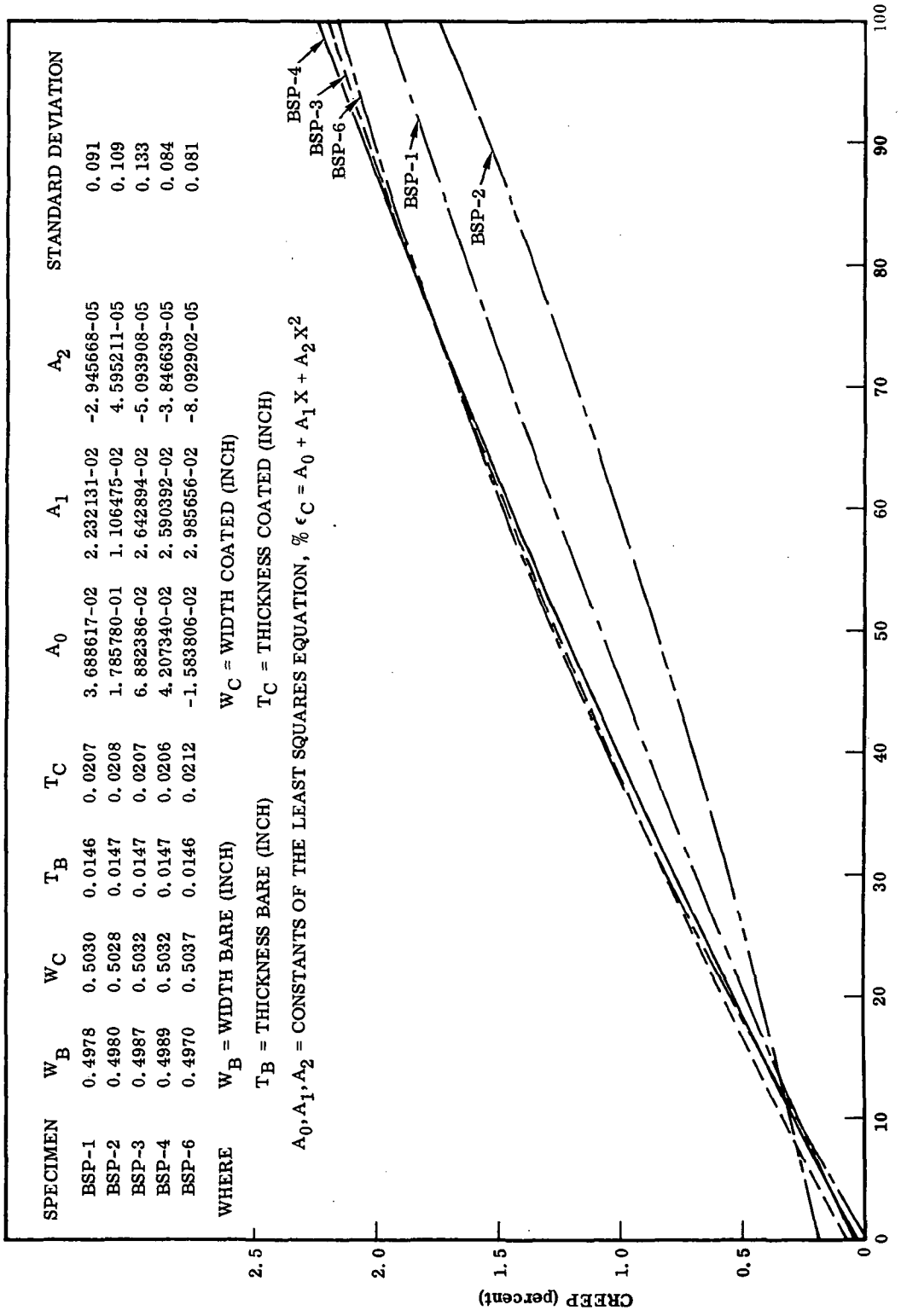


Figure B-14. Least Squares Fit of Cyclic Creep Test Data for Cb-752/R-512E Parent Specimens

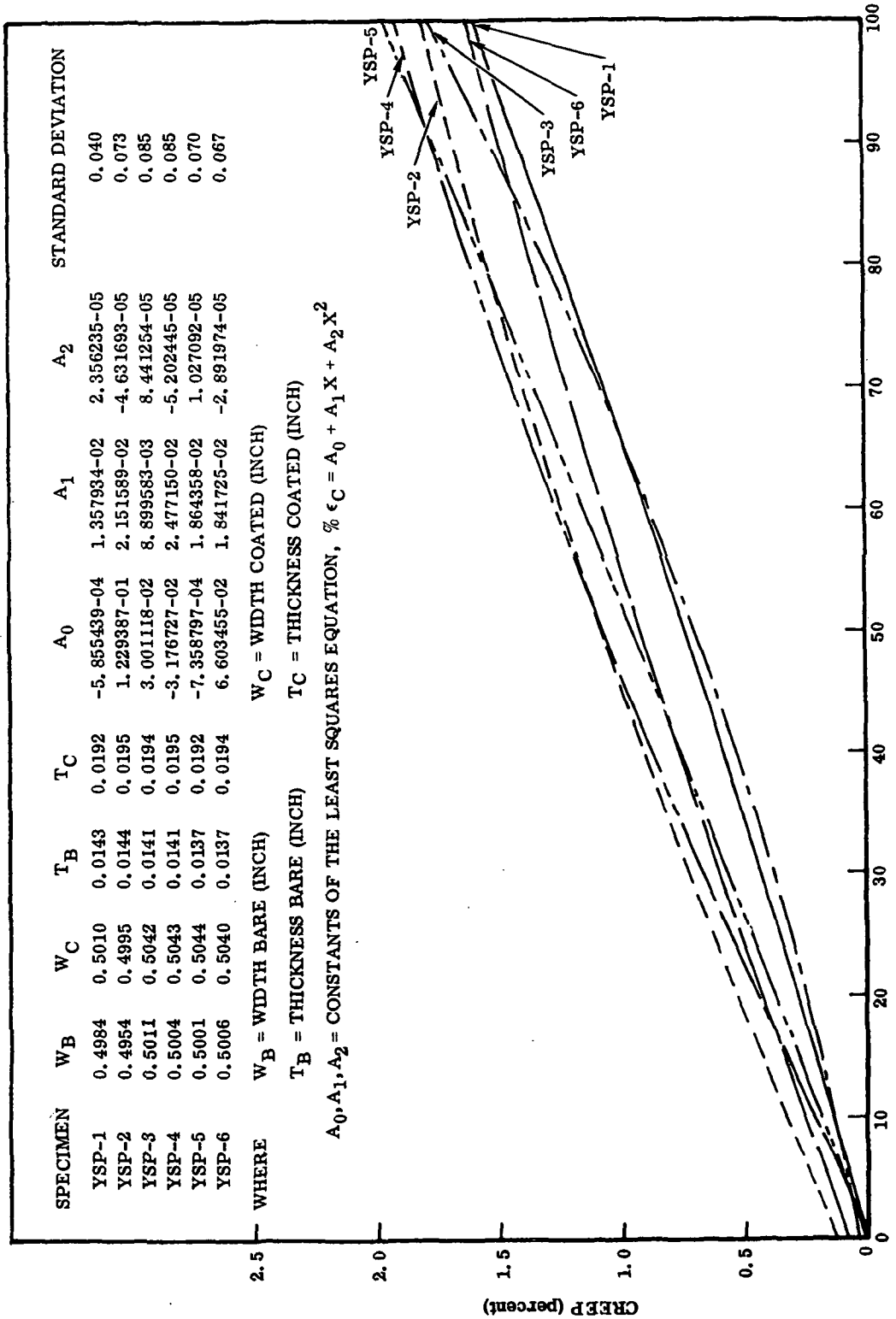


Figure B-15. Least Squares Fit of Cyclic Creep Test Data for C-129Y/R-512E Parent Specimens

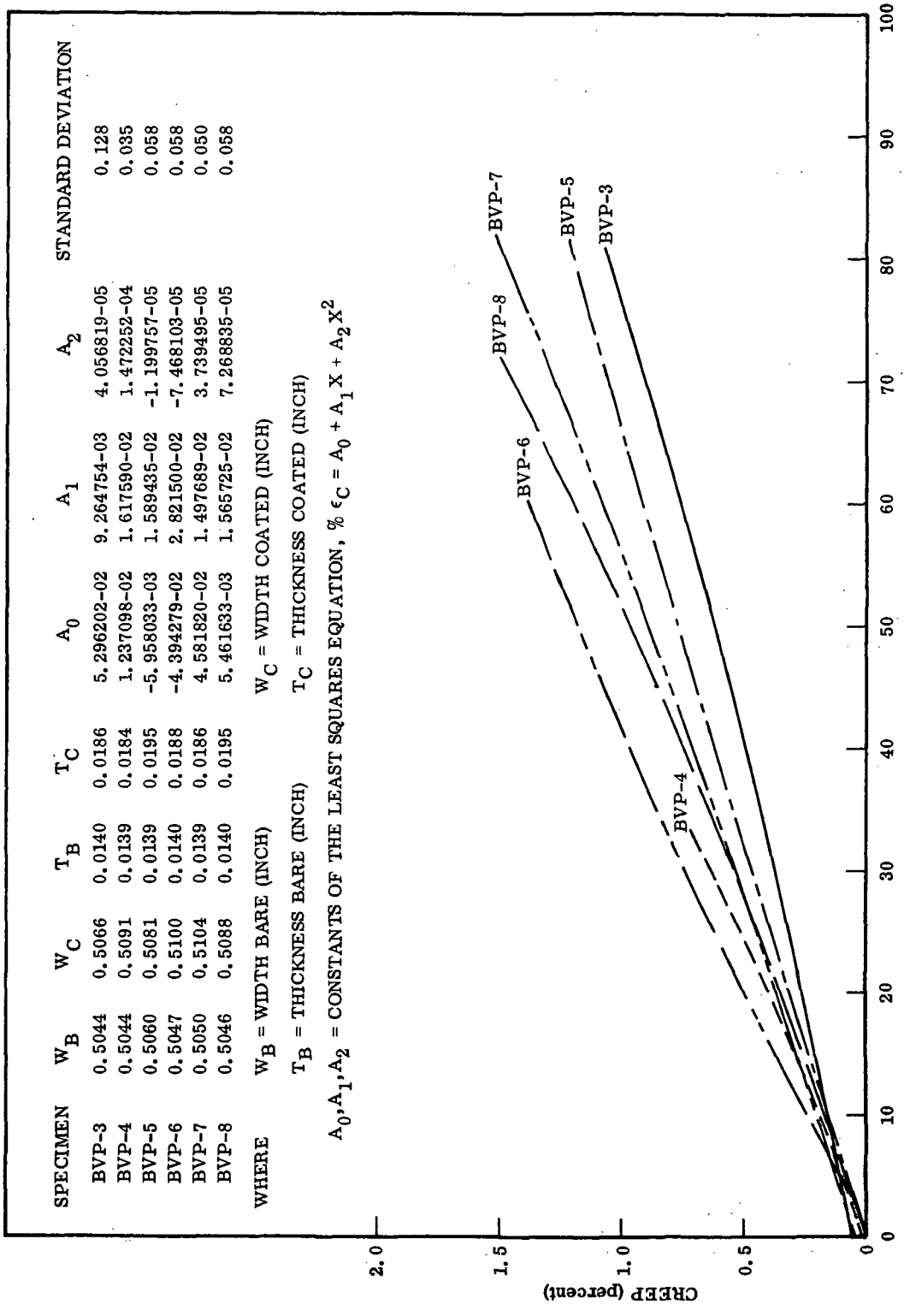


Figure B-16. Least Squares Fit of Cyclic Creep Test Data for Cb-752/VH-109 Parent Specimens

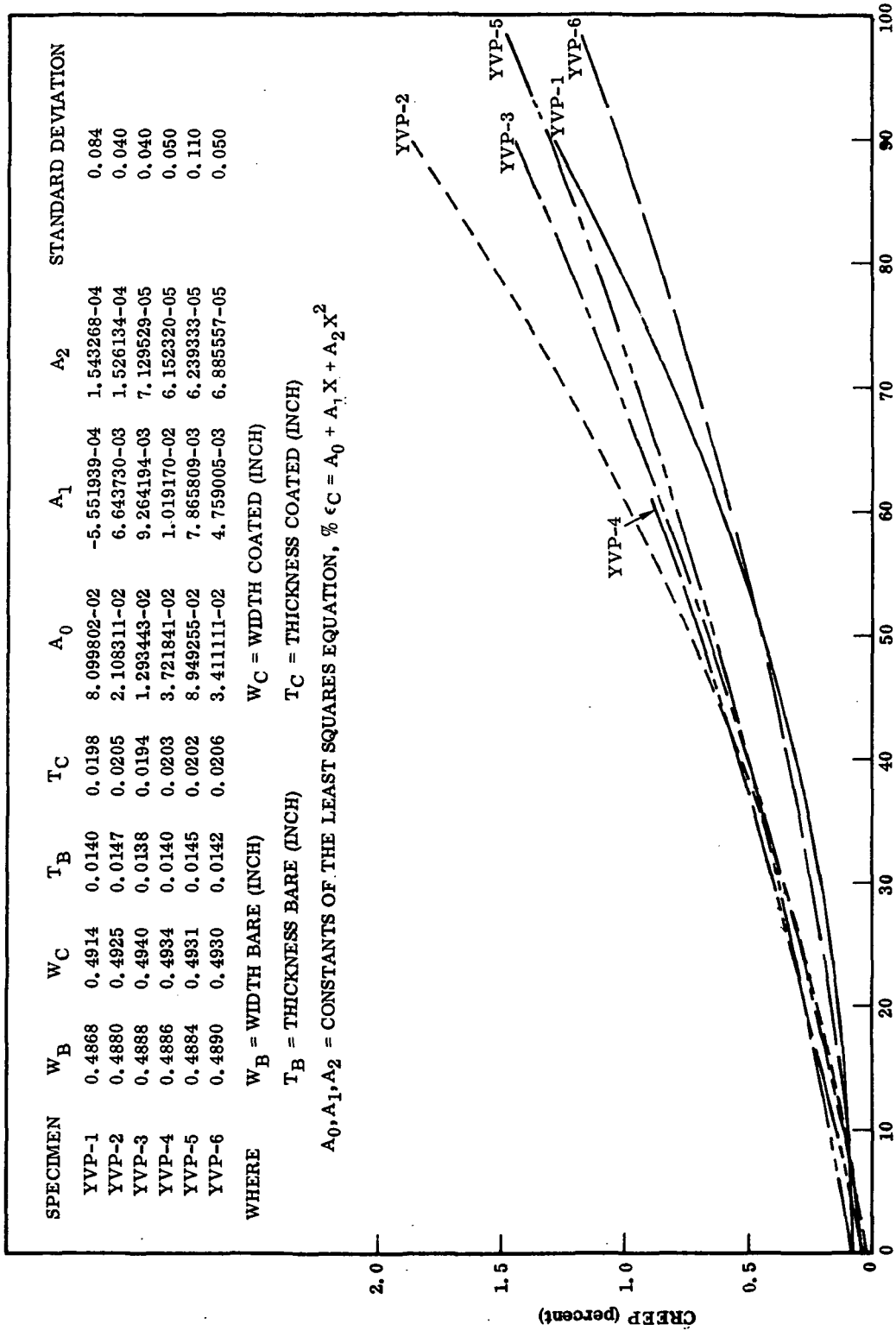


Figure B-17. Least Squares Fit of Cyclic Creep Test Data for C-129Y/VH-109 Parent Specimens

# APPENDIX C

## ANALYSES OF MECHANICAL PROPERTIES AND CREEP TEST DATA

This appendix reviews the tensile properties derived and subsequently used under this program in comparison with concurrent NASA programs involving coated columbium alloys. Correction factors for coating diffusion are employed, and recommended design curves suitable for preliminary design applications are presented. In view of the reported apparent discrepancy between the standard creep data and cyclic creep data generated under this program, an attempt is made to produce correlation factors to use for design when encountering cyclic phenomena. It is to be understood that the approaches and the factors advocated are interim solutions only and must rest on the challenge of future, more in-depth studies of material properties.

## MECHANICAL PROPERTY DATA

The tensile test data for Cb-752/R-512E and C-129Y/R-512E generated under this program were derived on the basis of uncoated cross-sectional areas (Tables 4-10 through 4-19). These tensile values have been adjusted on the basis of the estimated area remaining after coating (and after cycling, where applicable). These calculations assume a non-structural diffusion zone. Tables C-1 and C-2 present the original calculations from Section 4 and the coating compensated values. This data is considered more useful for design purposes, since properties based on original area only are applicable only to material of the same gage as the test specimens.

## CORRECTION FACTORS FOR COATING DIFFUSION

Factors to correct the aforementioned tensile values are computed for individual specimens from before-and-after coating measurements, where these measurements are applicable. (All specimens were accurately measured before coating; however, after coating, measurements were taken for only approximately 50% of the parent specimens and 35% of the welded and diffusion bonded specimens.) For specimens not measured after coating, the average coating/substrate diffusion per side was taken as one-half times the growth per side. That is, for the application of 3 mils (0.076 mm) of coating per side, 1 mil (0.025 mm) of substrate is consumed and 2 mils (0.051 mm) of growth is evidenced.

Plots of substrate consumption versus exposure cycles from References 19 and 45 are shown in Figure C-1. The value of 0.0005 inch (0.0013 cm) per side for Cb-752 alloy as determined in this program gives good agreement with an extrapolation of the

## Table C-1. Cb-752/R-512E Tensile Test Data

| Specimen Number | Exposure Cycles | Test Temperature °F | Test Temperature (°K) | Based on Uncoated Area $F_{TU}$ ksi | $F_{TU}$ ($MN/m^2$) | $F_{TY}$ ksi | $F_{TY}$ ($MN/m^2$) | E psi x $10^6$ | E ($GN/m^2$) | Based on Effective Area $F_{TU}$ ksi | $F_{TU}$ ($MN/m^2$) | $F_{TY}$ ksi | $F_{TY}$ ($MN/m^2$) | E psi x $10^6$ | E ($GN/m^2$) |
|---|---|---|---|---|---|---|---|---|---|---|---|---|---|---|---|
| BSP-21 | 0 | 75 | 297 | 67.1 | 463 | 50.7 | 350 | 12.8 | 88.3 | 89.9 | 620 | 67.9 | 468 | 17.2 | 118.2 |
| BSP-22 | 0 | 75 | 297 | 67.4 | 465 | 50.6 | 349 | 11.5 | 79.3 | 90.5 | 624 | 68.0 | 469 | 15.4 | 106.5 |
| BSP-23 | 0 | 75 | 297 | 67.4 | 465 | 50.4 | 348 | 12.3 | 84.8 | 88.6 | 611 | 66.3 | 457 | 16.2 | 111.5 |
| Average | | | | 67.3 | 464 | 50.6 | 349 | 12.2 | 84.1 | 89.7 | 618 | 67.4 | 465 | 16.3 | 112.0 |
| BSE-18 | 0 | 75 | 297 | 67.0 | 462 | 51.0 | 352 | 11.3 | 77.9 | 81.2 | 560 | 61.8 | 426 | 13.7 | 94.4 |
| BSE-19 | 0 | 75 | 297 | 69.6 | 480 | 52.5 | 362 | 11.6 | 80.0 | 88.5 | 610 | 66.7 | 460 | 14.7 | 101.6 |
| BSE-20 | 0 | 75 | 297 | 68.0 | 469 | 50.9 | 351 | 11.8 | 81.4 | 86.0 | 593 | 64.4 | 444 | 14.9 | 102.9 |
| Average | | | | 68.2 | 470 | 51.5 | 355 | 11.6 | 80.0 | 85.2 | 588 | 64.3 | 443 | 14.5 | 99.6 |
| BSD-16 | 0 | 75 | 297 | 62.8 | 433 | 51.7 | 357 | 15.2 | 104.8 | 78.1 | 538 | 64.3 | 443 | 18.9 | 130.2 |
| BSD-17 | 0 | 75 | 297 | 70.0 | 483 | 52.1 | 359 | 15.3 | 105.5 | 88.0 | 607 | 65.5 | 452 | 19.2 | 132.6 |
| BSD-23 | 0 | 75 | 297 | 71.0 | 490 | 53.0 | 365 | 13.9 | 95.8 | 88.6 | 611 | 66.1 | 456 | 17.4 | 119.6 |
| Average | | | | 69.7 | 481 | 52.3 | 360 | 14.8 | 102.0 | 84.9 | 585 | 65.3 | 450 | 18.5 | 127.5 |
| BSP-7 | 0 | 1400 | 1033 | 30.8 | 212 | - | - | - | - | 38.8 | 268 | - | - | - | - |
| BSP-8 | 0 | 1400 | 1033 | 30.6 | 211 | 30.4 | 210 | - | - | 39.1 | 270 | 38.9 | 268 | - | - |
| BSP-9 | 0 | 1400 | 1033 | 30.3 | 209 | 29.4 | 203 | - | - | 38.5 | 266 | 37.4 | 258 | - | - |
| Average | | | | 30.6 | 211 | 29.9 | 206 | - | - | 38.8 | 268 | 38.1 | 263 | - | - |
| BSE-1 | 0 | 1400 | 1033 | 32.7 | 225 | 32.2 | 222 | - | - | 40.8 | 281 | 40.2 | 277 | - | - |
| BSE-21 | 0 | 1400 | 1033 | 29.2 | 201 | - | - | - | - | 36.7 | 252 | - | - | - | - |
| Average | | | | 31.0 | 213 | 32.2 | 222 | - | - | 38.7 | 267 | 40.2 | 277 | - | - |
| BSD-13 | 0 | 1400 | 1033 | 31.4 | 217 | - | - | - | - | 39.9 | 275 | - | - | - | - |
| BSD-14 | 0 | 1400 | 1033 | 30.2 | 208 | - | - | - | - | 38.3 | 264 | - | - | - | - |
| BSD-15 | 0 | 1400 | 1033 | - | - | - | - | - | - | - | - | - | - | - | - |
| Average | | | | 30.8 | 212 | - | - | - | - | 39.1 | 270 | - | - | - | - |
| BSP-10 | 0 | 2000 | 1366 | 32.0 | 221 | 29.0 | 200 | - | - | 41.7 | 288 | 37.8 | 261 | - | - |
| BSP-11 | 0 | 2000 | 1366 | - | - | 28.3 | 195 | - | - | - | - | 36.4 | 251 | - | - |
| BSP-12 | 0 | 2000 | 1366 | 32.7 | 225 | 28.9 | 199 | - | - | 41.9 | 289 | 37.0 | 255 | - | - |
| Average | | | | 32.4 | 223 | 29.0 | 200 | - | - | 41.8 | 288 | 37.1 | 256 | - | - |
| BSE-4 | 0 | 2000 | 1366 | 29.3 | 202 | 28.2 | 194 | - | - | 36.6 | 253 | 35.3 | 243 | - | - |
| BSE-9 | 0 | 2000 | 1366 | 34.4 | 237 | 32.0 | 221 | - | - | 42.7 | 294 | 39.7 | 274 | - | - |
| BSE-12 | 0 | 2000 | 1366 | 31.9 | 220 | - | - | - | - | 39.5 | 272 | - | - | - | - |
| Average | | | | 31.9 | 220 | 30.1 | 208 | - | - | 39.6 | 273 | 37.5 | 258 | - | - |
| BSD-12 | 0 | 2000 | 1366 | 32.2 | 222 | - | - | - | - | 41.0 | 283 | - | - | - | - |
| BSD-18 | 0 | 2000 | 1366 | 32.4 | 223 | - | - | - | - | 41.2 | 284 | - | - | - | - |
| BSD-19 | 0 | 2000 | 1366 | 32.6 | 224 | - | - | - | - | 41.5 | 286 | - | - | - | - |
| Average | | | | 32.4 | 223 | - | - | - | - | 41.2 | 284 | - | - | - | - |

## Table C-1. Cb-752/R-512E Tensile Test Data, Contd

| Specimen Number | Exposure Cycles | Test Temperature °F | Test Temperature (°K) | Based on Uncoated Area | | | | | | Based on Effective Area | | | | | |
|---|---|---|---|---|---|---|---|---|---|---|---|---|---|---|---|
| | | | | $F_{TU}$ | | $F_{TY}$ | | E | | $F_{TU}$ | | $F_{TY}$ | | E | |
| | | | | ksi | ($MN/m^2$) | ksi | ($MN/m^2$) | psi x $10^6$ | ($GN/m^2$) | ksi | ($MN/m^2$) | ksi | ($MN/m^2$) | psi x $10^6$ | $GN/m^2$) |
| BSP-13 | 0 | 2400 | 1589 | 25.1 | 173 | 17.3 | 119 | 9.5 | 65.5 | 32.2 | 222 | 22.2 | 153 | 12.2 | 84.1 |
| BSP-14 | 0 | 2400 | 1589 | 25.6 | 177 | 18.2 | 126 | 8.9 | 61.4 | 32.8 | 226 | 23.4 | 161 | 11.4 | 78.7 |
| BSP-15 | 0 | 2400 | 1589 | 25.7 | 177 | 18.2 | 126 | 9.2 | 63.4 | 33.0 | 227 | 23.4 | 161 | 11.8 | 81.4 |
| Average | | | | 25.5 | 176 | 17.9 | 123 | 9.2 | 63.4 | 32.7 | 225 | 23.0 | 158 | 11.8 | 81.4 |
| BSE-8 | 0 | 2400 | 1589 | 25.7 | 177 | 18.9 | 130 | 9.3 | 64.1 | 32.1 | 221 | 23.6 | 163 | 11.6 | 80.1 |
| BSE-17 | 0 | 2400 | 1589 | 24.8 | 171 | 18.9 | 130 | 8.7 | 60.0 | 31.7 | 219 | 24.2 | 167 | 11.4 | 78.4 |
| BSE-22 | 0 | 2400 | 1589 | 24.8 | 171 | 16.7 | 115 | 6.9 | 47.6 | 31.1 | 215 | 21.0 | 145 | 8.7 | 59.7 |
| Average | | | | 25.1 | 173 | 18.2 | 125 | 8.3 | 57.2 | 31.6 | 218 | 22.9 | 158 | 10.6 | 72.7 |
| BSD-20 | 0 | 2400 | 1589 | 24.5 | 169 | - | - | - | - | 31.1 | 214 | - | - | - | - |
| BSD-21 | 0 | 2400 | 1589 | 27.1 | 187 | - | - | - | - | 34.2 | 236 | - | - | - | - |
| BSD-22 | 0 | 2400 | 1589 | 23.4 | 161 | - | - | - | - | 26.6 | 204 | - | - | - | - |
| Average | | | | 25.0 | 172 | - | - | - | - | 31.6 | 218 | - | - | - | - |
| BSP-1 | 100 | 75 | 297 | 59.1 | 407 | 45.0 | 310 | 13.2 | 91.0 | 81.8 | 564 | 62.3 | 429 | 18.3 | 126.0 |
| BSP-2 | 100 | 75 | 297 | 59.2 | 408 | 44.9 | 310 | 13.6 | 93.8 | 81.7 | 563 | 62.0 | 427 | 18.8 | 129.4 |
| BSP-5 | 100 | 75 | 297 | 56.0 | 386 | 46.4 | 320 | 16.6 | 114.5 | 77.5 | 534 | 64.2 | 443 | 23.0 | 158.4 |
| Average | | | | 58.1 | 401 | 45.4 | 313 | 14.5 | 99.8 | 80.3 | 554 | 62.8 | 433 | 20.0 | 137.9 |
| BSE-5 | 100 | 75 | 297 | 56.6 | 390 | 45.1 | 311 | 8.5 | 58.6 | 78.6 | 542 | 62.6 | 432 | 11.8 | 81.4 |
| BSE-6 | 100 | 75 | 297 | 59.2 | 408 | 42.4 | 292 | 8.5 | 58.6 | 81.7 | 563 | 58.5 | 403 | 11.7 | 80.9 |
| BSE-11 | 100 | 75 | 297 | 59.5 | 410 | 48.8 | 336 | 14.6 | 100.7 | 81.0 | 558 | 66.4 | 458 | 19.9 | 137.0 |
| Average | | | | 58.4 | 403 | 45.4 | 313 | 10.5 | 72.6 | 80.4 | 554 | 62.5 | 431 | 14.5 | 99.8 |
| BSD-3 | 100 | 75 | 297 | 61.3 | 423 | 49.7 | 343 | 14.6 | 100.7 | 83.5 | 576 | 67.7 | 467 | 19.9 | 137.1 |
| BSD-4 | 100 | 75 | 297 | 57.9 | 399 | 44.8 | 309 | 15.7 | 108.3 | 80.3 | 554 | 62.1 | 428 | 21.8 | 150.2 |
| BSD-10 | 100 | 75 | 297 | 60.5 | 417 | 47.9 | 330 | 15.5 | 106.9 | 85.4 | 589 | 67.6 | 466 | 21.9 | 150.9 |
| Average | | | | 59.9 | 413 | 47.5 | 327 | 15.3 | 105.3 | 83.1 | 573 | 65.8 | 454 | 21.2 | 146.0 |
| BSP-3 | 100 | 2400 | 1589 | 25.8 | 178 | 20.7 | 143 | 9.9 | 68.3 | 35.4 | 224 | 28.4 | 196 | 13.6 | 93.6 |
| BSP-4 | 100 | 2400 | 1589 | 26.3 | 181 | 20.7 | 143 | 9.6 | 66.2 | 36.0 | 248 | 28.3 | 195 | 13.1 | 90.5 |
| BSP-6 | 100 | 2400 | 1589 | 25.5 | 176 | 20.6 | 142 | 11.1 | 76.5 | 36.1 | 249 | 29.2 | 201 | 15.7 | 108.5 |
| Average | | | | 25.9 | 178 | 20.7 | 143 | 10.2 | 70.3 | 35.8 | 247 | 28.6 | 197 | 14.2 | 97.6 |
| BSE-7 | 100 | 2400 | 1589 | 27.9 | 192 | 22.4 | 154 | 9.1 | 62.7 | 38.8 | 267 | 31.1 | 215 | 12.6 | 87.2 |
| BSE-13 | 100 | 2400 | 1589 | 23.8 | 164 | - | - | 7.4 | 51.0 | 32.4 | 223 | - | - | 10.1 | 69.4 |
| BSE-10 | 97 | 2400 | 1589 | - | - | - | - | - | - | - | - | - | - | - | - |
| Average | | | | 25.9 | 179 | 22.4 | 154 | 8.3 | 56.9 | 35.6 | 245 | 31.1 | 215 | 11.4 | 78.3 |
| BSD-5 | 100 | 2400 | 1589 | 25.8 | 178 | - | - | - | - | 37.3 | 257 | - | - | - | - |
| BSD-6 | 100 | 2400 | 1589 | 24.6 | 170 | - | - | - | - | 34.5 | 238 | - | - | - | - |
| BSD-9 | 100 | 2400 | 1589 | 25.9 | 179 | - | - | - | - | 36.5 | 251 | - | - | - | - |
| Average | | | | 25.4 | 175 | - | - | - | - | 36.1 | 249 | - | - | - | - |

## APPENDIX C – Continued

### Table C-2. C-129Y/R-512E Tensile Test Data

| Specimen Number | Exposure Cycles | Test Temperature °F | Test Temperature (°K) | Based on Uncoated Area $F_{TU}$ ksi | $F_{TU}$ ($MN/m^2$) | $F_{TY}$ ksi | $F_{TY}$ ($MN/m^2$) | E $psi \times 10^6$ | E ($GN/m^2$) | Based on Effective Area $F_{TU}$ ksi | $F_{TU}$ ($MN/m^2$) | $F_{TU}$ ksi | $F_{TU}$ ($MN/m^2$) | E $psi \times 10^6$ | E ($GN/m^2$) |
|---|---|---|---|---|---|---|---|---|---|---|---|---|---|---|---|
| YSP-20 | 0 | 75 | 297 | 69.0 | 476 | 54.5 | 376 | 12.3 | 84.8 | 89.1 | 614 | 70.4 | 485 | 15.9 | 109.5 |
| YSP-21 | 0 | 75 | 297 | 70.2 | 484 | 54.7 | 377 | 12.2 | 84.1 | 91.1 | 628 | 71.0 | 489 | 15.8 | 109.1 |
| YSP-22 | 0 | 75 | 297 | 70.0 | 483 | 54.9 | 379 | 12.4 | 85.5 | 91.2 | 629 | 71.5 | 493 | 16.2 | 111.4 |
| Average | | | | 69.7 | 481 | 54.7 | 377 | 12.3 | 84.8 | 90.5 | 624 | 71.0 | 489 | 16.0 | 110.0 |
| YSE-18 | 0 | 75 | 297 | 76.8 | 530 | 59.4 | 410 | 12.5 | 86.2 | 92.4 | 637 | 71.5 | 493 | 15.0 | 103.7 |
| YSE-19 | 0 | 75 | 297 | 75.5 | 521 | 58.8 | 405 | 12.1 | 83.4 | 90.4 | 623 | 70.4 | 485 | 14.5 | 99.8 |
| YSE-20 | 0 | 75 | 297 | 75.9 | 523 | 59.1 | 408 | 12.2 | 84.1 | 92.4 | 637 | 71.9 | 496 | 14.9 | 102.4 |
| Average | | | | 76.1 | 525 | 59.1 | 408 | 12.3 | 84.6 | 91.7 | 632 | 71.3 | 491 | 14.8 | 102.0 |
| YSD-9 | 0 | 75 | 297 | 75.4 | 520 | 58.4 | 403 | 14.6 | 100.7 | 95.5 | 658 | 73.9 | 510 | 18.5 | 127.4 |
| YSD-19 | 0 | 75 | 297 | 74.4 | 513 | 57.3 | 395 | 14.7 | 101.4 | 94.0 | 648 | 72.4 | 499 | 18.6 | 128.0 |
| YSD-24 | 0 | 75 | 297 | 70.3 | 485 | 55.1 | 380 | 13.8 | 95.2 | 93.5 | 645 | 73.3 | 505 | 18.4 | 126.5 |
| Average | | | | 73.4 | 506 | 56.9 | 392 | 14.4 | 99.1 | 94.3 | 650 | 73.2 | 505 | 18.5 | 127.4 |
| YSP-7 | 0 | 1400 | 1033 | 35.2 | 243 | 34.9 | 241 | - | - | 42.8 | 295 | 42.5 | 293 | - | - |
| YSP-8 | 0 | 1400 | 1033 | 34.7 | 239 | 34.3 | 237 | - | - | 43.0 | 296 | 42.5 | 293 | - | - |
| YSP-11 | 0 | 1400 | 1033 | 34.4 | 237 | 33.7 | 232 | - | - | 42.7 | 294 | 41.8 | 288 | - | - |
| Average | | | | 34.8 | 240 | 34.3 | 237 | - | - | 42.8 | 295 | 42.3 | 291 | - | - |
| YSE-7 | 0 | 1400 | 1033 | 35.2 | 243 | 35.2 | 243 | - | - | 43.0 | 296 | 43.0 | 296 | - | - |
| YSE-8 | 0 | 1400 | 1033 | 36.3 | 250 | 36.3 | 250 | - | - | 44.0 | 306 | 44.0 | 306 | - | - |
| YSE-9 | 0 | 1400 | 1033 | 36.6 | 252 | 35.4 | 244 | - | - | 44.7 | 308 | 43.2 | 298 | - | - |
| Average | | | | 36.0 | 248 | 35.6 | 246 | - | - | 44.0 | 303 | 43.5 | 300 | - | - |
| YSD-13 | 0 | 1400 | 1033 | 35.2 | 243 | - | - | - | - | 44.7 | 308 | - | - | - | - |
| YSD-14 | 0 | 1400 | 1033 | 35.3 | 243 | - | - | - | - | 45.0 | 310 | - | - | - | - |
| YSD-15 | 0 | 1400 | 1033 | 34.3 | 237 | - | - | - | - | 43.7 | 301 | - | - | - | - |
| Average | | | | 34.9 | 241 | - | - | - | - | 44.5 | 307 | - | - | - | - |
| YSP-9 | 0 | 2000 | 1366 | - | - | 33.0 | 228 | - | - | - | - | 41.0 | 282 | - | - |
| YSP-12 | 0 | 2000 | 1366 | 36.7 | 253 | 34.1 | 235 | - | - | 45.1 | 311 | 41.9 | 289 | - | - |
| YSP-19 | 0 | 2000 | 1366 | 36.6 | 252 | 32.2 | 222 | - | - | 45.9 | 317 | 40.4 | 279 | - | - |
| Average | | | | 36.7 | 253 | 33.1 | 228 | - | - | 45.5 | 314 | 41.1 | 283 | - | - |
| YSE-10 | 0 | 2000 | 1366 | - | - | - | - | - | - | - | - | - | - | - | - |
| YSE-11 | 0 | 2000 | 1366 | 39.4 | 272 | 35.7 | 246 | - | - | 48.2 | 332 | 43.7 | 301 | - | - |
| YSE-12 | 0 | 2000 | 1366 | 38.1 | 263 | 35.6 | 246 | - | - | 46.6 | 321 | 43.5 | 300 | - | - |
| Average | | | | 38.8 | 267 | 35.7 | 246 | - | - | 47.4 | 326 | 43.6 | 301 | - | - |
| YSD-16 | 0 | 2000 | 1366 | 38.6 | 266 | - | - | - | - | 49.2 | 339 | - | - | - | - |
| YSD-17 | 0 | 2000 | 1366 | 34.0 | 234 | - | - | - | - | 43.2 | 298 | - | - | - | - |
| YSD-20 | 0 | 2000 | 1366 | 32.2 | 222 | - | - | - | - | 40.1 | 277 | - | - | - | - |
| Average | | | | 34.9 | 241 | - | - | - | - | 44.2 | 305 | - | - | - | - |

## Table C-2. C-129Y/R-512E Tensile Test Data, Contd

| Specimen Number | Exposure Cycles | Test Temperature °F | Test Temperature (°K) | Based on Uncoated Area $F_{TU}$ ksi | $F_{TU}$ ($MN/m^2$) | $F_{TY}$ ksi | $F_{TY}$ ($MN/m^2$) | E psi x $10^6$ | E ($GN/m^2$) | Based on Effective Area $F_{TU}$ ksi | $F_{TU}$ ($MN/m^2$) | $F_{TY}$ ksi | $F_{TY}$ ($MN/m^2$) | E psi x $10^6$ | E ($GN/m^2$) |
|---|---|---|---|---|---|---|---|---|---|---|---|---|---|---|---|
| YSP-15 | 0 | 2400 | 1589 | 25.1 | 173 | 17.9 | 123 | 8.6 | 59.3 | 31.3 | 216 | 22.3 | 154 | 10.7 | 74.0 |
| YSP-17 | 0 | 2400 | 1589 | 24.2 | 167 | 18.1 | 125 | 8.6 | 59.3 | 30.3 | 209 | 22.6 | 156 | 10.8 | 74.1 |
| YSP-18 | 0 | 2400 | 1589 | 25.3 | 174 | 18.4 | 127 | 7.5 | 51.7 | 31.1 | 215 | 22.6 | 156 | 9.2 | 63.6 |
| Average | | | | 24.9 | 172 | 18.1 | 125 | 8.2 | 56.7 | 30.9 | 213 | 22.4 | 155 | 10.2 | 70.5 |
| YSE-17 | 0 | 2400 | 1589 | 26.7 | 184 | - | - | 7.9 | 57.5 | 32.5 | 224 | - | - | 9.6 | 66.3 |
| YSE-22 | 0 | 2400 | 1589 | 27.4 | 189 | 18.3 | 126 | 7.8 | 53.9 | 33.6 | 232 | 22.4 | 155 | 9.5 | 65.8 |
| YSE-23 | 0 | 2400 | 1589 | 26.7 | 184 | 18.2 | 125 | 8.9 | 61.4 | 32.7 | 226 | 22.3 | 154 | 10.9 | 75.2 |
| Average | | | | 26.9 | 186 | 18.3 | 126 | 8.2 | 56.5 | 32.9 | 227 | 22.4 | 155 | 10.0 | 69.1 |
| YSD-21 | 0 | 2400 | 1589 | 23.8 | 164 | - | - | - | - | 29.6 | 204 | - | - | - | - |
| YSD-22 | 0 | 2400 | 1589 | 26.7 | 184 | - | - | - | - | 33.3 | 229 | - | - | - | - |
| YSD-23 | 0 | 2400 | 1589 | 25.7 | 177 | - | - | - | - | 32.1 | 222 | - | - | - | - |
| Average | | | | 25.4 | 175 | - | - | - | - | 31.7 | 218 | - | - | - | - |
| YSP-1 | 100 | 75 | 297 | 65.9 | 454 | 57.9 | 399 | 13.5 | 93.1 | 88.0 | 607 | 77.4 | 533 | 18.0 | 124.4 |
| YSP-3 | 100 | 75 | 297 | 64.2 | 443 | 57.4 | 395 | 14.0 | 96.5 | 88.6 | 611 | 77.4 | 533 | 18.9 | 130.2 |
| YSP-4 | 100 | 75 | 297 | 61.3 | 423 | 55.4 | 381 | 13.5 | 93.1 | 83.1 | 573 | 75.1 | 518 | 18.3 | 126.2 |
| Average | | | | 63.8 | 440 | 56.9 | 392 | 13.7 | 94.3 | 86.6 | 597 | 76.6 | 528 | 18.4 | 126.9 |
| YSE-2 | 100 | 75 | 297 | 56.1 | 387 | 54.9 | 379 | 14.1 | 97.2 | 76.5 | 527 | 74.8 | 516 | 19.2 | 132.5 |
| YSE-13 | 100 | 75 | 297 | 64.6 | 445 | 57.3 | 395 | 13.5 | 93.1 | 86.3 | 595 | 76.6 | 528 | 18.0 | 124.4 |
| YSE-15 | 100 | 75 | 297 | 57.9 | 399 | 57.3 | 395 | 14.0 | 96.5 | 77.6 | 535 | 76.8 | 529 | 18.8 | 129.4 |
| Average | | | | 59.5 | 411 | 56.5 | 390 | 13.9 | 95.6 | 80.1 | 552 | 76.1 | 524 | 18.7 | 128.7 |
| YSD-4 | 100 | 75 | 297 | 57.2 | 394 | 56.8 | 392 | 15.3 | 105.5 | 78.8 | 544 | 78.3 | 540 | 21.1 | 145.3 |
| YSD-5 | 100 | 75 | 297 | 62.2 | 429 | 57.1 | 394 | 15.9 | 109.6 | 85.5 | 589 | 78.5 | 541 | 21.9 | 150.7 |
| YSD-7 | 100 | 75 | 297 | 65.3 | 450 | 56.8 | 392 | 16.2 | 111.7 | 91.3 | 629 | 79.4 | 548 | 22.7 | 156.2 |
| Average | | | | 61.6 | 425 | 56.9 | 392 | 15.8 | 108.9 | 85.2 | 587 | 78.7 | 543 | 21.9 | 150.7 |
| YSP-2 | 100 | 2400 | 1589 | 27.9 | 192 | 22.0 | 152 | 10.0 | 69.0 | 37.0 | 255 | 29.2 | 201 | 13.3 | 91.5 |
| YSP-5 | 100 | 2400 | 1589 | 29.1 | 201 | 22.7 | 157 | 10.9 | 75.2 | 40.1 | 276 | 31.3 | 216 | 15.0 | 103.4 |
| YSP-6 | 100 | 2400 | 1589 | 28.4 | 196 | 23.6 | 163 | 13.2 | 91.0 | 39.5 | 272 | 32.8 | 226 | 18.4 | 126.6 |
| Average | | | | 28.5 | 196 | 22.8 | 157 | 11.4 | 78.4 | 38.9 | 268 | 31.1 | 214 | 15.5 | 107.2 |
| YSE-16 | 100 | 2400 | 1589 | 25.5 | 176 | 22.9 | 158 | 8.7 | 60.0 | 34.1 | 235 | 30.6 | 211 | 11.6 | 80.1 |
| YSE-1 | 100 | - | - | - | - | - | - | - | - | - | - | - | - | - | - |
| YSE-14 | 100 | - | - | - | - | - | - | - | - | - | - | - | - | - | - |
| Average | | | | 25.5 | 176 | 22.9 | 158 | 8.7 | 60.0 | 34.1 | 235 | 30.6 | 211 | 11.6 | 80.1 |
| YSD-3 | 100 | 2400 | 1589 | 24.8 | 171 | - | - | - | - | 34.3 | 236 | - | - | - | - |
| YSD-6 | 100 | 2400 | 1589 | 23.5 | 162 | - | - | - | - | 32.9 | 227 | - | - | - | - |
| YSD-8 | 100 | 2400 | 1589 | 26.3 | 181 | - | - | - | - | 36.8 | 254 | - | - | - | - |
| Average | | | | 24.9 | 171 | - | - | - | - | 34.6 | 239 | - | - | - | - |

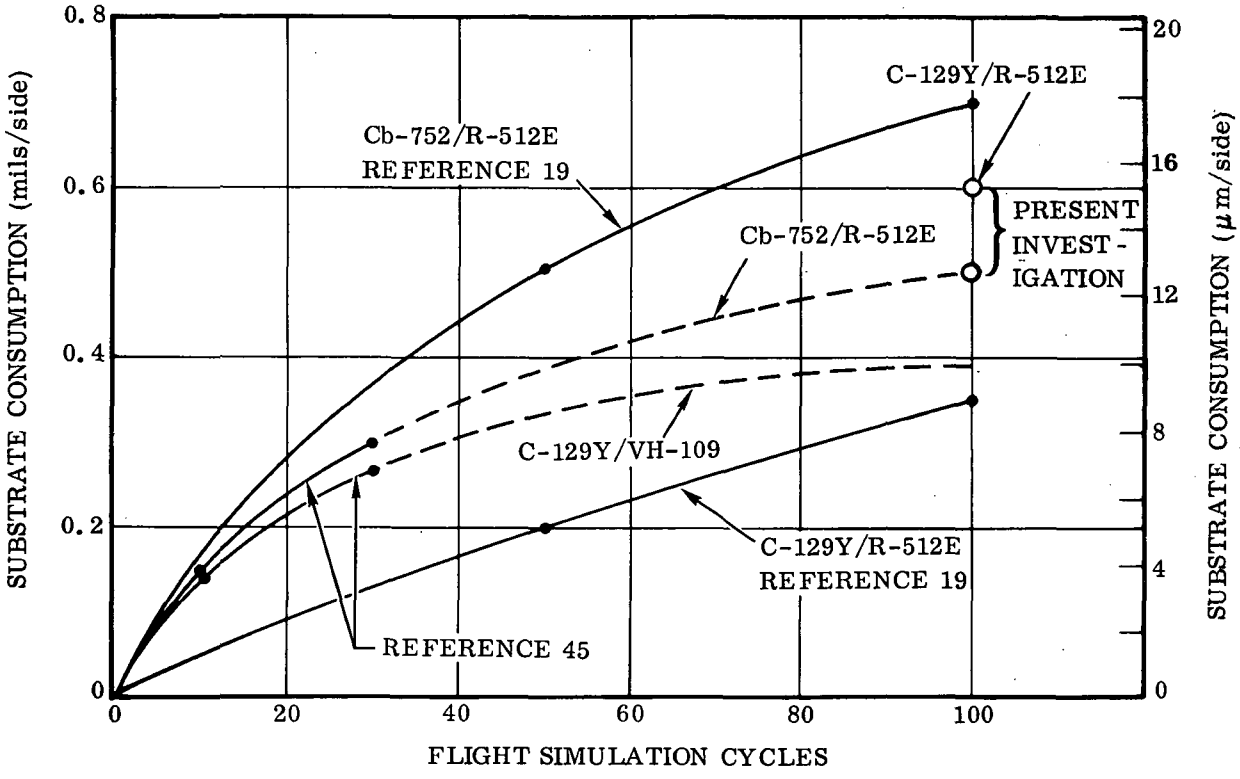


Figure C-1. Substrate Consumption Versus Flight Simulation Cycles

Reference 45 data. The value of 0.0006 to 0.0007 inch (0.0015 to 0.0018 cm) found for C-129Y alloy is somewhat greater than values given by either reference. The correction factors for specimens tested after 100 flight simulation cycles (the adjusted values are listed in Tables C-1 and C-2) are based on a value of 0.0005 inch (0.0013 cm) per side for both alloys.

The factor required to correct test stresses for substrate consumption is:

$$F = \frac{t_{initial}}{t_{initial} - 2\,(t_s)}$$

where

$t_{initial}$ = thickness before coating

$t_s$ = substrate consumption per side

Plots of the adjusted test data for ultimate strength, tensile yield, and elastic modulus versus temperature are presented in Figures C-2 through C-6 for Cb-752/R-512E and in Figures C-7 through C-11 for C-129Y/R-512E. Additional data points from Reference 19 and curves from Reference 45 are included. Preliminary and recommended design curves are also given. The recommended design curves generally follow the "A" values of Reference 45 except where data points from other sources fall below the Reference 45 curve. The curves are presented as conservative approximations only, since in general axial tension properties are not critical for design. Permissible stress levels were dictated by limiting creep strain and/or deflection criteria for this program.

Typical stress-strain diagrams for Cb-752/R-512E are C-129Y/R-512E at room temperature after 100 exposure cycles are presented in Figures C-12 and C-13.

## ANALYSIS OF CREEP TEST RESULTS

Creep tests conducted in this program consisted of both cyclic flight simulation and conventional creep test (Sections 4.3 and 4.5, respectively).

A comparison of creep prediction, made using the static creep data, with cyclic simulation test results gives large discrepancies. The predicted creep strain values were much lower than values from the simulation tests. A limited number of simulation tests for a reduced load profile indicate that the discrepancy between prediction and test increases as stress is reduced.

Correlation factors that bring predictions into agreement with test results have been determined for each alloy/coating combination. The factors are given by an expression of the form $F = C - m(\sigma)$ obtained by fitting a straight line to the simulation test results.

### Larson-Miller Plots for 1% Creep Strain and Comparison with Preliminary Data

The conventional creep test results for 1% creep strain generated in this program (Tables 4-23 and 4-25) for Cb-752/R-512E and C-129Y/R-512E are presented in Larson-Miller plots. This form of presentation was required for use in subsequent creep analysis. Preliminary curves presented in Reference 46 are shown for comparison. The plots for both materials cross the preliminary curves at a stress of approximately 2.0 ksi (13.8 $MN/m^2$), indicating increased times to 1% creep strain above this stress and reduced times for lower values. The C-129Y data for all test

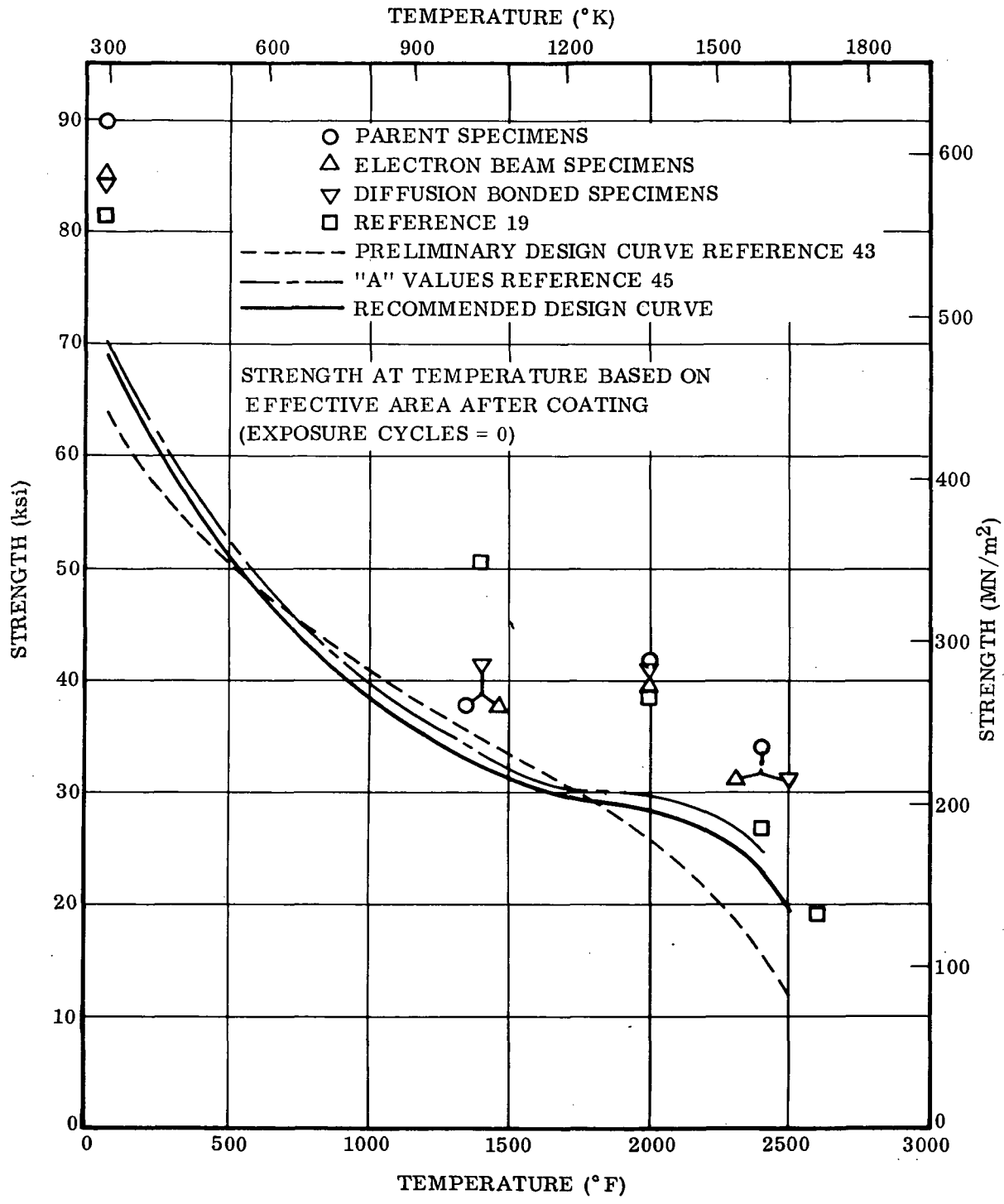


Figure C-2. Ultimate Strength of Cb-752/R-512E

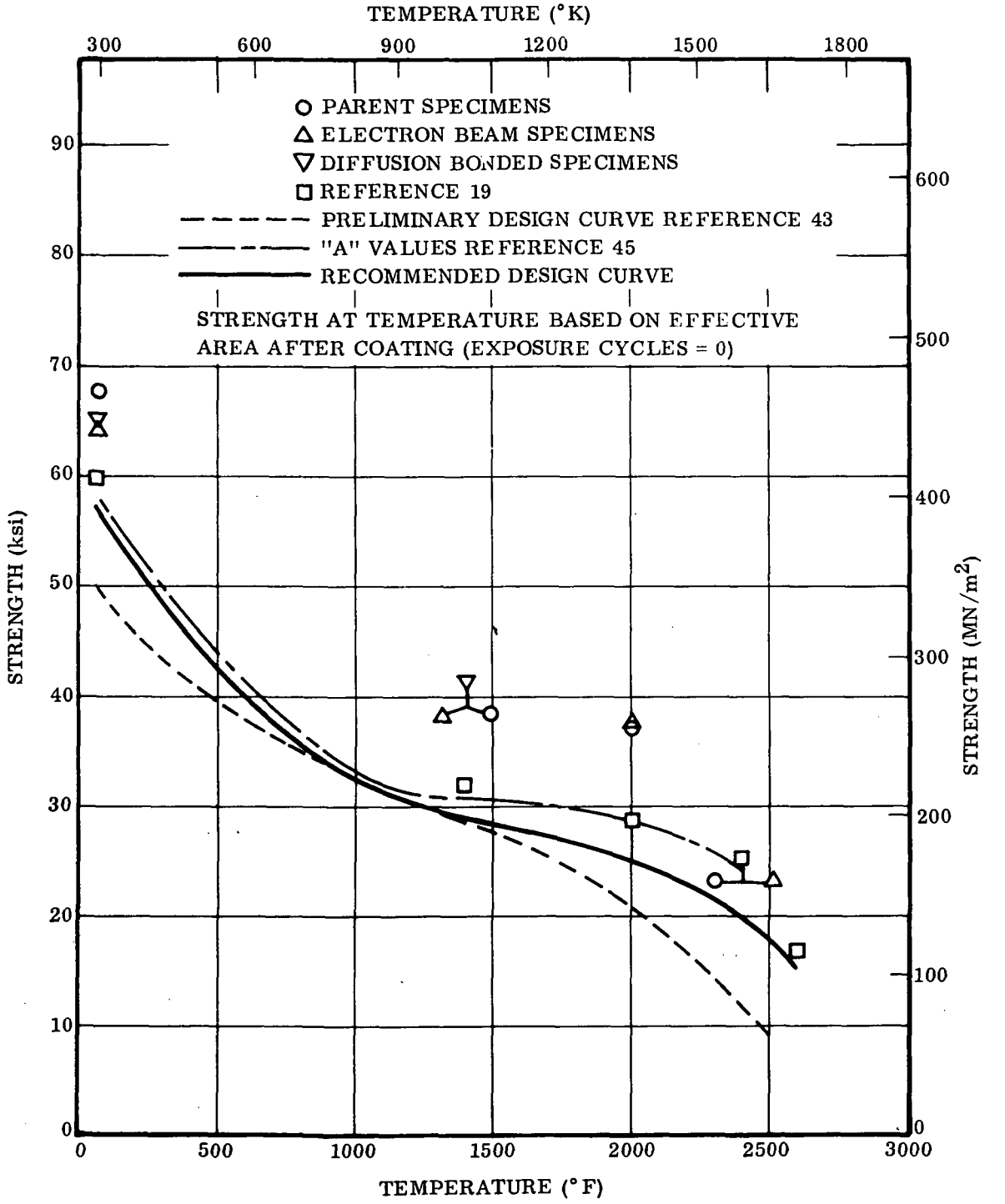


Figure C-3. Yield Strength of Cb-752/R-512E

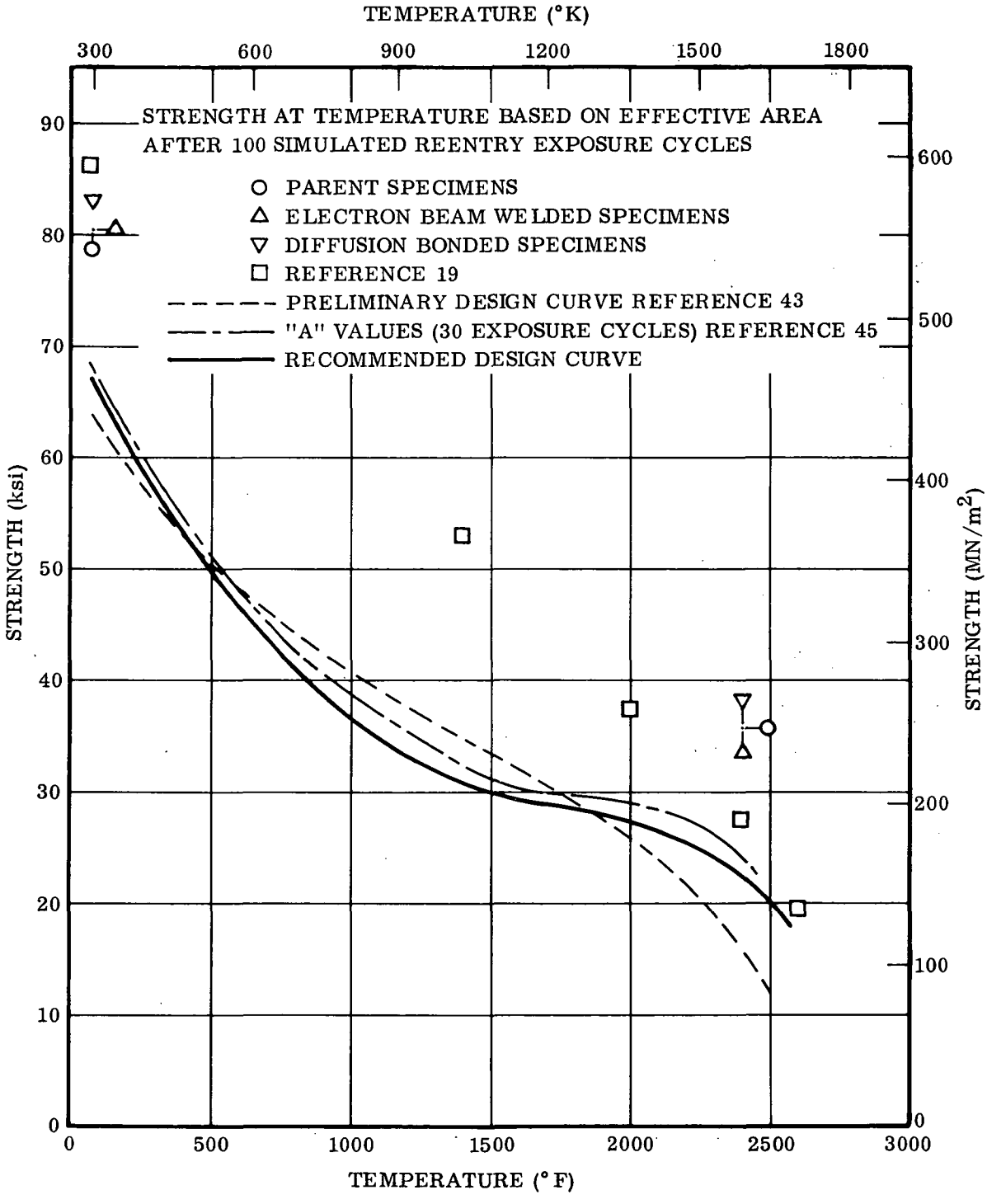


Figure C-4. Ultimate Strength of Cb-752/R-512E

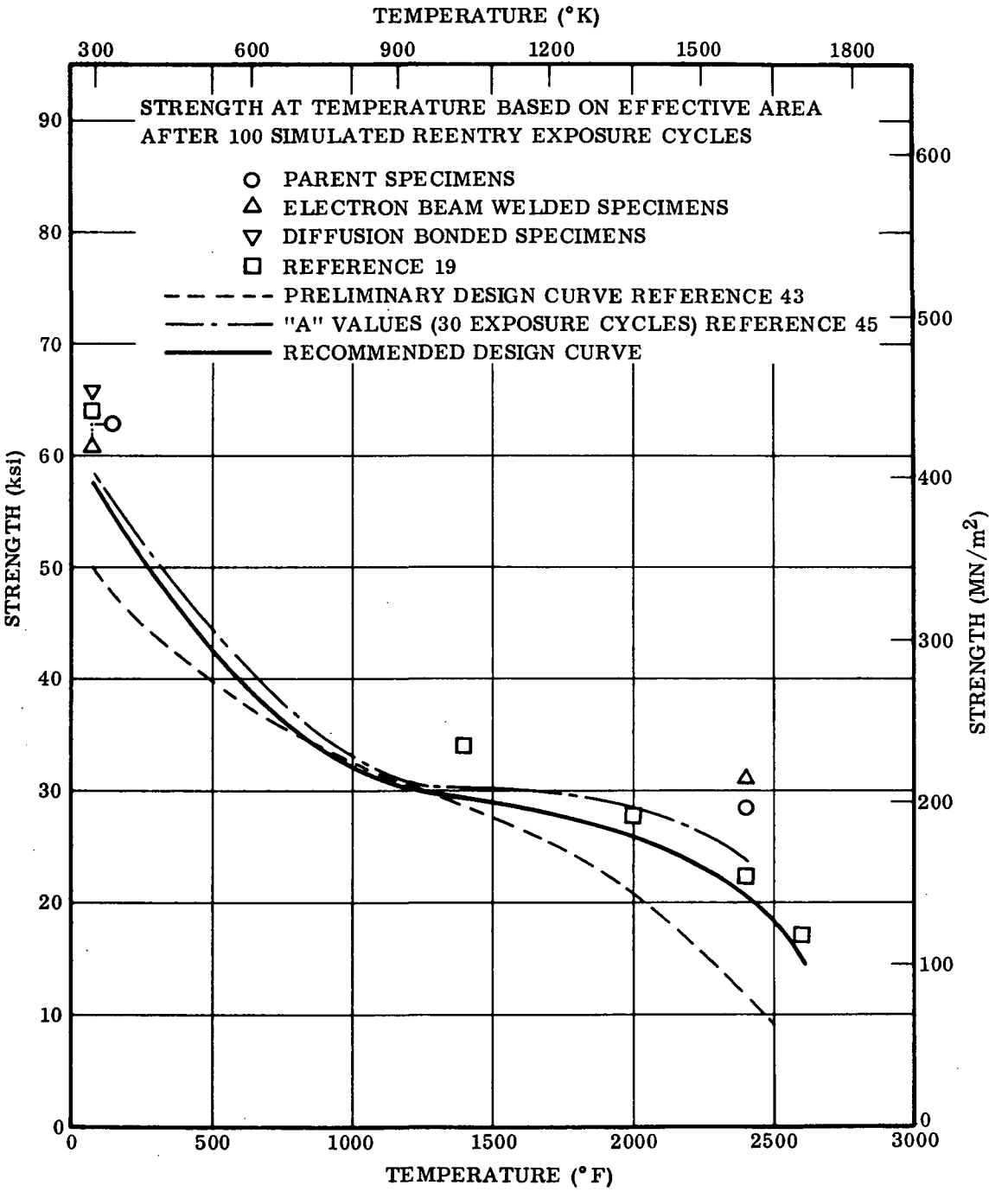


Figure C-5. Yield Strength of Cb-752/R-512E

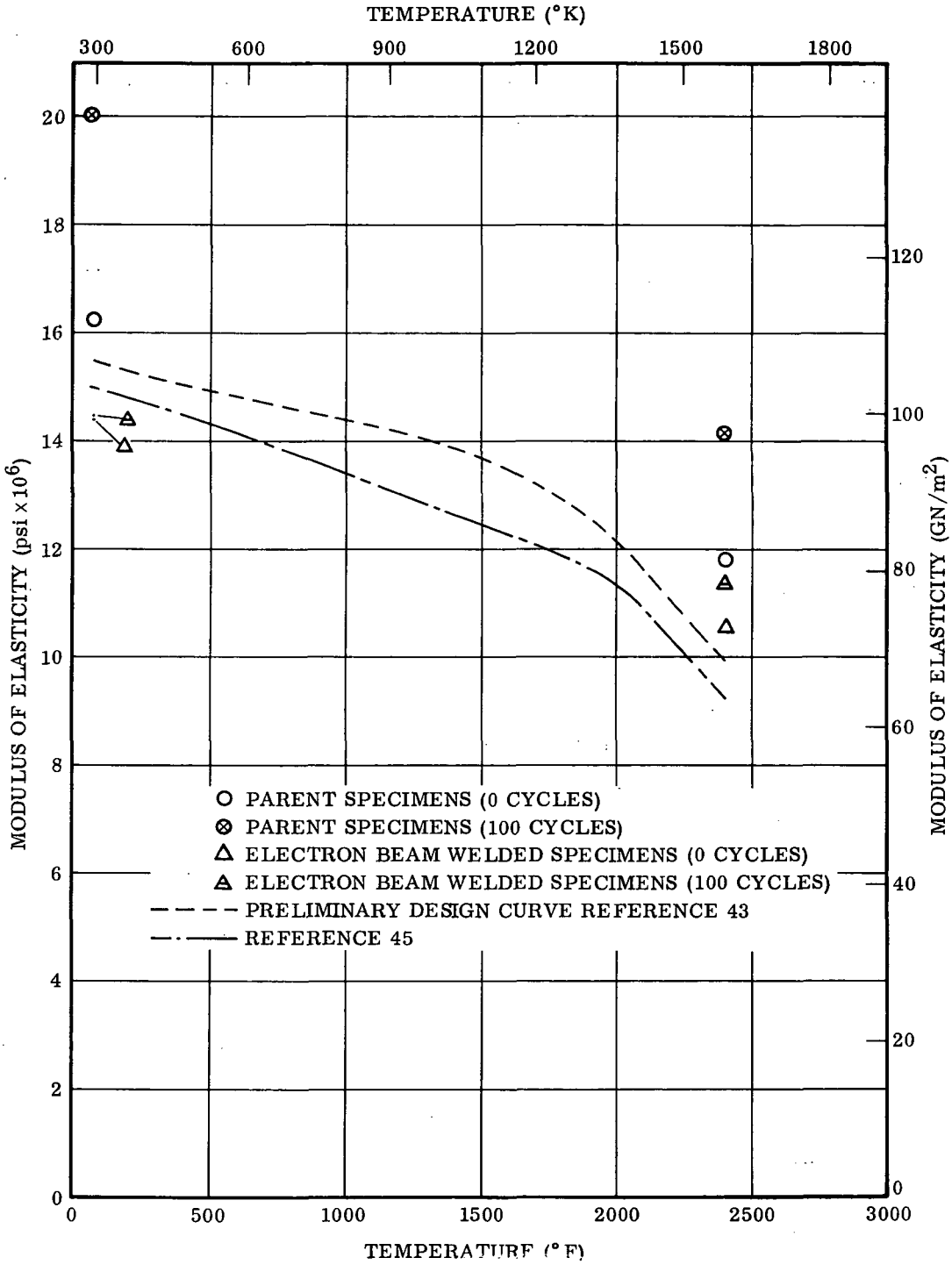


Figure C-6. Modulus of Elasticity of Cb-752/R-512E

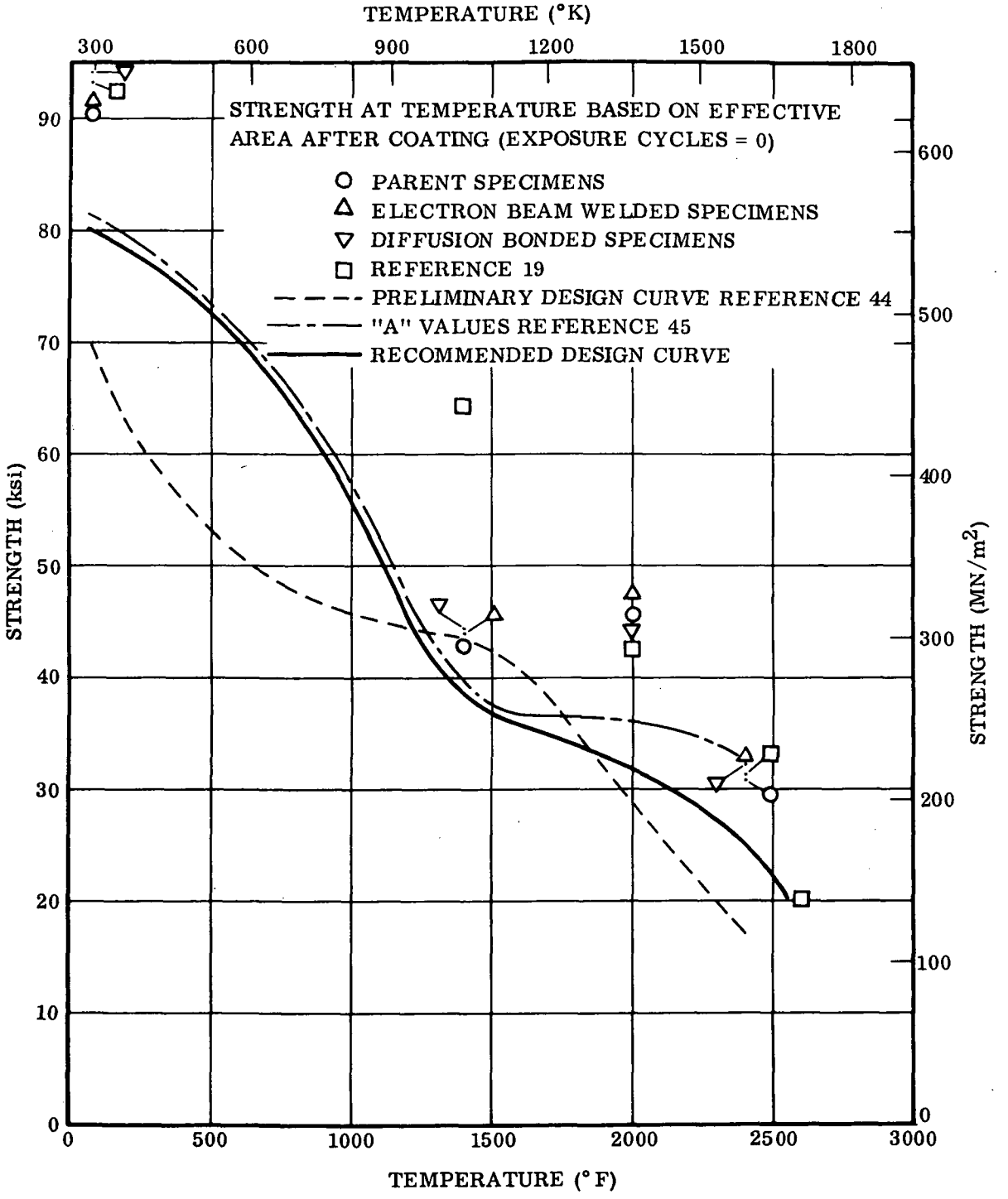


Figure C-7. Ultimate Strength of C-129Y/R-512E

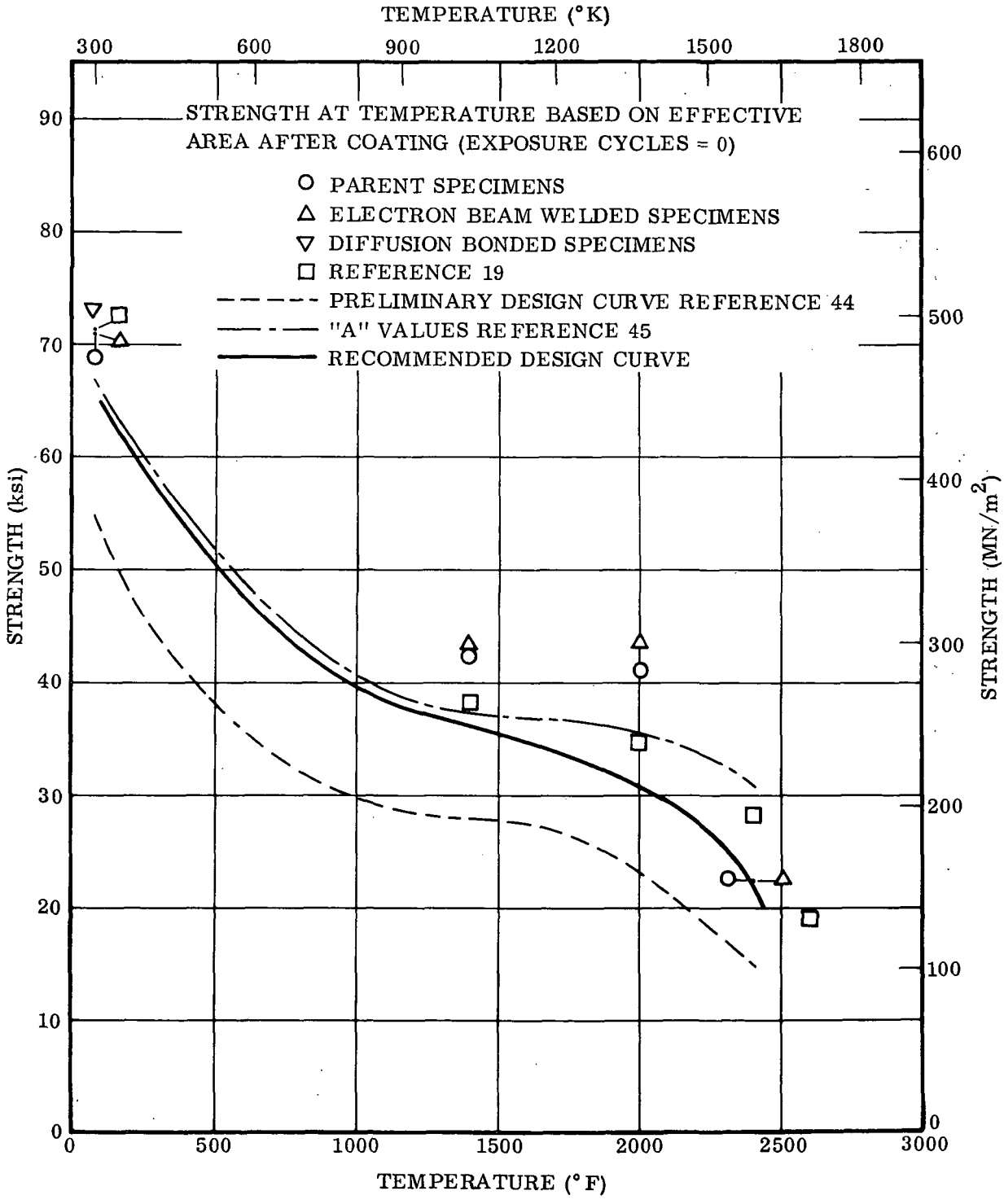


Figure C-8. Yield Strength of C-129Y/R-512E

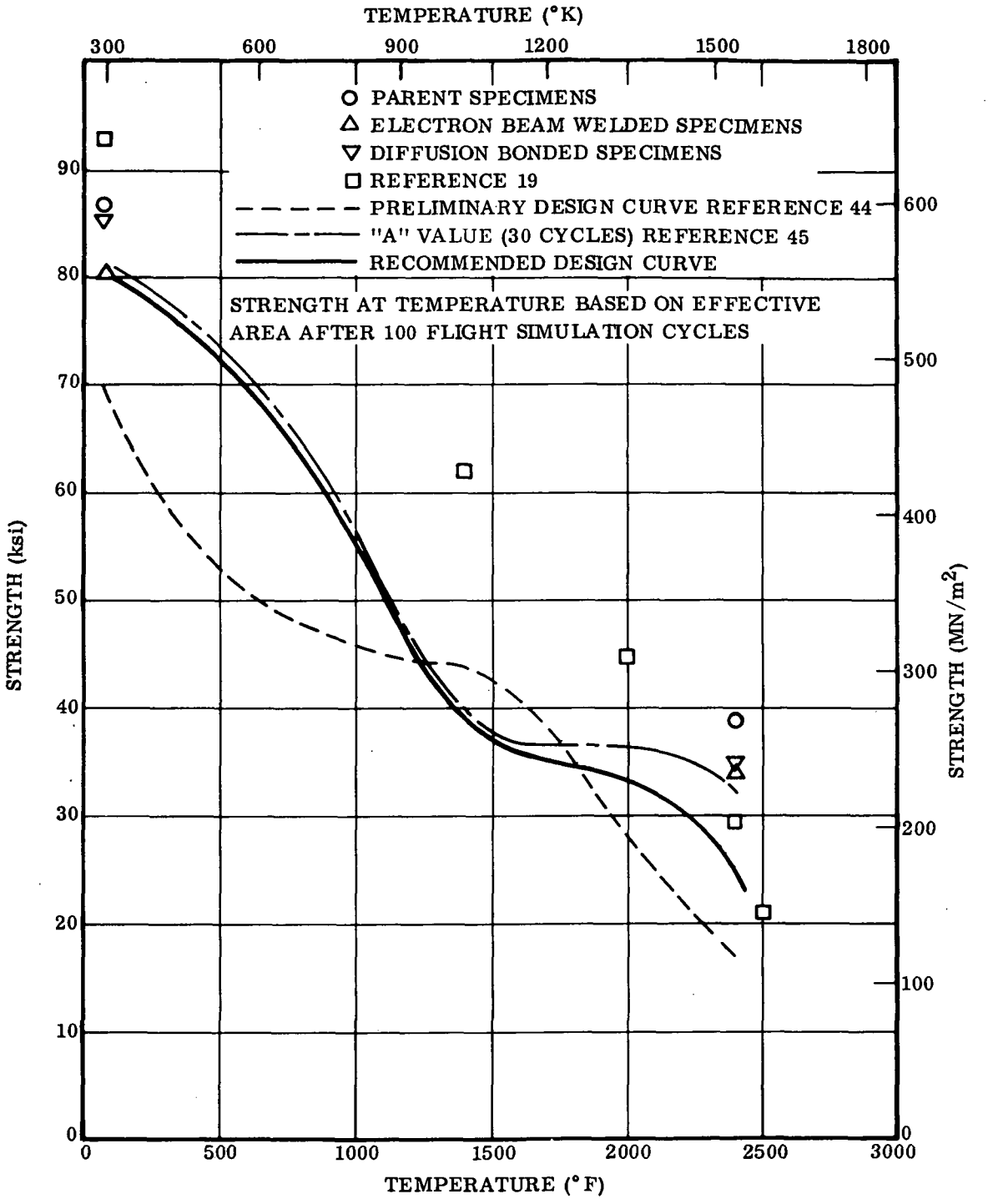


Figure C-9. Ultimate Strength of C-129Y/R-512E

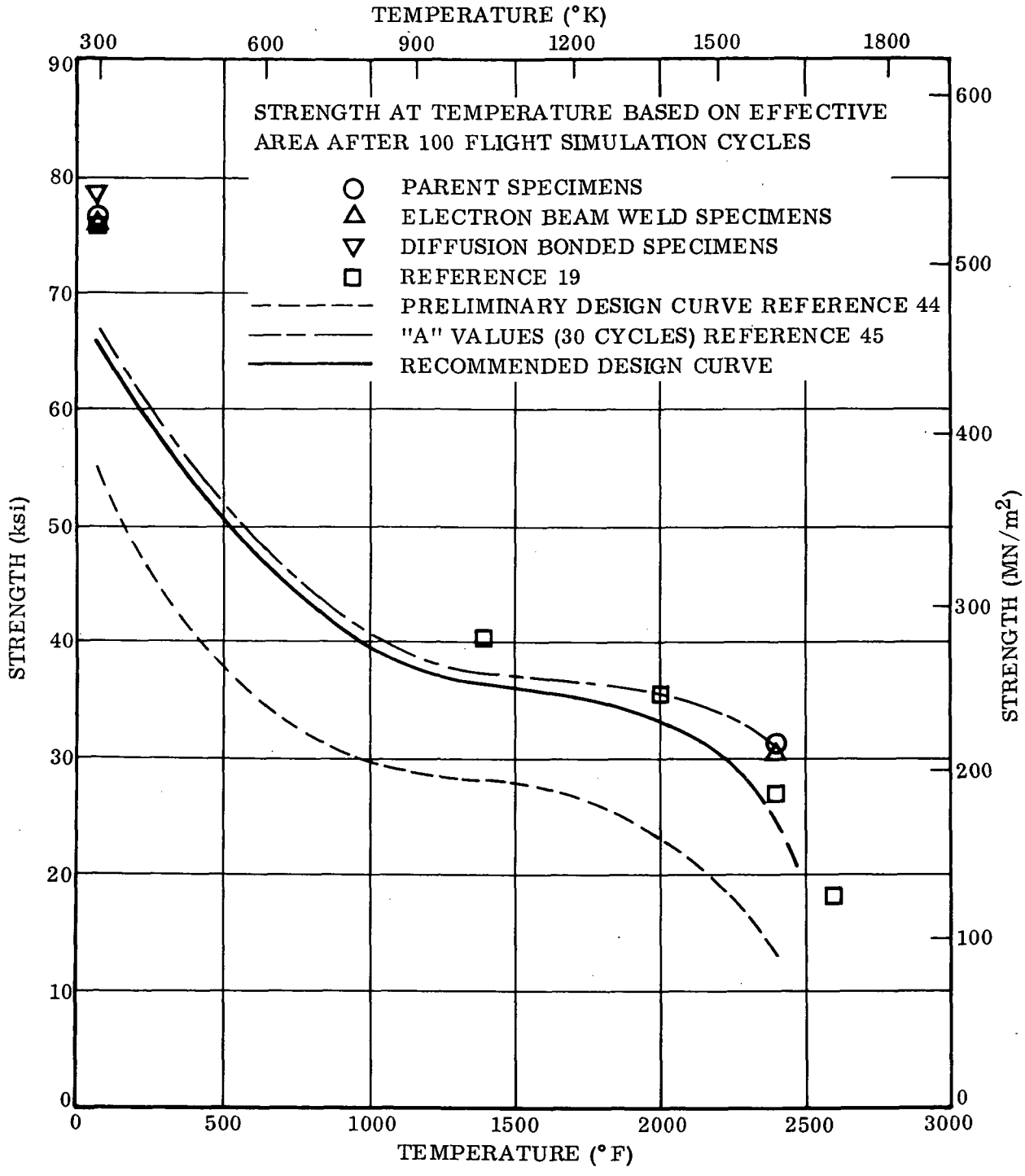


Figure C-10. Yield Strength of C-129Y/R-512E

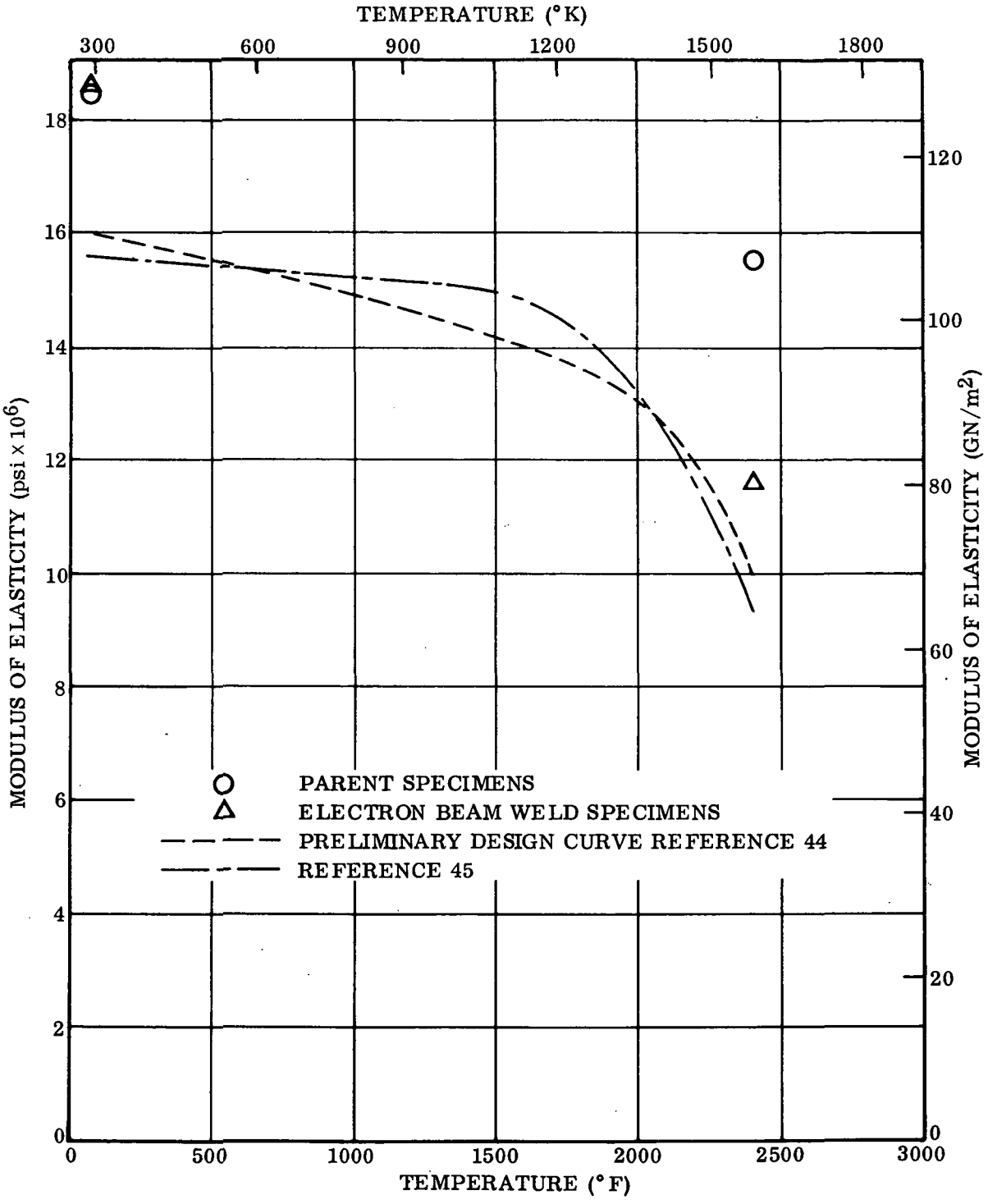


Figure C-11. Modulus of Elasticity of C-129Y/R-512E

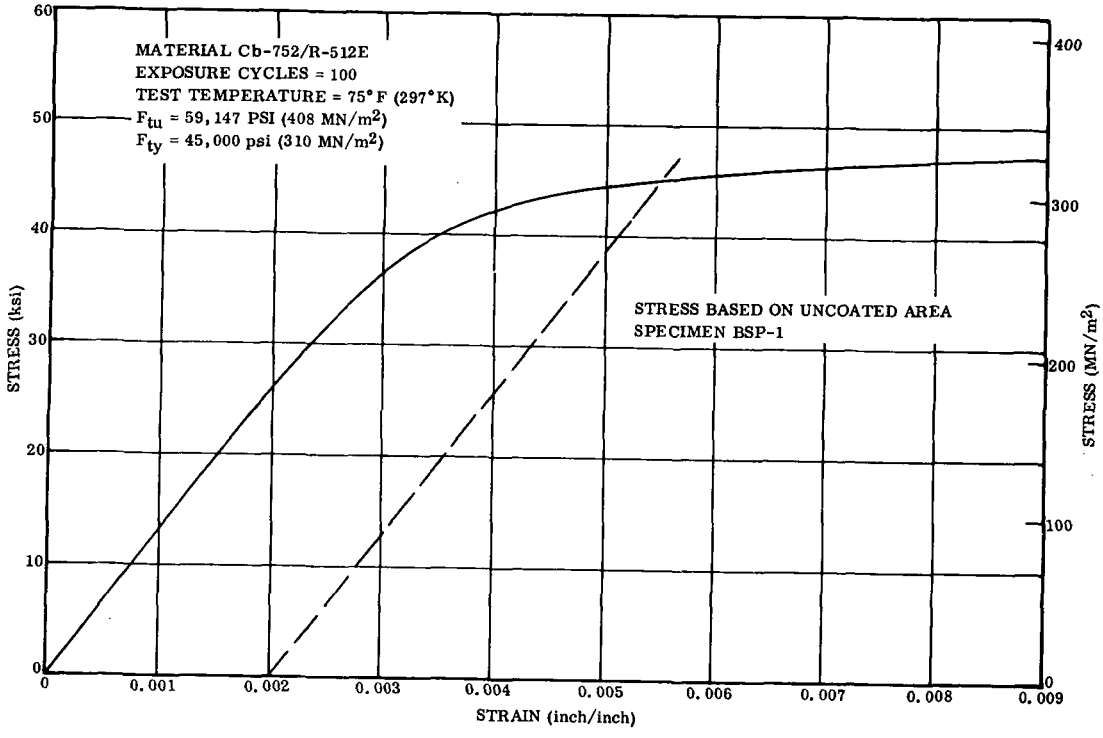


Figure C-12. Typical Stress-Strain Curve for Cb-752/R-512E After Exposure

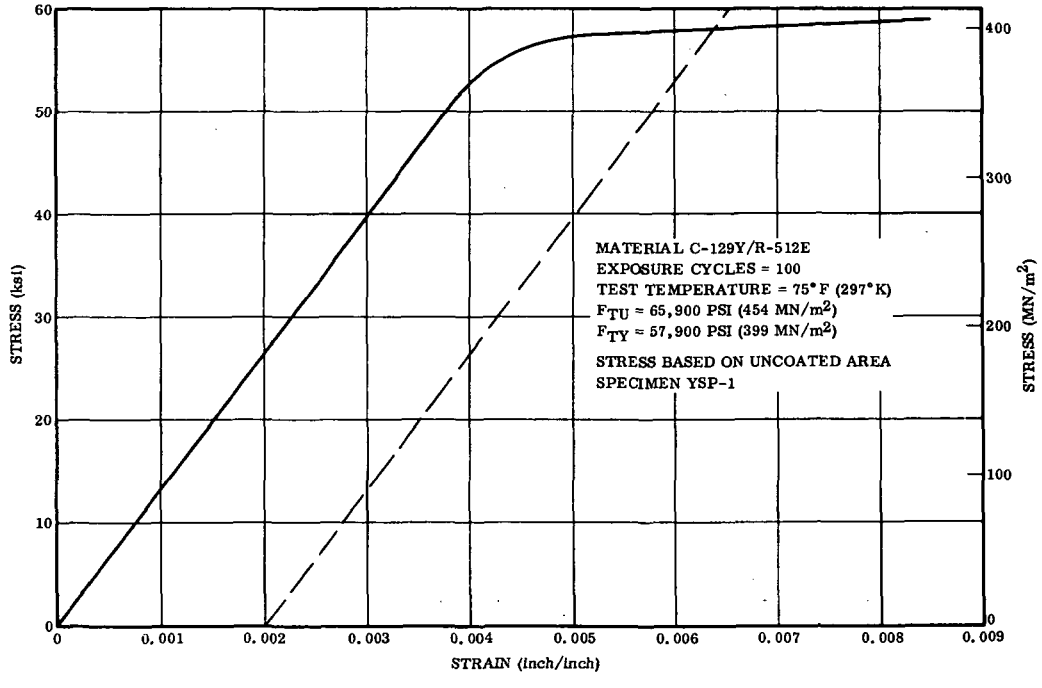


Figure C-13. Typical Stress-Strain Curve for C-129Y/R-512E After Exposure

temperatures correlate well with a Larson-Miller constant (C) equal to 13.7 (Table C-3) as used for the preliminary data. The best correlation for the Cb-752 data is obtained with a Larson-Miller constant equal to 10.2 rather than the value of 15 used for the preliminary curve (Table C-4).

The Larson-Miller curve for C-129Y is given in Figure C-14. Two plots are presented for Cb-752 in Figures C-15 and C-16. Figure C-15 using (C) equal to 15.0 shows the test data and the preliminary curve on a common basis for comparison only.

Table C-3. Creep Test Data for C-129Y/R-512E (See Table 4-23)

| Temperature | | | $\sigma$(1) | | $t_{1\%}$ | Larson-Miller Parameter(2) |
|---|---|---|---|---|---|---|
| °F | (°R) | (°K) | ksi | ($MN/m^2$) | hours | C = 13.7 |
| 2400 | 2860 | 1589 | 1.27 | 8.8 | 38.5 | 43,716 |
| | | | 1.90 | 13.1 | 23.0 | 43,076 |
| | | | 2.54 | 17.5 | 13.8 | 42,442 |
| 2200 | 2660 | 1478 | 3.81 | 26.3 | 56.2 | 41,096 |
| | | | 5.08 | 35.0 | 45.8 | 40,860 |
| | | | 6.35 | 47.8 | 26.4 | 40,223 |
| 2000 | 2460 | 1366 | 10.8 | 74.5 | >100 | 38,622 |
| | | | 12.7 | 87.6 | 92.8 | 38,542 |
| | | | 15.9 | 109.6 | 52.8 | 37,940 |

(1) Based on effective area after coating.
(2) $P = (T+460)(C+\log t_{1\%})$.

Table C-4. Creep Test Data for Cb-752/R-512E (See Table 4-25)

| Temperature | | | $\sigma$(1) | | $t_{1\%}$ | Larson-Miller Parameter(2) | |
|---|---|---|---|---|---|---|---|
| °F | (°R) | (°K) | ksi | ($MN/m^2$) | hours | C = 15 | C = 10.205 |
| 2400 | 2860 | 1589 | 1.27 | 8.8 | 98 | 48,595 | 34,881 |
| | | | 1.90 | 13.1 | 44.2 | 47,606 | 33,892 |
| | | | 2.54 | 17.5 | 24.5 | 46,873 | 33,159 |
| 2200 | 2660 | 1478 | 3.81 | 26.3 | 91.2 | 45,114 | 32,359 |
| | | | 5.08 | 35.0 | 58.7 | 44,605 | 31,850 |
| | | | 6.35 | 47.8 | 46.0 | 44,323 | 31,568 |
| 2000 | 2460 | 1366 | 12.7 | 87.6 | 145 | 42,217 | 30,421 |
| | | | 15.9 | 109.6 | 46 | 40,990 | 29,195 |
| | | | 19.0 | 131.0 | 20.5 | 40,126 | 28,331 |

(1) Based on estimated thickness of substrate remaining after coating.
(2) $P = (T+460)(C+\log t_{1\%})$

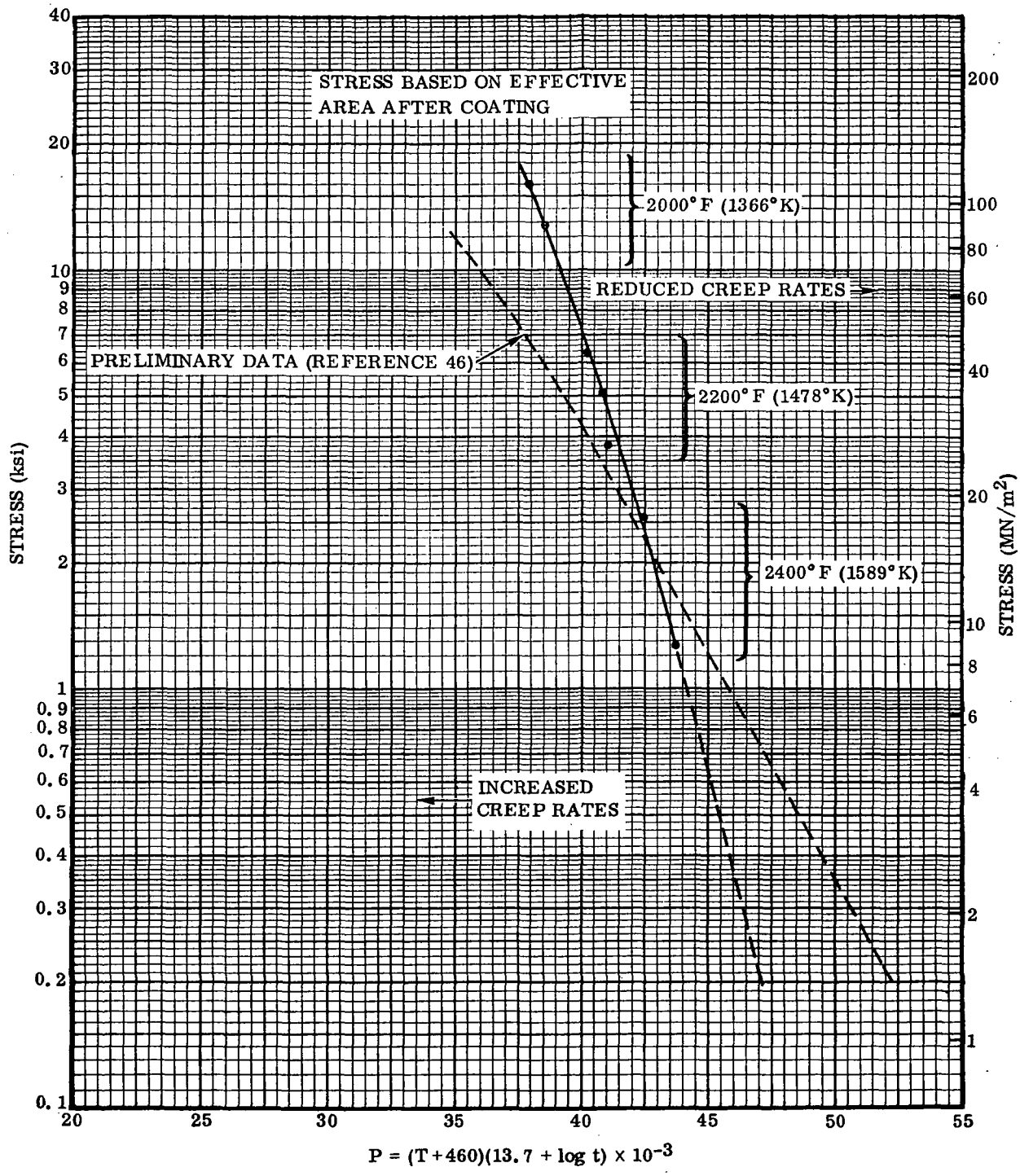


Figure C-14. Larson-Miller Comparison of 1% Creep Test Results with Preliminary Data for C-129Y/R-512E

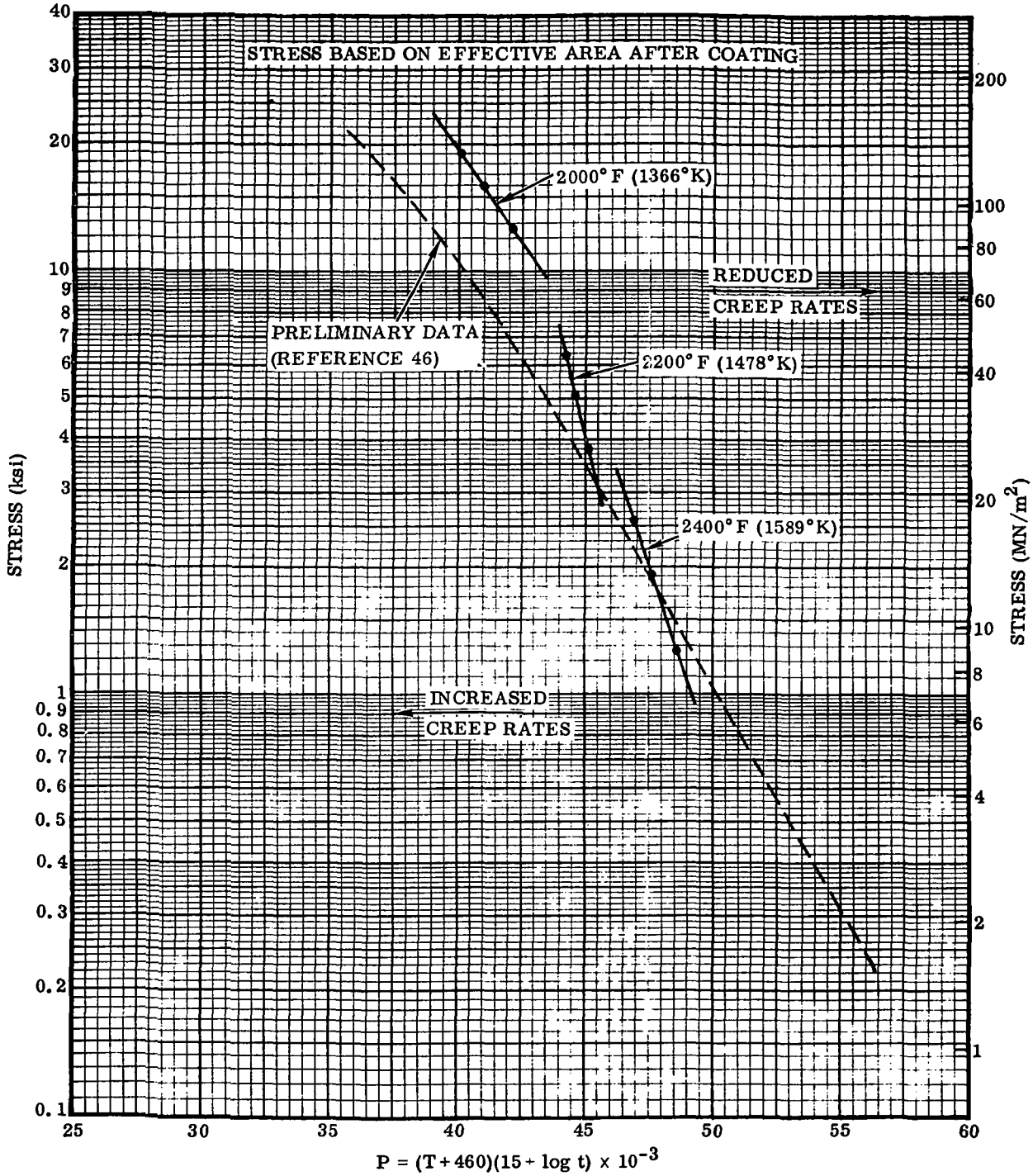


Figure C-15. Larson-Miller Comparison of 1% Creep Test Results with Preliminary Data for Cb-752/R-512E

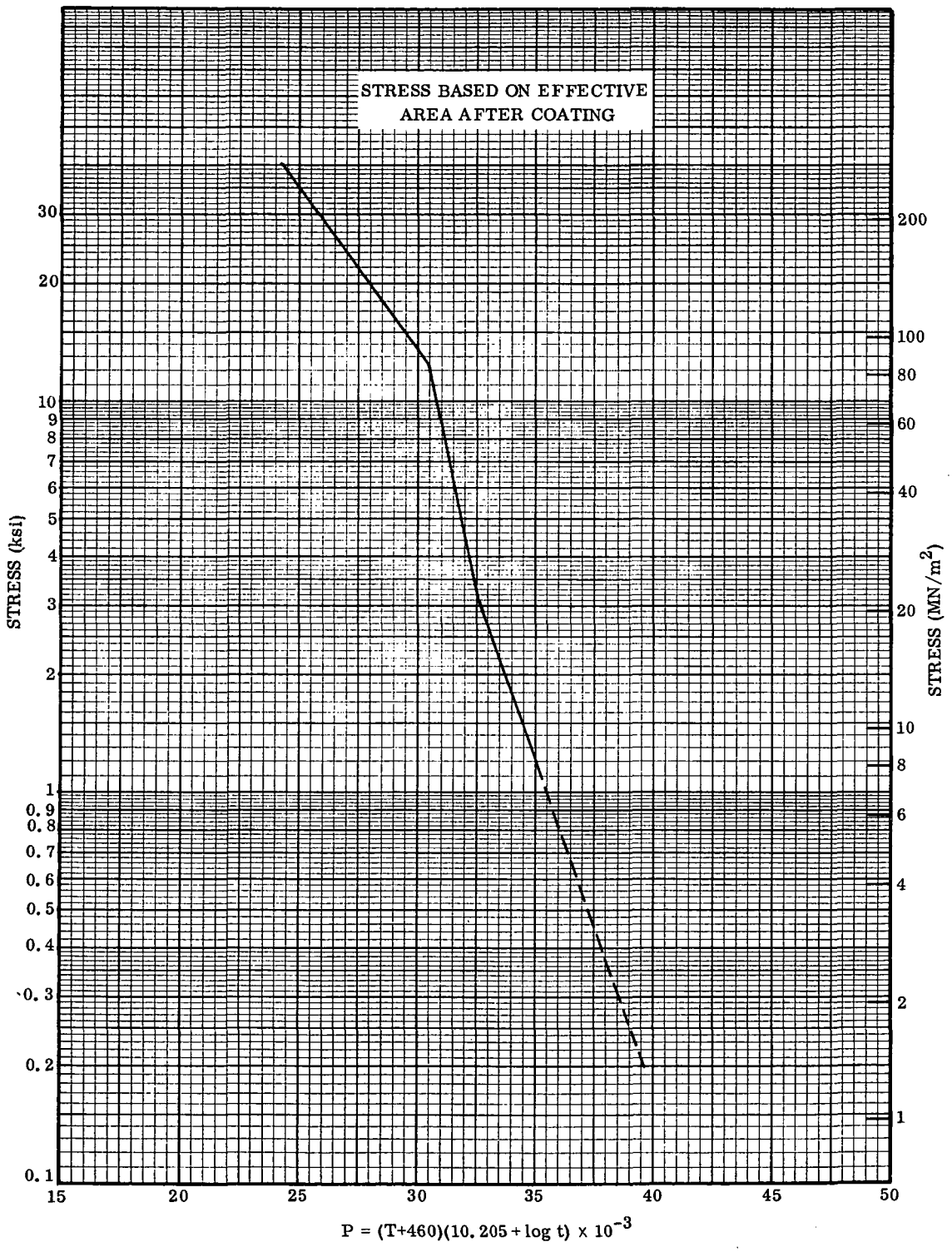


Figure C-16. Larson-Miller Plot for 1% Creep for Cb-752/R-512E

## Predicted Creep Strain for Flight Simulation Test Specimens

To compare and correlate the creep analysis method used for panel design with flight simulation test results, creep predictions have been made for nominal Cb-752 and C-129Y simulation specimens. For convenience, the analysis was made for a range of reference stress levels. The results are presented as curves of creep strain versus reference stress in Figures C-17 and C-18. The reference stress is the minimum stress in the simulation test cycle, occurring at time of maximum temperature [2400° F (1589° K)] and is based on the effective thickness after coating.

The creep analysis is accomplished by subdividing the simulation test profile into 20 time intervals as shown in Figure C-19. The instantaneous stress and creep rate are computed for each time interval. Hence the creep strain per flight is given by

$$\epsilon = \sum_{i=1}^{n} \dot{\epsilon}\, \Delta t$$

To account for the loss of substrate due to coating diffusion, the analysis was made repetitively with the effective thickness progressively reduced. The 100 simulation cycles were approximated by 10 creep summations. A diffusion rate of 0.00001 inch (0.000254 mm) per side per flight was assumed.

The analysis was performed using a computer program that requires the input creep data in the form of Larson-Miller parameter versus stress. The plots for 1% creep strain given in Figures C-14 and C-16 were used.

The creep rate $\dot{\epsilon}$ is derived as follows.

$$P = (T+460)(C+\log t_{1\%})$$

Hence the time to 1% creep strain is given by:

$$t_{1\%} = 10^{\left(\frac{P}{T+460} - C\right)}$$

and

$$\dot{\epsilon} = \frac{0.01}{t_{1\%}}$$

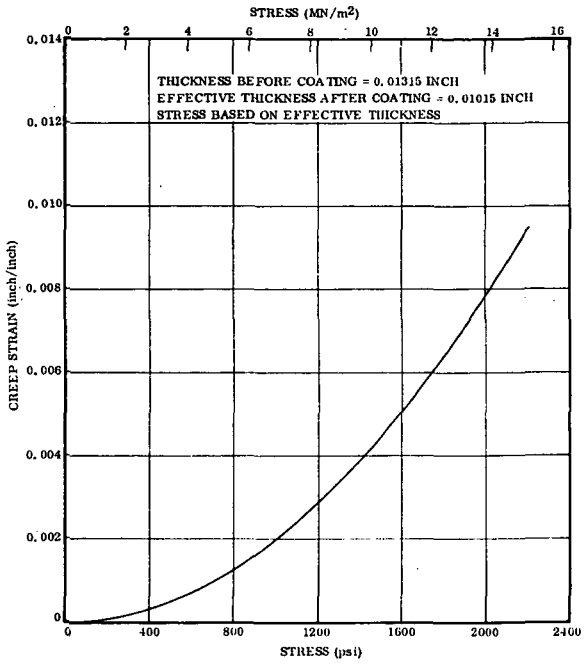


Figure C-17. Predicted Creep Strain Versus Stress for Nominal Cb-752/R-512E Simulation Specimen

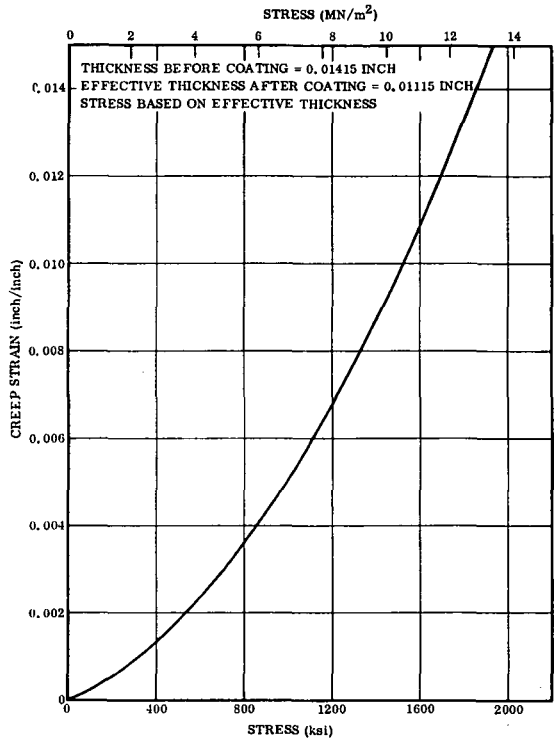


Figure C-18. Predicted Creep Strain Versus Stress for Nominal C-129Y/R-512E Simulation Specimen

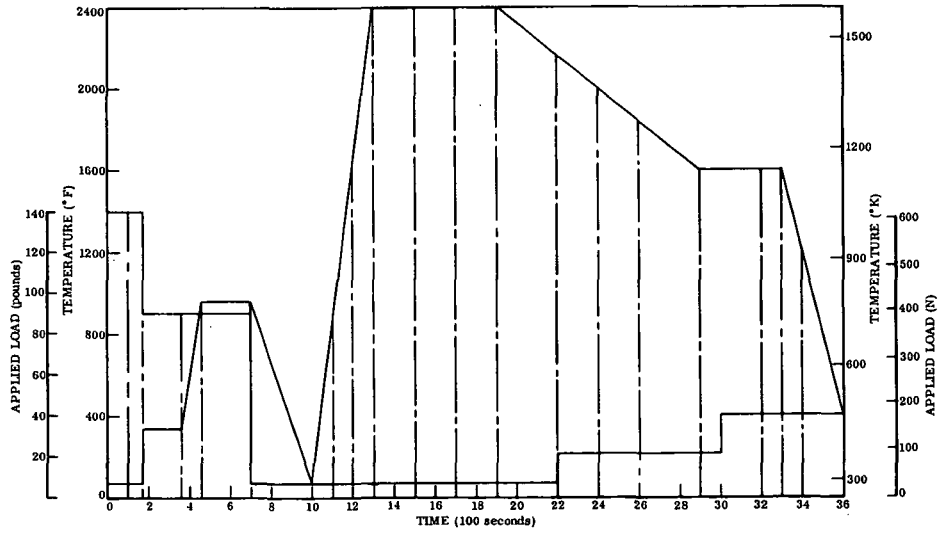


Figure C-19. Analytical Time Intervals of the Flight Simulation Test Profile

## Correlation of Creep Predictions with Simulation Test Results

The basic flight simulation tests were conducted using the test load and temperature profiles shown in Figure 4-5. The minimum nominal test load of 7.0 pounds (0.32 kg) acting at time of maximum temperature [2400° F (1589°K)] represents a stress level of 1270 psi (8.8 $N/m^2$) in a nominal [0.5 by 0.015 in. (1.27 by 0.038 cm)] specimen. Tests at this stress level yielded creep strains greater than 2.0% and hence a limited number of reduced load specimens at a nominal stress level of 820 psi (5.7 $N/m^2$) were tested. While these specimens yielded reduced creep strain (approximately 1.3%), a comparison with predicted values indicates that the ratio of test to predicted creep is increased over that found for the normal load specimens. This result indicates that the relationship between creep predictions, based on conventional creep data, and cyclic test is a function of stress. The number of reduced load specimens is too small to give a high degree of confidence in this trend, however. Since criteria for limiting creep strain and deflection require the establishment of design stress levels below the minimum flight simulation test values, it is necessary to evaluate the relationship as accurately as possible using the available data.

The procedure outlined in the following steps related creep predictions based on conventional creep data generated under this program with simulation test results. Stress values are those occurring during time of minimum load and maximum temperature [2400° F (1589°K)] in the simulation test profile and are based on actual measured specimen dimensions taken before and after coating. The effective thickness after coating is computed assuming a substrate consumption per side equal to 50% of the growth due to coating (per side).

(1) Compute applied stress level ($\sigma$) for all specimens in each set, including appropriate reduced load specimen(s).

(2) Predict creep strain for each specimen using contract creep data.

(3) Compute (R) for each specimen: the ratio of simulation test value to predicted creep strain from (2).

(4) Determine the linear regression equation of (R) on ($\sigma$).

(5) Compute the standard error of estimate ($S_{R\sigma}$) for each set of data.

The analyses for Cb-752/R-512E parent, C-129Y/R-512E parent, and electron beam weld specimens are given in Tables C-5, C-6, and C-7 respectively.

## Table C-5. Correlation Factors for Cyclic Creep Material – Cb-752/R-512E Parent Specimens

| Specimen Number | ① Area Before Coating | | ② $t_o$ | | ③ $t_i$ | | ④ $\sigma$ $\frac{P \times ②}{① \times ③}$ | | ⑤ Predicted $\epsilon$ | ⑥ Test $\epsilon$ | ⑦ R |
|---|---|---|---|---|---|---|---|---|---|---|---|
| | $in^2$ | $(mm^2)$ | inch | (mm) | inch | (mm) | psi | $MN/m^2$ | % | % | ⑥/⑤ |
| BSP-1 | 0.00727 | 4.691 | 0.0146 | 0.3708 | 0.01154 | 0.2931 | 1217 | 8.39 | 0.30 | 2.07 | 6.90 |
| BSP-2 | 0.00732 | 4.723 | 0.0147 | 0.3734 | 0.01164 | 0.2957 | 1207 | 8.32 | 0.29 | 2.07 | 7.13 |
| BSP-3 | 0.00733 | 4.729 | 0.0147 | 0.3734 | 0.01170 | 0.2972 | 1200 | 8.27 | 0.29 | 2.27 | 7.83 |
| BSP-4 | 0.00733 | 4.729 | 0.0147 | 0.3734 | 0.01174 | 0.2982 | 1195 | 8.24 | 0.29 | 2.27 | 7.83 |
| BSP-6 | 0.00729 | 4.704 | 0.0146 | 0.3708 | 0.01130 | 0.2870 | 1240 | 8.55 | 0.30 | 2.17 | 7.23 |
| BSE-3 | 0.00642 | 4.142 | 0.0130 | 0.3302 | 0.01050 | 0.2667 | 868 | 5.98 | 0.15 | 1.18 | 7.87 |

$\bar{R} = \frac{\Sigma R}{N} = 7.465$; standard deviation (S) = 0.4283

The regression line of R on $\sigma$ is given by $R = 9.289 - 0.00158\ (\sigma)$

Coefficient of correlation ($\nu$) = -0.5211

Therefore the standard error of estimate $= S\sqrt{1-\nu^2}$

$= 0.4283\sqrt{1-0.5211^2} = 0.3655$

## Table C-6. Correlation Factors for Cyclic Creep Material – C-129Y/R-512E Parent Specimens

| Specimen Number | ① Area Before Coating | | ② $t_o$ | | ③ $t_i$ | | ④ $\sigma$ $\frac{P \times ②}{① \times ③}$ | | ⑤ Predicted $\epsilon$ | ⑥ Test $\epsilon$ | ⑦ R |
|---|---|---|---|---|---|---|---|---|---|---|---|
| | $in^2$ | $(mm^2)$ | inch | (mm) | inch | (mm) | psi | $MN/m^2$ | % | % | ⑥/⑤ |
| YSP-1 | 0.00713 | 4.600 | 0.0143 | 0.3632 | 0.01170 | 0.2972 | 1200 | 8.27 | 0.677 | 1.58 | 2.33 |
| YSP-2 | 0.00713 | 4.600 | 0.0144 | 0.3658 | 0.01185 | 0.3010 | 1193 | 8.23 | 0.665 | 1.88 | 2.83 |
| YSP-3 | 0.00707 | 4.562 | 0.0141 | 0.3581 | 0.01145 | 0.2908 | 1220 | 8.41 | 0.695 | 1.67 | 2.40 |
| YSP-4 | 0.00706 | 4.555 | 0.0141 | 0.3581 | 0.01140 | 0.2896 | 1226 | 8.45 | 0.700 | 1.87 | 2.67 |
| YSP-5 | 0.00685 | 4.420 | 0.0137 | 0.3480 | 0.01095 | 0.2781 | 1279 | 8.82 | 0.750 | 1.88 | 2.51 |
| YSP-6 | 0.00686 | 4.426 | 0.0137 | 0.3480 | 0.01085 | 0.2756 | 1288 | 8.88 | 0.760 | 1.67 | 2.20 |
| YSP-10 | 0.00737 | 4.755 | 0.0147 | 0.3734 | 0.01200 | 0.3048 | 748 | 5.16 | 0.330 | 1.35 | 4.09 |

$\bar{R} = \frac{\Sigma R}{N} = 2.7186$; standard deviation (S) = 0.6404

The regression line of R on $\sigma$ is given by $R = 6.534 - 0.00328\ (\sigma)$

Coefficient of correlation ($\nu$) = -0.9587

Therefore the standard error of estimate $= S\sqrt{1-\nu^2}$

$= 0.6404\sqrt{1-0.9587^2} = 0.1821$

Table C-7. Correlation Factors for Cyclic Creep Material – C-129Y/R-512E E. B. Weld Specimens

| Specimen Number | ① Area Before Coating | | ② $t_o$ | | ③ $t_i$ | | ④ $\sigma = \frac{P \times ②}{① \times ③}$ | | ⑤ Predicted $\epsilon$ | ⑥ Test $\epsilon$ | ⑦ R |
|---|---|---|---|---|---|---|---|---|---|---|---|
| | $in^2$ | $(mm^2)$ | inch | (mm) | inch | (mm) | psi | $MN/m^2$ | % | % | ⑥/⑤ |
| YSE-1 | 0.00686 | 4.426 | 0.0136 | 0.3454 | 0.01105 | 0.2807 | 1256 | 8.66 | 0.725 | 2.07 | 2.86 |
| YSE-2 | 0.00692 | 4.465 | 0.0137 | 0.3480 | 0.01105 | 0.2807 | 1254 | 8.65 | 0.725 | 2.16 | 2.98 |
| YSE-4 | 0.00708 | 4.568 | 0.0140 | 0.3556 | 0.01145 | 0.2654 | 777 | 5.36 | 0.350 | 1.32 | 3.77 |
| YSE-13 | 0.00686 | 4.426 | 0.0139 | 0.3531 | 0.01140 | 0.2896 | 1244 | 8.58 | 0.720 | 2.27 | 3.15 |
| YSE-14 | 0.00676 | 4.362 | 0.0137 | 0.3480 | 0.01120 | 0.2845 | 1267 | 8.74 | 0.740 | 2.56 | 3.46 |
| YSE-15 | 0.00679 | 4.381 | 0.0138 | 0.3505 | 0.01130 | 0.2870 | 1259 | 8.68 | 0.730 | 2.37 | 3.25 |
| YSE-16 | 0.00685 | 4.420 | 0.0139 | 0.3531 | 0.01140 | 0.2896 | 1246 | 8.59 | 0.720 | 2.17 | 3.01 |

$\bar{R} = \frac{\Sigma R}{R} = 3.2114$; standard deviation (S) = 0.3154

The regression line of R on $\sigma$ is given by $R = 4.797 - 0.00134\ (\sigma)$

Coefficient of correlation ($\nu$) = -0.7653

Therefore the standard error of estimate $= S\sqrt{1-\nu^2}$

$= 0.3154\sqrt{1-0.7653^2} = 0.203$

Plots of R ($\epsilon_{test}/\epsilon_{predicted}$) versus stress together with the linear regression line and plus and minus ($2\ S_{R\sigma}$) lines are shown in Figures C-20, C-21, and C-22. All of the test points plot within these bounds. It should be noted that in each case a single reduced load specimen is weighed as heavily as the grouped normal load data. Additional simulation tests at low stress levels would be desirable either to confirm or modify the results.

The given equations plus ($2\ S_{R\sigma}$) will be used to compute correction factors for cyclic creep prediction in subsequent phases of this program.

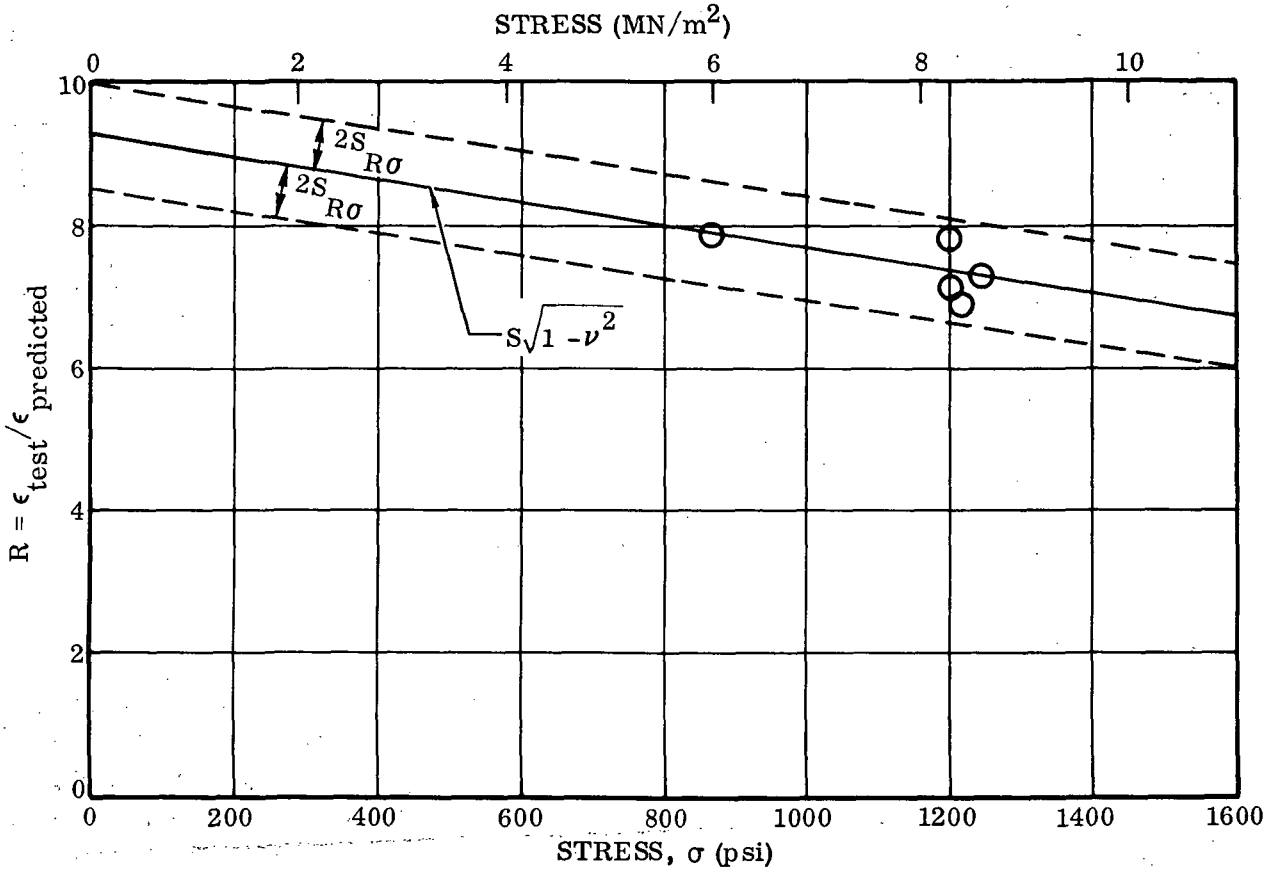


Figure C-20. Ratio $\epsilon_{test}/\epsilon_{predicted}$ Versus Stress for Cb-752/R-512E Parent Specimens

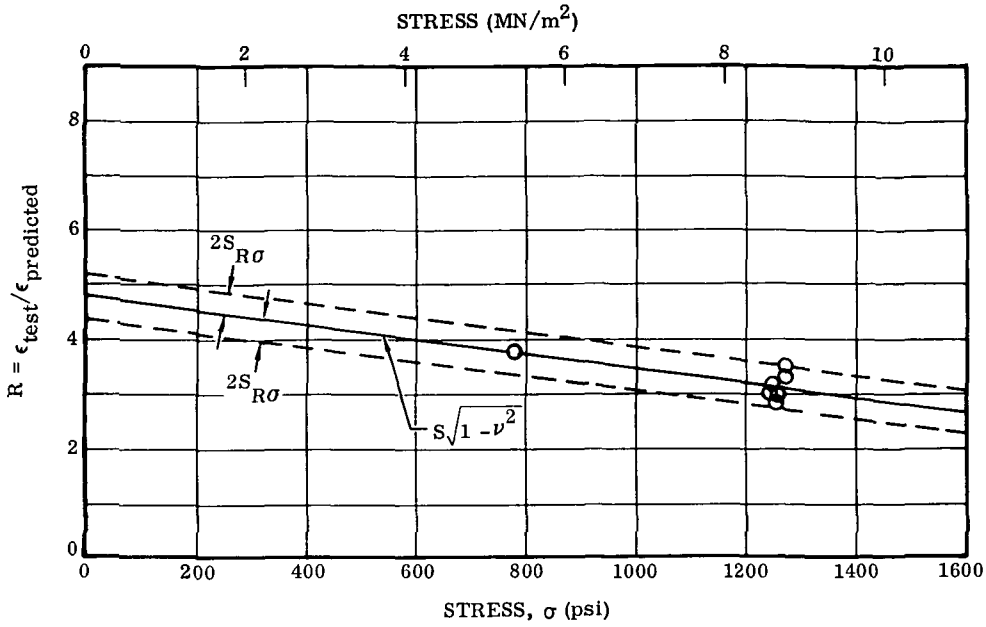


Figure C-21. Ratio $\epsilon_{test}/\epsilon_{predicted}$ Versus Stress for C-129Y/R-512E Electron Beam Weld Specimens

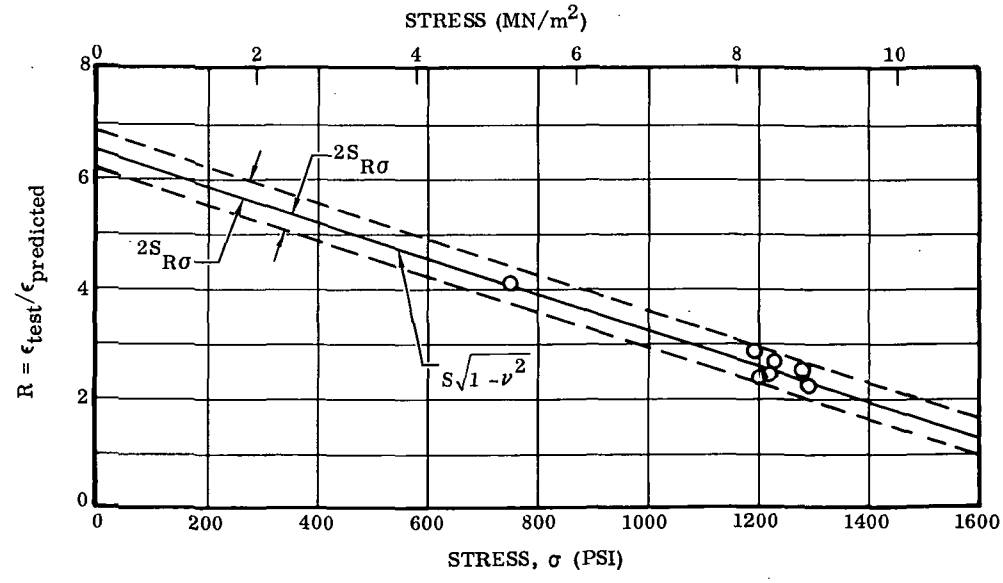


Figure C-22. Ratio $\epsilon_{test}/\epsilon_{predicted}$ Versus Stress for C-129Y/R-512E Parent Specimens

## REFERENCES


1. Stratham, C. L.; and Dupaquier, P. M.: Flight Environments, Aerothermal Loads and Dynamic Loads — Contract NAS 1-9793. North American Rockwell Internal Letter No. SSP/FT/70-265, revised Jan. 3, 1971.
2. Cole, J. N.; von Gierke, H. E.; et al.: Noise Radiation From Fourteen Types of Rockets in the 1,000 to 130,000 Pounds Thrust Range. WADC TR 57-354.
3. Franken, P. A.; and Kerwin, E. M.: Methods of Space Vehicle Noise Prediction. WADC TR 58-343, vol. II.
4. Getline, G. L.: Space Shuttle Booster Acoustic Environments. Convair Aerospace Division Report 76-549-4-151/AD-71-28, May 26, 1971.
5. Coe, C. F.; and Rechtien, R. D.: Scaling and Spatial Correlation of Surface Pressure Fluctuations in Separated Flow at Supersonic Mach Numbers. AIAA Structural Dynamics and Aeroelasticity Specialists Conference, New Orleans, Apr. 1969.
6. Ailman, C. N.: On Predicting Fluctuating Pressure at a Wall Beneath Turbulent Boundary Layer. NASA vol. 41, no. 6, June 1967, p. 1583.
7. Robertson, J. E.: Characteristics of the Static and Fluctuating Pressure Environments Induced by Three Dimensional Proturberances at Transonic Mach Numbers. Wiley Labs Report WR 69-3, June 1969.
8. Lowson, M. V.: Prediction of Boundary Layer Pressure Fluctuations. AFFDL-TR-67-167.
9. Bies, D. A.: A Review of Flight and Wind Tunnel Measurements of Boundary Layer Pressure Fluctuations and Inducted Structural Response. NASA CR-626.
10. Anon.: NASA/ARC 6 by 6 Wind Tunnel Data on Faget 1% Space Shuttle Model (Preliminary Data).
11. Anon.: Test No. 99 — NASA ARC 3.5 feet HWT. Aug. 1970.
12. Anon.: Test No. 509-NASA ARC 6 by 6 SSWT. Sept. 1970.
13. Palcheff, G. L.; and Gaumer, G. R.: Structural Thermal Protection System Criteria. Memo MRS-71 MDAC-East, Mar. 28, 1967.
14. Fitzgerald, B. G.; and Rusert, E. L.: Evaluation of the Fused Slurry Silicide Coating Considering Component Design and Reuse. AFML-TR-70-154, Dec. 1970.
15. Lewis, J. W.: Material Evaluation of a High Temperature Structural Test Component. Lockheed-California Company, Burbank, California, May 1968.
16. Black W. E.: Radiative Thermal Protection Systems Development for Maneuverable Reentry Spacecraft. Convair Division of General Dynamics Report GDC-ERR-1272, Feb. 1969.

17. Black, W.E.: Space Shuttle Vehicle High-Temperature Load-Carrying Structure and Radiative Thermal Protection Systems. Convair Division of General Dynamics Report GDC-ERR-1497, June 1970.
18. Gross, E.W.: Columbium Alloy Plate, Sheet and Strip-Specification for. General Dynamics Convair Division Specification 0.00947, Mar. 20, 1969.
19. Tavassoli, A.A.: Development of Columbium Alloy WC-3015, NASA TN MSFC-366, Mar. 1971.
20. Davis, J.W.; and Fitzgerald, B.G.: Fused Slurry Silicide Coatings for Columbium Alloy Reentry Heat Shields. Third Quarterly Technical Progress Narrative, McDonnell Douglas Astronautics Company — East, May 14, 1971.
21. Fischer, J.F.: Time-Temperature-Stress Profiles for Columbium Alloys Flight Simulation Testing. General Dynamics Convair Aerospace Division Memo SA-72-01, Jan. 1971.
22. Gerardi, S.J.: Coating and Processing of Columbium Panels for Space Shuttle Application — Contract NAS8-27280. Vac-Hyd Processing Corp. Report VHP-SDC-572, May 1972.
23. Priceman, S.; and Sama, L.: Protectiveness of Fused Silicide Coatings in Simulated Reentry Environments. *STR 67-5501.23, 13th Meeting of Refractory* Composites Working Group, Seattle, Washington, July 18-20, 1967.
24. Korb, L.J.; Beuyukian, C.S.; and Rowe, J.: The Design and Fabrication of Diffusion Bonded Columbium Panels for the Shuttle Heat Shield. National SAMPE Conference, Huntsville, Alabama, Oct. 5-7, 1971.
25. Anon.: Procedures for Evaluating Coated Refractory Metal Sheet. Report MAB-201-M, National Academy of Sciences — National Research Council (Material Advisory Board), Washington, D.C., Aug. 10, 1964.
26. Anon.: Tension Testing of Metallic Materials. ASTM Designation E8-69, ASTM Standards, Part 31, July 1970, p. 194.
27. Anon.: Standard Elevated Temperature Testing Procedures for Metallic Materials. ATC Report ARTC-13, Aerospace Research and Testing Committee, Aerospace Industries Association of America, Inc., Washington, D.C., July 1964.
28. Anon.: Verification and Classification of Extensometers. ASTM Designation E83-67, ASTM Standards, Part 31, July 1970, p. 351.
29. Wurst, J.; and Gerdeman, D.: Hot Bend Ductility of Columbium Base Alloys. Summary of the Eleventh Refractory Composites Working Group Meeting, AFML-TR-66-179, July 1966.
30. Bartlett, E.; and Allen, B.: Low Ductility at Intermediate Temperatures of Coated Columbium Alloys. Summary of the Twelfth Refractory Composites Working Group Meeting, AFML-TR-67-228, Aug. 1967.
31. Kerr, J.R.: Effect of Elevated Temperatures on Mechanical Properties of Fifteen Silicide Coating/Columbium Alloy Systems. GDC-ERR-AN-1217, Convair Division of General Dynamics Report GDC-ERR-AN-1217, Dec. 1967.

32. Kerr, J.R.: Evaluation of Nickel and Cobalt Base Superalloys and Silicide Coated Columbium Alloys for Use in Radiative Thermal Protection Systems, Convair Division of General Dynamics Report GDC-ERR-1345, Dec. 1968.
33. Metcalfe, A.G.; and Rose, F.K.: Advanced Methods for Testing Thin Gage Materials. AFML-TR-65-259, Nov. 1965.
34. Stephenson, R.L.: Creep Rupture Properties of C-129Y in Vacuum. J. Vacuum Sci. and Technology, vol. 7, no. 6, Nov./Dec. 1970.
35. Holloway, Jr., J.F.: Evaluation of Coated Columbium Alloys for Burner Applications. AFML-TR-71-127, Aug. 1971.
36. Stephenson, R.L.: The Creep Rupture Properties of Some Refractory Metal Alloys. J. Less-Common Metals, 15, 1968.
37. Stephenson, R.L.: Evaluation of the High Temperature Creep Properties of Refractory Metal Alloys in Vacuum. Trans. Vacuum Metallurgy Conference 1968, American Vacuum Society, New York, New York.
38. Anon.: Creep Properties of Cb-752/R-512E, NAR Lab Report LR9018, North American Rockwell unpublished data.
39. Fitzgerald, B.G.; and Rusert, E.L.: Evaluation of the Fused Silicide Coating Considering Component Design and Reuse. AFML-TR-70-154, Dec. 1970.
40. Culp, J.D.: Field Repair of Coated Columbium Thermal Protection Panels. McDonnell Douglas Astronautics Co. — East Report MDC E0456, Aug. 18, 1971.
41. DeLacy, T.J.: Spacecraft Heat Shield Testing Method. Convair Aerospace Division of General Dynamics Docket 6257, U.S. Patent applied for.
42. DeLacy, T.J.: The Use of Radioactive Labeling To Measure Reusability of Radiative Thermal Protection Systems Employing Coated Columbium. Convair Research Summary CRS-5, Convair Aerospace Division of General Dynamics, 1970.
43. Anon.: Material Properties for Columbium Alloy Cb-752 (Preliminary) Number 08.10.01.01, North American Rockwell Space Division, 1 October 1969.
44. Anon.: Material Properties for Columbium Alloy C-129Y (Preliminary) Number 08.11.01.01, North American Rockwell Space Division, 10 November 1969.
45. Favor, R. J.; Maykuth, D. J.; Bartlett, E. S.; and Mindlin, H.: Determination of Design Allowable Strength Properties of Elevated-Temperature Alloys, Part 1 — Coated Columbium Alloys. Contract NAS 8-26325, Battelle Columbus Laboratories, March 31, 1972.
46. Black, W. E.: Evaluation of Coated Columbium Alloy Heat Shields for Space Shuttle Application. Report 509-71L-12, Contract NAS 1-9793 Monthly Progress Report No. 4, Convair Aerospace Division of General Dynamics, February 1971.

GENERAL DYNAMICS

*Convair Aerospace Division*